Developing Optical Coatings for Laser Optics using Novel High Energy Ion Beam Sputter Deposition Technique

PhD Thesis

Chalisa Gier

PhD Student

Precision Measurement Research Group
Biomedical Engineering Department
University of Strathclyde, Glasgow

April 2024

This thesis is the result of the author's original research. It has been composed by the author and has not been previously submitted for examination which has led to the award of a degree.

The copyright of this thesis belongs to the author under the terms of the United Kingdom Copyright Acts as qualified by University of Strathclyde Regulation 3.50. Due acknowledgement must always be made of the use of any material contained in, or derived from, this thesis.

Signed: Chalisa Gier

Date: 04/04/2024

Abstract

This thesis outlines the fundamental aspects of various coating fabrication methods as well as the fundamentals of thin films and coatings that are typically studied and utilised to achieve high laser induced damage threshold (LIDT) properties. An overview of the two different novel high energy electron cyclotron resonance ion beam sputter deposition (ECR-IBSD) setups used to fabricate the coatings are described, along with the fundamental theory and setups of all the characterisation methods used for the films discussed. The materials of interest were hafnium oxide (HfO_2), scandium oxide (Sc_2O_3), and different mixture percentages of these two materials with silica (SiO_2). The effects of the reactive and sputtering oxygen partial pressures on the structure, stoichiometry, and optical properties of the HfO_2 and Sc_2O_3 thin films were systematically investigated. The amorphous structures of both films were determined using X-ray Diffraction. Energy-dispersive X-ray Spectroscopy and Rutherford Backscattering Spectrometry were carried out for the composition and stoichiometry analysis, which suggested the formation of over-stoichiometric films. The transmission and reflectance spectra of the films were measured using a spectrophotometer, where the spectra were analysed by an optical fitting software SCOUT, which utilises the model modified by O'Leary, Johnson and Lim, to extract the optical properties of the films. In addition to this study, by utilising a novel 24-beam ECR-IBSD system, mixed films of HfO_2:SiO_2 and Sc_2O_3:SiO_2 with different mixture percentages were investigated. The as-deposited mixed films were also found to possess an amorphous structure. The optical constants of the mixed films were extracted in the same manner as those of pure HfO_2 and Sc_2O_3 films. In addition to studying the films at as-deposited, the effects of post-deposition

heat treatment on the structure and optical properties of all the films were also investigated.

From this work, it was established that the influence of oxygen incorporation in pure materials from an optical and structural perspective shows that ECR-IBSD provides over-stoichiometric HfO_2 and Sc_2O_3 films. From the HfO_2 study, it was found that both the refractive index and extinction coefficient decreased with the increase of the oxygen content, whereas the bandgap energy increased. For Sc_2O_3 films, there was no real correlation with changing the oxygen content during deposition on the optical properties, except for the OJL bandgap energy, which increased as the oxygen percentage increased. The effects of annealing are as follows: the HfO_2 films remained amorphous after annealing to 500°C and became crystalline with a monoclinic structure after annealing to 700°C, whereas Sc_2O_3 films remained amorphous even after annealing to 900°C.

For mixed materials, this study focused on the influence of different mixture percentages on the optical, structural, and LIDT properties of the films. The mixture materials filled the values for the refractive index between the two pure materials, indicating that the refractive index can be tuned by changing the mixture percentage, which is the case for both HfO_2:SiO_2 and Sc_2O_3:SiO_2 mixed films. The same results were also found for both the extinction coefficient values and OJL bandgap energies of the mixed films, leading to the ability to easily fabricate films with tunable optical properties. The structure of the films in this study is as follows: in both cases, the films remained amorphous when heat treated up to 700°C. As the annealing temperature reached 900°C, the mixed films with less than 10% SiO_2 became more crystalline. In addition to the heat treatment study, LIDT testing was also carried out for these films, which provided unexpected results, where the main damage morphologies suggest that the main types of damage observed were absorption induced damage and pits due to inclusions. Laser damage is very sensitive to contamination within the nanosecond regime, and a large amount of discharge occurs inside the chamber during deposition, which leads to contamination of the films, which can lower the LIDT values.

For future studies, working towards different methods to mitigate the discharges during deposition is important, as this will provide a better understanding of the causes laser induced damage of the films fabricated by ECR within the nanosecond regime. Further discussion of future work and experiment utilising ECR-IBSD have also been presented in details.

Contents

Abstract **ii**

List of Figures **x**

List of Tables **xxiii**

Abbreviations **xxvi**

Acknowledgements **xxx**

Preface **xxxii**

1 Thin Film Optical Coatings **1**

1.1 Introduction to Thin Films 1

1.2 Thin Films Structure 2

1.3 Thin Film Mechanisms 3

1.4 Thin Film Structure Zone Model 5

1.5 Optical Coatings for Laser Optics 6

1.6 Previous Studies on High LIDT Materials 8
1.7 Damage Mechanisms of Optical Materials 15
2 Coating Development Techniques **24**
2.1 Introduction 24
2.2 Chemical Vapour Deposition Techniques 25
2.2.1 Thermal CVD 25
2.2.2 Plasma Enhanced CVD 25
2.2.3 Pulsed CVD 26
2.3 Physical Deposition Techniques 26
2.3.1 Pulsed Laser Deposition 26
2.3.2 Thermal Evaporation 27
2.3.3 Sputtering 29
3 Coating Characterisations **38**
3.1 Introduction 38
3.2 Optical Properties 38
3.2.1 Optical Transmittance and Reflectance 38
3.2.2 Refractive Index and Extinction Coefficient 40
3.2.3 Absorption and Absorption Coefficient 42
3.2.4 Bandgap Energy 44

3.3 Spectrophotometer . . . 48
3.4 SCOUT . . . 49
3.4.1 The OJL Model . . . 50
3.4.2 The Drude Model . . . 51
3.4.3 Harmonic Oscillator . . . 51
3.5 X-ray Powder Diffraction . . . 51
3.5.1 Bragg-Brentano Geometry . . . 53
3.5.2 Grazing-Incidence Geometry . . . 54
3.6 Energy Dispersive X-ray Spectroscopy . . . 55
3.7 Rutherford Backscattering Spectroscopy . . . 56
3.8 Post-deposition Heat Treatment . . . 56
3.9 Laser Induced Damage Threshold . . . 57
3.9.1 Fundamental . . . 57
3.9.2 LIDT Protocol . . . 58

4 Experimental Setup **60**

4.1 Introduction . . . 60
4.2 Substrate Cleaning Procedure . . . 60
4.3 System Setup . . . 61
4.3.1 600-System . . . 61

4.3.2 Combimat 63

4.3.3 Experimental Configuration 68

4.4 Characterisation Setup 78

4.4.1 Spectrophotometer 78

4.4.2 XRD Setup 79

4.4.3 EDS Setup 80

4.4.4 RBS Setup 80

4.4.5 LIDT Setup 81

4.4.6 Post-deposition Heat Treatment 82

5 Hafnium Oxide **84**

5.1 Introduction 84

5.2 As-Deposited HfO_2 Films 86

5.2.1 Results 86

5.2.2 Discussion 102

5.3 Effects of Annealing on HfO_2 Films 108

5.3.1 Results 109

5.3.2 Discussion 127

5.4 Conclusion 131

6 Scandium Oxide **134**

6.1 Introduction 134

6.2 As-Deposited Sc_2O_3 Films 137

6.2.1 Results and Discussion 137

6.3 Effects of Annealing on Sc_2O_3 Films 147

6.3.1 Results and Discussion 147

6.4 Conclusion 158

7 Hafnia Silica Mixture **160**

7.1 Introduction 160

7.2 As-Deposited HfO_2:SiO_2 Films 162

7.2.1 Results and Discussion 162

7.3 Effects of Annealing on HfO_2:SiO_2 Films 180

7.3.1 Results and Discussion 181

7.4 Conclusion 193

8 Scandia Silica Mixture **196**

8.1 Introduction 196

8.2 As-Deposited Sc_2O_3:SiO_2 Films 197

8.2.1 Results and Discussion 198

8.3 Effects of Annealing on Sc_2O_3:SiO_2 Films 212

8.3.1 Results and Discussion 213

8.4 Conclusion 226

9 Conclusion **229**

Bibliography **234**

List of Publications and Conferences **263**

List of Figures

1.1 Schematic illustration of the different structures thin films can be organised once fabricated, where (a) crystalline, (b) polycrystalline and (c) amorphous . . . 3

1.2 Schematic illustration of the three basic modes of thin film growth, where (a) Volmer-Weber, or island growth, (b) Frank-Van der Merwe, or layer-by-layer growth, and (c) Stranski-Krastanov, or island and layer growth [1]. 4

1.3 A schematic diagram of the structure zone model, representing the effects of substrate temperature and argon discharge gas pressure on the structure of metal films (deposited by magnetron sputtering). This image is extracted from [2], where the author has extracted this from Thornton [3] (Copyright 1974, American Vacuum Society). . . . 5

1.4 Single-shot LIDT at 1030 nm and pulse duration of 500 fs as a function of the optical bandgap energy. Each point corresponded to a different sample. Figure extracted from [4]. . . . 10

1.5 Single-shot LIDT at 1030 nm and 500 fs pulse as a function of the refractive index. Each point corresponds to a different sample. Figure extracted from [4]. . . . 10

1.6 The high and low refractive index materials from 10 different damage competitions. The figures were extracted from [5]. . . . 12

1.7 Intrinsic LIDT values of mixture thin films tested with single shot 1030 nm, 500 fs pulse duration. Each point corresponds to a different sample, with different mixture percentages. Both figures extracted from [4]. . . . 13

1.8 Single shot (or 1-on-1) LIDT at 1030 nm as a function of (a) Scandium fraction in the films, and (b) the optical bandgap. The films were deposited by reactive deposition from a metal target. Both figures are extracted from [6]. 14

1.9 Different laser induced processes and mechanisms that may arise as a function of the pulse duration. Image extracted from [7]. 15

1.10 Examples of thermal damages on optical coatings due to laser irradiation. The images are examples of the following: (a) and (b) delamination [8,9], (c) absorption induced [8], (d) melting [10], (e) recrystallisation [10], and (f) stress due to absorption [10]. The scales for (a) and (b) are not displayed as they were not provided by the source. 16

1.11 (a) - (c) shows examples of craters within the damage sites due to inclusions on the thin films. The images have been extracted from Ristau *et al.* for (a) [8], LIDARIS for (b) [9] and Laseroptik for (c) [10]. The scale for (b) is not displayed as it was not provided by the source. 18

1.12 Examples of femtosecond laser induced damages on thin films. (a) is an example of melting and ablation, extracted from [9], and (b) is an example of ablation, extracted from [11]. The scale for (a) is not displayed as this was not provided by the source. 19

1.13 A schematic diagram of (a) One photon ionisation, (b) Multiphoton ionisation, (c) Tunnel ionisation and (d) Avalanche ionisation, which are examples of non-linear effects that can occur due to laser irradiation. The figures are reproduced from [12–15]. 21

1.14 Schematic diagram of defect's layers on the optics, reproduced from [9]. 22

1.15 Example of bulk damage, extracted from [9]. The scale is not displayed as it was not provided by the source. 23

2.1 A schematic diagram of E-beam Evaporation reproduced from [16]. . . . 28

2.2 A schematic diagram of Molecular Beam Epitaxy reproduced from [17]. 28

2.3 A schematic diagram of Magnetron Sputtering reproduced from [18,19]. 30

2.4 A schematic diagram of (a) IBSD and (b) DIBSD reproduced from [20,21]. 32

2.5 A schematic diagram of different types of ion sources reproduced from [20]. 33

2.6 Schematic diagram of the electron and ion orbits, where **E** = 0, based on the Right-Hand rule, where the magnetic field **B** is travelling upwards through the paper. 35

2.7 Images of ECR sources used in this study. 37

3.1 Schematic diagram of bandgap transitions, where: (a) direct allowed, (b) direct forbidden, (c) indirect allowed and (d) indirect forbidden transitions [22, 23] 45

3.2 Density of states in the OJL band gap model [24, 25] 46

3.3 Schematic diagram of a single beam spectrophotometer, reproduced from [26] 49

3.4 Schematic diagram of electron shell distribution, showing K_α X-ray being produced, reproduced from [27, 28] 52

3.5 Schematic illustration of Bragg condition and Bragg's law 53

3.6 Schematic illustration of Bragg-Brentano Geometry, reproduced from [29] 54

3.7 Schematic illustration of Grazing-Incidence Geometry, reproduced from [29] 55

3.8 Different locations where there can be damages on an optics due to the laser irradiation. The different types of damage morphologies are shown in the figure. This figure has been extracted from LIDARIS [9]. 58

4.1 Schematic and photographed images of the custom-built ECR-IBSD system used. The figures also contain numbered labels for each of the components that were described in the text, along with labels in the schematic diagram of all the important components. 63

4.2 Schematic and photographed images of the Combimat system. The figures also contain numbered labels for each of the components that were described in the text, along with labels in the schematic diagram of all the important components. Again, this system utilises ECR ion sources, where the Combimat has a total of 24 ion sources. 64

4.3 Schematic (a,b) and photographed (c) images of the Combimat system. The figures contain numbered labels for each of the components that were described in the text, along with labels in the schematic diagram of all the important components. 66

4.4 A schematic diagram showing the electrical feed-through for the different components in the chamber, as well as the mass flow controllers for the gases used during the deposition. #6a is the high frequency feed-through for the individual sources, #8 and #9 is the sputtering and reactive gas mass flow controller, respectively. 67

4.5 A schematic diagram of the combimat's sputtering process. The schematic is showing one source and one target for simplicity. 68

4.6 A schematic of IBSD process, outlining the geometric factors which can contribute to differing sputter plume distributions (ion incidence angle (α), polar emission angle (β) and scattering angle (γ)). The schematic has been reproduced from [20]. 71

4.7 The target set-up for the HfO_2:SiO_2 coatings, where the white targets are HfO_2 and the clear targtes are SiO_2. 75

4.8 The target set-up for the Sc_2O_3:SiO_2 coatings, where the white targets are Sc_2O_3 and the clear targtes are SiO_2. 77

4.9 Photon RT UV-VIS-IR Spectrophotometer, where (b) is showing the setup for transmittance, and (c) is showing the setup for reflectance. The number labels are as follow: (1) Light source, (2) Detector, and (3) Substrate holder. 79

4.10 XRD system used within this project. The setup shown is for the BB-XRD method, where a collimator is used. 80

4.11 The schematics diagram of the S-on-1 LIDT setup provided by RhySearch [30] 82

4.12 The Carbolite Furnace for annealing samples 83

5.1 The transmittance and reflectance data obtained for the three configurations by utilising the Photon RT, where the data for blank substrate has been included. 88

5.2 Example of Experimental and Fitted data from SCOUT for one of the samples discussed in this chapter. 90

5.3 The refractive index of all three configurations. 92

5.4 The extinction coefficient of all three configurations. 94

5.5 The average bandgap energy of the films acquired from SCOUT for all three configurations. The error bars show the standard deviation of five separate fittings for each sample. 95

5.6 The average thicknesses of the films acquired from SCOUT for all three configurations. 96

5.7 EDS data for configurations (i) and (ii), where configuration (iii) and 0% Oxygen Background samples were not measured. 100

5.8 RBS data acquired for the films discussed in this chapter. The data was measured by M. Chicoine. 101

5.9 XRD data acquired for the as-deposited films in this study, by utilising the Bragg-Brentano method. (*) denotes the peaks that are emerging for the annealed sample, in comparison to the as-deposited samples. 102

5.10 Transmittance and reflectance data of as-deposited, 500°C and 700°C annealed samples from configuration (i) 110

5.11 Transmittance and reflectance data of as-deposited, 500°C and 700°C annealed samples from configuration (ii). 112

5.12 Transmittance and reflectance data of as-deposited, 500°C and 700°C annealed samples from configuration (iii). 113

5.13 The refractive index of all three configurations. 115

5.14 The extinction coefficient of all three configurations. 118

5.15 The average bandgap energy of the films acquired from SCOUT for all three configurations at As-deposited (black), 500°C (red) and 700°C (green). The error bars show the standard deviation of five separate fittings for each sample. 120

5.16 The average thickness of the films acquired from SCOUT for all three configurations at As-deposited (black), 500°C (red) and 700°C (green). The error bars show the standard deviation of five separate fittings for each sample. 122

5.17 BB-XRD data acquired for the 500°C films within this study. 124

5.18 BB-XRD data acquired for the 700°C films within this study. 125

5.19 GIXRD data acquired for the 500°C films within this study. 126

5.20 GIXRD data acquired for the 700°C films within this study. 127

6.1 Transmittance and reflectance data for as-deposited Sc_2O_3 138

6.2 The refractive index of all films in the study with differing oxygen percentages. 140

6.3 The extinction coefficient of all films in the study with differing oxygen percentages. 141

6.4 The average bandgap energy of the films acquired from SCOUT. The error bars show the standard deviation of five separate fittings for each sample. 142

6.5 The average thicknesses of the films acquired from SCOUT. The error bars show the standard deviation of five separate fittings for each sample. 144

6.6 RBS data acquired for the films discussed in this chapter. The data was measured by M. Chicoine. 145

6.7 XRD data acquired for the as-deposited films in this study, by utilising the GIXRD method. 146

6.8 Transmittance and reflectance data of as-deposited, 500°C, 700°C, and 900°C annealed samples. 148

6.9 The refractive index at λ = 1064 nm for as-deposited (black), 500°C (red), 700°C (green) and 900°C (blue) annealed temperature. The error bars show the standard deviation of five separate fittings for each sample. 150

6.10 The extinction coefficient at λ = 1064 nm for as-deposited (black), 500°C (red), 700°C (green) and 900°C (blue) annealed temperature. The error bars show the standard deviation of five separate fittings for each sample. 151

6.11 The average bandgap energy of the films acquired from SCOUT at as-deposited (black), 500°C (red), 700°C (green) and 900°C (blue) annealed temperature. The error bars show the standard deviation of five separate fittings for each sample. 152

6.12 The average thickness of the films acquired from SCOUT at as-deposited (black), 500°C (red), 700°C (green) and 900°C (blue) annealed temperature. The error bars show the standard deviation of five separate fittings for each sample. 154

6.13 GIXRD data acquired for the annealed films within this study. 156

7.1 Transmittance and Reflectance data for as-deposited HfO_2:SiO_2 samples with different mixture percentages. 163

7.2 Dispersion of the refractive index for the range of λ = 200 - 2500 nm of the films with different mixture percentages 165

7.3 The refractive index at λ = 1064 nm of the films with different mixture percentages. The error bars show the standard deviation of five separate fittings for each sample. 166

7.4 Dispersion of the extinction coefficient for the range of λ = 200 - 2500 nm. Y-axis displays the extinction coefficient on a logarithmic scale. . . 167

7.5 The extinction coefficient at λ = 1064 nm. The error bars show the standard deviation of five separate fittings for each sample. 168

7.6 The average bandgap energy of the films acquired from SCOUT. The error bars show the standard deviation of five separate fittings for each sample. 169

7.7 The average thicknesses of the films acquired from SCOUT. The error bars show the standard deviation of five separate fittings for each sample. 170

7.8 Different EMA models and its refractive index at different volume fraction of HfO_2 172

7.9 XRD data acquired for the as-deposited films in this study, by utilising the GIXRD method. 173

7.10 Example of Damage Probability Curves based on the ISO-standards for pure thin films studied in this chapter. The damage occurrence corresponds to a value of 100% and when no damage appears the fluence sites is designated at 0%. 175

7.11 LIDT values for all the films studied in this chapter as a function of the refractive index and bandgap energy. 176

7.12 Observed damage sites for pure HfO_2 film with (a) low and (b) high fluence. 178

7.13 Observed damage sites for HfO_2(92%):SiO_2(8%) film with (a) low and (b) high fluence. 178

7.14 Observed damage sites for the HfO_2(80%):SiO_2(20%) film with (a) low and (b) high fluence. 179

7.15 Observed damage sites for the HfO_2(41%):SiO_2(59%) film with (a) low and (b) high fluence. 179

7.16 Observed damage sites for the pure SiO_2 film with (a) low and (b) high fluence. 179

7.17 Transmittance and reflectance of annealed spectra for some of the samples investigated in this chapter. Three different samples are shown: pure HfO_2, pure SiO_2 and one of the mixed materials (HfO_2(41%):SiO_2(59%)). 182

7.18 The refractive index at $\lambda = 1064$ nm. The error bars show the standard deviation of five separate fittings for each sample. 184

7.19 The extinction coefficient at $\lambda = 1064$ nm. The error bars show the standard deviation of five separate fittings for each sample. 185

7.20 The average bandgap energy of the films acquired from SCOUT. The error bars show the standard deviation of five separate fittings for each sample. 186

7.21 The average thicknesses of the films acquired from SCOUT. The error bars show the standard deviation of five separate fittings for each sample. 187

7.22 GIXRD data acquired for the annealed films within this study. 188

7.23 LIDT vs HfO_2 percentage for both as-deposited and annealed films . . . 190

7.24 Cracks observed on the films due to annealing. 191

7.25 Observed damage sites for annealed pure HfO_2 film with (a) low and (b) high fluence. 192

7.26 Observed damage sites for annealed HfO_2(92%):SiO_2(8%) film with (a) low and (b) high fluence. 192

7.27 Observed damage sites for the annealed pure SiO_2 film with (a) low and (b) high fluence. 192

8.1 Transmittance and reflectance data for as-deposited 198

8.2 Dispersion of the refractive index for the range of λ = 200 - 2500 nm . . 200

8.3 The refractive index at λ = 1064 nm. The error bars show the standard deviation of five separate fittings for each sample. 200

8.4 Dispersion of the extinction coefficient for the range of λ = 200 - 2500 nm for the different mixed percentages. Y-axis displays the extinction coefficient on a logarithmic scale. 201

8.5 The extinction coefficient at λ = 1064 nm for the different mixed percentages. The error bars show the standard deviation of five separate fittings for each sample. 202

8.6 The average bandgap energy of the films acquired from SCOUT. The error bars show the standard deviation of five separate fittings for each sample. 203

8.7 The average thicknesses of the films acquired from SCOUT. The error bars show the standard deviation of five separate fittings for each sample. 204

8.8 Different EMA models and its refractive index at different volume fraction of Sc_2O_3 206

8.9 XRD data acquired for the as-deposited films in this study, by utilising the GIXRD method. 207

8.10 Damage probability curve for pure Sc_2O_3 film 208

8.11 LIDT values for all the films studied in this chapter as a function of the refractive index and bandgap energy. 209

8.12 Observed damage sites for pure Sc_2O_3 film with (a) low and (b) high fluence. 210

8.13 Observed damage sites for Sc_2O_3(94%):SiO_2(6%) film with (a) low and (b) high fluence. 210

8.14 Observed damage sites for the Sc_2O_3(78%):SiO_2(22%) film with (a) low and (b) high fluence. 211

8.15 Observed damage sites for the Sc_2O_3(52%):SiO_2(48%) film with (a) low and (b) high fluence. 211

8.17 Transmittance and Reflectance of annealed spectra for some of the samples investigated in this chapter. The samples shown are pure Sc_2O_3 and Sc_2O_3(52%):SiO_2(48%). 214

8.18 The refractive index at $\lambda = 1064$ nm. The error bars show the standard deviation of five separate fittings for each sample. 216

8.19 The extinction coefficient at $\lambda = 1064$ nm. The error bars show the standard deviation of five separate fittings for each sample. 217

8.20 The average bandgap energy of the films acquired from SCOUT. The error bars show the standard deviation of five separate fittings for each sample. 218

8.21 The average thicknesses of the films acquired from SCOUT. The error bars show the standard deviation of five separate fittings for each sample. 219

8.22 GIXRD data acquired for the annealed films within this study. 220

8.23 The LIDT values for all the films studied in this chapter (a) and (b) annealed at 480°C, (c) for both as-deposited and annealed films. 222

8.24 Cracks observed on the films due to annealing. 223

8.25 Observed damage sites for annealed pure Sc_2O_3 film with (a) low and (b) high fluence. 224

8.26 Observed damage sites for annealed Sc_2O_3(94%):SiO_2(6%) film with (a) low and (b) high fluence. 224

List of Tables

4.1 The gases configurations through the ion sources, neutraliser and background for all 3 setup that were carried out in this experiment 69

4.2 The gases configurations through the ion sources, neutraliser and background for this experiment 73

4.3 The number of targets that are being sputtered by the ion sources for differing percentages 74

4.4 The number of targets that were sputtered for each run 76

5.1 The different thicknesses of HfO_2 thin films with different configurations 97

5.2 The different thicknesses of HfO_2 thin films with different configurations at 500°C and 700°C annealed temperatures 123

6.1 The different thicknesses of Sc_2O_3 thin films with different oxygen concentrations 144

6.2 The different thicknesses of Sc_2O_3 thin films with different configurations at 500°C, 700°C and 900°C annealed temperatures 155

7.1 The different bandgap energies of HfO_2:SiO_2 thin films with different HfO_2 volume percentages. 169

7.2 The different thicknesses of HfO_2:SiO_2 thin films with different HfO_2 volume mixture percentages 171

7.3 Different EMA models for HfO_2 volume fraction in the mixed coatings studied in this chapter. 173

7.4 The different refractive indices of HfO_2:SiO_2 thin films with different mixture concentration at as-deposited, 500°C, 700°C and 900°C annealed temperatures. 184

8.1 The different bandgap energies of Sc_2O_3:SiO_2 thin films with different Sc_2O_3 volume percentages. 203

8.2 The different thicknesses of Sc_2O_3:SiO_2 thin films with different Sc_2O_3 volume percentages. 205

8.3 Different EMA models for Sc_2O_3 volume fraction in the mixed coatings studied in this chapter. 206

8.4 The different refractive indices of Sc_2O_3:SiO_2 thin films with different mixture concentration at as-deposited, 500°C, 700°C and 900°C annealed temperatures. 216

Abbreviations

A – Absorption

Al_2O_3 – Aluminium Oxide/Alumina

ALD – Atomic Layer Deposition

AlF_3 – Aluminium Fluoride

AMRL – Advanced Materials Research Laboratories

AR – Anti-Reflective

Ar – Argon

BB – Bragg-Brentano

CRD - Cavity Ring Down

Cu – Copper

CVD – Chemical Vapour Deposition

d – Thickness

DC – Direct Current

DIBS – Dual Ion Beam Sputtering

DIBSD – Dual Ion Beam Sputter Deposition

E-beam – Electron Beam

E_c – Conduction Band

ECR – Electron Cyclotron Resonance

EDS (or EDX) – Energy Dispersive X-ray Spectroscopy

EFI – Electric Field Intensity

E_{gap} – Bandgap Energy

EMA – Effective Medium Approximation

$\boldsymbol{E_\mathrm{v}}$ – Valence Band

FM – Frank-Van der Merwe

GIXRD – Grazing Incidence X-ray Powder Diffraction

H – Hydrogen

He – Helium

Hf – Hafnium

HfO_2 – Hafnium Oxide/Hafnia

HfO_2:SiO_2 – Hafnia-Silica

HIPIMS – High-power Impulse Magnetron Sputtering

HPPMS – High-power Pulsed Magnetron Sputtering

HPRS – High Pressure Reactive Sputtering

HR – Highly Reflective

IAD – Ion Assisted Deposition

IBD – Ion Beam Deposition

IBS – Ion Beam Sputtering

IBSD – Ion Beam Sputter Deposition

ICDD – International Centre for Diffraction Data

IR – Infrared

ISO – International Standard Organisation

JCPDS – Joint Committee on Powder Diffraction Standards

$\boldsymbol{k}$ – Extinction Coefficient

KKR – Kramers-Kronig Relation

LEDs – Light-emitting Diodes

LID – Laser Induced Damage

LIDT – Laser Induced Damage Threshold

LRO – Long Range Order

MBE – Molecular Beam Epitaxy

MgF_2 – Magnesium Fluoride

$\boldsymbol{n}$ – Refractive Index

Nb_2O_5 – Niobium Oxide

Nd:YAG - Neodymium-doped Yttrium Aluminium Garnet

O (or O_2) – Oxygen

OJL – O'Leary, Johnson and Lim

PCI - Photothermal Common-path Interferometry

PDF – Powder Diffraction File

PECVD – Plasma Enhanced Chemical Vapour Deposition

PLD – Pulsed Laser Deposition

ppm - Parts per million

PVD – Physical Vapour Deposition

R – Reflectance

RBS – Rutherford Backscattering Spectroscopy

RF – Radio Frequency

RLVIP – Reactive Low Voltage Ion Plating

RT – Room Temperature

Sc – Scandium

Sc_2O_3 – Scandium Oxide/Scandia

Sc_2O_3:SiO_2 – Scandia-Silica

SEM – Scanning Electron Microscope

SiO_2 – Silica/Silicon Dioxide

SK – Stranski-Krastanov

SMA – SubMiniature version A

SRO – Short Range Order

T – Transmittance

Ta_2O_3 – Tantalum Oxide/Tantala

TiO_2 – Titanium Dioxide/Titania

UHV – Ultra High Vacuum

UM – Unbalanced Magnetron

UV – Ultraviolet

VIS-NIR – Visible to Near Infrared

VM – Volmer-Weber

XRD – X-ray Powder Diffraction

Y_2O_3 – Yttrium Oxide/Yttria

ZrO_2 – Zirconium Dioxide/Zirconia

Acknowledgements

First, I would like to thank my supervisor, Professor Stuart Reid, for providing me with the opportunity to complete my PhD in his group. Without Prof. Reid's guidance, encouragement, and support, this experience would have been unachievable. I would like to thank him for his patience in correcting my paper and thesis, as well as answering all the silly questions I have had for him over the years. I have been very lucky to have a supervisor who has cared so much about my PhD.

I would also like to thank my second supervisor, Professor Alan Kemp, for his support, encouragement, and understanding in helping me to succeed in my studies. I would like to thank Prof. Kemp for the recommendation of different studies that would be beneficial and relevant to my PhD.

I would like to express my deepest gratitude to Dr. Marwa Ben Yaala for her additional support, extensive knowledge, insight, and guidance over the years, for being someone that I can bounce my ideas and steer me towards the right path. This has allowed me to grow as a researcher and being able to guide my own PhD to its end, and for this, I am indebted to you.

I would also like to acknowledge Dr. Kieran Craig for his additional support in my research. His extensive knowledge, insight, wisdom, and invaluable constructive criticism helped me complete my PhD efficiently.

I would like to thank my former and current group members for the good atmosphere, the support we have provided for each other, and all the discussions we have had

throughout the years. Thank you Dr. Imogen Birney, Dr. Svetoslava Angelova, Sean MacFoy, Callum Wiseman, Dr. Gavin Wallace, Dr. Mariana Fazio, and Steven Armstrong for making this PhD a positive experience.

I would like to extend my gratitude to Gooch and Housego for their support, especially Dr. Peter MacKay and his direct support of the work that was carried out. I would like to thank him for his time in discussing my project with me and offering advice on different aspects of the project.

I would like to recognise Dr. Maider Olasolo at AMRL (University of Strathclyde) for her assistance in setting up XRD and EDS measurements, along with Dr. Martin Chicoine and Professor François Schiettekatte for their assistance in carrying out the RBS measurements at the University of Montreal.

Finally, I would like to express my deepest appreciation to my parents, my siblings, and my partner throughout my academic journey. Words cannot express my gratitude to my mother and my best friend, Phuangpen Buachum. Your love and support in everything that I do has made me who I am today, and I would like to say thank you for always believing in me and pushing me to be the best version of myself. I would also like to take this opportunity to thank my stepfather, John Bannerman, for not only being my father figure but also for supporting and encouraging me every step of the way, and thank you for accepting me into your family with open arms. I am also extremely grateful for having a partner like Axel Ngoy, who understands the pressure of academia, always supports me in completing my PhD, and is always around to keep me grounded and cheer me up whenever I have a difficult day. Last but certainly not least, I would like to thank my cat, Cruise, for his quiet and comforting presence during my late-night writing sessions and for keeping me entertained during these times.

Preface

This thesis is a record of research carried out on optical coatings deposited using novel high energy ion beam sputter deposition technique, known as electron cyclotron resonance technology. This study was conducted between October 2018 and October 2023. The main focus of these coatings is to yield a high laser damage threshold. This research was mainly conducted at the University of Strathclyde, with the exception of LIDT testing and RBS measurements.

In Chapter 1, an introduction to thin films is provided, along with the film structure and mechanisms. Then, an introduction to optical coatings that are typically used for laser optics is described, along with a literature review of previous studies by other authors on high laser induced damage threshold materials, which give way to the materials studied in this thesis. Finally, typical laser damage mechanisms of optical materials are shown and described, along with the causes and examples of the damage that can be seen.

In Chapter 2, the different coating development techniques are presented and described. Particular attention was given to ion beam sputter deposition and the novel high energy electron cyclotron resonance ion sources used in this research.

In Chapter 3, different coating characterisation techniques that have been used in this research are described. This chapter presents a comprehensive overview of the various techniques used in this study and their operational principles.

In Chapter 4, the experimental setup is described. First, the substrate cleaning procedure before the coating fabrication is described. This was followed by the setup of

the two ECR-IBSD systems used to fabricate the coatings in this research. Then, the experimental configuration of each fabricated optical coating material (HfO_2, Sc_2O_3, and mixed materials) is described. Finally, the setup and configuration of each characterisation method are described. All characterisation techniques were carried out and analysed by the author, with the exception of LIDT testing and RBS measurements, which were carried out by RhySearch and M. Chicoine at the University of Montreal, respectively.

In Chapter 5, research on HfO_2 optical coatings produced by the author is presented and discussed. All spectrophotometry measurements and SCOUT fittings were performed by the author at the University of Strathclyde. The RBS measurements were performed by M. Chicoine at the University of Montreal. EDS and XRD measurements and analysis were carried out by the author at the Advanced Materials Research Laboratories within the University of Strathclyde, with the assistance of Dr. M. Olasolo with the system setup for measurement. The effects of the heat treatment on the films were also investigated and discussed.

In Chapter 6, research on Sc_2O_3 optical coatings produced by the author is presented and discussed. All spectrophotometry measurements and SCOUT fittings were performed by the author at the University of Strathclyde. The RBS measurements were performed by M. Chicoine at the University of Montreal. EDS and XRD measurements and analysis were carried out by the author at the Advanced Materials Research Laboratories within the University of Strathclyde, with the assistance of Dr. M. Olasolo with the system setup for measurement. The effects of the heat treatment on the films were also investigated and discussed.

In Chapter 7, research on HfO_2:SiO_2 mixed films produced by the author is presented and discussed. All spectrophotometry measurements and SCOUT fittings were conducted by the author at the University of Strathclyde. LIDT measurements were carried out by RhySearch. XRD measurements and analysis were carried out by the author at the Advanced Materials Research Laboratories at the University of Strathclyde with the assistance of Dr. M. Olasolo with the system setup for measurement. The effects

of heat treatment on the films were also carried out and discussed.

In Chapter 8, research on Sc_2O_3:SiO_2 mixed films produced by the author is presented and discussed. All spectrophotometry measurements and SCOUT fittings were conducted by the author at the University of Strathclyde. LIDT measurements were carried out by RhySearch. XRD measurements and analysis were carried out by the author at the Advanced Materials Research Laboratories at the University of Strathclyde with the assistance of Dr. M. Olasolo with the system setup for measurement. The effects of heat treatment on the films were also carried out and discussed.

The list of publications includes a list of published works and contributions from the author of this thesis:

1. The author has contributed to the fabrication of the co-sputtered Ta_2O_5:ZrO_2 thin films used in this paper by utilising the ECR-IBSD, along with a review and editing of the ECR-IBSD sections [31].

2. The author of this thesis is the first author of this paper, and the results are described in this thesis. Contribution includes conceptualisation, methodology which includes the fabrication of the HfO_2 thin films, characterisation and analysis, writing of the first original draft, and review and editing [32].

Please note that the author is also part of the LIGO Scientific Collaboration; however, those publications are not listed here.

1 Thin Film Optical Coatings

1.1 Introduction to Thin Films

Thin film materials are fabricated using different deposition or growth methods, which are divided into two categories: Physical Vapour Deposition (PVD) and Chemical Vapour Deposition (CVD), which are further discussed in Chapter 2. These different deposition methods provide different characteristics and structural properties for each thin film, such as amorphous, polycrystalline, crystalline, or even mixed phases [33]. There are a variety of thin films based on the structure such as amorphous, crystalline, polycrystalline, nanocomposite, multilayer, and superlattice structures. In contrast to thick films, which can be created through methods such as screen printing, thin films are formed by the deposition of atoms, ions, and molecules from gaseous or liquid phases [33]. Thin films can be used in a wide range of fields and industries, including semiconductor electronics, LEDs, integrated circuits, optical coatings, pharmaceuticals, and medicine, for example, where the properties of the films can be manipulated to be used for the application needed.

The main focus is the fabrication and characterisation of optical coatings, where the main application is focused on laser optics for different fields, for example: medical (optical systems for surgical instruments, fluorescence microscopy, dentistry, eye surgery, optical tweezers [34–37]), astronomy [38–40], biotechnology [35], defence (optical-based imaging, communications [41]), energy (fusion, energy mining [34, 42]), quantum technology [43], and sensing (distance sensing, chemical detection [44]). An optical coating

can be described as one or more layers (or combinations) of thin films deposited on an optical component (i.e. lens, mirror, or prism), where they are used to enhance the transmission, reflection, or polarisation properties of light through the optical component. Optical coatings can be used in various ways, depending on their application; for example, they can be designed to be used as anti-reflective (AR) coatings, where the reflection is reduced to less than 0.1%; highly reflective (HR) coatings, where the reflectivity is more than 99.9%; designed to enhance the polarisation properties of an optical component, that is, s- or p-polarised, or a combination of both; or optical filters, which selectively transmit or reflect light at certain wavelength range through the addition of interference coatings, with Dichroic filter being commonly used in optical systems [7]. An optical coating can be designed to have a combination of thin layers of materials (i.e. oxides or metals), and the performance of the coating is dependent on the number of layers, individual thicknesses, and refractive indices of the layers [7]. Typically, to design these multilayer optical coatings, one would have to study the properties of individual single layers that are of interest in order to design a full stack of optical layers that fits the original purpose of the optical component.

1.2 Thin Films Structure

In thin film coatings, three typical atomic structures can be produced: crystalline, amorphous, and polycrystalline. For crystalline materials, the atoms are arranged in a regular pattern, which repeats over long-range, in three dimensional order, or both short- and long-range for polycrystalline materials [45].

Amorphous materials lack long range order (LRO) in crystalline materials, but the short range order (SRO) still exists, where the atoms are arranged in a random pattern [46]. However, this random pattern can be described in many forms including topological, substitutional, and vibrational disorders [47, 48]. Topological disorder is the type that is used to describe amorphous materials, as it has no LRO and there are various degrees depending on the SRO a structure may have [49].

For polycrystalline materials, the structure can be described as having several crystalline grains, where they are randomly orientated in different parts of the lattice [49]. Hence, with this structure, there is also a lack of LRO. Figure 1.1 below shows the differences between the three structures.

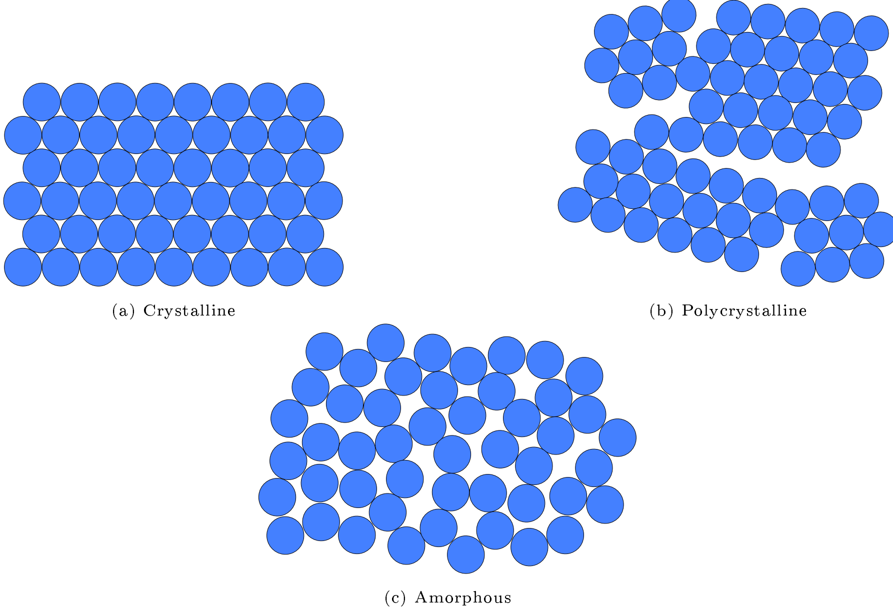

Figure 1.1: Schematic illustration of the different structures thin films can be organised once fabricated, where (a) crystalline, (b) polycrystalline and (c) amorphous

1.3 Thin Film Mechanisms

Thin film growth typically has three modes, which are briefly described below and are known as: Volmer-Weber (VM), Frank-Van der Merwe (FM), and Stranski-Krastanov (SK) modes.

The Volmer-Weber (VM) mode occurs as island growth when the cohesion between the atoms of the target material is greater than the adhesion between the target atoms and substrate. In turn, adatoms are more bound to each other than to the substrate, forming clusters or islands [50–53].

Frank-Van der Merwe (FM) mode is a layer-by-layer growth, which occurs when the adhesion between the adatoms and the substrate are greater than that of the adatom-adatom interactions. This method is the preferred method for producing smooth films because of layer-by-layer growth [50, 52–54].

Both layer and island growth modes occur in the Stranski–Krastanov (SK) mode. In the SK mode, islands are formed after a few monolayers are formed on the surface of the substrates. This transition from layer to island growth occurs at a critical layer thickness, which is highly dependent on chemical and physical properties, such as the surface energies of the substrate and film [50–54].

In Figure 1.2, three possible thin film formations are shown, where each of the three scenarios can be observed during the formation. Hence, these three methods complement each other.

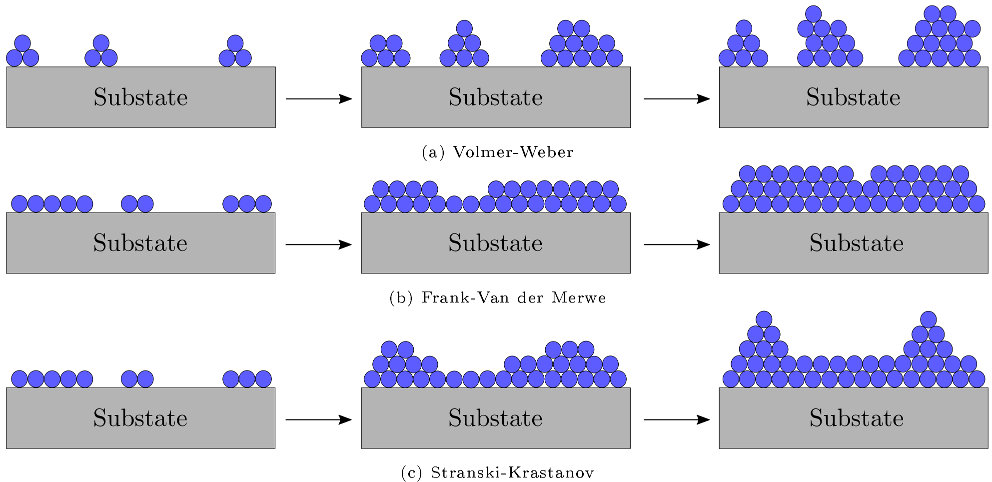

Figure 1.2: Schematic illustration of the three basic modes of thin film growth, where (a) Volmer-Weber, or island growth, (b) Frank-Van der Merwe, or layer-by-layer growth, and (c) Stranski-Krastanov, or island and layer growth [1].

1.4 Thin Film Structure Zone Model

As discussed previously, the growth and properties of thin films depend on several factors. These include the film material, substrate and its temperature, background pressure, and the energy and flux of the film forming particles [20,55–57]. Typically, thin films deposited by PVD at room temperature can achieve amorphous or polycrystalline structures [20, 58].

Movchan and Demchishin [59] when first characterised the structure of evaporation deposited coatings, realised that there are three different structure zones as a function of $\frac{T}{T_\mathrm{m}}$, where T is the substrate temperature and T_m is the bulk melting temperature of the film material [52, 60]. Later, Thornton [3, 61, 62] developed a zone diagram for sputtering deposited thin films, where it describes the correlation between the film's morphology and the process parameters, and taking into account the effect of sputtering gas by adding an additional zone, Zone T. The structure zone model is illustrated in Figure 1.3.

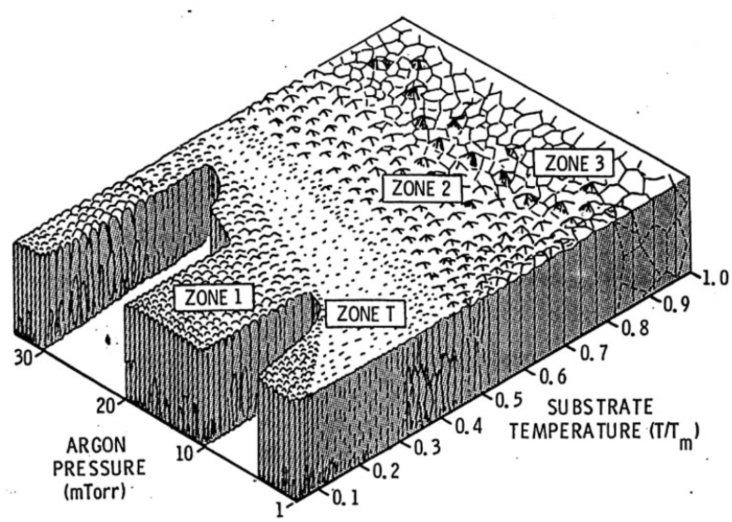

Figure 1.3: A schematic diagram of the structure zone model, representing the effects of substrate temperature and argon discharge gas pressure on the structure of metal films (deposited by magnetron sputtering). This image is extracted from [2], where the author has extracted this from Thornton [3] (Copyright 1974, American Vacuum Society).

In Zone 1, the film's structure is open-voided tapered fibrous structure. This is because of the low-angle incidence of the particles as a result of the collision between the sputtered and gas particles during the transportation of the sputtered material particles to the substrate. Another reason for this structure is due to the limited diffusion of adatoms on the substrate surface, which results from the low substrate temperature, where this also leads to the material structure to be amorphous [2, 57].

For Zone T, the film texture is now wider columns with flat surfaces, due to the interaction between the thermally enhanced surface diffusion filling the space between the columns, and the bombardment of the energetic particles leads to the flattening of the column surface [2, 57]. At this stage, the material structures remained amorphous.

In Zone 2, the thermal surface and grain boundary adatom diffusion increases with the increase of substrate temperature, where the columns are widened and the spaces between the columns are reduced. The material structure in this zone have increased in crystallinity, and many properties of the film are comparable to those of bulk materials [2, 57].

Lastly, in Zone 3, the spaces between the column boundaries are narrowed and internal thermal crystallisation of the columns occurs, where bulk diffusion is dominant in the final structure of the material, leading to highly crystallised internal structures [2,57,60].

1.5 Optical Coatings for Laser Optics

HR mirrors are crucial components in any laser system and play a critical role in laser operation and performance. In an optical cavity, light is amplified by repeatedly reflecting between two mirrors, where one of these is the HR mirror. HR mirrors also provide the necessary feedback mechanism for stimulated emission to occur, facilitate mode selection, and ensure efficient light amplification within the optical cavity. Their contribution is essential for the overall functioning and performance of laser systems. Hence, optical coatings that are utilised in laser optics are of interest in this study.

Laser optics are designed for use in many different laser applications and systems. Laser optics typically uses a specific substrate, coating, or both to provide a specific performance for a certain wavelength of the laser. Many laser optics require low absorption and high laser damage threshold coatings to avoid damage to the optical component, which can lead to the failure of laser systems. Several factors can affect the damage threshold of the thin film used in laser optics, including the substrate and its roughness, the deposition process and parameters, and the target materials used during deposition.

The substrate used plays an important role in providing a stable base where the films are grown, and the grinding and polishing marks on the substrates can also influence the uniformity and roughness of the thin films. These defects can lead to a decrease in laser damage resistance owing to subsurface impurities that are trapped in the polishing marks [63–66].

The deposition process used to fabricate thin films also has a large effect on the physical and chemical properties of the films, which in turn affects the laser damage threshold of the thin films and optics. As previously mentioned, there are two categories of deposition processes, where CVD processes tend to leave behind organic contaminants in the films, which compromises the films for high laser fluence applications; hence, PVD processes are typically preferred [63]. Most high damage threshold optics that have been reported are created by utilising PVD process, where electron beam (E-beam) evaporation has been the preferred process for high fluence applications [63]. However, E-beam evaporated films provide a porous thin film, which leads to higher posibilities of contaminants that can fill the surface voids, and these films typically have lower refractive indices compared to their bulk forms. With undesirable properties associated with the porous structure, denser films are often sought after. Ion assisted deposition (IAD) can be utilised in an E-beam process by adding a plasma source to the system to overcome the porosity of the coating. The use of IAD can provide a denser coating because of the bombardment of ions on the coated surface [55, 56]. Another method to fabricate denser coatings is by utilising ion beam sputter deposition (IBSD, further discussed in Chapter 2) to fabricate thin films, which provides characteristics

that are desirable in laser damage resistant films. IBSD is a high energy process which can fabricate amorphous thin films with properties close to those of bulk, with high density, high refractive indices, and less porous structure. Coatings fabricated by IBSD can exhibit high laser damage threshold which provides evidence that this technique is promising for creating thin films required for laser optics in high-power laser systems [63].

However, while different groups acquired different values of the measured laser induced damage threshold (LIDT) based on different coating fabrication methods, it has been found that the damage typically can be found in the high index material of a coating stack of laser optics [63, 67]. With HR and AR coatings being the common designs of laser optics coatings, any improvements that can be carried out for the high index materials of these stacks are highly sought after [63]. This leads to the investigation of fabricating thin film optical coatings by utilising IBSD technique within this project to obtain a high LIDT by manipulating the different deposition parameters, as well as investigating mixture materials to be utilised as the high index material within a multilayer stack.

1.6 Previous Studies on High LIDT Materials

As mentioned previously, the laser damage resistance of optical components is the main concern for most high power laser systems, where optical coatings are typically the first source of failure for laser optics. With numerous methods that can be explored and utilised to fabricate coatings, as well as to carry out LIDT testing, it is often challenging to select which materials are suitable for use in the design of laser optics.

Many groups have confirmed that high index materials in a multilayer stack are the main cause of failure in the LIDT testing of optical coatings, where dielectric coatings are typically used. Several factors must be considered for these dielectric thin films, including the optical, thermal, mechanical, and electronic properties that can affect the

laser damage resistance upon laser exposure, where these properties are also dependent on the deposition conditions. The choice of material can influence the LIDT of optics through its refractive index and bandgap energy values. This is because the refractive index can modify the electric field intensity values and distribution, as well as the spectral response. The materials typically used in high power laser systems are oxides and fluorides [5].

Several groups have reported a linear dependency between the intrinsic LIDT and the optical bandgap energy for different materials [4, 68–71], as well as the refractive index. This is due to the linear dependency on the bandgap energy and the refractive index that have been found [4].

Gallais *et al.* [4] have reported an extensive study of optical thin films which have been fabricated by different methods, where they have been characterised and damage tested in similar conditions. The study was carried out at 1030 nm for a pulse duration of 500 fs for single layers of oxide, fluoride, and mixture of materials. For pure oxides, a linear dependence of the LIDT on the bandgap value has been observed in IBSD oxide films, and this has been further discussed by Mero *et al.* [69]. There is a very low dispersion of results which is important because the films have been fabricated by different deposition techniques, where the samples have very different intrinsic and physical properties, such as the band structure, density of defect states, thermal properties, density, and adherence of the films, which can cause the laser damage. Gallais *et al.* suggests that the linear behaviour can be explained by taking into account the physical process involved in the ionisation processes and their dependency with the bandgap (i.e. photoionisation or impact ionisation). The intrinsic LIDT, or internal LIDT, vs. bandgap energy is shown in Figure 1.4, which was extracted from [4]. The materials that have been studied are: AlF_3, Al_2O_3, HfO_2, MgF_2, Nb_2O_5, Sc_2O_3, SiO_2, Ta_2O_3, TiO_2, Y_2O_3 and ZrO_2. The different methods of fabrication include electron beam evaporation (with and without ion assistance), IBSD, and magnetron sputtering, which are further described in Chapter 2.

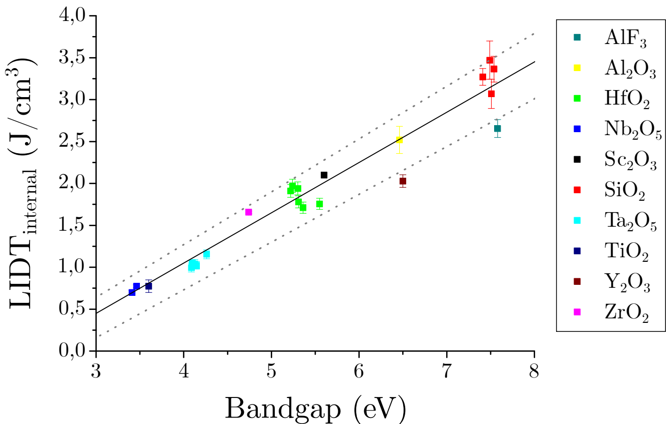

Figure 1.4: Single-shot LIDT at 1030 nm and pulse duration of 500 fs as a function of the optical bandgap energy. Each point corresponded to a different sample. Figure extracted from [4].

As mentioned, the relationship between the bandgap energy and refractive index exhibits linear behaviour, leading to an observed linear tendency between the LIDT and refractive index, as shown below in Figure 1.5 [4].

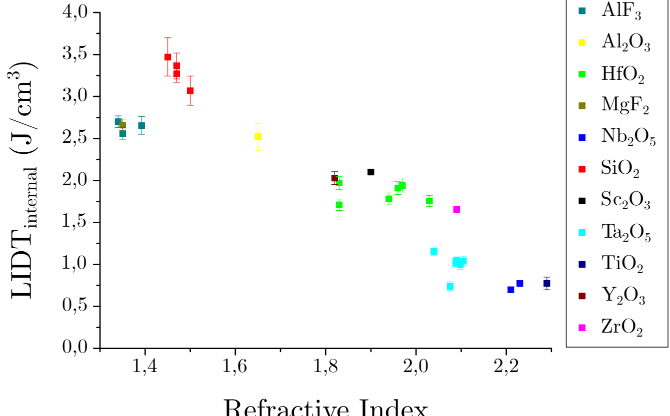

Figure 1.5: Single-shot LIDT at 1030 nm and 500 fs pulse as a function of the refractive index. Each point corresponds to a different sample. Figure extracted from [4].

For oxide materials, the dispersion of the results shown is related to the dependency on the refractive index, where this is dependent on the density and optical bandgap [4]. Both the density and optical bandgap are also dependent on the manufacturing process, which is an important consideration in the fabrication of oxide layers for laser optics.

Gallais *et al.*, with agreement from other authors, showed that HfO_2 is one of the most attractive high index materials for multilayer coatings for laser applications. Another material that provides high LIDT for high refractive index layer is Sc_2O_3, both of which are of interest and have been investigated in this project. For low index materials, SiO_2 exhibits the highest LIDT value [4]. Thus, SiO_2 is typically used as a low index material in laser optic multilayer stacks.

Stolz [5] presented at the *Optical Interference Coating* conference (2019) the findings of the trends observed during the last ten years in the thin film laser damage competition, where the best pair of low and high refractive index materials are consisted of SiO_2/HfO_2 pairs, within the picosecond regime. This pair of thin film coatings remains the preferred pair of materials in the design of multilayer dielectric optics which are used in high power laser systems and have been widely studied by many researchers [38, 72–76]. Figure 1.6(a) shows the high refractive index material that has been tested within the competition from the years 2008-2017, and Figure 1.6(b) shows the low refractive index materials that have been submitted for the damage competitions, where one can see that SiO_2 is the most common material used.

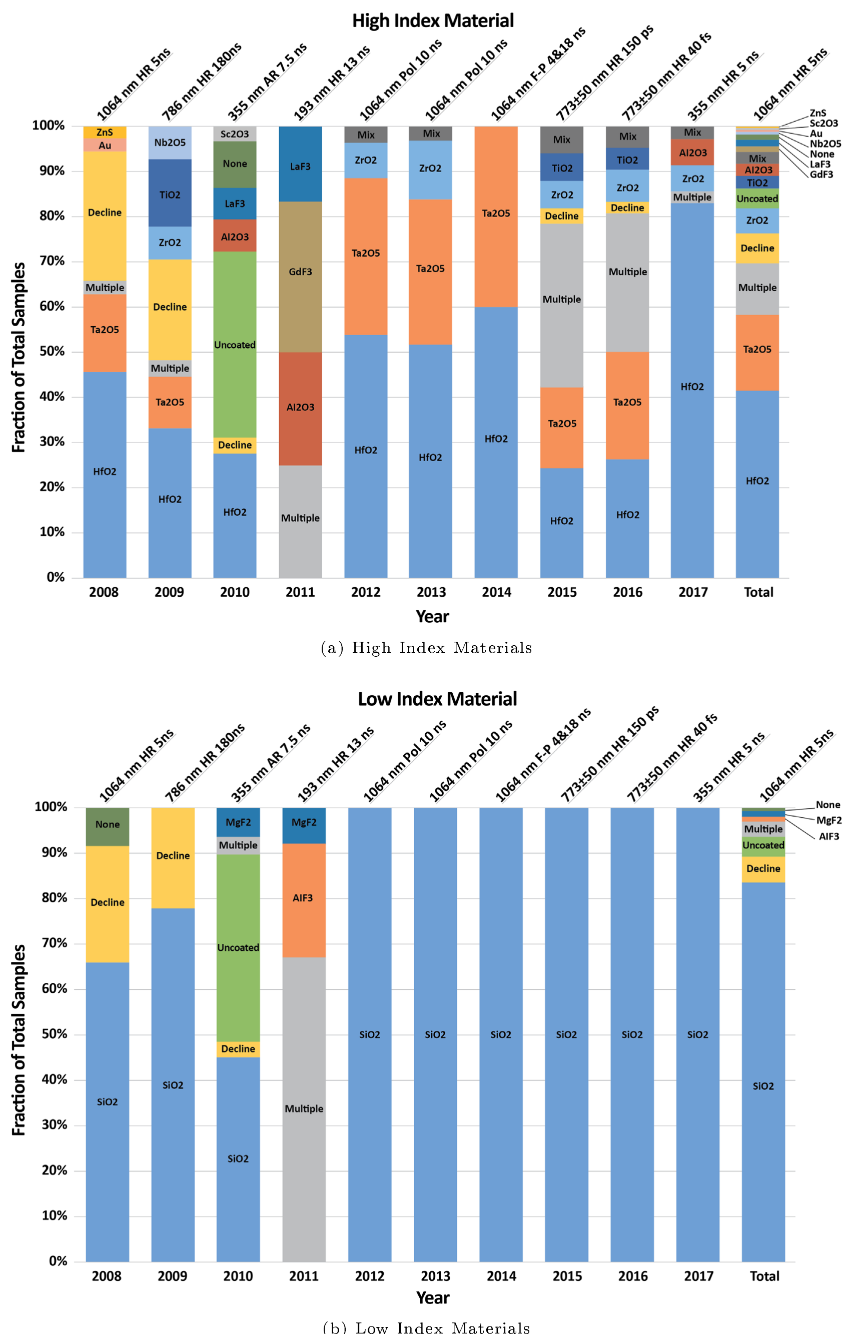

(a) High Index Materials

(b) Low Index Materials

Figure 1.6: The high and low refractive index materials from 10 different damage competitions. The figures were extracted from [5].

For mixture materials, also investigated and reported by Gallais *et al.* [4], the films were fabricated by IBSD technique, where the pure materials were placed side-by-side and the targets were moved to acquire the desired percentage of the mixture. By

mixing different materials, this leads to the possibility to tune the optical constants, microstructural properties and reduce the roughness and/or residual stress [4, 77]. By optimising the electric field distribution by using mixture materials, this can lead to the improvement of LIDT of the multilayer compared to utilising pure oxide materials only [4, 78]. Figure 1.7 below shows the mixture materials versus the bandgap energy and refractive index. The mixtures that were investigated are as follows: AlF_3-Al_2O_3, Al_2O_3-SiO_2, HfO_2-SiO_2, Nb_2O_5-SiO_2, Sc_2O_3-SiO_2, Ta_2O_5-SiO_2, and ZrO_2-SiO_2.

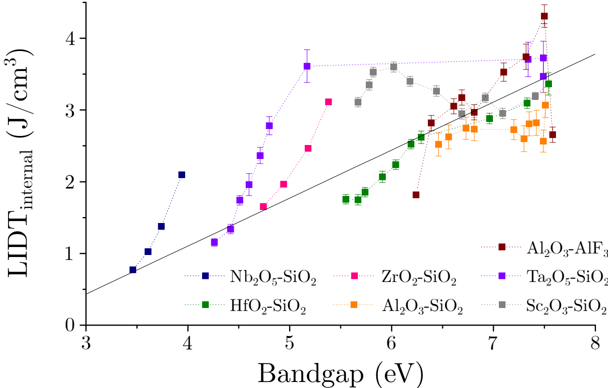

(a) LIDT as a function of bandgap energy. The black solid line corresponds to the pure material bandgap energy trend.

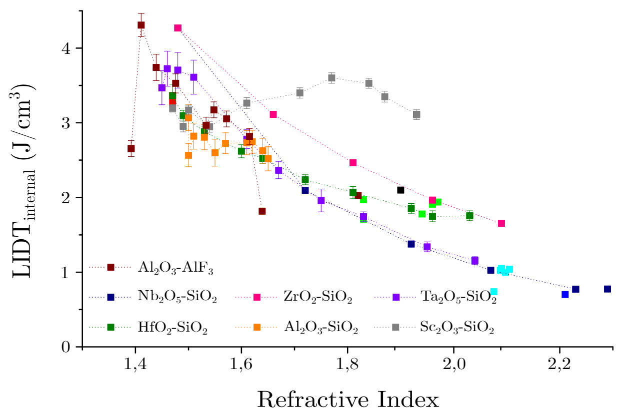

(b) LIDT as a function of refractive index

Figure 1.7: Intrinsic LIDT values of mixture thin films tested with single shot 1030 nm, 500 fs pulse duration. Each point corresponds to a different sample, with different mixture percentages. Both figures extracted from [4].

From this study, the authors have found that the Sc_2O_3-SiO_2 mixture is of interest

because it has a relatively high damage threshold compared to other mixture materials that have been studied. This material is said to be an interesting choice for high index material to produce the coatings for the optics for high power laser systems [4]. Mende *et al.* [6] have also carried out the study of varying the mixture percentages of Sc_2O_3-SiO_2 films. From this study, it was found that the mixture with 75% Sc_2O_3 and 25% SiO_2 yielded the highest LIDT value, which was also higher than the values obtained for pure materials (Figure 1.8). These studies show that mixture materials are an interesting concept to investigate for the use of laser optics; hence, they were also investigated in this study.

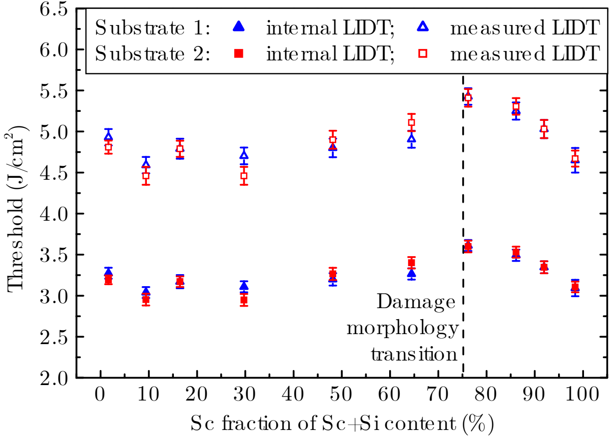

(a) Measured and intrinsic LIDT as a function of Sc fraction in the films.

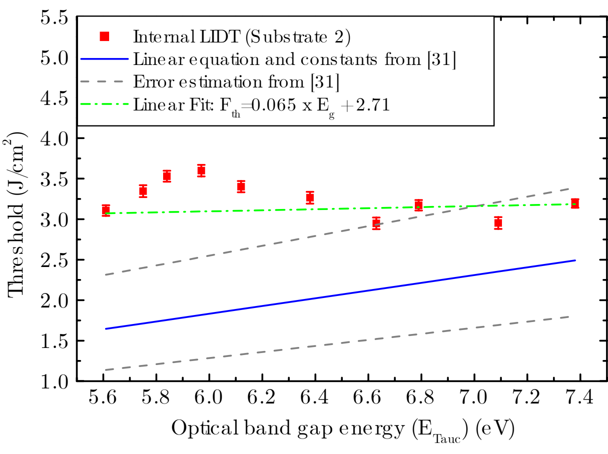

(b) Intrinsic LIDT as a function of the optical bandgap energy.

Figure 1.8: Single shot (or 1-on-1) LIDT at 1030 nm as a function of (a) Scandium fraction in the films, and (b) the optical bandgap. The films were deposited by reactive deposition from a metal target. Both figures are extracted from [6].

1.7 Damage Mechanisms of Optical Materials

Many types of defects can alter the LIDT values of a laser optic, where defects can exist in the substrate or thin films. The presence of these defects creates an intensification of light, which leads to laser damage at the defect location and can propagate further, thereby degrading the film [68]. Once the damage is initiated, further exposure of the site to the laser will allow the damage site to become larger.

The first point of focus in the discussion of the damage mechanism is that for optical materials, the pulse duration of the laser beam during LIDT testing has a large impact on which mechanism leads to damage [12]. Figure 1.9 below shows the dependence of various laser induced damage mechanisms and processes that may occur after laser irradiation on the pulse duration, extracted from [7]. The main damage mechanisms are strongly dependent on the optics material and thin films, including their optical properties, thermal conduction, absorption, and defects.

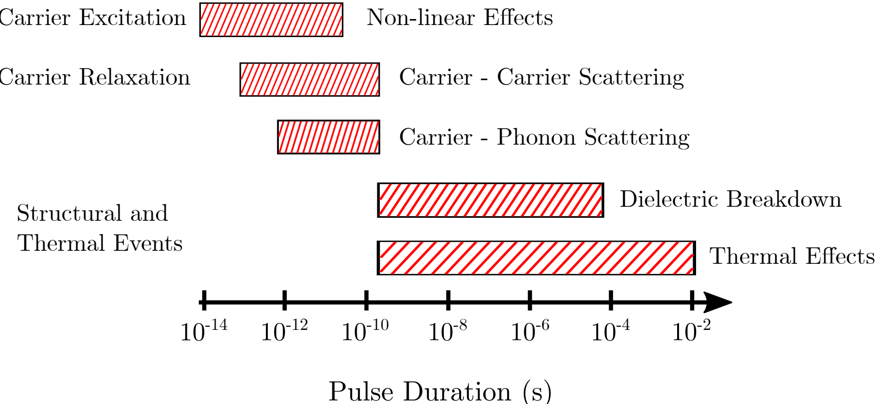

Figure 1.9: Different laser induced processes and mechanisms that may arise as a function of the pulse duration. Image extracted from [7].

For long pulses, where the time duration is longer than the relaxation time of the irradiated material, is typically in the microsecond to nanosecond regime. In this case, laser damage is typically linked to thermal effects, shock waves, or dielectric breakdown. The films absorb light through free electrons that were excited by the first photons.

These damages are based on heating the films until melting, material expansion, or modification of the optic and film has occur. In many cases within this regime, the laser induced damage can be attributed to an excess of thermal energy and the film absorbing the laser radiation, leading to catastrophic failure by mechanical disruption [8]. This can also be attributed to the increase in mechanical stress in the coating from the thermal expansion of the materials due to the laser heating of the coating; at a certain thermal stress level, the coating can crack or delaminate from the optic. In another case, absorption is the main cause of damage, where the film reaches the melting point before delamination occurs, and the film structure changes (the film becomes more crystalline). With this type of damage mechanism, the damage to the films is usually shown as discolouration or an increase in surface roughness [8]. Below are some examples of these damages extracted from [8–10].

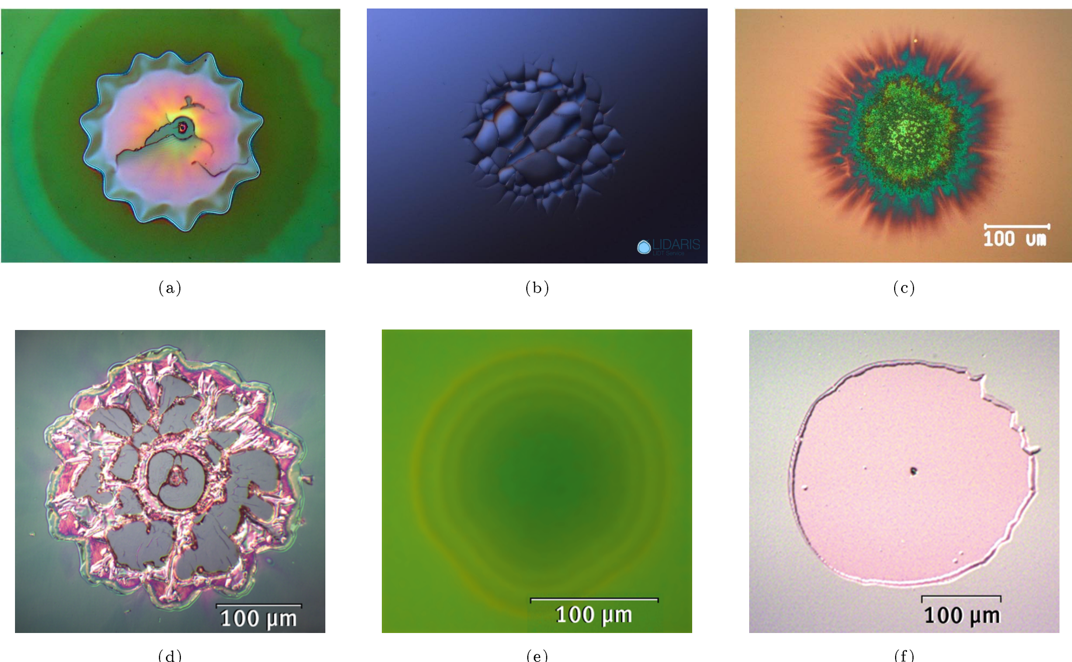

Figure 1.10: Examples of thermal damages on optical coatings due to laser irradiation. The images are examples of the following: (a) and (b) delamination [8,9], (c) absorption induced [8], (d) melting [10], (e) recrystallisation [10], and (f) stress due to absorption [10]. The scales for (a) and (b) are not displayed as they were not provided by the source.

Laser damage within the nanosecond regime is also due to defects, such as particles, nodules, or structural defects. With these defects, they can be absorbers which induce thermal defects, i.e. melting or evaporation of the films or mechanical failure, or they can also lead to light intensification that causes further damage to the material than the top layer of the films [68]. When there are inclusions in the films within the crystals of the transparent material, this can be either dust or metal inclusions from the targets or the system walls. When the inclusion is small (10 – 0.1 µm), they will absorb the laser radiation and causes stress to build up between the absorbing inclusion and the crystals due to the thermal expansion of the inclusion - which can lead to craters within the damage sites [79, 80], as shown in Figure 1.11 below [8–10]. These types of defect-induced damages are the most commonly observed mechanism and have been studied exhaustively [10,80–82], where a deposition process that can reduce the inclusion defects is sought after. The geometry and orientation of the inclusions are also important for the damage threshold, where several groups have modelled a sphere, plate, and rod shaped inclusions, where it was found that the plate and rod shaped inclusions failed at lower laser fluences than the sphere [79, 82, 83].

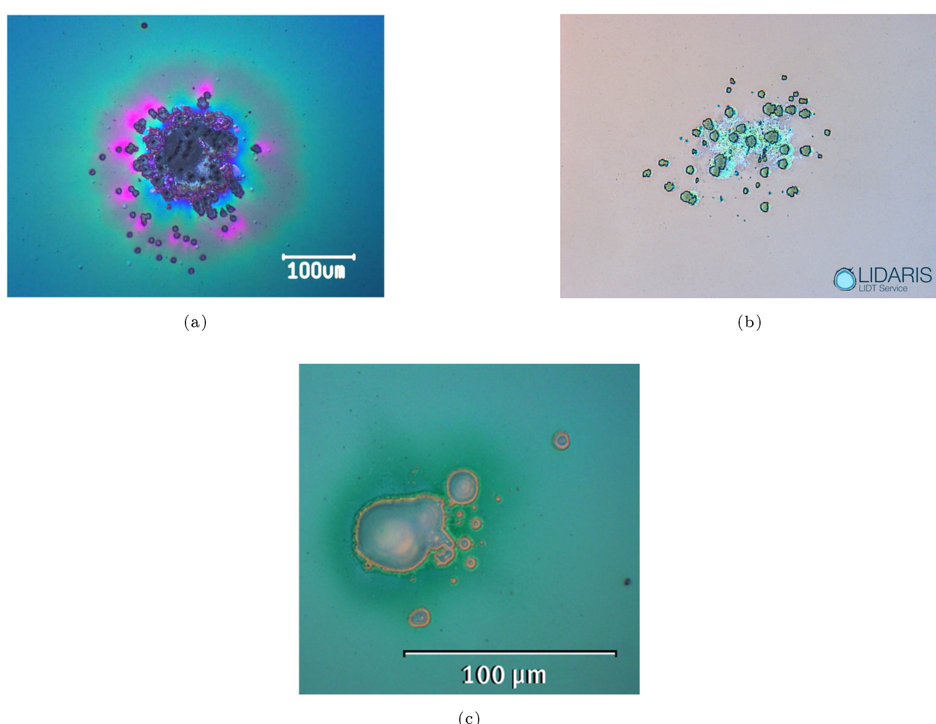

(a) (b) (c)

Figure 1.11: (a) - (c) shows examples of craters within the damage sites due to inclusions on the thin films. The images have been extracted from Ristau *et al.* for (a) [8], LIDARIS for (b) [9] and Laseroptik for (c) [10]. The scale for (b) is not displayed as it was not provided by the source.

This thermal damage mechanism discussed should also be considered for short pulse lasers, where the films cannot cool down in between the pulses. The crack damages due to thermal absorption can be observed differently depending on the laser pulse length. For example, at very long pulses (microsecond), melting of the films are most common, whereas at very short pulses (femtosecond), ablation is often witnessed [83].

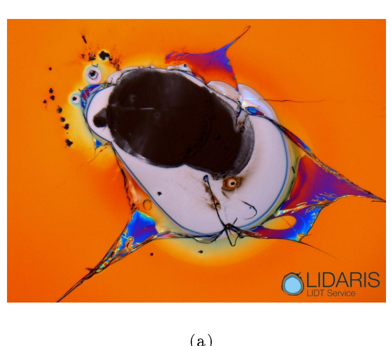

(a)

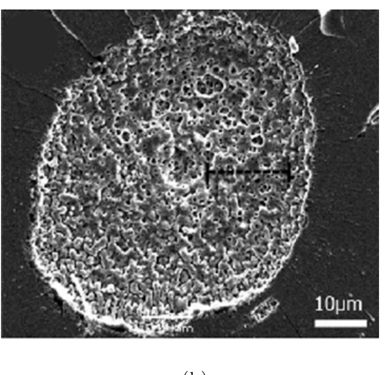

(b)

Figure 1.12: Examples of femtosecond laser induced damages on thin films. (a) is an example of melting and ablation, extracted from [9], and (b) is an example of ablation, extracted from [11]. The scale for (a) is not displayed as this was not provided by the source.

Dielectric breakdown occurs in dielectric materials under the influence of strong electric fields, where this can lead to either avalanche or multiphoton phenomena. Typically, avalanche ionisation happens at the pulse lengths of $10^{-10} - 10^{-13}$ s, and multiphoton absorption occurs at pulse lengths lower than 10^{-13} s [79, 80]. At short nanosecond pulses, thermal effects are less likely to occur, and dielectric breakdown occurs due to the little time for the heat to diffuse in between pulses, and there is less energy needed to be deposited in order to induce the dielectric breakdown [7, 84]. Once this breakdown begins, plasma formation and the associated ablation mechanisms can occur. With slightly longer pulses than the nanosecond regime, the combination of thermal and dielectric breakdown damage mechanisms can be observed [7]. However, for ultrashort pulses of around 10 picoseconds or less, the thermal damage mechanism are negligible [85]. In this case, non-linear effects can occur, including multiphoton ionisation, tunnel ionisation, and avalanche ionisation [7, 86].

For short pulses, the heat conduction time significantly exceeds the pulse duration, where this is typically in the order of picosecond or shorter [68, 87]. At this range, the LIDT of optics are mostly due to the material limitations rather than the presence of defects [68, 88], and a linear scaling between the LIDT and the electric field intensity (EFI) enhancement has been reported [68, 88–90]. With this knowledge, it can be used as a model to calculate the measured LIDT as the product of the intrinsic properties of

the films (also known as the intrinsic LIDT) and the maximum EFI.

Within the short pulse regimes, laser induced processes may occur as follows: the electron excitation from ground state to the conduction band (photoelectric effect) requires the electron to absorb the photons with total energy higher than that of the bandgap energy. This electron excitation is a result of non-linear excitation, where this can be due to multiphoton ionisation or tunnel ionisation. The excitation rate can be described by the Keldysh theory [8, 68, 91] for the photon ionisation and the Drude model of free carrier absorption [8]. Multiphoton ionisation is due to one single electron absorbing a few photons, leading to the cumulative energy of these photons being higher than the bandgap energy, and allowing the transition of the electron to the conduction band. The Keldysh theory can also be applied to the tunnelling effect [8]. In the tunnel ionisation case, the bandgap is deformed by the extremely high electric field from the laser, lowering the Coulomb barrier, which allows the electron to tunnel into the conduction band [8,68]. The electrons in the conduction band can still absorb more photons, allowing them to reach even higher energy states, leading to other non-linear excitations to occur. These excitations are a direct result of electron-to-electron relaxation, which can cause impact ionisation. With impact ionisation, the electron with high energy states can ionise another electron from the valence band, leading to two excited electrons in the conduction band [12]. They can then be heated by the laser, and once they have enough energy, they can impact more valence electrons [12]. With the repetition of the impact ionisation, this can lead to the avalanche effect to occur. With these types of laser induced processes, it shows that a way to increase LIDT is to utilise film materials that have higher bandgap energies in order to reduce the multiphoton ionisation and tunnel ionisation, where it then leads to the impact ionisation and avalanche effect [68]. Figure 1.13 shows the schematic of single photon, multiphoton, tunnel and avalanche ionisation.

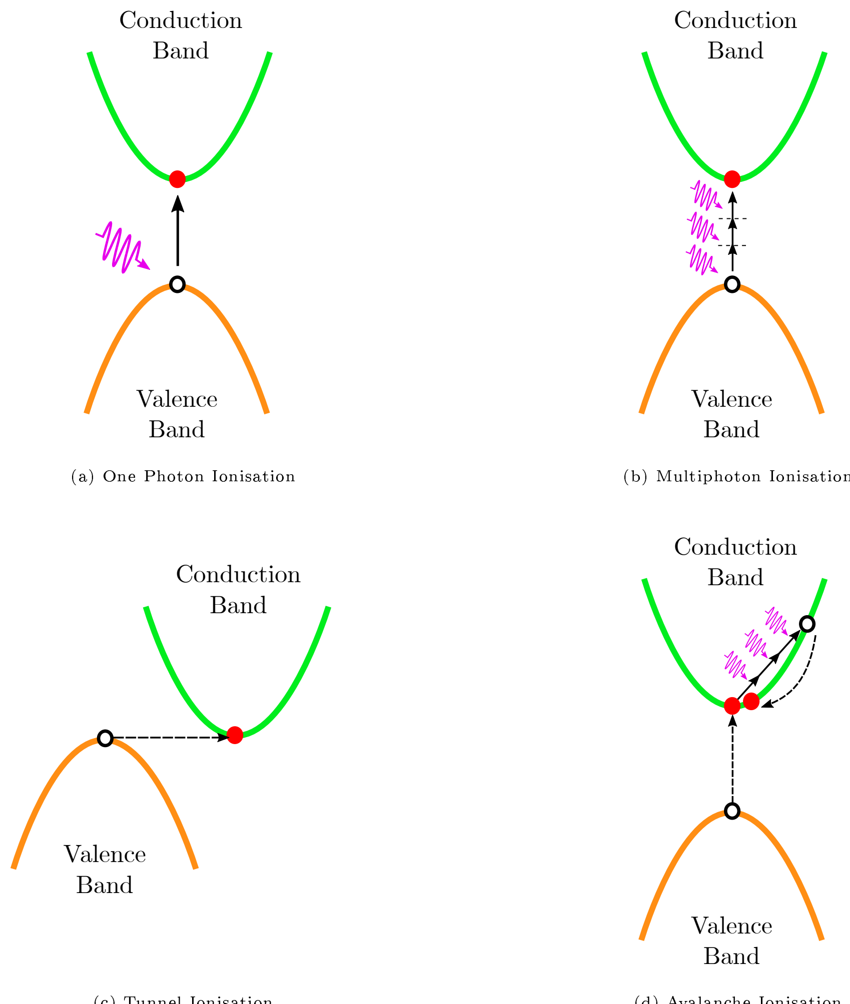

Figure 1.13: A schematic diagram of (a) One photon ionisation, (b) Multiphoton ionisation, (c) Tunnel ionisation and (d) Avalanche ionisation, which are examples of non-linear effects that can occur due to laser irradiation. The figures are reproduced from [12–15].

Other laser induced processes that can occur, based on Figure 1.9, in thin films are: carrier-carrier scattering and carrier-phonon scattering. The former can be described as when the electrons are accelerated by an electric field, they can collide with other electrons, scatter them, and causing them to collide with more electrons. In the latter process, this is where the electrons are once again accelerated by the electric field, where they then excite the phonons, or they cause the vibrations within the lattice of the materials, where this process can result in thermal effects in the films when irradiated by the laser, leading to damage that can be observed on the films [7].

Damages on laser optics can also occur as subsurface damage in addition to bulk damage. For subsurface damage, these are present in every optic at the top surface, often observed as cracks, residual stress, contaminants or voids due to the manufacturing processes of the optics [7, 92]. When a laser is exposed on the optic, subsurface damage can increase the absorption and scatter, increasing heat at these areas, leading to system failure in high power laser systems due to mechanical stress. Scattering can also occur from inclusions present in the optics due to contamination during melting or bubbles due to the reactions occurring during melting. However, these are mostly removed during polishing, although it is almost impossible to avoid these defects during the manufacturing and polishing of the optics [7]. Again, the thin film coatings on these optics can also enhance the defects, leading to the damages that have been discussed, and lowering the LIDT. Figure 1.14 below also shows a schematic diagram of defect layers that can possibly be found on an optic, extracted from [9].

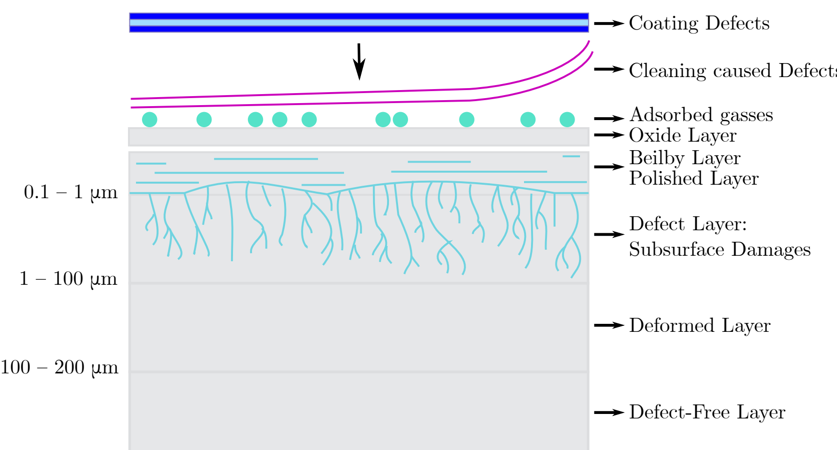

Figure 1.14: Schematic diagram of defect's layers on the optics, reproduced from [9].

For bulk damage, significant absorption can take place at high laser intensity, leading to localised heating. This optical breakdown occurs when a large number of electrons are excited into the conduction band, leading to large degree of free electron density, allowing non-linear absorption to increase. This will also lead to electron avalanche ionisation [7, 93]. When utilising ultrafast laser pulses, the bulk material does not have time to heat through localised absorption, leading to Coulomb explosion [7]. This is

where the build-up of the electrostatic force can break the molecular bonds, and causes lattice fracturing due to the high electric field from the ultrafast pulses [7, 94]. Below is an example of what a bulk damage may look like (Figure 1.15), where the image is extracted from [9].

Figure 1.15: Example of bulk damage, extracted from [9]. The scale is not displayed as it was not provided by the source.

2 Coating Development Techniques

2.1 Introduction

In this chapter, different techniques for the fabrication of optical thin films are discussed based on the available literature, where the method used for the films described in this thesis is discussed in more detail in Section 2.3.3.2, under "High Energy ECR Ion Sources". Many different deposition technologies have been used throughout the years, in both industry and research, in order to fabricate thin film optical coatings, where these are categorised into two main processes: physical and chemical process. The choice of deposition technique is essential for the fabrication of thin film materials, as the deposition technique can essentially determine all the properties and characteristics of the films and can also be used to modify existing properties. However, attention must be given to the choice of technique, as not all deposition techniques result in identical properties such as microstructure, surface morphology, electrical properties, biocompatibility, and optical properties [95]

2.2 Chemical Vapour Deposition Techniques

Chemical vapour deposition (CVD) is a term used for techniques of thin film deposition via a series of chemical reactions. In PVD, thin films are created by evaporation, ion bombardment, or sputtering of target materials, whereas CVD involves chemical reactions under specific conditions, such as temperature, pressure, momentum, mass, and energy transport. CVD technique provides high growth rate and offers good reproducibility of coatings with the same or similar properties, such as: mechanical, optical, chemical and physical [95]. CVD is commonly used to fabricate coatings from materials with low porosity properties which are problematic to evaporate or sputter. Some CVD techniques have been discussed below:

2.2.1 Thermal CVD

Thermal CVD process typically utilises heating lamps to rapidly heat the substrate to activate the energy needed for the reaction to take place. The film surface is exposed to thermal energy from either the condensing atoms or substrate heater to create the films. The thermal surface energy is responsible for mobilising the atoms, which leads to a uniform thickness of the films. The surface chemistry and surface atom mobility are aided by the substrate temperature. [55, 56, 95]

2.2.2 Plasma Enhanced CVD

Plasma Enhanced CVD (PECVD) is used to deposit thin films from gaseous state to solid state on the substrates. The chemical reaction takes place after the creation of plasma in the chamber, which leads to the deposition of the films. PECVD utilises electrical energy to generate plasma and sustain the reaction process rather than thermal energy. Hence, this is the main benefit of utilising PECVD, as the deposition process can be carried out close to ambient temperature [95, 96].

2.2.3 Pulsed CVD

Pulsed CVD is also known as atomic layer deposition (ALD). ALD is the technique of choice for ultra-thin films, as it is based on self-limiting reactions between two gaseous precursors, where the thin films are deposited layer-by-layer on the substrate. It uses only surface chemical reactions to build up the ultra-thin films, with the ability to achieve very precise control of the thin film thickness down to the atomic level - where currently, this cannot be achieved by any other PVD or CVD techniques [55, 56, 95, 97].

2.3 Physical Deposition Techniques

Physical vapour deposition (PVD) technique is a technique that involves the transfer of materials at the atomic level. PVD is an atomistic deposition process in which there is a physical dissociation of atoms, condensation, and nucleation of these atoms onto a substrate in either a vacuum or low pressure gaseous environment [95].

Generally, PVD processes are used to deposit films with thicknesses in the range of a few to thousands of nanometers; this process can also be used to fabricate multilayer coatings [95]. Typically, the entire deposition chamber is kept under vacuum, which allows particles to travel freely [96]. PVD covers a wide range of deposition techniques, which are discussed below:

2.3.1 Pulsed Laser Deposition

Pulsed laser deposition (PLD) utilises a high-power laser as a source to sputter the target material. The laser beam is focused inside a vacuum chamber to eject atoms from the target material, which is then deposited onto a substrate [96, 98]. The target absorbs the laser pulses, which leads to electronic excitation, and is converted into thermal, chemical, and mechanical energy. This conversion then results in evaporation and plasma formation, where the ejected atoms travel through vacuum and are deposited

on a typically hot substrate [96].

2.3.2 Thermal Evaporation

Thermal evaporation is a deposition process which has been extensively used to fabricate thin films on solid materials [55, 56, 95]. During the thermal evaporation process, it is often carried out under high to ultra-high vacuum, and the trajectory path of the target material to the substrate is a straight path, with minimal interference - essentially a collisionless path for the atoms to arrive on the substrate surface [55, 56, 95, 96]. The vapour flux is created by heating the target surface in vacuum using an electric resistance heater [96], where the flux is then condensed onto the substrate to form a thin film. As mentioned, this process is carried out under vacuum, where the vapour does not collide with other atoms in the chamber, which reduces the impurities in the films being grown [96]. Typically, the thermal evaporation process provides a higher deposition rate than other PVD processes [95].

The evaporation process has also been reported for different configurations, as discussed in the following sections [55, 56, 95, 96]:

2.3.2.1 Electron Beam Evaporation

Electron beam (E-beam) evaporation occurs when the target material is bombarded with an E-beam created from a charged tungsten filament to evaporate and convert it to a gaseous state for deposition onto the substrate. This technique is carried out under high vacuum, where these atoms that are in a vapour phase can precipitate and form a thin film coating [55]. A magnetic field can also be added to focus the electrons' trajectory.

E-beam evaporation is one of the most commonly used process to fabricate thin films, due to several advantages: (i) it can yield significantly higher deposition rates compared to other techniques; and (ii) it has very high material utilisation efficiency, leading to cost reduction, which is highly sought after in industry. A schematic of E-beam

evaporation is shown in Figure 2.1. An ion-assist source can also be added to the E-beam setup, which is known as ion assist deposition (IAD), where the assisting ions can further manipulate the film's properties (i.e. hardness, surface morphology, and density) by adding energy to the outermost layers as the films are being formed. This can also lead to better bonding and adhesion of the films to the substrate [55, 56].

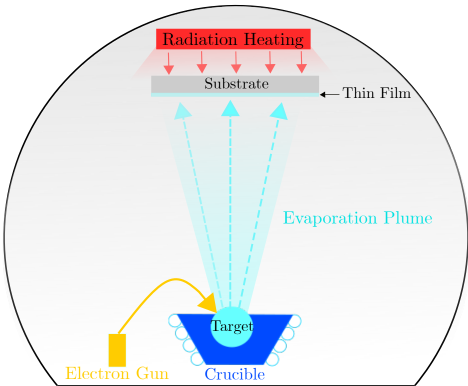

Figure 2.1: A schematic diagram of E-beam Evaporation reproduced from [16].

2.3.2.2 Molecular Beam Epitaxy

Molecular Beam Epitaxy (MBE) is used to grow epitaxy through active interaction of single or numerous molecular beams on the surface of a heated crystalline substrate material. This method is used to fabricate finely controlled single-crystal epitaxial films in ultra high vacuum. Fast shutters are employed inside the chamber between the sources and substrate for precise control of thickness, lattice match, composition, dopant concentration, and interfaces at the atomic layers [55, 56, 95]. A schematic of the MBE is shown in Figure 2.2.

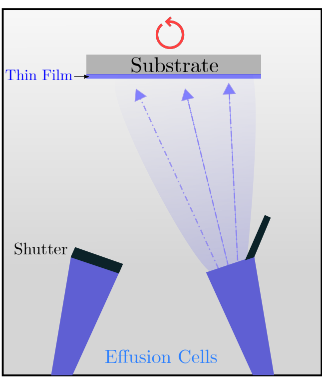

Figure 2.2: A schematic diagram of Molecular Beam Epitaxy reproduced from [17].

2.3.2.3 Reactive Evaporation

Reactive evaporation involves the evaporation of atoms from the target material in the presence of a reactive gas inside the chamber. During the evaporation process, the atoms react with the gas chemically to form a thin film layer on the substrate. Reactive evaporation is used to fabricate stoichiometric oxides and alloys by introducing oxygen (for oxide coatings) or nitrogen (for nitride coatings) as reactive gases. [95, 99, 100].

2.3.3 Sputtering

Sputtering process is a non-thermal vaporisation techniques where individual atoms are "knocked-off", or ejected, from the target surface due to atomic collision by high energy particle bombardment. This is the direct result of collisions between the incident energetic particles with the target's surface atoms. These energetic particles can be generated using an ion or plasma source. Once the atoms are liberated from the surface of the target, they travel through the vacuum chamber and deposit onto suitably positioned substrates, creating thin films. [55, 56, 60, 95, 96, 101]. Sputtering techniques can also be used to etch the surfaces of substrates to clean or further improve its roughness, due to its ability to remove atoms [95].

Sputtering deposition is a name given to a variety of sputtering processes, and an overview of how different sputtering deposition techniques operate is discussed below:

2.3.3.1 Magnetron Sputtering

During the sputtering process, due to ion bombardment, typically secondary electrons are emitted from the target's surface. Magnetron sputtering uses the magnetic field to restrict the movement of these electrons as close to the target surface as possible (Figure 2.3) [95]. The magnets are typically placed behind the target to confine the secondary electrons to the target, prevent them from reaching the substrates, and allow heavier atoms to travel [52, 60]. With magnetron sputtering, the electrons follow cycloidal trajectories along the target, which increases the probability of ionisation of the

sputtering gas, leading to denser plasma formation, which in turn leads to an increase in the deposition rate [52, 60, 102].

There are many methods of magnetron sputtering; for example, DC magnetron sputtering is used for conductive target material, whereas RF sputtering is used with insulating materials as well as conductive materials. This is due to the alternating current with high frequency is required to eliminate charge accumulation due to the ceramic target materials [103]. Other methods of magnetron sputtering include unbalanced magnetron sputtering (UM), high-power impulse magnetron sputtering (HIPIMS), and high-power pulsed magnetron sputtering (HPPMS), which have been widely discussed in the literature [52, 55, 56, 60, 95, 103].

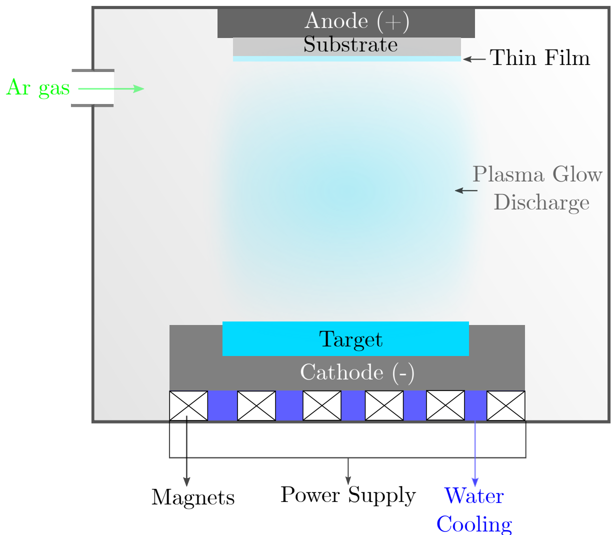

Figure 2.3: A schematic diagram of Magnetron Sputtering reproduced from [18, 19].

2.3.3.2 Ion Beam Sputter Deposition

Ion beam sputtering (IBS), also known as ion beam deposition (IBD) or ion beam sputter deposition (IBSD), is a PVD technique which has some advantages over other PVD techniques [20]. IBSD typically uses a broad beam ion sources with low energy ions to sputter a target. The sputtered particles condenses on the substrate, where a thin film is form. IBSD is a known PVD technique which produces thin films with desirable

properties, close to those of bulk materials. Examples of these desirable properties are dense film structures, improved adhesion of films to substrates, less defects, and better controlled composition of the materials [20, 95].

IBSD setup consists of an ion beam source, a target, and a substrate holder. IBSD relies on impinging the target surface with ions to remove the material, where the atoms that have been removed travel towards the substrate to form a thin film layer [20]. If there are any reactive gases involved in the process, this is known as reactive sputter deposition and is briefly described in later section. Another setup available in combination with IBSD is to add an assist source, where the assisting ions provide additional energy to the growing films, which can further manipulate the film's properties. This process is known as dual ion beam sputter deposition (DIBSD) [20]. A schematic drawing of typical IBSD and DIBSD is shown in Figure 2.4.

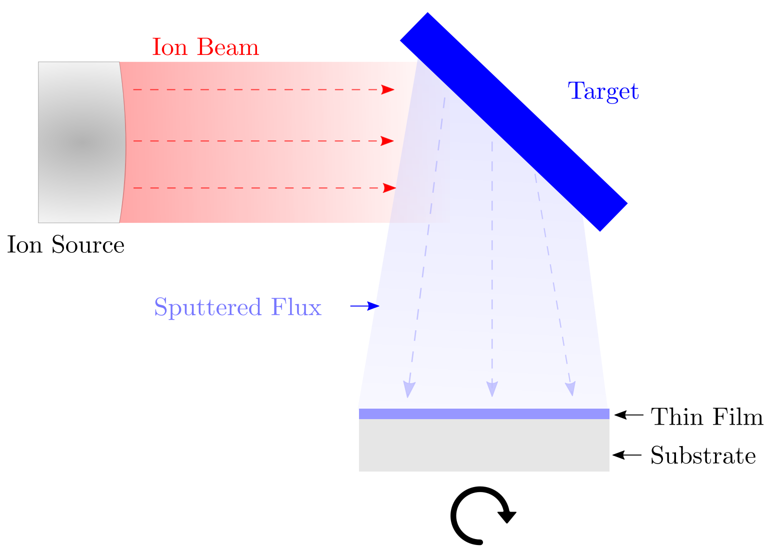

(a) Ion beam sputter deposition

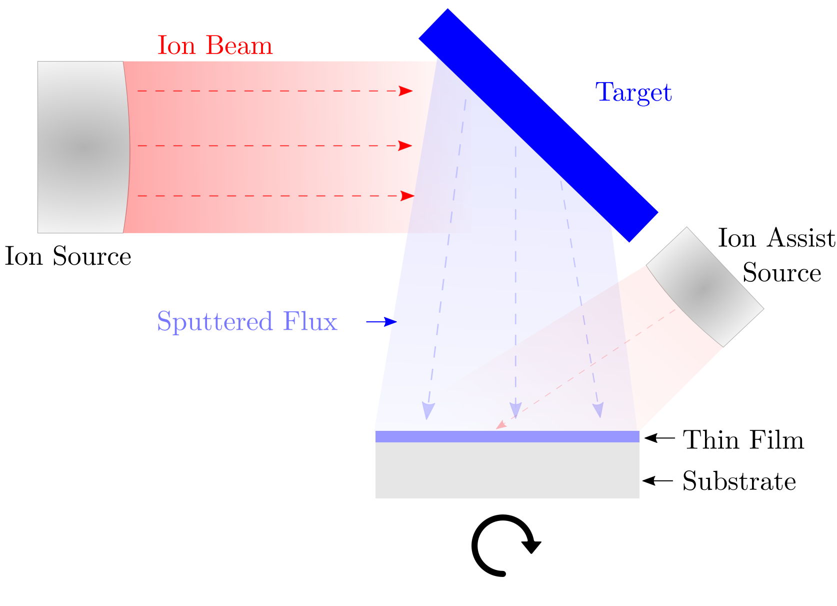

(b) Dual ion beam sputter deposition

Figure 2.4: A schematic diagram of (a) IBSD and (b) DIBSD reproduced from [20,21].

There are many advantages of using the sputtering process, for example, being able to control the stoichiometry and regulate the film thickness. Nevertheless, IBSD does have disadvantages compared with other PVD techniques. The growth rate is typically much lower than that of other methods, upscaling can be more complicated, and the ion source components are more complex; therefore, it can be more challenging to maintain than that of magnetron or evaporation sources [20, 95].

In IBSD, there are several different types of ion sources that can be used to create ion beams to bombard the target material. These sources are shown in Figure 2.5, with a brief description of each type of source. High energy ECR was the type of source used throughout this thesis.

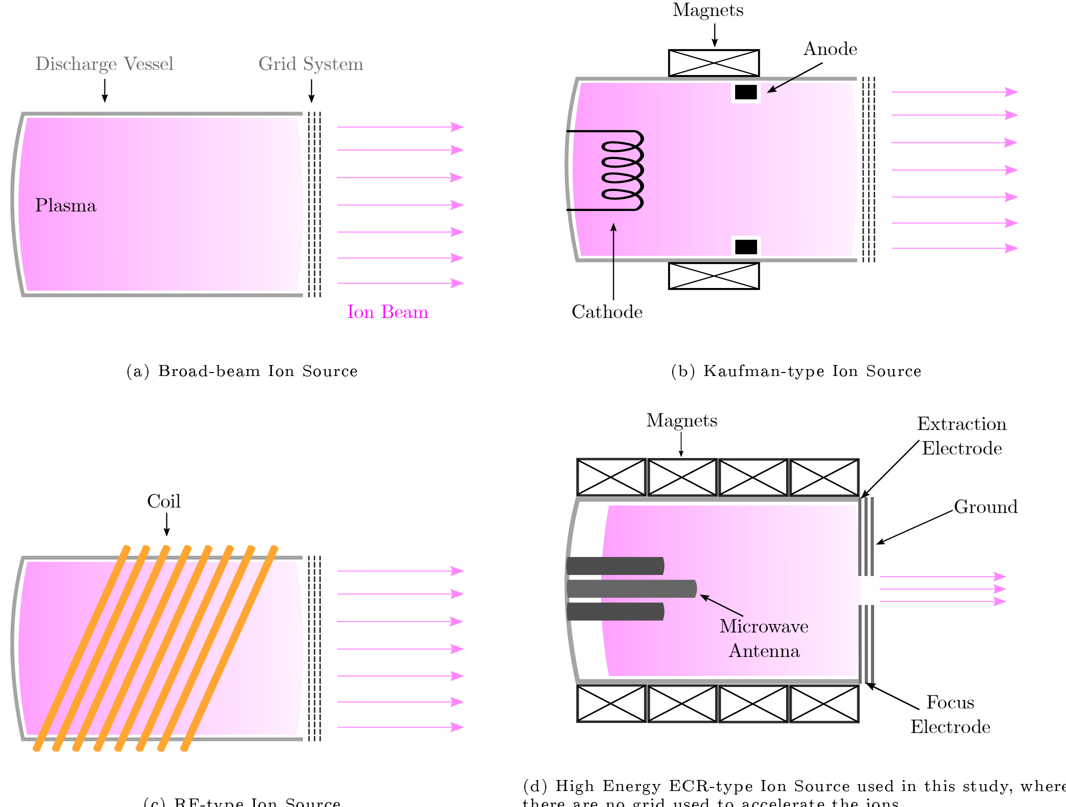

(a) Broad-beam Ion Source

(b) Kaufman-type Ion Source

(c) RF-type Ion Source

(d) High Energy ECR-type Ion Source used in this study, where there are no grid used to accelerate the ions

Figure 2.5: A schematic diagram of different types of ion sources reproduced from [20].

Broad-beam Ion Source

Typically, gridded broad-beam ion sources are used in IBSD systems, where the sources consist of a discharge vessel for ion generation and a multi-aperture grid system for ion acceleration and extraction (Figure 2.5a). Inside the discharge vessel, plasma is generated by electron impact, where the electrons are accelerated and collide with the injected gas atoms, where the ions are then formed [20].

Kaufman-type Ion Source

In Kaufman-type ion sources, or DC-type, electrons are emitted by the hot cathode that is heated using a direct current (Figure 2.5b). These electrons then collide with the injected gas atoms, creating ions and electrons along with secondary electrons from

the ion impact on the cathode surface [104]. With these types of sources, their lifetimes are limited because of the bombardment of ions on the cathode. This bombardment leads to the erosion of the cathode as well as possible contamination of the cathode material on the films. A solution for this problem is to utilise RF-type ion sources or ECR ion sources [104].

RF-type Ion Source

With RF-type ion sources, electrons are accelerated by a capacitively or inductively coupled radio frequency (RF) field, where the most commonly used type is the inductively coupled RF ion source (Figure 2.5c). In an inductively coupled system, an electric field is generated by time variation of the magnetic field. The electric field is strongest near the coil and does not drive the ions into the conductor surface and hence, reduces the damage to them. RF ion sources typically use low RF frequencies, and they do not attempt to couple to any plasma resonance; thus, they behave similarly to Kaufman-type sources but with different electron acceleration mechanisms [104].

High Energy ECR-type Ion Source

With ECR-type sources, the plasma is created by the use of a magnetic field and a microwave to heat the electrons, where they cause electron impact ionisation on the injected gas molecules (Figure 2.5d). The charged electrons make a circular orbit in the direction perpendicular to the magnetic field lines inside the cavity due to the Lorentz force:

$$\mathbf{F} = e^{-}(\mathbf{E} + \mathbf{v} \times \mathbf{B}), \tag{2.1}$$

where e^{-} is the electron charge, $\mathbf{E}$ is the electric field, $\mathbf{v}$ is the velocity of the electron, and $\mathbf{B}$ is the magnetic field.

To understand the behaviour of the electron orbit, presume a case where the electric field

is $\mathbf{E} = 0$. A particle in motion perpendicular to a magnetic field experiences a force perpendicular to both the particle velocity and magnetic field [105]. As this force is transverse to the velocity and field, the particle moves in a circular orbit, perpendicular to the magnetic field [105]. As the electrons spin counter-clockwise with respect to the direction of the magnetic field (due to the Right Hand rule), the ions spin clockwise due to the opposite electric charges of the particles (Figure 2.6). Hence, in ECR processes, right-hand polarised waves are typically used in order to have the electric wave field travelling in the same direction as the electrons [105].

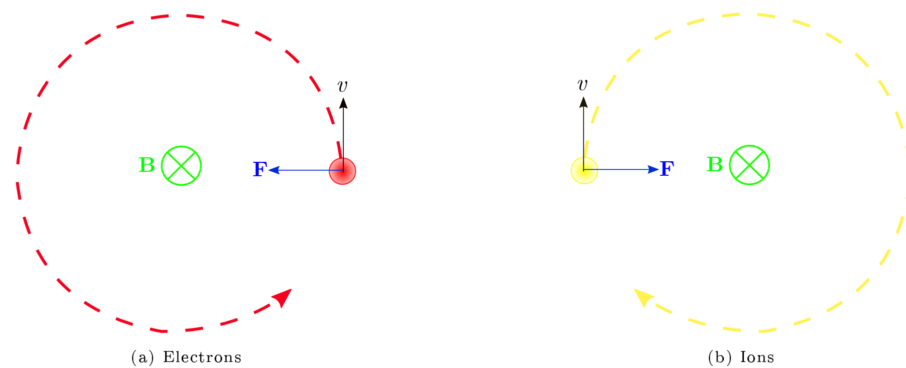

Figure 2.6: Schematic diagram of the electron and ion orbits, where $\mathbf{E} = 0$, based on the Right-Hand rule, where the magnetic field $\mathbf{B}$ is travelling upwards through the paper.

The motion of these electrons occurs at an angular frequency known as the electron cyclotron frequency:

$$f_c = \frac{e^{-}\mathbf{B}}{2\pi m_{\mathrm{e}}}, \tag{2.2}$$

where m_e is the mass of the electron.

The orbiting radius, also known as the cyclotron radius, is given by:

$$\rho = \frac{mv_{\perp}}{e^{-}\mathbf{B}}, \tag{2.3}$$

where $v_\perp$ denotes the transverse electron velocity.

With the injection of microwaves and an alternating electromagnetic field perpendicular to the magnetic field, a condition can be met, where the microwave frequency matches the electron cyclotron frequency. This leads to the electric field component of the wave to be in resonance with the electron orbit, accelerating the electrons [105].

The ECR sources used in this thesis, developed by Polygon Physics (*Grenoble, France*) [106], contain a compact $\frac{\lambda}{4}$ microwave cavity tuned to 2.45 GHz, which can operate for a range of extraction potentials (from 0 - 10 kV in this case). Alongside the permanent magnets around the cavity, and the electric field at the cavity exit being positively biased with respect to ground, a plasma can be ignited with the help of microwave power and ionisation of the injected gas molecules by the accelerated free electrons. The ion beam goes through the extraction electrode, towards the focus electrode, which can be used to manipulate the shape of the beam - depending on the voltage at which the focus electrode is held [106].

As mentioned, these ECR sources use aperture electrodes rather than an extraction grid to extract the beam, leading to minimal contact between the beam and the electrodes. This is advantageous as, firstly, there will be a lack of contamination in the films due to the extraction grid, which can be seen in films grown by other ion sources [106]. Secondly, the lifetime and associated maintenance cycles of the ECR sources are extended due to the limited erosion of the electrodes. Lastly, these ECR can operate at a wider range of extraction potentials (0–10 kV) compared to that of RF-ion sources, which typically have a working voltage no higher than 2 kV [102, 107]. However, even with a higher extraction potential, the deposition rate was observed to be considerably slower in the ECR-IBSD process than in RF-IBSD, leading to a longer run time required to achieve the same thicknesses of the thin films. Images of the ECR sources used in this study are shown in Figure 2.7.

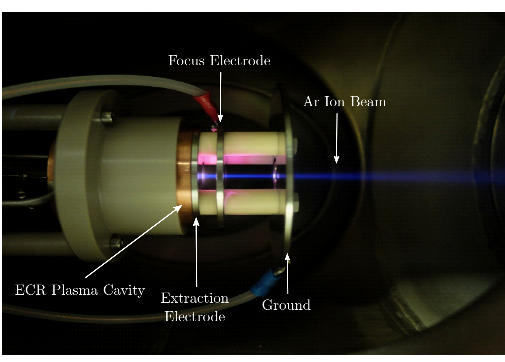

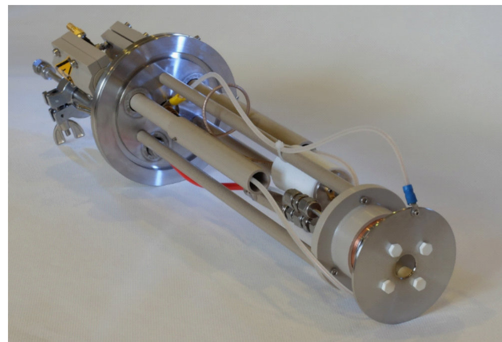

Figure 2.7: Images of ECR sources used in this study.

As mentioned, the films that were produced and discussed in this thesis were fabricated using the ECR-IBSD technique, which is a novel process that has previously yielded the lowest IR absorption in amorphous silicon thin films [108], but otherwise underexplored for optical coating development. This study is the first to report the study of laser optics by utilising the novel ECR-IBSD technique, which includes optical and structural characterisations, as well as the first reported LIDT results that have been carried out.

For IBSD processes, inert gases, such as argon or xenon, are typically used. However, other gases such as oxygen or nitrogen can also be used. These latter gases are of interest in the growth of oxide or nitride thin films to avoid contamination of films with inert gases [20].

2.3.3.3 Reactive Sputter Deposition

Reactive sputter deposition is typically used to fabricate compound thin films. During the sputtering process, reactive gases, such as oxygen or nitrogen, are introduced into the deposition chamber, and the gas reacts with the target material to form a compound thin film. The inert gas typically used for this process is argon, and there is a possibility of combining the inert gas with ionised reactive gas, or the reactive gas can be introduced into the chamber on its own [52, 60, 95]. The percentage of reactive gas added to the chamber can be controlled to produce a certain stoichiometric ratio of the compound material.

3 | Coating Characterisations

3.1 Introduction

In this chapter, the different characterisation methods used to extract information about the fabricated thin films are discussed. The basic background of each characterisation method has been described, and a literature review of the optical properties which have been investigated is also discussed in this section.

3.2 Optical Properties

When light is incident on thin films, three main phenomena occur: transmission, reflection, and absorption. This information can be obtained by utilising a spectrophotometer (Section 3.3) or by similar methods (i.e. ellipsometry). By utilising these measurements, optical fitting can be performed to determine the optical constants and properties of thin films.

3.2.1 Optical Transmittance and Reflectance

When photons of a selected wavelength with beam intensity I_0 are directed towards a film, photons with energies greater than that of the film's bandgap energy (E_{gap}) can excite the electrons in the valence band into higher states (absorption), and those

with energies less than E_{gap} are transmitted. This is due to the fact that the photons with less energy than E_{gap} does not excite the electrons in the valence band into higher states [101, 109]. The transmittance can be calculated by,

$$T(\%) = \frac{I_{\text{t}}}{I_0} \times 100, \tag{3.1}$$

where $T(\%)$ is the transmittance in percentage; I_{t} and I_0 are the intensity of transmitted photons and incident light, respectively.

The T spectra can be divided into three distinct regions [60]:

- **UV Region** - where there is a strong absorption edge, which is related to the band edge
- **Visible Region** - where there are extreme maxima and minima which are modified by interference effects, which can be related to the thickness of thin films
- **Infrared Region** - where the film enters a reflecting regime with metallic properties

As for the reflectance, this is the percentage of the ratio of the intensity of light reflected to that of the incident light. To measure the reflectance of thin films using a spectrophotometer, incident light of known wavelength is directed onto the surface of the film, and the intensity of the reflected light is measured [101]. The reflectance can be calculated by,

$$R(\%) = \frac{I_{\text{r}}}{I_0} \times 100, \tag{3.2}$$

where $R(\%)$ is the reflectance in percentage and I_{r} is the intensity of the reflected light.

3.2.2 Refractive Index and Extinction Coefficient

Optical properties are typically obtained from how light interacts with thin films, where the refractive index (n) and extinction coefficient (k) of a coating are very important parameters in thin film research. Both n and k are related to the dielectric function (ε) and can be computed over a wide range of wavelengths. The determination of the refractive index and its dispersion in thin films has wide applications in the modelling of optical coatings, where one can define the complex refractive index ($\tilde{n}$) as [101,110–112]:

$$\tilde{n} = n + ik, \tag{3.3}$$

where this is related to the velocity of propagation by [110]:

$$v = \frac{c}{\tilde{n}}. \tag{3.4}$$

As previously mentioned, both n and k are related to the dielectric constant (ε), which is expressed as [110],

$$\varepsilon_{\mathrm{r}} = \tilde{n}^2, \tag{3.5}$$

where the dielectric constant is defined by [101, 110–113]

$$\varepsilon_{\mathrm{r}} = \varepsilon_{\mathrm{r1}} - i\varepsilon_{\mathrm{r2}}, \tag{3.6}$$

where

$$\varepsilon_{\mathrm{r1}} = n^2 - k^2, \tag{3.7}$$

and

$$\varepsilon_{\mathrm{r}2} = 2nk \tag{3.8}$$

where $\varepsilon_{\mathrm{r}1}$ and $\varepsilon_{\mathrm{r}2}$ are the real and imaginary parts of the dielectric function, respectively [101,110–112]. Hence, the complex dielectric functions of materials and their variations with wavelength can be used to comprehend the different features of the T and R spectra of thin films [113].

As n and k cannot be calculated directly, several methods can be carried out through indirect measurements. In this project, the method is carried out by calculating and fitting the measured T and R spectra, where SCOUT programme is utilised. Within SCOUT, the Kramers-Kronig Relation (KKR) was used to calculate the real and imaginary parts of the dielectric functions as a function of wavelengths [102, 113, 114].

Other methods that have been studied for the determination of n and k are as follows [110, 115]:

- The Cauchy equation [116]
- The Sellmeier relations [116, 117]
- The Lorentz classical oscillator model [116–118]
- Swanpoel envelope method [119]

where Poelman and Smet [115] have carried out these methods and have reported the same kind of dispersion behaviour of the refractive index being observed based on the different techniques [110].

Additionally, many factors can affect the refractive index of thin films, such as deposition techniques, deposition parameters, substrate temperature, annealing temperature, film thickness, material mixing ratio, and the stoichiometry of the films [110].

As k can be related to the absorption of the coating materials (further discussed in

Section 3.2.3), it can be used to provide information about the optical absorption properties of a material when absorption measurements cannot be carried out directly. This is important for the optics utilised in laser systems, as they can be directly related to the mechanisms that cause LIDT. By calculating both n and k of the materials of interest, this allows for precise modelling of coatings that will be utilised in laser systems, aid the understanding of the materials which can help with the design to minimise loss due to absorption, leading to enhanced system efficiency.

The correlation between k and LIDT is significant, as higher absorption (higher k) leads to greater local heating, reducing LIDT owing to thermal damage mechanisms. Additionally, absorption can also influence non-linear effects such as multiphoton ionisation, tunnel ionisation, and avalanche ionisation, impacting the LIDT, as discussed in Section 1.7. For example, in multiphoton ionisation, materials with high values of k will absorb more photons at the laser wavelength, which leads to a lower LIDT by increasing the possibility of defects or free carriers which further damages the coatings, as well as leads to non-linear absorption, which can lower the material's resistance to laser damage.

Thus, understanding and accurately measuring both the refractive index and extinction coefficient is essential for optimising optical material performance and durability, especially in high-intensity laser applications. The uncertainty in the measurement of both n and k depends on the technique and equipment used, along with data interpretation. In the latter case, this depends on the model used to calculate both n and k, where different methods provide slightly different values for n and k. In this thesis, the uncertainty quoted is the standard deviation of the results based on five different fittings, using the optical fitting software SCOUT, unless explicitly stated otherwise.

3.2.3 Absorption and Absorption Coefficient

Optical absorption occurs when photons of given wavelengths are directed onto a sample, where photons with energies higher than that of E_{gap} are absorbed. This optical absorption can aid in the determination of the E_{gap} or forbidden gap energy [101].

For any given material, one can calculate the absorption (A) based on the T and R data by utilising the following assumption:

$$T + R + A = 1, \tag{3.9}$$

where the scattering of light is assumed to be negligible. However, for thin films, the T and R data tend to have "fringes", where one will have to correct for this by correcting the transmission (T_{C}) [25], where:

$$T_{\mathrm{C}} = T + A, \tag{3.10}$$

and

$$T_{\mathrm{C}} + R = 1, \tag{3.11}$$

where T_{C} can also be written as:

$$T_{\mathrm{C}} = \frac{T}{1 - R}. \tag{3.12}$$

The absorption coefficient can then be calculated based on the Beer-Lambert law:

$$I_{\mathrm{T}} = I_0 e^{-(\alpha d)}, \tag{3.13}$$

where I_{T} is the transmitted intensity after the correction. Hence,

$$\frac{I_{\mathrm{T}}}{I_0} = \frac{T}{1 - R} = e^{-(\alpha d)}, \tag{3.14}$$

where if the thickness (d) of the film is known (which can be extracted through an optical fitting software, or, for example, by using a surface profilometer), one can calculate the absorption coefficient (α) by,

$$\alpha = \frac{-\ln(\frac{T}{1-R})}{d}, \tag{3.15}$$

where α contains the relevant information for analysing the E_{gap}. There are several ways to compute E_{gap}, for example, by utilising the OJL method or Tauc's method, which will be discussed in the following sections (Section 3.2.4.1 and Section 3.2.4.2).

As α is also dependent on the wavelength of light that is being absorbed, as well as the material of the films, it can also be described in relation to the extinction coefficient (k) as,

$$\alpha = \frac{4\pi k}{\lambda}. \tag{3.16}$$

3.2.4 Bandgap Energy

The bandgap energy (E_{gap}), or the forbidden gap energy, is the difference between two bands: the valence band (E_{v}), which is the lowest energy level, and the conduction band (E_{c}), which is the highest level where an electron can be considered free for conduction. In other words, E_{gap} is the minimum energy required to excite electrons so that they can participate in conduction.

There are two types of band-to-band (interband) transitions in bandgaps: allowed and forbidden, where both of these transitions also exist in direct and indirect transitions [22]. In allowed transitions, the probability of photon-induced electron transitions is high, occurring without significant restrictions. In forbidden transitions, the probability is much lower due to the small momentum of photons which makes it difficult to satisfy the momentum conservation requirement, where forbidden transitions often

require multiple steps or the assistance of phonons to satisfy momentum conservation, which reduces the overall probability of such transitions. Figure 3.1 shows the optical transitions that may occur between the E_v and E_c.

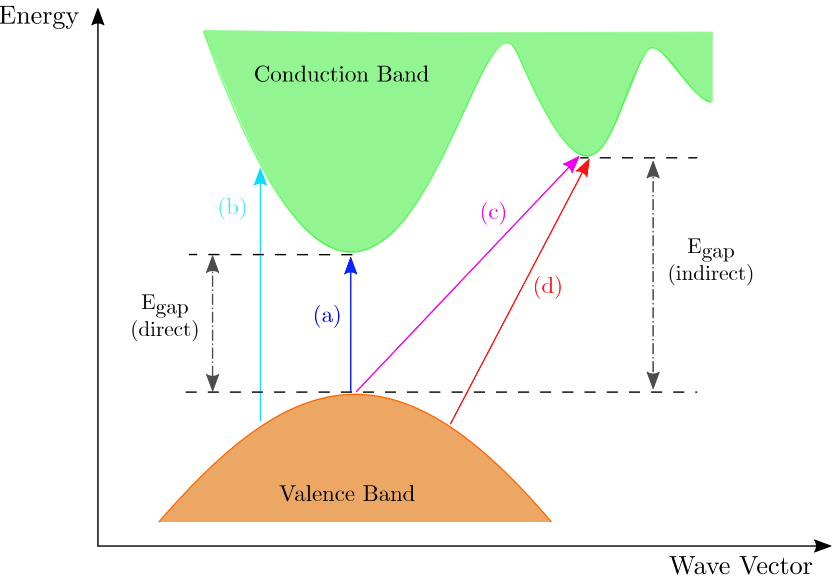

Figure 3.1: Schematic diagram of bandgap transitions, where: (a) direct allowed, (b) direct forbidden, (c) indirect allowed and (d) indirect forbidden transitions [22,23]

As shown in Figure 3.1, for direct transitions, the bandgap is formed between the energy maximum of the lowest band (valence band) and the minimum of the highest band (conduction band), which is at the same position as the electron momentum. For indirect transitions, the maximum energy of the valence band occurs at a different value of momentum to the minimum of the conduction band energy [101]. A photon of energy E_gap can easily produce an electron-hole pair in a direct bandgap semiconductor, whereas in the indirect bandgap semiconductor, an electron must undergo a significant change in its momentum for a photon of energy E_gap to produce an electron-hole pair. In an indirect transition, the electron will have to interact with both the photon to gain energy, and with a lattice vibration (phonon) in order to gain or lose momentum [101].

In the case of semiconductors and insulators, the absorption coefficient can be used to

determine the optical gap. The methods used in this thesis to obtain E_{gap} are described below.

3.2.4.1 OJL Bandgap Energy

The empirical OJL model [120] was used to describe the effects of interband transitions on dielectric functions. The OJL model was originally developed for amorphous materials, where the bandtails exists into the bandgap is taken into account. With this model, the parabolic bands are assumed with tail states exponentially decaying into the bandgap, as shown in Figure 3.2 below [24, 120]:

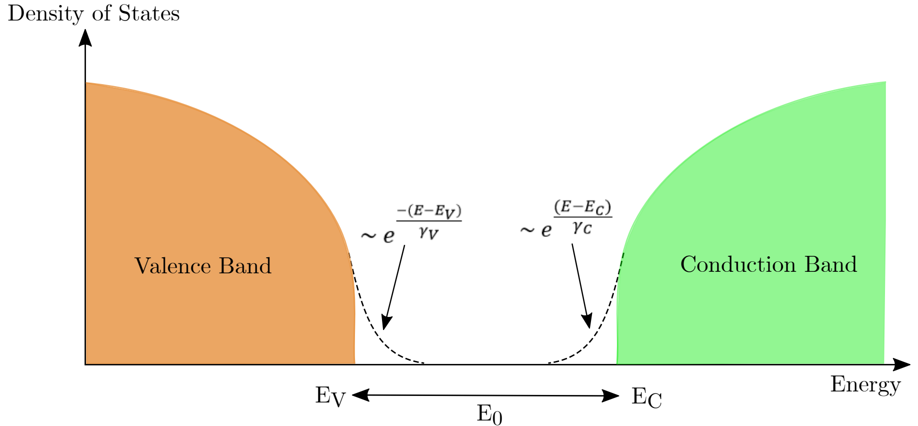

Figure 3.2: Density of states in the OJL band gap model [24, 25]

with the expressions for the mobility edges of the valence and conduction bands:

$$E_{\text{M,V}} = E_{\text{V}} - \frac{1}{2}\gamma_{\text{V}}, \tag{3.17}$$

and

$$E_{\text{M,C}} = E_{\text{C}} + \frac{1}{2}\gamma_{\text{C}}, \tag{3.18}$$

where we can then extract the mobility gap (E_{o}) by,

$$E_{\mathrm{C}} + \frac{1}{2}\gamma_{\mathrm{C}} - [E_{\mathrm{V}} - \frac{1}{2}\gamma_{\mathrm{V}}] = E_{\mathrm{o}}, \tag{3.19}$$

where γ_{V} and γ_{C} are the tail state exponents of the valence and conduction band. The γ given in the SCOUT model is equivalent to the Urbach energy (E_{U}), which is the sub-gap absorption that could arise from either the tail states or general disorders [25].

The OJL model is similar to Tauc's model, where both assume a parabolic density of states. However, as previously mentioned, OJL takes into account the exponential decaying of tail states in to the gap region, which is a more realistic description of amorphous materials.

3.2.4.2 Tauc's Bandgap Energy

In Tauc's method, he proposed a method for estimating the bandgap energy of a material by using the optical absorption spectra [121]. This method is based on the assumption that the energy-dependant absorption coefficient (α) can be expressed by,

$$(\alpha h\nu)^{\frac{1}{r}} = B(h\nu - E_{\mathrm{gap}}), \tag{3.20}$$

where h is the Planck constant, ν is the photon frequency, and B is a constant. The r factor depends on the nature of the electron transitions where this could be equal to $\frac{1}{2}$, 2, 3, and $\frac{3}{2}$ for direct allowed, indirect allowed, indirect forbidden, and direct forbidden transitions, respectively. The absorption is linearised by the function $(\alpha h\nu)^{\frac{1}{r}}$, where to extract the E_{gap} information, one must plot $(\alpha h\nu)^{\frac{1}{r}}$ against $h\nu$, where the linear region of the spectra can be extrapolated to cross the x-axis. The value of the x-intercept of this line is the value for E_{gap}.

One can also extract E_{U} values from Tauc's method by plotting $\ln(\alpha)$ against $h\nu$. By fitting the linear portion of the curve with a straight line, the reciprocal of the slope yields the value of E_{U}.

However, Tauc's method is not an ideal representation of the density of states in a real experiment for amorphous materials, where tail states are an important feature in the amorphous forbidden gap, where the OJL method is preferred, and hence, is used in SCOUT.

3.3 Spectrophotometer

Typically, the first measurements carried out on the films discussed in this thesis are the transmittance and reflectance measurements as a function of the wavelength of light, where this data can be input into the optical fitting software SCOUT to extract the optical properties of the films.

Spectroscopy allows for the study of how matter interacts with or emits electromagnetic radiation. Generally, there are two types of spectrophotometer: (i) single beam spectrophotometer and (ii) double beam spectrophotometer. The single beam spectrophotometer operates by utilising the light from the source lamp inside the system, which is collimated and passed through a monochromator, where the lights are diffracted into each individual wavelength. Then, the intensity of light transmitted and reflected through the sample is measured by a detector, which converts it into transmittance and reflectance spectra typically observed [26].

The absolute values of the transmittance and reflectance were acquired by calibrating the baseline data without a sample inside the spectrophotometer (where the read out for the transmittance is 100%). Then, the transmittance and reflectance data can be measured and obtained for the samples. Once the spectra are obtained, optical modelling fitting software (SCOUT) can be used to estimate the optical properties of the thin films. Figure 3.3 shows the schematic diagram of a single beam spectrophotometer which is used in this project.

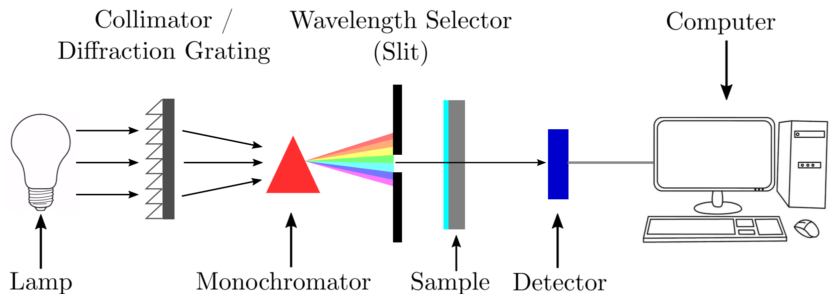

Figure 3.3: Schematic diagram of a single beam spectrophotometer, reproduced from [26]

3.4 SCOUT

SCOUT is a thin film analysis software used to extract information from optical measurements. This can be achieved by comparing the measured spectra for T and R, acquired from the spectrophotometer, with simulated spectra which are based on the user-defined layer stack. By fitting the spectra on SCOUT, optical constants can be extracted, for example, the refractive index, extinction coefficient, bandgap energy, and thickness of the films.

To carry out the optical fittings in SCOUT, the following steps must be taken based on dielectric modelling [60]:

1. Define the structure of the layer stack
    - In this case the layer stack are as follow: air - thin film - substrate - air
2. Define the optical constants of all relevant materials
    - The optical constant models are comprised of susceptibility terms, which are enabled to adjust the optical constants for better fit with experimental data. The susceptibility terms selected for modelling in this thesis are described in more detail below.

3. Define the type of spectra that will be used to be simulated and compared to the experimental data
    - This can be the T, R, A, or ellipsometry spectra, dependant on the user. In this case, the T and R spectra obtained from the spectrophotometer were selected.
4. Select the fit parameters
    - This is the parameters of the model that are to be adjusted in order to reach optimal agreement between the simulations and experimental data can be selected.
5. Fit the model
    - This can be done manually by the user or automatically, where the downhill simplex method is used.

3.4.1 The OJL Model

The OJL model is based on parabolic densities of states of the bandgap, and an exponential tails that are characterised by damping constants for the valence and conduction bands, as described in Section 3.2.4.1.

The "OJL2" model in SCOUT is under the KKR susceptibilities, where it is used to connect the real and imaginary parts of the dielectric functions, where this is implemented already in SCOUT. KKR is important for modelling the dielectric function model, where one would use this in combination with other contributions that add to the real part of the dielectric functions (i.e. "Constant Refractive Index") [24]. By utilising KKR susceptibilities, one can also extract the refractive index, extinction coefficient, and thickness of the films, along with the OJL model.

The OJL interband transition model simulates the direct bandgap absorption with tail states [24, 25, 60]. The model had four parameters: strength, gap energy, gamma, and

decay. The gap strength determines how sharp the gap onset is; the gap energy expresses the width of the bandgap; the Gamma parameter expresses the sub-gap absorption that are exponentially decaying into the bandgap which could arise from tail states, otherwise known as Urbach tail, or disorder; and Decay is a number that dictates the way the imaginary part of the dielectric function decays to zero for high frequencies [24,25,109].

3.4.2 The Drude Model

This model is used to describe the transport properties of electrons in a material by linking the optical and electrical properties of the material with the behaviour of its electrons or holes.

The Drude model neglects any long-range interaction between the electrons and ions and assumes that the electrons do not interfere with each other, where the only possible interaction is the instantaneous collision between a free electron and an ion, which occurs with a fixed probability per unit time [101].

3.4.3 Harmonic Oscillator

The microscopic vibrational motion of atomic nuclei typically has resonance frequencies in the infrared region. These characteristic frequencies depend on the oscillating masses and the strength of their bonding, which can be used to identify materials [24,101].

3.5 X-ray Powder Diffraction

X-ray powder diffraction (XRD) is a technique used to acquire information about the crystallography, crystallinity, atomic structure, crystallite size, and preferred orientation in thin film samples. The X-ray radiation used is created by bombardment of an anode by an electron beam produced by a tungsten filament [52].

The generation of X-ray is made when the electrons that are bombarding the target have sufficient kinetic energy; they can knock an electron out of the K shell, leaving the atom in an excited, high-energy state. One of the outer electrons will fall into the vacancy, emitting energy in the process, which is a form of X-ray radiation with a specific wavelength. The K shell vacancy can be filled with an electron from any other outer shells, giving rise to K_α and K_β lines. K_α is created when an electron from the L shell fills the vacancy and K_β is created when an electron from M shell fills the K shell vacancy, where the former is most probable. A schematic of the electron shell distribution showing the K_α characteristic X-ray photon emitted by an electron being ejected is shown in Figure 3.4 below [27].

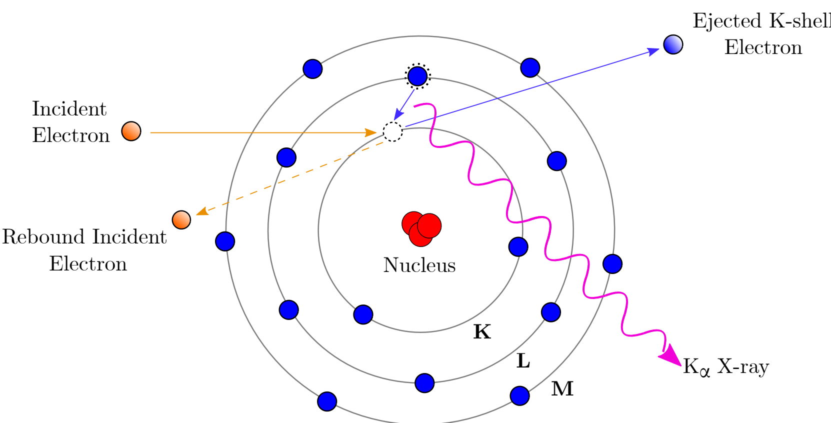

Figure 3.4: Schematic diagram of electron shell distribution, showing K_α X-ray being produced, reproduced from [27, 28]

The X-ray beam created was then focused on the sample with the help of a collimator placed in front of the X-ray gun. The X-ray detector picks up the interaction between the incident rays and the sample, where constructive interference is created to satisfy Bragg's Law (Figure 3.5),

$$n\lambda = 2d \sin\theta, \tag{3.21}$$

where n is the diffraction order, λ is the wavelength of the incident X-ray, d is the lattice

spacing, and θ is the incidence angle of electromagnetic radiation.

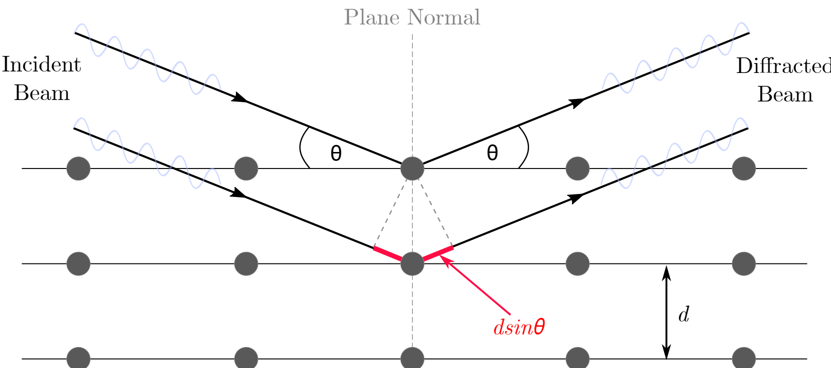

Figure 3.5: Schematic illustration of Bragg condition and Bragg's law

To satisfy Bragg's law, the condition is usually obtained by varying either the wavelength or θ. In this case, when a monochromatic X-ray beam is used, θ is varied to satisfy the Bragg condition. Once the condition is met, it can be used to determine the atomic orientation or the inter-planar distance between adjacent atomic planes. In polycrystalline and crystalline materials, the orientation of the lattice relative to the incident rays will alter the diffraction pattern, whereas in amorphous materials, the orientation should have no influence. In other words, the pattern of angular position (2θ) and intensities (I) of the resultant diffraction peaks are unique characteristics for each sample, whereas for an amorphous sample, this will result in featureless XRD scans [27].

Two different XRD methods have been carried out, which are described in the following sections:

3.5.1 Bragg-Brentano Geometry

The Bragg-Brentano (BB) method is typically used to analyse thin films. However, this method uses large incident angles, which leads to the X-ray beam to penetrate pass the coating and into the substrate, giving inaccurate data for the coating's crystallinity due to influence of the substrate. In this mode, the distance between the sample and

detectors are constant, as the samples are kept constant. The diffracting pattern was collected by varying the incidence angle of the incoming X-ray beam (θ) and the scattering angle (2θ), while measuring the scattered intensity I as a function of 2θ [52,122]. As mentioned, the sample remained fixed while the X-ray source and detector rotated by θ/min clockwise and anticlockwise, respectively. Figure 3.6 shows the schematics of the typical set-up of Bragg-Brentano geometry.

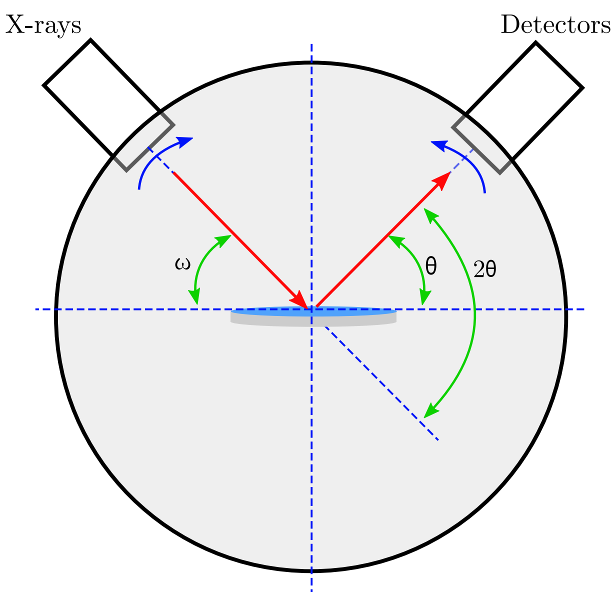

Figure 3.6: Schematic illustration of Bragg-Brentano Geometry, reproduced from [29]

3.5.2 Grazing-Incidence Geometry

To obtain information on the very thin layers on the sample, grazing-incidence XRD (GIXRD) was used. In GIXRD, a very small angle ($< 5°$) is used. This is so that X-rays are focused only on the topmost layer with small penetration depths into the samples [97]. During the collection of the diffraction spectrum, both the sample and incident angle of the X-ray beam were fixed, while the detector was rotated to collect information at different angles. By using GIXRD, it is possible to resolve information as a function of depth by collecting diffraction patterns with varying incident angles (ω). Figure 3.7 shows the schematics of the typical set-up of GIXRD geometry.

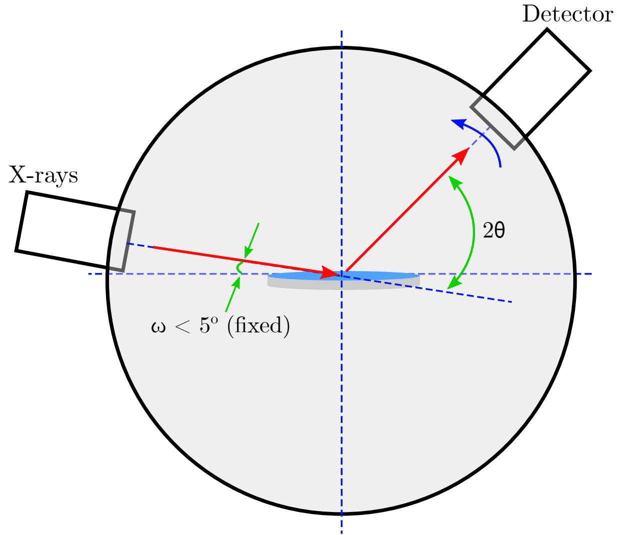

Figure 3.7: Schematic illustration of Grazing-Incidence Geometry, reproduced from [29]

3.6 Energy Dispersive X-ray Spectroscopy

Energy dispersive X-ray spectroscopy (EDS or EDX) was used to analyse the elemental composition or chemical characterisation of the thin films. X-ray emission is stimulated by focusing the X-ray beam or high energy charged particles on the surface of the samples, which excites the electronic structure of an atom. As the core atoms are "kicked" out, leaving behind a hole, electrons from higher binding energy levels then falls to fill in this hole, emitting an X-ray with the energy difference of the electron binding energies (see Figure 3.4). EDS analysis yields a spectrum which displays the peaks that are correlated to the elemental composition of the investigated samples, where each element in the periodic table has its own unique "fingerprint" spectrum [123,124]. EDS has three extremely important components: an emitter, a collector, and an analyser. The combination of these three components allows the analysis of the number of X-rays released along with their energies to provide both quantitative and qualitative information about the samples [125,126]. Typically, EDS is equipped with an electron microscope, which in this case is a Scanning Electron Microscope (SEM).

SEM focuses a beam of electrons over the sample area, where it interacts with atoms to emit electrons (secondary electrons), X-rays, and backscattered electrons. With these interactions, an image can be formed and the elemental properties of the material can be determined using EDS [127].

3.7 Rutherford Backscattering Spectroscopy

Rutherford backscattering spectroscopy (RBS) is an ion scattering technique used for thin film analysis and is unique in that it allows the quantification of elements without the use of reference standards. Light elements, such as helium or hydrogen, are typically used in the energy range of a few MeV to probe the samples. The ions were directed onto the sample, and the energy distribution and yield of the backscattered ions at a given angle were measured. The energy of the backscattered ions was used to identify the atoms in the samples and the depth at which the atoms were located. The number of detections of the elements allows for the determination of the stoichiometry of the films [122, 128, 129].

3.8 Post-deposition Heat Treatment

Post-deposition heat treatment (sometimes referred to as annealing) is commonly carried out in many device fabrication processes, and it is extremely significant for the stability and reproducibility of the process and devices [60, 130]. With post-deposition annealing, there are three possible effects that can occur [60, 131]:

- Improvement of crystallinity
- Formation of oxygen vacancies
- Release of excess oxygen

Nevertheless, the effectiveness of post-deposition annealing depends on the as-deposited properties of the films [60, 130].

Annealing of thin films in air at high temperatures can incorporate oxygen into thin film coatings if the films are oxygen deficient and reduce oxygen if the films are over-stoichiometric (oxygen-rich). Hence, post-deposition annealing was used to optimise the film properties. Alongside the optimisation of thin film properties, annealing may also be able to enhance grain growth and aid in the recovery of disordered structures [60, 130], that is, changing from a disordered structure known as amorphous to a crystalline nature.

3.9 Laser Induced Damage Threshold

3.9.1 Fundamental

When an optical sample is exposed to intense laser radiation, it can become damaged. Laser induced damage (LID) is understood to be an irreversible modification of the properties of a material caused by surface or bulk melting, material softening, cracking, pitting, or shattering.

According to the International Standard Organisation (ISO), LID is defined as,

"...any permanent laser radiation induced change of the surface characteristics of the specimen which can be observed by an inspection carried out with an incident light microscope having Nomarski-type differential interference contrast. A magnification in the range from 100× to 150× shall be used." [9, 132]

Throughout the years, it has been found that the formation and growth of LID depends on three main components: laser irradiation parameters (i.e. wavelength and pulse duration), environmental conditions (i.e. air, temperature, and contamination), and material properties (i.e. defects, absorption coefficient, and electric field effects).

Laser damage can be broadly classified into two types: absorption-driven damage and dielectric breakdown damage, where the type of damage is dependent on the conditions previously mentioned. LID can form at different locations of the optics: the bulk material, surface of the sample, or in the optical coating, where this is shown in Figure 3.8 below. The morphology of the LID can be associated with the damage mechanism and provides a small insight into the causes of the damage. Further discussion of the damage mechanisms is provided in Section 1.7.

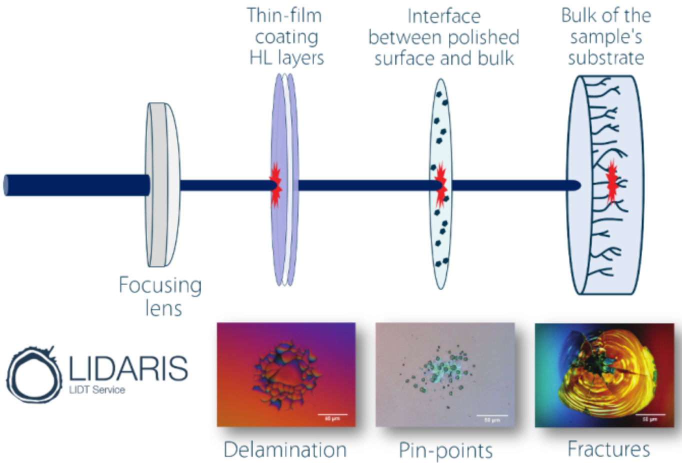

Figure 3.8: Different locations where there can be damages on an optics due to the laser irradiation. The different types of damage morphologies are shown in the figure. This figure has been extracted from LIDARIS [9].

3.9.2 LIDT Protocol

As for laser induced damage threshold (LIDT), this is a physical characteristic of optical components which defines the critical power or peak fluence of laser irradiation which causes irreversible changes in the material structure. The technical definition of LIDT is the limit of the material that can withstand the laser irradiation without any observable changes. According to ISO 21254-1, 2, 3 and 4, LIDT is the highest quantity of laser radiation incident upon the optical component for which the extrapolated probability of damage is zero where the quantity of laser radiation may be expressed in energy density, power density, or linear power density. [132–135]

LIDT is typically carried out by irradiating laser beam on to an optic. There are two main different tests typically carried out: 1-on-1 (single pulse per site) and S-on-1 (multiple shots per site). The S-on-1 method was carried out for this thesis, and the setup will be discussed in a later section. In the S-on-1 method, the test sample is irradiated at several different fluence levels at a certain number of sites at each level based on the ISO 21254 standard. The higher fluences were chosen to produce a high probability of damage, whereas the lower levels are for lower probability of damage existing. The percentage of failures is plotted against the fluence values, where a least-square linear fit to these data is calculated, and the 0% failure intercept most often defines the damage threshold level. However, the LIDT values quoted are dependent on the use of the optics, where there may be small damage, but for usage, this is negligible. The plot mentioned is also known as the "Damage Probability Curve".

4 Experimental Setup

4.1 Introduction

In this chapter, the experimental and characterisation setup used throughout this project are described. The substrate cleaning procedure was first discussed, followed by the two ECR-IBSD setups that were utilised: the 600-System and the Combimat system, where detailed descriptions of each component in each system have been discussed and shown. The final section that has been discussed is the description and parameters used for each of the different characterisation methods that have been carried out.

4.2 Substrate Cleaning Procedure

The cleanliness of the substrates is extremely important for laser optics, as this is a factor which can affect the LIDT of an optic. Throughout this thesis, a 3-step process was performed to clean the substrates:

1. Substrates placed in acetone, inside an ultrasonic bath for 20 minutes.
2. Then, placed in isopropyl alcohol inside an ultrasonic bath for a further 20 minutes.
3. Finally, dried by utilising nitrogen, before placing on the substrate holder.

The substrates utilised throughout this thesis are JGS-3 fused silica substrates, with

dimensions of 20 mm in diameter, and 1 mm thick, and Corning 7979 substrates, which are 1 inch in diameter and 6.35 mm thick. Typically, JGS-3 substrates are used for the characterisation of thin films, as described in Chapter 3 and also later in this chapter. Corning 7979 substrates were used for LIDT testing because they are highly polished substrates and are suitable for laser optics.

4.3 System Setup

4.3.1 600-System

The 600-system is shown in Figure 4.1, where it can occupy up to six ECR ion sources. These ion sources generate highly confined (mm-scale) parallel beams extracted through a single aperture and extracted with 10 kV potential. The experimental setup consisted of a dry scroll vacuum pump (Scrollvac 7, *Leybold, Germany*) and turbo pump (Turbovac MAG W 400 P, *Leybold, Germany*) to achieve ultra-high vacuum (UHV). The schematic shows an example of the experimental setup used to fabricate HfO_2 and Sc_2O_3 thin films.

Neutralisers (*Polygon Physics, France*) were added to the chamber (Figure 4.1, #4) to solve the previous arching issues that occurred, which were caused by the accumulation of charges on the non-conductive target surface. For improved thickness uniformity of the coatings, four samples are placed on a rotating substrate holder (Figure 4.1, #1), on a ferrofluidic drive, driven by a stepper motor at 0.6 rpm for each deposition. The location of the substrate holder coincides with the placement of the target (Figure 4.1, #2), where the greatest sputtered flux can be found. The growth rate was measured *in situ* by utilising a quartz microbalance, which was placed on the system door next to the substrate holder, and the thickness of the coatings was later determined by fitting T and R spectra and extracting the data from SCOUT. In addition, there are gas lines which introduce gas directly into the chamber (also known as the background gas), along with another set of gas lines which lead directly through the ion sources to create

ion beams.

The ion source parameters were controlled using the LabVIEW software (Version 16.0 NI), where the following parameters were controlled for each individual ion source: gas flow through the ion sources, microwave power for plasma generation, beam voltage, and focus voltage.

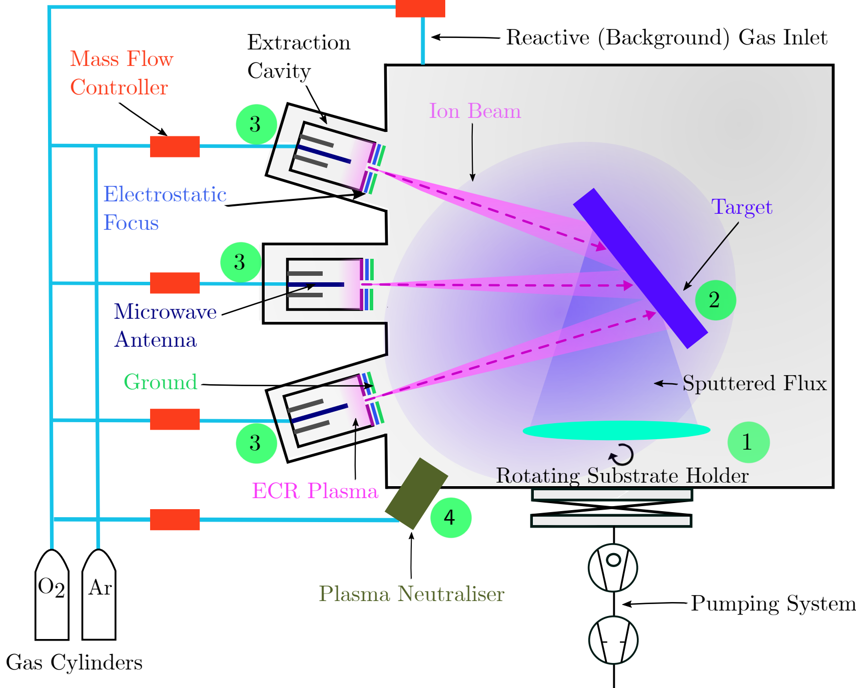

(a) Schematic diagram of the 600 System.

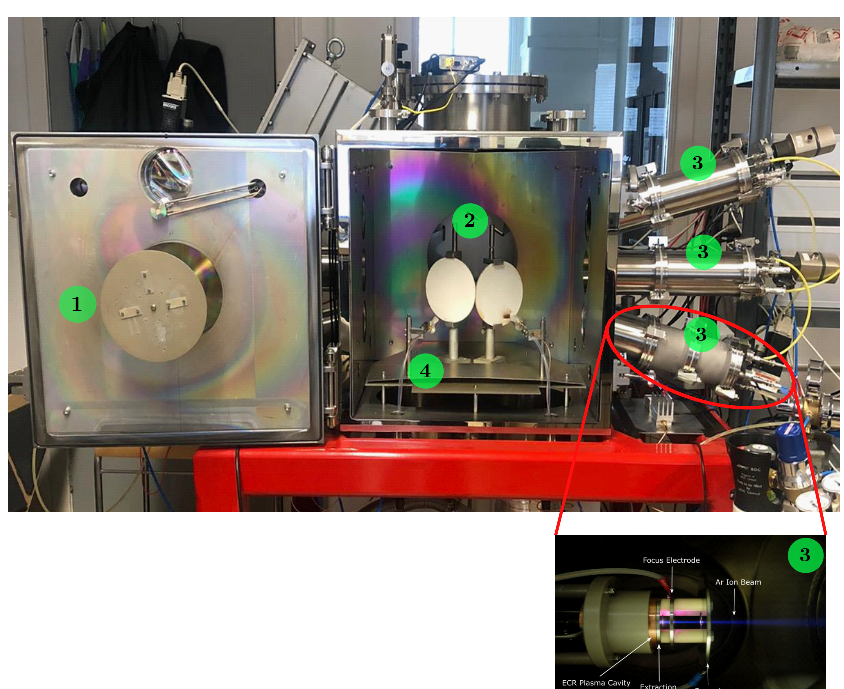

(b) Photographed image of the custom-built ECR-IBSD system. The blown-up image of the ECR ion source is the same as that in Figure 2.7.

Figure 4.1: Schematic and photographed images of the custom-built ECR-IBSD system used. The figures also contain numbered labels for each of the components that were described in the text, along with labels in the schematic diagram of all the important components.

4.3.2 Combimat

The combimat system is a steel vacuum chamber with the dimensions of $50 \times 50 \times 50$ cm^3, where inside the chamber, it contains 24 ECR ion sources, which is formed as a ring, targets holder for conical targets, substrates holder, shutter, and a quartz microbalance. The system also consists of a dry scroll vacuum pump (adixen ACP 15G, *Pfeiffer Vacuum, Germany*) and a turbo pump (TC 400, *Pfeiffer Vacuum, Germany*) to reach UHV, along with high voltage power supplies for the sources. Figure 4.2 shows the schematic cross sectional view of the system, along with the real image of the system.

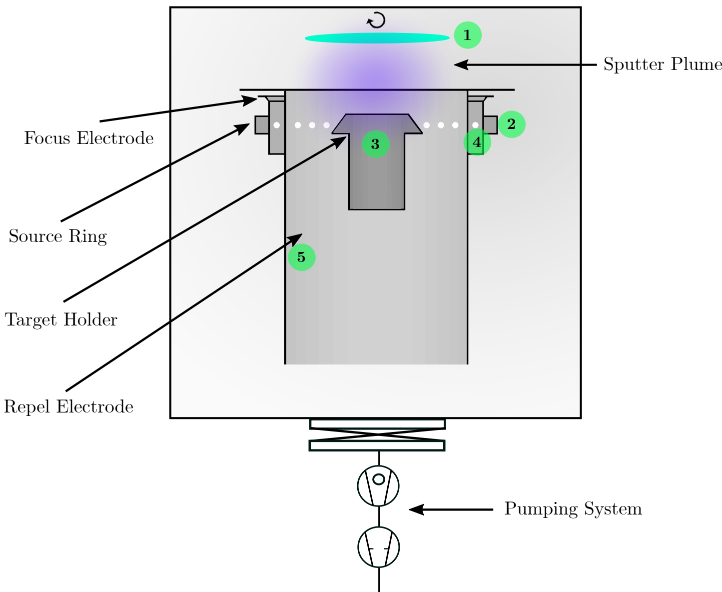

(a) Schematic of the Combimat system, where this is a cross section view

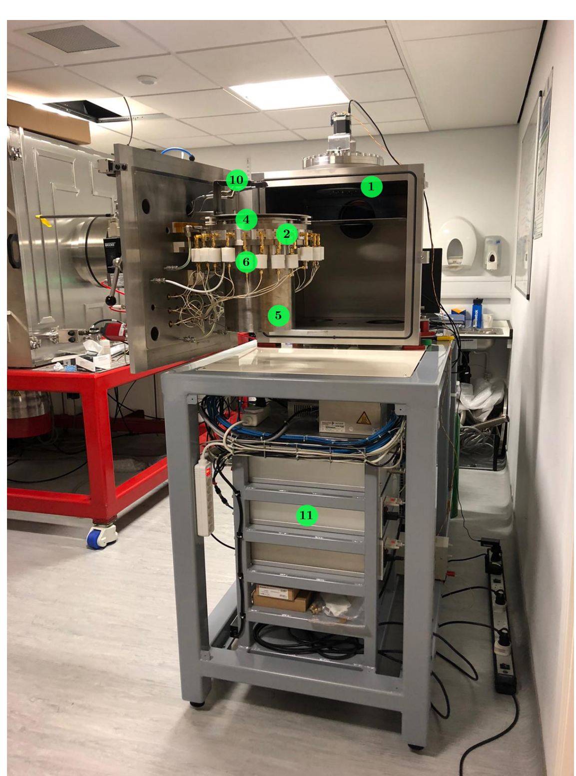

(b) Image of the Combimat system

Figure 4.2: Schematic and photographed images of the Combimat system. The figures also contain numbered labels for each of the components that were described in the text, along with labels in the schematic diagram of all the important components. Again, this system utilises ECR ion sources, where the Combimat has a total of 24 ion sources.

In Figure 4.2, important components are labelled in both images. The labels are as follows: #1 is the rotating substrate holder, #2 is the ion source ring, #3 is the targets holder, #4 is the focus electrode, #5 is the repel electrode, #6 is the individual high frequency generator, #10 is the quartz microbalance, and #11 are the power supplies for the system.

The arrangement of this system is novel owing to the compactness of the sources. Within this system, there are 24 ion sources that form a ring, where each ion source faces its own target, with conical geometry. This can be seen in Figure 4.2, as well as in Figure 4.3 below, where #7 label represents the ion sources.

Side View

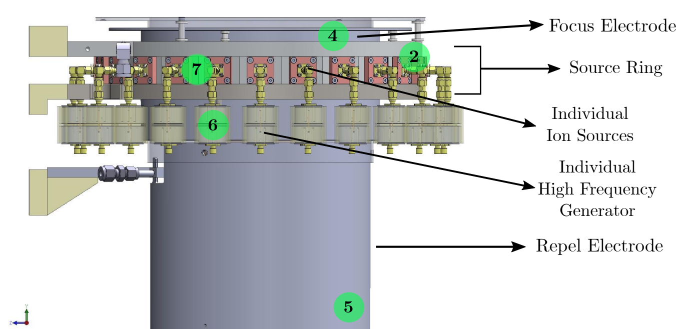

(a) Side view schematics of the Combimat's source ring

Tilted Top View

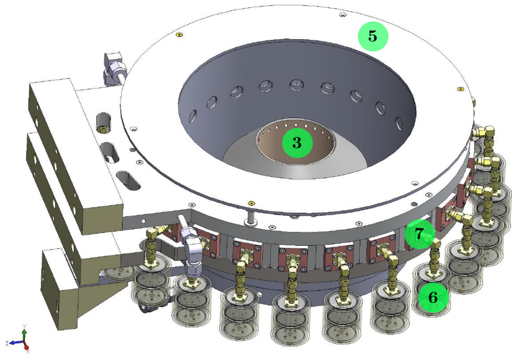

(b) Schematic of the Combimat's source ring, also showing the target holder

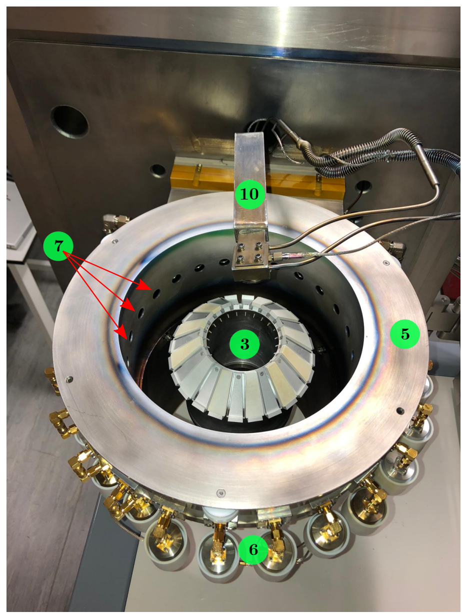

(c) Top-view image of the Combimat's source ring, and targets holder

Figure 4.3: Schematic (a,b) and photographed (c) images of the Combimat system. The figures contain numbered labels for each of the components that were described in the text, along with labels in the schematic diagram of all the important components.

The ion energy is set by polarising the source ring (#2) at a high positive voltage, and the ion beam shape can be controlled by polarising the focus electrode (#4). The beam shape can be controlled by controlling the focus voltage, which in turn can be used to control the spot size on the target. The polarisations on the source ring and the focus electrode can be controlled by utilising LabVIEW, where these polarisations are obtained using two independent high voltage supplies, which can be controlled between 0 - 15 kV. There is also a repel electrode (#5) that can be seen between the focus electrode (#4) and the target holder (#3), and it can be set between -25V to -2000V in order to deflect secondary electrons produced by the ions hitting the target. This repel electrode is important because the secondary electrons can accelerate backwards to the ion sources, causing damage. Each of the ion sources is connected to an individual high frequency generator via its own SMA cables to form the plasma, where the microwave power of the sources can be controlled using LabVIEW. All the high voltage biased

components were inside the vacuum chamber. The values of the parameters used are discussed in subsequent sections.

To create ion beams, gas must be injected into the system, which can be controlled using LabVIEW via mass flow controller. The gas distribution was performed by a stainless-steel rig that divided the total flux for the individual sources. Reactive gas (or background gas) is injected directly into the system above the source ring and targets, which can also be controlled via LabVIEW. A schematic diagram of the door, where all the electrical feed-through and mass flow controllers are shown in Figure 4.4.

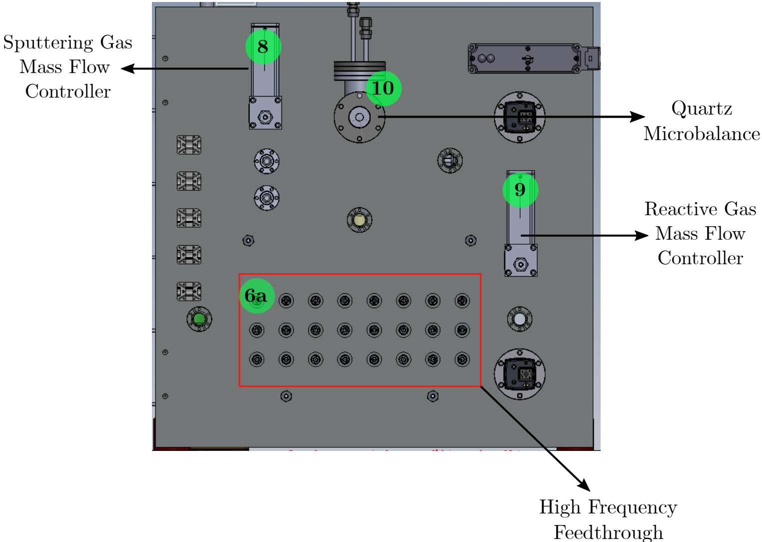

Figure 4.4: A schematic diagram showing the electrical feed-through for the different components in the chamber, as well as the mass flow controllers for the gases used during the deposition. #6*a* is the high frequency feed-through for the individual sources, #8 and #9 is the sputtering and reactive gas mass flow controller, respectively.

The substrate holder is also placed at the top of the chamber, where it also utilises a stepper motor to rotate the holder, at 0.9 rpm for each deposition, to provide a more uniform coating. The location of the substrate holder is where the greatest sputter flux can be found for the combination of individual ion sources/target fluxes. A schematic diagram of the sputtering process with Combimat's geometry is shown in Figure 4.5, where the substrate holder is at the top of the chamber. The growth rate can also be measured *in situ* by utilising a quartz microbalance, which is placed between the substrate holder and the source ring and targets.

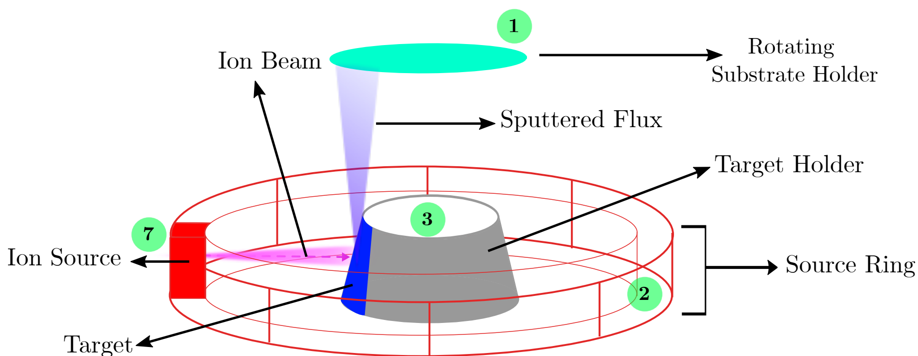

Figure 4.5: A schematic diagram of the combimat's sputtering process. The schematic is showing one source and one target for simplicity.

As shown, the combimat system relies on multiple small ion sources rather than one large ion source, which has its advantages. Each individual ion source faces its own target, allowing mixed materials or multilayer coatings to be easily fabricated. In addition, with the combimat system, one does not have to move the targets to fabricate multilayer coatings, as individual ion sources can be turned on and off depending on which target material is needed. By contrast, in a conventional IBSD system with one ion source, one would need a motor is required to move the targets to different positions to fabricate multilayer coatings.

4.3.3 Experimental Configuration

In this section, the different experimental configurations of the materials studied in this thesis are described.

4.3.3.1 Hafnium Oxide

The hafnium oxide (HfO_2) thin films presented in this thesis were fabricated in a custom-built IBSD system using three compact ECR ion sources (*Polygon Physics, France*), as shown in Figure 4.1. The system can occupy up to six ECR ion sources, three of which were utilised in this experiment to generate ion beams (Figure 4.1, #3). For the target,

a 99.99% HfO_2 target (*Scotech, Scotland*) was used, which was placed in the centre of the chamber (Figure 4.1, #2). A schematic and image of the custom-built ECR-IBSD system are shown in Figure 4.1. Owing to the nature of the ECR sources and their low deposition rate ($\sim$ 0.01 Å/s), the deposition time for each run was 72 hours for this experiment.

The main aim of this experiment was to investigate the optical properties of HfO_2 coatings with varying oxygen background partial pressures and using different percentage of oxygen through the ion sources. Table 4.1 shows the different percentages and gases used for each deposition, and has been split into the three different configurations, which has been further described below.

Table 4.1: The gases configurations through the ion sources, neutraliser and background for all 3 setup that were carried out in this experiment

OXYGEN PERCENTAGE (%)	**TOTAL PRESSURE (mbar)**	**GASES**		
		Ion Sources	Neutraliser	Background
Configuration (i)				
0%	2.5×10^{-4}	Argon	Argon	–
10%	2.5×10^{-4}	Argon	Argon	Oxygen
20%	2.5×10^{-4}	Argon	Argon	Oxygen
35%	2.5×10^{-4}	Argon	Argon	Oxygen
50%	2.5×10^{-4}	Argon	Argon	Oxygen
70%	2.5×10^{-4}	Argon	Argon	Oxygen
90%	2.5×10^{-4}	Argon	Argon	Oxygen
Configuration (ii)				
10%	2.5×10^{-4}	1 Source: Oxygen 2 Sources: Argon	Argon	–
30%	2.5×10^{-4}	3 Sources: Oxygen	Argon	–
Configuration (iii)				
100%	2.5×10^{-4}	Oxygen	Oxygen	–

The base pressure in this experiment was lower than 3×10^{-6} mbar, and as shown in Table 4.1, the total pressure was fixed at 2.5×10^{-4} mbar during the deposition, where the gas from the neutraliser was considered for the overall gas percentages and fixed total pressure. The deposition was performed at room temperature. The gases were

introduced into the chamber using the following three configurations:

(i) Varying oxygen background partial pressure from 0% to 90% of the fixed total pressure value, with argon being introduced through the sources and neutraliser to account for the remaining percentage. This configuration will also be referred to as "Reactive Oxygen"

(ii) Varying the sputtering oxygen partial pressure through 1 or 3 ion sources with no background gas, where this will be referred to as: "10% Sputtering Oxygen" when 1 source is utilising oxygen while the remaining 2 sources and the neutraliser are utilising argon; and "30% Sputtering Oxygen" when all 3 sources are utilising oxygen and the neutraliser is utilising argon.

(iii) Using pure oxygen gas for the full process through the sources and the neutraliser, where this will be referred to as "Pure Oxygen Process".

Figure 4.1 shows a schematic diagram of the experimental setup for this experiment, where three ion sources and one neutraliser were focused on a HfO_2 target. The beam sputtered the target and the material was deposited on a rotating substrate to provide a uniform coating. The position of the substrate was optimised to obtain the highest flux of the sputtered particles, where this is further discussed by C. Bundesmann and H. Neumann [20], and is shown in Figure 4.6.

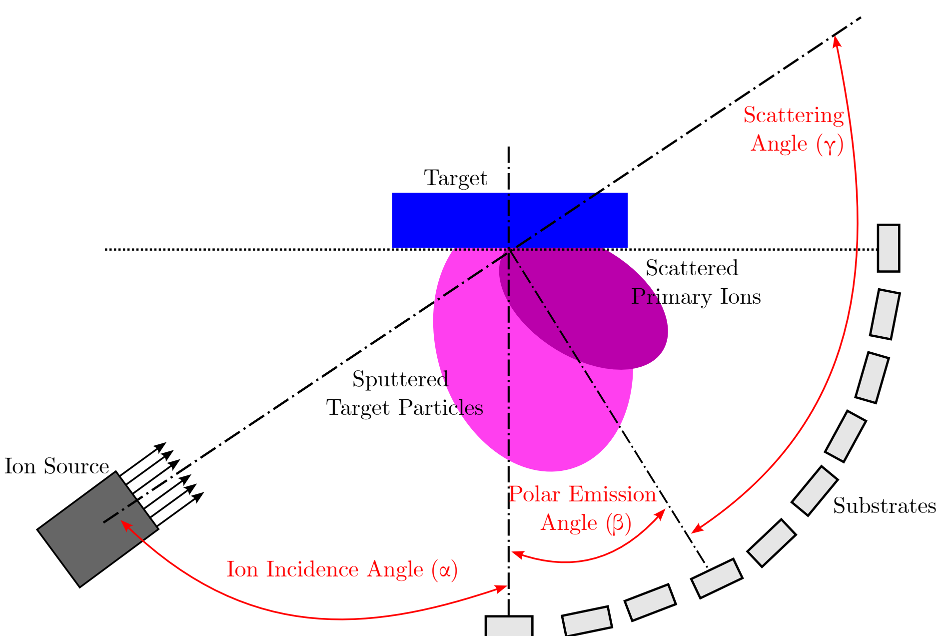

Figure 4.6: A schematic of IBSD process, outlining the geometric factors which can contribute to differing sputter plume distributions (ion incidence angle (α), polar emission angle (β) and scattering angle (γ)). The schematic has been reproduced from [20].

The geometric parameters that are integral to the properties of IBSD coatings include the beam angle of incidence (α), polar emission angle (β), and scattering angle (γ), given by,

$$\gamma = 180° - (\alpha + \beta), \tag{4.1}$$

where it has been reported that for the largest sputter yield, this can be achieved where $60° < \alpha < 80°$, with respect from the target material [20].

As previously mentioned, the ion source parameters are controllable via LabVIEW; in this experiment, the microwave power input was between 3 - 5 W, the focus voltage was between 3 - 6 kV, and the beam voltage was kept constant at 10 kV for all sources. The chosen parameters were used to provide the highest extraction current, minimal beam divergence, and highest ion energies and to provide the most stable beam for each

deposition.

For this custom-built system, the neutraliser is crucial for this experiment because it is used to control the accumulation of charges on the non-conductive target surface, which leads to arching and can cause damage to both the ion sources and substrates. The neutraliser utilises the same ECR technology as the ion sources, and the extraction system connected to the cavity determines the nature of the particles that exit the source; in this case, it is used to control the accumulation of charges. During each deposition, gas was injected into the neutraliser, where a separate controller from the ion sources was used to switch it on. The gas was introduced through the neutraliser until the pressure reached 1.8×10^{-4} mbar, which is the minimum pressure required to start the neutraliser.

4.3.3.2 Scandium Oxide

The scandium oxide (Sc_2O_3) thin films presented herein were fabricated using a custom-built ECR-IBSD system with three compact ECR ion sources (*Polygon Physics, France*), as shown in Figure 4.1. The target used was a 99.99% Sc_2O_3 target (*Scotech, Scotland*), which was placed at the centre of the chamber (Figure 4.1, #2). A schematic and image of the custom-built ECR-IBSD system is shown in Figure 4.1. In this experiment, the sputtering time was maintained constant at 72 hours, similar to that in the HfO_2 experiment.

In this experiment, six different coating runs were carried out, which consisted of varying the reactive oxygen background percentage and using oxygen as sputtering gas. Table 4.2 shows the different percentages and gases used for each deposition.

Table 4.2: The gases configurations through the ion sources, neutraliser and background for this experiment

OXYGEN PERCENTAGE	**TOTAL PRESSURE**	**GASES**		
(%)	**(mbar)**	Ion Sources	Neutraliser	Background
0%	2.5×10^{-4}	Argon	Argon	–
20%	2.5×10^{-4}	Argon	Argon	Oxygen
40%	2.5×10^{-4}	Argon	Argon	Oxygen
60%	2.5×10^{-4}	Argon	Argon	Oxygen
80%	2.5×10^{-4}	Argon	Argon	Oxygen
100%	2.5×10^{-4}	Oxygen	Oxygen	Oxygen

The base pressure in this experiment was lower than 3×10^{-6} mbar, and as shown in Table 4.2, the total pressure was fixed at 2.5×10^{-4} mbar during deposition, where the gas from the neutraliser was considered for the overall gas percentages and fixed total pressure. The deposition process were carried out at room temperature.

Figure 4.1 shows a schematic diagram of the experimental setup for this experiment, where three ion sources and one neutraliser were focused on a Sc_2O_3 target. The beam sputtered the target, and the material was deposited on a rotating substrate to provide a uniform coating, the setup of which was the same as that described for the HfO_2 experiment.

As previously mentioned, the ion source parameters were controllable via LabVIEW, in which the microwave power input was between 3 - 5 W, the focus voltage was between 3 - 6 kV, and the beam voltage was kept constant at 10 kV for all sources. As described for the HfO_2 setup, during every deposition, the gas was injected into the neutraliser, where a separate controller from the ion sources was used to switch it on. The gas was introduced through the neutraliser until the pressure reached 1.8×10^{-4} mbar, which was the minimum pressure required to start the neutraliser.

4.3.3.3 Hafnia Silica Mixture

Hafnia-silica mixed (HfO_2:SiO_2) films were fabricated using the Combimat system (*Polygon Physics, France*), as shown in Figures 4.2, 4.3, and 4.4. The system consists of a source ring with 24 ion sources (Figures 4.2 and 4.3, #2) – however, within this experiment, one of the sources' microwave power is used to control the neutraliser to help the repel plate with the discharging inside the system. The targets used in these experiments were 11 × HfO_2 conical targets with a purity of 99.99% (*Testbourne, United Kingdom*) and 12 × SiO_2 conical targets with a purity of 99.99% (*Testbourne, United Kingdom*). The targets were placed on the target holder, which was located in the middle of the source ring (Figure 4.2, #3). The deposition time for all the deposition runs in this study was 24 hours.

The main aim of this experiment was to investigate the optical properties of different percentage mixtures of HfO_2:SiO_2 and the LIDT of the coatings. In this study, five different coatings were investigated: pure HfO_2, pure SiO_2 and mixed oxide coatings. Table 4.3 below shows the numbers of targets that were sputtered in order to vary the mixture percentages.

Table 4.3: The number of targets that are being sputtered by the ion sources for differing percentages

RUN NAME	**TARGETS**	
	HfO_2	SiO_2
C21F2310	11	–
C21F2416	–	12
C21F2910	11	12
C21G0810	10	4
C21G1210	11	2

In this experiment, the base pressure was approximately 1×10^{-6} mbar or lower, and the total pressure during the deposition was 4×10^{-4} mbar. This total pressure includes the reactive oxygen gas (1.1 sccm), argon gas for the sources (5 sccm), and pressure for argon through the neutraliser (5×10^{-5} mbar). The deposition process were carried out

at room temperature.

Figure 4.5 shows a schematic diagram of the system's sputtering process, where all sources are behaving the same as the singular source shown in that figure. As for the placement of the targets, half of the target holders consist of HfO_2 targets, and the other half are SiO_2 targets, as shown in Figure 4.7.

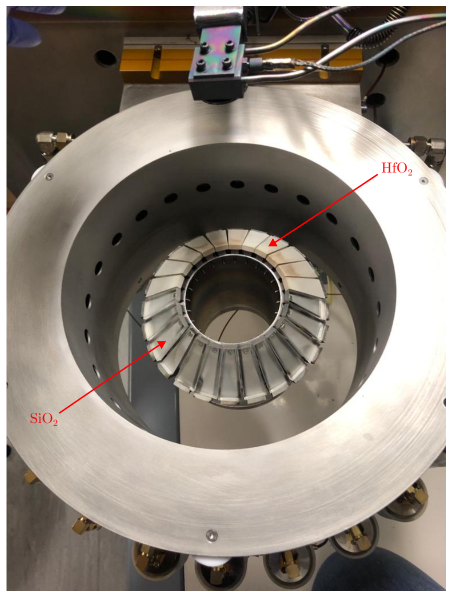

Figure 4.7: The target set-up for the HfO_2:SiO_2 coatings, where the white targets are HfO_2 and the clear targtes are SiO_2.

Each source was focused on the individual target in front of it, where it was then sputtered, and the material was deposited onto the rotating substrates for a uniform coating. To obtain different mixture percentages, a certain number of sources will remain on, while others will remain off, depending on the target percentages. This is also observed in Table 4.3. All the ion source parameters were controlled via LabView, where in this experiment, the microwave power for each of the individual sources was kept constant at 2 – 3 W, the focus voltage was 2 kV, the high beam voltage was 6 kV, and the repel voltage is -0.5 kV. The chosen parameters were utilised to provide the most stable process for each deposition, with the highest possible extraction current.

4.3.3.4 Scandia Silica Mixture

Similar to the HfO_2:SiO_2 films discussed in the previous section, the scandia-silica mixture (Sc_2O_3:SiO_2) films were fabricated using the Combimat system (*Polygon Physics, France*), as shown in Figures 4.2, 4.3, and 4.4. Similar to HfO_2:SiO_2, the targets used in these experiments were 12 × Sc_2O_3 conical targets with a purity of 99.99% (*Testbourne, United Kingdom*) and 11 × SiO_2 conical targets with a purity of 99.99% (*Testbourne, United Kingdom*). The targets were placed on the target holder, which was situated in the middle of the source ring (Figure 4.2, #3). The deposition time for all the deposition runs in this study was 24 hours.

The main aim of this experiment was to investigate the optical properties of different percentage mixtures of Sc_2O_3:SiO_2 and the LIDT of the coatings. In this study, four different coatings are discussed: pure Sc_2O_3 and mixed with SiO_2 coatings. Table 4.4 below shows the numbers of targets that were sputtered in order to vary the mixture percentages.

Table 4.4: The number of targets that were sputtered for each run

RUN NAME	TARGETS	
	Sc_2O_3	SiO_2
C21H3110	12	–
C21J0710	12	11
C21J2011	12	4
C21L0112	12	2

In this experiment, the base pressure was approximately 1×10^{-6} mbar or lower, and the total pressure during deposition was 4×10^{-4} mbar. This total pressure includes the reactive oxygen gas (1.1 sccm), argon gas for the sources (5 sccm), and pressure for the argon through the neutraliser (5×10^{-5} mbar). The deposition was performed at room temperature.

Figure 4.5 shows a schematics diagram of the system's sputtering process, where all

sources are behaving the same as the singular source shown in that figure. Regarding the placement of the targets, half of the target holder consists of Sc_2O_3 targets and the other half consists of SiO_2 targets, as shown below.

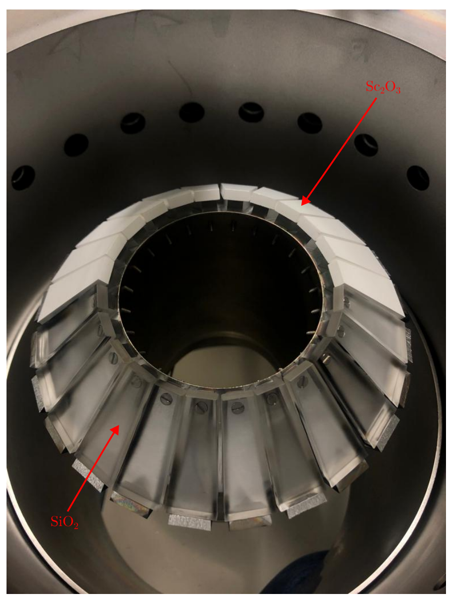

Figure 4.8: The target set-up for the Sc_2O_3:SiO_2 coatings, where the white targets are Sc_2O_3 and the clear targtes are SiO_2.

Each source was focused on the individual target in front of it, where it then sputtered the target, and the material was deposited onto the rotating substrates for a uniform coating. To obtain different mixture percentages, a certain number of sources will remain on, whereas others will remain off, depending on the aimed percentages. This is also observed in Table 4.4. All the ion source parameters were controlled via LabView, where in this experiment, the microwave power for each of the individual sources was kept constant at 2 – 3 W, the focus voltage was 2 kV, the high beam voltage was 6 kV, and the repel voltage is -0.5 kV. The chosen parameters were utilised to provide the most stable process for each deposition, with the highest possible extraction current.

4.4 Characterisation Setup

4.4.1 Spectrophotometer

The spectrophotometer used to acquire the transmittance and reflectance data is the Photon RT UV-Vis-IR Spectrophotometer *(EssentOptics Ltd., Belarus)*. The measurements were performed on JGS-3 substrates for the coatings discussed in this thesis unless stated otherwise. Photon RT can perform measurements in the wavelength range of 185 - 5000 nm. Photon RT utilises a deuterium lamp as the UV light source, a halogen lamp as the VIS-NIR light source, and IR-source is used for IR measurements. Figure 4.9a shows an image of the Photon RT.

To acquire the transmittance and reflectance spectra, the relevant light sources within Photon RT must be switched on. A calibration is carried out in the transmittance mode, with no samples inside, to obtain the baseline data. For the transmittance data, the sample was placed in front of the detector at a normal incidence, as shown in Figure 4.9b. To measure the absolute reflectance, the detector has to be 8° from normal for technical reasons, as shown in Figure 4.9c. At a small angle, the measured reflectance was not significantly different from that measured from normal incidence. As previously mentioned, once the spectra are obtained, optical modelling fitting software (in this case, SCOUT) can be used to estimate the optical properties of the thin films.

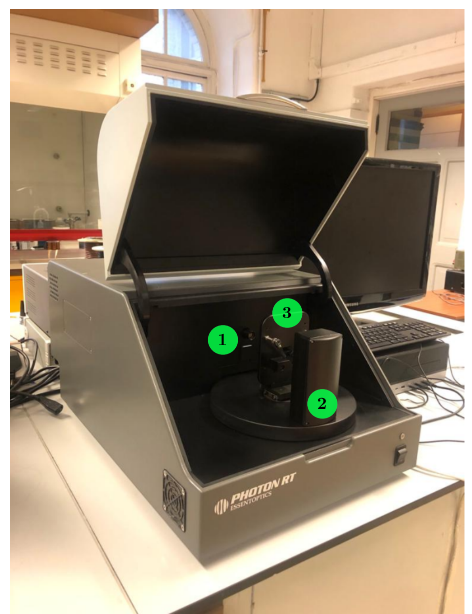

(a) Photon RT

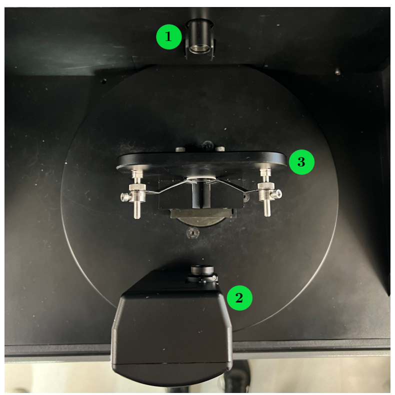

(b) Transmittance

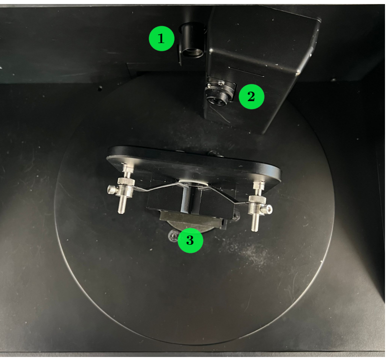

(c) Reflectance

Figure 4.9: Photon RT UV-VIS-IR Spectrophotometer, where (b) is showing the setup for transmittance, and (c) is showing the setup for reflectance. The number labels are as follow: (1) Light source, (2) Detector, and (3) Substrate holder.

4.4.2 XRD Setup

The XRD measurements in this thesis were carried out at Advanced Materials Research Laboratories (AMRL), situated at the University of Strathclyde (*Scotland, UK*), using a Bruker D8 Advance system with a Cu K_α X-ray source at $\lambda = 1.541$Å. Throughout this thesis, the BB method is used to measure the angles of $2\theta = 10 - 80°$, with 0.05°

steps. For the GIXRD method, this method was used to measure between the angles of $2\theta = 10 - 70°$, with 0.03° steps, and ω fixed at 0.5°. An image of the XRD system is shown in Figure 4.10.

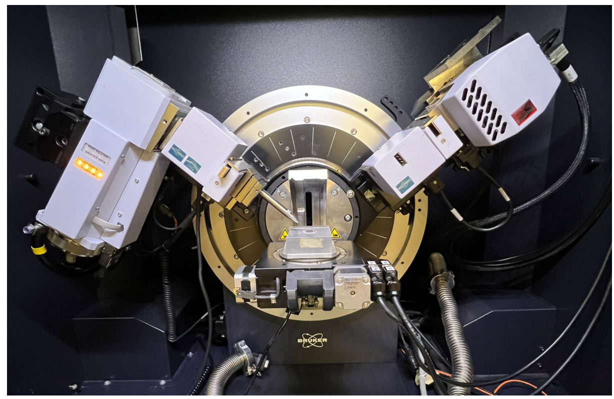

Figure 4.10: XRD system used within this project. The setup shown is for the BB-XRD method, where a collimator is used.

4.4.3 EDS Setup

EDS measurements taken in this thesis were performed at the Advanced Materials Research Laboratories (AMRL), situated at the University of Strathclyde (*Scotland, UK*). Elemental analysis and mapping of the samples were performed using a Hitachi S3700-N Scanning Electron Microscope (SEM) equipped with an Energy Dispersive Spectroscopy (EDS) system (Oxford Instruments X-Max 80). The measurements were performed at room temperature and operated at an accelerating voltage of 10 kV.

4.4.4 RBS Setup

The RBS measurements that were carried out on the samples in this study uses a 2 MeV ^{4}He beam. The beam was incident at an angle of 7° from the surface normal to minimise channelling effects and the detector was placed at a scattering angle of 170°. The atomic concentrations and layer thicknesses were determined by fitting the experimental spectra using the SIMNRA programme [136]. The RBS measurements

quoted in this thesis were performed by M. Chicoine at the University of Montreal, situated in Montreal, Canada.

4.4.5 LIDT Setup

The test setup used to carry out S-on-1 testing is shown in Figure 4.11. LIDT tests were carried out at RhySearch (*Buchs, Switzerland*) [30]. A pulsed Nd:YAG laser with a wavelength of 1064 nm and 100 Hz pulses was used as the laser source. The number of pulses per site (S) was 10, and the pulse duration was 11.6 ns. The laser travels towards the attenuator and HR mirrors, and then through the focusing lens towards the optics being tested. A focusing lens was used to set the irradiated spot size to the desired value. An energy monitoring photodiode was included in the setup to monitor the energy of the laser beam throughout the experiment. The optics is mounted on an XY-stage, which is used to position different test sites in the beam and to set the incidence angle (5° in this case). For *in situ* measurements, scattered light detection was used to measure any damage that may have occurred during LIDT testing. A Nomarski microscope was used *ex situ* to capture images of the damages after different energy fluences were carried out, which is not shown in Figure 4.11.

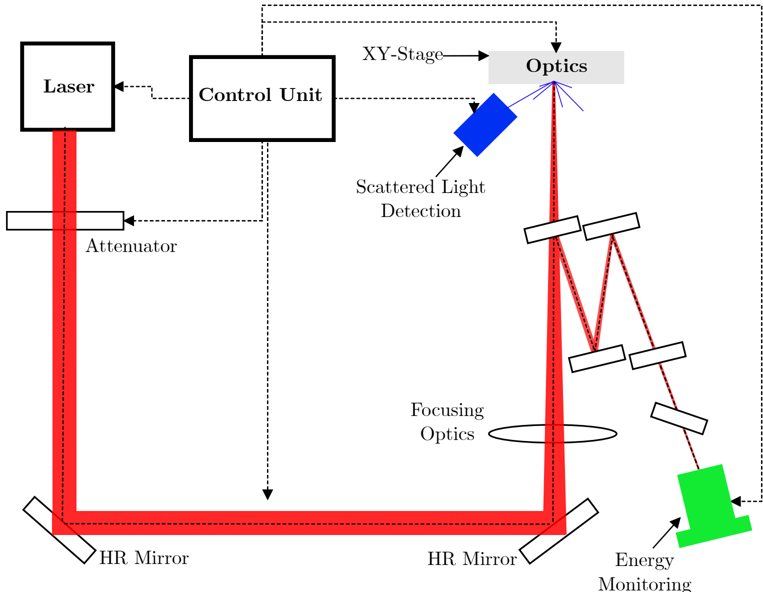

Figure 4.11: The schematics diagram of the S-on-1 LIDT setup provided by RhySearch [30]

The optics used to carry out LIDT testing were highly polished Corning 7979, and the tests were carried out in air. Two different tests were performed on the same sample. First, the samples were tested at as-deposited, then secondly, they were tested after annealing at 480° for 1 hour in air to observe any differences that may have occurred in the LIDT results.

4.4.6 Post-deposition Heat Treatment

All the samples investigated in this thesis were deposited at room temperature (RT), where some of these samples underwent post-deposition annealing treatment. The post-deposition annealing treatments were carried out in air using a Carbolite Gero CWF 1100 furnace (*Carbolite Gero Ltd.*). The samples were heated at a rate of 5°/min and held constant for a specific dwell time of 60 minutes, unless otherwise stated. The samples which underwent post-deposition annealing were annealed in steps of 100°C for the investigation. Finally, the samples were allowed to cool naturally to room temperature before further investigation.

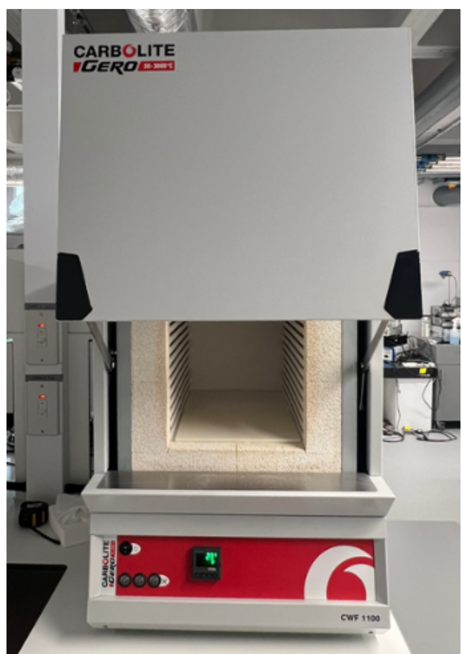

Figure 4.12: The Carbolite Furnace for annealing samples

5 | Hafnium Oxide

5.1 Introduction

Hafnium oxide, also known as Hafnia (HfO_2) is one of the most attractive high refractive index materials (n = 1.85 - 2.10) [137], high-κ dielectric, with excellent thermal and chemical stability [138] that are widely used in optical coating applications. They are also commonly used in multilayer coatings as the high index material, alongside low index materials like silica, where it can be utilised in interference filters, anti-reflective (AR) coatings, metal-oxide-semiconductor transistors [139], and cameras that can be used for space applications [137, 140, 141]. Other applications that HfO_2 films has been utilised aside for optical coatings are memory applications [138, 142, 143], ferroelectrics transistors which can be used for in-memory computing devices, as well as neuromorphic devices [144–146] and as HfO_2 based nanoagent in clinical trials for radio-sensitised tumour therapy [147]. HfO_2 has optical transparency over a wide spectral range, from ultraviolet (UV) to mid-infrared (mid-IR) region, due to its wide bandgap of 5.3 - 5.7 eV [38, 137, 148–151] alongside high laser induced damage threshold (LIDT), allowing it to often be utilised as the coating for optics in high power laser systems [4, 40, 150, 152–154]. These HfO_2 coated optics are utilised in filters or mirrors for laser spectroscopy, laser diodes, and multilayer high reflection mirrors for gravitational-wave interferometric detectors, for example [38–40]. Thus, understanding the optical properties and LIDT is extremely crucial for design and fabrication of high power laser optical devices. Although, from previous studies by many authors over the years, it

shows that HfO_2 has its favourable and advantages characteristics for different applications, but the optical and structural properties of the thin films can vary depending on the deposition methods, as well as deposition parameters [138, 140].

Thus, leading to HfO_2 films being deposited by common techniques, including e-beam evaporation [4, 74, 149], dual ion beam sputtering (DIBS) [154, 155], reactive low voltage ion plating (RLVIP), RF magnetron sputtering [156], high pressure reactive sputtering (HPRS) [157], pulsed laser deposition (PLD) [138] and ion beam sputtering deposition (IBSD) [72, 158], yielding inconsistent optical, electronic and structural properties. These inconsistencies reported in literature includes differences in films' stoichiometry due to the deposition method, crystalline phases, polycrystallinity, amorphous nature, density and defect states [138, 159–161]. These inconsistencies can also be largely associated with the deposition parameters, such as different beam power, working pressure and different percentages of argon and oxygen flow in the system during the fabrication of the films [161], where it can also affect the optical properties of the films (i.e. refractive index, bandgap energy and absorption) [162]. With these inconsistencies reported in film properties, it has been previously demonstrated that IBSD is a technique that is capable of the fabrication of high quality thin films, with properties close to those of bulk materials.

As for LIDT aspects within the literature, HfO_2 thin films that provides the highest LIDT are reported to be produced by utilising e-beam evaporation [74, 152–154]. However, these coatings demonstrated to have porous structures, where this is suitable for very demanding applications, typically in harsh environments for coatings, for example, high humidity, high temperature or even in space vacuum [141]. Due to the porous nature of e-beam evaporated coatings, there is a demand for denser films to be fabricated. Therefore, IBSD films have been shown to be a technique that is capable of fabrication of high quality thin films, where the high quality includes low scattering, high density, high refractive index, low absorption, good mechanical structural properties, and good environmental stability. The investigation of the purity, stoichiometric defects, and optical properties are of great significance for the preparation of high-quality coatings.

In this chapter, it is reported here a strategy for the optimisation of HfO_2 film properties by controlling the oxygen to argon ratio during the IBSD process. The films were produced by utilising ECR-IBSD (further discussed in Section 2.3.3.2), which is a novel process that has previously yielded the lowest IR absorption in amorphous silicon thin films [108], but otherwise under explored for optical coating development. The stoichiometry and elemental analysis of the films were carried out by EDS along with RBS. The structural properties of the films were determined by XRD, and the optical properties, such as refractive index (n), extinction coefficient (k) and bandgap energy (E_{gap}), were obtained by fitting the transmittance and reflectance spectra on SCOUT software, have been reported and discussed. The correlation between the reactive oxygen partial pressure and HfO_2 films properties are presented. Furthermore, the effects of annealing of these thin films on the structure and optical properties are presented and discussed, where the results and discussion of the as-deposited and the annealing studies have been split into two separate parts.

5.2 As-Deposited HfO_2 Films

Within this first part, the results for as-deposited HfO_2 thin films fabricated by ECR-IBSD have been presented and discussed.

5.2.1 Results

5.2.1.1 Transmittance and Reflectance Measurement

The main goal of the experiment is to investigate the effects of different oxygen partial pressure on the optical properties of the thin film coatings. The optical properties that are in focused are: refractive index (n), extinction coefficient (k) and Bandgap energy (E_{gap}). The thickness (d) of the coatings are also obtained the same way. In order to extract these properties, the transmittance and reflectance data were obtained using

the Photon RT.

Figure 5.1 shows the transmittance and reflectance measurements for all three configurations of the experiment. As previously mentioned, all the deposition runs has the same overall pressure during deposition, same deposition time and also the same base pressure. The absorption peaks measured at 2700 nm (very predominant in the transmittance data) are the water absorption peaks, which are associated with the substrate material. As described in Section 4.3.3.1, for varying oxygen content configuration (i) are shown as solid lines in Figure 5.1a; configuration (ii) is shown as dashed lines in Figure 5.1b; and configuration (iii) is shown as dotted lines in Figure 5.1b.

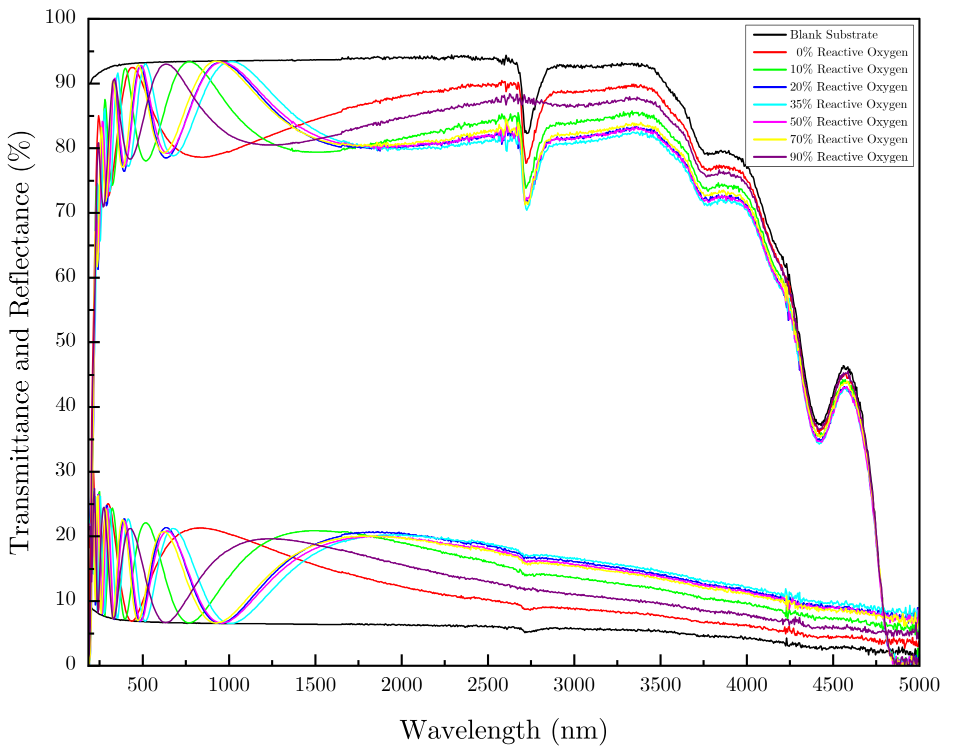

(a) Transmittance and reflectance data for configuration (i)

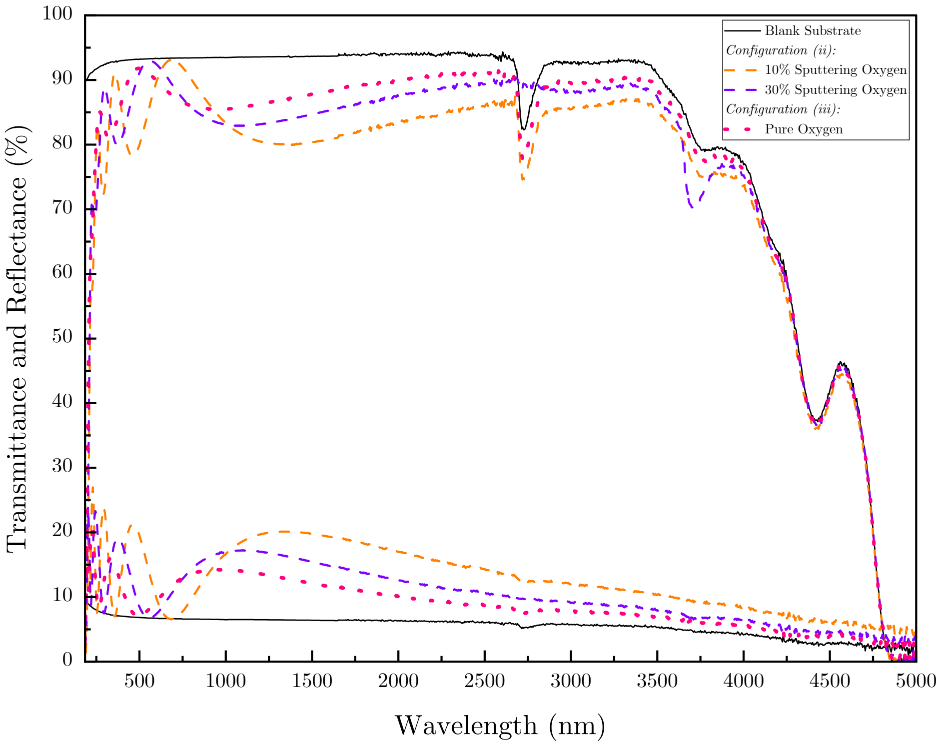

(b) Transmittance and reflectance data for configuration (ii) and (iii)

Figure 5.1: The transmittance and reflectance data obtained for the three configurations by utilising the Photon RT, where the data for blank substrate has been included.

As shown in Figure 5.1, the higher the oxygen content percentage, the transmittance also increases - where this can be seen the most prominently in the range of 1500 - 3000 nm. In example, for configuration (i) 10% reactive oxygen (green, solid line, Figure 5.1a) has a lower transmittance (and higher reflectance) than that of 90% reactive oxygen (purple, solid line, Figure 5.1a) in this wavelength range. This is also true for configuration (ii), where 10% sputtering oxygen (orange, dashed line, Figure 5.1b) has a lower transmittance (and higher reflectance) than that of 30% sputtering oxygen (violet, dashed line, Figure 5.1b) within this wavelength range. Alongside, configuration (iii), where this is the pure oxygen process (pink, dotted line, Figure 5.1b) has the highest transmittance, and lowest reflectance out of all three configurations.

It can also be observed that the transmittance data of samples shown exhibit interference effects. These interference fringes can be used as an indicator for the thickness of the films [163], where it can be observed that the films have different thickness due to the different configurations and oxygen percentages. As previously mentioned, all coatings have the same deposition time of 72 hours, where the thicknesses variations are shown in Section 5.2.1.4, dependent on the deposition configurations. From Figure 5.1, the data shows that by varying the oxygen content, for all three configurations, this has an effect on the transmittance and reflectance data, along with other optical properties, which will be discussed in the following sections.

However, in Figure 5.1a, at 0% oxygen partial pressure, where there is only argon inside the chamber through the ion sources, has yielded unexpected results. It can be seen that for this data, it has the highest transmittance (and lowest reflectance), and also with the least number of fringes - indicating a much thinner sample - compared to the other samples within this configuration. The possible explanation for this will be further discussed in the discussion section.

5.2.1.2 Refractive Index and Extinction Coefficient

As previously mentioned, by utilising SCOUT optical fitting software to fit the transmittance and reflectance data acquire from the Photon RT, one can obtain the optical constants. In Figure 5.2 below shows an example of the experimental data and the stimulated of transmittance and reflectance by utilising SCOUT, where an ideal fit has been obtained. From this, the n, k, E_{gap} and thickness can be extracted, where the "OJL2" model is utilised in SCOUT (further discussed in Section 3.4.1). From Figure 5.2, it can be seen that there are minimal differences between the experimental data and the simulated data (an ideal fit), which is important as this provides the confidence that the extracted data from SCOUT is accurate.

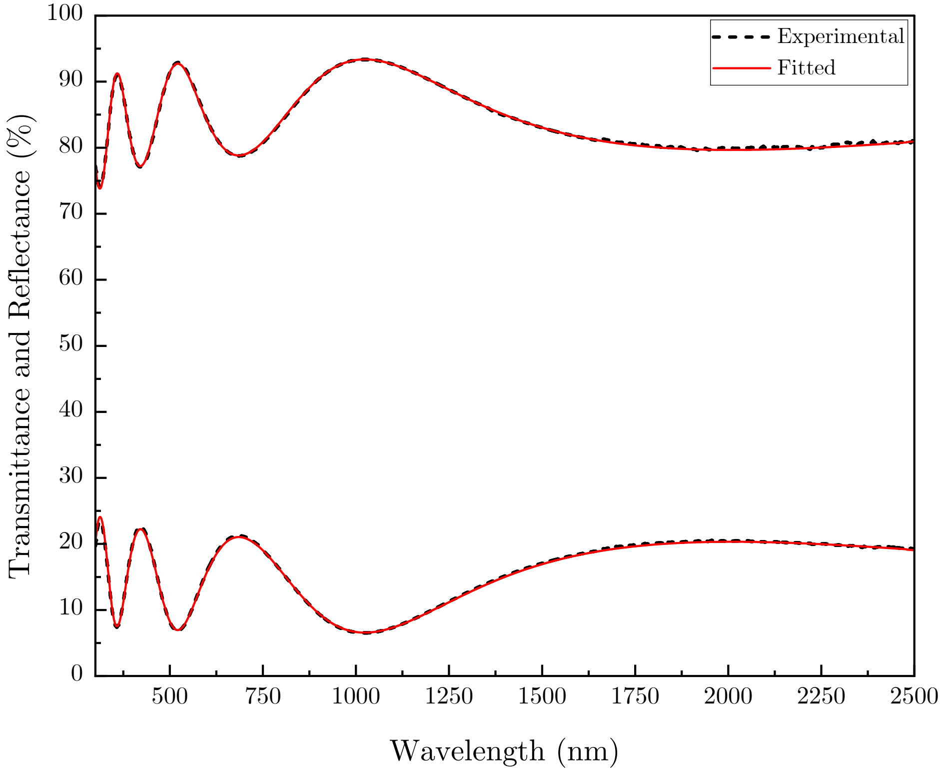

Figure 5.2: Example of Experimental and Fitted data from SCOUT for one of the samples discussed in this chapter.

In Figure 5.3 below, shows the refractive index of the HfO_2 films investigated in this chapter. Figure 5.3a and Figure 5.3b shows the refractive index of the three configurations, where Figure 5.3a shows the dispersion of the refractive index from the wavelength range of 200 - 2500 nm, and Figure 5.3b shows the refractive index extracted for a fixed wavelength of 1064 nm. This wavelength is chosen as Nd:YAG lasers operating at 1064 nm are widely used in many high power laser systems, including for military, medicine, and spectroscopy purposes.

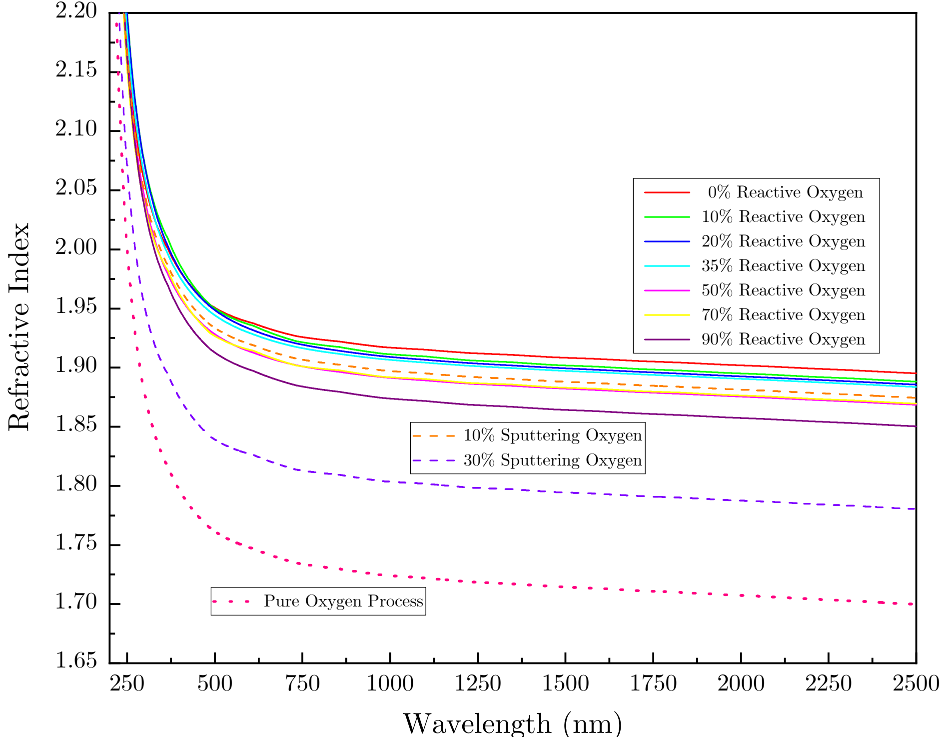

(a) Dispersion of the refractive index for the range of λ = 200 - 2500 nm.

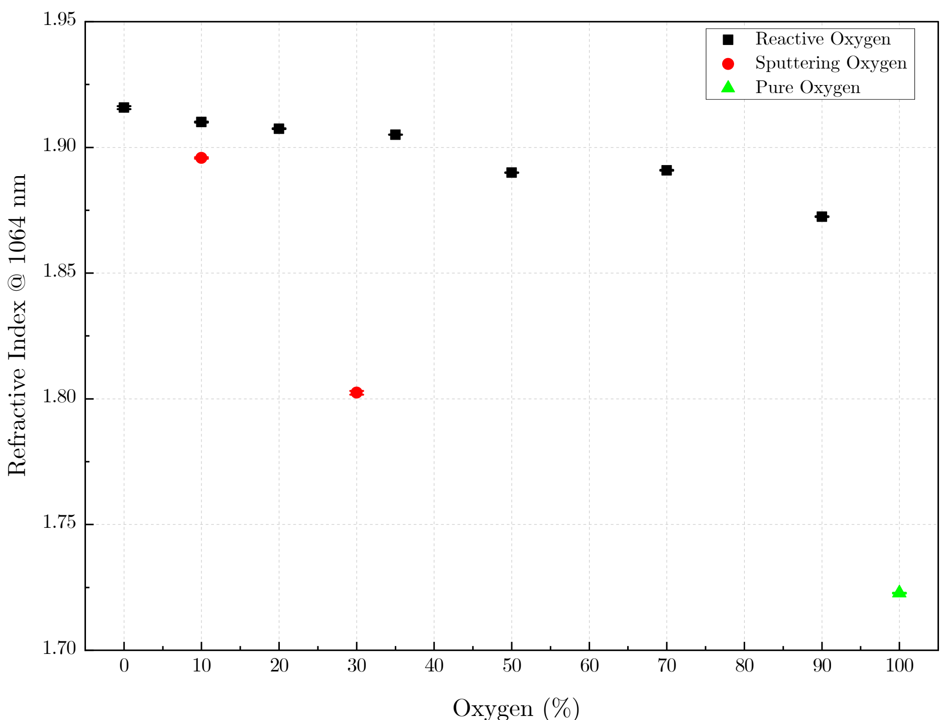

(b) The refractive index at $\lambda = 1064$ nm. The error bars show the standard deviation of five separate fittings for each sample.

Figure 5.3: The refractive index of all three configurations.

Figure 5.3a shows that as the oxygen concentration increases, the refractive index decreases for all three configurations. Here, it can be seen that the pure oxygen process possesses the lowest refractive index, and the 0% reactive oxygen process possesses the highest refractive index. Figure 5.3b also shows that 0% reactive oxygen has the highest refractive index of $n = 1.92$ at 1064 nm, and this decreases as the oxygen background percentage increases, where at 90% reactive oxygen, $n = 1.87$. The overall lowest refractive index at 1064 nm is for the pure oxygen process with the value of $n = 1.72$. The data and results shown here are quoted from the average values from SCOUT fittings, where the coatings from each run were fitted five times. The errors quoted are from the standard deviation of these fits, which are consistent across all errors referenced in this thesis, unless explicitly noted otherwise.

As shown in both Figure 5.3a and Figure 5.3b, the refractive index decreases with increasing oxygen. While for configuration (i), the refractive index decreases $\sim$3% from

the highest value at 1.92 (0%) to the lowest value of 1.87 (90%), configurations (ii) and (iii) for sputtering with oxygen has a higher impact - where from 10% oxygen to 100%, the refractive index value decreases by 10% (from 1.90 to 1.72).

In Figure 5.4 below shows the extinction coefficient of the HfO_2 films investigated within this chapter. Figure 5.4a and Figure 5.4b shows the extinction coefficient of the three configurations, where Figure 5.4a shows the dispersion of the extinction coefficient from the wavelength range of 200 – 2500 nm, and Figure 5.4b shows the extinction coefficient at a fixed wavelength of 1064 nm, similar to that of the refractive indices figures (Figure 5.3a).

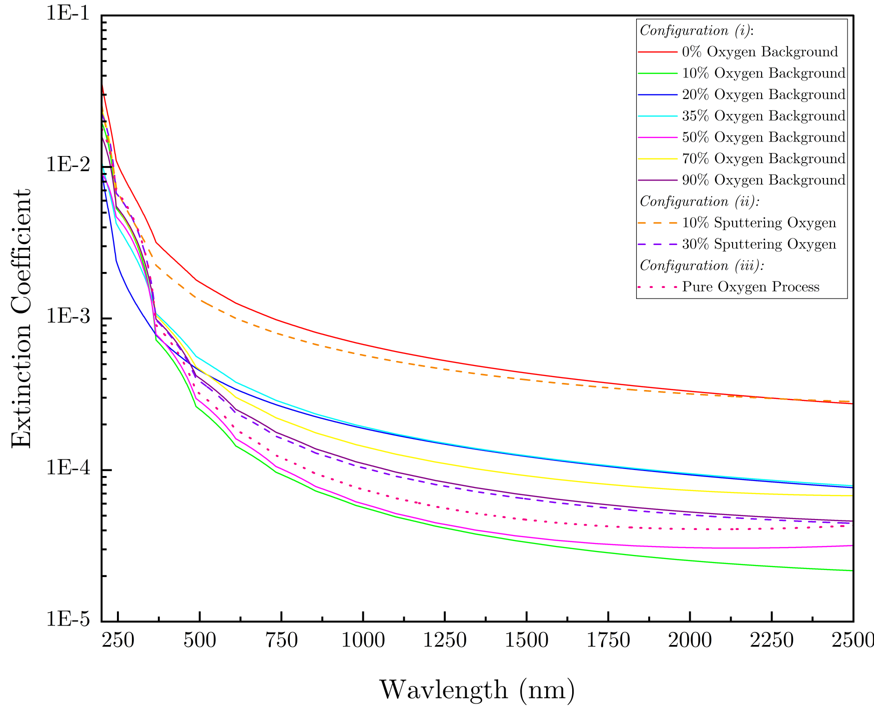

(a) Dispersion of the extinction coefficient for the range of λ = 200 - 2500 nm. Y-axis displays the extinction coefficient on a logarithmic scale.

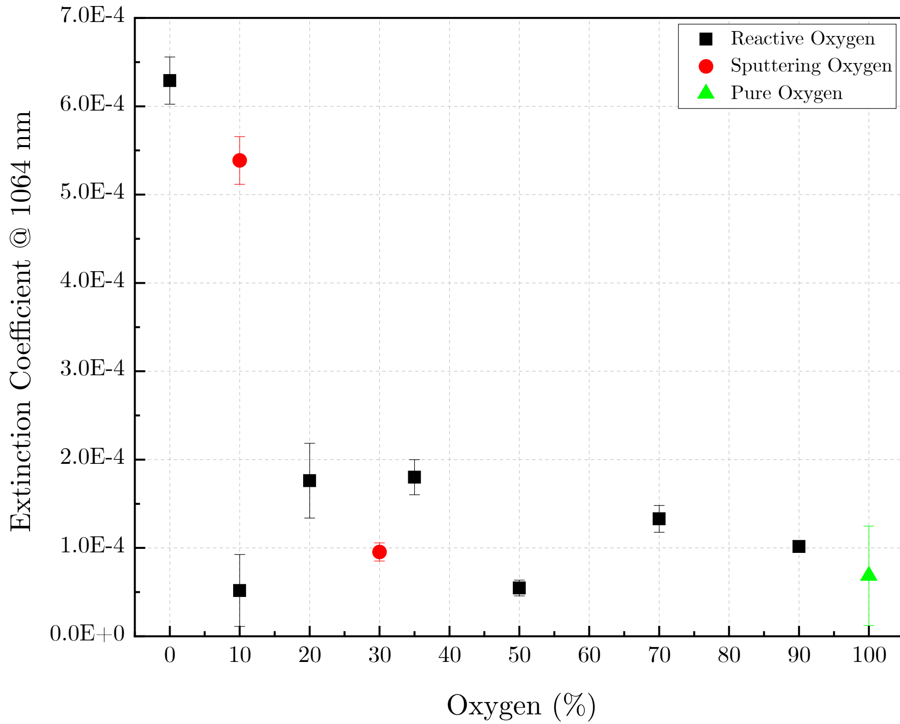

(b) The extinction coefficient at λ = 1064 nm. The error bars show the standard deviation of five separate fittings for each sample.

Figure 5.4: The extinction coefficient of all three configurations.

Figure 5.4 shows that as the oxygen concentration increases for configuration (i), the extinction coefficient decreases, where at 10% and 50% reactive oxygen posses the lowest values. The same can also be seen for configuration (ii) and (iii), where as the sputtering oxygen percentage increases, the extinction coefficient also decreases. In Figure 5.4a also shows a sharp decline of the extinction coefficient with increase in wavelength in the UV region, where this then slowly continues to decrease as it reaches mid-IR for all samples.

From Figure 5.4b, it can be seen that for configuration (i), at 0% reactive oxygen yielded the highest value of $k = 6.29 \times 10^{-4}$, whereas at 10% yielded the lowest value of $k = 5.18 \times 10^{-5}$. Although at higher reactive oxygen percentage than 10%, the extinction coefficient has increased, then decrease as the reactive oxygen is increase, it still shows a similar trend to that of configuration (ii) and (iii), where as the oxygen

incorporation increases, the extinction coefficient decreases. For configuration (ii) and (iii), the highest and lowest extinction coefficient values are 5.39×10^{-4} and 6.85×10^{-5}, respectively.

5.2.1.3 Bandgap Energy

Figure 5.5 shows the bandgap energy of HfO_2 films, extracted from the OJL gap energy model. For configuration (i) [black square], Figure 5.5 shows that at 35% reactive oxygen partial pressure has the lowest bandgap energy of 5.6 eV, however, within the error range, from 0 – 50% reactive oxygen partial pressure, the bandgap energies are within the same values of 5.65 ± 0.05 eV. For configuration (ii) [red circle], the bandgap energy increases with the increasing percentage of oxygen used as sputtering gas, from 5.69 eV at 10% sputtering oxygen to 5.82 eV at 30% sputtering oxygen. As for configuration (iii) [green triangle], the pure oxygen process provides the highest bandgap energy at 6 eV. The overall trend that can be concluded from Figure 5.5 is that as the oxygen concentration increases for each configuration, the bandgap energy also increases.

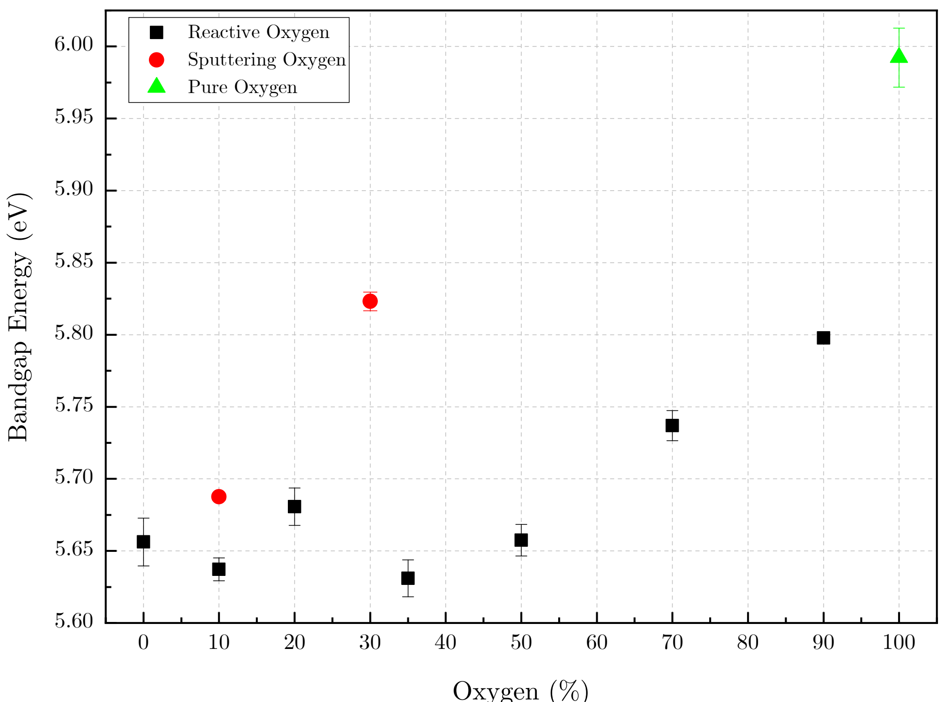

Figure 5.5: The average bandgap energy of the films acquired from SCOUT for all three configurations. The error bars show the standard deviation of five separate fittings for each sample.

5.2.1.4 Thickness

Another value that can be extracted from SCOUT fittings is the estimated thin film thickness. Figure 5.6 shows the thicknesses of the coatings at each oxygen percentage for the three configurations. As mentioned, all coating depositions has the same deposition time of 72 hours.

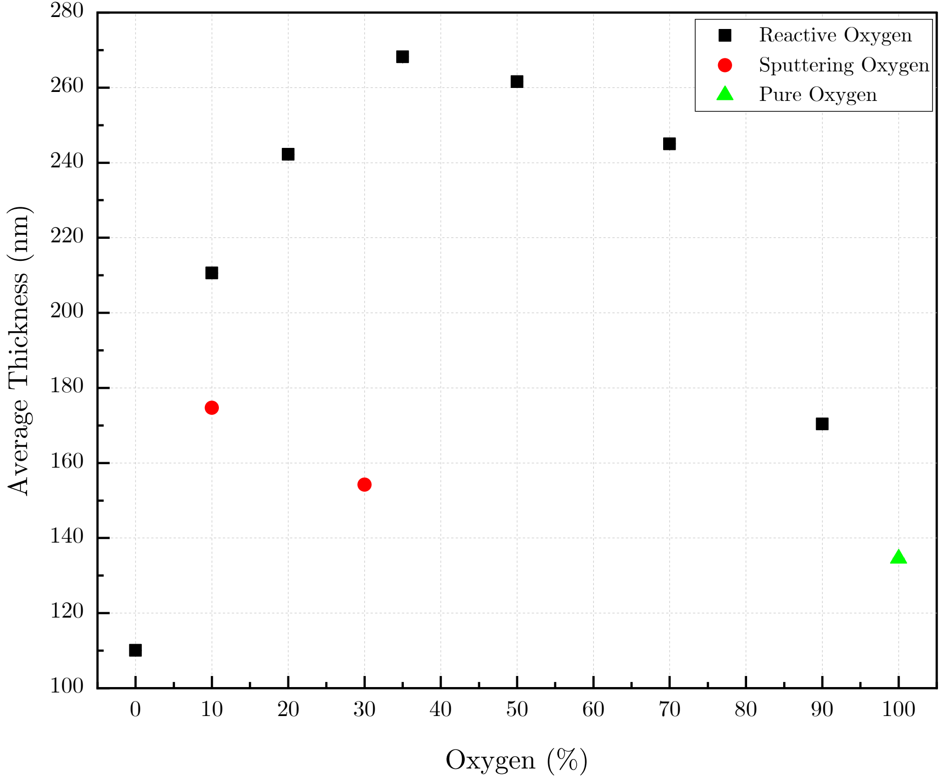

Figure 5.6: The average thicknesses of the films acquired from SCOUT for all three configurations.

From Figure 5.6, it can be seen that at 35% reactive oxygen has the highest thickness of 268 nm and at 0% oxygen background has the lowest thickness of 110 nm for configuration (i). As previously mentioned, this is an unexpected result for 0% Reactive Oxygen, as one would expect this to yield the highest deposition rate, and hence, highest thickness. Further discussion in to the possible explanation will be discussed in later section. As for configuration (ii), the highest thickness is at 10% sputtering oxygen at 175 nm, whereas for configuration (iii), the pure oxygen Process has the overall lowest

thickness of 135 nm. The thicknesses values are also shown in Table 5.1 below.

Table 5.1: The different thicknesses of HfO_2 thin films with different configurations

OXYGEN PERCENTAGE (%)	THICKNESS (nm)
Configuration (i)	
0%	110
10%	211
20%	242
35%	268
50%	262
70%	245
90%	170
Configuration (ii)	
10%	175
30%	154
Configuration (iii)	
100%	135

5.2.1.5 EDS / RBS Results

The atomic composition of the deposited HfO_2 films measured by EDS is shown in Figure 5.7. The only elements detected by utilising EDS in all coatings are O, Hf, and Ar. In Figure 5.7a and Figure 5.7b, the atomic percentage of oxygen and hafnium present in the films are provided. Figure 5.7d shows the ratio between oxygen and hafnium present. By increasing the background oxygen partial pressure over 35%, an increase of the oxygen concentration in the films is observed. The highest value of oxygen concentration in the films was acquired by 30% sputtering oxygen, where the O:Hf ratio is 4.45:1 [red circle]. Note that the composition for the pure oxygen process and 0% oxygen was not measured by EDS. From Figure 5.7d, it can be seen that all coatings have an excess of oxygen, and are over-stoichiometric due to the measured O:Hf ratios being above 2:1, where the lowest is 2.4:1 at 20% background oxygen [black square]. Figure 5.7c shows the Ar atomic percentage measured by EDS. For all films within this study,

the Ar concentration is lower than 2.5%. The decrease in Ar concentration is correlated with the oxygen increase, as shown in Figure 5.7a. However, at 30% sputtering oxygen (red circle), there are no Ar incorporated within the films.

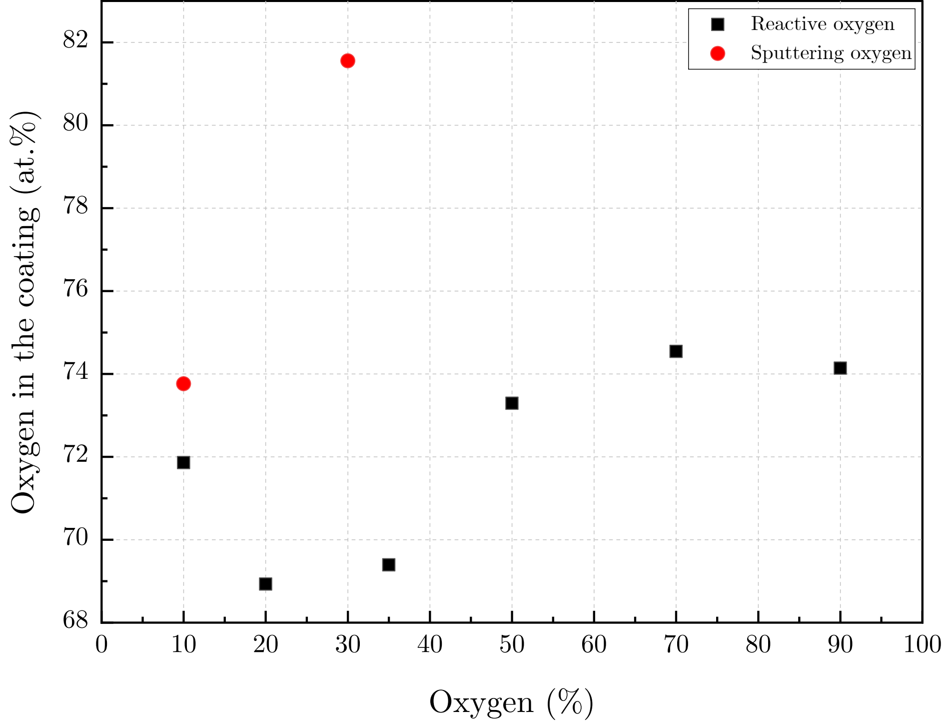

(a) Atomic oxygen percentage in the films vs oxygen percentage of total gas flow during deposition

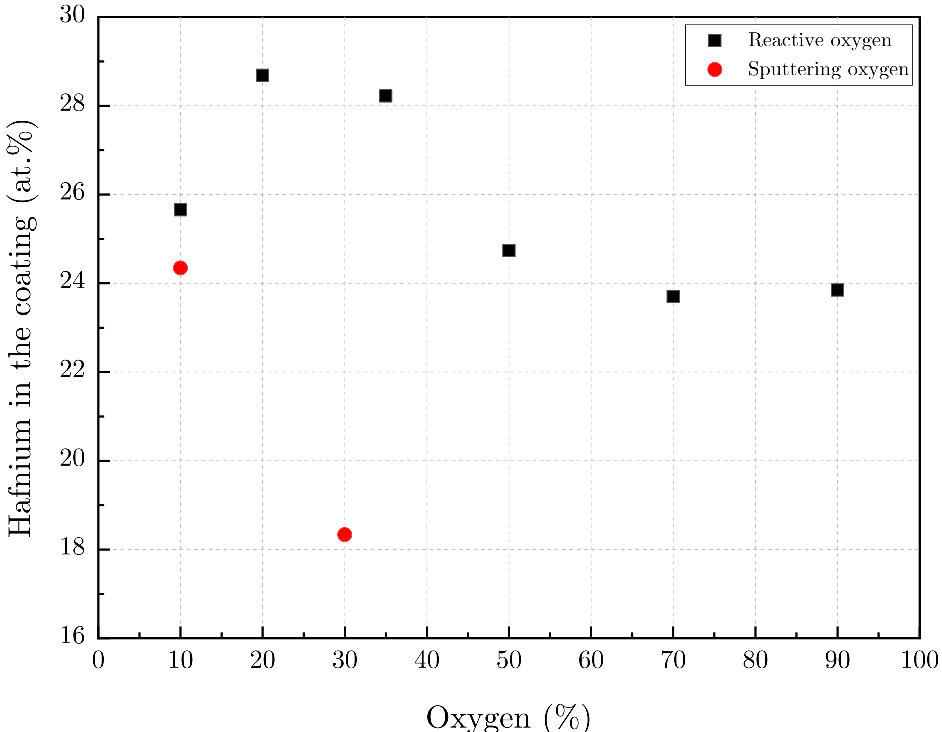

(b) Hafnium percentage in the films vs oxygen percentage of total gas flow during deposition

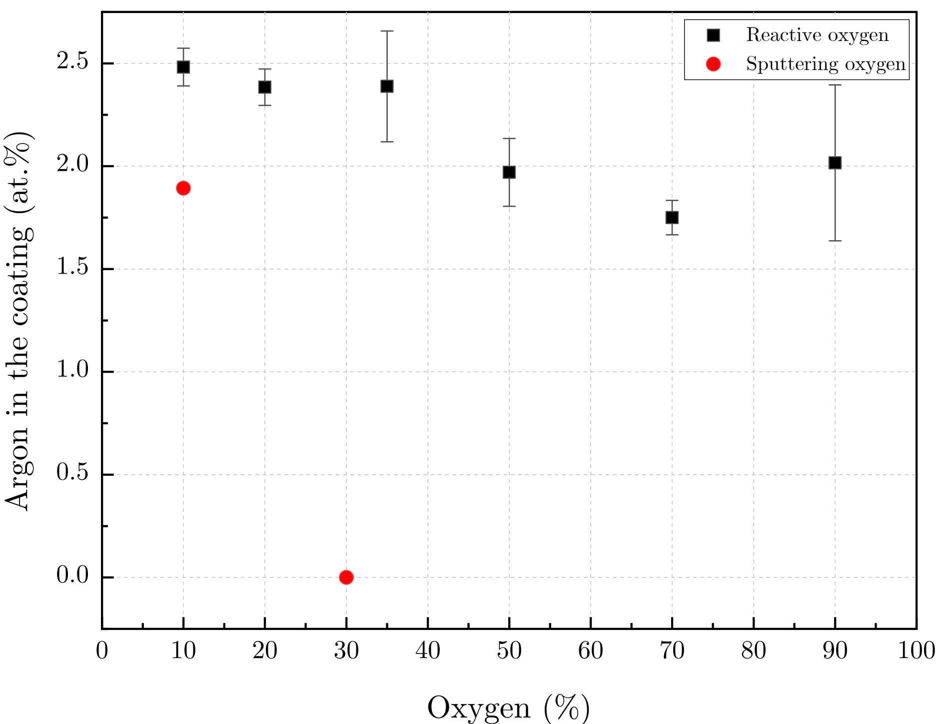

(c) Argon percentage in the films vs oxygen percentage of total gas flow during deposition

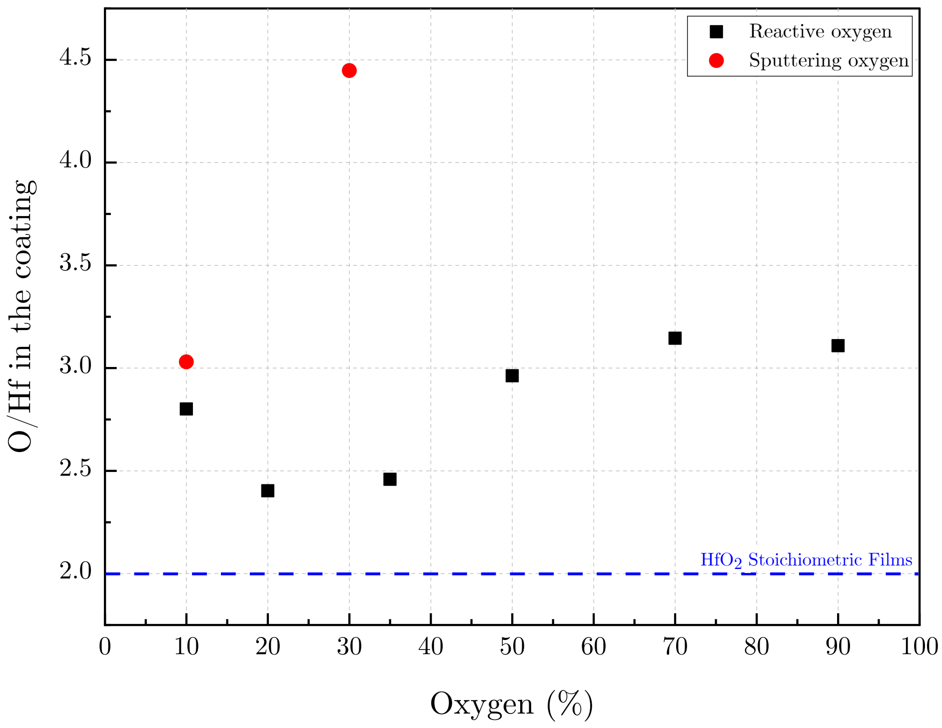

(d) O to Hf Ratio in the films vs oxygen percentage of total gas flow during deposition

Figure 5.7: EDS data for configurations (i) and (ii), where configuration (iii) and 0% Oxygen Background samples were not measured.

Due to the high O:Hf content shown in Figure 5.7d, RBS measurements were also carried out to confirm the O:Hf content and the stoichiometry of the films. Figure 5.8 shows the O:Hf content acquired by utilising RBS method. As shown, the results are slightly different to that of EDS results (Figure 5.7d). However, the RBS results are in agreement with EDS results, where the films discussed within this study are all over-oxygenated, and therefore, over-stoichiometric. As previously mentioned, for stoichiometric HfO_2 thin films, the O:Hf ratio must be 2:1, where in this case (based on RBS results, Figure 5.8), the lowest O:Hf ratio in this study has the value of 2.5:1 at 0% background oxygen [black square]. Alongside, the highest O:Hf ratio in this study, based on RBS results, is 3.89:1 at pure oxygen process [green triangle].

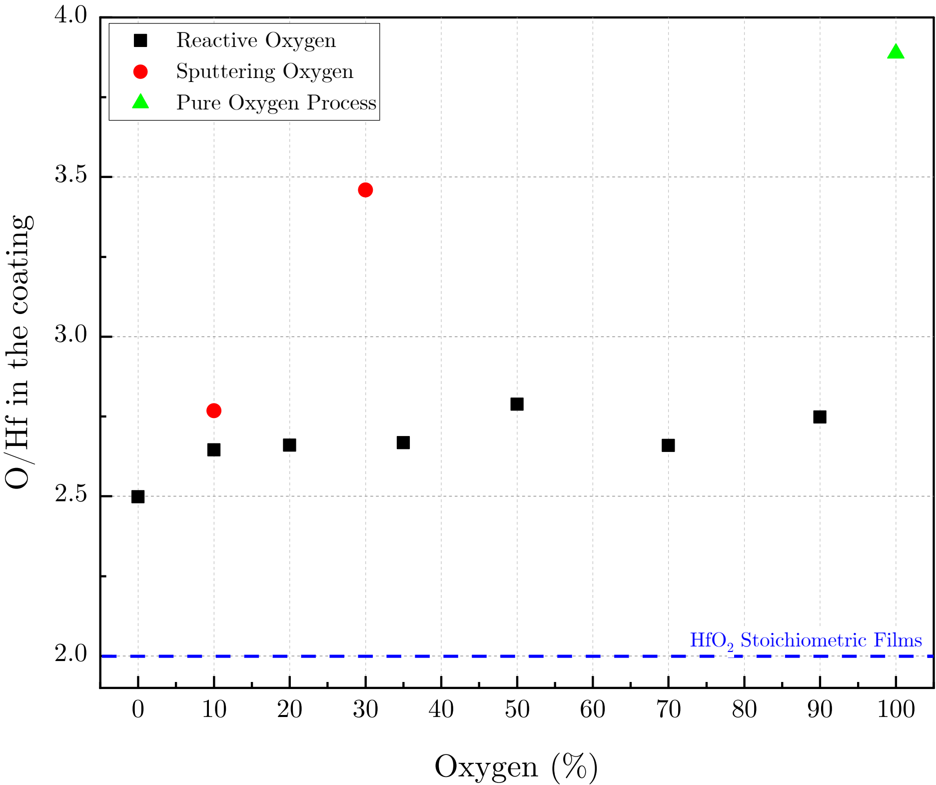

Figure 5.8: RBS data acquired for the films discussed in this chapter. The data was measured by M. Chicoine.

5.2.1.6 XRD Results

Figure 5.9 shows the XRD pattern of pure HfO_2 films with varying oxygen content of all three configurations. As can be seen from the XRD data, all HfO_2 films show a broad weak band, which indicates that all of the films in this study are amorphous. XRD data for a blank substrate is also included to show the peak centred at $\sim 21°$ in all samples is from the substrate. The XRD data shows minimal difference between the blank substrate and coated substrates, which further demonstrates that the HfO_2 thin films in this experiment are amorphous. Also included in the figure is a sample annealed to 500°C from the pure oxygen process, which shows the emergence of narrow peaks compared to the as-deposited films. These narrow peaks are an indicator to the increasing crystalline structure when the films are annealed, and are denoted by * in Figure 5.9. This is further confirmation that the as-deposited samples investigated are

in fact amorphous.

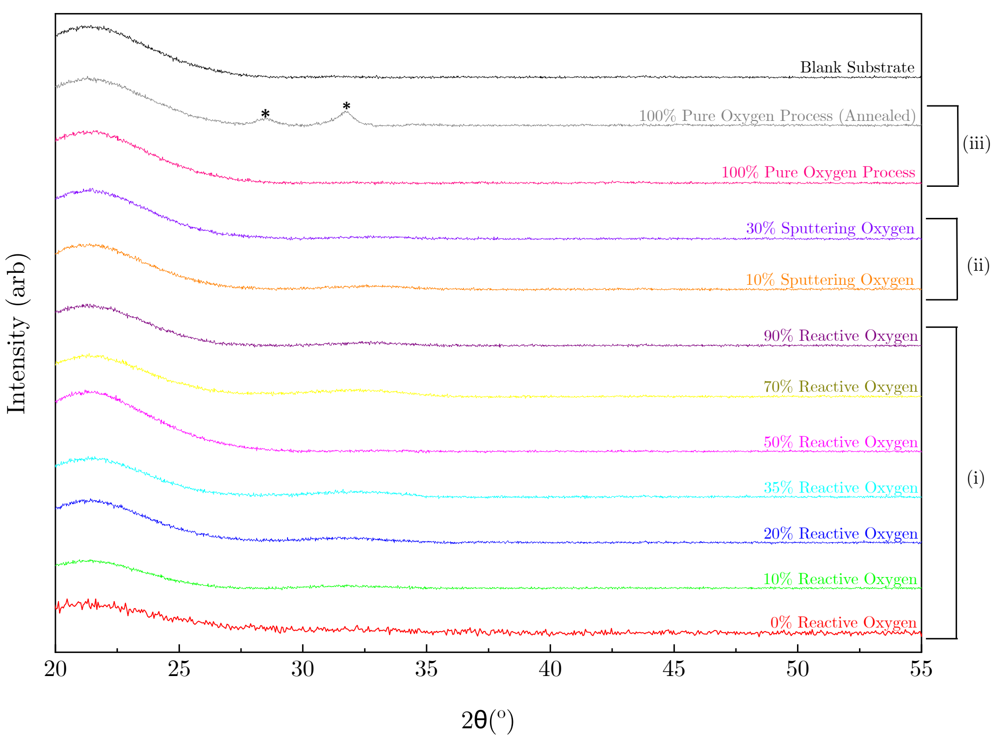

Figure 5.9: XRD data acquired for the as-deposited films in this study, by utilising the Bragg-Brentano method. (*) denotes the peaks that are emerging for the annealed sample, in comparison to the as-deposited samples.

5.2.2 Discussion

The transmission spectra measured for all films presented in Figure 5.1 show a high transmission from the UV to mid-IR (~300-3000 nm) which makes HfO_2 an interesting material for optical applications. At the wavelength of ~2700 nm, it can be seen that in the transmittance data, there are absorption peaks. This absorption is common in fused silica substrates, where this band corresponds to the OH absorption band (or "water band") [164]. It can also be seen that they are substrate-dependent, as not all of the transmittance data shown in Figure 5.1 possess this absorption peak. As this absorption peak is only due to the substrates, it is negligible when it comes to the discussion of the films optical constants in this study as the optical fittings in SCOUT were only carried out from 200 to 2500 nm to avoid the absorption peak that is only prominent in certain

samples.

The XRD data in Figure 5.9 shows that all coatings within this experiment exhibit a very broad wide band and minimal difference compared to blank substrates, which demonstrates that the HfO_2 films in this experiment are amorphous. The XRD data for annealed HfO_2 fabricated within the same pure oxygen process is shown to exhibit narrow peaks, where this shows that the film is becoming more crystalline in nature. This is in contrast to the broad peak of the films within this investigation, further verifying that the films are amorphous, even with the increase of oxygen content at room temperature.

The EDS compositional analysis presented in Figure 5.7 shows that, within the measurement certainty of circa 0.1%, only Ar, O, and Hf species are observed. High purity films are expected from the ECR-IBSD process, due to a highly confined, filament-free plasma generation in addition to the extraction of ions through a single aperture. The single aperture extraction allows high extraction potentials and eliminates the requirement for extraction grids that are a source of contamination in standard IBSD processes. As shown in Figure 5.7c, the films contain interstitial argon in the range 1.7 – 2.5%, which is typical in IBSD processes, where inert gases are used as the sputtering species, and trapped atoms can create "nanobubbles" [158]. However, the 30% sputtering oxygen process (configuration (ii), where argon is only utilised via the neutraliser) and pure oxygen process (configuration (iii), based on RBS results), does not have any Ar within the films, due to no use of ionised argon during the deposition process. The amount of Ar that exists within the films in this study is slightly higher than the Ar solubility in solid materials ($\sim$1%) [158,165], however, this is still less than that of conventional RF-IBSD systems (6 – 10%) [158]. This surplus of Ar quantity is associated with the implantation of the reflected neutral atoms with high kinetic energies, where the backscattered argon are incorporated into the coatings, along with the film-forming particles, as the angular distribution of each of these have some overlap as they leave the target surface [20,158,166]. These Ar atoms will accumulate to form bubbles within the HfO_2 matrix due to the inert nature of the gas. Whilst the fraction of argon in these

samples are low, the quantity of implanted argon bubbles [158] decreases with increasing oxygen adsorption in the films. It is likely that the different oxygen regimes across the range of the samples within this investigation play different roles in the deposition process and resultant thin film properties. The presence of nanobubbles, both due to the entrapment of Ar and O_2 molecules, may have an effect on the absorption of thin films, alongside the LIDT if used in laser systems, as the trapped nanobubbles can lead to optical breakdown due to laser exposure. Further investigation into the nanobubbles and the effect on absorption and LIDT results produced by films utilising ECR-IBSD will be of interest to study.

In addition, from both the EDS measurements and RBS measurements, the films presented are all over-stoichiometric in relation to the composition of the HfO_2 target (2:1 is the expected O:Hf ratio). Different mechanisms are thought to be the cause for the over-stoichiometry:

I. Interstitial oxygen in the films, where the oxygen molecules are supplanted in the interstitial sites within the HfO_2 lattice, where the oxygen aggregates in the films [167];

II. Higher coordination number compounds are bonded during the deposition due to the high energy process (e.g. HfO_x, where x $>$ 2) [168].

However, as Hf does not have a stable oxidation state to allow for bonding of three O atoms, the possibility of higher coordination compound like HfO_3 can be ruled out. In turn, this leads to the conclusion that the over-stoichiometry observed are due to the interstitial oxygen within the films.

The decreasing refractive index of the films at higher reactive oxygen partial pressure, as shown in Figure 5.3, where the literature value reported is $n = 1.88$ at 1064 nm for HfO_2 thin films, and $n = 2.1$ (at 550 nm) for bulk HfO_2 [148, 149, 169, 170] can be attributed to the interstitial oxygen that exists within the lattice. Alongside the decrease in refractive index observed due to interstitial oxygen, this also leads to the

increasing bandgap behaviour (Figure 5.5), particularly increasing to greater than the reported bandgap values (5.3 – 5.7 eV) [149,151].

With the increase of oxygen content and O:Hf ratios, changes can be observed most prominently in the increased transmittance data (Figure 5.1), especially in the mid-IR region of the samples deposited (λ = 1300 – 3000 nm). At 90% reactive oxygen (configuration (i)), where the O:Hf ratio is ~3:1, the transmittance has increased the most compared to other spectra in the same configuration (i), as shown in Figure 5.1a. At 30% sputtering oxygen (configuration (ii)), where the O:Hf ratio is ~4.45:1 (from EDS, and ~3.5:1 from RBS), provides an even higher transmittance than that of reactive oxygen configuration; and the pure oxygen process (configuration (iii)), where this has the highest transmittance out of all three configurations (Figure 5.1b) with O:Hf ratio of ~4:1 (Figure 5.8, green triangle).

Figure 5.3 shows that as the oxygen content increases, for all configurations, the refractive index decreases. This reduction in refractive index related to the increase of reactive oxygen partial pressure in configuration (i) could also be associated to the reduced packing density, which also leads to the increase in the bandgap energy when comparing between the samples within the same configuration. As previously stated, in literature, the refractive index of HfO_2 thin films is n = 1.88 at 1064 nm, where the films were fabricated by electron beam evaporation [148,149]. For films in configuration (i), the overall refractive index at differing reactive oxygen percentages is higher than reported values, where this could be due to the higher overall packing density through the use of ECR-IBSD when compared to films fabricated by other processes, such as electron beam evaporation or magnetron sputtering, when the films are still amorphous. Figure 5.3 also shows that the refractive index is lower when utilising oxygen as sputtering gas compared to argon, where this is most apparent in the pure oxygen process (configuration (iii)).

As for the optical bandgap energy, this is affected by many factors: defect density, purities, packing density, stoichiometry, etc. As previously stated, the bandgap energy

of HfO_2 reported in the literature is 5.3 – 5.7 eV [149,151]. It can be seen that in this work, by increasing the oxygen content during the deposition, the bandgap energy can be manipulated to be higher than that of the reported values, as shown in Figure 5.5. Other researchers [38] have reported the values of 5.59 – 5.68 eV with increasing reactive oxygen partial pressure, and another group [161] have reported the values of 5.58 – 5.83 eV, where the work within this study provides the values in the range of 5.6 – 5.8 eV by increasing the reactive oxygen partial pressure (configuration (i)). As for configuration (ii) and (iii), the bandgap energies are in the range of 5.69 – 6.0 eV. This shows that as the oxygen content increases, the bandgap energy increases, which is in agreement with other groups' findings [161,171]. In addition, there is also a slight blue-shift of the transmittance data (Figure 5.1), at the UV range for the absorption edge, that can be seen with the increase of oxygen content. This absorption edge is associated with the bandgap energy, and the shift seen is known as Burstein-Moss shift, where this shift to lower wavelengths of the absorption edge is associated with the increase of bandgap energy.

As stated earlier, the decrease in refractive index and increase of bandgap energy as the oxygen content increases within this study can also be due to the decrease in the packing density of the films. Additionally, it is known that the refractive index is closely related to the packing density of the thin films, where the packing density of the films can be derived from the expression [172]:

$$n^2 = \frac{(1-p)n_{\mathrm{v}}^4 + (1+p)n_{\mathrm{v}}^2 n_{\mathrm{s}}^2}{(1+p)n_{\mathrm{v}}^2 + (1-p)n_{\mathrm{s}}^2}, \tag{5.1}$$

where p is the packing density, n is the refractive index of the films, n_{s} is the refractive index of bulk ($n_{\mathrm{s}} = 2.1$ for bulk HfO_2), and n_{v} is the refractive index of voids, where $n_{\mathrm{v}} = 1$ for dry air voids, or $n_{\mathrm{v}} = 1.33$ for when the voids are fully filled with water.

By utilising equation 5.1, it was found that the highest packing density within this study can be found for 0% reactive oxygen (configuration (i)) where $p = 0.91$, and the

lowest packing density within this study is found when utilising pure oxygen process (configuration (iii)) where $p = 0.79$. This is in agreement with the results extracted from SCOUT, where at highest packing density calculated (0% reactive oxygen, configuration (i)), the refractive index is highest ($n = 1.92$, Figure 5.3b), with the bandgap energy of 5.67 eV (Figure 5.5). Alongside, at lowest packing density calculated in this study (pure oxygen process, configuration (iii)), the refractive index is lowest ($n = 1.72$, Figure 5.3b), with the highest bandgap energy ($E_{\text{gap}} = 6$ eV, Figure 5.5). The values of the refractive index used for equation 5.1 within this study for the films are based on the refractive values at $\lambda = 1064$ nm.

The film growth rate for all films sputtered with argon is ~ 0.01 Å/s, which is around two orders of magnitude lower than that of conventional IBSD. The slow deposition rate may be one of the reasons for the over-stoichiometry where the oxygen adatoms have a longer time for reacting and diffusing in the forming thin film. The high energy of the ECR process could also produce highly reactive oxygen that sputters the targets and are bonded to the hafnium atoms. The rate decreases further with the introduction of oxygen in the sources as sputtering gas (configuration (ii) and (iii)). This rate is directly related to the momentum transfer between the bombarding ions and the target atoms, which is directly correlated to the difference in atomic mass between the working gas and the target atoms. In particular, for Hf, the sputtering yield is ~ 3 times higher with Ar than with O_2 [173].

As for the extinction coefficient, shown in Figure 5.4, it is related to the absorption loss of thin films. Several factors can be attributed to the trend observed for the extinction coefficient within this study. Based on the nanobubbles theory described earlier [158], the entrapment of argon can have an effect on the absorption, which in turns, can have an effect on the extinction coefficient. In example, for configuration (i) at 0% reactive oxygen, in which the sample possess the highest argon content, also yielded the highest extinction coefficient, and as the oxygen content increases (with decreasing the argon content), the extinction coefficient also decreases. This trend can also be observed for configuration (ii) and (iii), where for 10% sputtering oxygen, this yielded

the highest extinction coefficient, where this is then decreased as the oxygen content increases, which leads to the decrease in argon. Another factor that can affect the extinction coefficient is that as the bandgap energy increases, the extinction coefficient decreases [174], where this trend can be observed clearly for configuration (ii) and (iii). As the extinction coefficient is related to the absorption loss, it can be seen that the films with higher oxygen contents shows lower loss as the extinction coefficient value is decreased, which is in agreement with other authors [175].

As previously mentioned, the films fabricated at 0% reactive oxygen have yielded some unexpected results, especially the thickness and within the transmittance and reflectance. The hypothesis for the low thickness, which in turns also leads to high transmittance and low reflectance, could be due to target erosion. The 0% reactive oxygen films were fabricated around 20 months after all the other samples discussed within this study, which raises the possibility of target erosion and composition changed on the target's surface. However, other than the unexpectedly lower thickness acquired, the optical and structural properties of the 0% reactive oxygen film have yielded the expected results. Hence, the slow deposition rate of this film, which did not provide films that were too thin, has negligible effects on the optical and structural properties of the films.

5.3 Effects of Annealing on HfO_2 Films

In this section, the results for annealed HfO_2 films at 500°C and 700°C have been presented and discussed.

5.3.1 Results

5.3.1.1 Transmittance and Reflectance

Figures 5.10, 5.11, 5.12 shows the transmittance and reflectance of some samples from the three configurations, where they are being compared between as-deposited, 500°C and 700°C annealing temperature, to show the differences within the same coatings due to annealing. As previously mentioned in Section 4.4.6, all samples were annealed for 1 hour in air at each temperature with the rate of 5°C/min, and left to cool down naturally. In each of the figures, the blank substrate is shown as black solid line. As for the as-deposited samples, the data is shown as red solid lines. For the annealed samples, at 500°C is shown as green dashed lines, and annealed at 700°C is shown as pink dashed-dotted lines. This information is also shown within each of the figures.

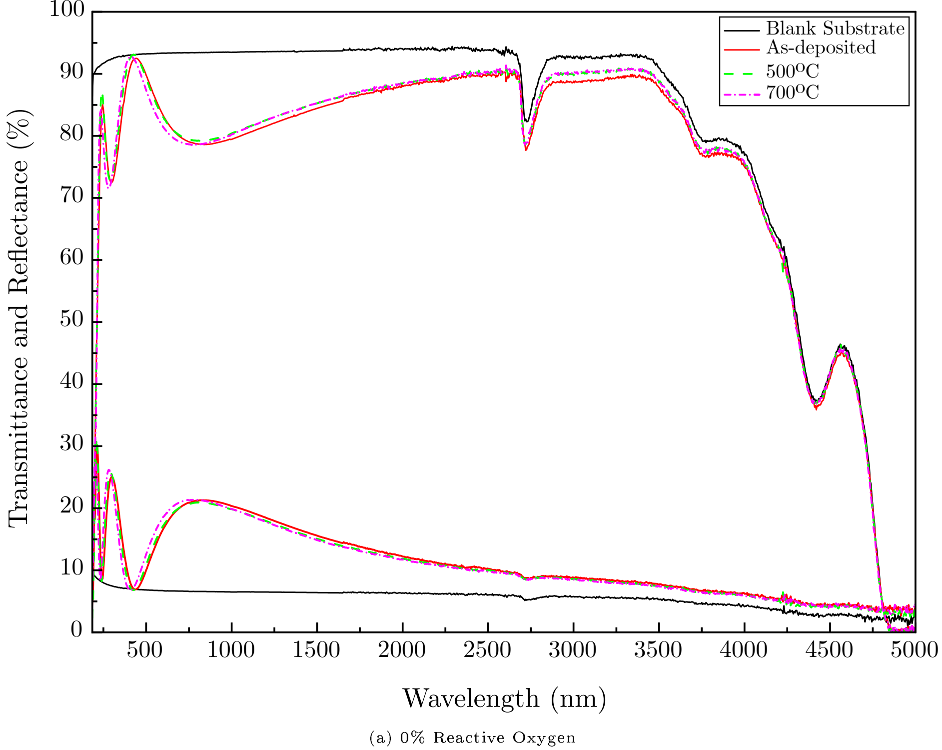

(a) 0% Reactive Oxygen

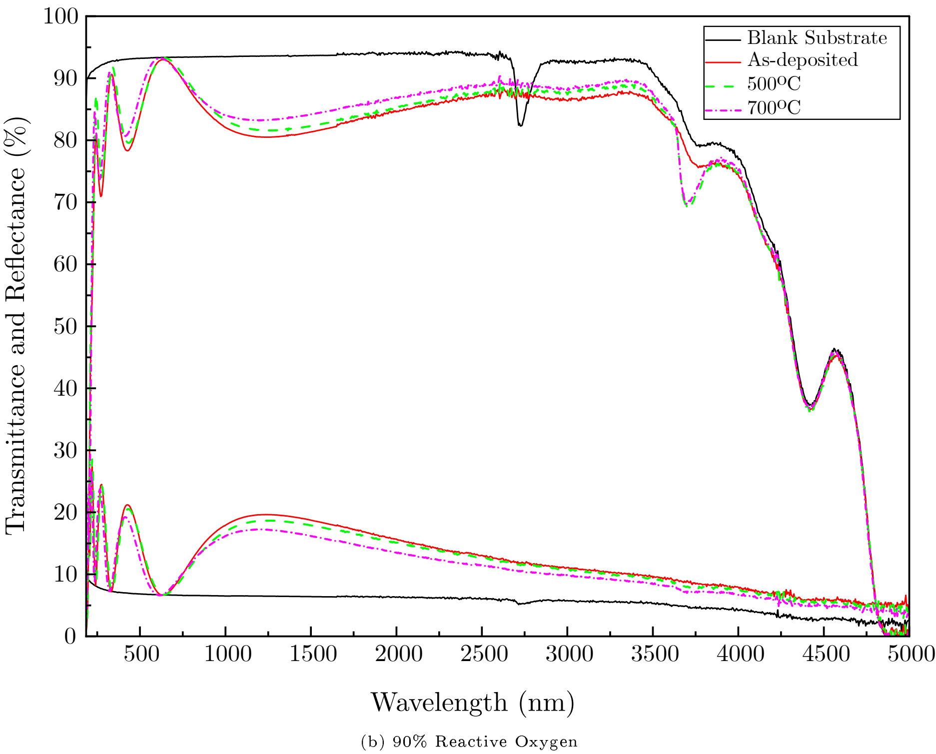

(b) 90% Reactive Oxygen

Figure 5.10: Transmittance and reflectance data of as-deposited, 500°C and 700°C annealed samples from configuration (i)

In Figure 5.10a shows the spectra are slightly shifted towards lower wavelengths as the annealing temperature increases. This shift is an indication that there is an increase in bandgap energy as the annealing temperature increases - otherwise known as Burstein-Moss shift. This shift towards the lower wavelengths as the annealing temperature increases can also indicate the thickness change within the coatings, and this shift can also affect the refractive index and density of the thin film coatings. There are no major changes in the transmittance and reflectance percentages, except for a slight increase in transmittance and decrease in reflectance as the temperature increases, however, the changes are not drastic. As for Figure 5.10b, shown for samples with 90% reactive oxygen, the results are similar to that of 0% reactive oxygen data, where there is a slight shift towards the lower wavelengths as the annealing temperature increases. Again, this indicates an increase in bandgap energy, as well as a change in the thickness. From these two figures, they show that as the reactive oxygen percentage increases, as well

as the annealing temperature, there are noticeable changes that can be seen which is the shifts in the data towards lower wavelengths, as well as some changes within the transmittance and reflectance percentages. The latter change is much more pronounce in the higher reactive oxygen percentage sample (only 90% is shown here).

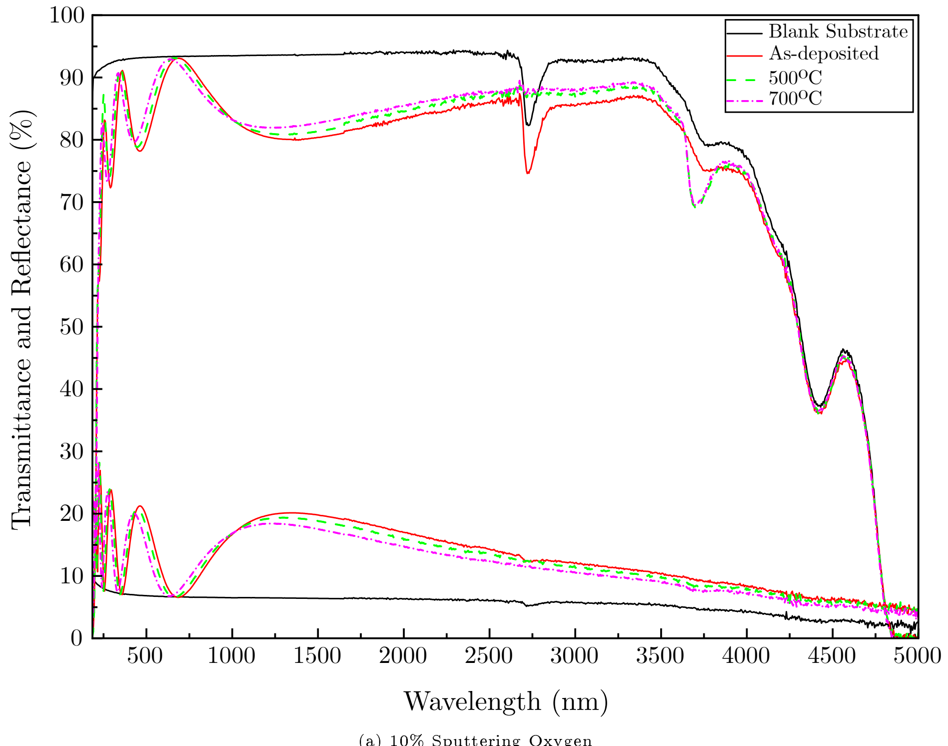

(a) 10% Sputtering Oxygen

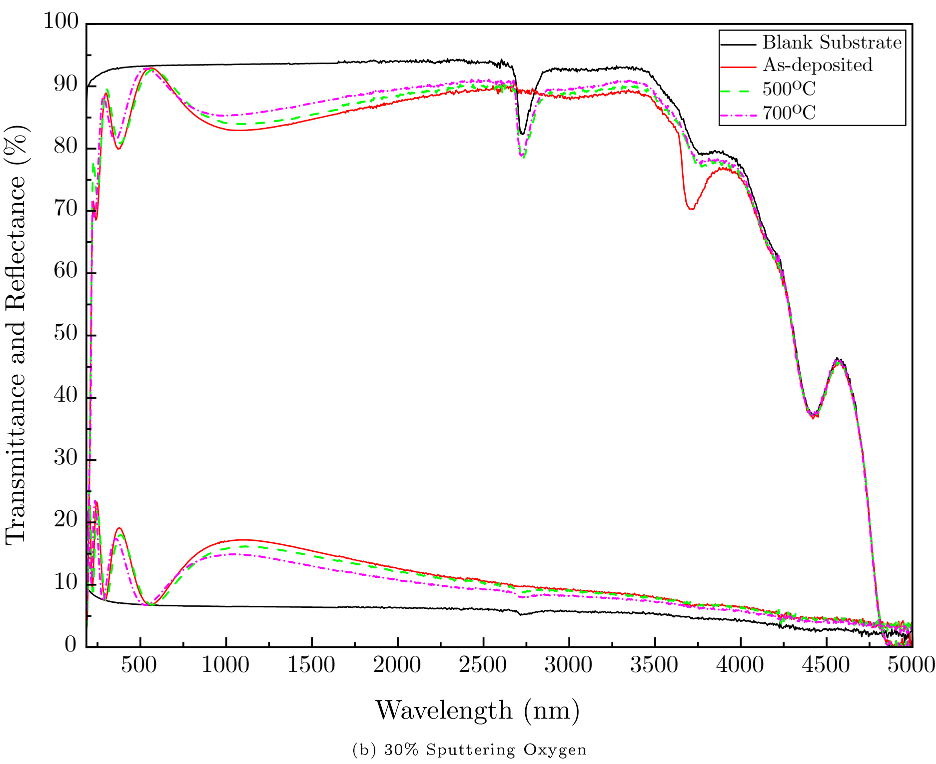

(b) 30% Sputtering Oxygen

Figure 5.11: Transmittance and reflectance data of as-deposited, 500°C and 700°C annealed samples from configuration (ii).

Here in Figure 5.11, both (a) and (b) shows a shift towards the lower wavelengths, similar to those in Figure 5.10. This indicates a slight increase in the bandgap energy as the annealing temperature increases, as well as changes with the thicknesses. Both Figure 5.11a and 5.11b shows a small increase in transmittance and small decrease in reflectance as the annealing temperature increases, similar to the case of configuration (i). Please note that between the as-deposited and annealed samples shown for these two figures are from different substrates, but within the same coating runs - where this give rise to some differences in the data at around 2700 nm and 3700 nm, which are absorption peaks due to the nature of the JGS substrates. However, this does not affect the optical fittings and the optical data that has been extracted for these samples.

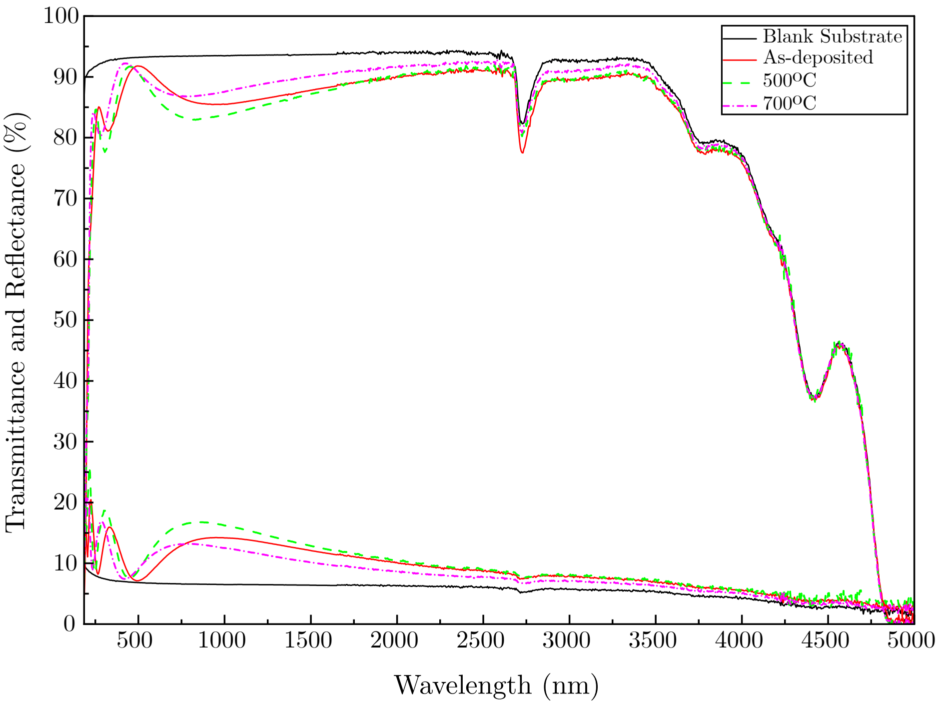

Figure 5.12: Transmittance and reflectance data of as-deposited, 500°C and 700°C annealed samples from configuration (iii).

Figure 5.12 shows a similar trend as the other configurations, where the data is shifted to lower wavelengths, leading to an increase in bandgap energy and changes to the thickness as the annealing temperature increases. In this case, at 500°C the transmittance decreases and reflectance increases, which can be due to the change in the structure of the films, where they are becoming more crystalline in nature. However, as the sample has been annealed to 700°C, the transmittance have increase, and the reflectance decreases.

5.3.1.2 Refractive Index and Extinction Coefficient

As previously mentioned, by utilising SCOUT to fit the experimental data acquired for the transmittance and reflectance of each samples, one can extract the optical properties of the films. Figure 5.13 below shows the refractive index of the three configurations, where Figure 5.13a shows the dispersion of the films at 500°C and Figure 5.13b shows the dispersion of the films at 700°C. As for Figure 5.13c, this shows the comparison between as-deposited, 500°C and 700°C for each films at the wavelength of 1064 nm.

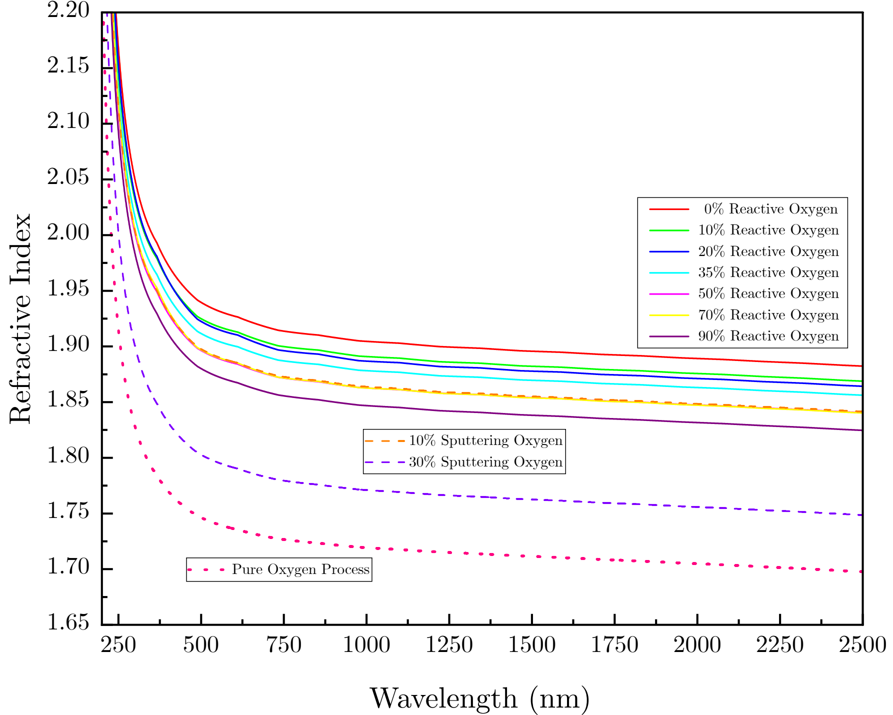

(a) Dispersion of the refractive index for the range of λ = 200 - 2500 nm for 500°C annealed samples

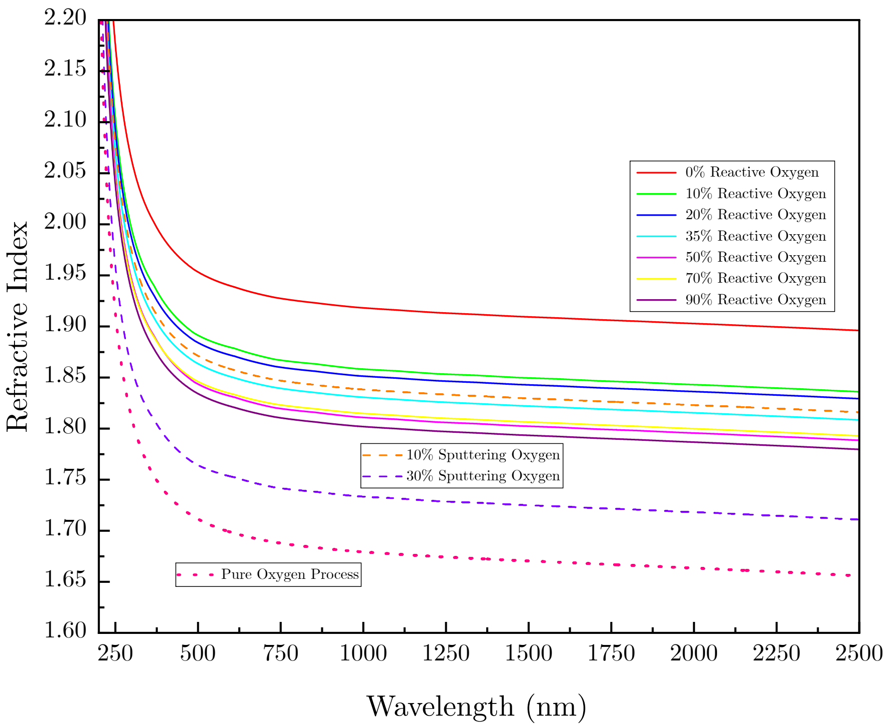

(b) Dispersion of the refractive index for the range of λ = 200 - 2500 nm for 700°C annealed samples

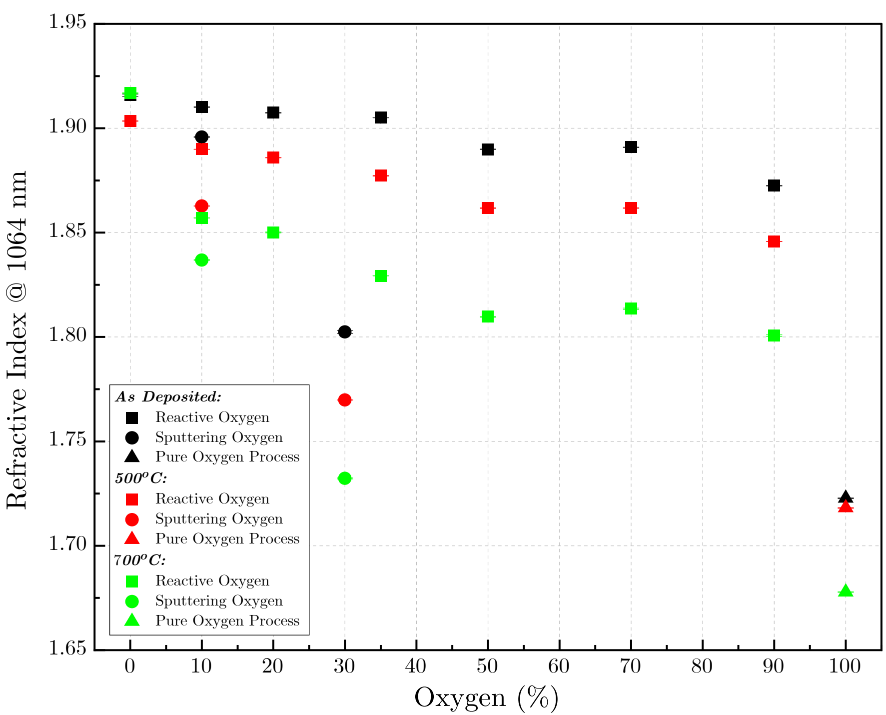

(c) The refractive index at $\lambda = 1064$ nm of all three configuration for As-deposited, 500°C and 700°C annealed temperature. The error bars show the standard deviation of five separate fittings for each sample.

Figure 5.13: The refractive index of all three configurations.

Similar to as-deposited results, 500°C annealed samples shown in Figure 5.13a shows that as the oxygen concentration increases, the refractive index decreases for all three configurations. The same is also shown for 700°C annealed samples in Figure 5.13b, where in both of these figures, the highest refractive index dispersion is for 0% reactive oxygen (configuration (i)) and the lowest refractive index dispersion is for the pure oxygen process (configuration (iii)). This is consistent with the as-deposited results shown in Section 5.2.1.2.

Figure 5.13c shows the refractive indices at 1064 nm for all three temperature: As-deposited (black), 500°C (red) and 700°C (green). All three configurations are also shown in the figure, where: Reactive Oxygen (square), Sputtering Oxygen (circle) and Pure Oxygen (triangle). From Figure 5.13c, it shows that 0% reactive oxygen has the highest refractive index at all three temperatures with n = 1.92, 1.91, and 1.92 for as-deposited, 500°C and 700°C, respectively. Comparing within configuration (i) only, 90%

reactive oxygen has the lowest refractive index at all three temperatures, where $n = 1.87$, 1.85, and 1.80 for as-deposited, 500°C and 700°C, respectively. As previously mentioned, for configuration (i), at as-deposited, the refractive index values decreases ~3% as the oxygen content increases. As the annealing temperature increases to 500°C, the overall refractive index decreases by ~3% from lowest reactive oxygen percentage (with highest n) to highest reactive oxygen percentage (with lowest n). As the annealing temperature continues to increase to 700°C, the overall refractive index decreases by ~6% from lowest reactive oxygen percentage (with highest n) to highest reactive oxygen percentage (with lowest n).

The overall lowest refractive index result is for pure oxygen process (configuration (iii)), where n = 1.72, 1.72 and 1.68 for as-deposited, 500°C and 700°C, respectively. When comparing configuration (ii) and (iii), as they are both utilising oxygen as the sputtering gas from 10% to 100%, a bigger impact on the refractive index change can be observed for all three temperatures. For as-deposited, refractive index decreased from 1.90 to 1.72, which is ~10% decrease. At 500°C, the refractive index decreases from 1.86 to 1.72, which is ~8% decrease. As the annealing temperature rises to 700°C, the refractive index decreases from 1.84 to 1.68, which is ~9% decrease in value.

In Figure 5.14 below shows the extinction coefficient of the annealed HfO_2 films. Figures 5.14a and 5.14b shows the dispersion of the extinction coefficient for both 500°C and 700°C, respectively. In Figure 5.14c, this shows the extinction coefficient values at 1064 nm, for as-deposited, 500°C and 700°C, to show the effects of annealing on the extinction coefficient.

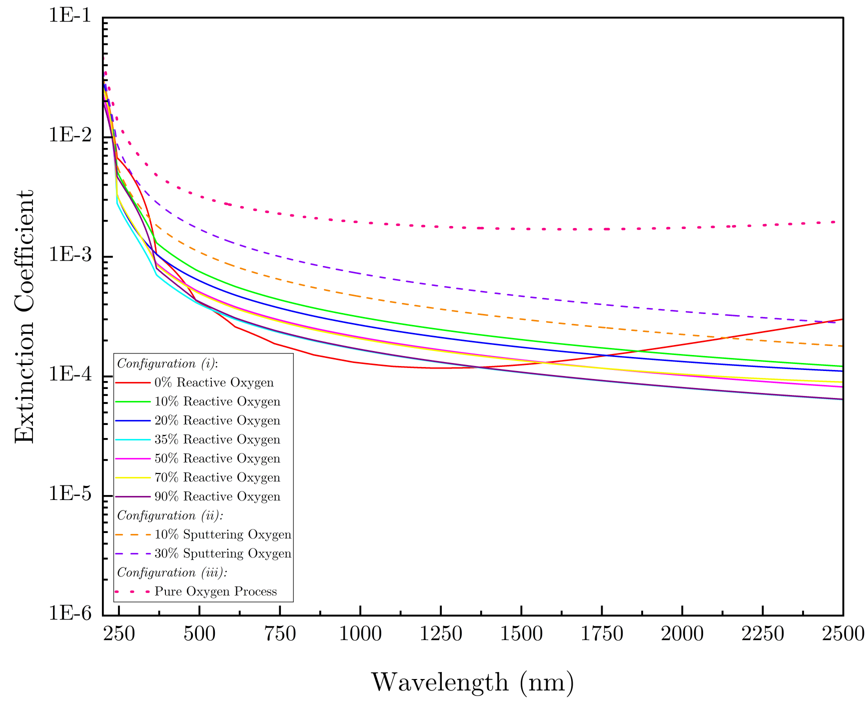

(a) Dispersion of the extinction coefficient for the range of λ = 200 - 2500 nm for samples annealed at 500°C. Y-axis displays the extinction coefficient on a logarithmic scale.

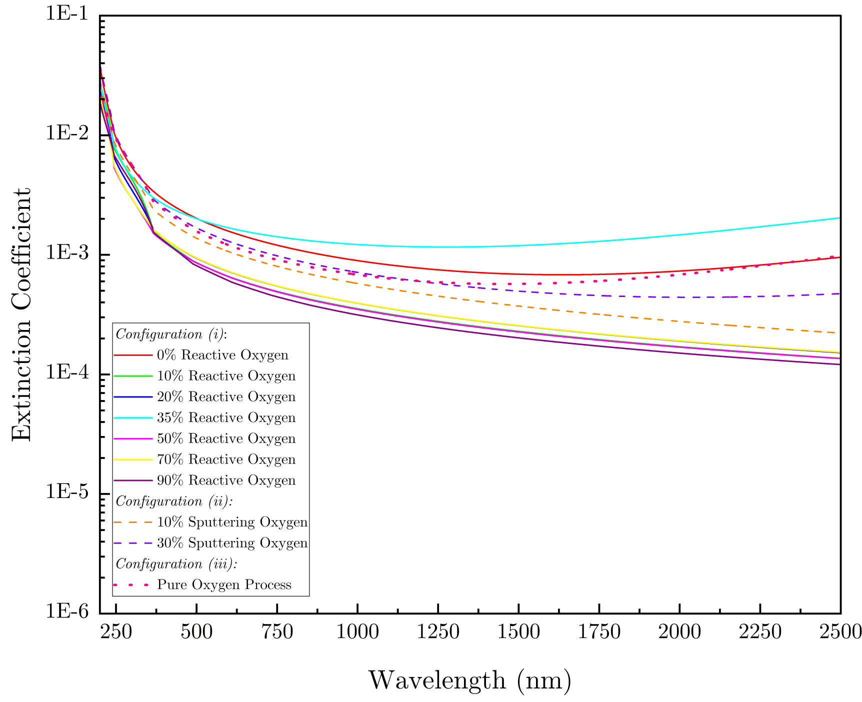

(b) Dispersion of the extinction coefficient for the range of λ = 200 - 2500 nm for samples annealed at 700°C. Y-axis displays the extinction coefficient on a logarithmic scale.

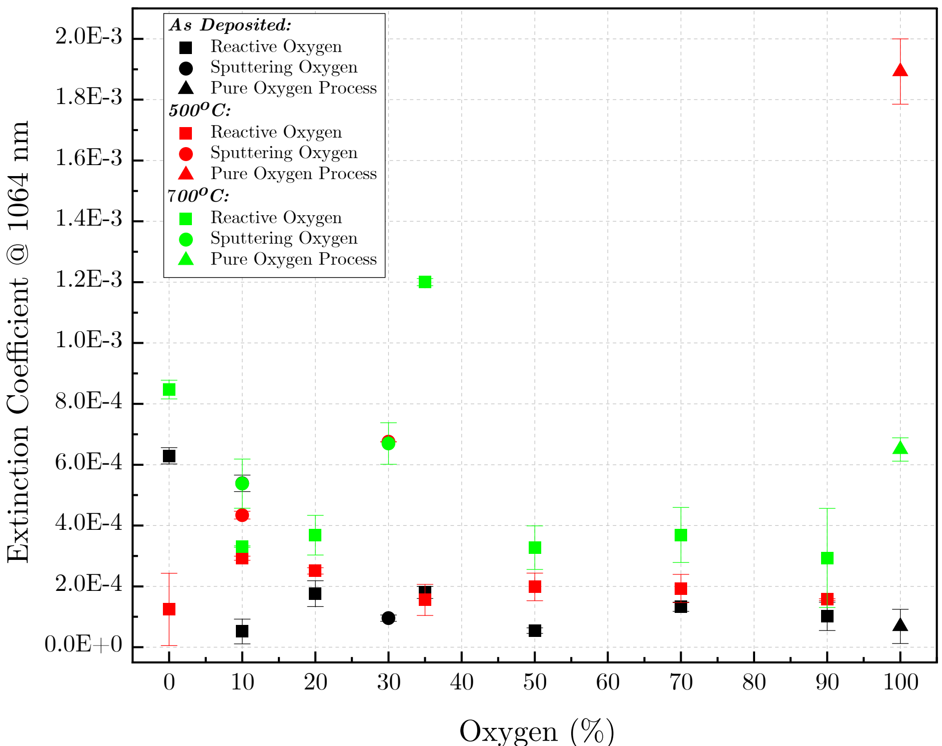

(c) The extinction coefficient at $\lambda = 1064$ nm of all three configuration for As-deposited, 500°C and 700°C annealed temperature. The error bars show the standard deviation of five separate fittings for each sample.

Figure 5.14: The extinction coefficient of all three configurations.

The dispersion of extinction coefficient is shown in Figures 5.14a and 5.14b for 500°C and 700°C, respectively. Similar to as-deposited results (shown in Figure 5.4a), the 500°C and 700°C annealed samples shows a sharp decline of extinction coefficient with increase in wavelength in the UV region, where this continues to decrease as it reaches mid-IR for all samples and temperature.

For configuration (i), it can be seen in Figure 5.14c that as the annealing temperature increases to 500°C, the extinction coefficient values increases, except for 0% and 35% reactive oxygen. When the annealing temperature continues to increase to 700°C, extinction coefficient values increases further for all reactive oxygen percentages. This leads to the understanding that the absorption is increasing as the annealing temperature increases, as the extinction coefficient is a function of absorption (α). At 500°C, a trend can be seen where at 10% reactive oxygen has the highest value of $k = 2.93 \times 10^{-4}$,

and the lowest value was found to be $k = 1.24 \times 10^{-4}$ for 0% reactive oxygen, where as the reactive oxygen percentage increases, the extinction coefficient slightly decreases. However, within the error range, at 500°C, the values for extinction coefficient does not differ hugely. As for at 700°C, the trend seems to be that as the reactive oxygen percentage increases, the extinction coefficient values decreases, with the exception of 35% reactive oxygen. However, at 10% - 90% reactive oxygen, within the error range, the extinction coefficient values can be said to have stayed constant despite the increase in oxygen content (with the exception of 35% reactive oxygen, where $k = 0.0012$).

For configuration (ii) and (iii), it can be seen that as the annealing temperature increases to 500°C, and as the sputtering oxygen content increases, so does the extinction coefficient values, where the highest value is $k = 0.0019$ for pure oxygen process (100% oxygen). As the annealing temperature increases to 700°C, the extinction coefficient value for the pure oxygen process decreases, whereas the 10% sputtering oxygen value slightly increases, and at 30% sputtering oxygen stays almost the same. The trend at 700° shows that as the sputtering oxygen percentage increases, so does the extinction coefficient. Although the values do not differ greatly, where this is the complete opposite for the as-deposited results.

5.3.1.3 Bandgap Energy

Figure 5.15 shows the OJL bandgap energy of the HfO_2 films for as-deposited (black), 500°C (red) and 700°C (green) of all three configurations. The configurations are shown as: (i) are shown as square, (ii) are shown as circle, and (iii) are shown as triangle.

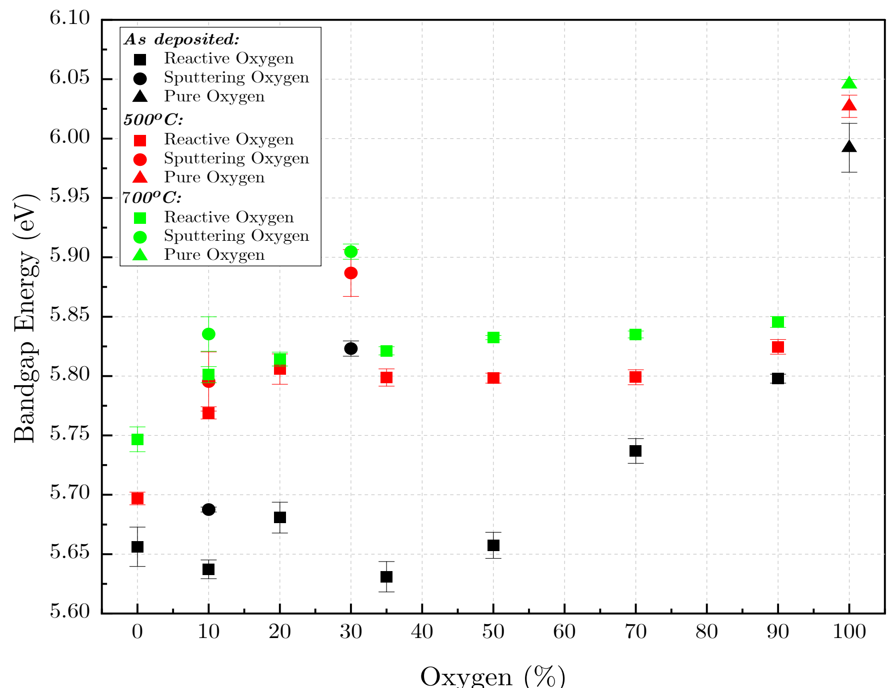

Figure 5.15: The average bandgap energy of the films acquired from SCOUT for all three configurations at As-deposited (black), 500°C (red) and 700°C (green). The error bars show the standard deviation of five separate fittings for each sample.

As the samples are annealed to 500°C, all configurations shows an increase in the bandgap energy with the increase in temperature. For configuration (i), the bandgap energies remained almost constant despite the differing reactive oxygen percentage from 10% to 90%, where $E_{\text{gap}} = 5.80 \pm 0.05$ eV. At 0% reactive oxygen, this possesses the lowest values of bandgap energy at 5.70 eV. For this configuration, the most notable increase in bandgap energy is observed at 10 - 50% reactive oxygen, however, the relative change is still low as the increase is $\sim 0.15 \pm 0.05$ eV. For configuration (ii), the bandgap energies increases with the increase in sputtering oxygen, as well as the increase in annealed temperature. The bandgap values for 10% and 30% sputtering oxygen are 5.80 and 5.89 eV, respectively. As for configuration (iii), this remained the highest bandgap energy, where this value has increased to 6.03 eV after annealing at 500°C.

As the samples are annealed to 700°C, all configurations once again shows an increase in the bandgap energy as the temperature increases. For configuration (i), the bandgap

energy increases ranges from 5.75 to 5.85 eV, from 0 - 90% reactive oxygen, where the highest percentage (90%) has the highest bandgap energy for this configuration - however, the values are within 0.1 eV range. For configuration (ii), there is also a small increase from the values at 500°C to 5.84 and 5.91 eV for 10% and 30% sputtering oxygen, respectively. As for configuration (iii), there is also a slight increase in bandgap energy to 6.05 eV.

The overall trend that can be observed from Figure 5.15 is that as the annealing temperature increases, so does the bandgap energy.

5.3.1.4 Thickness

Figure 5.16 shows the thickness extracted from SCOUT for the HfO_2 films of all three configurations for samples at as-deposited (black), 500°C (red) and 700°C (green). The three configurations are also shown as follows: (i) - square, (ii) - circle, and (iii) - triangle. As previously mentioned, all samples have the same deposition time of 72 hours, and have been annealed for 1 hour in air.

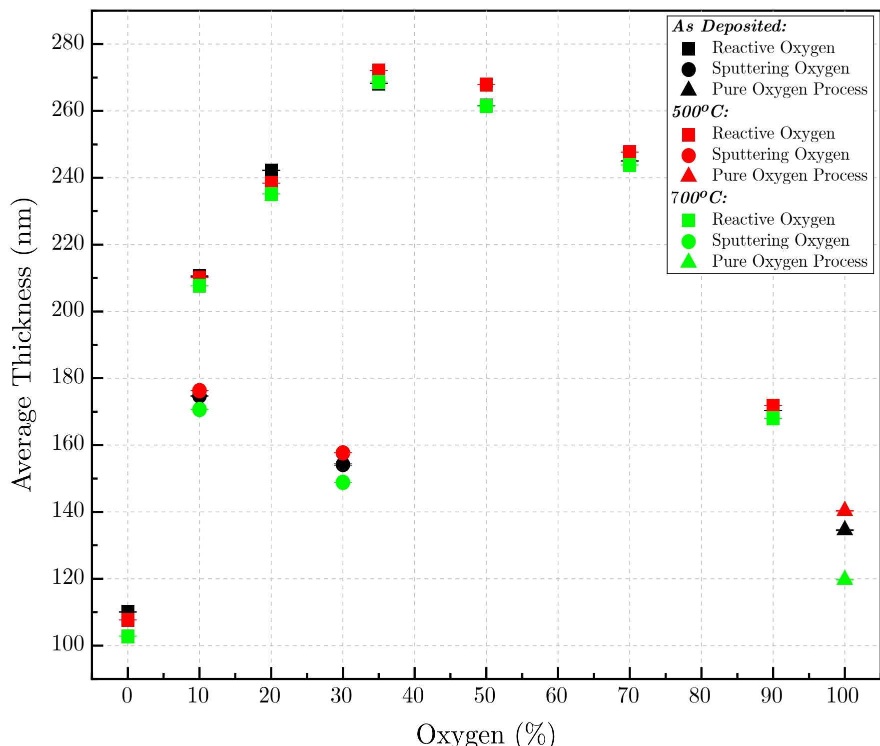

Figure 5.16: The average thickness of the films acquired from SCOUT for all three configurations at As-deposited (black), 500°C (red) and 700°C (green). The error bars show the standard deviation of five separate fittings for each sample.

From Figure 5.16, it can be seen that the annealed samples still follows the same trend for those at as-deposited (Figure 5.16, and also shown here). For the majority of the films, as the annealing temperature rises to 500°C, the thicknesses increases, then decreases again as the annealing temperature reaches 700°C.

For configuration (i), the highest change in thickness is 7 nm (0% reactive oxygen), and the lowest change is 3 nm (10% and 70% reactive oxygen). As for configuration (ii), 30% sputtering oxygen has the highest change of 9 nm, and 10% sputtering oxygen has a change of 5 nm. Lastly, configuration (iii) has the largest change overall of ∼20 nm. Below is a table to show the values of the thicknesses at 500°C and 700°C.

Table 5.2: The different thicknesses of HfO_2 thin films with different configurations at 500°C and 700°C annealed temperatures

OXYGEN PERCENTAGE	**THICKNESS (nm)**		
(%)	As-deposited	500°C	700°C
Configuration (i):			
0%	110	108	103
10%	211	210	208
20%	242	238	235
35%	268	272	268
50%	262	268	261
70%	245	248	246
90%	170	172	168
Configuration (ii):			
10%	175	176	171
30%	154	158	149
Configuration (iii):			
100%	135	140	120

5.3.1.5 XRD Results

In Figures 5.17 and 5.18 shows the XRD pattern of the HfO_2 films at 500°C and 700°C, respectively, by utilising the Bragg-Brentano setup.

As shown in Figure 5.17a, showing the 500°C data for configuration (i), where the films can be seen to still be amorphous as the data are showing broad weak bands. As for Figure 5.17b. this is showing the data for configuration (ii) and (iii) annealed at 500°C. For configuration (ii) [bottommost two bands], it can be seen the films are still amorphous due to the broad weak bands. As for configuration (iii), two small peaks are starting to form at (-111) and (111), favouring the latter growth orientation, indicating that the films are starting to crystallise, towards the polycrystalline state, at

this annealing temperature.

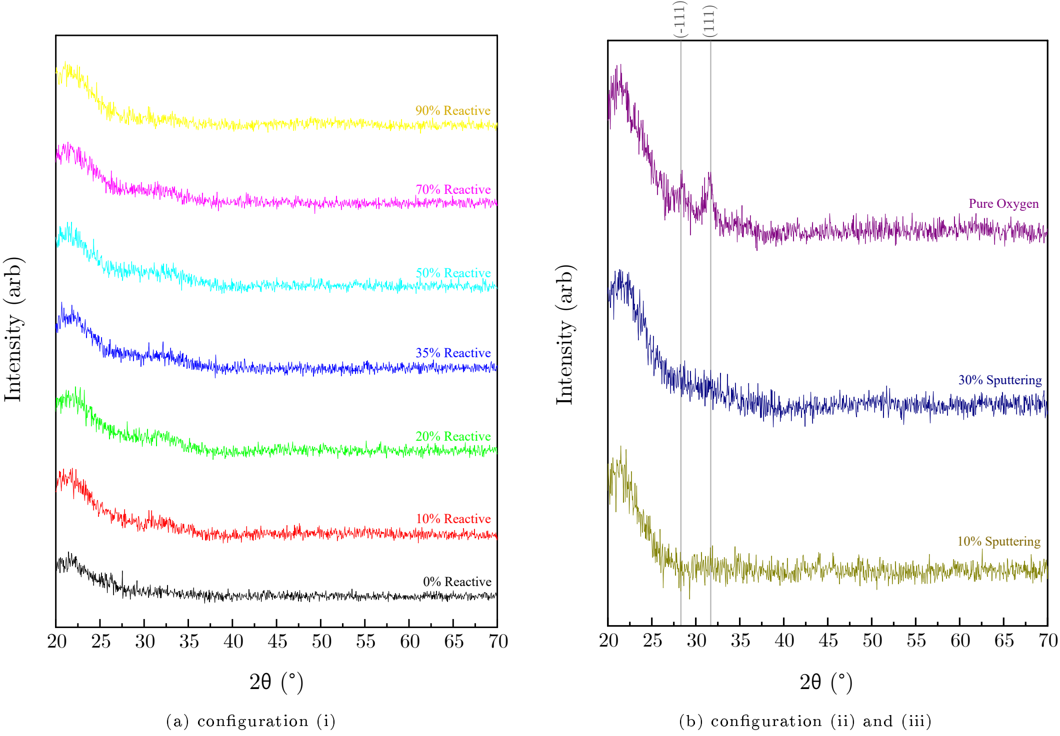

(a) configuration (i)

(b) configuration (ii) and (iii)

Figure 5.17: BB-XRD data acquired for the 500°C films within this study.

As for 700°C, the BB-XRD results are shown in Figure 5.18a for configuration (i) and Figure 5.18b for configuration (ii) and (iii). For all three configurations, it can be seen that sharp peaks have formed when annealed at this temperature. This indicates a more crystalline structure in all of the films in this investigation. It can be seen that for configuration (i), the films prefers the (-111) and (111) growth orientation as these are the sharpest peaks for all the different percentages in this configuration. The BB-XRD data shows that the phase of the films is monoclinic (PDF_01-074-4963) As for configuration (ii), as the films are annealed to 700°C, sharp peaks can be seen, where the films favours the (111) growth orientation, similar to configuration (iii), and the films in these configurations have monoclinic phase (PDF_01-074-4963). With all three configurations, the results suggests that there is an increase in grain size as the annealing temperature increases. The data for the peaks and phase of the film is from

the ICDD's Powder Diffraction File, where in this case it is PDF_01-074-4963. ICDD is the International Centre for Diffraction Data, who are a non-profit scientific organisation dedicated to collecting, editing, publishing, and distributing powder diffraction data for the identification of materials.

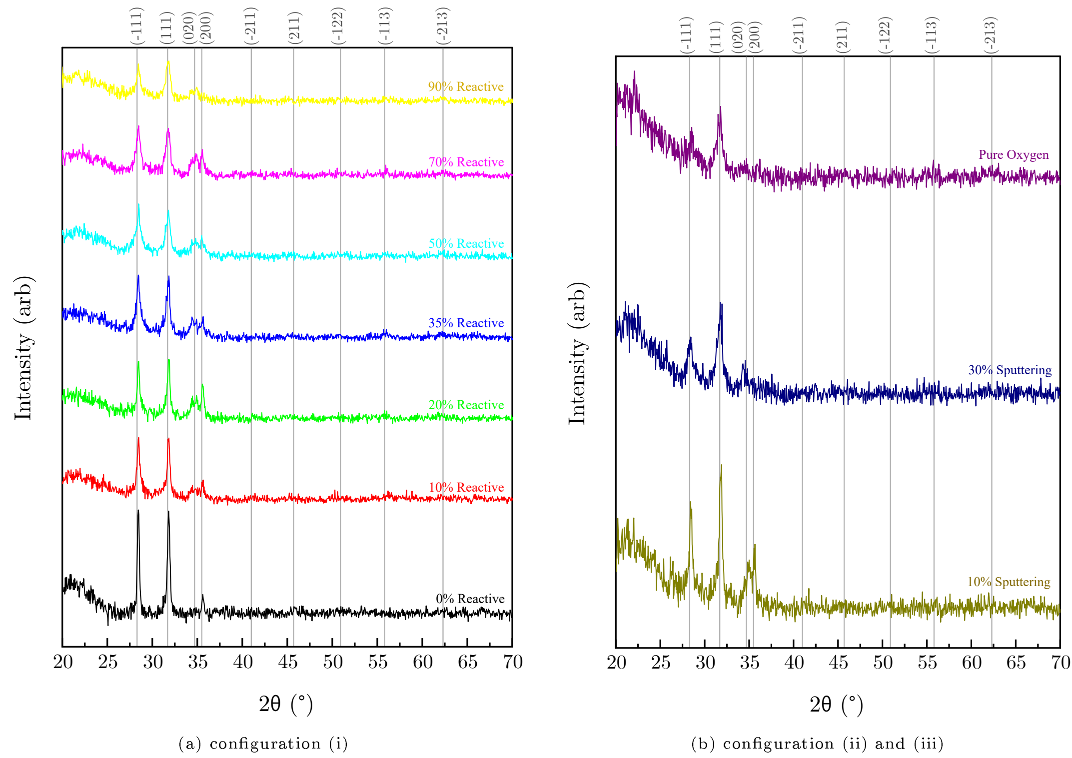

(a) configuration (i)

(b) configuration (ii) and (iii)

Figure 5.18: BB-XRD data acquired for the 700°C films within this study.

Below, the GIXRD data is also shown for the HfO_2 films at 500°C and 700°C in Figures 5.19 and 5.20, respectively. GIXRD is a more preferred method compared to BB-XRD, as GIXRD mainly only measures the film due to the angle of the incident x-ray beam is constant at 0.5°, providing a more accurate results of the films, excluding the substrate.

At 500°C, it can be seen that for configuration (i) [Figure 5.19a], there are broad weak bands, indicating that the films are still amorphous. As for configuration (ii), the bands are still broad, but slightly more prominent that those in configuration (i), leading to the films still being amorphous [Figure 5.19b, bottommost two bands]. As for configuration

(iii), shown in the same figure, shows a much more prominent peaks that are becoming sharp - indicating polycrystalline nature of the films, where it shows preferential (-111) and (111) growth orientation.

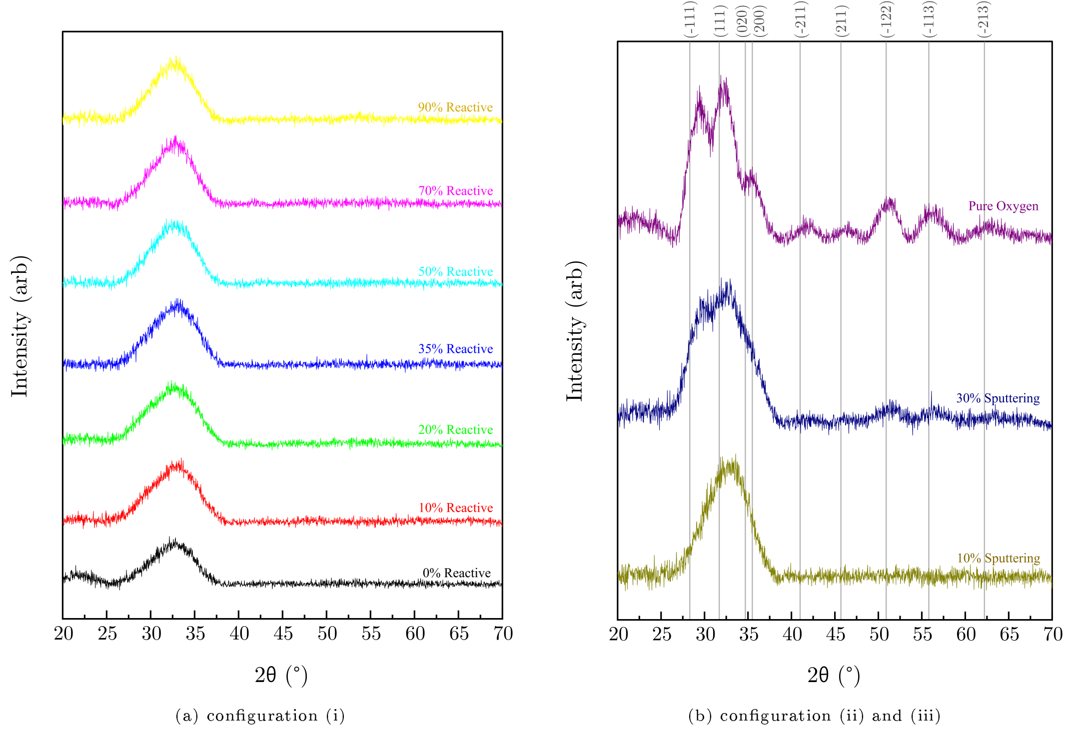

(a) configuration (i)

(b) configuration (ii) and (iii)

Figure 5.19: GIXRD data acquired for the 500°C films within this study.

At 700°C, it can be seen that for configuration (i) [Figure 5.20a], sharper peaks are formed. It can be seen that at 0% reactive oxygen shows a preferential (-111) growth orientation, where this is the preferred orientation for monoclinic HfO_2 films. As the oxygen percentage increases, it can be seen that the growth orientation (111) is becoming more favourable, alongside the (-111) orientation, with monoclinic phase. Overall, the GIXRD data for configuration (i) shows that the films are becoming more crystalline as it is annealed at 700°. As for configuration (ii), more peaks can be seen to have become sharper, indicating a more crystalline nature of the films [Figure 5.20b, bottom two bands]. The preferred growth orientation for both films is (111), which indicates that the films are monoclinic. As for configuration (iii), shown in the same figure, shows

that the peaks are becoming sharper, compared to that at 500°, where the growth orientation remains the same at (111), indicating the film is monoclinic. Overall, with all three configurations, the results suggests that there is an increase in grain size as the annealing temperature increases due to the increase in the number peaks, as well as the sharpness of the peaks.

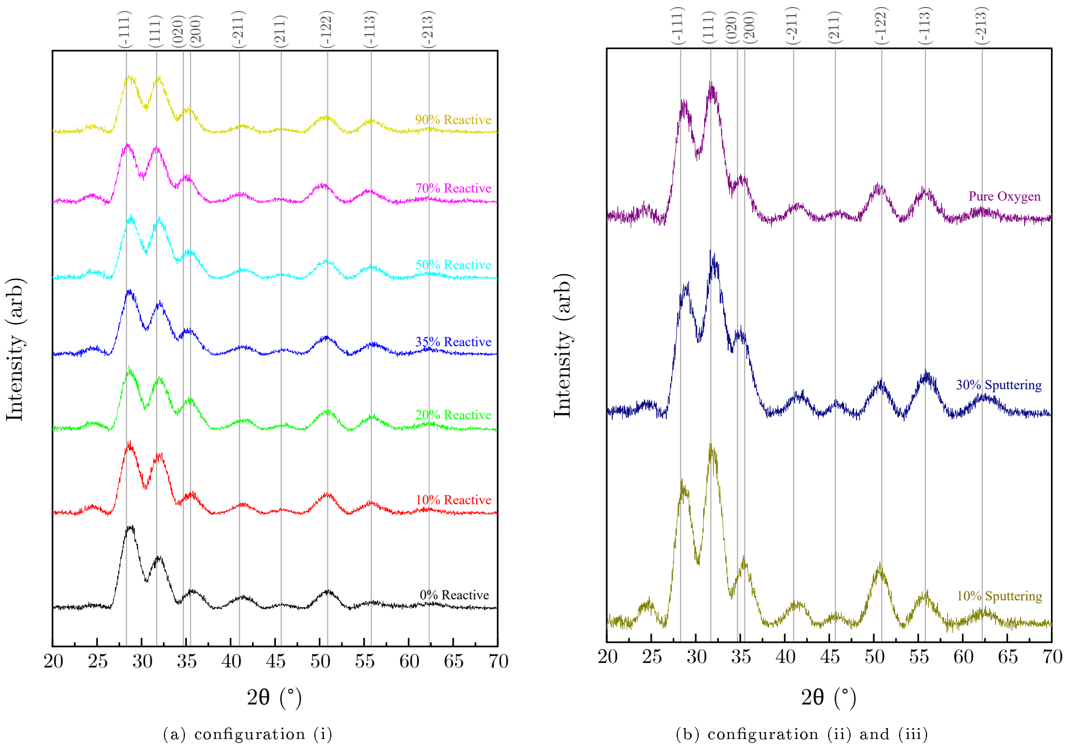

(a) configuration (i)

(b) configuration (ii) and (iii)

Figure 5.20: GIXRD data acquired for the 700°C films within this study.

5.3.2 Discussion

Both the BB-XRD and GIXRD are shown in the results section. For configuration (i), at 500°C the films are still amorphous, whereas at 700°C the films are crystallised. In Figures 5.18a and 5.20a shows that the preferred growth orientation is (-111), along with the other peaks that can be seen shows that the films are monoclinic. As the oxygen percentage increases in this configuration, the preferential growth orientation is now both (111) and (-111), which is also that of monoclinic HfO_2 films. As for

configuration (ii), at 500°C films are still amorphous as the data shown in Figures 5.17b and 5.19b is still broad for both 10% and 30% reactive oxygen. At 700°C, it can be seen that the films have become crystalline in nature as more prominent sharp peaks can be seen (Figures 5.18b and 5.20b). For this configuration, (111) is the preferred growth orientation, which can be seen for both BBXRD and GIXRD, alongside the (-111) peak. It can be seen that similar to configuration (i), the films are monoclinic. Shown in both BBXRD and GIXRD data that with less oxygen at 10% sputtering oxygen leads to sharper peaks, which shows that the crystallite sizes are slightly larger at 10% sputtering oxygen configuration (4.5 nm) compared to at 30% sputtering oxygen (4.1 nm). Lastly, for configuration (iii), at 500°C the data shows that there are peaks starting to show, where in this case it can be said that the film is crystalline in nature (Figures 5.17b and 5.19b). The preferred orientation is (111) and also (-111). As the annealing temperature reached 700°C, the peaks can be seen to be sharper, with the same preferred orientation as that at 500°C, where the pure oxygen sputtering film are in the monoclinic phase (Figures 5.18b and 5.20b). The other smaller peaks that can be seen in all films as the 2θ angle increases are also that of the monoclinic HfO_2 phase (PDF_01-074-4963).

As can be seen in the case of ECR-IBSD films, the films mostly remain amorphous at 500°C, whereas in most literature, HfO_2 films starts to crystalline between 400 – 500°C, depending on the film deposition techniques and conditions. Wiemer *et al.* studied ALD HfO_2 where they found that early stages of crystallisation occurs at 550°C in the monoclinic phase for one of their films, where at 700°C, the system is stabilised as monoclinic phase and at higher annealing temperature, the relative intensity of the diffraction peaks does not change much [176]. In their study, it is stated that at high annealing temperature, the system can crystallise with the preferential orientation which minimised the surface energy - where in the case of this thesis, for all three configurations, the films preferential orientation is in the monoclinic phase [176]. Khan *et al.* have found that their HfO_2 film fabricated by e-beam evaporation, after annealing at 400°C there are peaks that can be seen, where these peaks becomes more prominent and all the peak positions corresponds to monoclinic phase [150]. This shows that by utilising

the ECR-IBSD technique to fabricate HfO_2 thin films, the films remains amorphous whilst being annealed up to 500°C, leading to no risk of scatter due to crystallisation.

In regards to the transmittance and reflectance data (Figures 5.10 , 5.11 and 5.12), it can be seen that for all three configurations, after annealing at 500°C and 700°C, the transmittance and reflectance spectra shifts towards lower wavelengths. As previously mentioned, this is an indication that there is a change in the bandgap energy and the thicknesses of the films, which can be seen in Figure 5.15 and Figure 5.16, respectively. With these changes observed in the transmittance and reflectance data, it can also affect the refractive index and the density of the films.

As the annealing temperature increases for all three configurations, the refractive indices of the films decreases. This can be seen in Figures 5.13a, 5.13b and 5.13c. In some literature, other authors have found that the refractive index decreases while the films are in their polycrystalline state [177–179], where the refractive index then increases again as the films becomes crystalline. However, this is not the case in the films within this study as the films are fully crystalline at 700°C and the refractive indices are still lower than that at amorphous state. Additionally, refractive index relates to the density of the films, where the decrease in refractive indices can be due to the films being less optically dense as the annealing temperature increases [177–179]. Following this, past works also believed that the refractive index of amorphous HfO_2 films was higher than that of crystallised films [177]. With the decrease in refractive indices leading to reduction in the density, this could also result in compressive stress within the films (i.e. lattice contraction) [178]. Ramzan *et al.* also found that for their films, the refractive index also decreases after annealing, which can be due to the variation in the density of the films caused by crystallisation, as speculated for the films in this study [179]. Along with the decrease in packing density and refractive index with the increase in annealing temperature, the thicknesses of the films in all three configurations also decreases (Figure 5.16), where this can also be related to the stress in the films due to lattice contraction [150]. The decrease in the thicknesses after annealing is not commonly observed, which can be attributed to compressive stress within the films, or it

can also be attributed to the excess oxygen leaving the films after annealing, otherwise known as oxygen desorption, leading to a slight decrease in the thickness of the films. Regarding the extinction coefficient values, with the increase of annealing temperature, the extinction coefficient also increases for all three configurations. This is in agreement with Liu *et al.*, who found that with their films, as the substrate temperature increases, the extinction coefficient also tend to increase [180]. Any changes in the extinction coefficient is directly related to the absorption of the films, which shows that as the annealing temperature increases for the films in this study, so does the absorption.

As the annealing temperature increases for all three configurations, the bandgap energy also increases as shown in Figure 5.15. This increase in bandgap energy is related to the transformation of microstructure of the films from amorphous to crystalline, as can be seen in the XRD data [179, 181–184]. The variation in the bandgap energy can be associated with the rearrangement of atoms and molecules to a more favourable stable states due to post deposition annealing [179].

From the results, it can be seen that for most samples (in all three configurations), at 500°C, the thickness first increases (less than 4% overall), then decreases again once annealed to 700°C. The change in thicknesses of the films can also be an indication to the change in packing density and stress of the films, as previously mentioned. The shift in the transmittance data to shorter wavelengths of all films suggests the decrease in thicknesses of the films after annealing [185]. In regards to the stress of the films, it is suggested that lattice contraction leads to decrease in the film thicknesses – where for the HfO_2 films in this study shows an increase then decrease in film thickness. From the XRD data, it can be seen that the peaks are shifted towards higher angles at 500°C (Figure 5.17) when compared to the PDF database (also shown within the figure), which suggests compressive stress within the films – which suggests that the thickness increase of the films is due to another reason. This increase in film thickness at 500°C can be due to rearrangement of atoms to a more favourable stable states before they get into the final position where the films becomes crystallise [179]. As the films are annealed to 700°C, XRD data shows that there is still a shift towards higher angles compared

to the PDF data for monoclinic HfO_2 (Figure 5.18) and the thickness data shows that all the films has a reduction in thickness, suggesting that there is compressive stress within the films [27, 186–188]. In regards to stress within thin films, this is closely related to the film microstructure, which is dependent on the fabrication process, where gas entrapment at grain boundaries leads to compressive stress and attractive forces within pores leads to tensile stress [189]. It is widely reported that by utilising IBSD technique, this is known to produce films with high compressive stress due to higher ion bombardment, which leads to the production of denser films [56, 190–195].

5.4 Conclusion

The effect of the reactive oxygen partial pressure and sputtering oxygen through the ion sources plays an important role in the optical properties of HfO_2 thin films fabricated by ECR-IBSD technique. ECR gridless high-energy ion sources produced high-density pure hafnia films (with a lower backscattered Ar content of ∼2.5% compared to the conventional IBSD technique). By utilising ECR-IBSD, this technique is unique in the ability to study a wider rage of parameters, e.g. ion energy, allowing exploration that cannot be achieved via traditional IBSD technique. The structural analysis carried out by XRD confirmed that all as-deposited films in this study were amorphous. The compositional analysis demonstrated that the films in this study were all over-stoichiometric as the O:Hf ratio is higher than 2:1, even for 0% reactive O_2 partial pressure, which was found to be 2.5:1. The over-stoichiometry have been demonstrated by utilising both EDS and RBS methods for all films in this study. By utilising the OJL model implemented within SCOUT software, the refractive index of as-deposited films was found to be in the range of $n = 1.70 - 1.92$, the extinction coefficient was found to be in the range of $k = (0.52 - 6.29) \times 10^{-4}$ and the OJL bandgap energy was found to be in the range of 5.6 – 6.0 eV for the different oxygen concentrations that were investigated. The results indicate that both the refractive indices and extinction coefficients decreased with the increase of oxygen content within the chamber, whereas the bandgap energies

increased. This shift of the bandgap to higher energies can also be seen from the slight shift towards lower wavelengths (blue shift) in the transmittance measurement in the UV range as the oxygen content increases.

The effect of annealing on the optical properties of the HfO_2 films has also been shown and discussed. It was shown that as the films were annealed to 500°C, the refractive indices of all films decreased, and this also decreased further as the films were annealed to 700°C. For the extinction coefficient, as the films are annealed to 500°C (with the exception of 0% reactive oxygen), the extinction coefficient increases and continues to increase as the annealing temperature reaches 700°C. As for the bandgap energy, as the films are annealed to 500°C, it has been reported that the bandgap energies increase and continue to do so as the temperature reaches 700°C. The shift of the bandgap energies to higher values can also be seen in the transmittance measurement in the UV range, where there is a blue-shift. The structural properties of the films were determined using both BB-XRD and GIXRD, which provided the same conclusion. For configuration (i), the films are still amorphous when annealed to 500°C, and then become crystalline with monoclinic structure when annealed to 700°C. For films in configuration (ii), the films are still amorphous, as broad bands can be seen, and at 700°C, the films become crystalline with monoclinic structure. For the film in configuration (iii), at 500°C, the films are polycrystalline, and they then become crystalline once annealed to 700°C with monoclinic structure, similar to the other films in this study. The films with oxygen as the sputtering gas (configurations (ii) and (iii)) showed preferential growth at (111), whereas configuration (i) showed preferential growth at (-111). However, as the oxygen content increases in this configuration, the peak at (111) also increases. Based on the literature, it has been concluded that the changes in the refractive index, extinction coefficient, and bandgap energy observed for the films in this study could be attributed to the changes in the stress of the films, or attribute to oxygen desorption, as the annealing temperature increased. Furthermore, by utilising ECR-IBSD to fabricate HfO_2 films, the films remained amorphous until they were annealed at temperatures higher than 500°C, whereas with other techniques, the films could crystallise at much lower temperatures.

From optical characterisation, it was found that by controlling both the reactive and sputtering oxygen concentrations during deposition, the bandgap energy and refractive index could be tuned to the desired value, depending on the application. In addition to tuning the oxygen content and sputtering percentages during deposition, post-deposition annealing can also aid in tuning the optical constants to the desired value for different applications.

6 | Scandium Oxide

6.1 Introduction

Scandium oxide, or scandia (Sc_2O_3), is an important optical film material that consists of high refractive index, low absorption in the UV to mid-IR, low extinction coefficient, and slightly higher optical bandgap compared to HfO_2. Its wide bandgap is found in the range of 5.8 - 6.0 eV, compared to 5.3 - 5.7 eV typically found in HfO_2. This wide bandgap is important as it is regularly found to be linearly correlated with LIDT; hence, it should yield high LIDT values [196]. Scandia also has a high melting point, and high damage resistance to laser irradiation, which is important for high power laser applications [187, 196]. The refractive index of Sc_2O_3 ranges between n = 1.8 - 2.0, and it is sought after as the high refractive index components of dielectric coatings, especially those operating in the UV to mid-IR [188, 197]. However, despite the high bandgap and high refractive index, Sc_2O_3 thin films have not been investigated as often as HfO_2. This is likely due to the increased cost and difficulty to purify to create target materials [63]. Nevertheless, due to it being a high bandgap material, there is still a pull into investigating Sc_2O_3 as a high damage threshold coatings, where several groups have studied the results over the years [63], which will be further discussed.

There are various methods to fabricate Sc_2O_3 thin films, which includes e-beam evaporation [187,198,199], atomic layer deposition (ALD) [63,186,200,201], sol-gel [63,186,202], molecular beam epitaxy (MBE) [203], chemical vapour deposition (CVD) [204], pulse laser deposition (PLD) [205], RF magnetron sputtering [206] and ion beam sputter de-

position (IBSD) [63,186–188,207,208]. Similar to HfO_2 films, the Sc_2O_3 film properties are strongly dependent on the condition and method of thin film fabrication. However, by utilising IBSD to fabricate the films, this also has its own advantages where one can accurately control the transmittance and refractive index of the films. Furthermore, IBSD provide films with higher surface quality and ultra low loss compared to other techniques [196]. However, there are also disadvantages with IBSD process whilst fabricating Sc_2O_3 films as oxygen defects can easily formed in the films due to the different oxidation degree of the films with different oxygen flow rates [196].

As previously mentioned, Sc_2O_3 has been studied by several groups, where different optical properties can be found based on different deposition process and conditions. In example, Al-Kuhaili investigated Sc_2O_3 coatings fabricated by e-beam evaporation which has density gradients in the thickness of the films [198]. They also found that amorphous films were found with low growth temperature with refractive index of 1.75 at 800 nm, and crystalline films were found when deposited with heated substrates which has higher refractive index of 1.9 at 800 nm. Liu *et al.* [199] also utilised e-beam evaporation to fabricate Sc_2O_3 thin films, where they also found that at low substrate temperature, the films are amorphous and at higher substrate temperatures, the films become polycrystalline - in which they also found that the refractive index increases with the increase in temperature as the films becomes denser, whilst the bandgap energy decreases [199]. Grosso *et al.* [202] utilised sol-gel method, where the refractive index at 355 nm is 1.62, which is much lower than that of bulk ($n \approx 2$) [63, 186, 202]. As for IBSD methods, several groups have investigated Sc_2O_3 thin films: Krous *et al.* [207] utilised DIBSD, where they found that the refractive index is $n = 1.95$, which is higher than that of Al-Kuhaili [198, 207] - however, the film are said to be oxygen deficient; Langston *et al.* [188] found the refractive index to be $n = 2$ at 1μm, where they also found oxygen interstitial within their films [63, 186]; lastly, Belosludtsev *et al.* [187] extracted the refractive index to be 2.07 at 355 nm, where this is higher than films fabricated by e-beam evaporation, leading to higher density films being fabricated by IBSD. These are just some examples to show that the optical properties, like refractive index or crystallinity, can vary widely dependent on the method and condition during

the fabrication of thin films.

Aside from utilising Sc_2O_3 as coating material for high power laser systems due to its high bandgap energy and refractive index, various other applications of Sc_2O_3 have been investigated and utilised. In example, utilising Sc_2O_3 films as polarisers [187], superluminescent LEDs [209], nanometre scale e-beam lithography [210], quarter wave stacks [211], anti-reflection (AR) coatings [188, 196, 198], and high reflective (HR) multilayer utilised in the fabrication of capacitors and thin film transistors technology [197]. Also, with its high dielectric constants, high permittivity and chemical stability, Sc_2O_3 can be used as a gate oxide [212, 213], a candidate in replacing SiO_2 [188] and surface passivation [213, 214].

Sc_2O_3 is also typically utilised in mixed materials for different purposes, which is more commonly found within literature. In example, one group has utilised $(HfO_2)_{1-x}(Sc_2O_3)_x$ alloys as a replacement for SiO_2 in metal-insulator-semiconductor devices [188, 215]. Sc_2O_3/SiO_2 mixed oxide films deposited by IBSD have also been investigated at different percentages for its LIDT performances [6]. Sc_2O_3 thin films are also often studied as a dopant in thin film transistors, or use as a minor addition to alloys by the metallurgic industry [216], hence little research can be found within the literature for its use in the optical coatings field.

In this chapter, it is reported the study and strategy for the optimisation of Sc_2O_3 film properties by controlling the oxygen ratio during the IBSD process, utilising the ECR-IBSD technology, further discussed in Chapter 2.3.3.2. The stoichiometry and elemental analysis of the films were carried out by RBS. The structural properties of the films were determined by XRD, and the optical properties were obtained by fitting the transmittance and reflectance spectra on SCOUT software, have been reported and discussed. Furthermore, the effects of annealing of these films on the structure and optical properties are presented, where the results and discussion of the as-deposited and annealing studies have been split into two separate parts.

6.2 As-Deposited Sc_2O_3 Films

Within this first part, the results for as-deposited Sc_2O_3 thin films fabricated by ECR-IBSD have been presented and discussed.

6.2.1 Results and Discussion

6.2.1.1 Transmittance and Reflectance Measurement

As previously mentioned, within this experiment, the reactive oxygen have been varied in order to observe the effect this has on the coatings and its properties. Figure 6.1 below shows the transmittance and reflectance spectra obtained for the six films within this data set with different reactive oxygen percentage, including oxygen sputtering. The spectra were acquired by the use of the Photon RT, where this data is then used to extract the optical properties of the films, which will be discussed in later sections.

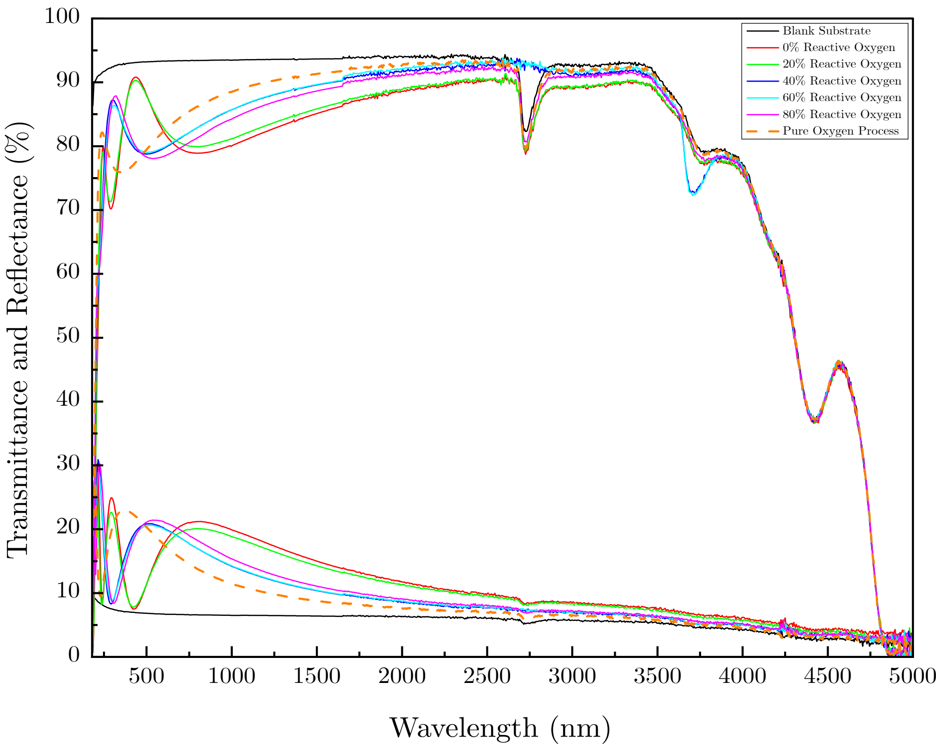

Figure 6.1: Transmittance and reflectance data for as-deposited Sc_2O_3

Here, it can be seen that as the oxygen content increases, the transmittance of the films increases, leading to a decrease of the reflectance. This is most notable in wavelength range of 750 – 2500 nm. In this wavelength range, the highest transmittance is for 100% sputtering oxygen and the lowest is for the 0% reactive oxygen process. It can also be seen that the data exhibits interference effects at lower wavelengths, where these fringes are indicators for the thickness of the films. It can also be seen that the number of interferences in this region decreased, leading to a decrease in the thickness of the films, which is in agreement with the extracted thickness values, as shown in Figure 6.5. As shown in Figure 6.1, for 0% and 20% reactive oxygen, the interference peaks in the transmittance data were very similar, yielding similar thicknesses. The slight variations in the minima and maxima values are due to the refractive indices and extinction coefficients of the films. Similar behaviour can be observed for 40%, 60%, and 80% reactive oxygen processes.

6.2.1.2 Refractive Index and Extinction Coefficient

In Figure 6.2 below shows the refractive index of the Sc_2O_3 films investigated in this chapter. Figure 6.2a shows the dispersion of the refractive indices in the range of 200 - 2500 nm, and Figure 6.2b shows the refractive index for a fixed wavelength at 1064 nm.

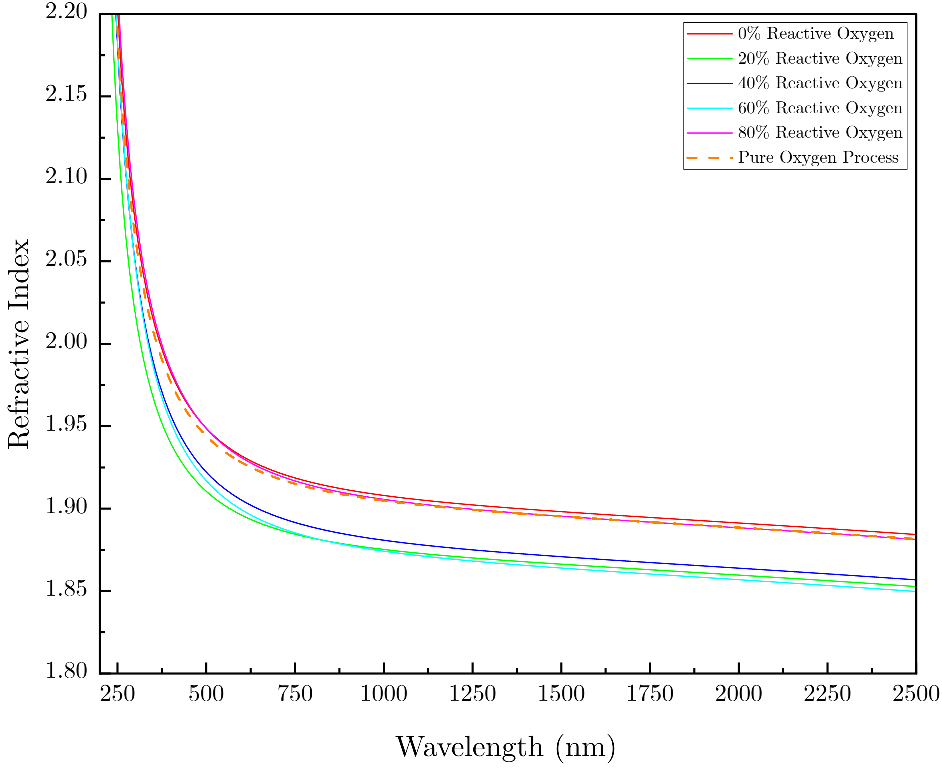

(a) Dispersion of the refractive index for the range of λ = 200 - 2500 nm

It can be seen in both figures that the lowest refractive index overall is from the 20% and 60% reactive oxygen deposition runs, where $n = 1.87$ at 1064 nm and the highest value is $n = 1.91$ at 0% reactive oxygen. It can also be seen in both figures that the refractive index for 0% and 80% reactive oxygen, along with the pure oxygen sputtering process have very close values for the refractive indices ($n = 1.91, 1.90$ and 1.90, respectively).

The refractive index values are correlated with the structure, chemical composition, and density of the films [187], where it was previously reported for zirconium dioxide that

the film composition is a dominant factor affecting the refractive index [217–219]. The refractive index values extracted from SCOUT (Figure 6.2) are very similar to those reported for Sc_2O_3 films which are $n = 1.8 - 2.0$ [63, 186–188, 196–199, 202, 207, 208]. Overall, the refractive indices of Sc_2O_3 fabricated under different oxygen content are similar, with an average of 1.89 ± 0.02, although there is an increase at 80% and 100%, but this is only by less than 2% from lower oxygen percentages.

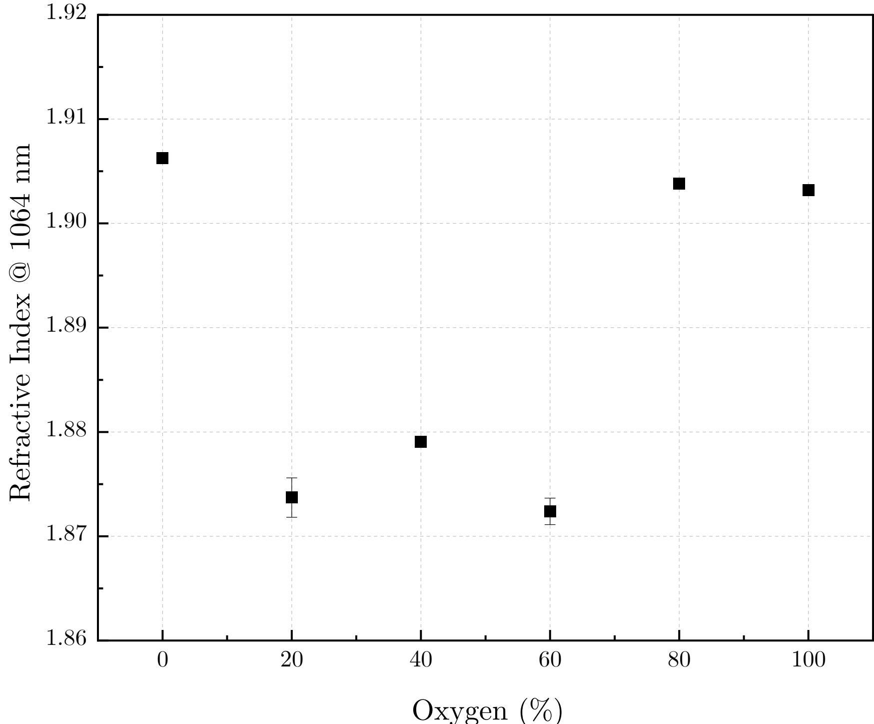

(b) The refractive index at $\lambda = 1064$ nm. The error bars show the standard deviation of five separate fittings for each sample.

Figure 6.2: The refractive index of all films in the study with differing oxygen percentages.

In Figure 6.3 below shows the extinction coefficient of the Sc_2O_3 films. Figures 6.3a and Figure 6.3b shows the extinction coefficient in the wavelength range of 200 - 2500 nm and at a fixed wavelength of 1064 nm, respectively.

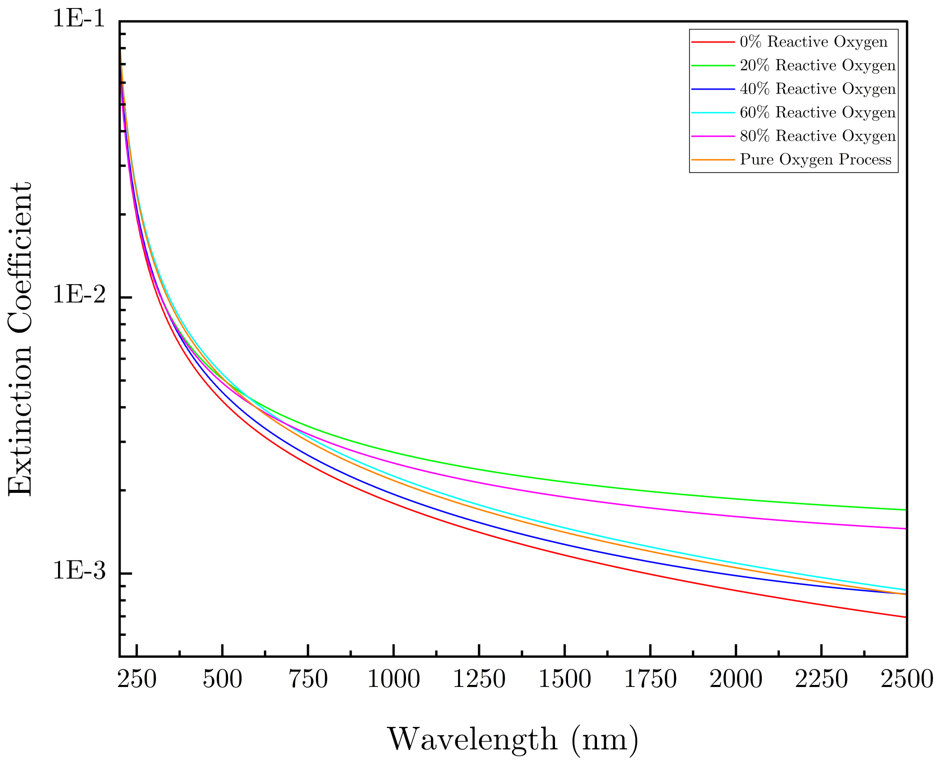

(a) Dispersion of the extinction coefficient for the range of λ = 200 - 2500 nm. Y-axis displays the extinction coefficient on a logarithmic scale.

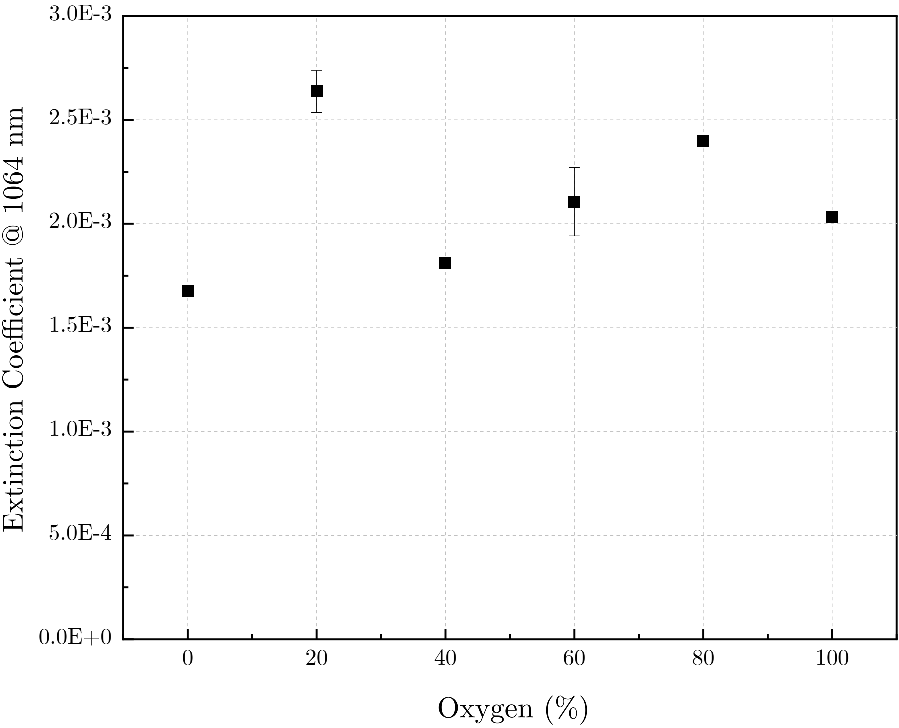

(b) The extinction coefficient at λ = 1064 nm. The error bars show the standard deviation of five separate fittings for each sample.

Figure 6.3: The extinction coefficient of all films in the study with differing oxygen percentages.

In Figure 6.3a, a sharp decline of the extinction coefficient with increase in wavelength in the UV region can be seen, where this then continues to decrease as it reaches mid-IR. As for Figure 6.3b, it can be seen that the highest value is $k = 2.6 \times 10^{-3}$, and the lowest is $k = 1.7 \times 10^{-3}$ for 20% and 0% reactive oxygen, respectively. However, similar to the refractive indices, the values for the extinction coefficient for all the films are very close to each other, where on average, $k = (2.1 \pm 0.4) \times 10^{-3}$.

6.2.1.3 Bandgap Energy

Figure 6.4 below shows the bandgap energy of Sc_2O_3 films, extracted from the OJL gap energy model. The figure shows that as the oxygen concentration increases, the bandgap energy also increases slightly from $E_{\text{gap}} = 5.86 - 6.13$ eV, which is within the range of energies reported in literature for Sc_2O_3 thin films.

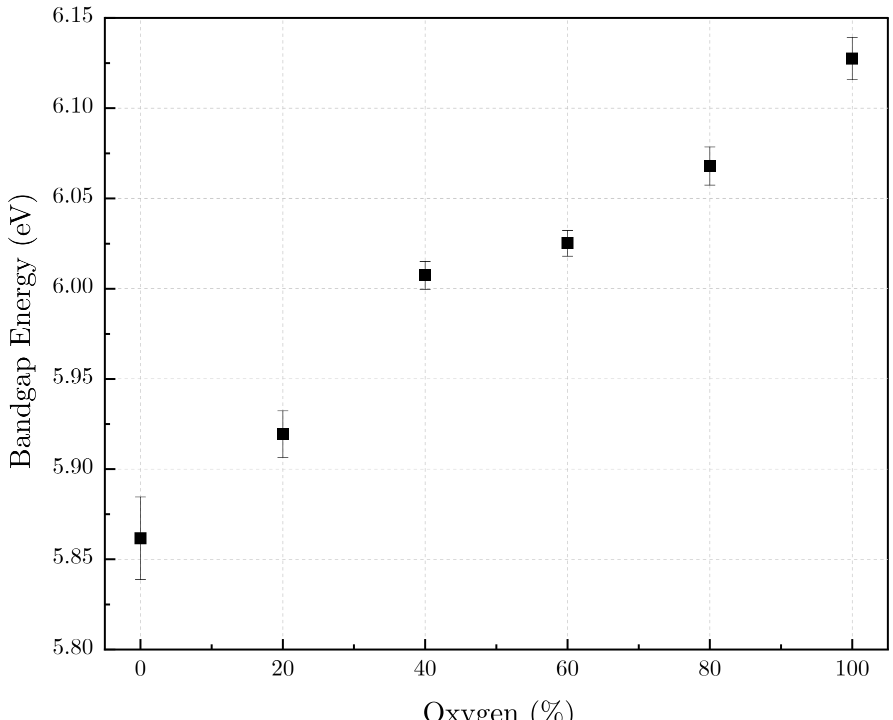

Figure 6.4: The average bandgap energy of the films acquired from SCOUT. The error bars show the standard deviation of five separate fittings for each sample.

As previously mentioned, the optical bandgap energies are affected by many factors, such as defect density, purity, packing density, and stoichiometry. In literature, the bandgap energy of Sc_2O_3 reported in literature is 5.8 – 6.0 eV [63, 196]. It can be seen in this work that by increasing the oxygen content during the deposition, the bandgap energy can be manipulated to be higher than the reported values, as shown in Figure 6.4. The increase of the bandgap energy with increasing oxygen partial pressure can be seen owing to the increase of interstitial oxygen within the films. Kong *et al.* [196] have found that with an increase of oxygen vacancies, this leads to a decrease in the concentration of free electrons as they getting trapped, leading to narrower bandgap due to high number of oxygen defects, whereas when they increase the oxygen flow rate, this increases the bandgap energy due to low number of oxygen defects. By correlating the values of bandgap energies with the transmittance measurement, it can be seen that the OJL values follow the same trend as can be seen in the UV section of the transmittance measurement. With the increase in oxygen content during deposition, there is a slight blue-shift in the transmittance data in the UV range for the absorption edge (Figure 6.1). This absorption edge is associated with the bandgap energy, and this Burstein-Moss shift shows that the shift to lower wavelengths of the absorption edge is associated with an increase in the bandgap energy.

6.2.1.4 Thickness

Figure 6.5 shows the thicknesses of the films at each oxygen percentages. As previously mentioned, all coating depositions has the same deposition time of 72 hours.

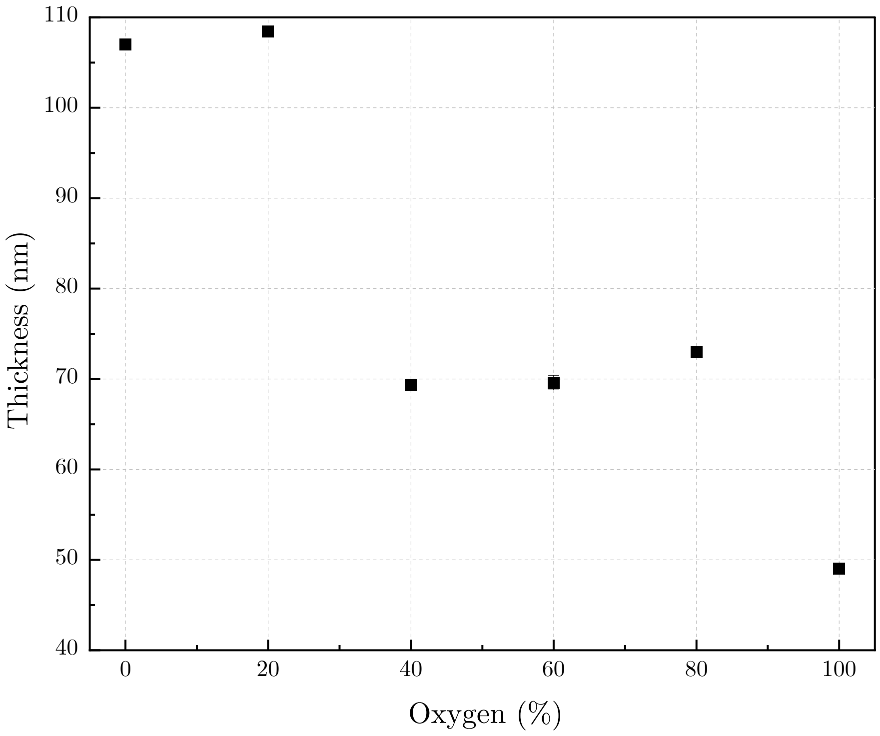

Figure 6.5: The average thicknesses of the films acquired from SCOUT. The error bars show the standard deviation of five separate fittings for each sample.

From Figure 6.5, it can be seen that at 20% reactive oxygen possesses the highest thickness, and the pure oxygen process has the lowest thickness. Table 6.1 below shows each value of the thicknesses of the films within this study:

Table 6.1: The different thicknesses of Sc_2O_3 thin films with different oxygen concentrations

OXYGEN PERCENTAGE (%)	THICKNESS (nm)
0%	107
20%	108
40%	69
60%	70
80%	73
100%	49

6.2.1.5 RBS Results

Figure 6.6 shows the ratio between the oxygen and scandium that are present within the coatings. For stoichiometric Sc_2O_3 films, O/Sc ratio has to be 1.5, which is denoted as the blue dashed line within the figure. It can be seen that all of the coatings are over-stoichiometric, where there are excess of oxygen within the films, as all films' ratio are over 1.5. The lowest value is for 20% reactive oxygen (1.58) and the highest value is for 60% reactive oxygen (2.17).

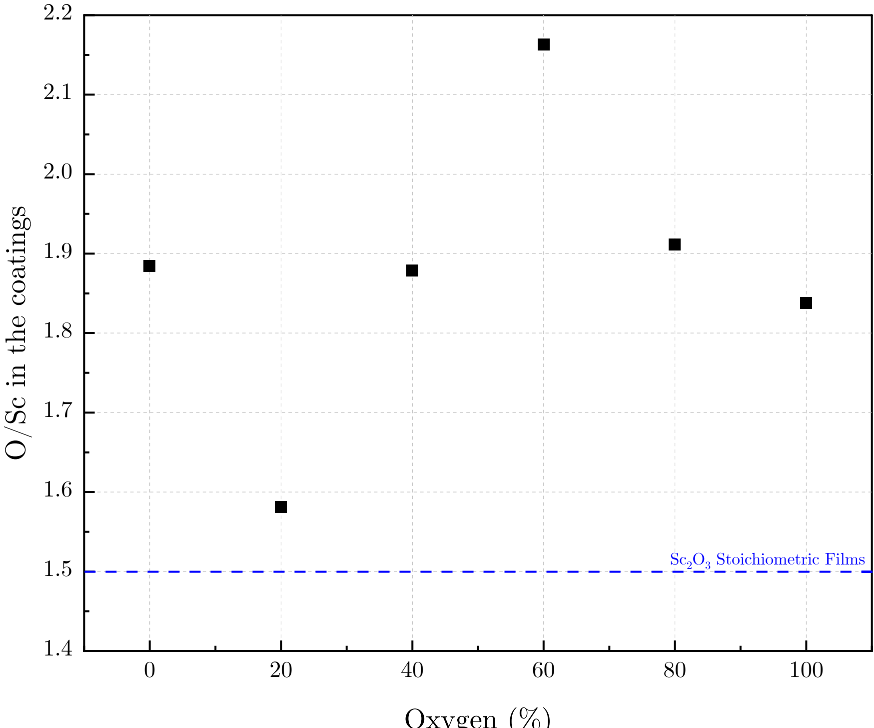

Figure 6.6: RBS data acquired for the films discussed in this chapter. The data was measured by M. Chicoine.

The RBS data show that all the films are overstoichiometric in relation to the composition of the Sc_2O_3 target (1.5:1 is the expected O:Sc ratio), where 20% reactive oxygen is closest to the stoichiometric value. In Figure 6.6, it can be seen that there is no obvious trend in the O:Sc ratio of the coatings as the oxygen percentage increases. However, if the average is taken for all films, the ratio of the films fabricated by ECR is 1.9 ± 0.2. This can be attributed to the interstitial oxygen within the films, which is common in

the literature for Sc_2O_3 thin films. As RBS is a surface technique, the overstoichiometric values can also be due the presence of additional oxygen-containing species, i.e. water in the atmosphere, which may increase the oxygen content in the films that have been measured.

6.2.1.6 XRD Results

Figure 6.7 below shows the GIXRD pattern of Sc_2O_3 films, with differing oxygen content. As can be seen from the XRD spectra, all of the films within this study shows broad weak bands, which indicates that all of the films at as-deposited are amorphous.

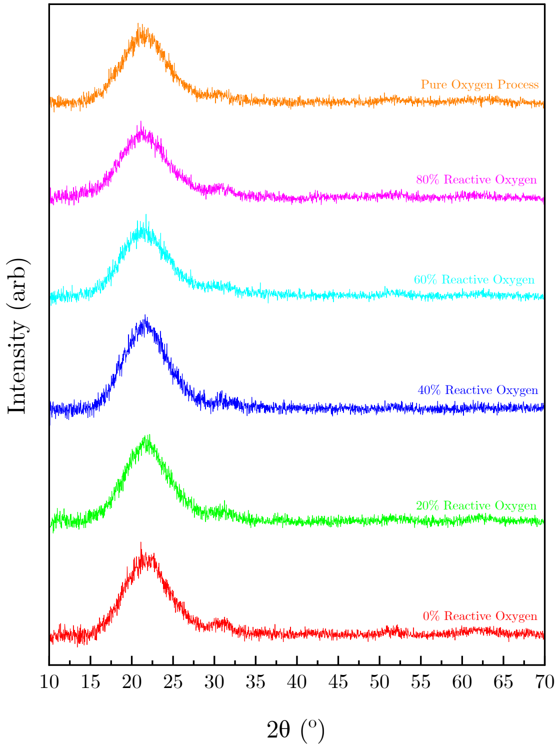

Figure 6.7: XRD data acquired for the as-deposited films in this study, by utilising the GIXRD method.

In the GIXRD data, the broad peak that can be seen is for (211) plane in a Sc_2O_3 cubic structure, which is also near the same position as that for fused silica substrate. It can be seen that as the oxygen content increases, the GIXRD peaks also shifts slightly towards

higher 2θ angle [27, 186]. However, as the change in 2θ is less than 1°, this increase in compressive stress is minimal [186–188]. The GIXRD spectra are in agreement with the RBS results of the overstoichiometric Sc_2O_3 films, where interstitial oxygen produces compressive stress [196].

6.3 Effects of Annealing on Sc_2O_3 Films

In this section, the results for annealed Sc_2O_3 films at 500°C, 700°C and 900°C have been presented and discussed.

6.3.1 Results and Discussion

6.3.1.1 Transmittance and Reflectance Measurement

Figure 6.8 shows the transmittance and reflectance of some samples within this study (0% reactive oxygen and pure oxygen sputtering), where they are being compared between as-deposited, 500°C, 700°C and 900°C annealing temperatures to show the differences within the same coatings due to annealing. As previously mentioned, all samples were annealed for 1 hour in air at each temperature, and left to cool down naturally before taking them out of the furnace.

In each of the figures, the black solid line are the spectra for the blank substrate, red solid line is for as-deposited, green dash is for annealed at 500°C, magenta dashed-dot is for annealed at 700°C, and blue dot is for annealed at 900°C.

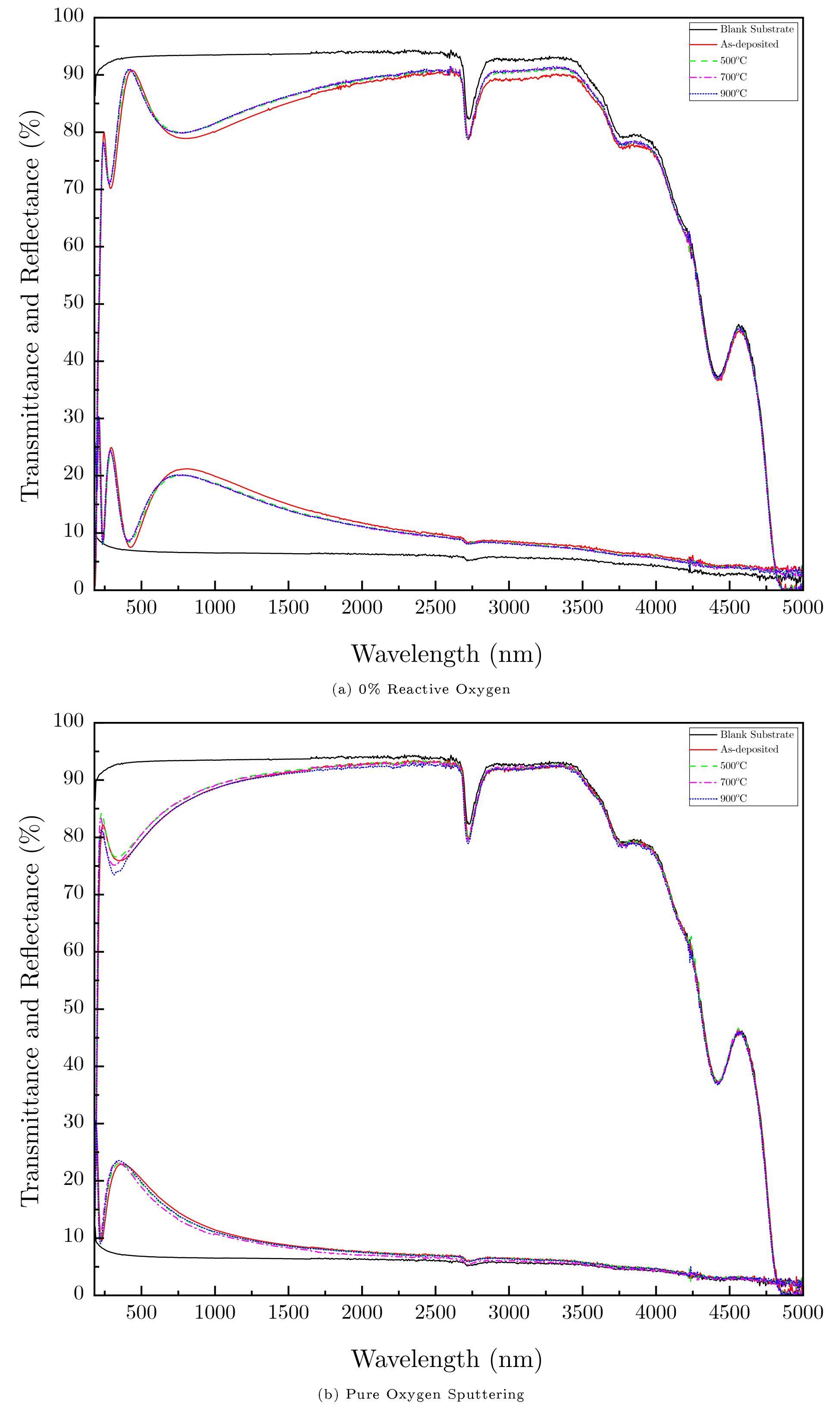

(a) 0% Reactive Oxygen

(b) Pure Oxygen Sputtering

Figure 6.8: Transmittance and reflectance data of as-deposited, 500°C, 700°C, and 900°C annealed samples.

Figure 6.8a shows that there is a slight shift of the data that can be seen towards lower wavelengths as the annealing temperature increases. This shift is an indication that there is an increase in the bandgap energy as the annealing temperature increases - otherwise known as the Burstein-Moss shift. This shift towards the lower wavelengths as the annealing temperature increases can also indicate the thickness change within the coatings, which in turn will also affect the refractive index and the density of the coating. There are no major changes in the transmittance and reflectance percentages, except for a slight increase in transmittance and decrease in the reflectance as the temperature increases, however, the changes are not drastic.

In Figure 6.8b shows a similar trend where the data is shifted towards the lower wavelengths, leading to an increase in the bandgap energy as the annealing temperature increases. It can be seen that at 900°C, the transmittance data shows the most drastic change at 280 - 400 nm, compared to other temperatures, as the transmittance decreases. The higher transmittance of the annealed films can also be attributed to the better homogeneity of the films [53, 220] or resulting from the arrangement of the microstructure of the films [192].

6.3.1.2 Refractive Index and Extinction Coefficient

Figure 6.9 shows the refractive index at 1064 nm for all temperature: As-deposited (black square), 500°C (red circle), 700°C (green upright triangle), and 900°C (blue downward triangle). It can be seen that when the samples have been annealed, they follow a similar trend, where from 0% to 40% reactive oxygen shows the refractive index value decreases with increasing oxygen content, then as the oxygen content increases from 60% to 100%, the refractive index also increases.

As the annealing temperature increases, the refractive index also decreases for all samples, except for at 900°C, where some values increase slightly. In example, for 20% reactive oxygen, from 700°C to 900°C annealing temperatures, the difference between the two refractive index values is 0.002, similar to the values for 80% reactive oxygen

sample. The largest change that can be observed by annealing from 700°C to 900°C is for pure oxygen process, where the highest refractive index value is at 900°C ($n = 1.91$).

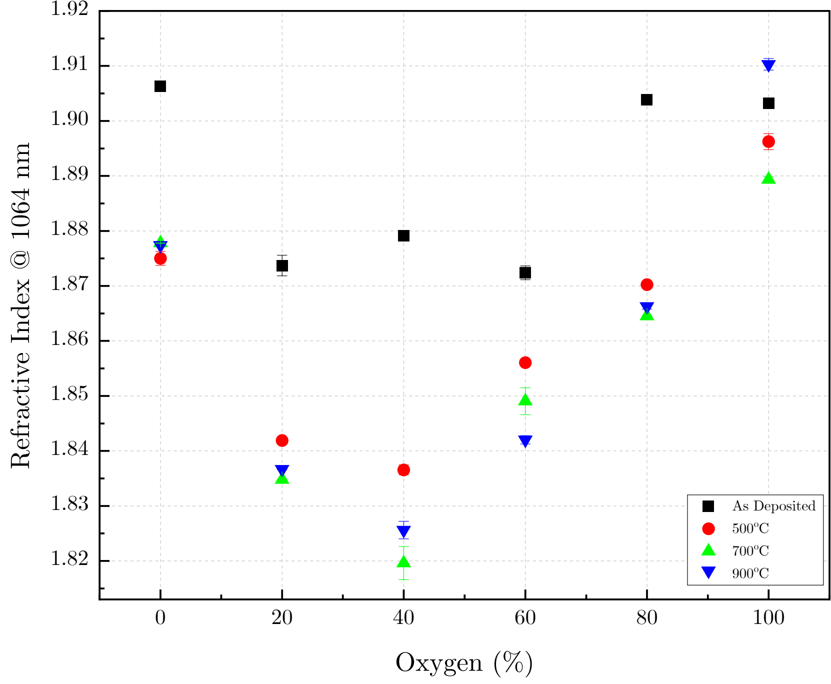

Figure 6.9: The refractive index at $\lambda = 1064$ nm for as-deposited (black), 500°C (red), 700°C (green) and 900°C (blue) annealed temperature. The error bars show the standard deviation of five separate fittings for each sample.

The less dense films can also be attributed to the stress of the thin films, i.e. lattice contraction. Other authors have also associated a decrease in the refractive index with the increase in the porosity of films [221], which in turn decreases the density of the films. However, this is reported for films that were fabricated by other deposition methods, rather than by IBSD [221]. Lv *et al.* have also observed the same phenomena for Ta_2O_5 films where they expressed that this leads to the decrease in packing density of the films, which is in agreement with the widely reported relationship between optical constant and annealing temperature [192, 222].

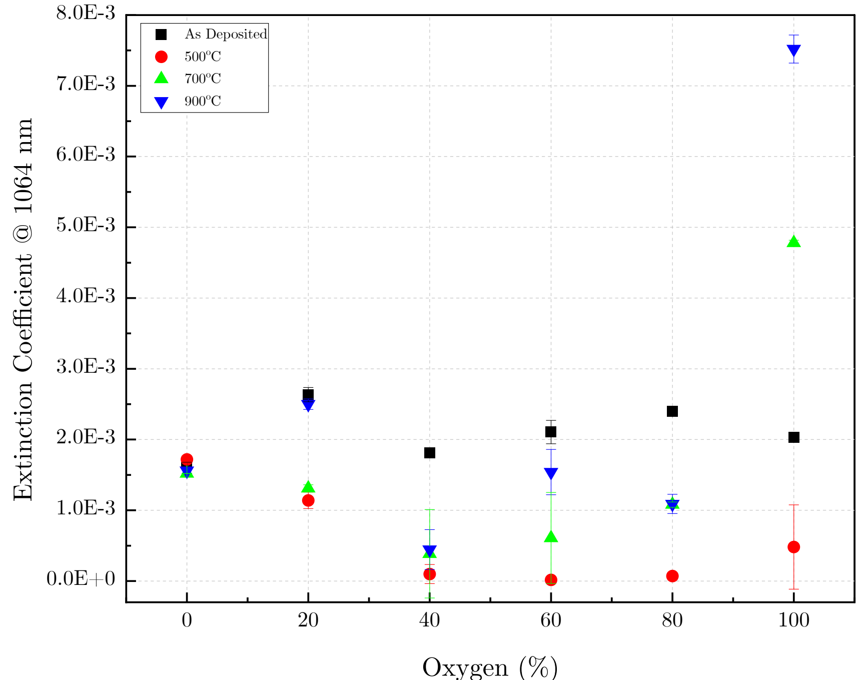

Figure 6.10: The extinction coefficient at $\lambda = 1064$ nm for as-deposited (black), 500°C (red), 700°C (green) and 900°C (blue) annealed temperature. The error bars show the standard deviation of five separate fittings for each sample.

Figure 6.10 above shows the extinction coefficient of the samples at 1064 nm, similar to the refractive index shown above in Figure 6.9. For all samples, as they are annealed to 500°C, the extinction coefficient decreases, leading to a decrease in absorption. The highest value is at 0%, where $k = 2 \times 10^{-3}$, and the lowest value is at 80%, where $k = 7 \times 10^{-5}$. As the annealing temperature increases to 700°C, the extinction coefficient increases for all samples, similar to those annealed to 900°C. The biggest change that can be observed is for the pure oxygen process, where the lowest value is $k = 4.81 \times 10^{-5}$ at 500°C, to the highest value at $k = 7.52 \times 10^{-3}$ at 900°C. As for the films with 0% reactive oxygen, this has the smallest variation in the extinction coefficient for the different annealing temperature ($k = 1.52 - 1.72 \times 10^{-3}$). In the case of Sc_2O_3 films in this study, the ideal annealing temperature in terms of lowest extinction coefficient is at 500°C, as when the temperature increases, so does the extinction coefficient.

6.3.1.3 Bandgap Energy

Figure 6.11 below shows the OJL bandgap energy of the Sc_2O_3 films for: as-deposited (black square), 500°C (red circle), 700°C (green upright triangle), and 900°C (blue downward triangle).

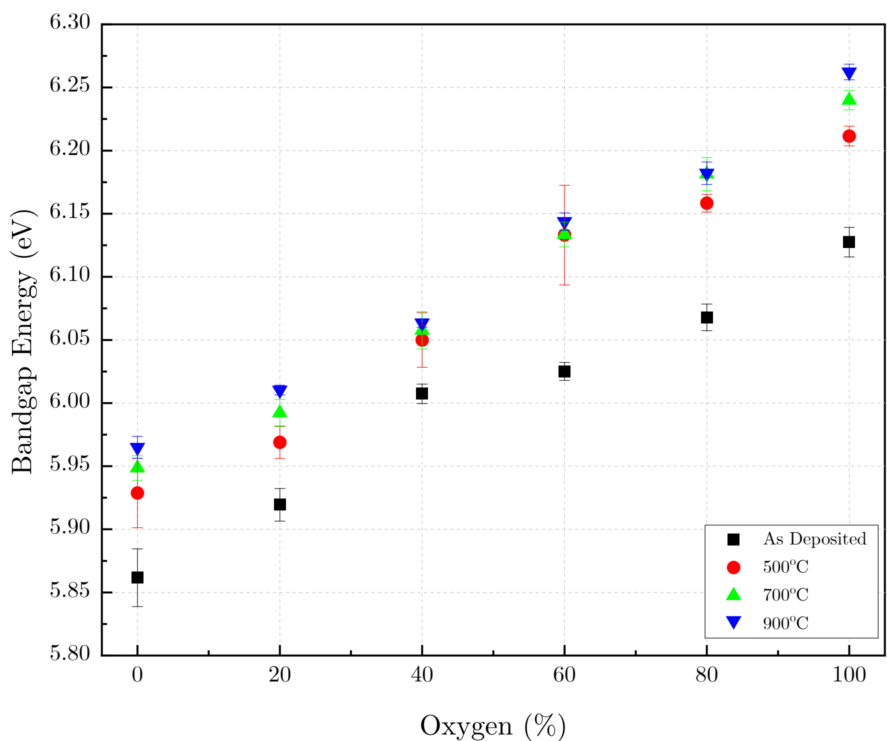

Figure 6.11: The average bandgap energy of the films acquired from SCOUT at as-deposited (black), 500°C (red), 700°C (green) and 900°C (blue) annealed temperature. The error bars show the standard deviation of five separate fittings for each sample.

As the samples are annealed to 500°C, all samples shows an increase in energy. At 0% reactive oxygen shows the lowest value for bandgap energy of 5.93 ± 0.03 eV, and pure oxygen process has the highest value of 6.21 ± 0.01 eV. As the samples are annealed to 700°C, there is also a slight increase in bandgap energy that can be observed for all samples. The same can also be observed as the annealing temperature increases to 900°C, where the lowest value is for 0% reactive oxygen at 5.96 ± 0.01 eV and the highest value is for pure oxygen process at 6.26 ± 0.01 eV.

As shown in Figure 6.11, it can be seen that as the annealing temperature increases, so does the bandgap energy, in agreement with the spectral shift towards lower wavelengths, which can be seen in the transmittance data. This increase in the bandgap energy as the annealing temperature increases can be attributed to changes in the microstructure of the films from amorphous to more polycrystalline structures, and can be related to the rearrangement of atoms to more favourable positions or stable states by post-thermal annealing [181]. Another explanation for the increase in bandgap energies by thermal annealing is the reduction in the number of unsaturated defects, which in turn decreases the density of localised states in the band structure, leading to an increase in the optical bandgap energy [221, 223–225].

The overall trend that can be observed from Figure 6.11 is that as the annealing temperature increases, so does the bandgap energy.

6.3.1.4 Thickness

Figure 6.12 shows the thickness extracted from SCOUT for the Sc_2O_3 films for samples at: as-deposited (black square), 500°C (red circle), 700°C (green upright triangle), and 900°C (blue downward triangle).

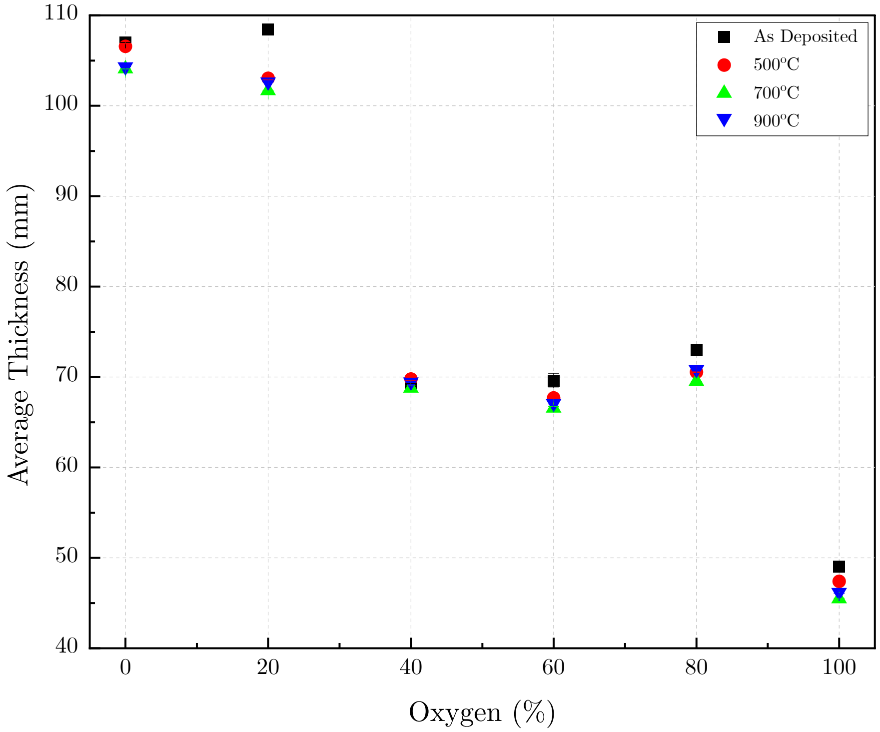

Figure 6.12: The average thickness of the films acquired from SCOUT at as-deposited (black), 500°C (red), 700°C (green) and 900°C (blue) annealed temperature. The error bars show the standard deviation of five separate fittings for each sample.

From Figure 6.12, it can be seen that the annealed samples are still following the same trend as those at as-deposited. For all the films, as the annealing temperature increases, the thickness decreases. The largest change that can be observed is for 20% reactive oxygen from as-deposited (108 nm) to 500°C (103 nm). For other configurations and annealing temperatures, the changes between the thickness are 2 nm or less, where this variation is within the fitting error range of SCOUT. Table 6.2 below shows the thicknesses of each sample at different annealing temperature.

Table 6.2: The different thicknesses of Sc_2O_3 thin films with different configurations at 500°C, 700°C and 900°C annealed temperatures

OXYGEN PERCENTAGE (%)	THICKNESS (nm)			
	As-deposited	500°C	700°C	900°C
0%	107.0	106.6	104.1	104.3
20%	108.4	103.0	101.7	102.6
40%	69.3	69.8	68.8	69.5
60%	69.6	67.7	66.5	67.1
80%	73.0	70.5	69.5	70.8
100%	49.1	47.4	45.5	46.2

6.3.1.5 XRD Results

Below, the GIXRD data for Sc_2O_3 films at 500°C, 700°C and 900°C are shown. GIXRD data has been chosen as the films in this study are relatively thin, and with this technique, the substrate's signal can be minimised.

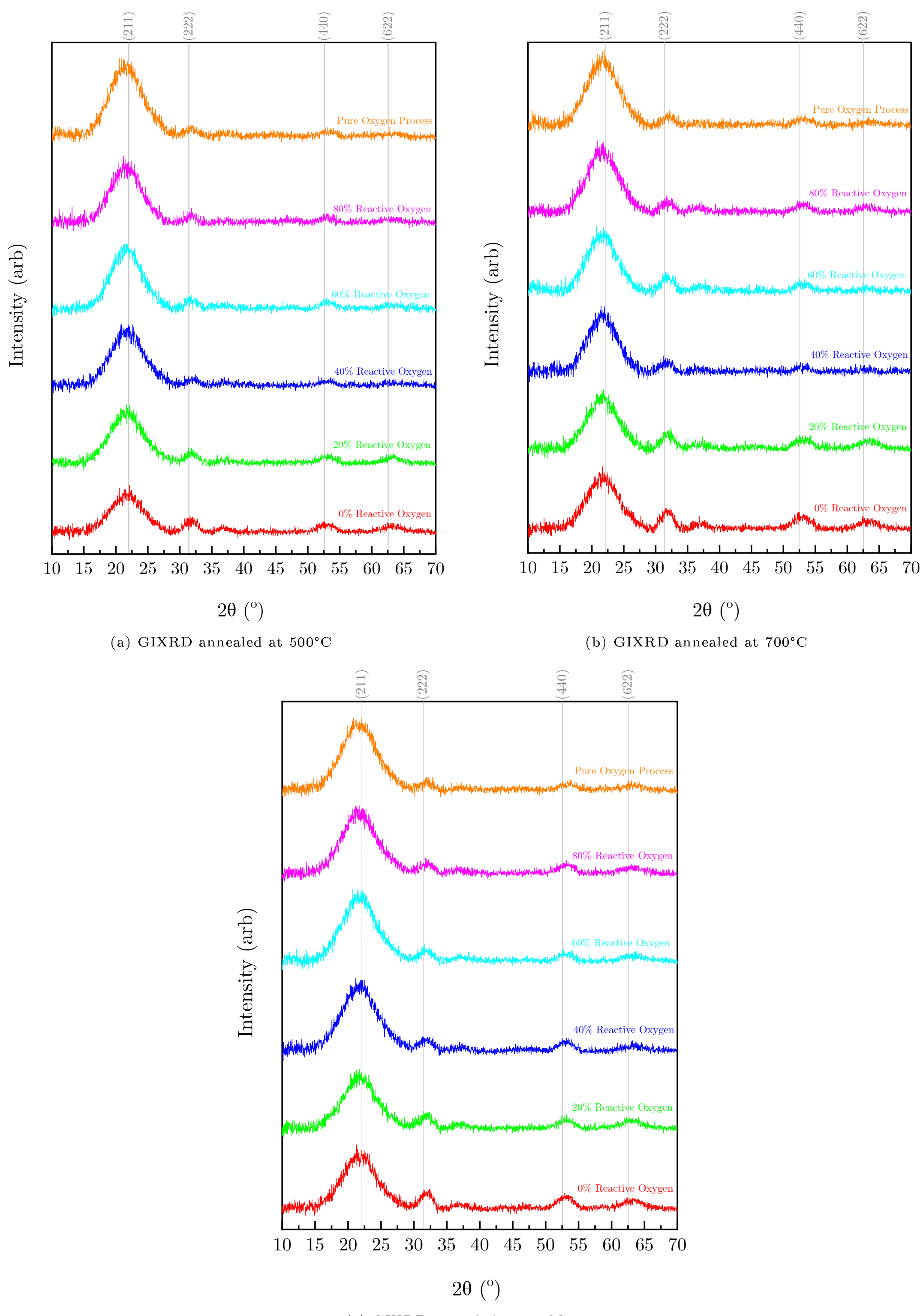

(a) GIXRD annealed at 500°C

(b) GIXRD annealed at 700°C

(c) GIXRD annealed at 900°C

Figure 6.13: GIXRD data acquired for the annealed films within this study.

At 500°C show in Figure 6.13a, it can be seen that the data still shows broad weak bands, indicating that the films are still amorphous. However, there are small peaks starting to show, but this is still so small that the films are said to still be amorphous for all samples. Similarly at 700°C (Figure 6.13b), where the spectra also shows broad weak bands, indicating that the amorphous nature still exists for the films. Again, small peaks are starting to form, indicating a slow shift into the polycrystalline nature. The same can also be observed when the films are annealed to 900°C (Figure 6.13c), where the peaks that are forming are still similar to those at 700°C. From this, it can be concluded that the films are still amorphous at this temperature, where it is slowly transitioning into polycrystalline nature.

As can be seen in Figure 6.13, as the annealing temperature increased, more diffraction peaks corresponding to cubic Sc_2O_3 can be seen to have appeared. However, the films remained amorphous. These peaks that can be observed as the temperature increases, can be seen that they all have shifted slightly towards higher 2θ values (particularly at (222), (440) and (622)). This suggests that lattice contraction occurred within the films, leading to compressive stress [27, 186–188]. Along with the slight decrease in thickness (Figure 6.12), lattice contraction can cause shrinkage in the films [150], further confirming the hypothesis of an increase in the compressive stress in the Sc_2O_3 films as the annealing temperature increases. Another reason that can be attributed to the decrease in thickness, along with a decrease in the refractive index and packing density as the annealing temperature increases, can be due to oxygen desorption, where the excess oxygen within the films are released from the films. As mentioned in Chapter 5, IBSD films typically exhibit compressive stress, where this is also expected in ECR-IBSD films. For Sc_2O_3, the crystallisation temperature is typically 500°C, where with some deposition methods, the films will possessed polycrystalline nature from fabrication without any annealing processes [187]. By utilising ECR-IBSD to fabricate Sc_2O_3 films and annealing the films up to 900°C, the films provides interesting results where they remain amorphous.

6.4 Conclusion

The effects of differing oxygen percentage during the fabrication of Sc_2O_3 thin films by utilising ECR-IBSD technique has been presented and discussed in this chapter. The structural analysis of the films was carried out by GIXRD, which confirmed that all the as-deposited films in this study were amorphous. The compositional analysis has been demonstrated by utilising RBS, where it was found that the films are all over-stoichiometric as the O:Sc ratio is higher than 1.5:1, at an average of 1.88:1. By utilising the OJL model implemented within SCOUT software, the refractive index of the as-deposited films was found be in the range of n = 1.87 – 1.91, where the average of all films is $n = 1.89 \pm 0.02$; the extinction coefficient was found to be in the range of k = (1.7 – 2.6) $\times 10^{-3}$, with an average of $k = (2.1 \pm 0.4) \times 10^{-3}$; and the OJL bandgap energy was found to be in the range of 5.86 – 6.13 eV for the different oxygen concentration that were investigated, where the increase in oxygen content leads to an increase of the bandgap energy. The shift in the bandgap to higher energies can also be seen from the slight shift towards lower wavelengths in the transmittance measurement in the UV range as the oxygen content increases. As can be seen from the refractive indices and extinction coefficients, there is no real trend of the effect of increasing the oxygen percentage during deposition, where the average value of the refractive index and the composition acquired from the RBS measurement confirms that these films are Sc_2O_3 with slight over-stoichiometry.

The effects of annealing on the optical and structural properties of the Sc_2O_3 films are also presented and discussed for the annealing temperature of 500°C, 700°C and 900°C. It was shown that, as the films were annealed at 500°C, the refractive indices for all films decreased, and this also decreased further as the annealing temperature increased. This also leads to the conclusion that the density of the films decreased as the annealing temperature increased. For the extinction coefficient, as the films were annealed at 500°C, the extinction coefficient decreased and then increased again as the annealing temperature increased. As for the bandgap energy, as the films are annealed to 500°C,

it has been reported that the bandgap energies increase and continue to do so as the temperature reaches 700°C and 900°C. The shift of the bandgap energies to higher values can also be observed in the transmittance measurement in the UV range, where there is a blue-shift in the spectra. The structural properties were determined using GIXRD, which showed that the films remained amorphous as the annealing temperature increased, reaching 900°C. There are peaks that can be observed as the annealing temperature increases relating to the cubic structure of the Sc_2O_3 films, where these are still broad weak bands. All the peaks show a slight shift towards higher angles, indicating compressive stress within the films, which goes hand-in-hand with the decrease in thickness and the decrease in the refractive index (and therefore, density) of the films. However, this decrease in the film thickness and refractive index can also be associated with oxygen desorption due to the annealing of the films.

From the optical characterisation, it was found that by controlling both the reactive and sputtering oxygen concentration during deposition, the bandgap energy could be tuned to the desired value depending on the application. In addition to tuning the oxygen content and sputtering percentages during deposition, post-deposition annealing can also aid in tuning the optical constants to the desired value for different applications. While the films are still amorphous after annealing at 900°C, where Sc_2O_3 films typically crystallises at 500°C, shows that Sc_2O_3 films fabricated by ECR-IBSD could be an interesting material for high-temperature applications.

7 | Hafnia Silica Mixture

7.1 Introduction

Research on mixed composite coatings is of interest due to their tunable bandgap energies, which are of great importance in the process of improving LIDT and their tunable refractive indices [70, 193, 226–228]. In the past few decades, the study of mixing oxide materials has been one of the most promising studies, as this mixed composite material allows several degrees of freedom in comparison to pure materials. Mixed materials not only give rise to the ability to tailor the refractive indices and bandgap energies, but also allow the tunability of absorption loss, as well as changing the mechanical, thermal, and structural characteristics. This also provides the ability to tailor the optical properties within a spectral range of interest, where the materials can be used to replace the typical high refractive index materials, whose LIDT can be improved by utilising mixed-material coatings [229].

The mixing of oxide dielectric coatings has been used in many different applications for many decades. For high precision optics, especially within optical coatings, the utilisation of mixed materials was introduced around the same time as the semiconductor industry. By utilising IBSD technique to fabricate mixed coatings, one of the main advantages is the reduction of stress within the coatings [230, 231], which provides high stability and repeatability of mixture coatings [72]. Along with the reduction in stress, mixed materials can be utilised to avoid discrete layer interfaces in multilayer coatings [230]. Mixed material coatings have also been used to produce rugate filter

designs [77, 193, 231–235], where gradual index profiles were utilised [231, 236] by co-deposition of two materials. This technique has been proven reliable and is a flexible method for the deposition of mixed materials [77]. However, as previously stated by Jensen *et al.*, within the last few years, it has been proven that spectral characteristics of rugate filters can be designed using the standard two material concept, without the use of mixed materials, which is further discussed by Pervak *et al* [231, 237]. Nevertheless, there are still many advantages of mixed material coatings, as previously mentioned.

The materials that are commonly investigated as mixed materials are Sc_2O_3:SiO_2, TiO_2:SiO_2, Ta_2O_3:SiO_2, and HfO_2:SiO_2, for example, [238]. Within this chapter, the mixture of interest is HfO_2:SiO_2. It has been observed that by adding SiO_2 to pure HfO_2, this can improve several properties of the thin films, such as: optical and mechanical properties, and LIDT [70, 77, 226]. A study by Jena *et al.* also showed that reduced surface roughness can be achieved by utilising mixed films of HfO_2:SiO_2 compared to that of pure HfO_2, which leads to the reduction in scattering loss [226]. HfO_2 is also known to crystallise at low temperatures and undergo certain phase transitions after heat treatment [239, 240]; and by mixing it with SiO_2, this can increase the crystallisation temperature. This also leads to better optical properties when the films are annealed, without the fear of scattering losses due to crystallisation. A lot of interest of HfO_2:SiO_2 mixture materials in literature are within the UV spectral range, where several groups have investigated the mixed coatings material with different mixture percentage and the effects this has on the LIDT, for example: Mende *et al.* reported double increased in LIDT values for S-on-1 testing at 355 nm for mixture coatings within the stack, compared to pure HfO_2 and SiO_2 multilyer coatings [72, 241]; another study by Mende *et al.* demonstrated successful application of mixed HfO_2:SiO_2 coating with an increased in LIDT for multiwavelength AR coating [242]; and Jensen *et al.* study also agrees with Mende *et al.*, where mirrors for 355 nm laser applications with mixed material has twice as high LIDT than pure material multilayer [239].

However, with the unique optical and physical properties of mixed coatings, along with different combinations of coating and substrate materials, the LIDT mechanisms of

mixed coatings are much more complex than those of pure materials [243]. To predict the optical properties of any mixed oxide material, several different effective medium approximation (EMA) models that can be utilised, such as: Lorentz-Lorenz, Drude, Needle, and Linear models, along with many others, have been used to compute the compositional dependence of the different mixed material coatings on the refractive index [193, 226].

In this chapter, it is reported the study of HfO_2:SiO_2 thin films with different mixture percentages, fabricated by ECR-IBSD technology. The stoichiometry and elemental composition of the films were calculated by EMA estimation, the structural properties of the films were determined by XRD, and the optical properties were obtained by fitting the transmittance and reflectance spectra using SCOUT software. The results have been reported and discussed, along with the LIDT results which were carried out by Rhysearch (*Buchs, Switzerland*). Furthermore, the effects of the annealing of these films on the structure, optical properties, and LIDT results are presented, where the results and discussion of the as-deposited and annealed films are split into two separate parts.

7.2 As-Deposited HfO_2:SiO_2 Films

Within this first part, the results for as-deposited HfO_2:SiO_2 thin films fabricated by ECR-IBSD have been presented and discussed.

7.2.1 Results and Discussion

7.2.1.1 Transmittance and Reflectance Measurement

In this study, the effects of different mixture percentages of HfO_2 and SiO_2 on the optical properties were investigated. Figure 7.1 below shows the transmittance and reflectance results. As previously mentioned, all of the depositions had the same pressure during

the deposition, the same base pressure, and the same deposition time (24-hours), the only difference was the number of sources that were on.

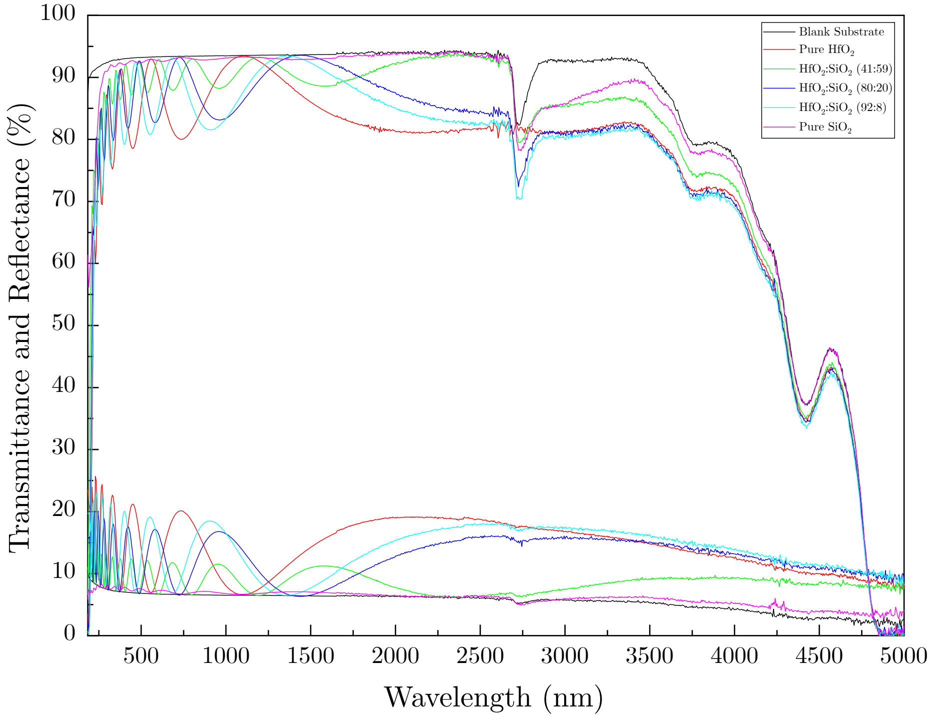

Figure 7.1: Transmittance and Reflectance data for as-deposited HfO_2:SiO_2 samples with different mixture percentages.

The figure shows six different spectra: blank JGS3 substrate, pure HfO_2, pure SiO_2, HfO_2(41%):SiO_2(59%), HfO_2(80%):SiO_2(20%), and HfO_2(92%):SiO_2(8%). The mixture percentages were extracted from EMA calculations, as discussed in Section 7.2.1.5, and the values quoted here and throughout the chapter are based on the Lorentz-Lorenz model.

Although the SiO_2 coating was deposited on fused silica (JGS-3) substrates, it can be seen that the transmittance and reflectance data for SiO_2 coating differs from the substrate's data - where interference details can be seen for the coatings which is an indication of the thickness of the film, and that there is a difference in the refractive indices of the thin film and bulk (the fused silica substrate in this case). With this interference data that can still be observed, it means that the optical constants (*n, k,*

E_{gap}, d) can still be extracted by performing the optical fittings on SCOUT.

In Figure 7.1, it can be seen that all the coatings have interference fringes, which can be used to extract the optical constants, as previously mentioned. It can be seen that varying the mixture percentages has an effect on the amplitude and number of fringes, which affects the optical constants that are extracted. The pure HfO_2 films have the largest amplitude, and pure SiO_2 has the smallest amplitude, with the different mixture amplitude sizes decreasing as the silica content increases in the mixture. The effects of the mixtures on the optical constants based on the optical fittings from the spectra in Figure 7.1 are discussed in the following sections.

7.2.1.2 Refractive Index and Extinction Coefficient

In Figures 7.2 and 7.3 below shows the refractive indices of the mixture films investigated in this study. Figure 7.2 shows the dispersion of the refractive index in the range of 200 - 2500 nm, and Figure 7.3 shows the refractive index extracted for a fixed wavelength of 1064 nm.

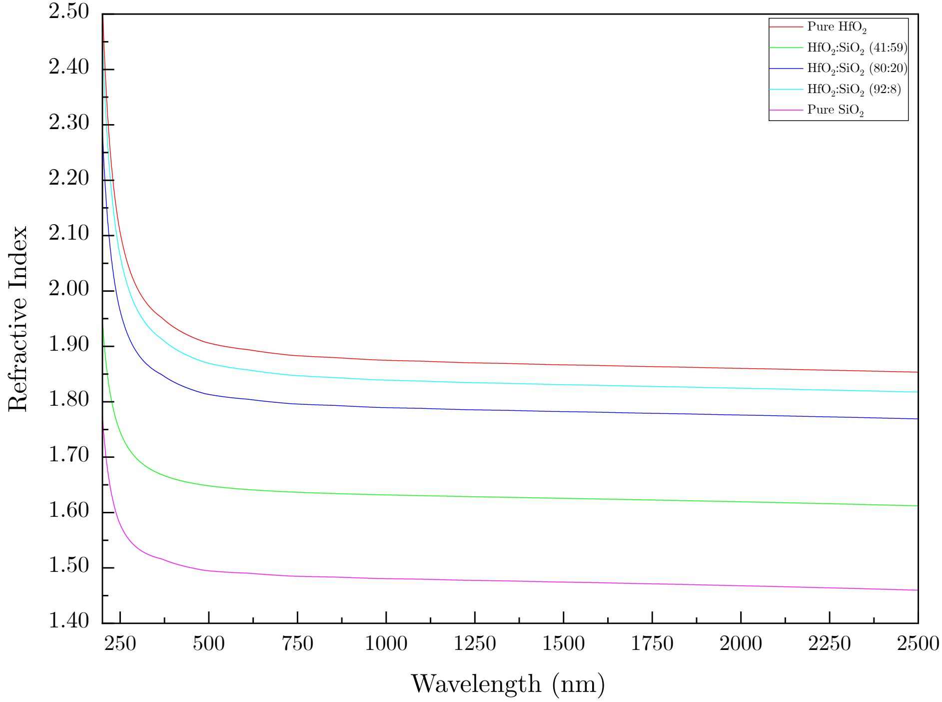

Figure 7.2: Dispersion of the refractive index for the range of λ = 200 - 2500 nm of the films with different mixture percentages

Because HfO_2 has a higher refractive index than SiO_2, it is expected that mixed films with a high HfO_2 content will have a higher refractive index. Figures 7.2 and 7.3 show that as the SiO_2 content increased in the films, the refractive index decreased, with pure SiO_2 possessing the lowest values and pure HfO_2 possessing the highest values. As shown, the mixture materials fill in the values for the refractive index between the two pure materials, indicating that the refractive index can be tuned by changing the mixture percentages. As previously discussed, the density is related to the refractive index, and it is known that SiO_2 is less dense than HfO_2. Hence, as the silica content increases, the density of the films decreases [226].

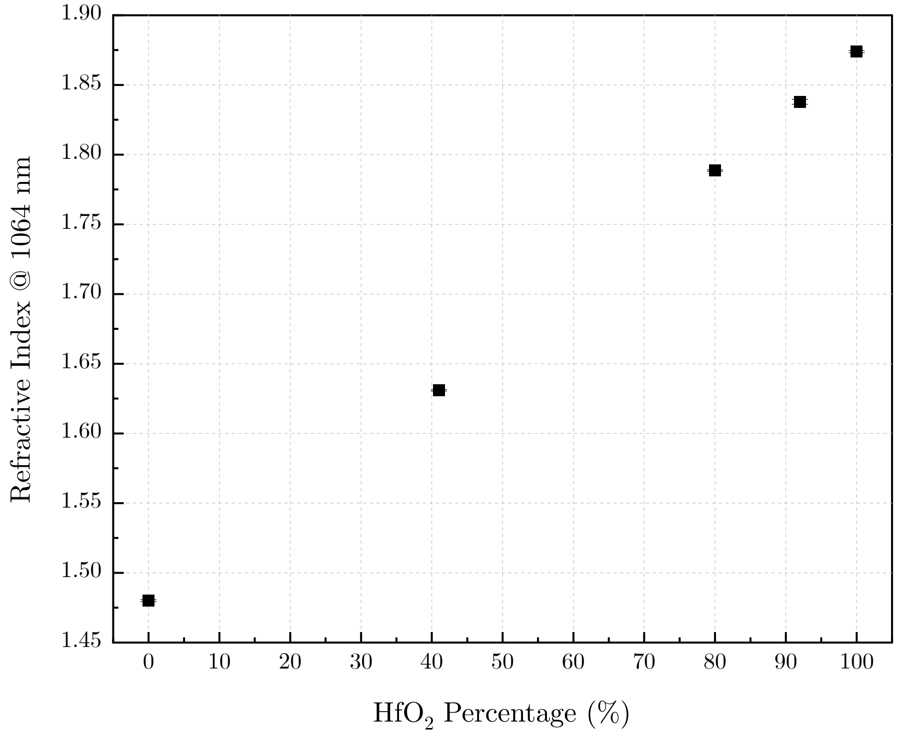

Figure 7.3: The refractive index at $\lambda = 1064$ nm of the films with different mixture percentages. The error bars show the standard deviation of five separate fittings for each sample.

In Figure 7.3, the refractive index at 1064 nm was utilised in the EMA models (Section 7.2.1.5) to extract the mixture percentages of the films. The lowest refractive index value was obtained for pure SiO_2 ($n = 1.48$) and the highest value was obtained for pure HfO_2 ($n = 1.87$). As can be seen, the increase in refractive index is linear with the increase in HfO_2 percentage. Hence, for a desired value of refractive index, extrapolation of these results can be carried out for a fixed percentage of HfO_2 that has to be deposit.

Figures 7.4 and 7.5 shows the extinction coefficient from the wavelength of 200 - 2500 nm and at a fixed wavelength of 1064 nm, respectively.

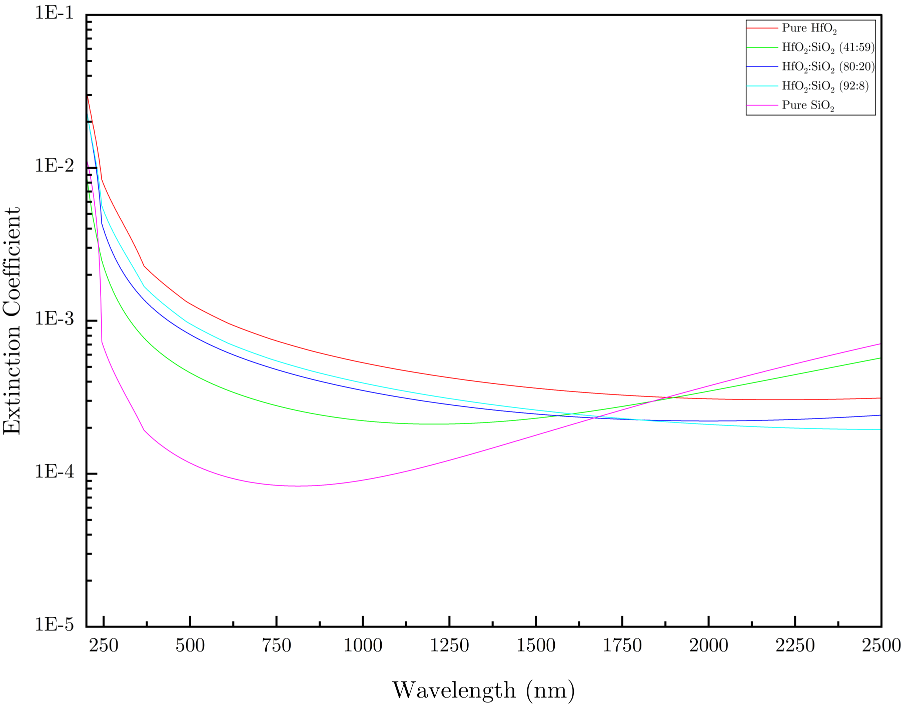

Figure 7.4: Dispersion of the extinction coefficient for the range of λ = 200 - 2500 nm. Y-axis displays the extinction coefficient on a logarithmic scale.

Figure 7.4 shows the dispersion of the extinction coefficient for the wavelength range of 200 - 2500 nm, which also exhibits a sharp decline of the extinction coefficient with the increase in wavelength within the UV region, where this then continues to slowly decrease as it reaches mid-IR.

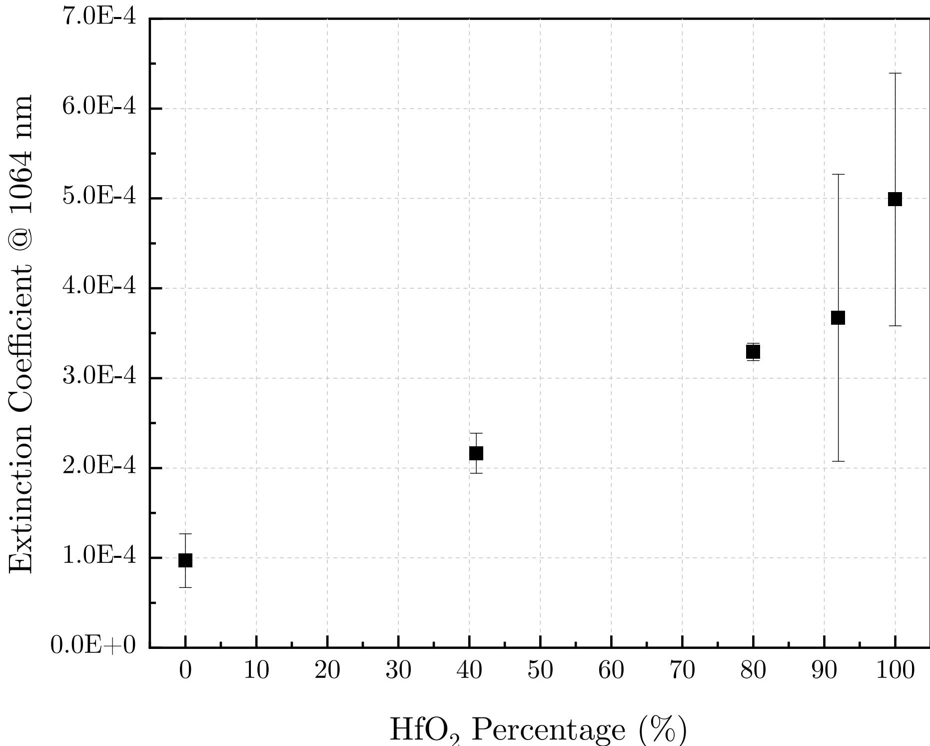

Figure 7.5: The extinction coefficient at $\lambda = 1064$ nm. The error bars show the standard deviation of five separate fittings for each sample.

In Figure 7.5, it can be clearly seen that the extinction coefficient increases as the HfO_2 volume percentage increases. This is expected because SiO_2 has a lower absorption, which is related to the extinction coefficient, than HfO_2, leading to an increase in the extinction coefficient as the HfO_2 volume percentage increases [226]. The lowest value is for pure SiO_2 ($k = 9.69 \times 10^{-5}$) and the highest value is for pure HfO_2 ($k = 4.99 \times 10^{-4}$).

7.2.1.3 Bandgap Energy

Figure 7.6 shows the bandgap energy of the mixture films as a function of the HfO_2 volume percentage in the films, where the bandgap energy was extracted from the OJL gap energy model, and the volume percentage was extracted from EMA calculations based on the Lorentz-Lorenz model.

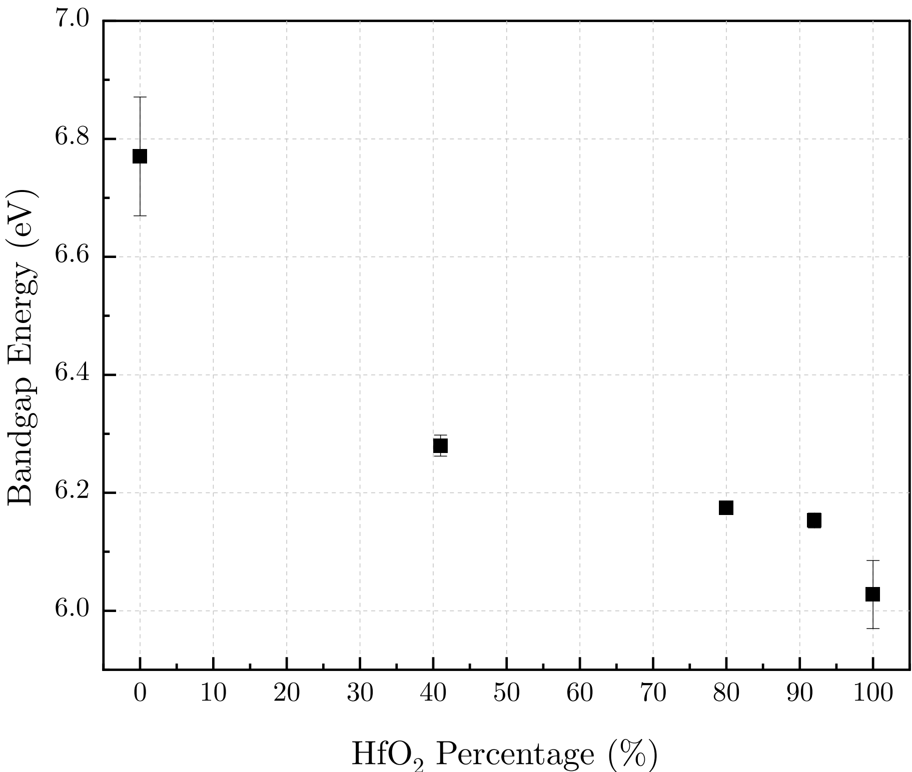

Figure 7.6: The average bandgap energy of the films acquired from SCOUT. The error bars show the standard deviation of five separate fittings for each sample.

As expected, with an increase in the SiO_2 content in the mixed films, the bandgap energy also increased [231]. This can also be observed by the blue shift observed in the transmittance data in Figure 7.1. The highest bandgap energy for the films in this study was for pure SiO_2 (6.77 eV), and the lowest was for pure HfO_2 (6.03 eV). The bandgap energies are also listed in Table 7.1:

Table 7.1: The different bandgap energies of HfO_2:SiO_2 thin films with different HfO_2 volume percentages.

HAFNIA PERCENTAGE (%)	BANDGAP ENERGY (eV)
0%	6.77
41%	6.28
80%	6.17
92%	6.15
100%	6.03

7.2.1.4 Thickness

Figure 7.7 shows the thickness of the coatings with different mixture percentages. As mentioned, all the coatings have the same deposition time and conditions, with the exception of the number of ion sources on a certain number of targets. The thicknesses were extracted from the number of fringes observed in the transmittance and reflectance spectra using SCOUT software.

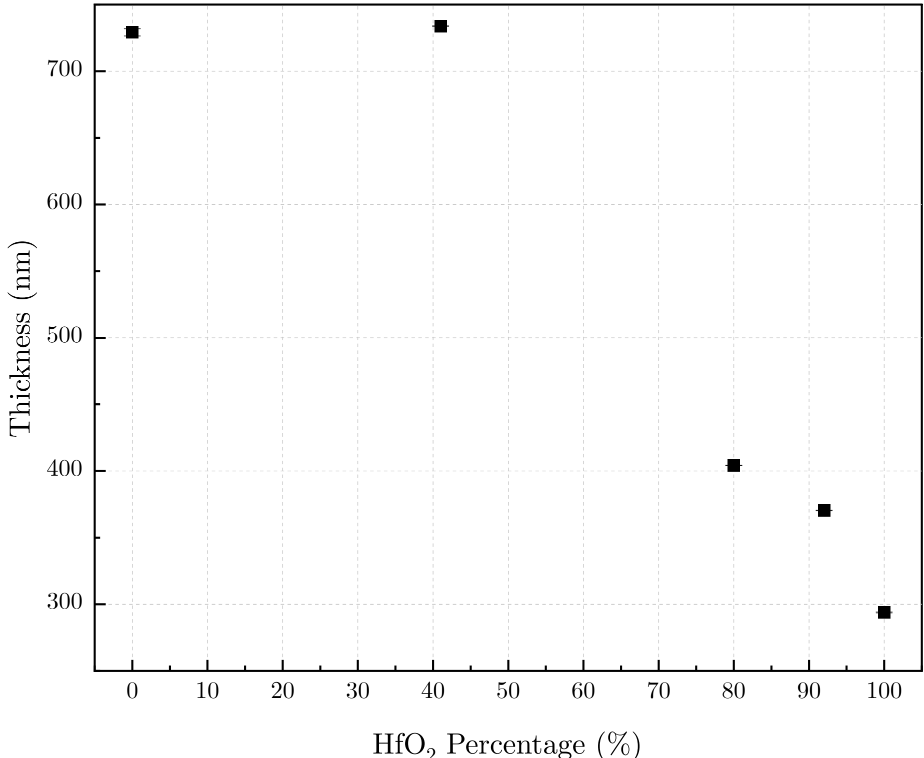

Figure 7.7: The average thicknesses of the films acquired from SCOUT. The error bars show the standard deviation of five separate fittings for each sample.

From Figure 7.7, it can be seen that the highest thickness is for HfO_2(41%):SiO_2(59%), and the lowest is for the pure HfO_2 films. The changes in the thicknesses can be associated to the fact that the sputtering rate of HfO_2 is lower than that of SiO_2. Table 7.2 below shows the thicknesses of the films based on the volume percentage of HfO_2 within the films.

Table 7.2: The different thicknesses of HfO_2:SiO_2 thin films with different HfO_2 volume mixture percentages

HAFNIA PERCENTAGE (%)	THICKNESS (nm)
0%	729
41%	734
80%	404
92%	370
100%	294

7.2.1.5 Effective Medium Approximation

Different EMA models have been derived to represent the refractive index of a homogeneous mixed-component system [193]. The models used in this thesis are as follows: Linear (Eq. 7.1), Lorentz-Lorenz (Eq. 7.2), Drude (Eq. 7.3, and Needle (Eq. 7.4), which are also frequently used in the literature:

$$n = f_a n_a + f_b n_b, \tag{7.1}$$

$$\frac{n^2 - 1}{n^2 + 2} = f_a \frac{n_a^2 - 1}{n_a^2 + 2} + f_b \frac{n_b^2 - 1}{n_b^2 + 2}, \tag{7.2}$$

$$n^2 = f_a n_a^2 + f_b n_b^2, \tag{7.3}$$

$$\frac{1}{n^2} = \frac{f_a}{n_a^2} + \frac{f_b}{n_b^2}, \tag{7.4}$$

where f_a and f_b are the volume fractions of the two pure materials and n_a and n_b are the refractive indices of the two pure materials. EMA models can be used to calculate the volume percentage of the materials by knowing the values for n_a, n_b and n of the

mixed material in question. The equations 7.3 and 7.4 are the Wiener absolute bounds of refractive index [193, 244]. For any given mixture film, the refractive index must lie on or within the region enclosed by equations 7.3 and 7.4. This can also be observed in Figure 7.8:

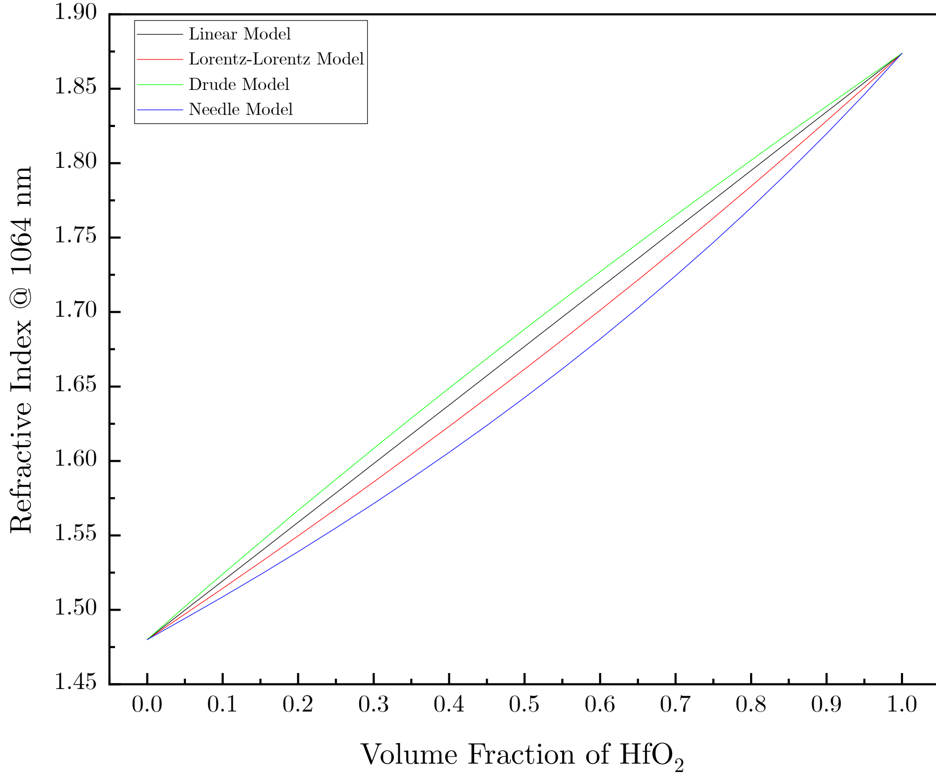

Figure 7.8: Different EMA models and its refractive index at different volume fraction of HfO_2

The Lorentz-Lorenz model values were used to quote the mixture percentages as the experimental values of the refractive indices of the mixed films are closest to the Lorentz-Lorenz model. This indicates that the microstructure of the mixed films was closer to point-like and mixed well [193]. The values for the volume fraction of HfO_2 based on the different EMA models is shown in Table 7.3:

Table 7.3: Different EMA models for HfO_2 volume fraction in the mixed coatings studied in this chapter.

RUN NAME	DRUDE	LINEAR	LORENTZ-LORENZ	NEEDLE
C21F2310 (Pure HfO_2)	1	1	1	1
C21F2910	0.36	0.38	0.41	0.47
C21F0810	0.76	0.78	0.80	0.84
C21G1210	0.90	0.91	0.92	0.94
C21F2416 (Pure SiO_2)	0	0	0	0

7.2.1.6 XRD Results

Figure 7.9 shows the GIXRD pattern of the mixed films with different mixture percentages. As can be seen from the GIXRD data, all the films, even with different mixture percentages, shows broad weak bands, which indicates that all the films are amorphous. It can be seen that with increase in HfO_2 content in the films, the peaks can be seen to increase at 32°, with the peak of SiO_2 at 22°can also be seen.

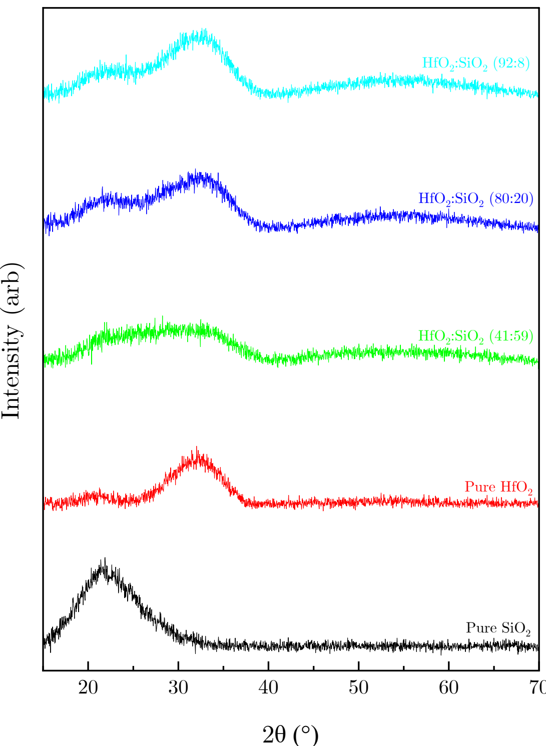

Figure 7.9: XRD data acquired for the as-deposited films in this study, by utilising the GIXRD method.

7.2.1.7 LIDT Results

Figure 7.10 below shows the damage probability curves for the two pure materials studied in this chapter as an example, where all the samples underwent the same protocol and fittings. As previously mentioned in Chapter 3.9, according to the ISO 21254 standards, LIDT is the highest quantity of laser radiation incident on the optical component for which the extrapolated probability of damage is zero, where the quantity of laser radiation is expressed in energy density. The percentage of failures is plotted against the energy density, where a least square linear fit to these data is calculated, and the 0% failure intercept most often defines the damage threshold level. The LIDT setup, this was previously mentioned in detail in Chapter 4.4.5, where the LIDT was carried out by RhySearch with a 10-on-1 test using a Nd:YAG laser at 1064 nm and 11.6 ns pulses.

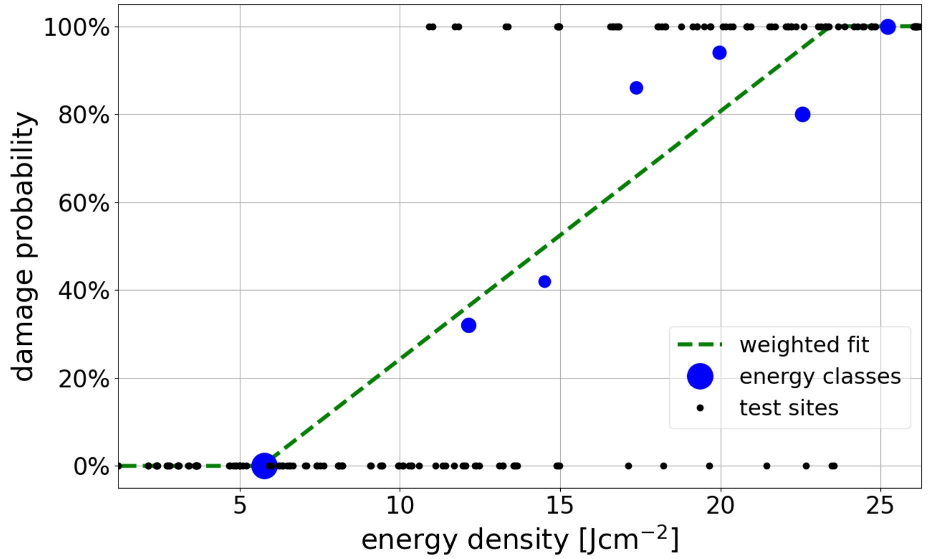

(a) Damage Probability Curve for Pure HfO_2 Films

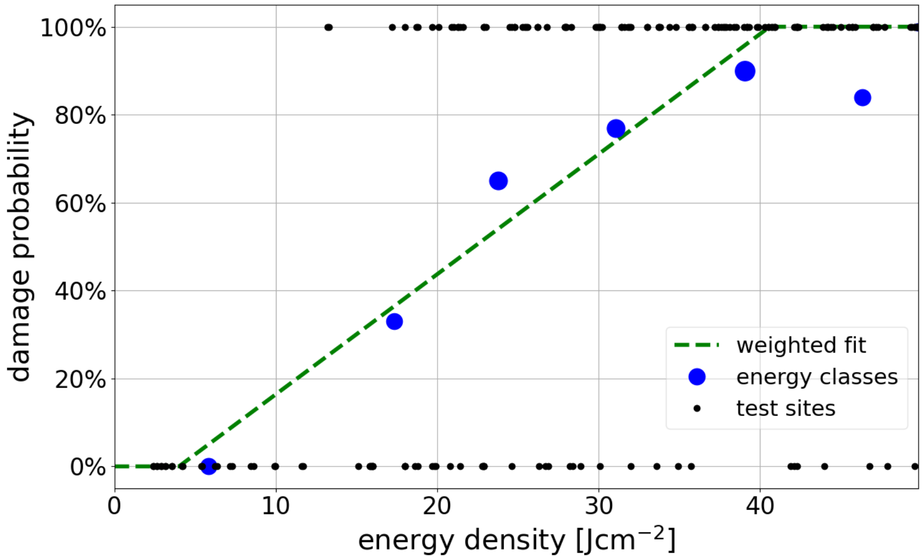

(b) Damage Probability Curve for Pure SiO_2 Films

Figure 7.10: Example of Damage Probability Curves based on the ISO-standards for pure thin films studied in this chapter. The damage occurrence corresponds to a value of 100% and when no damage appears the fluence sites is designated at 0%.

In Figure 7.11 below shows the LIDT of all coatings studied in this chapter versus refractive index (Figure 7.11a), and bandgap energy (Figure 7.11b), respectively.

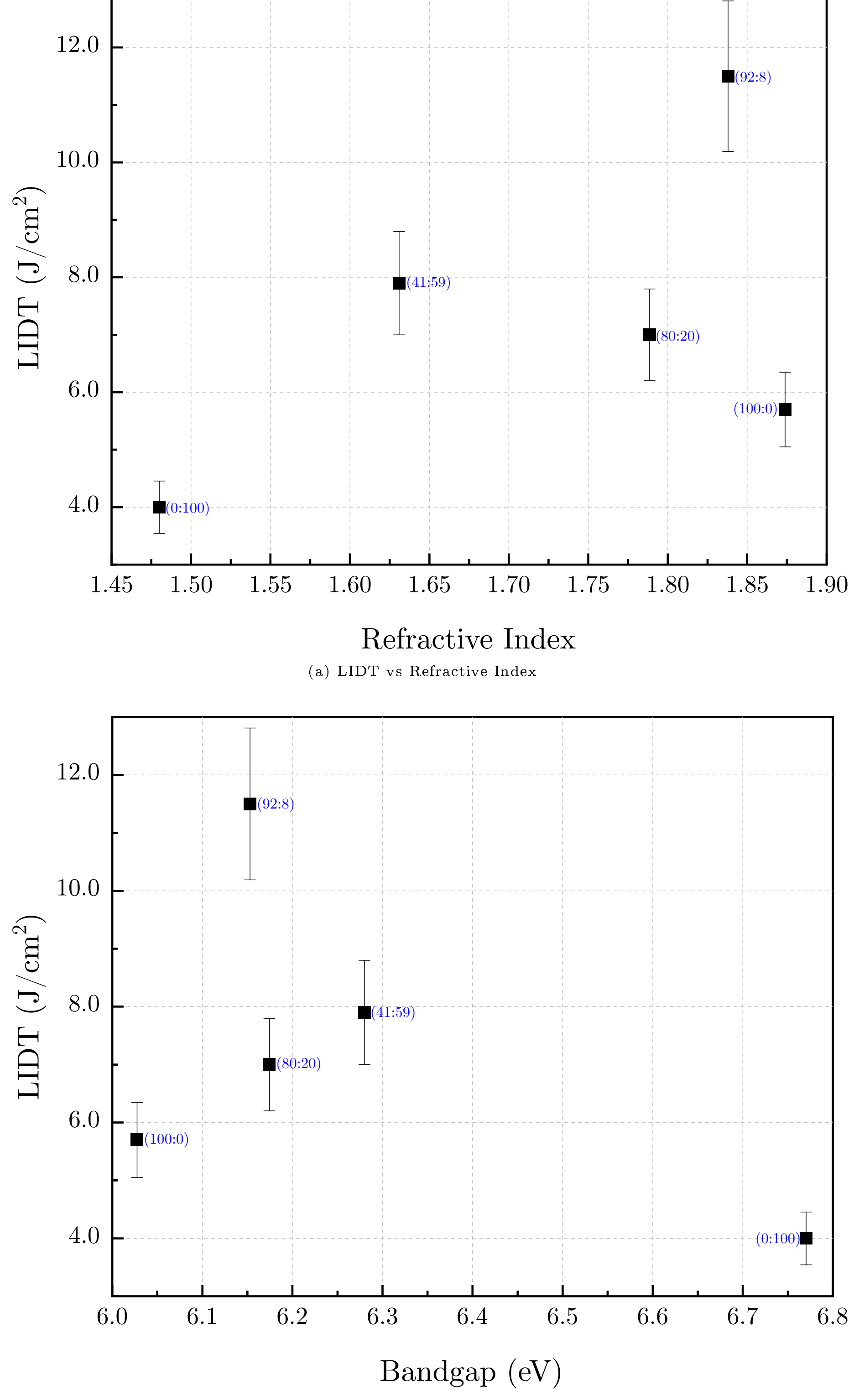

(a) LIDT vs Refractive Index

(b) LIDT vs Bandgap Energy

Figure 7.11: LIDT values for all the films studied in this chapter as a function of the refractive index and bandgap energy.

As shown, the highest LIDT was for HfO_2(92%):SiO_2(8%), and the lowest was for the pure SiO_2 film. By adding a small percentage of SiO_2 to the HfO_2 films, this increases the LIDT to 11.5 J/cm^2 from 5.7 J/cm^2 of pure HfO_2 coating. Based on Figure 7.11a for mixed films, as the refractive index increases, the LIDT values first decrease and then increase, and based on Figure 7.11b for mixed films, as the bandgap energy increases, first the LIDT decreases then increases again slightly.

As expected from the literature, the addition of SiO_2 to HfO_2 coatings reduces the refractive index and extinction coefficient of the films, where the absorbed power decreases, leading to an increase in the LIDT values for the mixed films compared to pure HfO_2 [226]. However, in this study, SiO_2 had the lowest LIDT among all the films. This is unexpected because a high LIDT of SiO_2 has been widely reported in the literature [4, 5, 71, 81, 231]. Within the nanosecond regime, the laser damage to the films is very sensitive to many technological factors, where during the production steps of the films, different origins of defects and contamination can occur [8, 229]. These defects includes but not limited to, substrate surface polishing, cleanliness of the substrate surface prior to coating, cleanliness of the deposition chamber, the deposition process and optics handling techniques [8,229]. In this study, contamination was likely to occur during the loading of substrates into the system and during the deposition process. During the deposition process, there was a large amount of discharge inside the system, which can cause contamination inside the system from delamination of the material coated on the inner walls [8]. Another source of contamination can be the sputtering of particles that may be on the targets. From the microscopic images that were taken by RhySearch of the damaged area, contamination on the coatings is very visible, showing that there is contamination and inclusions on the coatings, which likely affect the LIDT results. The figures are presented in Section 7.2.1.8 below. Therefore, during the deposition of the pure SiO_2 films, there was a significant amount of discharge inside the system, which caused the sources to be unstable. This could be the source of contamination in the SiO_2 film, leading to a much lower LIDT value than expected.

7.2.1.8 Damage Morphology

Figures 7.12 to 7.16 shows the damage morphologies of the pure and mixed films after laser irradiation, where (a) shows the low fluence damages and (b) shows the high fluence damages. There are two main types of damage that can be observed: absorption induced damage and pits due to inclusion.

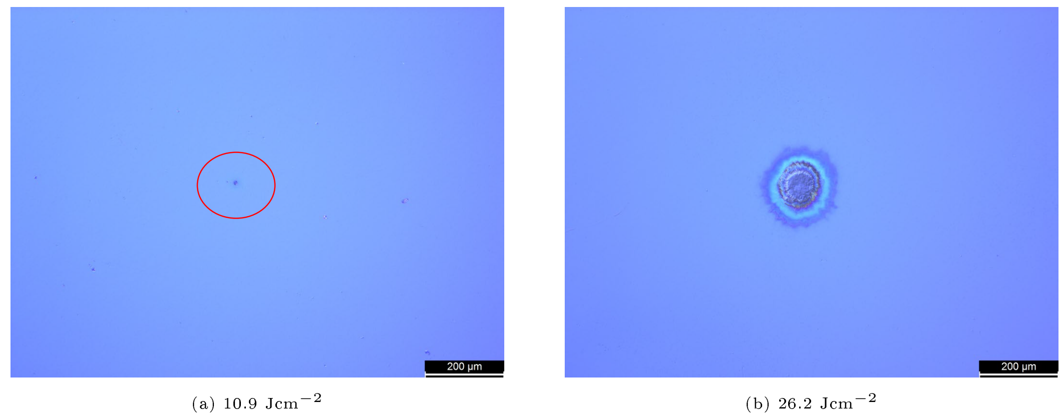

(a) 10.9 Jcm^{-2} (b) 26.2 Jcm^{-2}

Figure 7.12: Observed damage sites for pure HfO_2 film with (a) low and (b) high fluence.

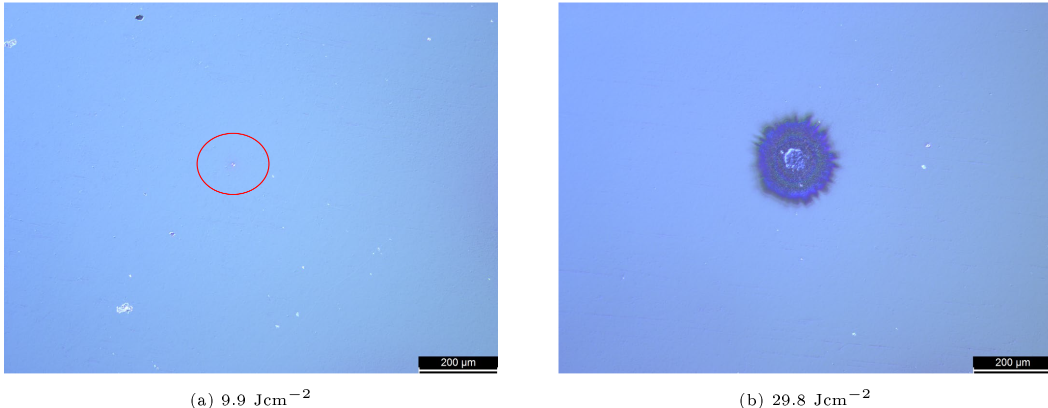

(a) 9.9 Jcm^{-2} (b) 29.8 Jcm^{-2}

Figure 7.13: Observed damage sites for HfO_2(92%):SiO_2(8%) film with (a) low and (b) high fluence.

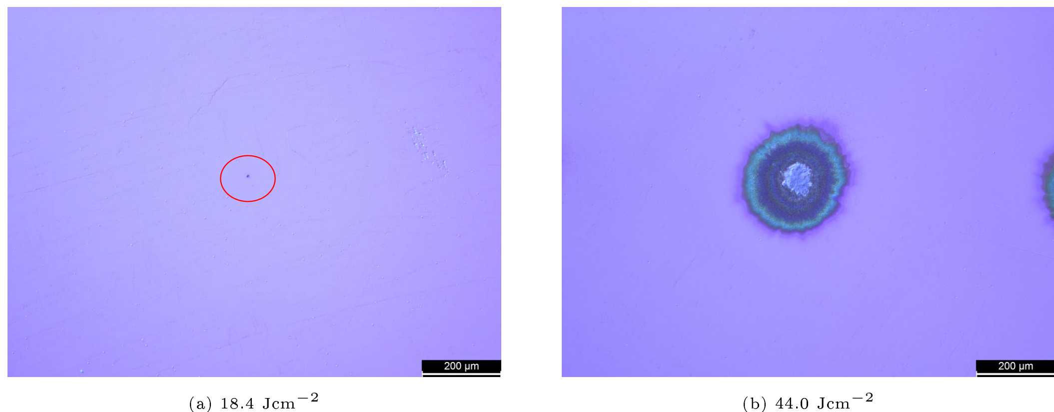

(a) 18.4 Jcm^{-2} (b) 44.0 Jcm^{-2}

Figure 7.14: Observed damage sites for the HfO_2(80%):SiO_2(20%) film with (a) low and (b) high fluence.

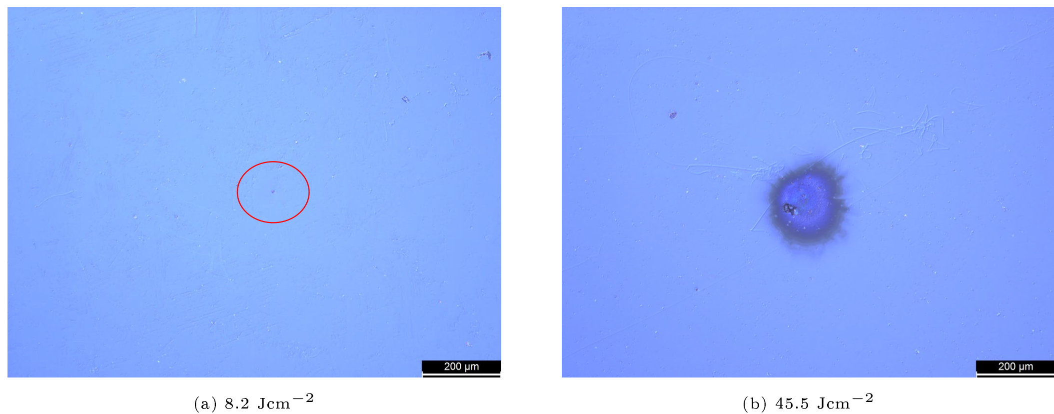

(a) 8.2 Jcm^{-2} (b) 45.5 Jcm^{-2}

Figure 7.15: Observed damage sites for the HfO_2(41%):SiO_2(59%) film with (a) low and (b) high fluence.

(a) 18.0 Jcm^{-2} (b) 49.8 Jcm^{-2}

Figure 7.16: Observed damage sites for the pure SiO_2 film with (a) low and (b) high fluence.

In Figures 7.12b, 7.13b, and 7.14b, it can be observed that the damage morpholo-

gies are very similar, which can be associated with absorption induced damage effect, where the films reached their melting point before delamination occurred [8, 243]. The characteristic morphology of absorption induced defect damage is often shown as discolouration or an increase in the surface roughness at the centre of the laser beam [8], which can be observed for samples of pure HfO_2 and mixed films with 20% or less SiO_2 contribution. This correlates with the extinction coefficient values (Figure 7.5), where the films in Figures 7.12b, 7.13b, and 7.14b have higher extinction coefficient values, which is related to the absorption of the film. In Figure 7.15b, it can be seen that the HfO_2(41%):SiO_2(52%) film exhibits both absorption induced damage morphology and pits, and as for Figure 7.16, pits can be observed for both high and low fluences. Damage initiated by defects embedded in the films typically shows craters or pits in the laser beam area [8, 80, 243]. This morphology could be attributed to inclusions which were rapidly heated during laser irradiation and exploded, creating pits [8, 80, 243]. Figure 7.16b shows the damage morphology of the pure SiO_2 film, where faint rings can also be observed at the damage site, which can be associated with the recrystallisation of the damage after laser irradiation [8]. All of the films observed in Figures 7.12 to 7.16 at low fluence laser irradiation (figures set (a)), only pits can be observed because of laser damage. In addition, contamination and inclusions can also be clearly observed in these figures near the damage site, confirming that the pit damage morphology is due to contamination of the coatings, which is the starting point of damage for all the films in this study, regardless of the mixture percentages. As mentioned, with an increase in fluence, absorption induced damage occurs for films with less than 20% SiO_2 within the mixture, including pure HfO_2 films.

7.3 Effects of Annealing on HfO_2:SiO_2 Films

In this section, the results for annealed HfO_2:SiO_2 films at 500°C, 700°C and 900°C have been presented and discussed.

7.3.1 Results and Discussion

7.3.1.1 Transmittance and Reflectance Measurement

Figure 7.17 shows the transmittance and reflectance of some samples studied in this chapter, where they are being compared between as-deposited, 500°C, 700°C and 900°C, to show the differences within the same coatings due to annealing. As previously mentioned, all samples were annealed for 1 hour in air at each temperature and allowed to cool naturally before being removed from the furnace. In each figure, the black solid lines are the spectra for the blank substrate, the red solid line represents the as-deposited substrate, the green dashed line represents 500°C, the magenta dash-dot line represents 700°C, and the blue dotted line represents 900°C.

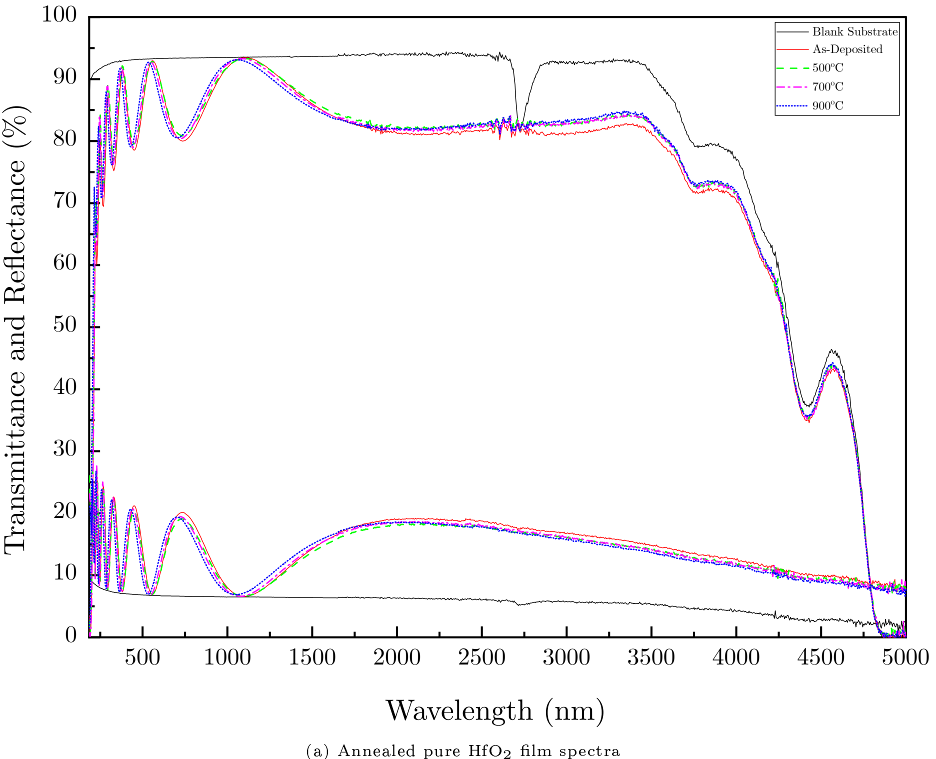

(a) Annealed pure HfO_2 film spectra

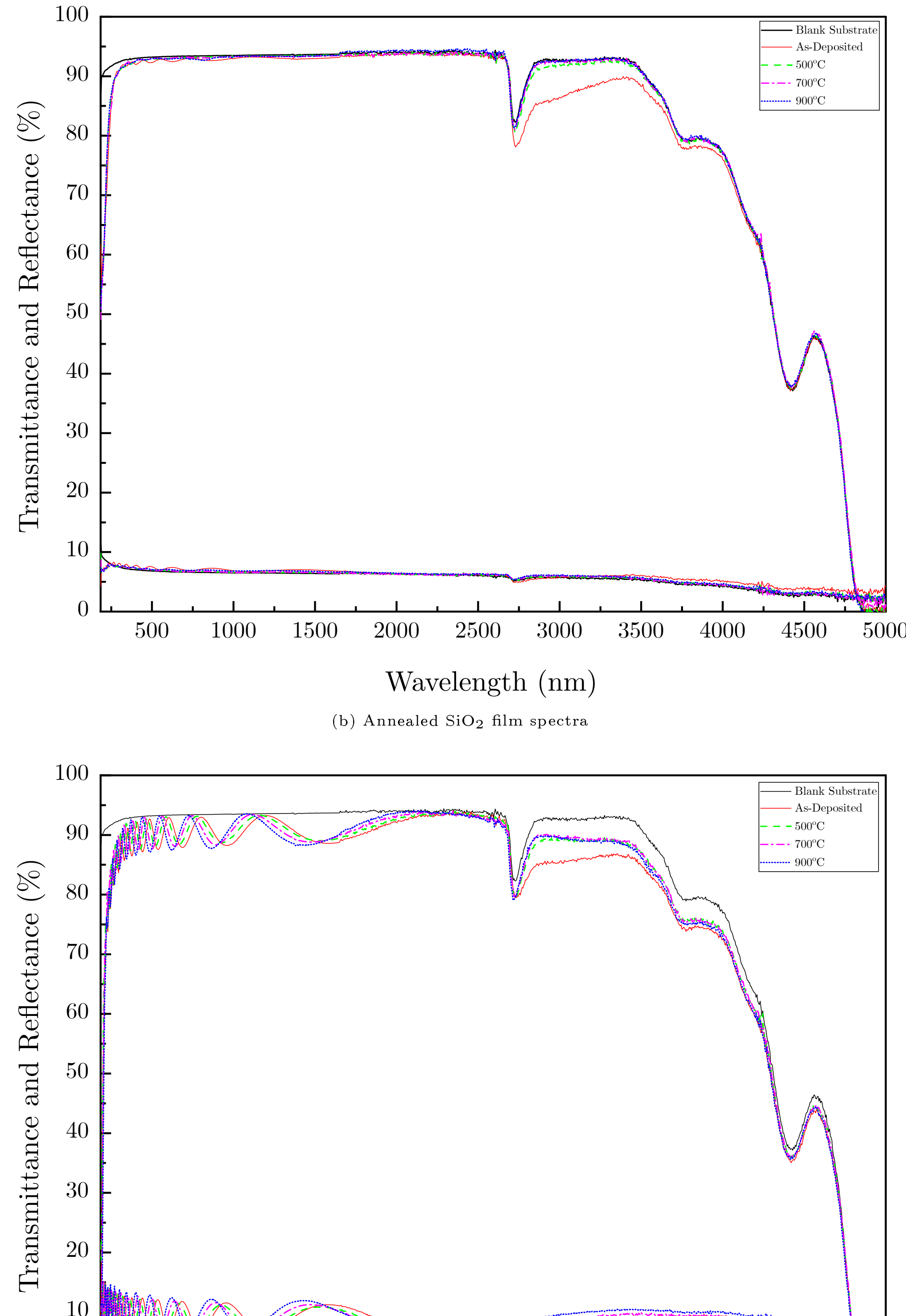

(b) Annealed SiO_2 film spectra

(c) Annealed HfO_2(41%):SiO_2(59%) film spectra

Figure 7.17: Transmittance and reflectance of annealed spectra for some of the samples investigated in this chapter. Three different samples are shown: pure HfO_2, pure SiO_2 and one of the mixed materials (HfO_2(41%):SiO_2(59%)).

Figure 7.17a shows that there is a slight shift of the data that can be seen towards lower wavelengths as the annealing temperature increases (Burstein-Moss shift). This shift towards lower wavelengths as the annealing temperature increases can also indicate a change in thickness, which in turn will also affect the refractive index and density of the coating. This shift also indicated an increase in the bandgap energy of the film. No major changes were observed in the transmittance and reflectance percentages as the temperature increased. The same can be said for the spectra in Figure 7.17b, where there is a small blue shift in the data, which is much smaller than the other spectra. This shows that annealing the SiO_2 film did not cause drastic changes in the bandgap energies or other optical constants. As for Figure 7.17c for one of the mixed materials' spectra, there is a much more notable blue shift in the spectra as the annealing temperature increases. Further discussion of the effects of annealing on the optical properties is discussed in the following sections.

7.3.1.2 Refractive Index and Extinction Coefficient

Figure 7.18 shows the refractive index at 1064 nm for all temperature: as-deposited (black square), 500°C (red circle), 700°C (green upright triangle) and 900°C (blue downward triangle), as a function of HfO_2 volume percentage in the films.

It can be seen that as the samples are annealed, they follow a similar trend, where the refractive index first decreases slightly, then increases slightly again. However, the changes in the refractive indices are very small and are within a few percentages of each other as the annealing temperature increases (~1–2%). The small reduction in the refractive index due to *ex situ* annealing has been widely reported by many authors [191, 229, 242], who also found that the coatings with SiO_2 mixtures remained amorphous, whereas the pure HfO_2 films crystallised at temperatures as low as 400°C [242] and 500°C [191, 229].

The most notable refractive index change is for the mixed material with 41% HfO_2, where as the temperature reaches 900°C, the refractive index increases to a value higher

than that of the as-deposited samples. However, this was still a very small percentage change. As can be seen, the trend for the refractive indices at each annealing temperature remains the same, where the higher the HfO_2 mixture content, the higher the value of the refractive index. Table 7.4 shows the values of the refractive index and of each samples at different annealing temperature.

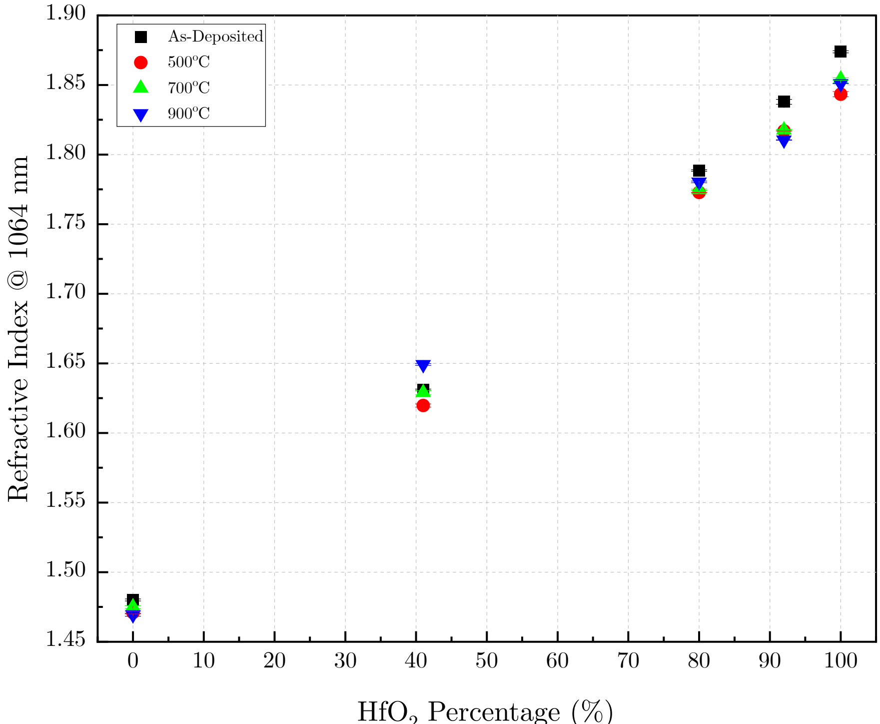

Figure 7.18: The refractive index at $\lambda = 1064$ nm. The error bars show the standard deviation of five separate fittings for each sample.

Table 7.4: The different refractive indices of HfO_2:SiO_2 thin films with different mixture concentration at as-deposited, 500°C, 700°C and 900°C annealed temperatures.

HAFNIA:SILICA CONTENT	AS-DEP	500°C	700°C	900°C
100:0 (Pure HfO_2)	1.87	1.84	1.85	1.85
92:8	1.84	1.82	1.82	1.81
80:20	1.79	1.77	1.77	1.78
41:50	1.63	1.62	1.63	1.65
0:100 (Pure SiO_2)	1.48	1.47	1.48	1.47

Figure 7.19 shows the extinction coefficient of the samples at 1064 nm, similar to that

of the refractive indices shown above. All samples were annealed at 500°C, 700°C, and 900°C. As the samples are annealed to higher temperatures, the overall trend shows that the extinction coefficient decreases for all films and continues to do so as the annealing temperature continues to increase. The extinction coefficient for the annealed samples followed the same trend as that for the as-deposited samples, where as the HfO_2 content increased, so did the extinction coefficient [226]. For the pure SiO_2 sample, the changes are extremely small and within the error bars, leading to the conclusion that annealing does not affect the extinction coefficient.

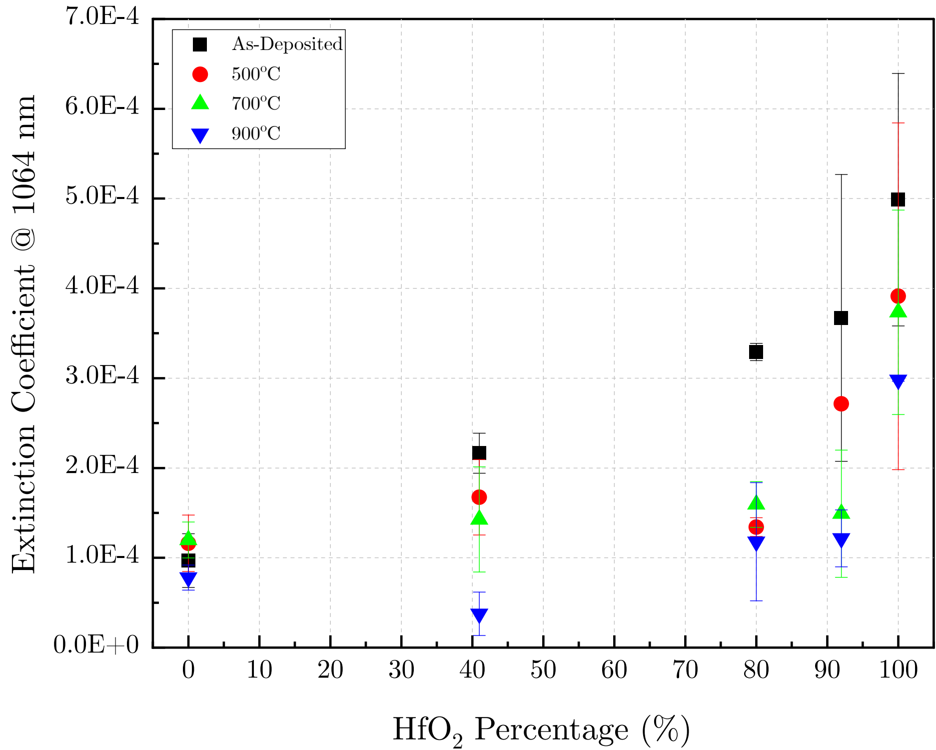

Figure 7.19: The extinction coefficient at $\lambda = 1064$ nm. The error bars show the standard deviation of five separate fittings for each sample.

7.3.1.3 Bandgap Energy

Figure 7.20 below shows the OJL bandgap energy extracted from SCOUT for films at: as-deposited (black square), 500°C (red circle), 700°C (green upright triangle) and 900°C (blue downward triangle).

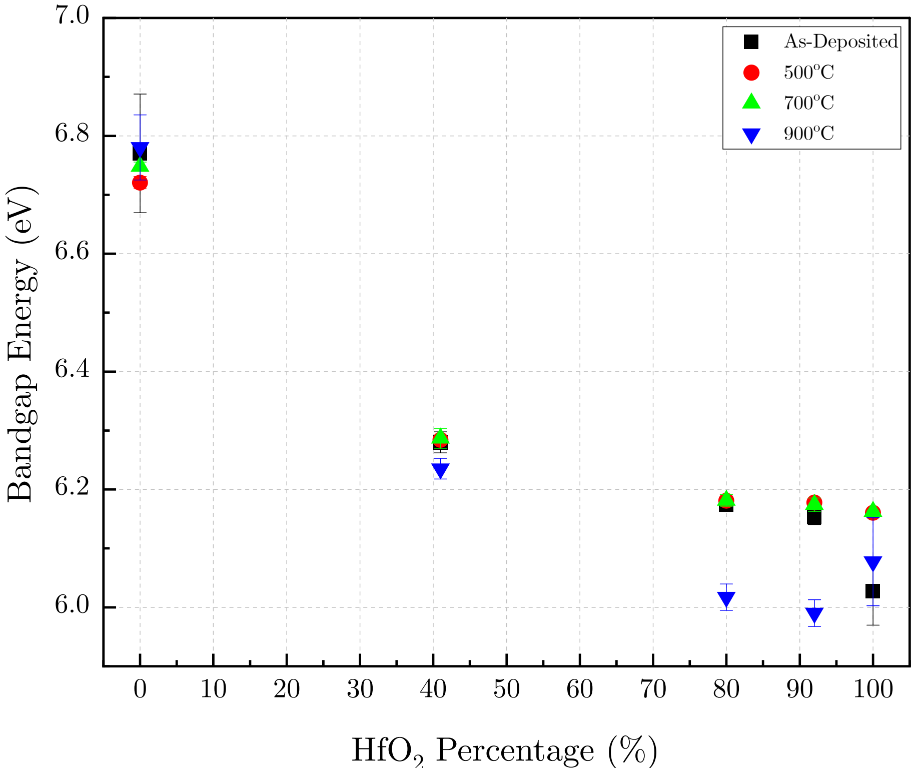

Figure 7.20: The average bandgap energy of the films acquired from SCOUT. The error bars show the standard deviation of five separate fittings for each sample.

As the samples were annealed to 500°C, there was a slight increase in the bandgap energies for films with more than 50% HfO_2 percentage in the coatings, where the bandgap energies remained almost the same at 700°C, and decreased as the annealing temperature reached 900°C. For samples with less than 50% HfO_2 percentage in the coatings, as the samples were annealed, the bandgap energies barely changed, and there was a slight decrease in the bandgap energy at 900°C for HfO_2(41%):SIO_2(59%). For the pure silica sample, the values for the bandgap energies at all temperatures are within the errors of each other, leading to the conclusion that the bandgap energy does not change with annealing. This coincides with the transmittance and reflectance data shown in Section 7.3.1.1, where there is a slight blue shift that can be seen, indicating an increase in the bandgap energies.

7.3.1.4 Thickness

Figure 7.21 below shows the thickness extracted from SCOUT for the mixed films: as-deposited (black square), 500°C (red circle), 700°C (green upright triangle) and 900°C (blue downward triangle).

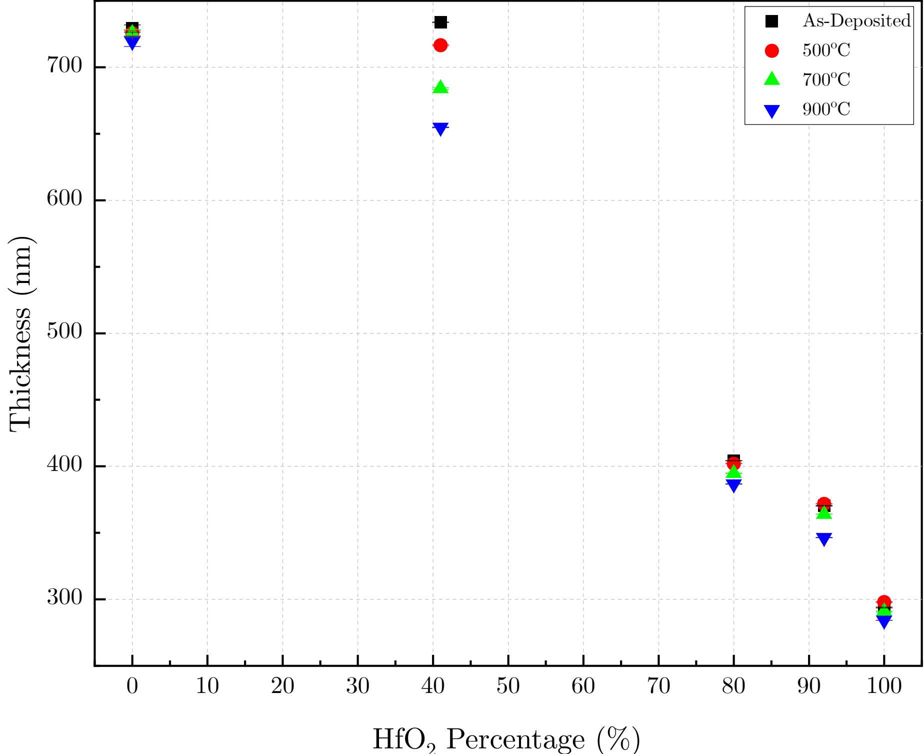

Figure 7.21: The average thicknesses of the films acquired from SCOUT. The error bars show the standard deviation of five separate fittings for each sample.

The annealed samples follow the same trend as that of the as-deposited samples. For all films, as the annealing temperature increased, the thickness decreased. The largest change was observed for HfO_2(41%):SiO_2(59%) films, where there was a large change in the thicknesses at each annealing step. This coincides with the transmittance and reflectance shown in Section 7.3.1.1, where this sample exhibits the largest change and shift in the fringes within the spectra compared with the other samples. For pure silica, there was virtually no change in thickness as the films were annealed. The decrease in

the thickness as the annealing temperature increases suggests that there is compressive stress within the films [27, 186–188], which is further confirmed by the XRD data, especially for the films that have crystallised.

7.3.1.5 XRD Results

GIXRD data for pure and mixed films annealed at 700°C and 900°C are presented below.

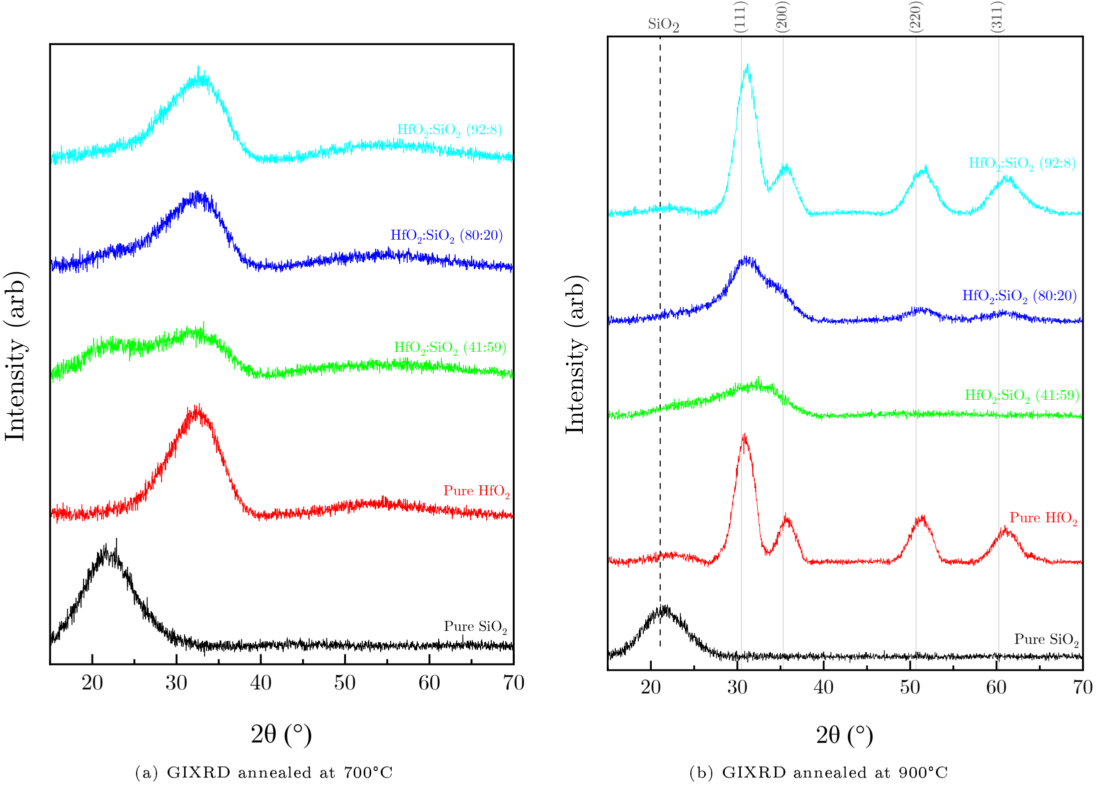

(a) GIXRD annealed at 700°C

(b) GIXRD annealed at 900°C

Figure 7.22: GIXRD data acquired for the annealed films within this study.

At 700°C, it can be see that all of the films still has broad weak bands, similar to the data shown at as-deposited. As the films were annealed at 900°C, some films showed sharp peaks, indicating that the films were crystalline. The pure HfO_2 and HfO_2(92%):SiO_2(8%) films showed a preferential (111) growth orientation, which is the preferred orientation for tetragonal HfO_2 films. It can also be observed that there

are more peaks at (200), (220), and (311), which further confirms the presence of the tetragonal phase. For the HfO_2(80%):SiO_2(20%) film, the data show that the film becomes more polycrystalline in nature, with the same peaks starting to appear in the same phases as the pure hafnia and HfO_2(92%):SiO_2(8%) films. The pure silica and HfO_2(41%):SiO_2(59%) films show broad weak bands, indicating that the films are still amorphous. This is expected because silica crystallises at a much higher temperature [245, 246], and the larger percentage of silica in the mixture films allows for the suppression of crystallisation in the mixed films [72]. Feng *et al.* have noted in their paper that there are several reasons as to why the mixture films remained amorphous, in example, the mixed films consists of more Si-O bonding than HfO_2 film, which have appeared to suppress crystallisation [245]. Figure 7.22b also shows that there is a shift in the pure hafnia and HfO_2(92%):SiO_2(8%) films towards higher values of 2θ, which indicates lattice contraction due to annealing, leading to compressive stress in the films [27, 178, 179, 186–188]. The same phenomena were observed and discussed in previous chapters for HfO_2 and Sc_2O_3 films.

The data for the peaks and phase of the film were obtained from the powder diffraction database, where in this case, it is JCPDS:no. 53-0550. The Joint Committee on Powder Diffraction Standards (JCPDS) is an organisation founded on powder diffraction data for the identification of materials.

7.3.1.6 LIDT Results

In Figure 7.23 below shows the LIDT of the films after annealing them at 480°C for 1 hour. The figure shows the LIDT as a function of HfO_2 percentage in the film for both the as-deposited and annealed films.

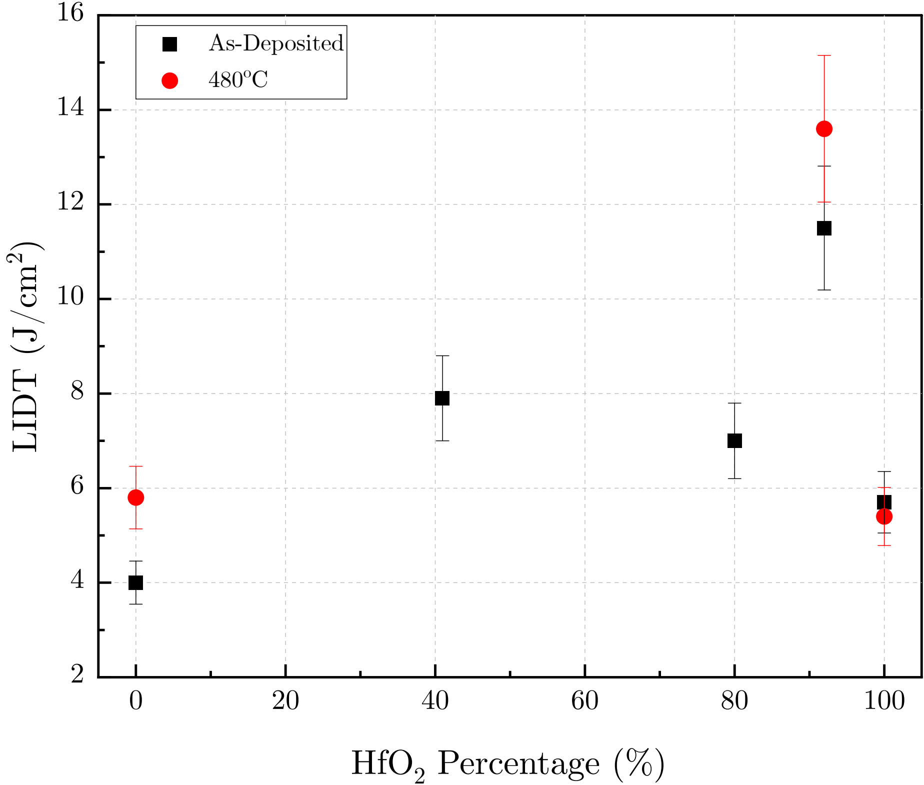

Figure 7.23: LIDT vs HfO_2 percentage for both as-deposited and annealed films

As shown in Figure 7.23, only some films underwent LIDT testing. This is because, after annealing, some films have cracks, which can be observed by a microscope. These cracks in the coatings can lead to misinterpretation of the values of LIDT, as structural defects can modify the electric field, therefore lowering the damage threshold of dielectric films [79]. The reason for the occurrence of cracks at this temperature can also be due to several damages already existing on the coatings from testing at as-deposited, which increases the chance of cracks as the films are annealed. For the tested samples, it can be seen that the LIDT for HfO_2(92%):SiO_2(8%) film remains the highest. By annealing the films, the pure silica and HfO_2(92%):SiO_2(8%) films' LIDT values increased, whereas for the pure HfO_2 film, the value decreased slightly by 0.3 J/cm^2, which is still within the error of the results. The overall increase in the LIDT values can be attributed to the decrease in the extinction coefficient, which in turn decreases the absorption of the films. This is similar to that reported in the literature, where an increase in the SiO_2 content

decreased the absorption power of the laser and enhanced the LIDT, and by annealing the films, this decreases the absorption, which may also decrease the absorption power of the laser [226].

Figure 7.24 below shows SEM images of cracks that can be observed due to annealing of the films:

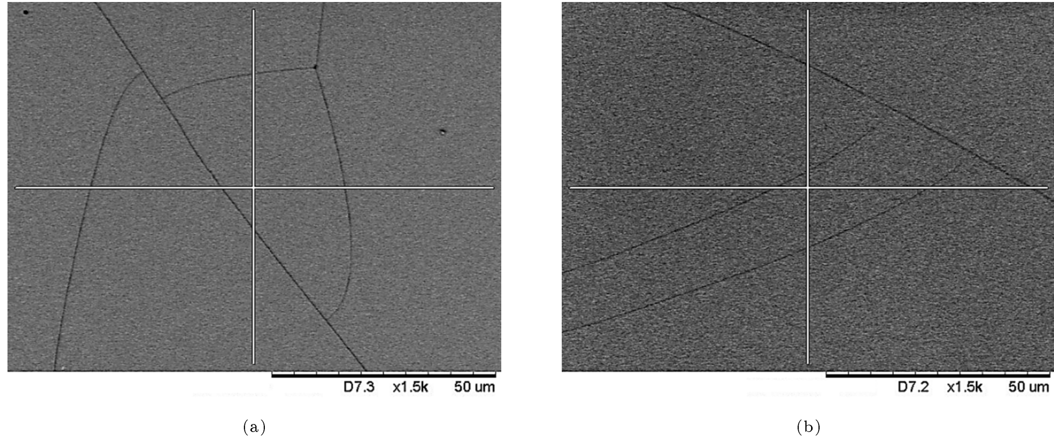

(a) (b)

Figure 7.24: Cracks observed on the films due to annealing.

The films in both figures were on JGS-3 substrates, which were only used for annealing studies to extract optical constants, where the films were annealed to 700°C before cracks were observed. As shown in Figure 7.24a, some of the cracks can be seen to have originated from pits, which can arise from contamination in the films and turn into pits as the annealing temperature increases. As mentioned, the samples which underwent LIDT showed cracks at a lower temperature because the previous damages were enhanced as the annealing temperature increased.

7.3.1.7 Damage Morphology

Figures 7.25 to 7.27 shows the damage morphologies of the pure and mixed films after laser irradiation, where (a) shows the low fluence damages and (b) shows the high fluence damages. It can be seen that similar to as-deposited samples, after annealing,

there are two main types of damage observed: absorption induced damage and pits due to inclusion.

(a) 12.2 Jcm^{-2} (b) 28.9 Jcm^{-2}

Figure 7.25: Observed damage sites for annealed pure HfO_2 film with (a) low and (b) high fluence.

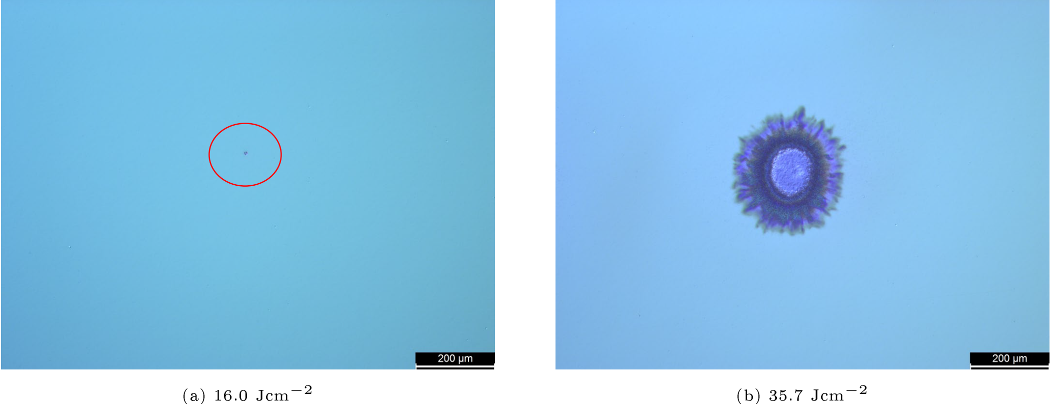

(a) 16.0 Jcm^{-2} (b) 35.7 Jcm^{-2}

Figure 7.26: Observed damage sites for annealed HfO_2(92%):SiO_2(8%) film with (a) low and (b) high fluence.

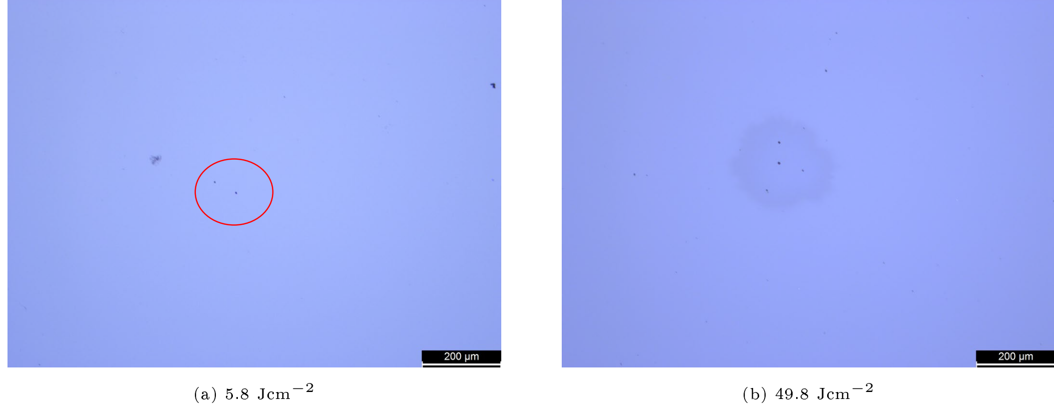

(a) 5.8 Jcm^{-2} (b) 49.8 Jcm^{-2}

Figure 7.27: Observed damage sites for the annealed pure SiO_2 film with (a) low and (b) high fluence.

In Figures 7.25b and 7.26b, it can be observed that the damage morphologies are similar and can be associated with the absorption induced damage effect [8, 243]. The characteristic morphology of absorption induced defect damage is often shown as discolouration or an increase in the surface roughness at the centre of the laser beam [8], which can be observed for samples of pure HfO_2 and mixed films with a 20% or less SiO_2 contribution, similar to those of the as-deposited. This correlates with the extinction coefficient values (Figure 7.19), where the films in Figures 7.25b and 7.26b have higher extinction coefficient values, which are related to the absorption of the film because of the higher percentage of HfO_2 in the films. For Figure 7.27, pits can be observed at both high and low fluences. Damage initiated by defects embedded in films typically results in craters or pits in the laser beam area [8, 80, 243]. This morphology can be attributed to inclusions which were rapidly heated during laser irradiation and exploded, creating pits [8, 80, 243]. All of the films observed in Figures 7.25, 7.26, and 7.27 at low fluence laser irradiation (figures set (a)), only pits can be observed because of laser damage. In addition, contamination and inclusions can also be clearly observed in these figures near the damage site, confirming that the pit damage morphology is due to contamination of the coatings, which is the starting point of damage for all films in this study, regardless of the mixture percentages. As mentioned, with an increase in fluence, absorption induced damage occurs in films with less than 20% SiO_2 within the mixture, including pure HfO_2 films.

7.4 Conclusion

The effects of different mixture percentages of HfO_2:SiO_2 thin films fabricated using the ECR-IBSD technique on the optical constants and LIDT are presented and discussed in this chapter. Structural analysis of the films was carried out by GIXRD, which confirmed that the as-deposited films in this study were amorphous, regardless of the mixture percentages. The volume mixture percentages of HfO_2 and SiO_2 in each film in this study were determined using EMA models based on refractive index values. By

utilising the OJL model implemented within SCOUT software, the refractive index of the as-deposited films was found to be in the range of $n = 1.48 – 1.87$, where the lowest value is for the pure SiO_2 film and the highest value is for the pure HfO_2 film. It was shown that the mixture materials filled in the values for the refractive index between the two pure materials, indicating that the refractive index can be tuned by changing the mixture percentages. As for the extinction coefficient, this was found to be in the range of $k = 9.69 \times 10^{-5} - 4.99 \times 10^{-4}$, where the highest value is for the pure HfO_2 film and the lowest is for the SiO_2 film, with the mixed film values lying in between these two values, where the higher the SiO_2 percentage, the lower the extinction coefficient value. The OJL bandgap energy was found in the range of 6.03 – 6.77 eV, where the increase in SiO_2 also increases the bandgap energy. The shift in the bandgap to higher energies can also be seen from the slight shift towards lower wavelengths in the transmittance measurement in the UV range as the SiO_2 content increases. The LIDT of the films was carried out by RhySearch with a 10-on-1 test using a Nd:YAG laser at 1064 nm and 11.6 ns pulses. From this, it was found that the highest LIDT was for HfO_2(92%):SiO_2(8%) at 11.5 J/cm^2 and the lowest for pure SiO_2 at 4 J/cm^2. Based on the damage morphologies, two main types of damage were observed: absorption induced damage and pits due to inclusions, where the latter can be observed for all films at low laser fluence. The laser damage is very sensitive to contamination within the nanosecond regime, and a large amount of discharge occurs inside the chamber during deposition, which leads to contamination of the films, which can lower the LIDT values.

The effects of annealing on the optical and structural properties and LIDT of HfO_2:SiO_2 mixed films are also presented and discussed for annealing temperatures of 500°C, 700°C and 900°C. As the annealing temperature increased, the refractive index and extinction coefficient values decreased, and the bandgap energy increased. The structural properties were determined using GIXRD, which showed that at 700°C, all films with different percentages of mixtures remained amorphous, and as the temperature reached 900°C, peaks were observed for pure HfO_2 and HfO_2(92%):SiO_2(8%) films, which show a crystalline tetragonal HfO_2 structure; however, films with a higher percentage of SiO_2

remained amorphous. All the crystalline films show a slight shift towards higher angles, indicating compressive stress within the films, which goes hand-in-hand with the decrease in refractive index and decrease in the film thickness due to annealing. The LIDT was carried out only for three films in this study after annealing owing to cracking in the films. It was found that as the films were annealed to 480°C, the LIDT values also increased. Similar to the as-deposited films, two main types of damage were observed: absorption induced damage and pits due to inclusions, where the latter can be observed for all films at low laser fluence.

From optical characterisation, it was found that by controlling the mixture percentage of HfO_2 and SiO_2, the refractive index, extinction coefficient, and bandgap energy can be tuned to the desired values depending on the application. In addition, post-deposition annealing can aid in tuning the optical constants of the mixed films. By including more than 10% of SiO_2 into the mixture of HfO_2:SiO_2, this can suppress the crystallisation temperature of the films and provide a higher damage threshold than that of the pure HfO_2 film.

8 | Scandia Silica Mixture

8.1 Introduction

As previously mentioned, mixed materials have the advantages of tunable bandgap energies and tunable refractive indices covering the range between the two materials [70, 193, 226–228], among other mechanical, thermal, and structural characteristics, as well as the avoidance of discrete layer interfaces and improved physical properties such as reduction of residual stress [4, 230]. With these advantages, mixed materials can be utilised in multilayer designs in place of high refractive index materials, which can improve the LIDT of the optics utilised in high power laser systems [4, 70, 229].

In the last few years, typically HfO_2 have been studied as a high refractive index material in combination with SiO_2 to create mixture materials, which has been the focus of investigations of high LIDT thin films [6, 154, 231, 239]. However, Sc_2O_3 has drawn some attention because of its high refractive index from UV to mid-IR [247] and slightly higher bandgap energy than that of HfO_2 [6] as mentioned in Chapter 6. Although the mixture of Sc_2O_3 and SiO_2 has not been studied as much as the mixture with HfO_2, there are still a few studies that have investigated this mixture using different thin film fabrication techniques, most commonly e-beam evaporation, and little with IBSD. This led to the interest in investigating this mixture material in this study, especially for films fabricated by ECR-IBSD and its properties. A study by Gallais *et al.* showed that Sc_2O_3:SiO_2 films have a relatively high damage threshold at 1030 nm, sub-ps laser applications compared to other materials within their study, and found

that Sc_2O_3(60%):SiO_2(40%) mixture as a high index material combined with SiO_2 as a low index material could be a promising combination for optical interference coatings utilised in high power laser systems [4, 248]. This finding was also supported by Mende *et al.* for the same combination percentage of mixture materials that can be utilised in optical coatings for fs-range laser applications [6]. A study by Fu *et al.* also agrees that mixtures of Sc_2O_3:SiO_2 can have high LIDT and low values of bandgap energy with a high refractive index, making it an interesting material for the design of high LIDT coatings for both ns- and fs-range with infrared lasers (1064 nm and 1030 nm, respectively) [230]. Kong *et al.* have also studied Sc_2O_3:SiO_2 mixtures in the UV-range (355 nm), where they found that the LIDT decreases with the increase of Sc_2O_3 in the coatings, and the residual stress increases with the increase of Sc_2O_3 which they believe is related to oxygen vacancies and interstitials in the Sc_2O_3:SiO_2 mixture films [247]. Overall, with the limited literature available, there is agreement that Sc_2O_3:SiO_2 is an interesting choice for high index material for high power applications.

In this chapter, Sc_2O_3:SiO_2 thin films with different mixture percentages fabricated by ECR-IBSD technology are reported. The stoichiometry and elemental composition of the films were calculated by EMA estimation previously explained in Chapter 7; the structural properties of the films were determined by XRD, and the optical properties were obtained by fitting the transmittance and reflectance spectra on SCOUT software have been reported and discussed, along with the LIDT results which were carried out by RhySearch (*Buchs, Switzerland*). Furthermore, the effects of the annealing of these films on the structure, optical properties, and LIDT results are presented, where the results and discussion of the as-deposited and annealed films are split into two separate parts.

8.2 As-Deposited Sc_2O_3:SiO_2 Films

Within this first part, the results for as-deposited Sc_2O_3:SiO_2 thin films fabricated by ECR-IBSD have been presented and discussed.

8.2.1 Results and Discussion

8.2.1.1 Transmittance and Reflectance Measurement

In this experiment, the effects of different mixture percentages of Sc_2O_3 and SiO_2 on optical properties were investigated. Figure 8.1 below shows the transmittance and reflectance measurements. As previously mentioned, all of the depositions had the same deposition pressure, base pressure, and time, with the only difference being the number of sources that were on.

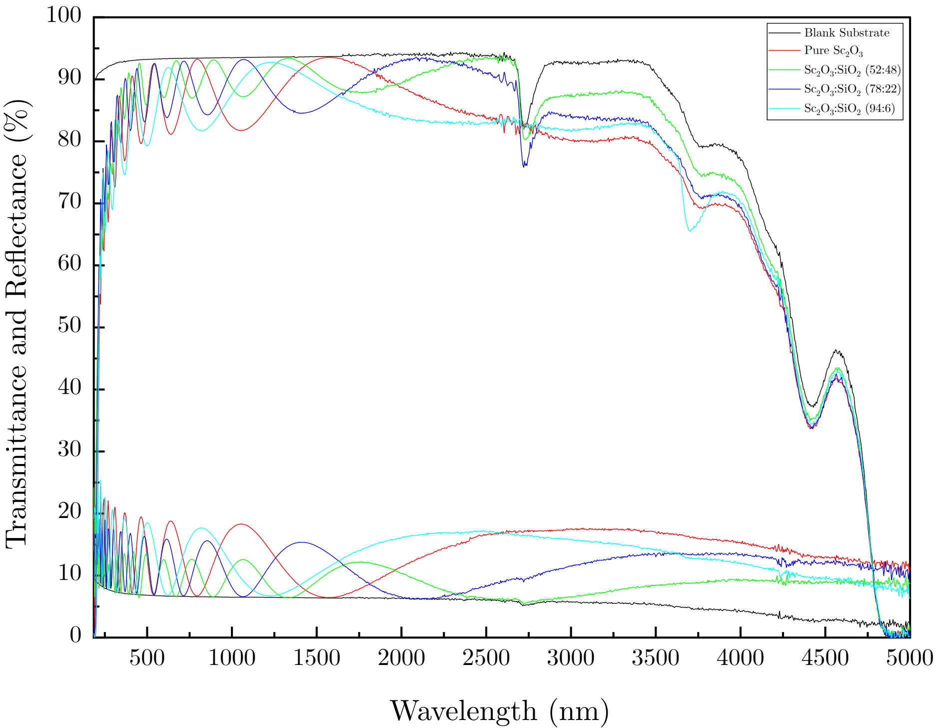

Figure 8.1: Transmittance and reflectance data for as-deposited

The figure shows five different spectra for the following samples: blank JGS3 substrate, pure Sc_2O_3, Sc_2O_3(52%):SiO_2(48%), Sc_2O_3(78%):SiO_2(22%), and Sc_2O_3(94%):SiO_2(6%). The mixture percentages quoted were extracted from the Lorentz-Lorenz EMA model, as previously discussed in Section 7.2.1.5.

In Figure 8.1, it can be seen that all the coatings have interference effects, which are utilised in SCOUT to extract the optical constants. It can be seen that by varying the mixture percentages, this has an effect on the amplitude and the number of fringes. As shown, pure Sc_2O_3 had the largest amplitude, and as the SiO_2 content increased, the amplitude decreased. This proves that tuning the volume fraction of Sc_2O_3 can change the transmittance of the films [247]. The effect of the mixtures on the optical constants based on the optical fittings from the spectra in Figure 8.1 is discussed in the following sections.

8.2.1.2 Refractive Index and Extinction Coefficient

In Figures 8.2 and 8.3, the refractive index of the mixed films investigated in this chapter is shown. Figure 8.2 shows the dispersion of the refractive index in the wavelength range of 200 - 2500 nm, and Figure 8.3 shows the refractive index extracted at a fixed wavelength of 1064 nm.

Figures 8.2 and 8.3 shows that as the SiO_2 content increases in the films, the refractive index decreases, where it can be see that the pure Sc_2O_3 possesses the highest refractive index values. As shown, the results agree with the literature, where the mixed percentages fill in the values of the refractive indices between the two pure materials, demonstrating that the refractive index can be tuned by simply changing the mixture percentages [77, 247]. The refractive index of pure SiO_2 is shown in Section 7.2.1.2.

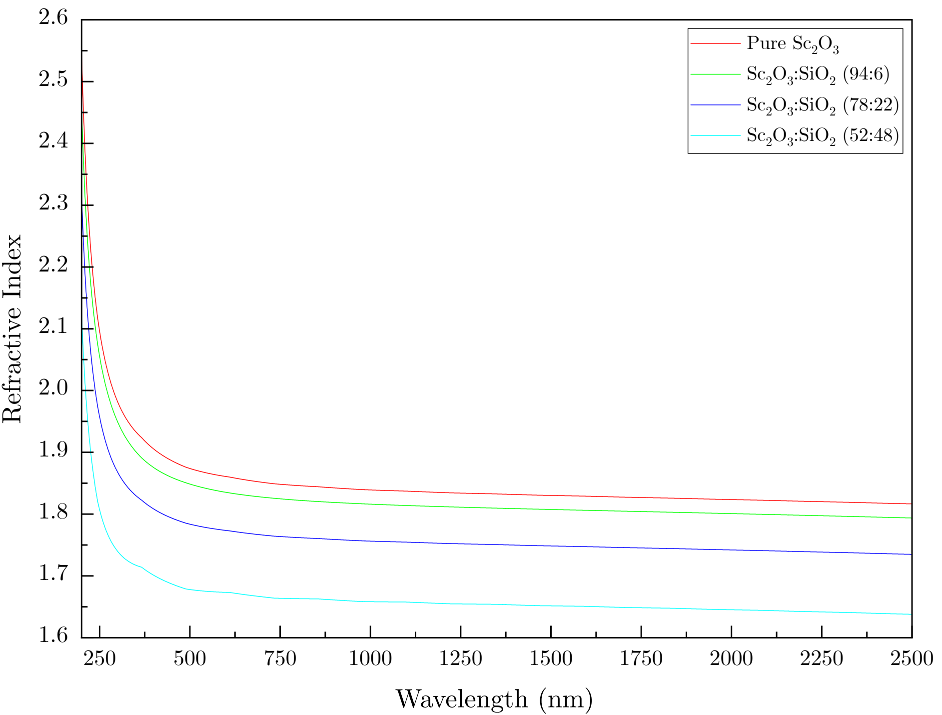

Figure 8.2: Dispersion of the refractive index for the range of λ = 200 - 2500 nm

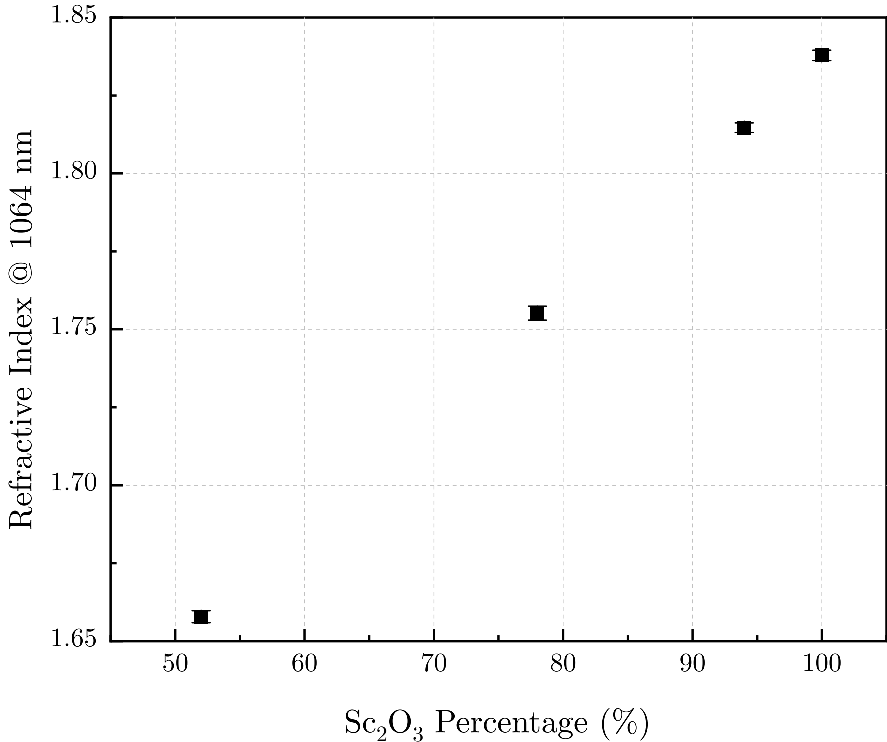

Figure 8.3: The refractive index at λ = 1064 nm. The error bars show the standard deviation of five separate fittings for each sample.

In Figure 8.3, the refractive index at 1064 nm was utilised in the EMA models (shown in Section 8.2.1.5) to extract the volume mixture percentages of the films. In this case, the lowest refractive index value, neglecting the SiO_2 values, was obtained for $Sc_2O_3(52\%)$:$SiO_2(48\%)$ ($n = 1.66$), and the highest value was obtained for pure Sc_2O_3 ($n = 1.84$). All the refractive indices at 1064 nm and the mixture percentages based on different EMA models are shown in Table 8.3 in Section 8.2.1.5.

Figures 8.4 and 8.5 shows the extinction coefficient from the range of wavelength of 200 - 2500 nm and at a fixed wavelength of 1064 nm, respectively.

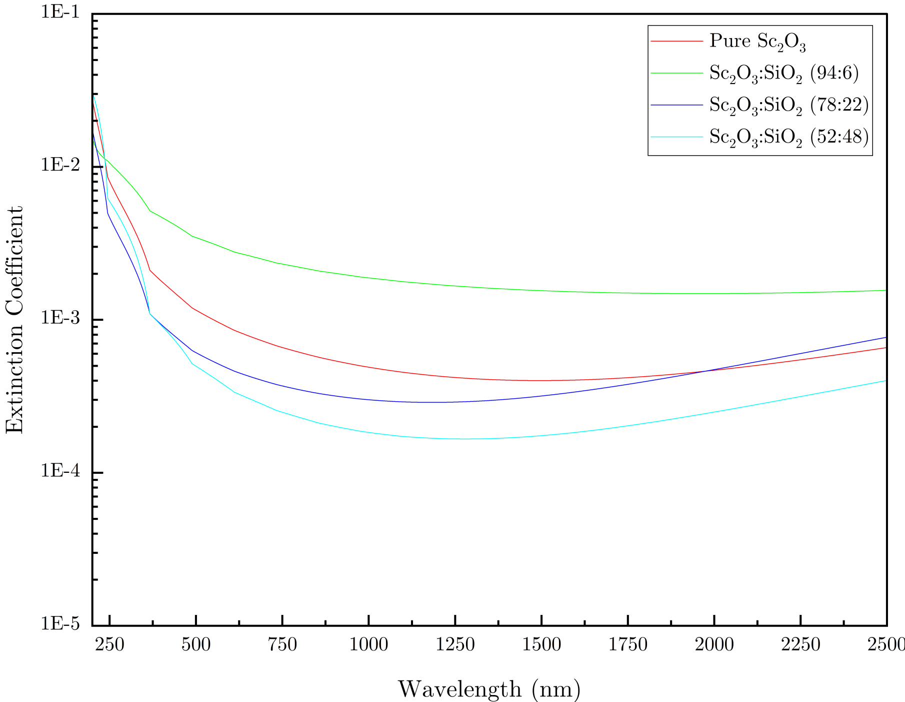

Figure 8.4: Dispersion of the extinction coefficient for the range of λ = 200 - 2500 nm for the different mixed percentages. Y-axis displays the extinction coefficient on a logarithmic scale.

Figure 8.4 shows that as the Sc_2O_3 content decreases, so does the extinction coefficient, with the exception of $Sc_2O_3(94\%)$:$SiO_2(6\%)$ which has a large increase. Figure 8.4 shows a sharp decline of the extinction coefficient in the wavelengths within the UV region, where this then continues to slowly decrease as it reaches mid-IR.

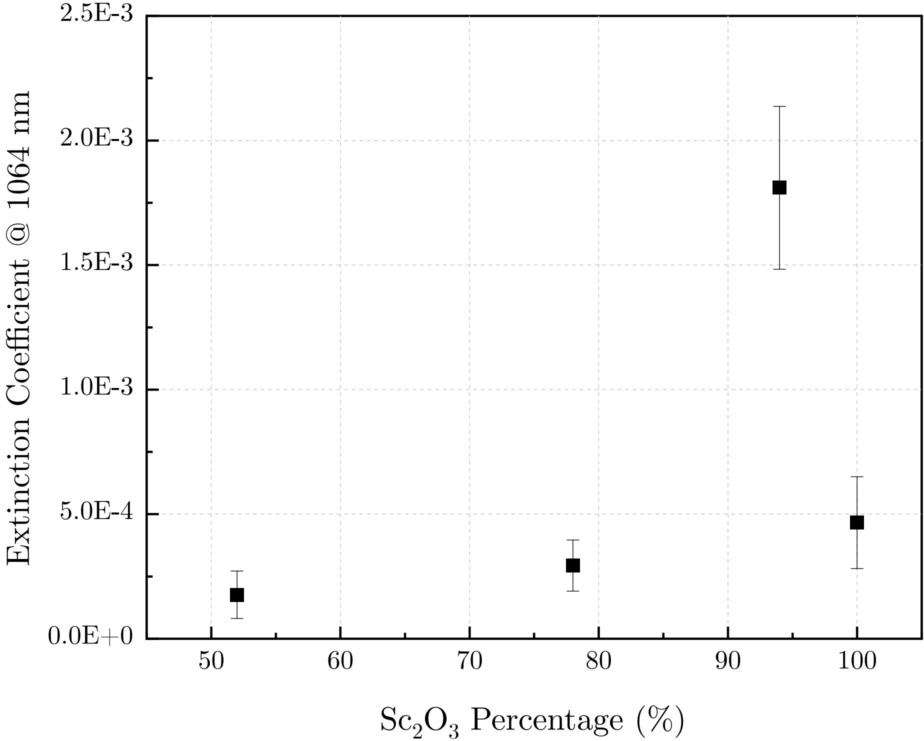

Figure 8.5: The extinction coefficient at $\lambda = 1064$ nm for the different mixed percentages. The error bars show the standard deviation of five separate fittings for each sample.

In Figure 8.5, it can be seen that the extinction coefficient increases as the volume percentage of Sc_2O_3 increases. The highest value was obtained for Sc_2O_3(94%):SiO_2(6%) with $k = 1.81 \times 10^{-3}$ and the lowest value was obtained for Sc_2O_3(52%):SiO_2(48%) with $k = 1.76 \times 10^{-4}$. The results for pure silica are presented in the previous chapter. This shows that, as the silica content increased in the mixed films, the extinction coefficient decreased, and therefore, the absorption also decreased.

8.2.1.3 Bandgap Energy

Figure 8.6 shows the bandgap energy of mixed films as a function of the Sc_2O_3 volume fraction in the films, where the bandgap energy is extracted from the OJL gap energy model, and the volume percentage is extracted from EMA model.

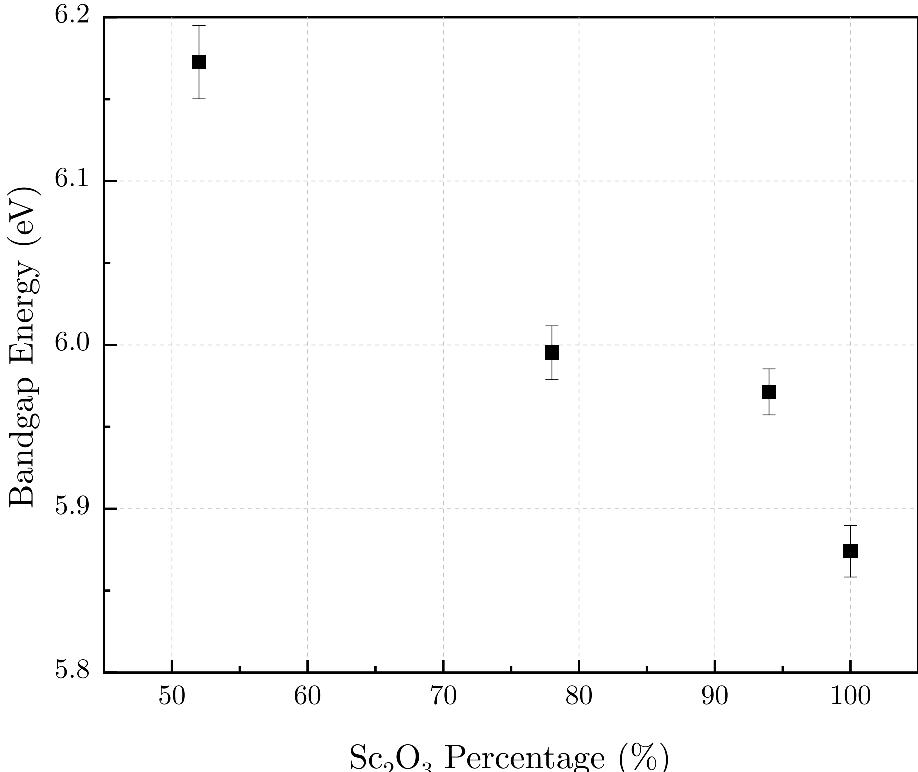

Figure 8.6: The average bandgap energy of the films acquired from SCOUT. The error bars show the standard deviation of five separate fittings for each sample.

It can be seen that the highest bandgap energy shown in the figure corresponds to Sc_2O_3(52%):SiO_2(48%) at 6.17 eV and the lowest is for the pure Sc_2O_3 film at 5.87 eV. The bandgap energies are listed in Table 8.1. Please note that the values for SiO_2 are not mentioned here but are shown in the previous chapter. From Figure 8.6, it can be observed that there is a linear relationship between the decrease in the bandgap energy and the decrease in the SiO_2 volume fraction in the coating. This phenomenon was observed and reported by Mende *et al.* [6].

Table 8.1: The different bandgap energies of Sc_2O_3:SiO_2 thin films with different Sc_2O_3 volume percentages.

SCANDIA PERCENTAGE (%)	BANDGAP ENERGY (eV)
52%	6.17
78%	6.00
94%	5.97
100%	5.87

8.2.1.4 Thickness

Figure 8.7 shows the thicknesses of the coatings with different mixture percentages. As previously mentioned, all coatings had the same deposition conditions. The thickness is typically extracted from the number of fringes observed in the transmittance and reflectance spectra.

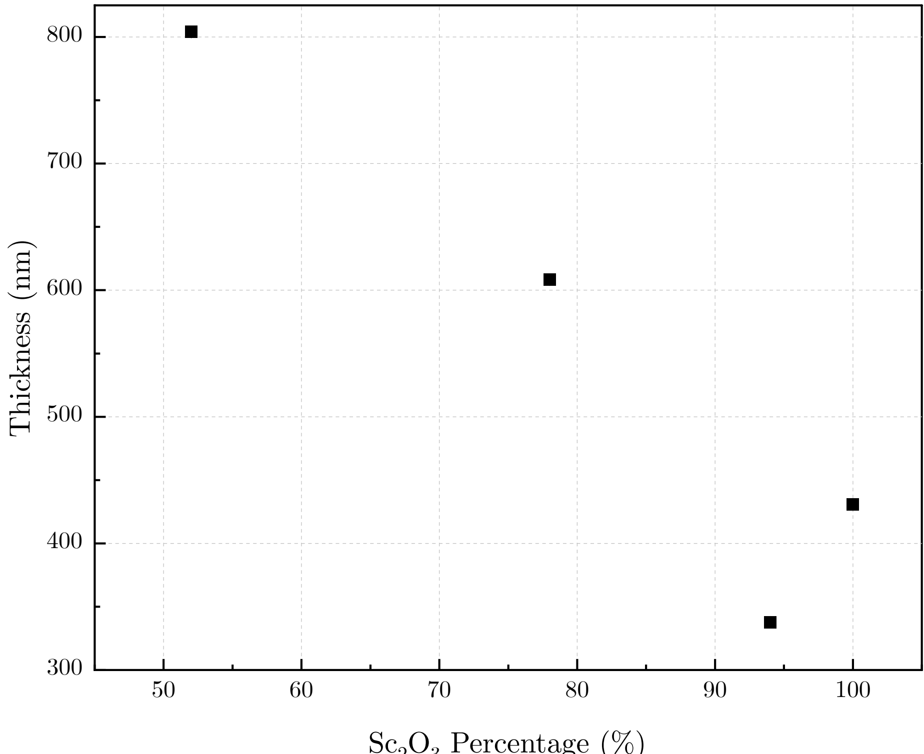

Figure 8.7: The average thicknesses of the films acquired from SCOUT. The error bars show the standard deviation of five separate fittings for each sample.

From Figure 8.7, it can be seen that the highest thickness is for Sc_2O_3(52%):SiO_2(48%) sample, and the lowest thickness is for Sc_2O_3(94%):SiO_2(6%) sample. Table 8.2 shows the thicknesses of the films based on the volume percentage of Sc_2O_3 within the films.

Table 8.2: The different thicknesses of Sc_2O_3:SiO_2 thin films with different Sc_2O_3 volume percentages.

SCANDIA PERCENTAGE (%)	THICKNESS (nm)
52%	804
78%	608
94%	338
100%	431

8.2.1.5 Effective Material Approximation

As previously mentioned in Section 7.2.1.5, there are different EMA models that can be utilised, in which the models in focus are Linear, Lorentz-Lorenz, Drude and Needle. In this case, the EMA models are used to calculate the volume percentage of the two host materials by knowing the refractive indices of the two pure materials and the mixed material in question. The values based on the refractive indices of Sc_2O_3 and SiO_2 at 1064 nm were used in the different models to map the values of the refractive indices at different volume fractions of Sc_2O_3, as shown in Figure 8.8.

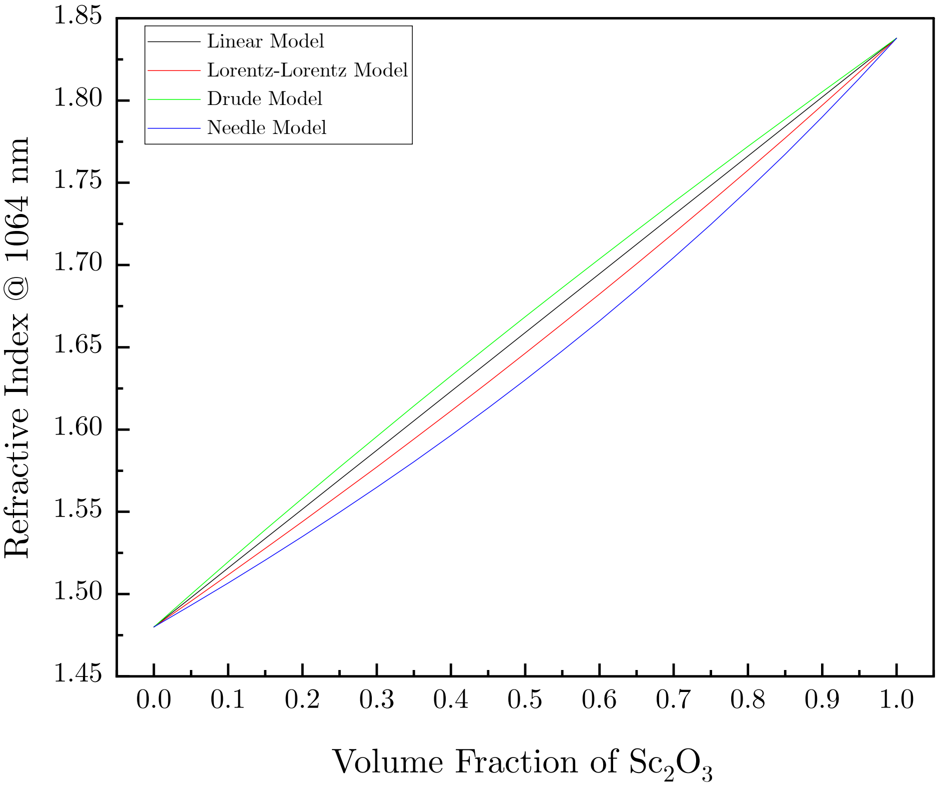

Figure 8.8: Different EMA models and its refractive index at different volume fraction of Sc_2O_3

As previously mentioned, the Lorentz-Lorenz model values were used to quote the mixture percentages, as the values provided by this model lie in the middle of the Wiener bounds (Drude and Needle models). The values of the volume fraction of Sc_2O_3 based on the different EMA models are listed in Table 8.3.

Table 8.3: Different EMA models for Sc_2O_3 volume fraction in the mixed coatings studied in this chapter.

RUN NAME	DRUDE	LINEAR	LORENTZ-LORENZ	NEEDLE
C21H3110 (Pure Sc_2O_3)	1	1	1	1
C21J0710	0.47	0.50	0.52	0.58
C21J2011	0.75	0.77	0.78	0.82
C21L0112	0.93	0.94	0.94	0.95

8.2.1.6 XRD Results

Figure 8.9 shows the GIXRD pattern of the mixed films with different mixture percentages. As can be seen from the GIXRD data, all the films showed broad weak bands, indicating that all the films were amorphous. It can also be seen that the films with a higher SiO_2 content show a more prominent peak at 22° compared to the peaks that can be seen slightly for Sc_2O_3. Again, although some peaks can be observed, the films are amorphous because of the broad weak bands mentioned.

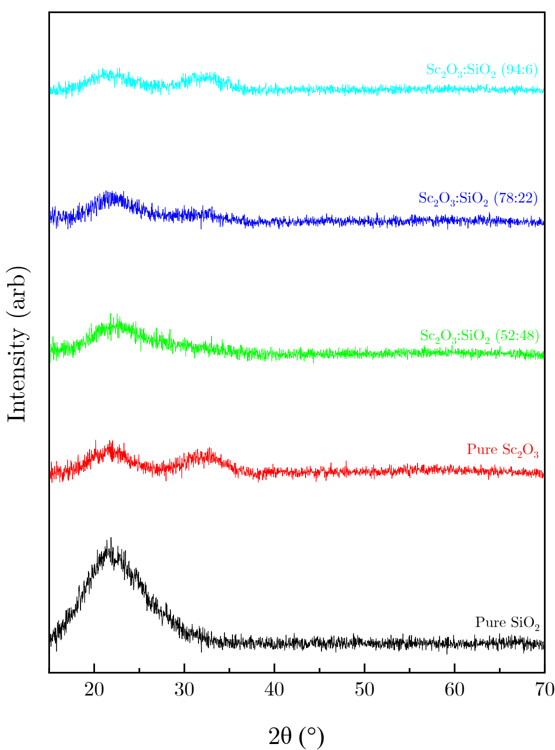

Figure 8.9: XRD data acquired for the as-deposited films in this study, by utilising the GIXRD method.

8.2.1.7 LIDT Results

Figure 8.10 shows the damage probability curves for the pure Sc_2O_3 coating studied in this chapter. As previously mentioned in Section 7.2.1.7, all samples follow the same protocol and fittings.

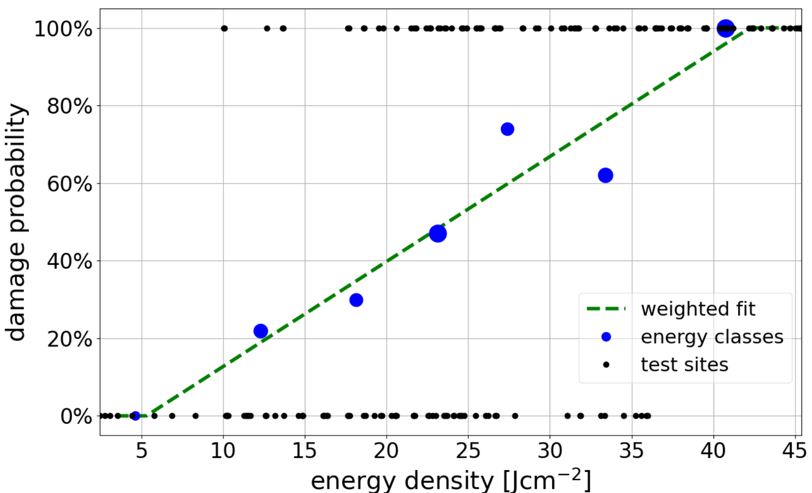

Figure 8.10: Damage probability curve for pure Sc_2O_3 film

Figure 8.11 shows the LIDT of the coatings studied in this chapter versus refractive index (Figure 8.11a) and bandgap energy (Figure 8.11b), respectively.

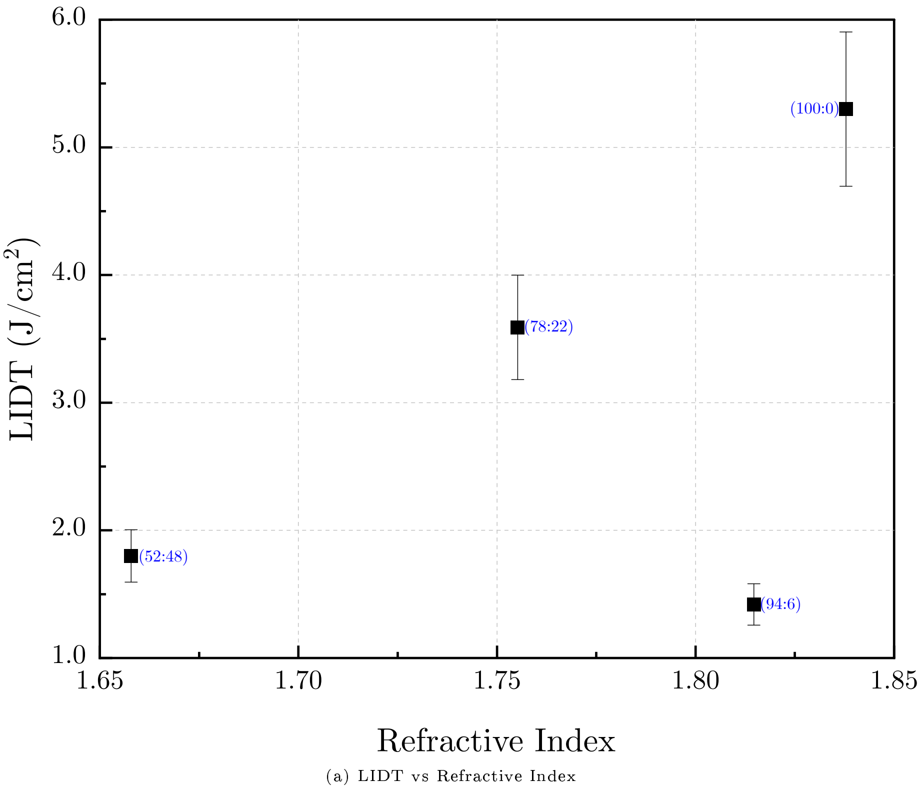

(a) LIDT vs Refractive Index

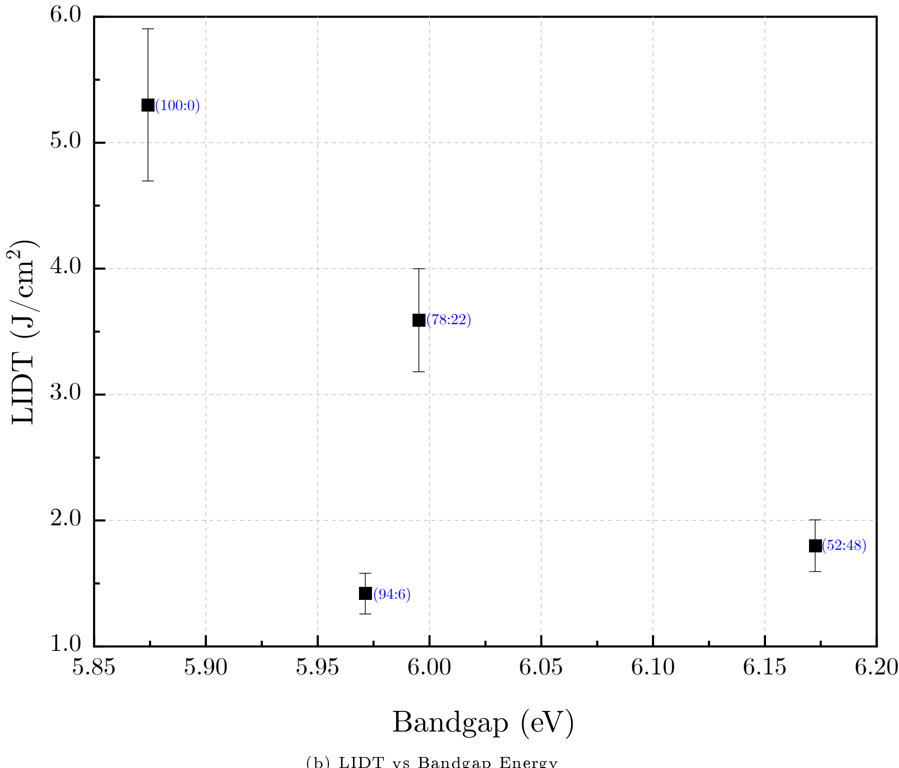

(b) LIDT vs Bandgap Energy

Figure 8.11: LIDT values for all the films studied in this chapter as a function of the refractive index and bandgap energy.

As shown, the highest LIDT value was for the pure Sc_2O_3 film (5.3 J/cm^2), and the lowest was for Sc_2O_3(94%):SiO_2(6%) (1.42 J/cm^2). Based on Figure 8.11a, as the refractive index increases, so do the LIDT values, and based on Figure 8.11b, as the bandgap energies decrease, so do the LIDT values, where both cases have the exception of Sc_2O_3(94%):SiO_2(6%) sample. The lowest value acquired for the Sc_2O_3(94%):SiO_2(6%) sample was most likely due to the large amount of contamination observed in the films (Figure 8.13), which provides a much lower than expected LIDT value. This observed increase in contamination could be due to the cleanliness of the chamber, where there is a lot of flaking of previous materials from the chamber, and when the ion sources discharge, this increases the contamination of the films. As previously mentioned, within the nanosecond regime, the laser damage to the films is very sensitive to defects and contaminations on the films and substrates [8, 229, 230].

8.2.1.8 Damage Morphology

Figures 8.12 to 8.15 shows the damage morphologies of the pure and mixed films after laser irradiation, where (a) shows the low fluence damages and (b) shows the high fluence damages. Two main types of damage can be observed: absorption induced damage and pits due to inclusion.

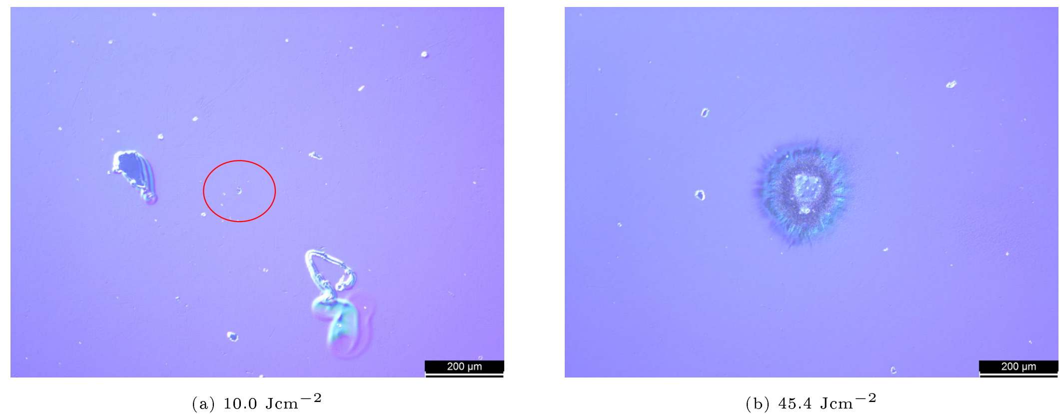

(a) 10.0 Jcm^{-2} (b) 45.4 Jcm^{-2}

Figure 8.12: Observed damage sites for pure Sc_2O_3 film with (a) low and (b) high fluence.

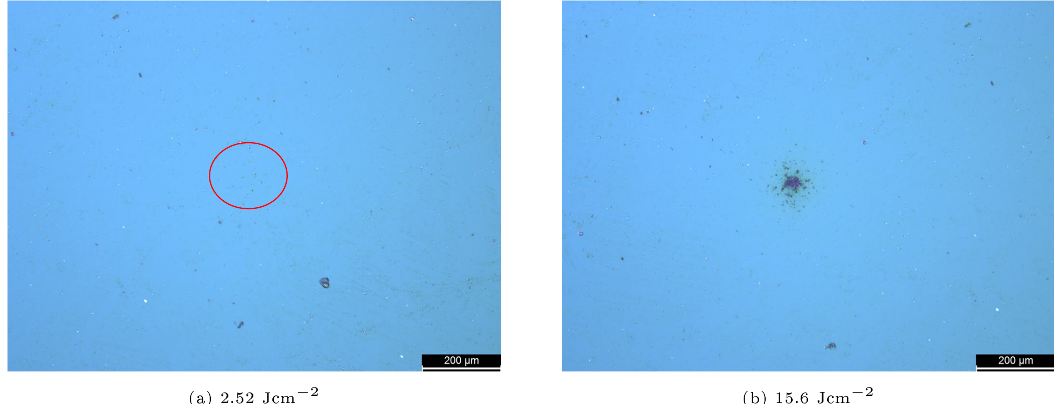

(a) 2.52 Jcm^{-2} (b) 15.6 Jcm^{-2}

Figure 8.13: Observed damage sites for Sc_2O_3(94%):SiO_2(6%) film with (a) low and (b) high fluence.

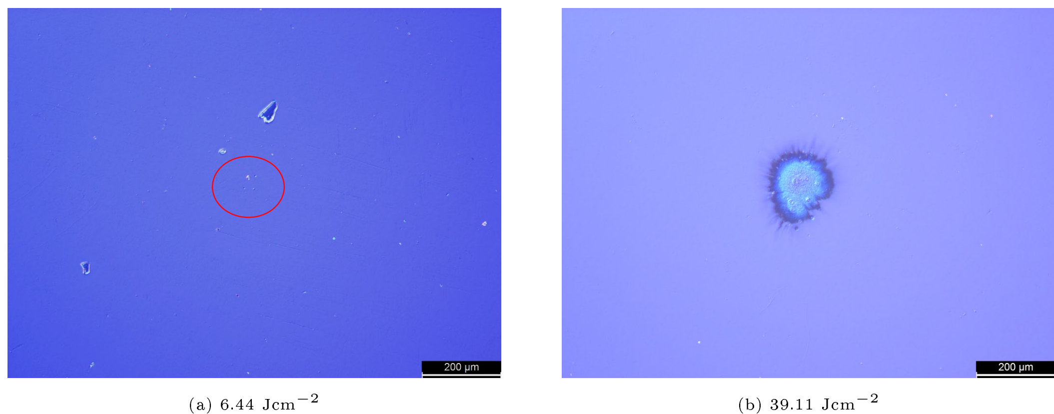

(a) 6.44 Jcm^{-2} (b) 39.11 Jcm^{-2}

Figure 8.14: Observed damage sites for the Sc_2O_3(78%):SiO_2(22%) film with (a) low and (b) high fluence.

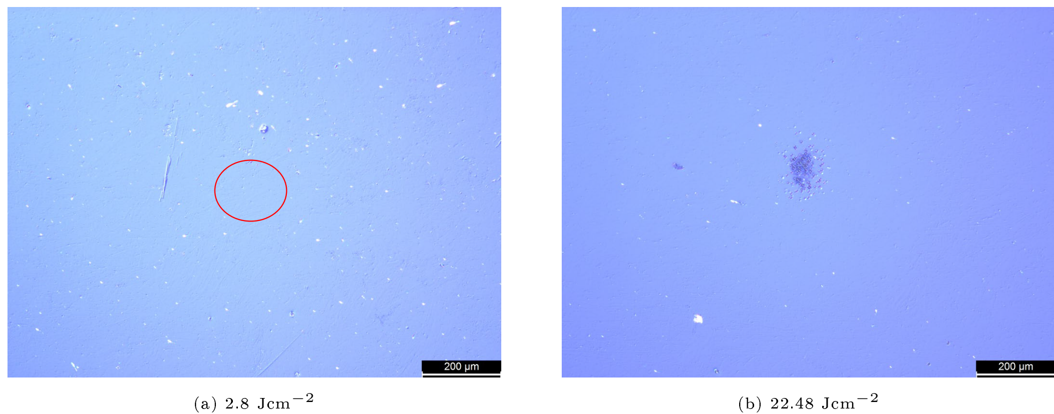

(a) 2.8 Jcm^{-2} (b) 22.48 Jcm^{-2}

Figure 8.15: Observed damage sites for the Sc_2O_3(52%):SiO_2(48%) film with (a) low and (b) high fluence.

In Figures 8.12b and 8.14b, it can be observed that the damage morphologies are very similar, which can be associated with absorption induced damage effect, where the films reach their melting point before delamination occurs [8, 243]. The characteristic morphology of absorption induced defect damage is often shown as discolouration or an increase in the surface roughness at the centre of the laser beam [8], which can be observed for samples of pure Sc_2O_3 and mixed films with 25% or less SiO_2 contribution, disregarding the Sc_2O_3(94%):SiO_2(6%) sample. This correlates with the extinction coefficient values (Figure 7.5), where the films in Figures 8.12b and 8.14b had higher extinction coefficient values, which are related to the absorption of the film. For the Sc_2O_3(94%):SiO_2(6%) sample, it can be seen that the surface quality of the film is terrible, where there are defects and contamination that can be seen. This significantly

affects the LIDT results acquired for films within the nanosecond regime. Although contamination can be seen quite obviously for all the films, the overall surface quality of the Sc_2O_3(94%):SiO_2(6%) sample can be seen to be the worst, with lots of small pits and damages. Hence, in Figure 8.13, pits can be observed at both high and low fluences. Damage initiated by defects embedded in films typically results in craters or pits in the laser beam area [8, 80, 243]. This morphology can be attributed to inclusions which were rapidly heated during laser irradiation and exploded, creating pits [8, 80, 243]. In Figure 8.15b, it can be observed that the Sc_2O_3(52%):SiO_2(48%) film exhibited both absorption induced damage morphology and pits. This shows that by having less than 25% SiO_2 content in the films, the main reason for the damage is absorption induced defects, and higher than 25% but less than 50% consists of both types of damage. Again, the Sc_2O_3(94%):SiO_2(6%) sample is an anomaly in this study because of its poor surface and film quality. All of the films observed in Figures 8.12 to 8.15 at low fluence laser irradiation (figures set (a)), only pits can be observed because of laser damage. In addition, contamination and inclusions can also be clearly observed in these figures near the damage site, confirming that the pit damage morphology is due to contamination of the coatings, which is the starting point of damage for all films in this study, regardless of the mixture percentages. The results reported here are similar to those reported and observed by Mangote *et al.* for Sc_2O_3:SiO_2 with respect to the change in damage morphology; the occurrence of thermal effects (i.e. absorption induced damage) is more pronounced when the Sc_2O_3 content increases [70].

8.3 Effects of Annealing on Sc_2O_3:SiO_2 Films

In this section, the results for annealed Sc_2O_3:SiO_2 films at 500°C, 700°C and 900°C have been presented and discussed.

8.3.1 Results and Discussion

8.3.1.1 Transmittance and Reflectance Measurement

Figure 8.17 shows the transmittance and reflectance of some samples studied in this chapter, where they are being compared between as-deposited, 500°C, 700°C and 900°C, to show the differences within the same coatings due to annealing. As previously mentioned, all samples were annealed for 1 hour in air at each temperature and allowed to cool naturally before removing them from the furnace. In each figures, the black solid lines represent the spectra for the blank substrate, the red solid line represents the as-deposited, the green dashed line represents 500°C, the magenta dash-dot line represents 700°C, and the blue dotted line represents 900°C.

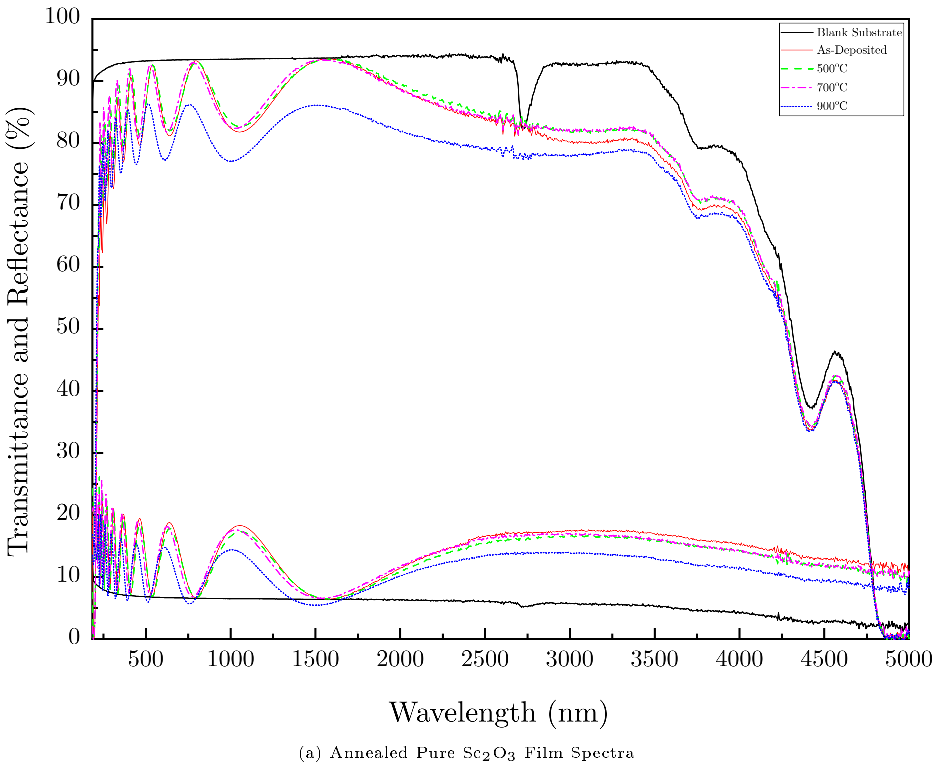

(a) Annealed Pure Sc_2O_3 Film Spectra

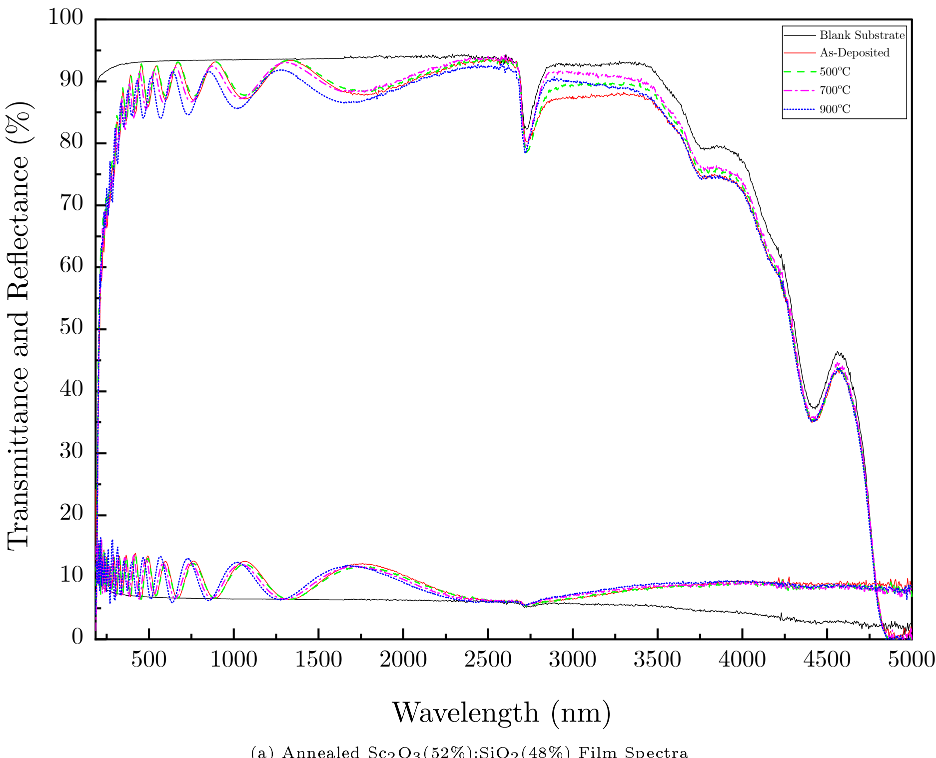

(a) Annealed Sc_2O_3(52%):SiO_2(48%) Film Spectra

Figure 8.17: Transmittance and Reflectance of annealed spectra for some of the samples investigated in this chapter. The samples shown are pure Sc_2O_3 and Sc_2O_3(52%):SiO_2(48%).

Figure 8.16a shows that there is a slight shift of the data that can be seen towards lower wavelengths as the annealing temperature increases (Burstein-Moss shift). This shift towards lower wavelengths as the annealing temperature increases can also indicate a thickness change within the coatings, which in turn will also affect the refractive index and density of the coating. There were no major changes in the transmittance and reflectance percentages as the temperature was increased to 700°C. As the annealing temperature reached 900°C, both transmittance and reflectance decreased. The same can be said for the spectra in Figure 8.17a, where there was a small blue shift in the data. It can also be seen that at 900°C, there is a reduction in the transmittance, although it is not as prominent as that of the pure scandia film. Further discussion of the effects of annealing on the optical properties is discussed in the following sections.

8.3.1.2 Refractive Index and Extinction Coefficient

Figure 8.18 shows the refractive index at 1064 nm for all temperature: as-deposited (black square), 500°C (red circle), 700°C (green upright triangle) and 900°C (blue downward triangle), as a function of Sc_2O_3 volume percentage in the films.

It can be seen that as the samples are annealed, they follow a similar trend where the refractive index decreases as the temperature increases, except for some films whose refractive index slightly increases at 700°C by a small amount of 0.01, then decreases again. The most notable refractive index change was observed for the mixed material with 94% Sc_2O_3. A small reduction in the refractive index owing to annealing has been reported for Sc_2O_3 by other authors [249] and also for other materials like HfO_2 [191, 229, 242]. As can be seen, the trend for the refractive indices at each annealing temperature is still the same, where the higher the Sc_2O_3 mixture content, the higher the value of the refractive index. Table 8.4 shows the values of the refractive index and of each samples at different annealing temperature.

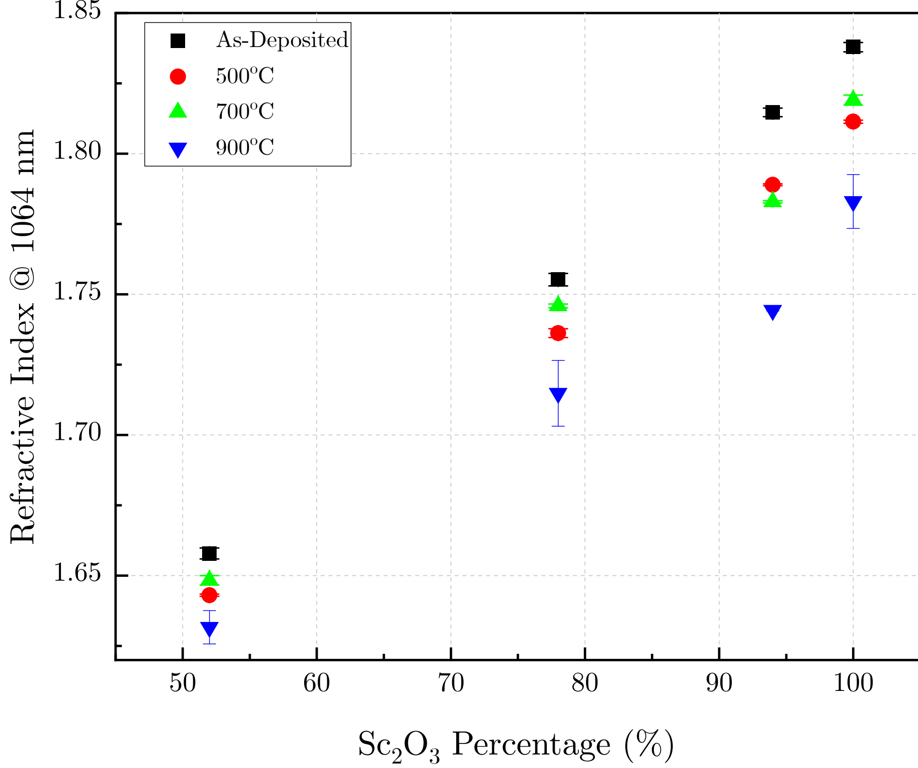

Figure 8.18: The refractive index at $\lambda = 1064$ nm. The error bars show the standard deviation of five separate fittings for each sample.

Table 8.4: The different refractive indices of Sc_2O_3:SiO_2 thin films with different mixture concentration at as-deposited, 500°C, 700°C and 900°C annealed temperatures.

SCANDIA:SILICA CONTENT	AS-DEP	500°C	700°C	900°C
100:0 (Pure Sc_2O_3)	1.84	1.81	1.82	1.78
94:6	1.81	1.79	1.78	1.74
78:22	1.76	1.74	1.75	1.71
52:48	1.66	1.64	1.65	1.63

Figure 8.19 shows the extinction coefficient of the samples at 1064 nm, similar to that of the refractive indices shown above. As the samples were annealed to higher temperatures, the overall trend showed that the extinction coefficient did not change significantly, with only a slight decrease. However, for most of the films, as the temperature reached 900°C, the extinction coefficient increased significantly, which led to an increase in absorption, as observed in the transmittance and reflectance examples shown

in Figure 8.17 for pure Sc_2O_3 and Sc_2O_3(52%):SiO_2(48%), where the transmittance and reflectance both decreased. This could be due to the occurrence of more cracks in the coating, which could lead to an increase in the absorption coefficient [247] This was also confirmed by the decrease in the LIDT value for the pure Sc_2O_3 film (Section 8.3.1.6).

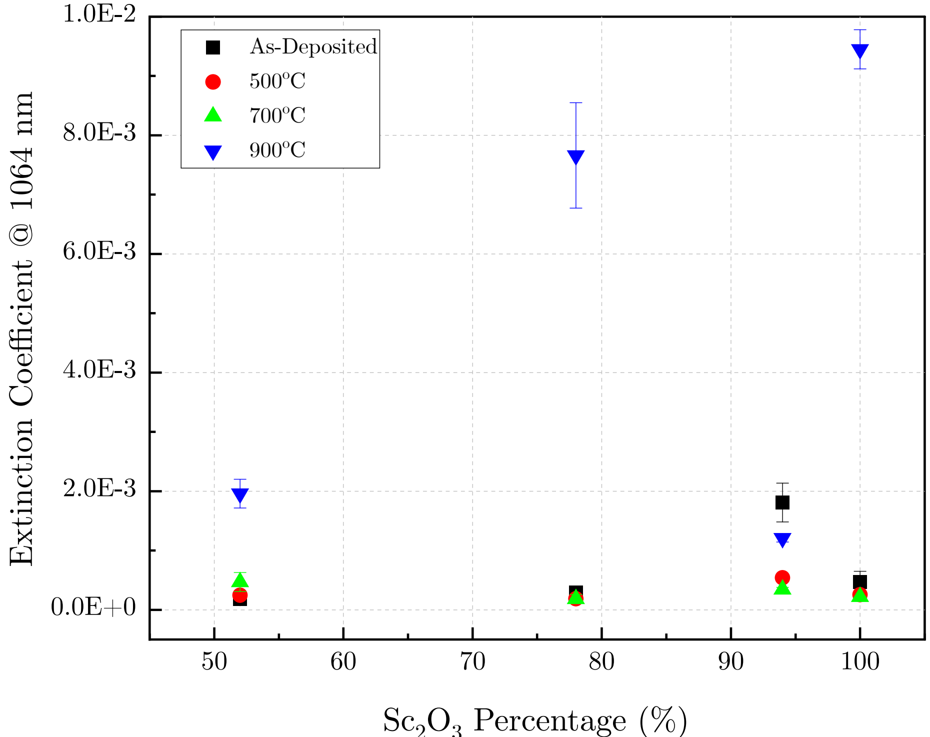

Figure 8.19: The extinction coefficient at λ = 1064 nm. The error bars show the standard deviation of five separate fittings for each sample.

8.3.1.3 Bandgap Energy

Figure 8.20 shows the OJL bandgap energy extracted from SCOUT for films at: as-deposited (black square), 500°C (red circle), 700°C (green upright triangle) and 900°C (blue downward triangle).

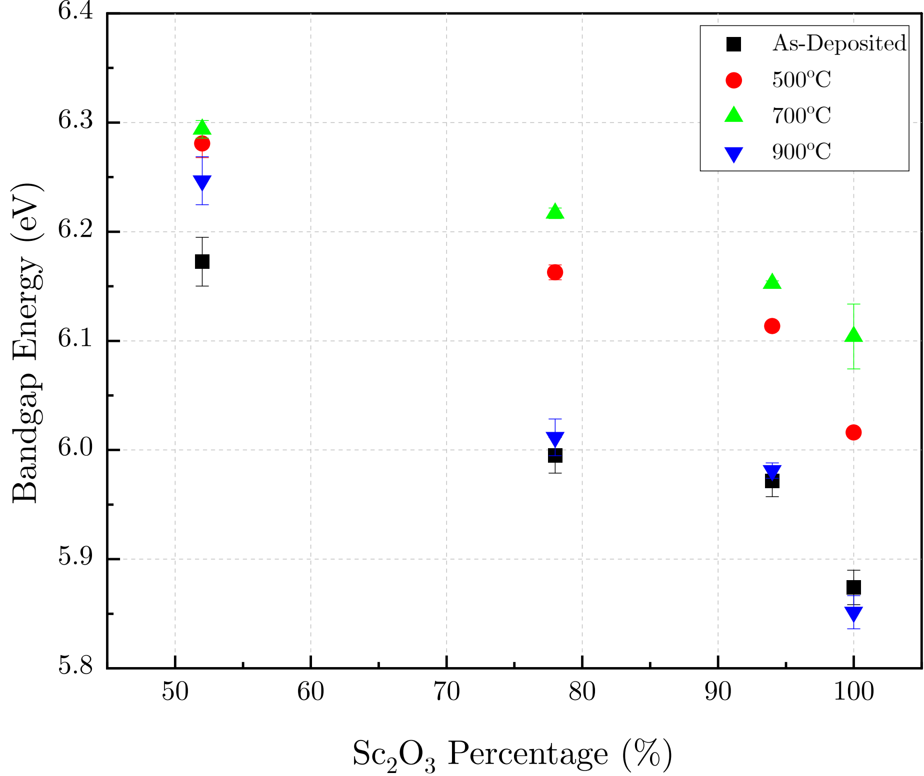

Figure 8.20: The average bandgap energy of the films acquired from SCOUT. The error bars show the standard deviation of five separate fittings for each sample.

As the samples were annealed to 700°C, there was an increase in the bandgap energies for all films, where the bandgap energies then decreased as the annealing temperature reached 900°C. All samples still follow the same trend after annealing as it does for the as-deposited film, where increasing the Sc_2O_3 content in the film lowers the bandgap energies.

8.3.1.4 Thickness

Figure 8.21 shows the thickness extracted from SCOUT for the mixed films: as-deposited (black square), 500°C (red circle), 700°C (green upright triangle) and 900°C (blue downward triangle).

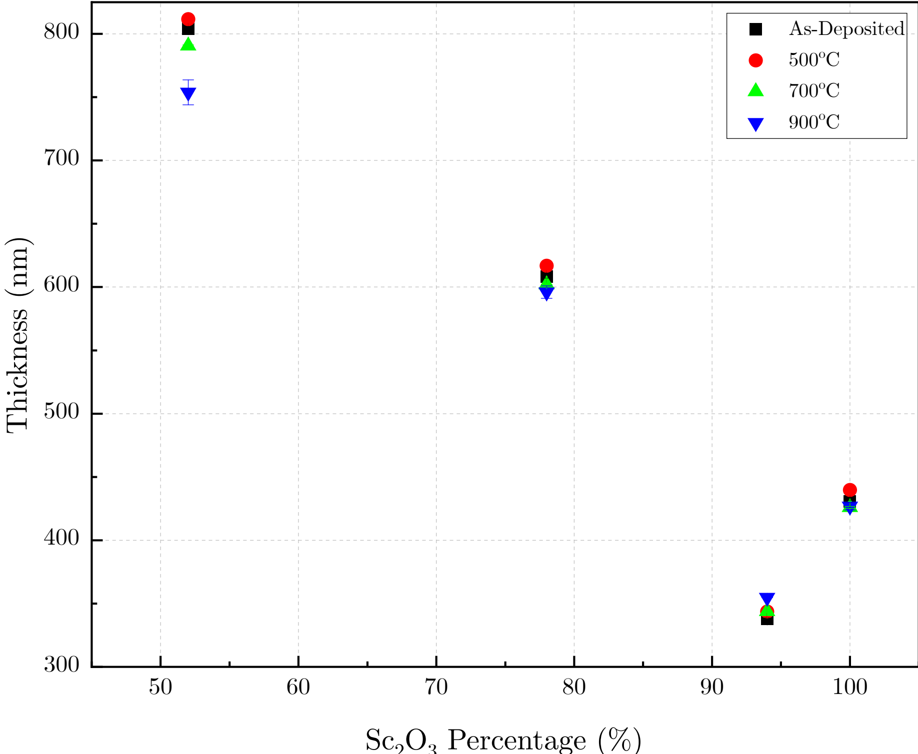

Figure 8.21: The average thicknesses of the films acquired from SCOUT. The error bars show the standard deviation of five separate fittings for each sample.

The annealed samples follow the same trend as that of the as-deposited samples. For all the films, as the annealing temperature increased, the thickness increased at 500°C, and then decreased at 700°C and 900°C. For the Sc_2O_3(94%):SiO_2(6%) film, there is a small increase at every annealing temperature. However, for all these films, the changes in thickness were very small (∼2%). The largest change was observed for Sc_2O_3(52%):SiO_2(48%) annealed at 900°C, where the highest value was $d = 812$ nm and the lowest value was 754 nm. The decrease in the thickness with increasing annealing temperature suggests that there is compressive stress within the films [27, 186–188], which is further confirmed by the XRD data, especially for the crystallised film.

8.3.1.5 XRD Results

GIXRD data for the mixed films at 700°C and 900°C are presented.

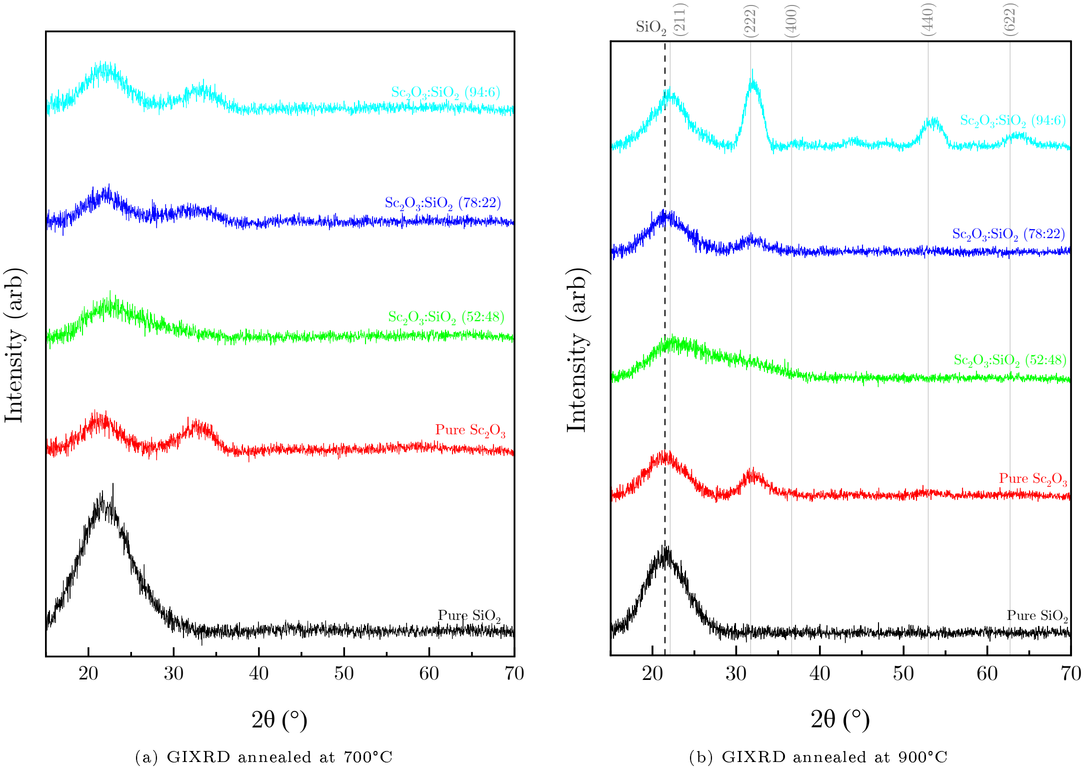

(a) GIXRD annealed at 700°C

(b) GIXRD annealed at 900°C

Figure 8.22: GIXRD data acquired for the annealed films within this study.

At 700°C, it can be seen that all of the films still have broad weak bands, similar to the data shown for the as-deposited film, with the pure Sc_2O_3 and Sc_2O_3(94%):SiO_2(6%) film peaks becoming slightly more prominent compared to the as-deposited films. As the films were annealed to 900°C, the Sc_2O_3(94%):SiO_2(6%) film showed sharp peaks, indicating that the film was crystalline. The Sc_2O_3(94%):SiO_2(6%) film showed a preferential (222) growth orientation, which is the preferred orientation for cubic Sc_2O_3 films. It can also be seen that there are more peaks at (440) and (622), which further confirms the cubic phase. As for the Sc_2O_3(78%):SiO_2(22%) and pure Sc_2O_3 films, the data show that the film is moving towards becoming polycrystalline, with the same peaks starting to appear at the same phases as the Sc_2O_3(94%):SiO_2(6%) film. The Sc_2O_3(52%):SiO_2(48%) film still shows broad weak bands similar to the pure silica data, indicating that the films are still amorphous. This is expected because silica crystallises at a much higher temperature, and the larger percentage of silica in the mixed films

allows for the suppression of crystallisation in the mixed film [72]. Figure 8.22b also shows that there is a shift in the pure hafnia and HfO_2(92%):SiO_2(8%) films towards higher values of 2θ, which indicates lattice contraction due to annealing, leading to compressive stress in the films [27, 178, 179, 186–188]. The same phenomena were observed and discussed in the previous chapters for the HfO_2 and Sc_2O_3 films. The data for the peaks and phase of the film is from ICDD's PDF_00-042-1463.

8.3.1.6 LIDT Results

In Figure 8.23 shows the LIDT of the films after annealing at 480°C for 1 hour are shown. The figures shows: Figure 8.23a LIDT versus refractive index, Figure 8.23b LIDT versus bandgap energy, and Figure 8.23c shows the LIDT as a function of Sc_2O_3 percentage in the film for both as-deposited and annealed films.

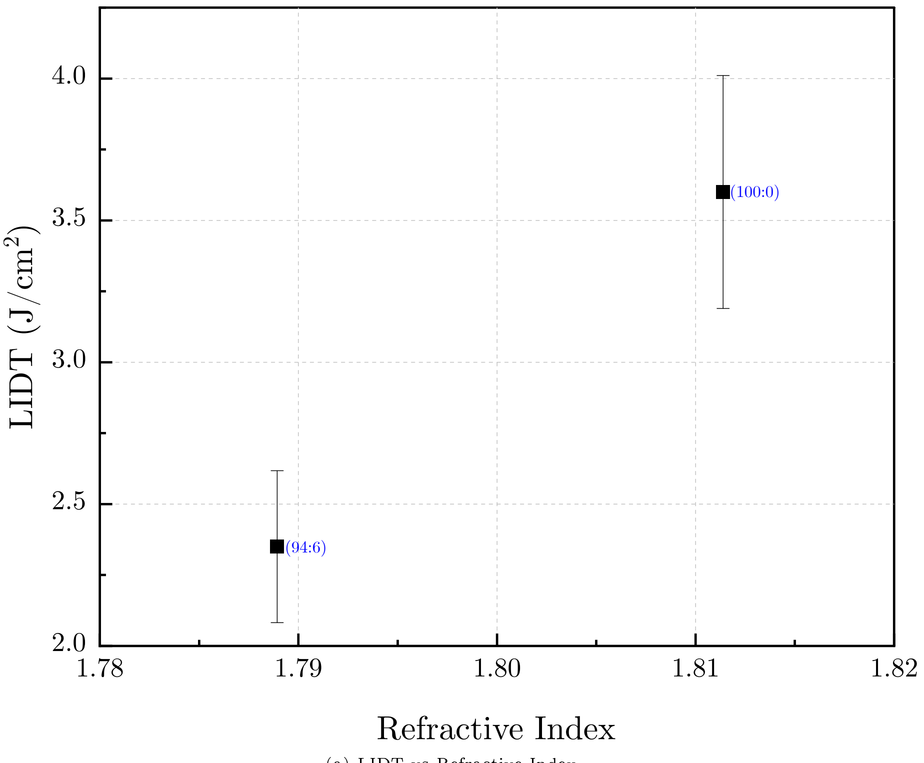

(a) LIDT vs Refractive Index

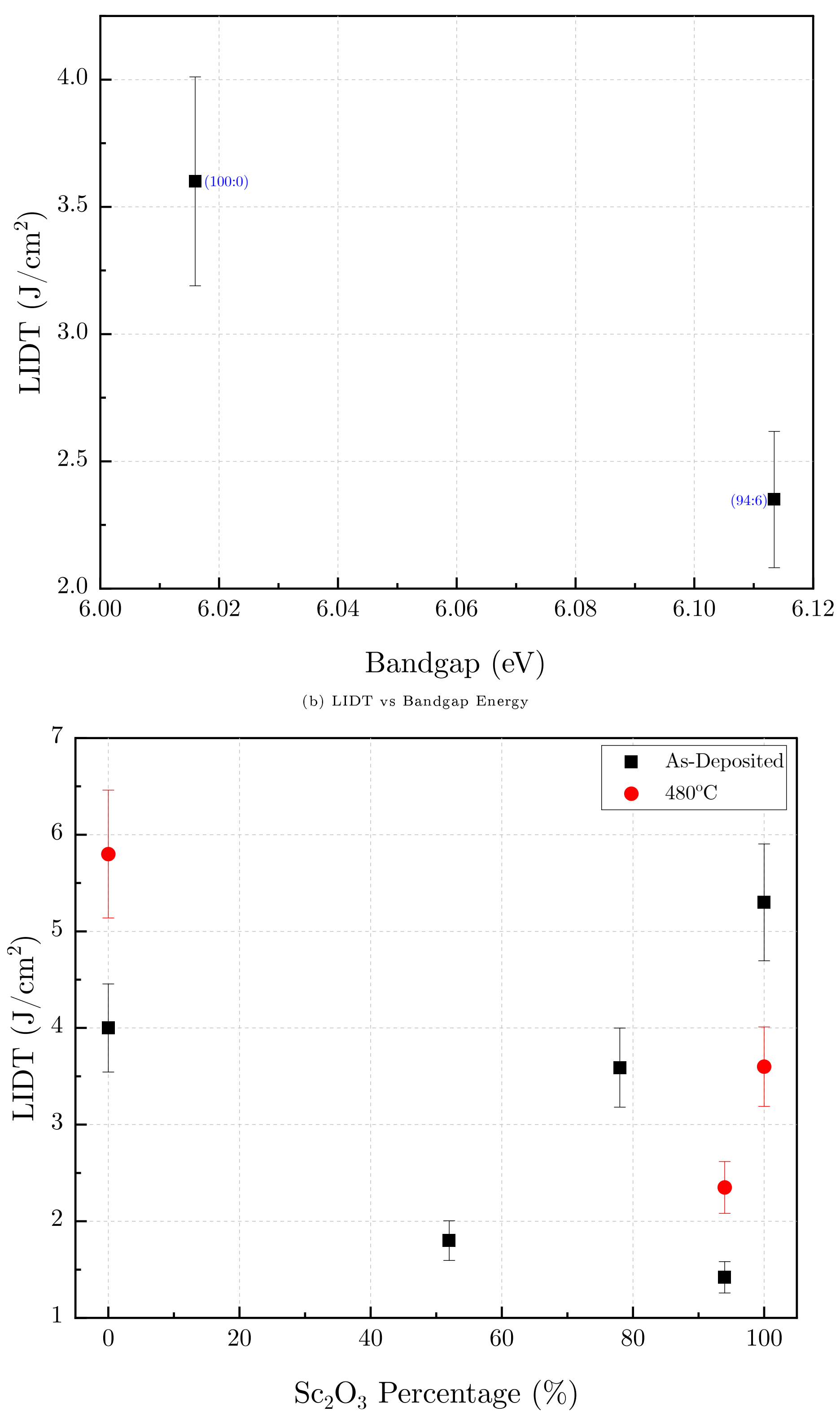

(b) LIDT vs Bandgap Energy

(c) LIDT vs Sc_2O_3 Percentage for both as-deposited and annealed films

Figure 8.23: The LIDT values for all the films studied in this chapter (a) and (b) annealed at 480°C, (c) for both as-deposited and annealed films.

As shown in Figure 8.23, only some films underwent LIDT testing. This is because, as previously mentioned, after annealing, some films have cracks, which can be seen under a microscope. These cracks in the coatings can lead to misinterpretation of the LIDT values, as structural defects can modify the electric field, thereby lowering the damage threshold of dielectric films [79]. One of the reasons for the occurrence of cracks at this temperature can also be due to several damages already existing on the coatings from testing at as-deposited, which increases the chance of cracks as the films are annealed. For the tested samples, it can be seen that the LIDT for Sc_2O_3(94%):SiO_2(6%) increased after annealing, whereas for pure Sc_2O_3, the value decreased. The significant decrease in the LIDT value for pure Sc_2O_3 can be attributed to the cracks on the coatings because this is the only sample to undergo LIDT testing with cracks.

Figure 8.24 shows SEM images of cracks that can be observed due to annealing of the films:

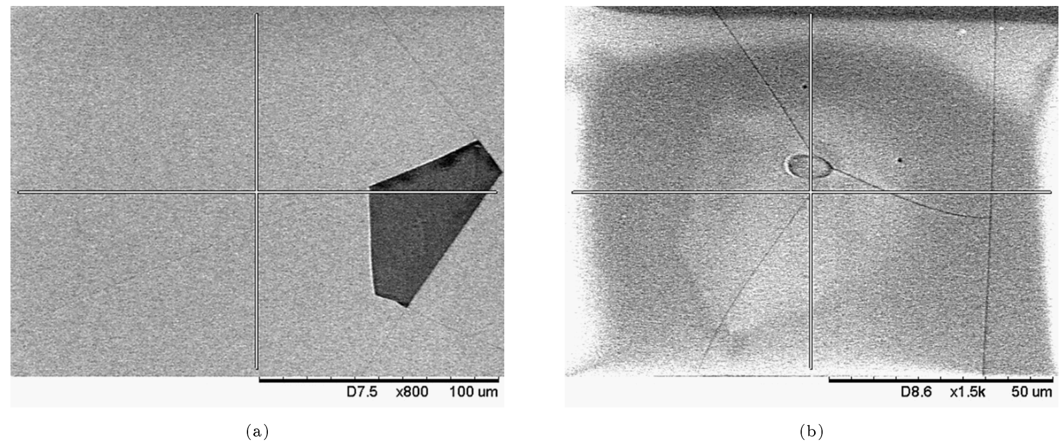

(a) (b)

Figure 8.24: Cracks observed on the films due to annealing.

The films in both figures were on JGS-3 substrates, which were only used for annealing studies to extract the optical constants, where the films were annealed to 700°C before cracks were observed. As shown in Figure 8.24b, some of the cracks can be seen to have originated from pits, which can arise from contamination in the films and become pits as the annealing temperature increases. In Figure 8.24a, it can be seen that the cracks originate where a portion of the film has broken off, or delaminated. This could

be due to contamination of the films being burned off, breaking off a large part of the thin film, similar to how pits are created. As mentioned, the samples which underwent LIDT showed cracks at a lower temperature because the previous damage was enhanced as the annealing temperature increased.

8.3.1.7 Damage Morphology

Figures 8.25 and 8.26 shows the damage morphologies of the pure and mixed film after laser irradiation, where (a) shows the low fluence damages and (b) shows the high fluence damages. It can be seen that similar to as-deposited samples, after annealing, there are two main types of damage observed: absorption induced damage and pits due to inclusion.

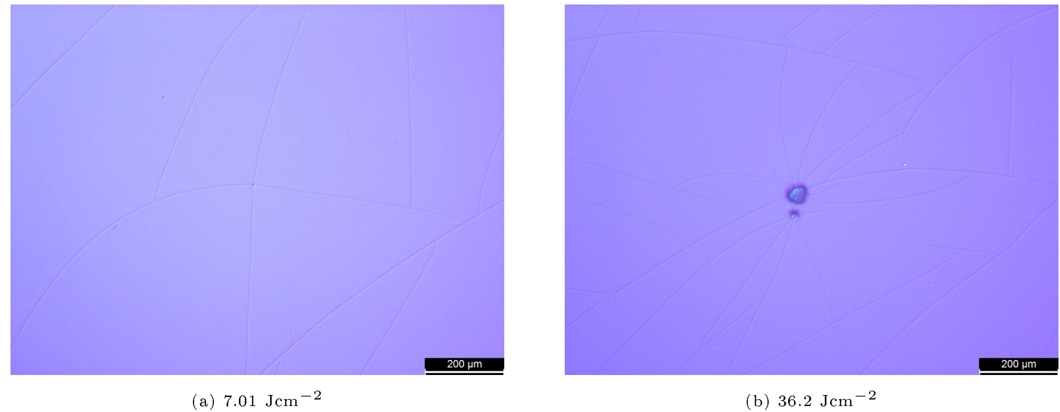

(a) 7.01 Jcm^{-2} (b) 36.2 Jcm^{-2}

Figure 8.25: Observed damage sites for annealed pure Sc_2O_3 film with (a) low and (b) high fluence.

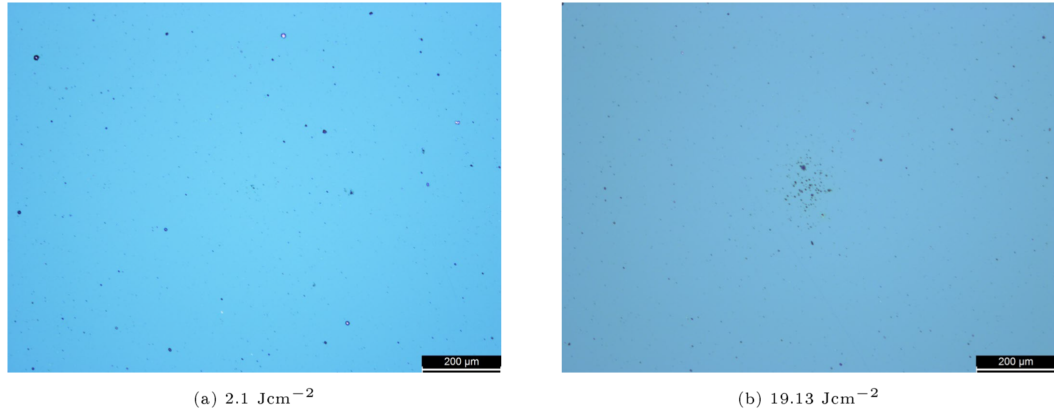

(a) 2.1 Jcm^{-2} (b) 19.13 Jcm^{-2}

Figure 8.26: Observed damage sites for annealed Sc_2O_3(94%):SiO_2(6%) film with (a) low and (b) high fluence.

In Figures 8.25b, it can be observed that the LIDT was performed on cracks that can be observed on the films, leading to a decrease in the LIDT value, as mentioned in Section 8.3.1.6. The damage morphology that can be observed here is similar to that at as-deposited, where the damage can be associated with absorption induced damage effect, where the films reach their melting point before delamination occurs [8, 243]. The characteristic morphology of absorption induced defect damage is often shown as a discolouration or an increase in the surface roughness at the centre of the laser beam [8], which can be observed for the pure Sc_2O_3 sample. It can also be observed that there are two different spots which have been damaged next to each other and within the size of the beam diameter, where the smaller damaged spot appears as a pit where some of the cracks originate. For the Sc_2O_3(94%):SiO_2(6%) sample, many defects and contamination were observed on the film, which leads to the decreased surface quality of the film. This significantly affects the LIDT results acquired for the films within the nanosecond regime. In Figure 8.26, pits are observed at both high and low fluences. Damage initiated by defects embedded in films typically results in craters or pits in the laser beam area [8,80,243]. This morphology can be attributed to inclusions which were rapidly heated during laser irradiation and exploded, thereby creating pits [8, 80, 243]. It can also be observed in Figures 8.25 that at low fluence laser irradiation, only pits can be observed because of laser damage. In addition, contamination and inclusions can also be clearly observed in these figures near the damage site, confirming that the pit damage morphology is due to contamination of the coatings, which is the starting point of damage for all the films in this study, regardless of the mixture percentages. As previously mentioned, the pure Sc_2O_3 sample is the only one which RhySearch carried out the LIDT testing despite the cracks in the films, which confirms the theory that this will provide a lower LIDT than expected owing to the improvement of the absorption coefficient of the films [247]. Another theory as to why cracks could lower the LIDT threshold was discussed by Ristau, who stated that structural defects can modify the electric field, thereby lowering the damage threshold of dielectric films [79].

8.4 Conclusion

The effects of different mixture percentages of Sc_2O_3:SiO_2 thin films fabricated using the ECR-IBSD technique on the optical constants, structure, and LIDT are presented and discussed in this chapter. Structural analysis of the films was carried out using GIXRD, which confirmed that the as-deposited films in this study were amorphous, regardless of the mixture percentages. The volume mixture percentages of Sc_2O_3 and SiO_2 in each film in this study were determined using EMA models based on the refractive index values. By utilising the OJL model implemented in SCOUT software, the refractive index of the as-deposited films was found to be in the range of $n = 1.66 - 1.84$, where the lowest value is for the Sc_2O_3(52%):SiO_2(48%) film and the highest value is for the pure Sc_2O_3 film. It was shown that the mixture materials filled the values for the refractive index between those of the two pure materials, indicating that the refractive index can be tuned by changing the mixture percentages. The extinction coefficient was found to be in the range of $k = 1.76 \times 10^{-4} - 1.81 \times 10^{-3}$, where the highest value was for the Sc_2O_3(94%):SiO_2(6%) film and the lowest was for the Sc_2O_3(52%):SiO_2(48%) film, with the other mixed film values lying in between these two values, where the higher the SiO_2 percentage, the lower the extinction coefficient value, with the Sc_2O_3(94%):SiO_2(6%) film being the anomaly. The OJL bandgap energy was found in the range of 5.87 – 6.17 eV, where the increase in SiO_2 also increases the bandgap energy. The shift in the bandgap to higher energies can also be seen from the slight shift towards lower wavelengths in the transmittance measurement in the UV range as the SiO_2 content increases.

The LIDT of the films was carried out by RhySearch with a 10-on-1 test using a Nd:YAG laser at 1064 nm and 11.6 ns pulses. From this, it was found that the highest LIDT was for the pure Sc_2O_3 film at 5.3 J/cm^2 and the lowest for Sc_2O_3(94%):SiO_2(6%) at 1.42 J/cm^2. Based on the damage morphologies, two main types of damage were observed: absorption induced damage and pits due to inclusions, where the latter could be observed for all films at low laser fluence. Laser damage is very sensitive to contamination

within the nanosecond regime, and a large amount of discharge occurs inside the chamber during deposition, which leads to contamination of the films, which can lower the LIDT values. Contamination of the films was clearly observed under the microscope, with the Sc_2O_3(94%):SiO_2(6%) film having the worst film surface quality.

The effects of annealing on the optical and structural properties and LIDT of Sc_2O_3:SiO_2 mixed films are also presented and discussed for annealing temperatures of 500°C, 700°C and 900°C. As the annealing temperature increased, the refractive index and extinction coefficient decreased, and the bandgap energy increased. However, the extinction coefficient at 900°C increases significantly. The structural properties were determined using GIXRD, which showed that at 700°C, all films with different percentages of mixtures remained amorphous, and as the temperature reached 900°C, peaks were observed for Sc_2O_3(94%):SiO_2(6%) films, which showed a cubic Sc_2O_3 structure; however, films with a higher percentage of SiO_2 remained amorphous. The pure Sc_2O_3 film also showed a slightly polycrystalline cubic structure; however, it did not fully crystallise at 900 °C. All the crystalline (and polycrystalline) films show a slight shift towards higher angles, indicating compressive stress within the films, which goes hand-in-hand with the decrease in refractive index and decrease in the film thickness due to annealing. The LIDT was carried out for only two films in this study after annealing, owing to cracking in the films. As the films were annealed to 480°C, the LIDT value for pure Sc_2O_3 film decreased due the tests being done on the cracks of the coatings, whereas the Sc_2O_3(94%):SiO_2(6%) mixed film's LIDT value increases. Similar to the as-deposited films, two main types of damage were observed: absorption induced damage and pits due to inclusions, where the latter could be observed for all films at low laser fluence.

From optical characterisation, it was found that by controlling the mixture percentage of Sc_2O_3 and SiO_2, the refractive index, extinction coefficient, and bandgap energy could be tuned to the desired values depending on the application. In addition, post-deposition can aid in tuning the optical constants of the mixed films. By including more than 10% of SiO_2 into a mixture of Sc_2O_3:SiO_2 films fabricated by ECR-IBSD, this can suppress the crystallisation temperature of the films, along with the pure Sc_2O_3

which typically crystallises at 500°C. This shows that the mixed Sc_2O_3:SiO_2 films, and pure Sc_2O_3 film, fabricated by ECR-IBSD could be an interesting material for high-temperature applications.

9 | Conclusion

The research presented in this thesis utilises ion beam sputter deposition to fabricate amorphous thin film coatings of materials with a high refractive index and high laser induced damage threshold, which is typically used in laser systems. Ion beam sputter deposition is an ideal deposition method for films that will be used in harsh environments with high fluence requirements and desirable properties close to those of bulk properties (i.e. high density films, improved adhesion of films to substrate, fewer defects, etc.). Typically, RF-type ion sources are used for IBSD processes, and as in this study, ECR-type ion sources were utilised. An overview of the two deposition setups of the ECR-IBSD processes used throughout this thesis, which were developed and operated by the author, to produce the coatings discussed in this thesis, alongside the fundamental theory of the ECR-IBSD process. The two ECR-IBSD setups are novel because the first system can employ six ECR ion sources, where the individual sources can be controlled separately, and the second set-up is the only setup in the world, to the author's knowledge, which employs 24-ion sources in a ring shape, where the microwave power of the individual sources can be controlled. In this thesis, the fundamental theory was discussed for all the characterisation methods carried out for the films discussed, which includes, but is not limited to, the optical software used (SCOUT), XRD, EDS, and LIDT testing carried out by RhySearch.

The materials of interest discussed in this thesis include both pure and mixed materials, where the focused materials are HfO_2, Sc_2O_3, HfO_2:SiO_2, and Sc_2O_3:SiO_2. In this work, it has established the influence of oxygen incorporation in pure materials from an optical

and structural perspective. This work has led to the understanding that utilising ECR-IBSD and ceramic targets provides over-stoichiometric HfO_2 and Sc_2O_3. For the mixed materials, the study focused on the influence of different mixture percentages on the optical, structural, and LIDT properties of the films.

For the pure HfO_2 study, three different configurations were used: differing reactive oxygen percentages, differing sputtering oxygen percentages, and pure oxygen sputtering. By utilising the OJL model, the refractive indices of the as-deposited films were found to be in the range of $n = 1.70 - 1.92$, the extinction coefficient was found to be in the range of $k = 0.52 - 6.29 \times 10^{-4}$, and the OJL bandgap energy was found to be in the range of 5.6 – 6.0 eV. From this study, it was found that both the refractive index and extinction coefficient decreased with an increase in the oxygen content, whereas the bandgap energy increased. The effects of annealing on the optical and structural properties of HfO_2 films were also investigated. It was found that the refractive indices for all the films decreased, and the extinction coefficient of the films increased, as did the bandgap energies. The effect of annealing was investigated at temperatures of up to 700°C. From the GIXRD results, it was found that the films fabricated by ECR-IBSD remained amorphous after annealing to 500°C, whereas they showed a monoclinic crystalline structure after annealing to 700°C. As for the pure Sc_2O_3 study, the effects of different reactive oxygen percentages and pure oxygen sputtering are presented and discussed. The refractive indices of the as-deposited films were found to be in the range of $n = 1.87 - 1.91$, the extinction coefficient was found to be in the range of $k = 1.7 - 2.6 \times 10^{-3}$, and the OJL bandgap energy was found to be in the range of 5.86 – 6.13 eV. From the study, it was found that neither the refractive index nor the extinction coefficient exhibit a real trend with differing oxygen percentages. However, the averages were found to be $n = 1.89 \pm 0.02$ and $k = (2.1 \pm 0.4) \times 10^{-3}$. As for the bandgap energy, this increased with an increase in the oxygen percentage in the process. The effects of annealing on the optical and structural properties of the Sc_2O_3 films were also investigated. It was found that the refractive indices for all the films decreased, and the extinction coefficient of the films first decreased and then increased after reaching an annealing temperature higher than 500°C. As for the bandgap energies, as the an-

nealing temperature increases, so does the bandgap energy. The effect of annealing was investigated at temperatures of up to 900°C. From the GIXRD results, it was found that the films fabricated by ECR-IBSD remained amorphous despite being annealed at 900°C. Typically, Sc_2O_3 films crystallise at 500°C, and this study shows that Sc_2O_3 films fabricated by ECR-IBSD could be an interesting material for high-temperature applications because the films remained amorphous. From the studies carried out in this thesis for pure materials, it was found that by controlling both the reactive and sputtering oxygen concentrations during deposition, the bandgap energy and refractive index could be tuned to the desired value. In addition, post deposition annealing can aid in tuning the optical constants to the desired values for different applications. Although, it is surprising that all of the films within the pure material study has excess oxygen within the coatings, where further investigation would be of value, this can still be of benefit in different applications depending on the optical properties that are required.

For both the mixed materials, the effects of different mixture percentages on the optical, structural, and LIDT properties were investigated. From these studies, it was found that as the silica content increased in the mixture, the refractive indices decreased. A similar trend was observed for the extinction coefficient. As for the bandgap energy, as the silica content increased, so did the bandgap energy of the mixed materials. It can be concluded that the optical constants of the mixed materials can fill in the optical values between the two pure materials, indicating that the optical properties can be tuned by changing the mixture percentages. It was also found that with more than 10% SiO_2 in the mixed films, silica suppressed the crystallisation of the mixed films, leading to amorphous films after annealing to 900°C. The LIDT was performed for the as-deposited and annealed to 480 °C. The LIDT of the annealed films increased slightly for the films that were tested. However, some films were not able to carry out LIDT testing after annealing because of the cracks in the coatings, which can provide lower values of LIDT than expected for the coatings. From this study, at as-deposited, the highest LIDT is for HfO_2(92%):SiO_2(8%) at 11.5 J/cm^2 and the lowest is for Sc_2O_3(94%):SiO_2(6%) at 1.42 J/cm^2. The main damage morphologies observed for the films fabricated by ECR-IBSD were absorption induced damage and pits owing

to inclusions. As the LIDT is very sensitive to contamination within the nanosecond regime, this is a downfall of the films studied in this thesis. Contamination can arise from many factors: during the production steps, substrate surface polishing, cleanliness of the substrate surface prior to coating, cleanliness of the deposition chamber, deposition process, and optics handling techniques. In these studies, contamination likely occurred during the loading of substrates into the system and during the deposition process. During the deposition process, there was a large amount of discharge inside the system which can cause contamination inside the system from delamination of the materials coated on the inner walls. With this knowledge, the most important next steps are to mitigate the discharge inside the chamber during deposition, and carry out LIDT tests again to be certain as to what causes the LIDT within the nanosecond regime.

For future work, further development and tweaking of the two ECR systems will have to be carried out to fully mitigate the discharging that occurs inside the system. Several methods can be employed, first by utilising metal targets instead of ceramic targets, as significant discharge can occur owing to the accumulation of charges on the non-conductive target surface; second, by employing more, or more effective, neutralisers in the system; and lastly, regular cleaning of the deposition chamber to minimise the materials on the chamber wall delaminating, leading to contamination in the system which can contaminate the substrates. Once the contamination has been minimised, further investigation of different mixture percentages of the mixed coatings on the LIDT can be carried out to determine the main cause of damage in the ECR-IBSD coatings in the nanosecond regime, that is, bandgap dependency or absorption dependency. Several studies have been thought of that could be carried out in order to understand more about the films that have fabricated by ECR-IBSD and its optical properties, including LIDT once the discharges have been mitigated:

- New set of studies between metallic and ceramic targets should be carried out to understand the properties of the films and the effects different types of targets has on the optical properties of the film,

- With metallic targets, different oxygen percentage in the background could be studied, alongside different sputtering gases (argon, oxygen, nitrogen, etc.),
- Mixed materials, including more than just mixing two different materials would be of interest (Hafnia/Scandia/Silica mixtures),
- Elevated substrate temperature inside the system during the deposition to investigate if high deposition temperature will decrease the defects in the coatings and the effects this has on the films' structural, optical and LIDT properties,
- Studying multilayers, as they are typically utilised in optical systems, which can provide "real-world" insights into the optical coatings that have been produced by ECR-IBSD.

Further investigation into the LIDT of films fabricated from both metallic and ceramic targets will help gain insight into the main cause of damage in the nanosecond regime once contamination and discharging issues have been mitigated. Alongside the set of studies mentioned, post-deposition annealing of the coatings will also be of interest to understand the effects of heat treatment on the optical, structural, and LIDT properties of the films.

For the 600 system, as the angle of the target relative to the ion sources can be moved, this will be an interesting study to carry out, where different target angles can be manipulated. The change in the target angle can affect the amount of argon trapped in the films, along with the study of backscattered argon and how this can change the film structure.

Since the studies within this thesis have been carried out and the group has expanded, new characterisation techniques are now available, such as: Mass spectrometer, where this can be used to study the ECR plasma and its energies which will provide an important and interesting insights into the ECR plasmas and films that have been fabricated; Photothermal Common-path Interferometry (PCI) and Cavity Ring Down (CRD) systems are also available, where they can be utilised to study the absorption

in parts per million (ppm) level, which can lead to the study of the correlation between the absorption of the films and its LIDT in the nanosecond regime.

The LIDT study presented in this thesis has focused on the wavelength of 1064 nm and within the nanosecond regime, and it would also be very interesting to investigate the LIDT at different laser parameters (different wavelengths and pulse durations), as well as the possibility of investigating continuous wave lasers.

Finally, a study that would also be very interesting in the future is to add another ECR source where it is operating at a lower energy to act as an ion assist source, which can be found in many other IBSD systems, where the assist source is typically used to further densify the films and reduce their stress. The optical, structural, and LIDT properties of these films will be very interesting and could provide further understanding of ECR-IBSD fabricated thin films.

Bibliography

[1] H. Brune, "Growth Modes," Pergamon, Tech. Rep., 2001.

[2] E. Kusano, "Structure-zone modeling of sputter-deposited thin films: a brief review," *Applied Science and Convergence Technology*, vol. 28, no. 6, pp. 179–185, 2019.

[3] J. A. Thornton, "The microstructure of sputter-deposited coatings," *Journal of Vacuum Science & Technology A*, vol. 4, no. 6, pp. 3059–3065, 1986.

[4] L. Gallais and M. Commandré, "Laser-induced damage thresholds of bulk and coating optical materials at 1030 nm, 500 fs," 2014.

[5] C. Stolz and R. Negres, "Ten-year summary of the Boulder Damage Symposium annual thin film laser damage competition," *Optical Engineering*, vol. 57, no. 12, 2018.

[6] M. Mende, S. Schrameyer, H. Ehlers, D. Ristau, and L. Gallais, "Laser damage resistance of ion-beam sputtered Sc_2O_3/SiO_2 mixture optical coatings," *Applied Optics*, vol. 52, no. 7, 2013.

[7] Edmund Optics. [Online]. Available: https://www.edmundoptics.co.uk/knowledge-center/application-notes/lasers/laser-optics-resource-guide/

[8] D. Ristau, M. Jupé, and K. Starke, "Laser damage thresholds of optical coatings," *Thin Solid Films*, vol. 518, no. 5, pp. 1607–1613, 2009.

[9] Lidaris. [Online]. Available: https://lidaris.com/

[10] Laseroptik. [Online]. Available: https://www.laseroptik.com/

[11] F. X. D'Abzac, A. M. Seydoux-Guillaume, J. Chmeleff, L. Datas, and F. Poitrasson, "In situ characterization of infrared femtosecond laser ablation in geological samples. part A: the laser induced damage," *Journal of Analytical Atomic Spectrometry*, vol. 27, pp. 99–107, 2012.

[12] S. Mao, F. Quéré, S. Guizard, X. Mao, R. Russo, G. Petite, and P. Martin, "Dynamics of femtosecond laser interactions with dielectrics," *Applied Physics A*, vol. 79, no. 7, pp. 1695–1709, 2004.

[13] B. Guo, J. Sun, Y. Hua, N. Zhan, J. Jia, and K. Chu, "Femtosecond laser micro/nano-manufacturing: theories, measurements, methods, and applications," *Nanomanufacturing and Metrology*, vol. 3, no. 1, pp. 26–67, 2020.

[14] L. Jonušauskas, D. Mackevičiūtė, G. Kontenis, and V. Purlys, "Femtosecond lasers: the ultimate tool for high-precision 3D manufacturing," *Advanced Optical Technologies*, vol. 8, no. 3-4, pp. 241–251, 2019.

[15] X. J. Wang, H. H. Fang, F. W. Sun, and H. B. Sun, "Laser writing of color centers," *Laser & Photonics Reviews*, vol. 16, no. 1, p. 2100029, 2022.

[16] N. Abbas, M. R. Shad, M. Hussain, S. M. Z. Mehdi, and U. Sajjad, "Fabrication and characterization of silver thin films using physical vapor deposition, and the investigation of annealing effects on their structures," *Materials Research Express*, vol. 6, no. 11, p. 116437, 2019.

[17] University of Warwick. [Online]. Available: https://warwick.ac.uk/fac/sci/physics/current/postgraduate/regs/mpagswarwick/ex5/growth/pvd/

[18] C. Bonafos, L. Khomenkhova, F. Gourbilleau, E. Talbot, A. Slaoui, M. Carrada, S. Schamm-Chardon, P. Dimitrakis, and P. Normand, "Nano-composite MOx materials for NVMs," *Metal Oxides for Non-volatile Memory*, pp. 201–244, 2022.

[19] P. N. Hishimone, H. Nagai, and M. Sato, "Methods of fabricating thin films for energy materials and devices," *Lithium-ion Batteries-Thin Film for Energy Materials and Devices*, 2020.

[20] C. Bundesmann and H. Neumann, "Tutorial: The systematics of ion beam sputtering for deposition of thin films with tailored properties," *Journal of Applied Physics*, vol. 124, no. 23, p. 231102, 2018.

[21] M. Agrawal, S. Biswas, and K. Vliet, "Vacuum-assisted biocompatible surface modification coating techniques: A new era in the synthesis of biotech-enabled products," *Vacuum Technology and Coating*, vol. 17, pp. 31–33, 2016.

[22] M. Balestrieri, "Transparent conductive oxides with photon converting properties in view of photovoltaic applications: The cases of rare earth-doped zinc oxide and cerium oxide," Ph.D. Dissertation, 2014.

[23] A. M. Hussein, E. M. A. Dannoun, S. B. Aziz, M. A. Brza, R. T. Abdulwahid, S. A. Hussen, S. Rostam, D. M. T. Mustafa, and D. S. Muhammad, "Steps toward the band gap identification in polystyrene based solid polymer nanocomposites integrated with tin titanate nanoparticles," *Polymers*, vol. 12, no. 10, p. 2320, 2020.

[24] W. Theiss, "Scout: Technical Manual" *W.Theiss Hard- and Software for Optical Spectroscopy.* [Online]. Available: https://wtheiss.com/.

[25] R. Lance, "Optical analysis of titania: Band gaps of brookite, rutile and anatase," Master's thesis, 2018.

[26] Z. Chen and T. Jaramillo, "The use of UV-visible spectroscopy to measure the band gap of a semiconductor," *Department of Chemical Engineering, Stanford University, Edited by Bruce Brunschwig*, vol. 9, pp. 19, 2017.

[27] B. D. Cullity and S. R. Stock, *Elements of X-ray Diffraction*, Third Edition, 2001.

[28] X-ray Production, Tubes, and Generators. [Online]. Available: https://radiologykey.com/x-ray-production-tubes-and-generators/

[29] I. Stabrawa, A. Kubala-Kukuś, D. Banaś, G. Pepponi, J. Braziewicz, M. Pajek, and M. Teodorczyk, "Characterization of the morphology of titanium and titanium (IV) oxide nanolayers deposited on different substrates by application of grazing incidence X-ray diffraction and X-ray reflectometry techniques," *Thin Solid Films*, vol. 671, pp. 103–110, 2019.

[30] Rhysearch. [Online]. Available: https://www.rhysearch.ch/

[31] M. Abernathy, A. Amato, A. Ananyeva, S. Angelova, B. Baloukas, R. Bassiri, G. Billingsley, R. Birney, G. Cagnoli, M. Canepa, M. Coulon, J. Degallaix, A. Di Michele, M. A. Fazio, M. M. Fejer, D. Forest, C. Gier, M. Granata, A. M. Gretarsson, E. M. Gretarsson, E. Gustafson, E. J. Hough, M. Irving, É. Lalande, C. Lévesque, A. W. Lussier, A. Markosyan, I. W. Martin, L. Martinu, B. Maynard, C. S. Menoni, C. Michel, P. G. Murray, C. Osthelder, S. Penn, L. Pinard, K. Prasai, S. Reid, R. Robie, S. Rowan, B. Sassolas, F. Schiettekatte, R. Shink, S. Tait, J. Teillon, G. Vajente, M. Ward, and L. Yang, "Exploration of co-sputtered Ta_2O_5–ZrO_2 thin films for gravitational-wave detectors," *Classical and Quantum Gravity*, vol. 38, no. 19, p. 195021, 2021.

[32] C. Gier, M. Ben Yaala, C. Wiseman, S. MacFoy, M. Chicoine, F. Schiettekatte, J. Hough, S. Rowan, I. Martin, P. MacKay, and S. Reid, "Controlling the optical properties of hafnium dioxide thin films deposited with electron cyclotron resonance ion beam deposition," *Thin Solid Films*, vol. 771, p. 139781, 2023.

[33] S. Kumar and D. K. Aswal, "Recent advances in thin films," 2020.

[34] P. A. Ribeiro and M. Raposo, "Optics, Photonics and Laser Technology", vol. 218, 2018.

[35] H. J. Eichler, J. Eichler, and O. Lux, "Medical Applications and Biophotonics", *Lasers: Basics, Advances and Applications*, pp. 423–458, 2018.

[36] S. Mittler, "Waveguide evanescent field fluorescence and scattering microscopy: The status quo," *Optics, Photonics and Laser Technology*, pp. 1–24, 2018.

[37] S. Seeger, S. Monajembashi, K. J. Hutter, G. Futterman, J. Wolfrum, and K. Greulich, "Application of laser optical tweezers in immunology and molecular genetics," *Cytometry: The Journal of the International Society for Analytical Cytology*, vol. 12, no. 6, pp. 497–504, 1991.

[38] S. Jena, R. Tokas, S. Tripathi, K. Rao, D. Udupa, S. Thakur, and N. Sahoo, "Influence of oxygen partial pressure on microstructure, optical properties, residual stress and laser induced damage threshold of amorphous HfO_2 thin films," *Journal of Alloys and Compounds*, vol. 771, pp. 373–381, 2019.

[39] D. Schiltz, D. Patel, C. Baumgarten, B. A. Reagan, J. J. Rocca, and C. S. Menoni, "Strategies to increase laser damage performance of Ta_2O_5/SiO_2 mirrors by modifications of the top layer design," *Applied Optics*, vol. 56, no. 4, p. C136–C139, 2017.

[40] Z. Balogh-Michels, I. Stevanovic, A. Borzi, A. Bächli, D. Schachtler, T. Gischkat, A. Neels, A. Stuck, and R. Botha, "Crystallization behavior of ion beam sputtered HfO_2 thin films and its effect on the laser-induced damage threshold," *Journal of the European Optical Society-Rapid Publications*, vol. 17, no. 1, 2021.

[41] H. J. Eichler, J. Eichler, and O. Lux, "Further Applications and Future Potential", *Lasers: Basics, Advances and Applications*, pp. 459–504, 2018.

[42] G. Magalhães-Mota, P. Farinha, S. Sério, P. A. Ribeiro, and M. Raposo, "Photochromic materials towards energy harvesting," *Optics, Photonics and Laser Technology*, pp. 223–241, 2018.

[43] Z. Ficek and R. Tanas, "Quantum-Limit Spectroscopy", 2017.

[44] H. J. Eichler, J. Eichler, and O. Lux, "Semiconductor Lasers", *Lasers: Basics, Advances and Applications*, pp. 165–203, 2018.

[45] Chemist Notes. [Online]. Available: https://chemistnotes.com/physical/crystalline-solid-and-amorphous-solid/

[46] A. B. Behboud, “Development of nanostructured metallic glasses with high toughness,” Ph.D. Dissertation, 2021.

[47] D. J. Igram, “A topological explanation of the Urbach tail,” Ph.D. Dissertation, Ohio University, 2016.

[48] S. R. Elliott, “Physics of amorphous materials”, 1990.

[49] A. Amato, “Low thermal noise coating for new generation gravitational-wave detectors,” Ph.D. Dissertation. Thèse de doctorat dirigée par Cagnoli, Gianpietro Canepa, Maurizio et Granata, Massimo Physique des matériaux Lyon, 2019.

[50] S. N. Ogugua, O. M. Ntwaeaborwa, and H. C. Swart, “Latest development on pulsed laser deposited thin films for advanced luminescence applications,” *Coatings*, vol. 10, no. 11, 2020.

[51] P. H. Le and C. W. Luo, “Thermoelectric and Topological Insulator Bismuth Chalcogenide Thin Films Grown Using Pulsed Laser Deposition,” *Applications of Laser Ablation*, ch. 3, 2016.

[52] M. F. Hasaneen, “Effect of oxygen doping on titanium nitride thin films preparedby reactive unbalanced magnetron sputtering,” Ph.D. Dissertation, 2013.

[53] L. A. Owino, “Effect of annealing ambient on the structural, optical and electrical properties of TiO_2:Ge thin films for photovoltaic application.” Ph.D. Dissertation, University of Nairobi, 2021.

[54] J. A. Venables, “Introduction to surface and thin film processes”, 2000.

[55] P. M. Martin, “Handbook of deposition technologies for films and coatings: science, applications and technology”, 2009.

[56] K. Seshan, “Handbook of thin film deposition techniques principles, methods, equipment and applications”, 2002.

[57] P. Martin, “Review ion-based methods for optical thin film deposition,” 1986.

[58] M. Ohring, "Materials science of thin films: deposition and structure", 2001.

[59] B. A. Movchan and A. Demchishin, "Structure and properties of thick condensates of nickel, titanium, tungsten, aluminum oxides, and zirconium dioxide in vacuum." *Fiz. Metal. Metalloved*, 1969.

[60] Z. Qiao, "Fabrication and study of ITO thin films prepared by magnetron sputtering," Ph.D. Dissertation, 2003.

[61] J. A. Thornton, "Influence of apparatus geometry and deposition conditions on the structure and topography of thick sputtered coatings," *Journal of Vacuum Science and Technology*, vol. 11, no. 4, pp. 666–670, 1974.

[62] J. A. Thornton, "High rate thick film growth," *Annual Review of Materials Science*, vol. 7, no. 1, pp. 239–260, 1977.

[63] P. F. Langston, "A study of the influence of process parameter variations on the material properties and laser damage performance of ion beam sputtered Sc_2O_3 and HfO_2 thin films," Ph.D. Dissertation, 2016.

[64] F. Y. Génin, A. Salleo, T. V. Pistor, and L. L. Chase, "Role of light intensification by cracks in optical breakdown on surfaces," *J. Opt. Soc. Am. A*, vol. 18, no. 10, pp. 2607–2616, 2001.

[65] E. Stenzel, S. Gogoll, J. Sils, M. Huisinga, H. Johansen, G. Kästner, M. Reichling, and E. Matthias, "Laser damage of alkaline-earth fluorides at 248 nm and the influence of polishing grades," *Applied Surface Science*, vol. 109-110, pp. 162–167, 1997.

[66] N. Bloembergen, "Role of cracks, pores, and absorbing inclusions on laser induced damage threshold at surfaces of transparent dielectrics," *Appl. Opt.*, vol. 12, no. 4, pp. 661–664, 1973.

[67] F. Rainer, W. H. Lowdermilk, D. Milam, C. K. Carniglia, T. T. Hart, and T. L. Lichtenstein, "Materials for optical coatings in the ultraviolet," *Appl. Opt.*, vol. 24, no. 4, pp. 496–500, 1985.

[68] M. Chorel, "Study of high damage threshold optical coatings used in environment with very low hygrometry for fusion class laser system," Ph.D. Dissertation, 2019.

[69] M. Mero, J. Liu, W. Rudolph, D. Ristau, and K. Starke, "Scaling laws of femtosecond laser pulse induced breakdown in oxide films," *Physical Review B*, vol. 71, no. 11, p. 115109, 2005.

[70] B. Mangote, L. Gallais, M. Commandré, M. Mende, L. Jensen, H. Ehlers, M. Jupé, D. Ristau, A. Melninkaitis, J. Mirauskas, V. Sirutkaitis, S. Kičas, T. Tolenis, and R. Drazdys, "Femtosecond laser damage resistance of oxide and mixture oxide optical coatings," *Opt. Lett.*, vol. 37, no. 9, pp. 1478–1480, 2012.

[71] A. Hervy, L. Gallais, G. Chériaux, and D. Mouricaud, "Femtosecond laser-induced damage threshold of electron beam deposited dielectrics for 1-m class optics," *Optical Engineering*, vol. 56, no. 1, p. 011001, 2016.

[72] G. Abromavičius, S. Kičas, and R. Buzelis, "High temperature annealing effects on spectral, microstructural and laser damage resistance properties of sputtered HfO_2 and HfO_2-SiO_2 mixture-based UV mirrors," *Optical Materials*, vol. 95, p. 109245, 2019.

[73] R. Tateno, H. Okada, T. Otobe, K. Kawase, J. K. Koga, A. Kosuge, K. Nagashima, A. Sugiyama, and K. Kashiwagi, "Negative effect of crystallization on the mechanism of laser damage in a HfO_2/SiO_2 multilayer," *Journal of Applied Physics*, vol. 112, no. 12, p. 123103, 2012.

[74] A. Hervy, L. Gallais, D. Mouricaud, and G. Chériaux, "Electron-beam deposited materials for high-reflective coatings: Femtosecond LIDT," *Optical Interference Coatings*, 2013.

[75] S. Papernov, A. Kozlov, and J. Oliver, "Interface absorption versus film absorption in HfO_2/SiO_2 thin-film pairs in the near-ultraviolet and the relation to pulsed-laser damage," *Proceedings of SPIE - The International Society for Optical Engineering*, vol. 9237, 2014.

[76] S. Papernov, A. Kozlov, J. Oliver, C. Smith, L. Jensen, D. Ristau, S. Günster, and H. Mädebach, "The role of film interfaces in near-ultraviolet absorption and pulsed-laser damage in ion-beam-sputtered coatings based on HfO_2/SiO_2 thin-film pairs," *Proceedings of SPIE - The International Society for Optical Engineering*, vol. 9632, p. 96320B, 2015.

[77] O. Stenzel, S. Wilbrandt, M. Schürmann, N. Kaiser, H. Ehlers, M. Mende, D. Ristau, S. Bruns, M. Vergöhl, M. Stolze, M. Held, H. Niederwald, T. Koch, W. Riggers, P. Burdack, G. Mark, R. Schäfer, S. Mewes, M. Bischoff, M. Arntzen, F. Eisenkrämer, M. Lappschies, S. Jakobs, S. Koch, B. Baumgarten, and A. Tünnermann, "Mixed oxide coatings for optics," *Applied optics*, vol. 50, no. 9, 2011.

[78] M. Jupé, M. Lappschies, L. Jensen, K. Starke, and D. Ristau, "Improvement in laser irradiation resistance of fs-dielectric optics using silica mixtures," *Laser-Induced Damage in Optical Materials*, vol. 6403, 2006.

[79] D. Ristau, "Laser-induced damage in optical materials", 2014.

[80] R. M. Wood, "Laser-induced damage by thermal effects," *Laser-induced damage in optical materials*, pp. 24–39, 2014.

[81] L. Gallais, "Laser damage resistance of optical coatings in the sub-ps regime: limitations and improvement of damage threshold," *Laser Sources and Applications III*, vol. 9893, pp.15–25, 2016.

[82] X. Cheng and Z. Wang, "Defect-related properties of optical coatings," *Advanced Optical Technologies*, vol. 3, no. 1, 2014.

[83] S. Papernov, "Defect-induced damage," *Laser-induced damage in optical materials*, pp. 25–74, 2014.

[84] RP Photonics. [Online]. Available: https://www.rp-photonics.com/laser_induced_damage.html

[85] R. Wood, R. Taylor, and R. Rouse, "Laser damage in optical materials at 1.06 μm," *Optics and Laser Technology* 1975.

[86] X. Jing, J. Shao, J. Zhang, Y. Jin, H. He, and Z. Fan, "Calculation of femtosecond pulse laser induced damage threshold for broadband antireflective microstructure arrays," *Opt. Express*, vol. 17, no. 26, pp. 24137–24152, 2009.

[87] E. G. Gamaly, A. V. Rode, B. Luther-Davies, and V. T. Tikhonchuk, "Ablation of solids by femtosecond lasers: Ablation mechanism and ablation thresholds for metals and dielectrics," *Physics of plasmas*, vol. 9, no. 3, pp. 949–957, 2002.

[88] J. Jasapara, A. Nampoothiri, W. Rudolph, D. Ristau, and K. Starke, "Femtosecond laser pulse induced breakdown in dielectric thin films," *Physical Review B*, vol. 63, no. 4, p. 045117, 2001.

[89] J. H. Apfel, "Optical coating design with reduced electric field intensity," *Applied Optics*, vol. 16, no. 7, pp. 1880–1885, 1977.

[90] A. A. Kozlov, J. C. Lambropoulos, J. B. Oliver, B. N. Hoffman, and S. G. Demos, "Mechanisms of picosecond laser-induced damage in common multilayer dielectric coatings," *Scientific reports*, vol. 9, no. 1, pp. 1–15, 2019.

[91] L. Keldysh, "Ionization in the field of a strong electromagnetic wave," *Sov. Phys. JETP*, vol. 20, no. 5, pp. 1307–1314, 1965.

[92] K. R. Fine, R. Garbe, T. Gip, and Q. Nguyen, "Subsurface damage is measured nondestructively," *Laser Focus World*, vol. 42, no. 6, pp. 131–134, 2006.

[93] N. Bloembergen, "Laser-induced electric breakdown in solids," *IEEE Journal of Quantum Electronics*, vol. 10, no. 3, pp. 375–386, 1974.

[94] D. Wang, Y. Wang, and C. Liao, "Femtosecond laser micromachining on optical fiber," in *Laser Surface Engineering*, pp. 359–381, 2015.

[95] O. O. Abegunde, , E. T. Akinlabi, O. P. Oladijo, S. Akinlabi, and A. U. U. and, "Overview of thin film deposition techniques," *AIMS Materials Science*, vol. 6, no. 2, pp. 174–199, 2019.

[96] L. De Los Santos Valladares, "Study of thin metal films and oxide materials for nanoelectronics applications," PhD Thesis, 2012.

[97] İ. Dönmez, "Atomic layer deposition of metal oxide thin films and nanostructures," Master's Thesis, 2013.

[98] R. Eason, "Pulsed laser deposition of thin films: applications-led growth of functional materials", 2006.

[99] H. K. Pulker, G. Paesold, and E. Ritter, "Refractive indices of TiO_2 films produced by reactive evaporation of various titanium–oxygen phases," *Appl. Opt.*, vol. 15, no. 12, pp. 2986–2991, 1976.

[100] D. Mergel, D. Buschendorf, S. Eggert, R. Grammes, and B. Samset, "Density and refractive index of TiO_2 films prepared by reactive evaporation," *Thin Solid Films*, vol. 371, pp. 218–224, 2000.

[101] R. G. Gitonga, "Characterization of Sn_xSe_y/SnO_2: Co p-n junction deposited by spray pyrolysis for photovoltaic application," Master's Thesis, 2016.

[102] S. Angelova, "Characterisation of ion-beam deposited thin-film coating materials for use in future gravitational wave observatories," Ph.D. Dissertation, 2021.

[103] A. Behera, S. Aich, and T. Theivasanthi, "Chapter 8 - Magnetron sputtering for development of nanostructured materials," *Design, Fabrication, and Characterization of Multifunctional Nanomaterials*, pp. 177–199, 2022.

[104] R. Scrivens, "Classification of ion sources."

[105] R. Geller, "Electron Cyclotron Resonance Ion Sources and ECR Plasmas," 1996.

[106] Polygon Physics. [Online]. Available: https://polygonphysics.com/

[107] R. Lossy and J. Engemann, "RF-broad-beam ion source for reactive sputtering," *Vacuum*, vol. 36, no. 11, pp. 973–976, 1986.

[108] R. Birney, J. Steinlechner, Z. Tornasi, S. MacFoy, D. Vine, A. Bell, D. Gibson, J. Hough, S. Rowan, P. Sortais, S. Sproules, S. Tait, I. Martin, and S. Reid, "Amorphous silicon with extremely low absorption: Beating thermal noise in gravitational astronomy," *Physical Review Letters*, vol. 121, no. 19, p. 191101, 2018.

[109] N. Musila, , M. Munji, J. Simiyu, E. Masika, and R. Nyenge, "Optical properties and analysis of OJL model's electronic inter-band transition parameters of TiO_2 films," *Path of Science*, vol. 4, no. 7, pp. 3001–3012, 2018.

[110] S. K. Al-Ani, "Methods of determining the refractive index of thin solid films (article review)," *Iraqi Journal of Applied Physics*, vol. 4, pp. 17–23, 2008.

[111] M. C. Moraro, "Optical and electrical characterization of $Cd_xSe_{1-x}S$ and Cu_2S thin films for solar cell application," Master's Thesis, 2016.

[112] J. Chebwogen, "Fabrication and characterization of cobalt pigmented anodized zinc for photocatalytic application," Master's Thesis, 2019.

[113] A. Solieman and A. Abu-Sehly, "Modelling of optical properties of amorphous selenium thin films," *Physica B: Condensed Matter*, vol. 405, no. 4, pp. 1101–1107, 2010.

[114] J. A. Dobrowolski, F. C. Ho, and A. Waldorf, "Determination of optical constants of thin film coating materials based on inverse synthesis," *Appl. Opt.*, vol. 22, no. 20, pp. 3191–3200, 1983.

[115] D. Poelman and P. F. Smet, "Methods for the determination of the optical constants of thin films from single transmission measurements: a critical review," *Journal of Physics D: Applied Physics*, vol. 36, no. 15, p. 1850, 2003.

[116] F. A. Jenkins and H. E. White, "Fundamentals of optics," *Indian Journal of Physics*, vol. 25, pp. 265–266, 1957.

[117] B. Tatian, "Fitting refractive-index data with the Sellmeier dispersion formula," *Applied optics*, vol. 23, no. 24, pp. 4477–4485, 1984.

[118] E. Hecht, "Optics 2nd edition," *Optics 2nd edition by Eugene Hecht Reading*, 1987.

[119] R. Swanepoel, "Determination of the thickness and optical constants of amorphous silicon," *Journal of Physics E: Scientific Instruments*, vol. 16, no. 12, p. 1214, 1983.

[120] S. O'Leary, S. Johnson, and P. Lim, "The relationship between the distribution of electronic states and the optical absorption spectrum of an amorphous semiconductor: An empirical analysis," *Journal of Applied Physics*, 1997.

[121] J. Tauc, R. Grigorovi, and A. Vancu, "Optical properties and electronic structure of amorphous germanium," *physica status solidi*, 1966.

[122] T. H. Nguyen, "Channelling investigation of the behaviour of Urania under low-energy ion irradiation," Ph.D. Dissertation, 2013.

[123] N. Mehrban and J. Bowen, "5 - monitoring biomineralization of biomaterials in vivo," *Monitoring and Evaluation of Biomaterials and their Performance In Vivo*, pp. 81–110, 2017.

[124] C. O. Colpan, Y. Nalbant, and M. Ercelik, "4.28 Fundamentals of fuel cell technologies," *Comprehensive Energy Systems*, pp. 1107–1130, 2018.

[125] C. P. Bobby Gaston, "Energy-Dispersive X-ray Spectroscopy (EDS)," 2018.

[126] P. M. V. Raja and A. R. Barron, "1.12 An Introduction to Energy Dispersive X-ray Spectroscopy," 2022. [Online]. Available: https://chem.libretexts.org/Bookshelves/Analytical_Chemistry/Physical_Methods_in_Chemistry_and_Nano_Science_(Barron)/01%3A_Elemental_Analysis/1.12%3A_An_Introduction_to_Energy_Dispersive_X-ray_Spectroscopy

[127] B. Stuart, "Deposition and characterisation of RF magnetron," Ph.D. Dissertation, 2016.

[128] C. J. Chirayil, J. Abraham, R. K. Mishra, S. C. George, and S. Thomas, "Instrumental techniques for the characterization of nanoparticles," *Thermal and Rheological Measurement Techniques for Nanomaterials Characterization*, pp. 1–36, 2017.

[129] P. S. Kumar, K. G. Pavithra, and M. Naushad, "Chapter 4 - characterization techniques for nanomaterials," *Nanomaterials for Solar Cell Applications*, pp. 97–124, 2019.

[130] T. Karasawa and Y. Miyata, "Electrical and optical properties of indium tin oxide thin films deposited on unheated substrates by D.C. reactive sputtering," *Thin Solid Films*, vol. 223, no. 1, pp. 135–139, 1993.

[131] N. Kikuchi, E. Kusano, E. Kishio, A. Kinbara, and H. Nanto, "Effects of excess oxygen introduced during sputter deposition on carrier mobility in as-deposited and postannealed indium-tin-oxide films," *Journal of Vacuum Science and Technology A*, vol. 19, pp. 1636–1641, 2001.

[132] "Lasers and laser-related equipment — test methods for laser-induced damage threshold — part 1: Definitions and general principles," International Organization for Standardization, Standard, 2011.

[133] "Lasers and laser-related equipment — test methods for laser-induced damage threshold — part 2: Threshold determination," International Organization for Standardization, Standard, 2011.

[134] "Lasers and laser-related equipment — test methods for laser-induced damage threshold — part 3: Assurance of laser power (energy) handling capabilities," International Organization for Standardization, Standard, 2011.

[135] "Lasers and laser-related equipment — test methods for laser-induced damage threshold — part 4: Inspection, detection and measurement," International Organization for Standardization, Standard, 2011.

[136] B. Garching, München, and M. Mayer, "SIMNRA user's guide," 1997.

[137] A. Wiatrowski, A. Obstarczyk, M. Mazur, D. Kaczmarek, and D. Wojcieszak, "Characterization of HfO_2 optical coatings deposited by MF magnetron sputtering," *Coatings*, vol. 9, no. 2, p. 106, feb 2019.

[138] L. Sun, J. G. Jones, J. T. Grant, N. R. Murphy, C. V. Ramana, K. G. Eyink, J. P. Vernon, and P. R. Stevenson, "Nanoscale-thick thin films of high-density HfO_2 for bulk-like optical responses," *ACS Applied Nano Materials*, vol. 4, no. 10, pp. 10836–10844, 2021.

[139] D. Franta, I. Ohlídal, D. Nečas, F. Vižd'a, O. Caha, M. Hasoň, and P. Pokorný, "Optical characterization of HfO_2 thin films," *Thin Solid Films*, vol. 519, no. 18, pp. 6085–6091, 2011.

[140] S. Fang, C. Ma, W. Liu, J. He, C. Wang, G. Chen, D. Liu, and R. Zhang, "Effect of oxygen flow on the optical properties of hafnium oxide thin films by dual-ion beam sputtering deposition," *Applied Physics A*, vol. 128, no. 12, 2022.

[141] D. Wernham and A. Piegari, "Optical coatings in the space environment," in *Optical Thin Films and Coatings*, pp. 789–811, 2018.

[142] C. Künneth, R. Materlik, M. Falkowski, and A. Kersch, "Impact of four-valent doping on the crystallographic phase formation for ferroelectric HfO_2 from first-principles: Implications for ferroelectric memory and energy-related applications," *ACS Applied Nano Materials*, vol. 1, no. 1, pp. 254–264, 2018.

[143] M. H. Park, Y. H. Lee, T. Mikolajick, U. Schroeder, and C. S. Hwang, "Review and perspective on ferroelectric HfO_2-based thin films for memory applications," *MRS Commun.*, vol. 8, p. 795, 2018.

[144] H. Joh, M. Jung, J. Hwang, Y. Goh, T. Jung, and S. Jeon, "Flexible ferroelectric hafnia-based synaptic transistor by focused-microwave annealing," *ACS Applied Materials & Interfaces*, vol. 14, no. 1, pp. 1326–1333, 2022.

[145] I. J. Kim and J. S. Lee, "Ferroelectric transistors for memory and neuromorphic device applications," *Advanced Materials*, pp. 2206864, 2022.

[146] Z. Li, T. Wang, Y. Liu, J. Yu, J. Meng, P. Liu, K. Xu, H. Zhu, Q. Sun, D. W. Zhang, and L. Chen, "Understanding the effect of oxygen content on ferroelectric properties of Al-doped HfO_2 thin films," *IEEE Electron Device Letters*, vol. 44, no. 1, pp. 56–59, 2023.

[147] Y. Li, Y. Qi, H. Zhang, Z. Xia, T. Xie, W. Li, D. Zhong, H. Zhu, and M. Zhou, "Gram-scale synthesis of highly biocompatible and intravenous injectable hafnium

oxide nanocrystal with enhanced radiotherapy efficacy for cancer theranostic," *Biomaterials*, vol. 226, p. 119538, 2020.

[148] M. Al-Kuhaili, "Optical properties of hafnium oxide thin films and their application in energy-efficient windows," *Optical Materials*, vol. 27, no. 3, pp. 383–387, 2004.

[149] M. F. Al-Kuhaili, S. M. A. Durrani, and E. E. Khawaja, "Characterization of hafnium oxide thin films prepared by electron beam evaporation," *Journal of Physics D: Applied Physics*, vol. 37, no. 8, pp. 1254–1261, 2004.

[150] S. B. Khan, Z. Zhang, and S. L. Lee, "Annealing influence on optical performance of HfO_2 thin films," *Journal of Alloys and Compounds*, vol. 816, p. 152552, 2020.

[151] E. Bersch, S. Rangan, R. A. Bartynski, E. Garfunkel, and E. Vescovo, "Band offsets of ultrathin high-κ oxide films with Si," *Phys. Rev. B*, vol. 78, p. 085114, 2008.

[152] L. Gallais, J. Capoulade, J.-Y. Natoli, M. Commandré, M. Cathelinaud, C. Koc, and M. Lequime, "Laser damage resistance of hafnia thin films deposited by electron beam deposition, reactive low voltage ion plating, and dual ion beam sputtering," *Applied Optics*, 2007.

[153] L. Gallais, J. Capoulade, J.-Y. Natoli, M. Commandré, M. Cathelinaud, C. Koc, and M. Lequime, "Laser damage of Silica and Hafnia thin films made with different deposition technologies," *Laser-Induced Damage in Optical Materials*, vol. 6720, 2007.

[154] L. Gallais, B. Mangote, M. Zerrad, M. Commandré, A. Melninkaitis, J. Mirauskas, M. Jeskevic, and V. Sirutkaitis, "Laser-induced damage of hafnia coatings as a function of pulse duration in the femtosecond to nanosecond range," *Applied Optics*, 2010.

[155] A. Ciapponi, F. R. Wagner, S. Palmier, J.-Y. Natoli, and L. Gallais, "Study of luminescent defects in hafnia thin films made with different deposition techniques," *Journal of Luminescence*, vol. 129, no. 12, pp. 1786–1789, 2009.

[156] L. Pereira, P. Barquinha, E. Fortunato, and R. Martins, "Influence of the oxygen/argon ratio on the properties of sputtered hafnium oxide," *Materials Science and Engineering: B*, vol. 118, no. 1-3, pp. 210–213, 2005.

[157] F. L. Martínez, M. Toledano-Luque, J. J. Gandía, J. Cárabe, W. Bohne, J. Röhrich, E. Strub, and I. Mártil, "Optical properties and structure of HfO_2 thin films grown by high pressure reactive sputtering," *Journal of Physics D: Applied Physics*, vol. 40, no. 17, pp. 5256–5265, 2007.

[158] C. Harthcock, S. R. Qiu, R. A. Negres, J. A. Hammons, T. Voisin, G. Guss, A. A. Martin, C. J. Stolz, M. G. Menor, G. Bhowmik, and M. Huang, "The impact of nano-bubbles on the laser performance of hafnia films deposited by oxygen assisted ion beam sputtering method," *Applied Physics Letters*, vol. 115, no. 25, p. 251902, 2019.

[159] T. Bright, J. Watjen, Z. Zhang, C. Muratore, and A. Voevodin, "Optical properties of HfO_2 thin films deposited by magnetron sputtering: From the visible to the far-infrared," *Thin Solid Films*, vol. 520, no. 22, pp. 6793–6802, 2012.

[160] J. Aarik, H. Mändar, M. Kirm, and L. Pung, "Optical characterization of HfO_2 thin films grown by atomic layer deposition," *Thin Solid Films*, vol. 466, no. 1, pp. 41–47, 2004.

[161] J. Gao, G. He, B. Deng, D. Xiao, M. Liu, P. Jin, C. Zheng, and Z. Sun, "Microstructure, wettability, optical and electrical properties of HfO_2 thin films: Effect of oxygen partial pressure," *Journal of Alloys and Compounds*, vol. 662, pp. 339–347, 2016.

[162] V. N. Peters, S. R. Qiu, C. Harthcock, R. A. Negres, G. Guss, T. Voisin, E. Feigenbaum, C. J. Stolz, D. Vipin, and M. Huang, "Investigation of UV, ns-laser damage

resistance of hafnia films produced by electron beam evaporation and ion beam sputtering deposition methods," *Journal of Applied Physics*, vol. 130, no. 4, p. 043103, 2021.

[163] A. Solieman, "Extracting the optical parameters of thermally evaporated Se film by modelling of transmittance spectra: Effect of heat treatment," *Journal of Taibah University for Science*, vol. 14, no. 1, pp. 470–478, 2020.

[164] A. M. Efimov, V. G. Pogareva, and A. V. Shashkin, "Water-related bands in the IR absorption spectra of silicate glasses," *Journal of Non-Crystalline Solids*, vol. 332, no. 1, pp. 93–114, 2003.

[165] M. Carroll and E. Stolper, "Argon solubility and diffusion in silica glass: Implications for the solution behavior of molecular gases," *Geochimica et Cosmochimica Acta*, vol. 55, no. 1, pp. 211–225, 1991.

[166] R. Feder, C. Bundesmann, H. Neumann, and B. Rauschenbach, "Ion beam sputtering of Ag – angular and energetic distributions of sputtered and scattered particles," *Nuclear Instruments and Methods in Physics Research Section B: Beam Interactions with Materials and Atoms*, vol. 316, pp. 198–204, 2013.

[167] A. S. Foster, F. Lopez Gejo, A. L. Shluger, and R. M. Nieminen, "Vacancy and interstitial defects in hafnia," *Phys. Rev. B*, vol. 65, p. 174117, 2002.

[168] J. Zhang, A. R. Oganov, X. Li, K.-H. Xue, Z. Wang, and H. Dong, "Pressure-induced novel compounds in the Hf-O system from first-principles calculations," *Phys. Rev. B*, vol. 92, p. 184104, 2015.

[169] M. Jerman, Z. Qiao, and D. Mergel, "Refractive index of thin films of SiO_2, ZrO_2, and HfO_2 as a function of the films' mass density," *Applied Optics*, vol. 44, no. 15, pp. 3006–3012, 2005.

[170] D. L. Wood, K. Nassau, T. Y. Kometani, and D. L. Nash, "Optical properties of cubic hafnia stabilized with yttria," *Applied Optics*, vol. 29, no. 4, pp. 604–607, 1990.

[171] S. Jena, R. B. Tokas, K. D. Rao, S. Thakur, and N. K. Sahoo, “Annealing effects on microstructure and laser-induced damage threshold of HfO_2/SiO_2 multilayer mirrors,” *Applied Optics*, vol. 55, no. 22, pp. 6108–6114, 2016.

[172] W. Liu, Z. Liu, F. Yan, T. Tan, and H. Tian, “Influence of O_2/Ar flow ratio on the structure and optical properties of sputtered hafnium dioxide thin films,” *Surface and Coatings Technology*, vol. 205, no. 7, pp. 2120–2125, 2010.

[173] N. Matsunami, Y. Yamamura, Y. Itikawa, N. Itoh, Y. Kazumata, S. Miyagawa, K. Morita, R. Shimizu, and H. Tawara, “Energy dependence of the ion-induced sputtering yields of monatomic solids,” *Atomic Data and Nuclear Data Tables*, vol. 31, no. 1, pp. 1–80, 1984.

[174] P. Eiamchai, P. Chindaudom, A. Pokaipisit, and P. Limsuwan, “A spectroscopic ellipsometry study of TiO_2 thin films prepared by ion-assisted electron-beam evaporation,” *Current Applied Physics*, vol. 9, pp. 707–712, 2009.

[175] S. Mahjabin, M. M. Haque, S. Khan, V. Selvanathan, M. Jamal, M. Bashar, H. I. Alkhammash, M. I. Hossain, M. Shahiduzzaman, N. Amin *et al.*, “Effects of oxygen concentration variation on the structural and optical properties of reactive sputtered WO_x thin film,” *Solar Energy*, vol. 222, pp. 202–211, 2021.

[176] C. Wiemer, S. Ferrari, M. Fanciulli, G. Pavia, and L. Lutterotti, “Combining grazing incidence X-ray diffraction and X-ray reflectivity for the evaluation of the structural evolution of HfO_2 thin films with annealing,” *Thin Solid Films*, vol. 450, no. 1, pp. 134–137, 2004.

[177] J. Ni, Z. Cao Li, and Z. Jun Zhang, “Influence of deposition temperature on the structure and optical properties of Hfo_2 thin films,” *Frontiers of Materials Science in China*, vol. 2, no. 4, pp. 381–385, 2008.

[178] S. Pandey, P. Kothari, S. K. Sharma, S. Verma, and K. J. Rangra, “Impact of post deposition annealing in O_2 ambient on structural properties of nanocrystalline hafnium oxide thin film,” *Journal of Materials Science: Materials in Electronics*, vol. 27, no. 7, pp. 7055–7061, 2016.

[179] M. Ramzan, M. Wasiq, A. Rana, S. Ali, and M. Nadeem, "Characterization of e-beam evaporated hafnium oxide thin films on post thermal annealing," *Applied Surface Science*, vol. 283, pp. 617–622, 2013.

[180] H. Liu, Y. Jiang, L. Wang, S. Li, X. Yang, C. Jiang, D. Liu, Y. Ji, F. Zhang, and D. Chen, "Effect of heat treatment on properties of HfO_2 film deposited by ion-beam sputtering," *Optical Materials*, vol. 73, pp. 95–101, 2017.

[181] A. Javed, M. Wasiq, A. Rana, M. Nadeem, N. Niaz, M. Mazhar, M. Usmani, R. Ciancio, and P. Orgiani, "Influence of post deposition thermal annealing on the optical characteristics of hafnia nanofilms," *Journal of Ovonic Research*, 2018.

[182] M. Modreanu, J. Sancho-Parramon, O. Durand, B. Servet, M. Stchakovsky, C. Eypert, C. Naudin, A. Knowles, F. Bridou, and M.-F. Ravet, "Investigation of thermal annealing effects on microstructural and optical properties of HfO_2 thin films," *Applied Surface Science*, vol. 253, no. 1, pp. 328–334, 2006.

[183] J. Robertson, "Band structures and band offsets of high-κ dielectrics on Si," *Applied Surface Science*, vol. 190, no. 1-4, pp. 2–10, 2002.

[184] M. Balog, M. Schieber, M. Michman, and S. Patai, "Chemical vapor deposition and characterization of HfO_2 films from organo-hafnium compounds," *Thin Solid Films*, vol. 41, no. 3, pp. 247–259, 1977.

[185] J. Liu, X. Ling, and X. Liu, "Mechanism of annealing effect on damage threshold enhancement of HfO_2 films in vacuum," *Vacuum*, vol. 189, pp. 110266, 2021.

[186] E. Krous, "Characterization of scandium oxide thin films for use in interference coatings for high-power lasers operating in the near-infrared," Ph.D. Dissertation, 2010.

[187] A. Belosludtsev, K. Juškevičius, L. Ceizaris, R. Samuilovas, S. Stanionytė, V. Jasulaitienė, and S. Kičas, "Correlation between stoichiometry and properties of scandium oxide films prepared by reactive magnetron sputtering," *Applied Surface Science*, vol. 427, pp. 312–318, 2018.

[188] P. F. Langston, E. Krous, D. Schiltz, D. Patel, L. Emmert, A. Markosyan, B. Reagan, K. Wernsing, Y. Xu, Z. Sun, R. Route, M. M. Fejer, J. J. Rocca, W. Rudolph, and C. S. Menoni, “Point defects in Sc_2O_3 thin films by ion beam sputtering,” *Applied Optics*, vol. 53, no. 4, pp. A276, 2014.

[189] L. Martinu and D. Poitras, “Plasma deposition of optical films and coatings: A review,” *Journal of Vacuum Science & Technology A: Vacuum, Surfaces, and Films*, 2000.

[190] E. Alfonso, J. Olaya, and G. Cubillos, “Thin film growth through sputtering technique and its applications,” in *Crystallization*, 2012.

[191] S. Kičas, U. Gimževskis, and S. Melnikas, “Post deposition annealing of IBS mixture coatings for compensation of film induced stress,” *Optical Materials Express*, vol. 6, no. 7, pp. 2236, 2016.

[192] Q. Lv, M. Huang, S. Zhang, S. Deng, F. Gong, F. Wang, Y. Pan, G. Li, and Y. Jin, “Effects of annealing on residual stress in Ta_2O_5 films deposited by dual ion beam sputtering,” *Coatings*, vol. 8, no. 4, pp. 150, 2018.

[193] H. Liu, S. Chen, P. Ma, Y. Pu, Z. Qiao, Z. Zhang, Y. Wei, and Z. Liu, “Ion beam sputtering mixture films with tailored refractive indices,” *Optics and Laser Technology*, vol. 55, pp. 21–25, 2014.

[194] M. Bischoff, T. Nowitzki, O. Voß, S. Wilbrandt, and O. Stenzel, “Postdeposition treatment of IBS coatings for UV applications with optimized thin-film stress properties,” *Applied Optics*, vol. 53, no. 4, pp. A212–A220, 2014.

[195] M. Falmbigl, “Effect of annealing on properties and performance of HfO_2SiO_2 optical coatings for UV-applications,” *Optics Express*, vol. 30, no. 8, 2022.

[196] P. Kong, Y. Pu, P. Ma, and J. Zhu, “Relationship between oxygen defects and properties of scandium oxide films prepared by ion-beam sputtering,” *Coatings*, vol. 9, no. 8, pp. 517, 2019.

[197] S. Dixon, A. Jiamprasertboon, C. Carmalt, and I. Parkin, "Luminescence behaviour and deposition of Sc_2O_3 thin films from Scandium(III) acetylacetonate at ambient pressure," *Applied Physics Letters*, 2018.

[198] M. Al-Kuhaili, "Optical properties of scandium oxide films prepared by electron beam evaporation," *Thin Solid Films*, vol. 426, no. 1-2, pp. 178–185, 2003.

[199] G. Liu, Y. Jin, H. He, and Z. Fan, "Effect of substrate temperatures on the optical properties of evaporated Sc_2O_3 thin films," *Thin Solid Films*, vol. 518, no. 10, pp. 2920–2923, 2010.

[200] P. de Rouffignac, A. P. Yousef, K. H. Kim, and R. G. Gordon, "ALD of Scandium Oxide from Scandium Tris(*N*,*N'*-diisopropylacetamidinate) and Water," *Electrochemical and Solid-State Letters*, vol. 9, no. 6, 2006.

[201] C. Adelmann, P. Lehnen, V. S., C. Zhao, B. Brijs, A. Franquet, T. Conard, M. Roeckerath, J. Schubert, O. Boissière, C. Lohe, and D. S., "Growth of dysprosium-, scandium-, and hafnium-based third generation high-κ dielectrics by atomic vapor deposition," *Chemical Vapor Deposition*, vol. 13, no. 10, pp. 567–573, 2007.

[202] D. Grosso and P. Sermon, "Scandia optical coatings for application at 351 nm," *Thin Solid Films*, 2000.

[203] D. O. Klenov, L. F. Edge, D. G. Schlom, and S. Stemmer, "Extended defects in epitaxial Sc_2O_3 films grown on (111) Si," *Applied Physics Letters*, vol. 86, no. 5, 2005.

[204] Z. Xu, A. Daga, and H. Chen, "Microstructure and optical properties of scandium oxide thin films prepared by metalorganic chemical-vapor deposition," *Applied Physics Letters*, vol. 79, no. 23, pp. 3782–3784, 2001.

[205] C. Liu, E. F. Chor, L. S. Tan, and A. Du, "Epitaxial growth of Sc_2O_3 films on GaN (0001) by pulsed laser deposition," *Journal of Vacuum Science & Technology*

B: Microelectronics and Nanometer Structures Processing, Measurement, and Phenomena, vol. 25, no. 3, pp. 754–759, 2007.

[206] D. C. Hays, B. P. Gila, S. J. Pearton, B.-J. Kim, F. Ren, and T. S. Jang, "Band offsets in Sc_2O_3/ZnO heterostructures deposited by RF magnetron sputtering," *Journal of Vacuum Science & Technology B*, vol. 33, no. 5, 2015.

[207] E. Krous, D. Patel, P. Langston, C. Menoni, A. Markosyan, R. Route, M. Fejer, D. Nguyen, L. Emmert, and W. Rudolph, "Scandium oxide thin films deposited by dual ion beam sputtering for high-power laser applications," *Optical Interference Coatings*, 2010.

[208] C. S. Menoni, E. M. Krous, D. Patel, P. Langston, J. Tollerud, D. N. Nguyen, L. A. Emmert, A. Markosyan, R. Route, M. Fejer, and W. Rudolph, "Advances in ion beam sputtered Sc_2O_3 for optical interference coatings," *Laser-Induced Damage in Optical Materials*, vol. 7842, 2010.

[209] I. Ladany, P. Zanzucchi, J. Andrews, J. Kane, and E. DePiano, "Scandium oxide antireflection coatings for superluminescent LEDs," *Applied Optics*, vol. 25, no. 4, pp. 472–473, 1986.

[210] J. Hollenbeck and R. Buchanan, "Oxide thin films for nanometer scale electron beam lithography," *Journal of Materials Research*, vol. 5, no. 5, pp. 1058–1072, 1990.

[211] F. Rainer, W. Lowdermilk, D. Milam, T. Hart, T. Lichtenstein, and C. Carniglia, "Scandium oxide coatings for high-power UV laser applications," *Applied Optics*, 1982.

[212] A. Liu, G. Liu, H. Zhu, H. Song, B. Shin, E. Fortunato, R. Martins, and F. Shan, "Water-induced scandium oxide dielectric for low-operating voltage n- and p-type metal-oxide thin-film transistors," *Advanced Functional Materials*, vol. 25, no. 46, pp. 7180–7188, 2015.

[213] R. Mehandru, B. Luo, J. Kim, F. Ren, B. Gila, A. Onstine, C. Abernathy, S. Pearton, D. Gotthold, R. Birkhahn *et al.*, "AlGaN/GaN metal–oxide–semiconductor high electron mobility transistors using Sc_2O_3 as the gate oxide and surface passivation," *Applied Physics Letters*, vol. 82, no. 15, pp. 2530–2532, 2003.

[214] B. Luo, J. Kim, F. Ren, J. Gillespie, R. Fitch, J. Sewell, R. Dettmer, G. Via, A. Crespo, T. Jenkins *et al.*, "Electrical characteristics of proton-irradiated Sc_2O_3 passivated AlGaN/GaN high electron mobility transistors," *Applied Physics Letters*, vol. 82, no. 9, pp. 1428–1430, 2003.

[215] L. Yakovkina, T. Smirnova, V. Borisov, V. Kichai, and V. Kaichev, "Synthesis and properties of dielectric $(HfO_2)_{(1-x)}(Sc_2O_3)_x$ films," *Inorganic Materials*, vol. 49, pp. 172–178, 2013.

[216] M. Fazio, L. Yang, A. Markosyan, R. Bassiri, M. M. Fejer, and C. S. Menoni, "Growth and characterization of Sc_2O_3 doped Ta_2O_5 thin films," *Applied Optics*, vol. 59, no. 5, 2019.

[217] G. Yu, B. Tay, and Z. Zhao, "Structure and properties of zirconium oxide thin films prepared by filtered cathodic vacuum arc," *Applied Physics A: Materials Science and Processing*, vol. 81, no. 2, pp. 405 – 411, 2005.

[218] A. Kao and G. Gorman, "Modification of zirconia film properties by low-energy ion bombardment during reactive ion-beam deposition," *Journal of Applied Physics*, vol. 67, no. 8, p. 3826 – 3834, 1990.

[219] A. Belosludtsev, J. Vlček, J. Houška, and R. Čerstvý, "Reactive high-power impulse magnetron sputtering of ZrO_2 films with gradient ZrO_x interlayers on pretreated steel substrates," *Journal of Vacuum Science & Technology A*, vol. 35, no. 3, 2017.

[220] G. Zhu, Z. Cheng, T. Lv, L. Pan, Q. Zhao, and Z. Sun, "Zn-doped nanocrystalline TiO_2 films for CdS quantum dot sensitized solar cells," *Nanoscale*, vol. 2, pp. 1229–1232, 2010.

[221] T. Siciliano, M. Di Giulio, M. Tepore, E. Filippo, G. Micocci, and A. Tepore, "Effect of thermal annealing time on optical and structural properties of TeO_2 thin films," *Vacuum*, vol. 84, no. 7, pp. 935–939, 2010.

[222] R. P. Netterfield, M. Gross, F. N. Baynes, K. L. Green, G. M. Harry, H. Armandula, S. Rowan, J. Hough, D. R. Crooks, M. M. Fejer *et al.*, "Low mechanical loss coatings for LIGO optics: progress report," in *Advances in Thin-Film Coatings for Optical Applications II*, 2005.

[223] M. Hafiz, M. Abdel-Rahim, and A. Abu-Sehly, "Optical absorption and electrical conductivity of amorphous AsTeGe thin films," *Physica B: Condensed Matter*, vol. 252, no. 3, pp. 207–215, 1998.

[224] S. Hasegawa, S. Yazaki, and T. Shimizu, "Effects of annealing on gap states in amorphous Si films," *Solid State Communications*, vol. 26, no. 7, pp. 407–410, 1978.

[225] A. Maan, D. Goyal, S. K. Sharma, and T. Sharma, "Optical absorption properties of amorphous $Ga_{40}Se_xTe_{60-x}$ alloys," *Journal of non-crystalline solids*, vol. 183, no. 1-2, pp. 186–190, 1995.

[226] S. Jena, R. B. Tokas, N. M. Kamble, S. Thakur, and N. K. Sahoo, "Optical properties and laser damage threshold of HfO_2-SiO_2 mixed composite thin films," *Applied Optics*, vol. 53, no. 5, p. 850, 2014.

[227] D. Nguyen, L. Emmert, I. Cravetchi, M. Mero, W. Rudolph, M. Jupe, M. Lappschies, K. Starke, and D. Ristau, "$Ti_xSi_{1-x}O_2$ optical coatings with tunable index and their response to intense subpicosecond laser pulse irradiation," *Applied Physics Letters*, vol. 93, no. 26, pp. 261903, 2008.

[228] D. Rademacher, G. Bräuer, B. Fritz, and M. Vergöhl, "Optical properties of silicon titanium oxide mixtures prepared by metallic mode reactive sputtering," *Applied Optics*, vol. 51, no. 33, pp. 8047–8051, 2012.

[229] S. Kičas, G. Batavičiūtė, K. Juškevičius, T. Tolenis, R. Drazdys, R. Buzelis, and A. Melninkaitis, “Characterization and application of HfO_2-SiO_2 mixtures produced by ion-beam sputtering technology,” *Laser-Induced Damage in Optical Materials*, 2013.

[230] X. Fu, M. Commandré, L. Gallais, M. Mende, H. Ehlers, and D. Ristau, “Laser-induced damage in composites of scandium, hafnium, aluminum oxides with silicon oxide in the infrared,” *Applied Optics*, vol. 53, no. 4, 2014.

[231] L. O. Jensen and D. Ristau, “Coatings of oxide composites,” *Laser-Induced Damage in Optical Materials*, 2012.

[232] M. Lappschies, B. Görtz, and D. Ristau, “Optical monitoring of rugate filters,” in *Advances in Optical Thin Films II*, vol. 5963, pp. 547–555, 2005.

[233] C. C. Lee, C. J. Tang, and J. Y. Wu, “Rugate filter made with composite thin films by ion-beam sputtering,” *Applied Optics*, vol. 45, no. 7, pp. 1333–1337, 2006.

[234] H. Bartzsch, S. Lange, P. Frach, and K. Goedicke, “Silicon oxynitride rugate filters grown by reactive pulse magnetron sputtering,” *Advances in Optical Thin Films*, vol. 5250, pp. 502–510, 2004.

[235] Z. Gou and F. Placido, “Aluminum oxynitride rugate filters grown by reactive RF sputtering,” *Fourth International Conference on Thin Film Physics and Applications*, vol. 4086, pp. 791–794, 2000.

[236] P. Baumeister, “Simulation of a rugate filter via a stepped-index dielectric multilayer,” *Applied Optics*, vol. 25, no. 16, pp. 2644–2645, 1986.

[237] V. Pervak, A. Tikhonravov, M. Trubetskov, J. Pistner, F. Krausz, and A. Apolonski, “Band filters: two-material technology versus rugate,” *Applied optics*, vol. 46, no. 8, pp. 1190–1193, 2007.

[238] H. Xing, M. Zhu, Y. Chai, F. Tu, H. Wang, K. Yi, and J. Shao, “Study of hafina-silica mixed coatings with different compositions prepared by e-beam co-

evaporation," *Pacific Rim Laser Damage 2015: Optical Materials for High-Power Lasers*, 2015.

[239] L. O. Jensen, M. Mende, H. Blaschke, D. Ristau, D. Nguyen, L. Emmert, and W. Rudolph, "Investigations on SiO_2-HfO_2 mixtures for nanosecond and femtosecond pulses," *Laser-Induced Damage in Optical Materials*, 2010.

[240] M. R. Visokay, J. J. Chambers, A. L. P. Rotondaro, A. Shanware, and L. Colombo, "Application of HfSiON as a gate dielectric material," *Applied Physics Letters*, vol. 80, no. 17, pp. 3183–3185, 2002.

[241] M. Mende, L. O. Jensen, H. Ehlers, W. Riggers, H. Blaschke, and D. Ristau, "Laser-induced damage of pure and mixture material high reflectors for 355 nm and 1064 nm wavelength," in *Advances in Optical Thin Films IV*, vol. 8168, pp. 491–501, 2011.

[242] M. Mende, L. O. Jensen, H. Ehlers, S. Bruns, M. Vergöhl, P. Burdack, and D. Ristau, "Applying hafnia mixtures to enhance the laser-induced damage threshold of coatings for third-harmonic generation optics," *Laser-Induced Damage in Optical Materials*, 2012.

[243] Q. Zhou, P. Ma, F. Qiu, Y. Pu, Z. Qiao, L. Lv, M. Zhang, P. Kong, R. Qiu, and Y. Jiang, "Role of nano-precursors in ultraviolet-laser damage of HfO_2/SiO_2 mixture coatings," *Thin Solid Films*, vol. 739, pp. 138963, 2021.

[244] O. Stenzel, "The physics of thin film optical spectra", 2015.

[245] L. P. Feng, Z. T. Liu, and Y. M. Shen, "Compositional, structural and electronic characteristics of HfO_2 and HfSiO dielectrics prepared by radio frequency magnetron sputtering," *Vacuum*, vol. 83, no. 5, pp. 902–905, 2009.

[246] J. D. Mackenzie, "High-pressure effects on oxide glasses: III, densification in Non-rigid State," *Journal of the American Ceramic Society*, vol. 47, no. 2, pp. 76–80, 1964.

[247] P. Kong, Y. Pu, P. Ma, and J. Zhu, "The characterization and properties of mixed Sc_2O_3:SiO_2 films," *Thin Solid Films*, vol. 714, pp. 138357, 2020.

[248] L. Gallais, B. Mangote, M. Commandré, M. Mende, L. Jensen, H. Ehlers, M. Jupé, D. Ristau, A. Melninkaitis, V. Sirutkaitis *et al.*, "An exhaustive study of laser damage in ion beam sputtered pure and mixture oxide thin films at 1030 nm with 500 fs pulse durations," in *Laser-Induced Damage in Optical Materials*, vol. 8530, pp. 117–124, 2012.

[249] A. Belosludtsev, Y. Yakimov, R. Mroczyński, S. Stanionytė, M. Skapas, D. Buinovskis, and N. Kyžas, "Effect of annealing on optical, mechanical, electrical properties and structure of scandium oxide films," *physica status solidi (a)*, vol. 216, no. 18, 2019.

List of Publications and Conferences

1. Abernathy, M., et al. "Exploration of co-sputtered Ta_2O_5–ZrO_2 thin films for gravitational-wave detectors." Classical and Quantum Gravity 38.19 (2021): 195021. `https://doi.org/10.1088/1361-6382/ac1b06`

2. **Gier, C.**, Reid S., Ben Yaala, M., Angelova, S., Birney, I., Hill, P., Hough, J., Martin, I., Murray, P., Rowan, S., Tait, S., Wallace, G., and Wiseman, C. "Developing Optical Coatings for Gravitational Wave Detectors and Laser Optics using Next Generation Ion Beam Deposition Technique", Society of Vacuum Coaters (SVC) TechCon, 2021.

3. **Gier, C.** "Developing Optical Coatings for Gravitational Wave Detectors and Laser Optics using Next Generation Ion Beam Deposition Technique". Gravitational-wave Excellence through Alliance Training (GrEAT) Webinar, 2021.

4. **Gier, C.**, Reid S., Ben Yaala, M., Angelova, S., Birney, I., Hill, P., Hough, J., Martin, I., Murray, P., Rowan, S., Tait, S., Wallace, G., and Wiseman, C. "Developing Optical Coatings for Gravitational Wave Detectors and Laser Optics using Next Generation Ion Beam Deposition Technique", Society of Vacuum Coaters (SVC) Fall Bulletin, 2022.

5. **Gier, C.**, Ben Yaala, M., Wiseman, C., MacFoy, S., Chicoine, M., Schiettekatte, F., Hough, J., Rowan, S., Martin, I., MacKay, P. and Reid, S. "Controlling the optical properties of hafnium dioxide thin films deposited with electron cyclotron resonance ion beam deposition." Thin Solid Films 771 (2023): 139781.

https://doi.org/10.1016/j.tsf.2023.139781

6. **Gier, C.** "Fabrication of Extreme-Performance Optical Coatings by ECR Ion Beam Sputter Deposition". Optical Coatings for Laser Applications (OCLA) Symposium, 2023.

IOP Publishing

Classical and Quantum Gravity

Class. Quantum Grav. 38 (2021) 195021 (39pp) https://doi.org/10.1088/1361-6382/ac1b06

Exploration of co-sputtered Ta_2O_5–ZrO_2 thin films for gravitational-wave detectors

M Abernathy[1,2], A Amato[3], A Ananyeva[4], S Angelova[5], B Baloukas[6], R Bassiri[7], G Billingsley[4], R Birney[5,8], G Cagnoli[3], M Canepa[9,10], M Coulon[11], J Degallaix[11], A Di Michele[12], M A Fazio[13], M M Fejer[7], D Forest[11], C Gier[5], M Granata[11,*], A M Gretarsson[14], E M Gretarsson[15], E Gustafson[4], E J Hough[16], M Irving[17], É Lalande[18], C Lévesque[18], A W Lussier[18], A Markosyan[7], I W Martin[16], L Martinu[6], B Maynard[17], C S Menoni[13,19], C Michel[11], P G Murray[16], C Osthelder[4], S Penn[17], L Pinard[11], K Prasai[7], S Reid[5], R Robie[16], S Rowan[16], B Sassolas[11], F Schiettekatte[18], R Shink[18], S Tait[16], J Teillon[11], G Vajente[4,*], M Ward[18] and L Yang[19]

[1] Department of Physics, American University, Washington, DC, United States of America

[2] Johns Hopkins University Applied Physics Laboratory, Laurel, MD, United States of America

[3] Université de Lyon, Université Claude Bernard Lyon 1, CNRS, Institut Lumière Matière, F-69622 Villeurbanne, France

[4] LIGO Laboratory, California Institute of Technology, Pasadena, CA, United States of America

[5] SUPA, Department of Biomedical Engineering, University of Strathclyde, Glasgow, United Kingdom

[6] École Polytechnique de Montréal, Montréal, Québec, Canada

[7] Edward L Ginzton Laboratory, Stanford University, Stanford, CA 94305, United States of America

[8] SUPA, Institute of Thin Films, Sensors and Imaging, University of the West of Scotland, Paisley, United Kingdom

[9] OPTMATLAB, Dipartimento di Fisica, Università di Genova, Via Dodecaneso 33, 16146 Genova, Italy

[10] INFN, Sezione di Genova, Via Dodecaneso 33, 16146 Genova, Italy

[11] Laboratoire des Matériaux Avancés, Institut de Physique des 2 Infinis de Lyon, CNRS/IN2P3, Université de Lyon, Université Claude Bernard Lyon 1, F-69622 Villeurbanne, France

[12] Dipartimento di Fisica e Geologia, Università degli Studi di Perugia, Via Pascoli, 06123 Perugia, Italy

* Authors to whom any correspondence should be addressed.

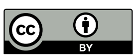

Original content from this work may be used under the terms of the Creative Commons Attribution 4.0 licence. Any further distribution of this work must maintain attribution to the author(s) and the title of the work, journal citation and DOI.

[13] Department of Electrical and Computer Engineering, Colorado State University, Fort Collins, CO, United States of America
[14] Embry-Riddle Aeronautical University, 3700 Willow Creek Rd., Prescott, AZ 86301, United States of America
[15] Wyant College of Optical Sciences, University of Arizona, 1630 E University Blvd., Tucson, AZ 85721, United States of America
[16] SUPA, Institute for Gravitational Research, University of Glasgow, Glasgow, United Kingdom
[17] Department of Physics, Hobart and William Smith Colleges, Geneva, NY, United States of America
[18] Département de physique, Université de Montréal, Montréal, Québec, Canada
[19] Department of Chemistry, Colorado State University, Fort Collins, CO, United States of America

E-mail: m.granata@lma.in2p3.fr and vajente@caltech.edu

Received 29 March 2021, revised 29 June 2021
Accepted for publication 5 August 2021
Published 13 September 2021

Abstract

We report on the development and extensive characterization of co-sputtered tantala–zirconia (Ta_2O_5-ZrO_2) thin films, with the goal to decrease coating Brownian noise in present and future gravitational-wave detectors. We tested a variety of sputtering processes of different energies and deposition rates, and we considered the effect of different values of cation ratio $\eta = \mathrm{Zr}/(\mathrm{Zr} + \mathrm{Ta})$ and of post-deposition heat treatment temperature T_a on the optical and mechanical properties of the films. Co-sputtered zirconia proved to be an efficient way to frustrate crystallization in tantala thin films, allowing for a substantial increase of the maximum annealing temperature and hence for a decrease of coating mechanical loss φ_c. The lowest average coating loss was observed for an ion-beam sputtered sample with $\eta = 0.485 \pm 0.004$ annealed at 800 °C, yielding $\overline{\varphi}_\mathrm{c} = 1.8 \times 10^{-4}$ rad. All coating samples showed cracks after annealing. Although in principle our measurements are sensitive to such defects, we found no evidence that our results were affected. The issue could be solved, at least for ion-beam sputtered coatings, by decreasing heating and cooling rates down to 7 °C h^{-1}. While we observed as little optical absorption as in the coatings of current gravitational-wave interferometers (0.5 parts per million), further development will be needed to decrease light scattering and avoid the formation of defects upon annealing.

Keywords: thin films, thermal noise, gravitational-wave detectors

(Some figures may appear in colour only in the online journal)

1. Introduction

The detection of gravitational-wave (GW) signals from astrophysical systems [9] has ushered in a new era in astronomy [10, 11], allowing the study of previously invisible systems. The current generation of GW interferometric detectors are sensitive enough to allow a confident candidate event about once per week [13, 14]. Increasing the sensitivity of the detectors is

important not only to increase the detection rate but also to improve the signal to noise ratio and sky localization of events, allowing for a more precise probing of the properties of nuclear matter in neutron stars [12] and of the fundamental physics of gravitation and general relativity [8].

Ironically, the sensitivity of current detectors to signals from very large and massive astrophysical systems is limited by random noise in microscopic systems, that is, fluctuations resulting from the internal mechanical dissipation in the material constituting the mirrors used as test masses [42]. In the most sensitive region of the detection band of Advanced LIGO [7] and Advanced Virgo [15], between 50 and 300 Hz, the sensitivity is limited by an equal contribution of quantum noise [26] and thermal noise, the latter being dominated by coating Brownian noise [72]. Indeed, all GW detectors currently operating are laser interferometers with km-scale optical resonators [56], where the test masses used to probe the space time metric fluctuations are high-quality fused silica mirrors with high-reflection (HR) dielectric coatings on the front surfaces [27, 46, 84]. Of all the sources of thermal noise in the mirrors, the Brownian motion of particles in the coating layers is the limiting factor and hence needs to be reduced for future sensitivity upgrades [40, 48, 50].

The dielectric coatings used in the current generation of GW detectors are Bragg reflectors [75] made of alternate ion-beam sputtered (IBS) thin layers of silica (SiO_2) and tantala–titania (Ta_2O_5–TiO_2) of optimized thickness [58]. Silica is the low refractive index material ($n = 1.45$ at 1064 nm), and the tantala–titania is the high refractive index material ($n = 2.07$ at 1064 nm) [32]. These materials and their synthesis by various methods have been extensively investigated in the context of optical materials in general and interferometric filters for photonic, lasers, and astronomy applications in particular [75], including for example their mechanical properties [3, 32, 38], showing that their performance is intimately related to parameters such as their internal stress and growth parameters [32].

The detection of GW signals is performed by monitoring the change in the relative distance between the mirrors, measured as a change in the phase of the laser beams [78]. Therefore, any fluctuation in the thickness or in the optical properties of the coating materials acts like a spurious displacement noise. Thermo-refractive and thermo-elastic fluctuations are not relevant [28], and the dominant source of phase noise is due to the Brownian motion of all the layers. The fluctuation dissipation theorem [1] links Brownian noise to the rate of energy dissipation in the coating material due to internal friction. The amount of friction is measured by the material loss angle φ, that is the fraction of energy lost per cycle when the material is driven by a sinusoidal external force. In the coating materials used so far, the worst offender is tantala–titania, with measured values $(2.3–3.4) \times 10^{-4}$ [32, 82]. The silica layers have one order of magnitude lower loss angle, $(2.3–4.0) \times 10^{-5}$ [32, 44].

The goal for the GW detector upgrades in the next 2–5 years is to roughly double the sensitivity to GW inspiral signals [40], which translates to an improvement of the same factor of the sensitivity in the 100 Hz region. In Advanced LIGO, for instance, this sets a target of 6.6×10^{-21} m $Hz^{-1/2}$ at 100 Hz in terms of coating Brownian noise, to be compared with the current estimated level of 1.3×10^{-20} m $Hz^{-1/2}$ [23]. The Brownian noise amplitude spectral density scales with the square root of the total loss angle of the HR coating [36]. Therefore the upgrade goal translates into improving the high refractive index material loss angle by at least of a factor 4. Marginal or no improvement is necessary for the low refractive index material. For this reason, most of the coating research in the Virgo and LIGO collaborations focused on finding an alternative material to replace the tantala–titania layers [33, 84], while keeping the same outstanding optical properties (absorption, scattering, etc) of the HR coatings. The main line of research explores the co-sputtering of other oxides with tantala, following the success of

co-sputtered tantala–titania coatings [37] which allowed a reduction of the coating loss angle by about 25% [32] with respect to tantala.

Beginning in 2012, one of the authors (SP) characterized a series of zirconia-based coatings. That investigation was motivated by zirconia (ZrO_2) being a high-index material ($n \geqslant 2$ at 1064 nm, like tantala) possessing a similar molecular structure and physical parameters to silica. However, unlike silica, when treated at high temperatures, zirconia will crystallize unless stabilized. Tewg *et al* [67] showed that the addition of zirconia to tantala thin films allowed for a higher maximum heating temperature, before the onset of crystallization. Post-deposition heat treatment, referred to as *annealing* hereafter, is a standard procedure to decrease the internal stress, the optical absorption and the mechanical loss of coatings [32]. As a general empirical rule, the higher the annealing peak temperature, the lower the resulting coating mechanical loss. In the work of Tewg *et al*, the annealing had a duration of 10 min, while typical annealing times for HR coatings used in GW detectors are of the order of 10 h [32]. Indeed, higher annealing temperatures (up to 900 °C) and duration would be beneficial also for the silica layers, decreasing their mechanical loss [17, 31] as a result of structural relaxation, leading to HR coatings with overall lower loss angle and hence lower thermal noise.

This paper focuses on collaborative work, carried out by several groups within the LIGO and Virgo Collaborations to produce and characterize co-sputtered tantala–zirconia thin films, for possible use as high refractive index layers for the new sets of mirrors of the Advanced LIGO + and Advanced Virgo + detector upgrades. We considered the effect of adding various amounts of zirconia, and measured the optical and mechanical properties of the films as functions of their chemical composition and annealing temperature. As coating mechanical loss depends in general on the nature of the growth technique, we tested a variety of sputtering processes of different energies and deposition rates. A detailed description of the coating samples is given in section 2. Different techniques and methodologies have been used to characterize the optical and mechanical properties of the coating samples, described with their results in sections 3 and 4. In sections 4 and 5 we show that the main effect of co-sputtering zirconia with tantala is a significant increase of the maximum annealing temperature T_a, hence a reduction of coating mechanical loss. The main issues we encountered are cracking of all annealed single-layer samples and bubble-like defects in annealed IBS HR coatings. Later we found that cracking could be avoided by drastically slowing down the annealing heating and cooling rates of the samples. Bubble-like defects, however, remain a pending issue to date. In section 6 we present the results of Raman spectroscopy measurements, and discuss the possibility of using Raman peaks as a probe of the state of relaxation or a predictor of the loss angle in a material. Finally, we discuss the results and their implications in section 7.

2. Deposition methods and film composition

The co-sputtered tantala–zirconia coating samples used for this work were produced by one industrial manufacturer and several academic research groups, using different growth techniques:

- Ion-beam sputtering (IBS), at MLD Technologies (MLD) and Laboratoire des Matériaux Avancés (LMA)
- Electron-cyclotron-resonance ion-beam deposition (ECR-IBD), at University of Strathclyde (UoS)
- Reactive biased-target deposition (RBTD), at Colorado State University (CSU), Fort Collins

Table 1. Measured atomic cation ratio $\eta = \text{Zr}/(\text{Zr} + \text{Ta})$, analysis method used to determine η and density ρ of co-sputtered Ta_2O_5–ZrO_2 thin films. RF-MS samples had Ta deposited by RF-MS and Zr deposited by DC-MS, HiPIMS samples had Ta deposited by HiPIMS and Zr deposited by RF-MS. Density values are plotted and discussed in section 3.5, where correlation between oxygen concentration, density and refractive index are considered.

Sample	Process	η (at.%)	Method	ρ (g cm^{-3})
MLD2014	IBS	48.5 ± 0.4	EDX	
MLD2018	IBS	50.2 ± 0.6	EDX	
LMA	IBS	19 ± 1	EDX	6.9 ± 0.1
UoS	ECR-IBD	34.0 ± 0.5	EDX	
UMP 551	RF-MS	41 ± 3	RBS	6.1 ± 0.2
UMP 554	RF-MS	43 ± 3	RBS	5.9 ± 0.2
UMP 658	HiPIMS	24 ± 3	RBS	7.0 ± 0.2
UMP 659	HiPIMS	24 ± 2	RBS	7.1 ± 0.2
UMP 542	HiPIMS	7 ± 2	RBS	7.3 ± 0.2
UMP 664	HiPIMS	7 ± 2	RBS	7.1 ± 0.2
UMP 678	HiPIMS	47 ± 2	RBS	6.6 ± 0.2
UMP 680	HiPIMS	47 ± 2	RBS	6.5 ± 0.2
CSU II	RBTD	23 ± 1	XPS	7.1[a]
CSU III	RBTD	54 ± 3	XPS	7.1[a]

[a]Estimated from component values and concentration.

- High-power impulse (HiPI) and radio-frequency (RF) magnetron sputtering (MS), at Université de Montréal and Polytechnique Montréal (UMP).

Acronyms of growth techniques and groups are used throughout this paper to identify the samples. The measured atomic cation ratio $\eta = \text{Zr}/(\text{Zr} + \text{Ta})$ and density ρ of all samples considered in this work are summarized in table 1 and plotted and discussed in section 3.5. Obtained values of η depended on the different coating facilities used, in terms of their equipment, configuration, accessible growth parameters, and availability. Considering all our sample sets, we eventually managed to reproduce almost every cation ratio already tested by Tewg *et al* in their study [67]. Details on the different growth processes, sample specifications and characterizations follow below.

After coating deposition, all coating samples were annealed in air at increasing peak temperature T_a by steps of 50 or 100 °C, starting from 300 °C, until they showed signs of crystallization. The annealing time for each soaking temperature T_a was 10 h, except for ECR-IBD samples for which it was 5 h.

2.1. IBS

Ion-beam-sputtered films where produced by MLD Technologies and by the LMA research group. Details are described below.

2.1.1. MLD Technologies. The provider is a manufacturer of high performance and specialty optical coatings located in Mountain View, CA, with coating facilities in Eugene, OR. The company deposited the coatings using standard IBS, where a beam of Ar ions is directed at a metal target and the sputtered metal atoms are oxidized in a low density O_2 atmosphere before striking the substrate. For all deposition runs, MLD coated: (i) thin super-polished disk substrates of Corning 7980 fused silica that were 76.2 mm in diameter and 2.5 mm thick; (ii) a ~100 μm thick fused-silica cantilever welded to a 10 mm × 10 mm × 3 mm

clamping block; (iii) and a number of 35 mm $\times$ 5 mm $\times$ $\sim$65 μm silicon cantilevers with a 10 mm $\times$ 5 mm $\times$ $\sim$550 μm clamping block. As is standard practice, each run included fused-silica witness samples with 25.4 mm diameter that were used to test the coating composition and thickness.

MLD conducted 2 runs, whose samples are referenced as MLD2014 and MLD2018, of identical specifications: the design goal was a single 500 nm thick tantala–zirconia coating with atomic cation ratio $\eta = \mathrm{Zr}/(\mathrm{Zr} + \mathrm{Ta}) \sim 36\%$, as specified by Tewg *et al* [67] for achieving amorphous coatings stable to peak annealing temperatures of 800 °C, where the ratio was intended to denote atomic number density. MLD performed post-deposition energy-dispersive x-ray spectroscopy (EDX) measurements that reported cation ratios in agreement with that goal. However, while Tewg *et al* reported atomic number densities, MLD reported ratios were later learned to be molecular number densities. Moreover, a reanalysis of the EDX data showed that the η was $48.5 \pm 0.4\%$ for MLD2014 and $50.2 \pm 0.6\%$ for MLD2018. Thus the actual molecular number densities were $ZrO_2 = 65.3 \pm 0.4\%$ and $Ta_2O_5 = 34.7 \pm 0.4\%$ for MLD2014 and $ZrO_2 = 66.8 \pm 0.6\%$ and $Ta_2O_5 = 33.2 \pm 0.6\%$ for MLD2018. MLD also reported coating thicknesses of 590 nm for MLD2014 and 483 nm for MLD2018.

After coating deposition, to test the effect of annealing on coating mechanical loss, the fused-silica disk and the silicon cantilevers were progressively annealed with steps of increasingly high temperatures, ranging from 300 to 800°C.

2.1.2. LMA. Co-sputtered Ta_2O_5–ZrO_2 coatings were produced with the custom-developed so-called *Grand Coater* (with a volume of 10 m^3) used to coat the mirrors of the Advanced LIGO, Advanced Virgo and KAGRA detectors [27, 32, 46]. Prior to deposition, the base pressure was less than 10^{-7} mbar. Ar gas was fed into the sputtering source while O_2 gas was fed directly into the vacuum chamber, for a total working pressure of 2×10^{-4} mbar. Energy and current of the sputtering Ar ions were of the order of 1 keV and 0.1 A, respectively. During deposition, the co-sputtered Ta_2O_5 and ZrO_2 particles impinged on substrates heated up to about 120 °C.

Single layers with a thickness between 500 and 650 nm have been grown on various substrates for different purposes: (i) on fused-silica witness samples (25.4 mm in diameter, 6 mm thick) for transmission spectrophotometry; (ii) on silicon wafers (75 mm in diameter, 0.5 mm thick) for reflection spectroscopic ellipsometry and EDX analyses; (iii) on a Corning 7980 fused-silica disk-shaped mechanical resonator of 75 mm in diameter and 1 mm thick for measuring coating mechanical loss, Young modulus, Poisson ratio and density.

Additionally, Ta_2O_5–ZrO_2/SiO_2 HR coatings with the same design of those of Advanced LIGO and Advanced Virgo most reflective mirrors (end test masses, ETMs) [32] have been deposited on micro-polished fused-silica witness samples for optical absorption and scattering measurements. By design, those ETM coatings have a transmission of 5 parts per million (ppm) at 1064 nm, determined by 38 layers of optimized thickness [58], for a total thickness of 5.9 μm [32].

Prior to coating deposition, to release the internal stress due to manufacturing and induce relaxation, the fused-silica disk was annealed in air at 900 °C for 10 h. After deposition, all coating samples were annealed in air for 10 h: optical samples were annealed at 500 °C, the disk underwent consecutive annealing treatments of increasing peak temperature (500, 600 and 700 °C) and the mechanical loss of its coating was measured after each annealing step.

We used an analytical balance to measure the mass of the disk before and after the coating deposition, as well as after the 500 °C annealing. To estimate the surface area coated in the deposition process, we measured its diameter with a Vernier caliper. As the coating thickness

was known with high accuracy from the optical characterization (see section 3.1.2), the coating density $\rho = 6.9 \pm 0.1$ g cm^{-3} was straightforwardly estimated as the mass-to-volume ratio.

We used a Zeiss LEO 1525 field-emission scanning electron microscope (SEM) and a Bruker Quantax system equipped with a Peltier-cooled XFlash 410 M silicon drift detector to analyze the surface and elemental composition of the single-layer coatings. The SEM beam was set to 15 keV for the survey. We performed multiple EDX analyses on different coating sample spots and with different magnifications (from 100$\times$ to 5000$\times$). Semi-quantitative (standardless) results were based on a peak-to-background evaluation method of atomic number, self-absorption and fluorescence effects (P/B-ZAF correction) and a series fit deconvolution model provided by the Bruker Esprit 1.9 software. Using the self-calibrating P/B-ZAF standard-based analysis, no system calibration had to be performed. According to our EDX analyses, our thin films had an average atomic cation ratio η = Zr/(Zr + Ta) = 19 $\pm$ 1%. We also found that they incorporated 2.9 $\pm$ 0.6 at.% of Ar.

2.2. ECR-IBD

Coatings were deposited using a custom-built ion beam deposition system that utilized three ECR ion sources for sputtering [20]. The ion beams are generated by injection of Ar gas into a resonance microwave cavity, with $\sim$3 W injected power at 2.45 GHz. The confinement of the plasma permits the extraction of ions through a single aperture, enabling a larger range of stable extraction potentials to be explored, with low ion current. The extraction potential was 10 kV and ion currents ranged between 0.2–0.6 mA per source, resulting in a deposition rate of 0.001 nm s^{-1}. Base pressure was below 1×10^{-5} mbar prior to deposition, with pressure rising to 8×10^{-5} mbar with Ar injected through the ion sources, and increasing to 1.2×10^{-4} mbar with reactive O_2 gas fed into the chamber. The targets used during the deposition process are two circular 152.4 mm diameter targets of pure tantala and zirconia provided by Scotech, UK, both with 99.99% purity. During the deposition process, two ion beams were directed onto the tantala target and one beam on the zirconia target, with the aim for cation ratio η = Zr/(Zr + Ta) of $\sim$33%. Fused-silica witness samples and cantilevers were placed on a rotating substrate holder to ensure coating uniformity.

The cantilevers, used for coating mechanical loss measurements [55], were fabricated from 45 mm $\times$ 5 mm $\times$(175 $\pm$ 3) μm strips of fused silica, flame welded to 10 mm $\times$ 10 mm $\times$ 3.1 mm clamping blocks [55]. They were cleaned in boiling H_2O_2 (30% w/w in H_2O) with 1 mol l^{-1} KOH dissolved, in order to remove the majority of particulates associated with the welding process, then annealed in air for 5 h at 950 °C prior to measurement and deposition.

EDX was used to quantify the cation ratio η = Zr/(Zr + Ta), found to be 34.0 $\pm$ 0.5%.

2.3. RBTD

Coatings were deposited using a LANS system by 4Wave, Inc. [63], where a low energy Ar ion plume is produced using an end-Hall ion source operated at 60 V and 5.8 A, with an Ar flow of 27 sccm. For neutralization, a hollow cathode electron source is employed at an emission current of 6.2 A with an Ar flow of 25 sccm. The Ar ions are attracted to a biased metallic target, leading to sputtering of the target material. For oxide coatings, O_2 is introduced into the chamber during the process. Substrates are placed in a sample holder facing the ion source, and rotating at 20 rpm during deposition to ensure uniformity of the film. The chamber base pressure is below 1×10^{-7} mbar, while the process pressure is about 9×10^{-4} mbar.

The LANS system has the ability to simultaneously bias up to three targets to produce mixed oxide coatings. An asymmetric, bipolar DC pulse is used to bias the targets with a negative voltage of -800 V and a positive voltage of 10 V and a period of 100 μs. For a

Table 2. Deposition conditions for Ta_2O_5–ZrO_2 thin films grown via RBTD. Pure Ta_2O_5 and ZrO_2 samples (I and IV, respectively) are included for reference.

Film	O_2 flow (sccm)	Target	Pulse width (μs)	Deposition rate (nm s^{-1})
CSU I	12	Ta	2	0.0212 ± 0.0001
CSU II	12	Ta–Zr	2–54	0.0294 ± 0.0001
CSU III	12	Ta–Zr	47–2	0.0217 ± 0.0001
CSU IV	12	Zr	2	0.0116 ± 0.0001

Table 3. Atomic concentrations obtained from XPS analysis at the surface of as-deposited Ta_2O_5–ZrO_2 thin films grown via RBTD.

	Elemental concentration (at.%)				Cation ratio
Film	C	O	Zr	Ta	Zr/(Zr + Ta)
CSU II	38 ± 1	44 ± 1	4.3 ± 0.1	14.1 ± 0.1	0.23 ± 0.01
CSU III	39 ± 1	42 ± 1	10.4 ± 0.4	8.7 ± 0.1	0.54 ± 0.03

binary oxide mixture, two targets are simultaneously biased and different mixture proportions of the materials are achieved by controlling the individual pulse duration of each target. Ta and Zr targets were employed to deposit tantala–zirconia thin films, and the corresponding deposition conditions are presented in table 2. Deposition rates for RBTD are typically an order of magnitude lower than with a gridded IBS system, ranging from 0.0212 nm s^{-1} for tantala to 0.0116 nm s^{-1} for zirconia. Films with a thickness between 200–300 nm were grown on: (i) 25.4 mm diameter and 6.35 mm thick UV grade fused-silica substrates; (ii) 75 mm diameter and 1 mm thick fused-silica substrates; and (iii) (111) Si wafer substrates.

X-ray photoelectron spectroscopy (XPS) measurements were performed on as-deposited coatings using a Physical Electronics PE 5800 ESCA/ASE system with a monochromatic Al Kα x-ray source. The photoelectron take-off angle was set at 45° and a charge neutralizer with a current of 10 μA was employed. The chamber base pressure was around 1×10^{-9} mbar. High resolution scans were recorded for the main peaks of the detected elements: C 1s, O 1s, Zr 3d and Ta 4f. No Ar can be detected by XPS in this case, because the peak associated with this element is superimposed with a Ta peak. Presence of carbon is due to normal surface contamination of samples exposed to the atmosphere. In the case of insulating samples the carbon is not removed but instead used for calibration of the binding energy scale, by employing the position of the adventitious carbon peak. CasaXPS software (version 2.3.19) was used to fit the high-resolution spectra [71].

Table 3 shows the atomic concentrations obtained from XPS for the thin films as deposited. The atomic percentage cation ratio, η = Zr/(Zr + Ta), resulted in 0.23 ± 0.01 for sample II and 0.54 ± 0.03 for sample III.

Figure 1 presents typical fits of the main XPS peaks. The C 1s peak was composed mainly of adventitious carbon, and up to 5% of carbon was found to be linked to an alcohol and/or ester functionality. This further confirmed that the presence of carbon was due to surface contamination. The O 1s peak had two components: lattice O, determined as such based on the tabulated position of O 1s for zirconia and tantala (around 530 eV), and non-lattice oxygen. In all cases, 1 to 3% of the oxygen was associated with hydroxide species based on the analysis of the C 1s peak, so the non-lattice peak could be attributed mainly to oxygen in defective sites. In the case of the Zr 3d peak, the doublet energy separation was found to be (2.39 ± 0.01) eV and the Zr $3d_{5/2}$ peak position was (182.1 ± 0.1) eV for both films. These values are in agreement with the tabulated values for zirconia [76]. For the Ta 4f doublet in both films,

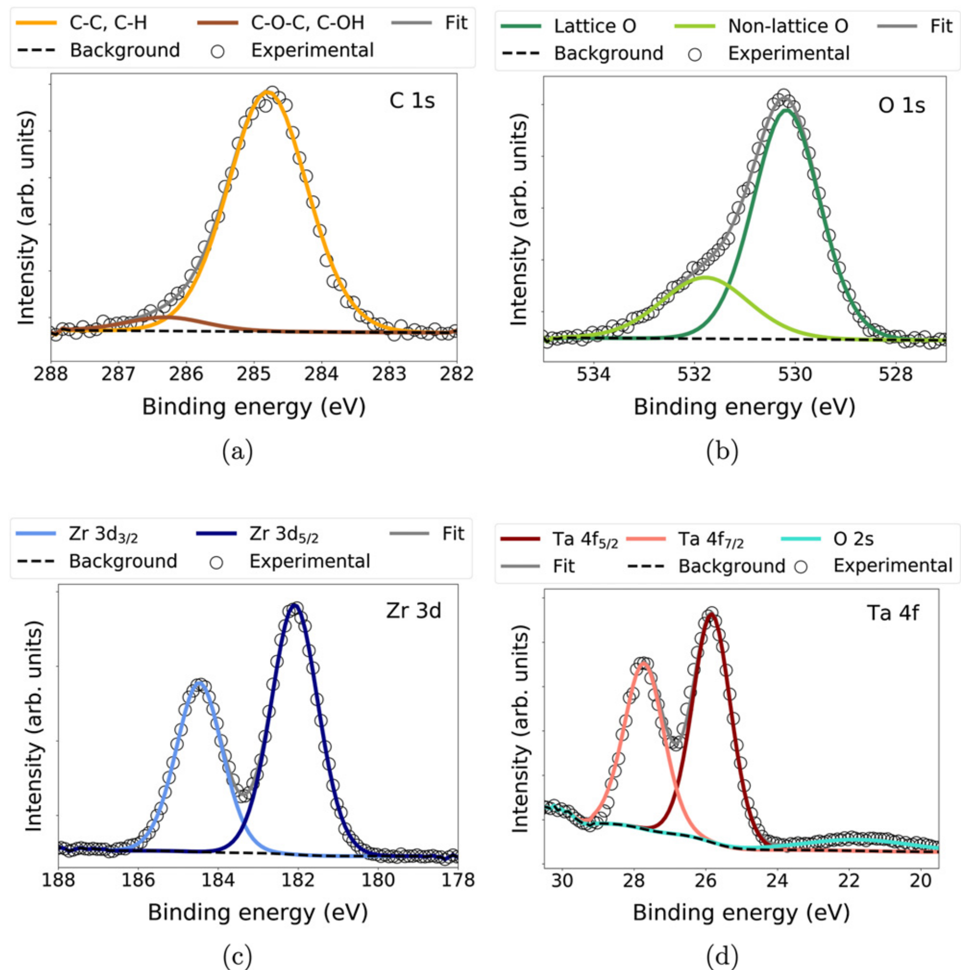

Figure 1. Typical fit of XPS peaks for an as-deposited Ta_2O_5–ZrO_2 thin film grown via RBTD with a cation ratio of 0.54: (a) C 1s, (b) O 1s, (c) Zr 3d and (d) Ta 4f.

the energy separation was determined as (1.89 ± 0.01) eV and the Ta $4f_{7/2}$ peak position as (26.0 ± 0.2) eV, which is in agreement with reported values for tantala [76]. Therefore, for the evaluated zirconia-doped tantala films as deposited, there was no noticeable modification of the chemical environment of either Ta or Zr, compared to their corresponding oxides.

2.4. HiPIMS/RF-MS

Layers of approximately 700 nm in thickness were synthesized in a Kurt J Lesker CMS-18 system, equipped with two 76 mm diameter metallic targets of Zr and Ta of 99.95% purity located ∼25 cm beneath the substrate holder. Prior to deposition, the base pressure in the system was less than 10^{-7} mbar. Depositions were carried out on different samples: (i) the 75 mm diameter fused-silica disks were placed face down, one at a time, on a rotating substrate holder featuring a wedged hole in the middle, such that they were supported by a 1 mm ledge; (ii) silica and (iii) silicon substrates were placed next to the disks as witness samples. During deposition, the pressure was 9 mbar with a 20% O_2:Ar gas ratio.

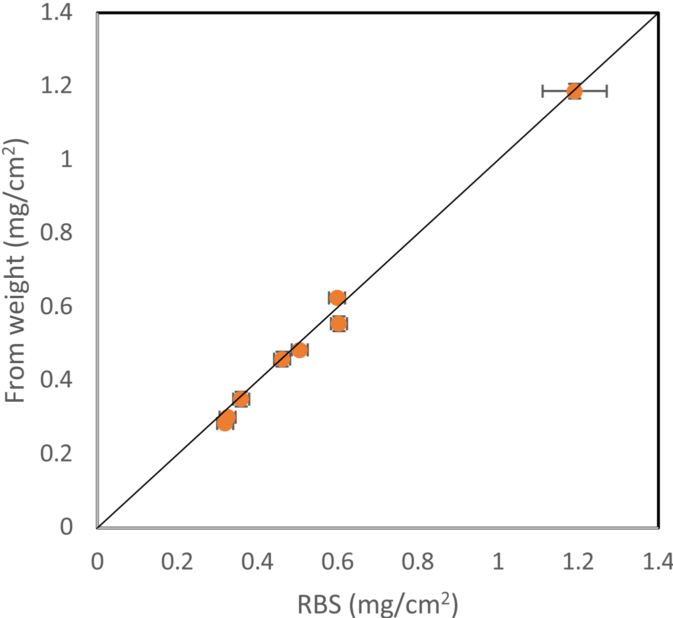

Figure 2. Areal mass density of Ta_2O_5–ZrO_2 thin films grown via MS: values measured by sample weighing are presented as a function of those measured by RBS, for comparison. The black line shows the 1:1 relationship.

For six samples, Ta was sputtered by HiPIMS [34, 35] using a Huttinger power supply, while the Zr was sputtered using an RF power supply (13.56 MHz) [22]. Two additional samples had their Ta deposited by RF-MS while the Zr was deposited by DC-MS, for comparison. The nominal duty cycle of the HiPIMS process was set at a voltage of 700 V, with a pulse duration of 80 μs at a frequency of 80 Hz. The nominal RF voltage applied to the Zr target varied between 200 V and 400 V, in order to achieve different doping levels. Both magnetrons were pre-sputtered for 12 min prior to deposition, in order to reach steady-state conditions before opening the main shutter. Depositions typically lasted 2 to 6 h.

Rutherford back scattering (RBS) measurements [68] were performed on the Si witness samples to measure the composition and areal atomic density of the films. Two ion beam configurations were implemented: a 2 MeV He ion beam to obtain the classical Rutherford cross section of O, and a 3.9 MeV He ion beam in order to separate the different peaks of Ta, Zr and Ar. The latter allowed for a higher precision of the concentration of these elements but with less precision on the O content, given the non-Rutherford cross-section and charging effects. The incidence angle was set at 7° and the scattering angle at 170° to maximize mass resolution. SIMNRA simulations [74] were compared to the experimental spectra in order to extract the composition and the areal atomic density of the deposited layers. Uncertainties were estimated by varying the concentrations until the simulation no longer fit the data. The resulting cation ratios η = Zr/(Ta + Zr) are reported in table 1, while the O content is discussed below. The coatings contain ∼1.5% Ar, as expected for samples deposited in Ar ambient. Elastic recoil detection analysis in other coatings usually also reveals the presence of 1.5 to 3.0% of hydrogen. We expect this to be the case in these films as well. No concentration gradients were identified within the sensitivity of our measurements.

Table 4. Measured refractive index n at 1064, 1550 and 2000 nm of co-sputtered Ta_2O_5–ZrO_2 thin films, and characterization method used to determine it (SP and SE indicate spectroscopic photometry and spectroscopic ellipsometry, respectively). The site of production and characterization is the same, and is indicated by the group acronym in each sample name. RF-MS samples had Ta deposited by RF-MS and Zr deposited by DC-MS, HiPIMS samples had Ta deposited by HiPIMS and Zr deposited by RF-MS. Index values are plotted and discussed in section 3.5.

Sample	Process	η (at.%)	n_{1064}	n_{1550}	n_{2000}	Method
MLD2014	IBS	48.5 ± 0.4	2.07 ± 0.01	2.06 ± 0.01		SP
MLD2018	IBS	50.2 ± 0.6	2.08 ± 0.01	2.07 ± 0.01		SP
LMA	IBS	19 ± 1	2.08 ± 0.01	2.07 ± 0.01	2.06 ± 0.02[a]	SE
UoS	ECR-IBD	34.0 ± 0.5	1.96 ± 0.01	1.95 ± 0.01	1.94 ± 0.01	SP
UMP 551	RF-MS	41 ± 3	2.01 ± 0.01	1.99 ± 0.01	1.99 ± 0.01	SE
UMP 554	RF-MS	43 ± 3	1.99 ± 0.01	1.97 ± 0.01	1.96 ± 0.01	SE
UMP 658	HiPIMS	24 ± 3	2.13 ± 0.01	2.11 ± 0.01	2.11 ± 0.01	SE
UMP 659	HiPIMS	24 ± 2	2.11 ± 0.01	2.10 ± 0.01	2.09 ± 0.01	SE
UMP 542	HiPIMS	7 ± 2	2.12 ± 0.01	2.11 ± 0.01	2.10 ± 0.01	SE
UMP 664	HiPIMS	7 ± 2	2.11 ± 0.01	2.10 ± 0.01	2.09 ± 0.01	SE
UMP 678	HiPIMS	47 ± 2	2.11 ± 0.01	2.10 ± 0.01	2.09 ± 0.01	SE
UMP 680	HiPIMS	47 ± 2	2.11 ± 0.01	2.10 ± 0.01	2.09 ± 0.01	SE
CSU II	RBTD	23 ± 1	2.07 ± 0.01	2.06 ± 0.01	2.05 ± 0.01[a]	SE
CSU III	RBTD	54 ± 3	2.10 ± 0.01	2.09 ± 0.01	2.08 ± 0.01[a]	SE

[a]Model extrapolation.

The mass density of the films was calculated by the following two methods. The first one relies on the areal atomic density (at./cm^2) and composition found by RBS. Knowing the atomic mass, it was possible to compute the areal mass density (g cm^{-2}). The second method consisted in measuring the substrate mass before and after deposition using a micro-balance, and dividing it by the coated area. The latter was measured from a photograph, in order to account for the area of the uncoated region near the edges of the sample. For both methods, the areal density was divided by the thickness found by ellipsometry (see section 3.4). We note that for the density calculation based on RBS, due to the presence of thickness gradients, both measurements needed to be carried out at the same location to avoid discrepancies. Likewise, in the case of the weighing method, it was important to consider an average thickness deduced from the thickness mapping obtained by ellipsometry. Figure 2 compares the areal mass density deduced from RBS measurements and by weighing the samples, that is, without considering the thickness. We can observe that both data sets closely follow a 1:1 relationship. Given the independence of both methods, we can assume that the measured values are accurate. Densities reported in table 1 are average values between the two methods.

3. Optical properties

The optical properties of the coating samples were characterized using different techniques. Table 4 presents the measured values for the refractive index n at the wavelengths of interest for current and future GW interferometers: 1064, 1550 and 2000 nm [7, 15, 48, 50]. In some case, the refractive index at 2000 nm was estimated by extrapolating the sample best-fit dispersion models through the infrared region, where optical absorption is expected to be negligible.

Optical absorption at 1064 nm was measured on RBTD single-layer samples and IBS multi-layer HR stacks. Light scattering at 1064 nm was measured on IBS multi-layer HR stacks.

At 1550 nm, where only ellipsometric and photometric measurements were available, extinction values were smaller than the sensitivity of the instruments ($k < 10^{-3}$). Measurements and their analyses are described below. A comparative summary is presented in section 3.5, where correlations between oxygen concentration, density and refractive index are discussed.

3.1. IBS

3.1.1. MLD. After deposition, MLD used a Cary spectrophotometer to measure the coating transmittance over the 400–1800 nm spectral range. The coating thickness and index of refraction were determined by a fit to this data.

At Embry-Riddle Aeronautical University, Prescott (Gretarsson Lab), we measured the optical thickness dependence on temperature for sample MLD2014 by monitoring the wavelength dependence of its transmission spectrum extrema as a function of temperature in the range 89°C–411°C. Details of the apparatus and method are given elsewhere [73]. Typical fits to the extrema locations are shown in figure 3(a). The measured coating optical thickness as a function of temperature, shown in figure 3(b), is linear. Note that, due to uncertainty in the physical thickness of the coating layer, optical thickness is not used here to estimate the absolute value of the index, only the change with temperature. The fractional optical thickness change as a function of temperature was found to be

$$\frac{1}{L}\frac{\mathrm{d}L}{\mathrm{d}T} = \alpha + \beta/n = (18.6 \pm 1) \times 10^{-6}\ \mathrm{K}^{-1}, \tag{1}$$

where α is the thermal expansion coefficient and β is the thermo-optic coefficient.

3.1.2. LMA. Refractive index and thickness of as-deposited coating samples were determined by spectroscopic ellipsometry, via coupled analysis of data sets acquired with two different J. A. Woollam Co. commercial instruments covering complementary spectral regions: a VASE for the 190–1100 nm range and a rotating-compensator M-2000 for the 245–1700 nm range. The wide range swept with both instruments allowed us to extend the analysis from ultraviolet to near infrared (0.7–6.5 eV). Consistent results were obtained in the overlapping range, within the uncertainty of the models used to fit the data. Analysis was carried out independently for VASE and M-2000 data, and eventually the information was combined in order to obtain the final results.

The optical constants were obtained by measuring the amplitude ratio Ψ and phase difference Δ of the p- and s-polarized light [64] reflected by the samples at different incidence angles $\theta = 55°, 60°, 65°$, close to the coating Brewster angle. The optical response of the substrates (silicon wafers with a thin native oxide layer and unpolished rear surface in order to avoid backside spurious reflections) was characterized with prior dedicated measurements and analyses [18]. As in previous works on similar systems [18, 47], we analyzed the data through a three-layer model consisting of substrate, thin film and surface layer. The latter, accounting for surface roughness, was defined via a Bruggeman effective medium approximation. The resulting coating roughness was less than 1 nm, a value comparable with those measured with an atomic-force microscope on similar samples [47]. Being less than 1% of the coating thickness, the surface layer did not substantially affect the data fit, especially in the near-infrared region.

The dielectric functions were reconstructed by using Kramers–Kronig-consistent Tauc–Lorentz [6] and Cody–Lorentz [80] models. Both models fit the data with comparable mean squared error, and yielded consistent results. We then obtained the complex refractive index of the as-deposited thin films from the best-fit dielectric functions. The Cody–Lorentz model provided a slightly better fit in the region of the absorption edge and included also the

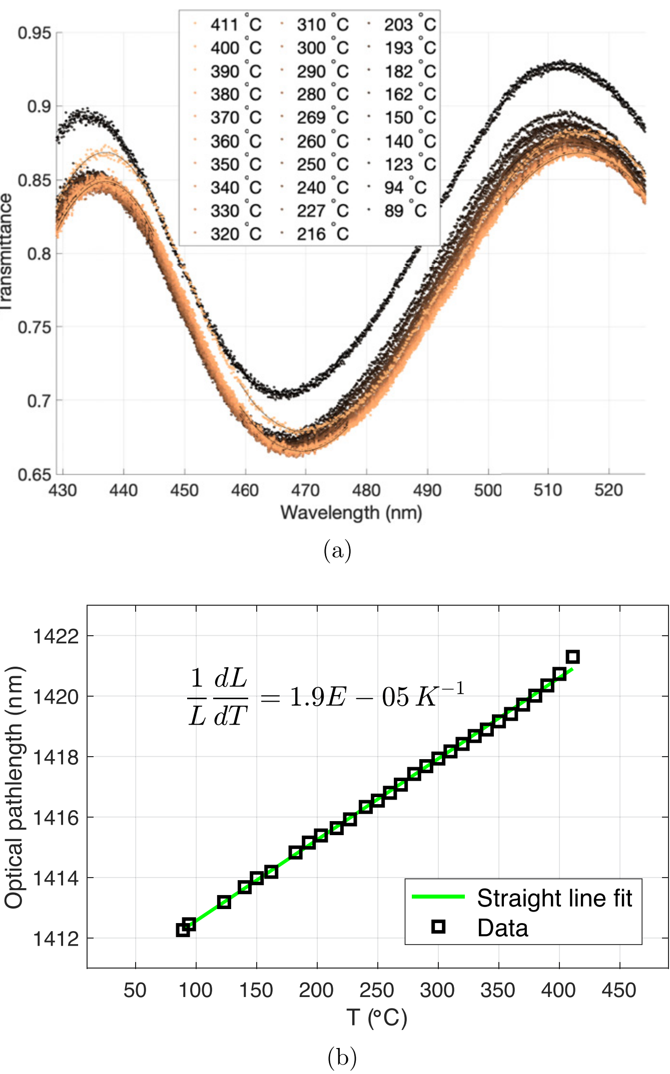

Figure 3. Characterization of optical thickness dependence on temperature of IBS Ta_2O_5–ZrO_2 thin film MLD2014. (a) Transmission spectrum extrema with parabolic fits to determine the extrema locations as a function of temperature. Higher temperatures shift the extrema to longer wavelengths, indicating an increasing optical thickness with temperature. (b) Optical thickness of the coating as a function of temperature.

Urbach tail absorption, which may be correlated to coating mechanical loss [19]. However, data quality for energies higher than the energy gap ($E > 4$ eV) was degraded and resulted in a large uncertainty for the Urbach energy $E_U = 130 \pm 30$ eV.

All measured spectra were fit with the same accuracy. Figure 4 shows exemplary spectra acquired at $\theta = 60°$ and their best fits with a Cody–Lorentz model. Figure 5(a) shows the reconstructed coating optical constants, and figure 5(b) is a Cody plot highlighting the coating energy gap, $E_g = 4.1 \pm 0.1$ eV, which is consistent with that of pure tantala coatings produced under identical conditions [18].

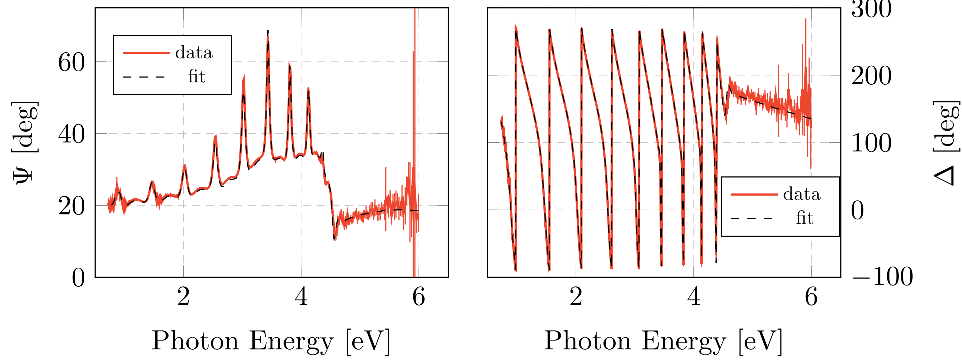

Figure 4. Measured ellipsometric spectra of an as-deposited IBS Ta_2O_5–ZrO_2 thin film with cation ratio $\eta = 0.19$ (LMA), acquired at an incidence angle $\theta = 60°$. The best-fit Cody–Lorentz model is shown (dashed line).

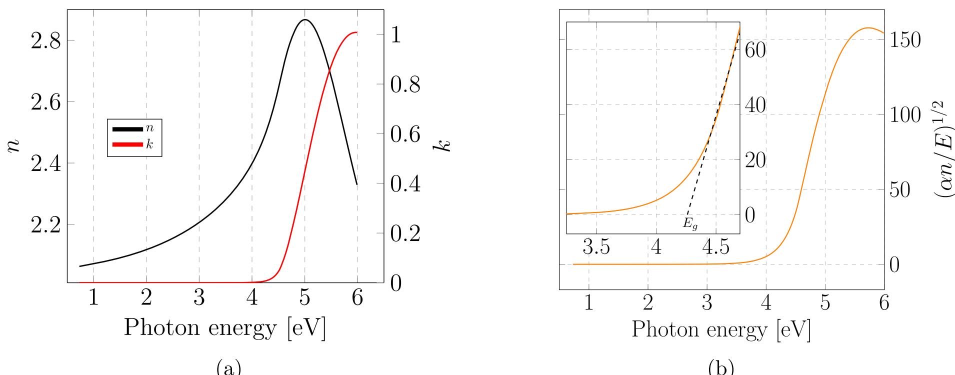

Figure 5. Measured optical properties of as-deposited IBS Ta_2O_5–ZrO_2 thin films with cation ratio $\eta = 0.19$ (LMA): (a) refractive index n and extinction coefficient k as function of photon energy E, the region of interest for present GW detectors is around $E = 1.2$ eV [7, 15] (corresponding to a wavelength of 1064 nm) and for future GW detectors is around $E = 0.8$ and $E = 0.6$ eV [48, 50] (corresponding to 1550 and 2000 nm, respectively); (b) Cody plot highlighting the energy gap E_g.

After annealing at 500 °C in air for 10 h, single-layer coating samples were characterized in their transparency region (400–1400 nm) with a Perkin Elmer Lambda 1050 spectrophotometer, at normal incidence. The annealing reduced the refractive index in the near-infrared region by about 3%. Samples of HR ETM stacks (see section 2), also annealed at 500 °C in air for 10 h, were characterized for optical absorption and light scattering with a custom-developed setup based on the photo-thermal deflection principle [21] and a commercial CASI scatterometer, respectively. We measured an optical absorption of 0.5 ppm, and 45 ppm of scattered light.

3.2. ECR-IBD

Optical-transmission spectra of as-deposited films, shown in figure 6, were measured in the 250–2100 nm range using a Varian 5000 spectrophotometer and fit to transmission simulations using SCOUT software by WTheiss. The behavior of the measured extinction coefficient,

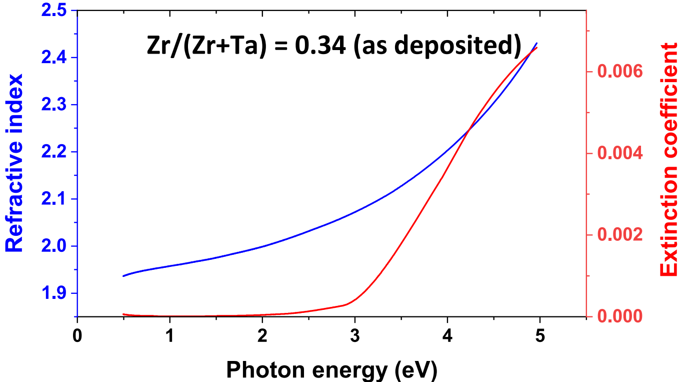

Figure 6. Refractive index n and extinction coefficient k as function of photon energy for as-deposited ECR-IBD Ta_2O_5–ZrO_2 thin films with cation ratio $\eta = 0.34$.

particularly the short-wavelength cut-off, is likely due to the deposition parameters associated with the ECR-IBD process, e.g. the higher ion energy and slower deposition rate. At 1064 nm and 1550 nm, the refractive index n was found to be 1.96 ± 0.01 and 1.95 ± 0.01, respectively, and the extinction coefficient $k < 10^{-3}$.

3.3. RBTD

Refractive index and extinction coefficient for the films were determined by spectroscopic ellipsometry using a Horiba UVISEL ellipsometer. Measurements were taken at an angle of 60°, for a spectral range of 0.59–6.5 eV. The films were evaluated as deposited and after annealing at the maximum temperature for which no crystallization was detected and mechanical loss minimized. A reduction of the refractive index was found after annealing, which could be due to oxygen incorporation during the process or due to formation of Ar bubbles [29]. Films previously grown by our group were found to contain 3 to 5% of Ar. When Ar bubbles are formed and coalesce upon annealing, the films usually feature a reduction in the refractive index that is accompanied by an increase in thickness. In our case, however, the thickness did not increase after annealing within the resolution of the instrument, indicating no significant presence of Ar bubbles in the coatings.

The dispersion of refractive index n and extinction coefficient k are presented in figure 7. The refractive index for both annealed films is presented in table 4. The film with the largest cation ratio featured the highest refractive index, as expected, given that the refractive index of zirconia is higher than that of tantala.

Optical absorption at $\lambda = 1064$ nm was determined by photothermal common-path interferometry [16]. We define the absorption normalized to a quarter wave thickness as

$$a_{\mathrm{QWT}} = \frac{a}{d}\frac{\lambda}{4n}, \tag{2}$$

with a being the absorption as measured in ppm, n the refractive index, d the coating thickness and $\lambda = 1064$ nm. a_{QWT} was 4.4 ± 0.8 ppm for the film with cation ratio $\eta = 0.54$ and 1.85 ± 0.05 ppm for the film with cation ratio $\eta = 0.23$. These results are summarized in table 5.

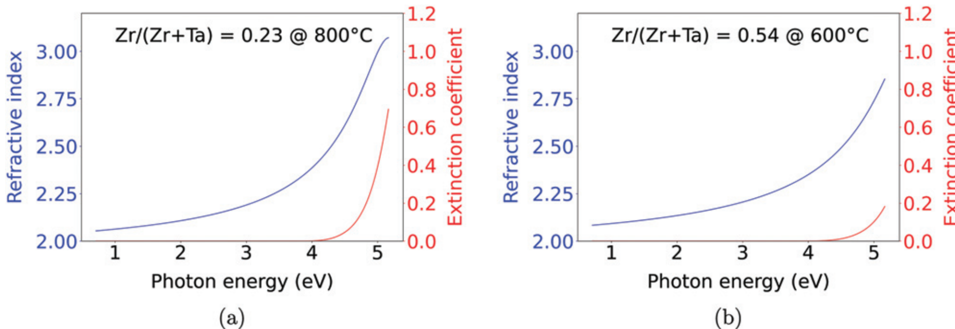

Figure 7. Refractive index n and extinction coefficient k as function of photon energy for RBTD Ta_2O_5–ZrO_2 thin films: (a) cation ratio $\eta = 0.23$, annealed at 800 °C for 10 h; (b) cation ratio $\eta = 0.54$, annealed at 600 °C for 10 h.

Table 5. Absorption loss normalized to a quarter wave thickness α_{QWT} at 1064 nm for RBTD Ta_2O_5–ZrO_2 thin films annealed at the maximum temperature T_a before crystallization (see equation (2) and section 5 for more details).

Sample	T_a (°C)	Cation ratio η	a_{QWT} @ 1064 nm (ppm)
CSU II	800	0.23	1.85 ± 0.05
CSU III	600	0.54	4.4 ± 0.8

3.4. HiPIMS/RF-MS

Similarly to what is described in sections 3.1.2 and 3.3, spectroscopic ellipsometry was carried out between wavelengths of 210 nm and 2500 nm with a J. A. Woollam Co., Inc. RC2-XI ellipsometer. Data analysis to obtain the complex refractive index and thickness mappings was carried out using the J. A. Woollam CompleteEASE software, with the optical properties being represented by a general oscillator model consisting of a Tauc–Lorentz and Gaussian oscillators for the UV absorption. The model parameters were first fit for each sample from a series of measurements at four different incidence angles, 45°, 55°, 65° and 75°, carried out at the center of the sample. The average thickness of the samples was then established through a mapping of 48 points, measured at 70° where only the thickness and surface roughness (Bruggeman effective medium approximation) were fit while keeping the optical model constant. The measured refractive index at 1064 and 1550 nm of all HiPIMS/RF-MS samples is presented in table 4.

3.5. Comparative summary

Figure 8(a) shows the refractive index values at 1064 nm and 1550 nm reported in table 4 as a function of the cation ratio η = Zr/(Zr + Ta), for all the samples. By way of example, a comparison of dispersion laws for samples where $\eta \sim 20\%$ is presented in figure 9.

The solid line in figure 8(a) corresponds to the rule of mixtures (addition according to molar fractions, also known as Arago–Biot rule [65] for the refractive index), assuming bulk values for pure oxides. The low dependence on η is expected, since tantala and zirconia have a similar refractive index at these wavelengths. Samples deposited by HiPIMS, IBS and RBTD feature values close to the rule of mixture. For samples where tantala is deposited by RF-MS or when the coating is deposited by ECR-IBD, the refractive index is significantly lower.

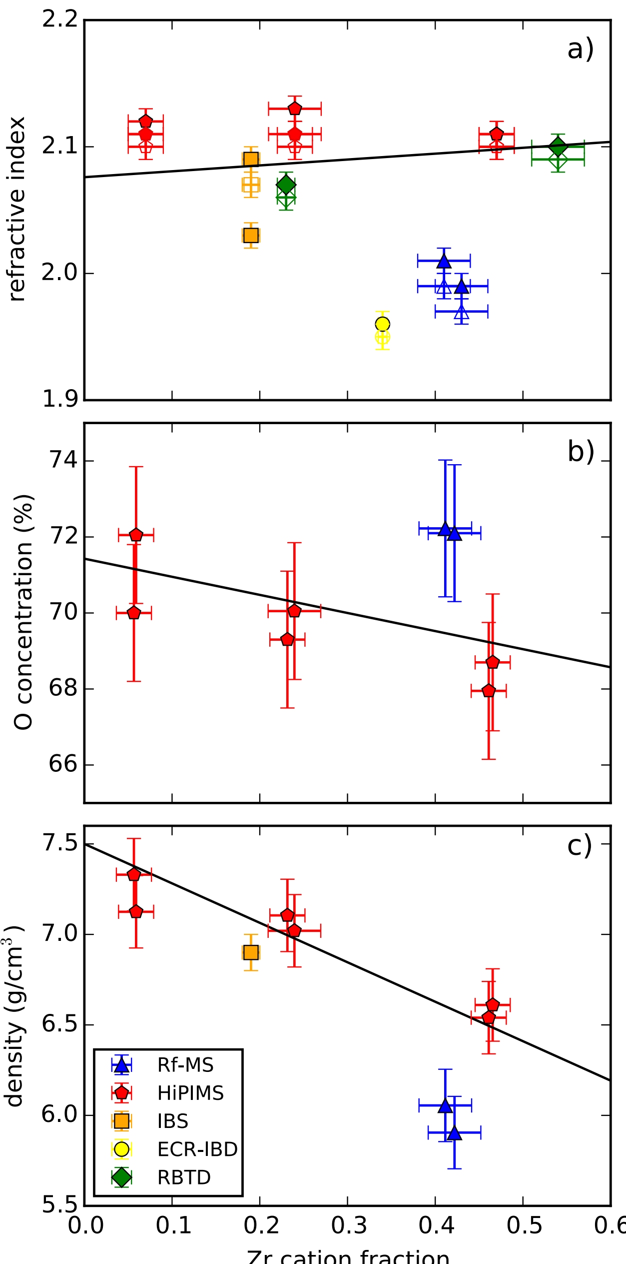

Figure 8. Correlation between oxygen concentration, density and refractive index of co-sputtered Ta_2O_5–ZrO_2 thin films, as a function of cation ratio $\eta = Zr/(Ta + Zr)$: (a) refractive index at 1064 nm (filled markers) and 1550 nm (empty markers), the black solid line is the value expected from the rule of mixtures (or Arago–Biot rule [65]) at 1064 nm when considering the refractive index found in reference [69] for bulk zirconia and reference [85] for that of bulk tantala; (b) oxygen concentration; (c) density. The solid lines in (b) and (c) are the expected oxygen content and density, respectively, according to the rule of mixture and assuming stoichiometric tantala and zirconia for the oxygen content, and density values for Ta_2O_5 and ZrO_2 taken from the literature [4, 55].

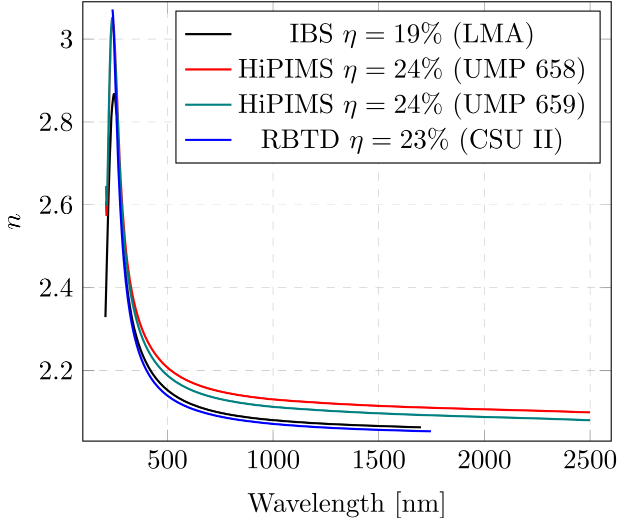

Figure 9. Comparison of refractive index n for Ta_2O_5–ZrO_2 thin films with cation ratio $\eta \sim 20\%$, as function of photon wavelength: as-deposited IBS sample (LMA), HiPIMS samples annealed at 700 °C before crystallization, RBTD sample annealed at 800 °C.

In figure 8(b), we find that the oxygen content in the layers where tantala is deposited by HiPIMS follows the rule of mixture (according to molar fractions) between stoichiometric tantala and zirconia, while there is an excess of oxygen in the films where tantala was deposited by RF-MS. Accordingly, as shown by figure 8(c), the density of films where tantala is deposited by HiPIMS or IBS follow the rule of mixture considering bulk densities of tantala and zirconia [4, 55], while those where tantala was deposited by RF-MS show a significantly lower density. Hence, the excess of oxygen leads to films with lower density and correspondingly lower refractive index. The explanation partly lies in the fact that atoms, when deposited by HiPIMS, have a higher kinetic energy than in RF-MS, which produces more compact films with less chances to have, for example, two oxygen atoms on the same bond. It is worth noting that we did not attempt to grow stoichiometric RF-MS layers, for example by changing the O_2:Ar ratio during deposition, as we wanted to compare HiPIMS and RF-MS under the same conditions.

Our results show the correlation between the oxygen concentration, the density, and the refractive index. Techniques such as HiPIMS and IBS feature atomic fluxes with higher kinetic energy, leading to higher dissociation rates of oxygen. This means that less oxygen may be used in the Ar/O_2 mixture to obtain stoichiometry. Also, the higher energy of species impinging on the growing film surface leads to coatings of higher density. Conversely, RF-MS films are generally less dense and have a lower refractive index. However, pores are frequently filled with water vapor that adds oxygen and hydrogen, leading to apparent oxygen over-stoichiometry. The former may therefore have more desirable properties for optical components. We will see in section 4 how that affects the loss angle.

4. Mechanical properties

The mechanical loss φ_c, Young modulus Y_c and Poisson ratio ν_c of the coating samples were measured using different setups, all based on the ring-down technique [83]: the mechanical resonances (modes) of a suspended coated resonator are excited using an actuator, and the

amplitude of their ring-down oscillations is monitored using an optical transducer. For a resonating mode of frequency f and ring-down time τ, the measured mechanical loss angle is $\varphi = (\pi f \tau)^{-1}$. The coating loss angle φ_c can be calculated as

$$\varphi_c = \frac{\varphi + (D-1)\varphi_s}{D}, \tag{3}$$

where φ_s is the measured loss angle of the substrate, φ is the measured loss angle of the coated sample and D is a so-called *dilution factor*, defined as the ratio of the coating elastic energy to the total elastic energy of the coated sample.

Coated samples were suspended under vacuum, in order to prevent systematic damping from ambient pressure. We used different suspension systems, each one specifically adapted to the different geometries of the substrates used as resonators. Because of the different suspension systems and samples, we also used different methods to estimate D, Y_c and ν_c. Specific measurements and their analyses are described in the following.

Results are summarized in table 6, where an average coating loss $\overline{\varphi}$, taken from every set of resonant modes of each sample, is used to ease comparisons. Since the lowest coating thermal noise occurs when the coating Young modulus matches that of the substrate [36], values of the parameter

$$\gamma = \overline{\varphi}_c \left(\frac{Y_c}{Y_s} + \frac{Y_s}{Y_c} \right) \tag{4}$$

are also presented, where $Y_s = 73.2$ GPa is the Young modulus of the fused silica substrate of Advanced LIGO and Advanced Virgo mirrors [7, 15].

A comparative summary is presented in figures 18 and 19 of section 4.5, where the effects of different cation ratios η = Zr/(Zr + Ta) and annealing temperatures T_a on the coating mechanical loss are discussed.

4.1. IBS

4.1.1. MLD. The coating samples used to measure coating mechanical loss, Young modulus and Poisson ratio were grown on fused-silica disks and cantilevers and on silicon cantilevers (see section 2.1.1). Samples grown on fused-silica substrates were used for measurements at ambient temperature, those on silicon cantilevers to perform cryogenic measurements.

Disks — the mechanical loss measurements were performed at Hobart and William Smith Colleges (HWS). The coated, fused silica substrates were welded to a monolithic, fused silica fiber suspension. The mechanical loss was measured for the samples' eight lowest vibrational modes, which span the frequency range from 2.5 to 18 kHz. Each mode was excited to resonance using an electrostatic comb exciter. The dissipation was measured using an ellipsometry detector to monitor the strain-induced birefringence during ring-down (see [37] for details). The loss for each mode was measured several times with both weighted and unweighted averages retained.

After each set of measurements, the samples have been annealed and remeasured. The annealing temperatures were 300, 600, 650, 700, 750 and 800 °C for MLD2014 and 400, 600 and 700 °C for MLD2018. For these experiments, the fused silica substrate is typically annealed to high temperature before being coated. The MLD2018 disk was properly annealed at 950 °C, whereas the MLD2014 disk was not annealed prior to coating. For the latter sample, the substrate loss was determined from the data using the frequency dependence of the loss as determined by finite-element modeling. The model, created using COMSOL, was used to

Table 6. Measured mechanical properties of co-sputtered Ta_2O_5–ZrO_2 thin films: frequency-averaged mechanical loss $\overline{\varphi}$ of samples annealed at the highest peak temperature T_a before the onset of crystallization, Young modulus Y_c, Poisson ratio ν_c, and coefficient $\gamma = \overline{\varphi}_c(Y_c/Y_s + Y_s/Y_c)$, where $Y_s = 73.2$ GPa is the Young modulus of a fused silica substrate. The characterization methods used to determine such properties are also listed, together with the site where the characterizations were performed. RF-MS samples had Ta deposited by RF-MS and Zr deposited by DC-MS, HiPIMS samples had Ta deposited by HiPIMS and Zr deposited by RF-MS. RF-MS, HiPIMS and IBS (LMA) samples have been annealed for 10 h, ECR-IBD samples for 5 h. Average coating loss values are plotted in figures 18 and 19 and discussed in section 4.5.

Sample	Process	T_a (°C)	η (at.%)	$\overline{\varphi}_c$ (10^{-4} rad)	Y_c (GPa)	ν_c	γ (10^{-4} rad)	Method
MLD2014	IBS	800	48.5 ± 0.4	4.26 ± 0.11	131 ± 2		10.0	[a]
MLD2018	IBS	700	50.2 ± 0.6	1.82 ± 0.04	130 ± 2		4.3	[a]
LMA	IBS	700	19 ± 1	4.41 ± 0.68	120 ± 3	0.32 ± 0.01	9.9	GeNS (LMA)
UoS	ECR IBD	750	34.0 ± 0.5	3.64 ± 0.45	176 ± 8		10.3	Clamped cantilevers (UoS)
UMP 551	RF-MS	800	41 ± 3	2.36 ± 0.85	125 ± 2	0.21 ± 0.05	5.4	GeNS (Caltech)
UMP 554	RF-MS	800	43 ± 3	2.52 ± 0.82	114 ± 2	0.36 ± 0.03	5.5	GeNS (Caltech)
UMP 658	HiPIMS	700	24 ± 3	5.59 ± 0.90	110.6 ± 1.2	0.31 ± 0.02	12.1	GeNS (Caltech)
UMP 659	HiPIMS	700	24 ± 2	5.04 ± 1.53	108 ± 5	0.35 ± 0.05	10.9	GeNS (Caltech)
UMP 542	HiPIMS	600	7 ± 2	5.69 ± 0.37	100.6 ± 1.1	0.34 ± 0.02	12.0	GeNS (Caltech)
UMP 664	HiPIMS	650	7 ± 2	4.45 ± 0.38	116.5 ± 1.3	0.33 ± 0.02	9.9	GeNS (Caltech)
UMP 678	HiPIMS	800	47 ± 2	4.38 ± 0.63	111 ± 4	0.28 ± 0.09	9.5	GeNS (Caltech)
UMP 680	HiPIMS	800	47 ± 2	4.87 ± 0.92	110 ± 4	0.28 ± 0.09	10.6	GeNS (Caltech)
CSU II	RBTD	800	23 ± 1	3.22 ± 0.53	145 ± 6	0.30 ± 0.09	8.0	GeNS (Caltech)
CSU III	RBTD	600	54 ± 3	2.67 ± 0.15	143 ± 5	0.37 ± 0.05	6.6	GeNS (Caltech)

[a] Disks suspended by welded glass fibers (HWS)/clamped cantilever blades, at ambient and cryogenic temperature (IGR)/nanoindentation (Caltech).

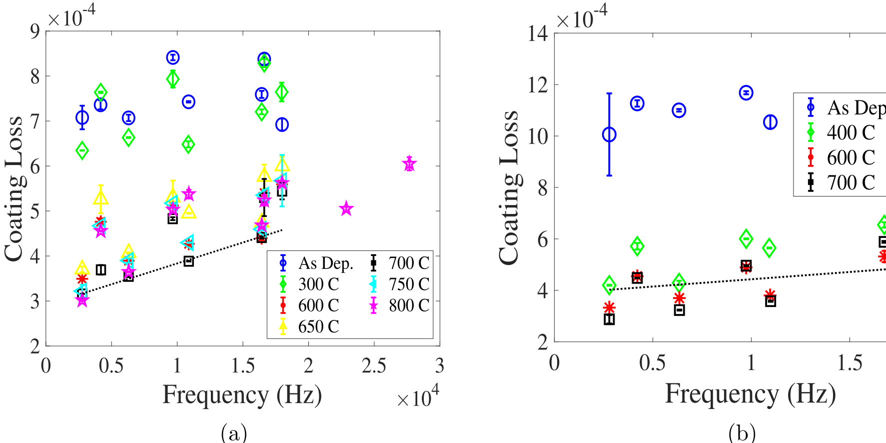

Figure 10. Coating loss as a function of frequency for IBS Ta_2O_5–ZrO_2 thin films, as measured on suspended disks: (a) sample MLD2014, (b) sample MLD2018. The loss is steadily reduced with increased annealing temperature T_a, until reaching a minimum near 700 °C. A weighted linear least-squares fit is shown (black line) for the data sets of the 700 °C annealing. In the MLD2014 data, panel (a), the fit line follows the low loss data due to their smaller uncertainties.

calculate the dilution factor for the total coating loss and for the decomposition of the coating loss into bulk and shear loss [86].

As shown in figure 10, the coating loss for both samples decreased with increasing annealing temperature, until reaching a minimum at 700 °C. A linear fit of the frequency-dependent coating loss after annealing at 700 °C gave:

$$\varphi_c(f) = (9.29 \pm 0.09) \times 10^{-9}\ \mathrm{Hz}^{-1} \quad f + (2.907 \pm 0.007) \times 10^{-4}\ \text{for MLD2014},$$

$$\varphi_c(f) = (5.7 \pm 0.2) \times 10^{-9}\ \mathrm{Hz}^{-1} \quad f + (3.87 \pm 0.02) \times 10^{-4}\ \text{for MLD2018}.$$

The variation in the ratio of bulk and shear energy with mode shape, which in turn depends on frequency, introduces a scatter of the data about any function of a single coating loss angle. Instead, a decomposition of the coating loss into shear and bulk components allows a more precise fit to the data, as shown in figure 11. A fit of each data set to bulk and shear coating loss resulted in the dependence of these values with annealing temperature T_a shown in figure 12: the shear loss steadily decreased for increasing T_a, whereas the bulk loss showed no clear dependence. The substrate barrel (edge) was polished. A fit to the data showed no significant contribution from edge dependent losses [24].

The coating Young modulus was measured after annealing at two different temperatures, using a nano-indentation facility at the California Institute of Technology (Caltech). The results, $Y_c = 130 \pm 2$ GPa for MLD2018 annealed at 800 °C and $Y_c = 131 \pm 2$ GPa for MLD2014 annealed at 600 °C, assume a coating Poisson ratio of 0.298 determined by molecular dynamics models [66].

Cantilevers — the mechanical loss of the MLD2018 coating was measured also on a fused-silica cantilever at ambient temperature, and on silicon cantilevers at cryogenic temperatures. Measurements were performed at the Institute for Gravitational Research of the University of Glasgow (IGR).

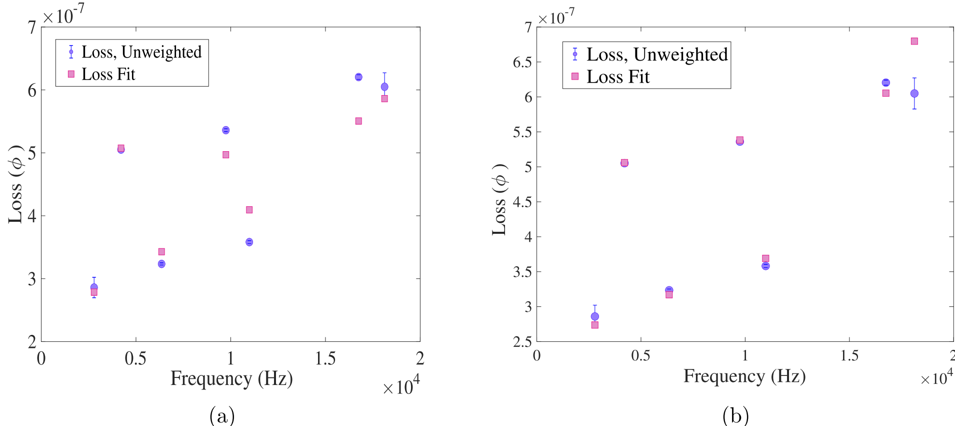

Figure 11. Comparison of analysis methods, as applied to coating loss data of IBS Ta_2O_5–ZrO_2 thin films (MLD) measured on suspended disks: (a) fit with single loss angle, (b) fit with bulk and shear loss angles. The need for separate analysis of bulk and shear coating loss angle is pointed out by the improved fit of panel (b).

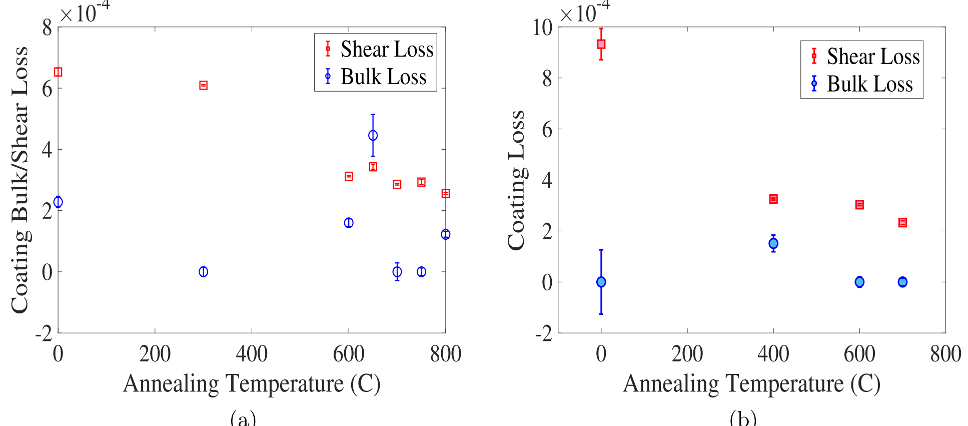

Figure 12. Bulk and shear coating loss as function of annealing temperature for IBS Ta_2O_5–ZrO_2 thin films, as measured on suspended disks: (a) sample MLD2014, (b) sample MLD2018. The shear loss is steadily reduced with increased annealing temperature, while the bulk loss shows no clear dependence.

The cantilevers were mounted in a clamp, under vacuum, and their bending modes were excited using an electrostatic actuator. The amplitude of the ring-down motion was monitored using an optical shadow sensor. The coating mechanical loss was then calculated using equation (3) and

$$D = \frac{3Y_c d_c}{Y_s d_s}, \tag{5}$$

where Y_c and d_c are the coating Young modulus and thickness, respectively, and Y_s and d_s are the substrate Young modulus and thickness, respectively.

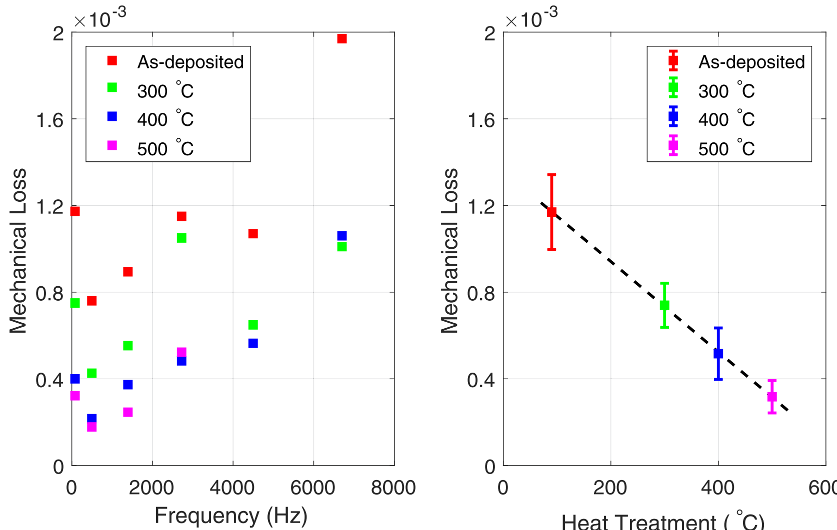

Figure 13. Coating loss of IBS Ta_2O_5–ZrO_2 thin film MLD2018, as measured on a clamped ∼100 μm thick fused-silica cantilever at ambient temperature. Left: (a) the loss was measured as a function of frequency on the as-deposited sample, then re-measured after progressive annealings at 300, 400 and 500 °C; right: (b) frequency-averaged coating loss $\overline{\varphi}$ as a function of annealing temperature. The coating loss decreased after each annealing treatment.

After each set of measurements, the coated fused-silica cantilever was progressively annealed at increasing peak temperatures, up to 500 °C. Figure 13(b) shows the effect of annealing on the coating mechanical loss as a function of frequency, and that the coating mechanical loss at 1 kHz decreased by over a factor of three upon annealing, from $\overline{\varphi} = 1.1 \times 10^{-3}$ in its as-deposited state to $\overline{\varphi} = 3.2 \times 10^{-4}$ after a 500°C annealing.

The coated silicon cantilevers were measured in a temperature-controlled, liquid-helium-cooled cryostat [77]. The coating mechanical loss was calculated using equations (3) and (5) for a large number of resonant modes, from ∼1 to 30 kHz, as extensively detailed in [77]. Here, for sake of conciseness, we present in figure 14 only the coating loss of the third- and fourth-order bending modes, at ∼1.4 kHz and ∼2.7 kHz respectively.

Figure 14 shows that IBS Ta_2O_5–ZrO_2 coating in its as-deposited state has a very small and broad loss peak of $\sim 6 \times 10^{-4}$ at ∼30 K. This peak narrowed to 1×10^{-3} after annealing at 300 and 400 °C, and further increased to 1.2×10^{-3} after an 800 °C anneal. Below 100 K, the coating loss temperature-dependent trend of the annealed Ta_2O_5–ZrO_2 samples is similar to that of pure IBS Ta_2O_5 films annealed at 600 °C [39]. After annealing at 800 °C, the coating loss of Ta_2O_5–ZrO_2 does not show the large and broad loss peak observed at 80 K for IBS poly-crystalline Ta_2O_5 thin films annealed to the same temperature [39]. This is a clear indication that co-sputtering ZrO_2 with Ta_2O_5 prevented the onset of crystallization for annealing at 800 °C.

As shown in figure 13, annealing reduced the coating loss at ambient temperature. At the same time, figure 14 suggests that annealing increased the coating loss at low temperatures, which is the opposite of what has been observed on IBS poly-crystalline Ta_2O_5–TiO_2 [41]. This is of interest for further understanding of coating loss and structure and modeling, and

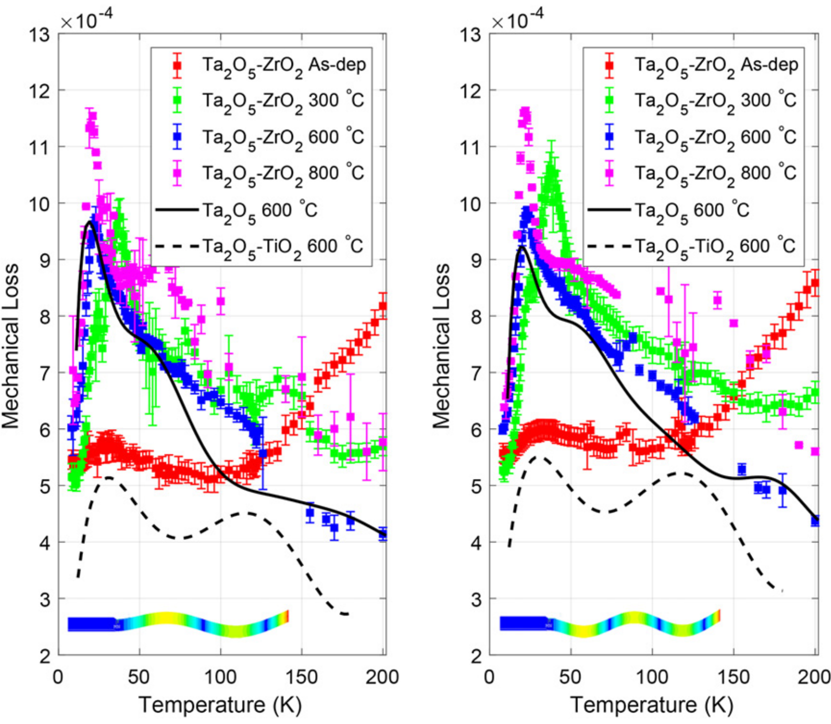

Figure 14. Cryogenic mechanical loss of IBS Ta_2O_5–ZrO_2 coatings as a function of sample temperature, as measured on clamped ∼65 μm thick silicon cantilevers. Left: (a) results for the third-order bending mode at ∼1.4 kHz; right: (b) results for the fourth-order bending mode at ∼2.7 kHz. The coating loss of sample MLD2018 as deposited and after a 300 °C annealing and of sample MLD2014 after 600 °C and 800 °C annealing are shown, and compared to data of IBS amorphous Ta_2O_5 and poly-crystalline Ta_2O_5–TiO_2 samples annealed to 600 °C [39, 41]. Finite-element representations of the measured resonant mode are visible at the bottom of each plot.

suggests that different values of the cation ratio $\eta = \mathrm{Zr}/(\mathrm{Zr} + \mathrm{Ta})$ need to be investigated at low temperatures.

4.1.2. LMA. We used a gentle nodal suspension (GeNS) system [25] to measure coating mechanical loss, Young modulus and Poisson ratio via the direct measurement of the disk dilution factor [32]. As a matter of fact, the dilution factor D in equation (3) can be written as a function of the resonator mode frequency (f_0, f) and mass (m_0, m) before and after coating deposition, respectively [52]:

$$D = 1 - \left(\frac{f_0}{f}\right)^2 \frac{m_0}{m}. \tag{6}$$

The advantage of measuring the dilution factor is that the ensuing coating loss estimation is then exclusively based on measured quantities: sample loss angle, mode frequency and mass. Therefore, unlike other experimental setups based on the ring-down method, our method does not require prior knowledge of coating Young modulus and thickness. Furthermore, one

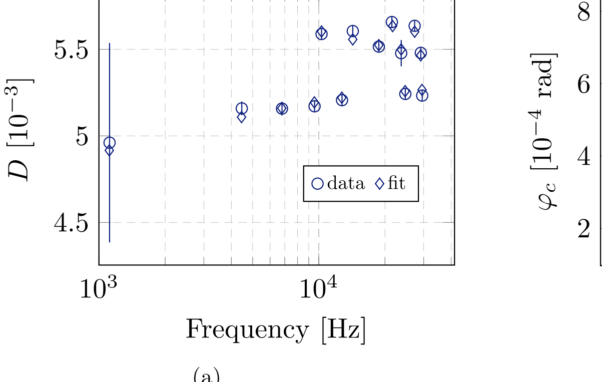

(a)

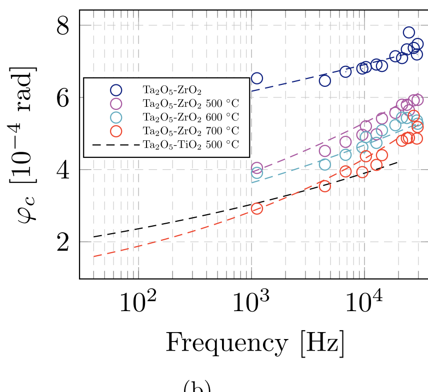

(b)

Figure 15. Measured mechanical properties of IBS Ta_2O_5–ZrO_2 thin films (LMA) as a function of frequency, as measured on a disk suspended with a GeNS system: (a) measured and best-fit simulated dilution factor D, for the first three families of disk mode shapes [32]; (b) coating loss angle φ_c, as measured after deposition and after annealing treatments at 500, 600 and 700 °C for 10 h, in air. Data of the annealed Ta_2O_5–TiO_2 layers of Advanced LIGO and Advanced Virgo is also shown, for comparison [32]. Dashed lines are least-squares fits using a power-law model $\varphi_c(f) = af^b$, best-fit parameters a and b are presented in table 7. Values at $f < 1$ kHz are model extrapolations.

can estimate coating Young modulus Y_c and Poisson ratio ν_c by fitting the results of finite-element simulations to measured values of D estimated via equation (6). Compared to nano-indentation, such method does not rely on the prior knowledge of ν_c, and does not depend on the nature of the substrate used nor on the model chosen for data analysis [32]. Figure 15(a) shows best-fit results for three mode families of different shapes and frequency [32], giving $Y_c = 120 \pm 3$ GPa and $\nu_c = 0.32 \pm 0.01$. Details about our fitting method and finite-element simulations can be found elsewhere [30, 32].

Figure 15(b) shows the coating loss angle before and after consecutive annealing treatments at 500, 600 and 700 °C for 10 h, in air. As expected, the annealing reduced the coating loss. However, the coating showed cracks after the 700 °C annealing. This issue is further discussed in section 5.

We used a power-law model $\varphi_c(f) = af^b$ to describe the observed frequency-dependent behavior of the coating internal friction [24, 53, 81], and applied least-squares linear regression in order to fit the data. Best-fit parameters are presented in table 7. It is worth noting that the b parameter increased after each annealing step, implying lower loss values in the most sensitive region (50–300 Hz) of GW detectors. Thus, by extrapolating our results to lower frequency, we obtain a loss angle of 1.8×10^{-4} at 100 Hz for the Ta_2O_5–ZrO_2 annealed at 700 °C. This value has to be compared to 2.4×10^{-4} for the Ta_2O_5–TiO_2 layers of GW detectors [32].

4.2. ECR-IBD

The coating mechanical loss at ambient temperature was characterized using fused-silica cantilevers. They were mounted in a stainless steel clamp within a vacuum chamber with residual pressure pressure below 5×10^{-6} mbar, and excited using an electrostatic actuator [49]. The freely-decaying amplitude of the resonant motion was monitored using an optical shadow sensor. We then used equations (3) and (5) to calculate the coating loss for the cantilever bending modes [79], and the results are presented in section 4.5.

Table 7. Best-fit parameters of a power-law internal friction model $\varphi_c(f) = af^b$ for data sets of IBS Ta_2O_5–ZrO_2 thin films (LMA) measured on a disk suspended with a GeNS system, as function of annealing peak temperature T_a (as-deposited coating samples are denoted by $T_a = 0°C$), shown in figure 15(b). Each annealing treatment was performed in air and lasted 10 h.

T_a (°C)	a (10^{-4} rad Hz^{-b})	b
0	4.4 ± 0.4	0.05 ± 0.01
500 °C	1.6 ± 0.2	0.13 ± 0.01
600 °C	1.7 ± 0.2	0.12 ± 0.01
700 °C	0.8 ± 0.1	0.18 ± 0.02

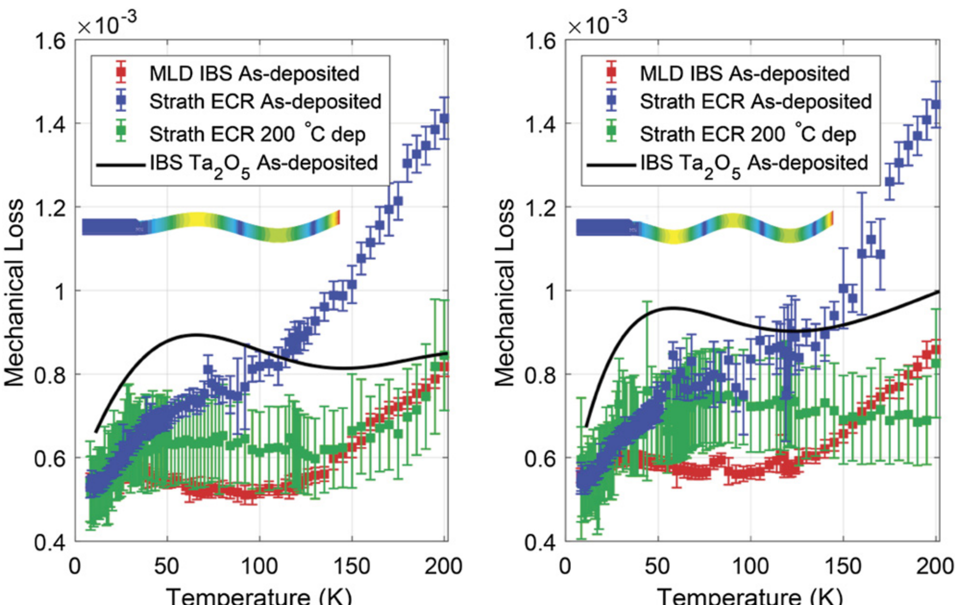

Figure 16. Cryogenic mechanical loss of as-deposited ECR-IBD Ta_2O_5–ZrO_2 coatings as a function of sample temperature, as measured on clamped ~65 μm thick silicon cantilevers. Left: (a) results for the third-order bending mode at ~1.4 kHz; right: (b) results for the fourth-order bending mode at ~2.7 kHz. Data of an ECR-IBD sample grown through standard deposition (blue markers) and that of an ECR-IBD grown on a substrate held at 200 °C (green markers) are shown, and compared to the data of as-deposited IBS Ta_2O_5–ZrO_2 MLD2018 (see figure 14) and Ta_2O_5 [39] coating samples. Finite-element representations of the measured resonant mode are visible in each plot.

The same method was applied to perform cryogenic loss measurements of coated silicon cantilevers, whose results are shown in figure 16 for the third- and fourth-order bending modes at ~1.4 kHz and ~2.7 kHz, respectively, and compared to the results obtained for the IBS sample MLD2018 (see section 4.1.1 and figure 14). Below ~100 K, both the ECR-IBD and IBS as-deposited Ta_2O_5–ZrO_2 coatings have a lower coating loss than that of as-deposited IBS Ta_2O_5 [39]. This shows that, prior to annealing, the addition of ZrO_2 already reduced the coating loss at low temperature. Below 30 K, the loss of the ECR-IBD coatings is comparable to that of IBS coatings.

Figure 16 also shows the data of coating loss for an ECR-IBD Ta_2O_5–ZrO_2 coating sample grown on a substrate held at 200 °C. By comparing the ECR-IBD samples, it can be seen that heating the substrate to a higher temperature had a considerable effect on the low-temperature coating loss, between 100 and 200 K: for instance, the coating loss of the sample grown at 200 °C is 1.8 times smaller at 200 K. Finally, we found that the coating loss of the ECR-IBD sample grown at 200 °C is similar to that of the IBS sample MLD2018 in its as-deposited state.

Coating Young modulus Y_c was measured using a Bruker Hysitron TriboScope nano-indenter system, with a three-sided Berkovich pyramid diamond tip ($Y_{\text{indenter}} = 1140$ GPa, and $\nu_{\text{indenter}} = 0.007$) and found to be $Y_c = 176 \pm 8$ GPa, assuming a coating Poisson ratio of $\nu_c = 0.297$ determined by molecular dynamics models [66]. Measurements were taken on as-deposited thin films grown on 1 mm thick JGS-1 fused-silica witness samples, following the Oliver–Pharr method [2].

4.3. RBTD

Coating mechanical loss, Young modulus and Poisson ratio were estimated by measuring suspended coated fused-silica disks. The disks were measured by the LIGO Laboratory group at Caltech, in a setup with four independent GeNS systems [25] installed in the same vacuum chamber to simultaneously measure all the accessible resonant modes of four samples [54].

Prior to coating deposition, the resonant frequencies and mechanical loss of the disks were characterized through specific measurements, which served as a reference and for background noise estimation for the subsequent series of measurements performed after deposition. All surfaces of the bare disks, including the edge, were polished to a standard optical grade to reduce the contribution of substrate surface losses [5, 24].

After coating deposition, the disks were measured again, and then repeatedly annealed at increasing peak temperature T_a, from 300 to 800 °C. After each annealing treatment, the resonant frequencies and mechanical loss of the disks were measured. Knowing the coating thickness and density from the previous characterizations (see sections 2 and 3), it was possible to compute the coating elastic properties, i.e. Young modulus Y_c and Poisson ratio ν_c, with a procedure similar to what explained in [32, 52] and in [57] and to what was done in analyzing the samples grown by LMA. The measured elastic properties, with their estimation uncertainties, were then used to compute the dilution factors D and extract the coating loss angle according to equation (3). The results are presented in table 6 and figures 18 and 19, and discussed in section 4.5.

4.4. HiPIMS/RF-MS

Coating mechanical loss, Young modulus Y_c and Poisson ratio ν_c were measured on suspended coated fused-silica disks by the LIGO Laboratory group at Caltech, using the same setup and analysis methods described in section 4.3.

HiPIMS coating samples with different cation ratios η = Zr/(Zr + Ta) were produced, in order to determine how ZrO_2 content affects the loss angle. Also, as mentioned in section 3.5, RF-MS coating samples were grown with the same Ar:O_2 gas ratio, which had higher oxygen content and hence lower densities and refractive index. Samples were then annealed at increasing peak temperature T_a by steps of 50 and 100 °C, starting from 400 °C, until they showed signs of crystallization. The annealing time for each soaking temperature T_a was 10 h. Depending on the cation ratio, the onset of crystallization was observed at temperatures which ranged from $T_a = 700$°C to $T_a = 850$°C.

Figure 17 presents the coating loss angle as a function of the cation ratio η at 650°C, where it can be seen that most values are overlapping. This means that, within the uncertainties of

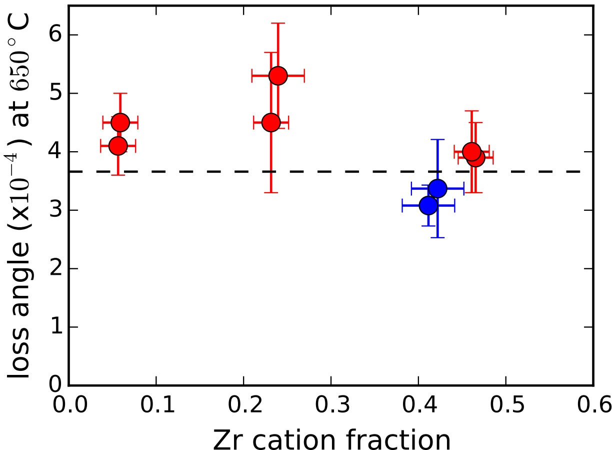

Figure 17. Coating loss of HiPIMS (red markers) and RF-MS (blue markers) Ta_2O_5–ZrO_2 thin films as a function of cation ratio $\eta = $ Zr/(Zr + Ta), as measured on suspended fused-silica disks after annealing at 650 °C. The dashed black line represents the loss angle value of the annealed Ta_2O_5–TiO_2 layers of Advanced LIGO and Advanced Virgo [32].

the measurements, η does not considerably affect the coating loss angle. Although still within measurement uncertainty, however, RF-MS samples feature a slightly lower coating loss angle. Therefore, even if HiPIMS samples were shown to be denser and closer to stoichiometry than RF-MS samples, this did not translate into a decrease of the coating loss angle.

4.5. Comparative summary

We discuss here the effects of different cation ratios $\eta = $ Zr/(Zr + Ta) and annealing peak temperatures T_a on the mechanical loss of our coating samples, limiting our analysis to the results obtained at ambient temperature so that we can compare samples from all the growth techniques presented in this work. To ease comparison, an average coating loss $\overline{\varphi}$ can be taken from every set of measured resonant modes of each sample.

Figure 18 shows the resulting $\overline{\varphi}$ as a function of cation ratio η, where it can be seen that η does not affect significantly the coating mechanical loss. Furthermore, coating loss seems to be fairly independent of the technique used to grow the samples.

The samples were progressively annealed through steps of increasingly high peak temperature T_a to test the effect of annealing on coating loss. For these experiments, the fused silica substrate is typically annealed to temperatures higher than 900 °C before being coated. The high temperature annealing of the bare substrate lowers its mechanical loss ($\varphi_s < 10^{-7}$) such that it is negligible compared to the coating loss. In addition, the substrate loss will not change with lower temperature annealing cycles, so that any change in the coated sample loss may be attributed solely to the coating.

Figure 19 shows that annealing significantly reduced the coating mechanical loss, from about 10^{-3} for as-deposited samples down to (2–4) $\times$ 10^{-4} for samples treated at 800 °C.

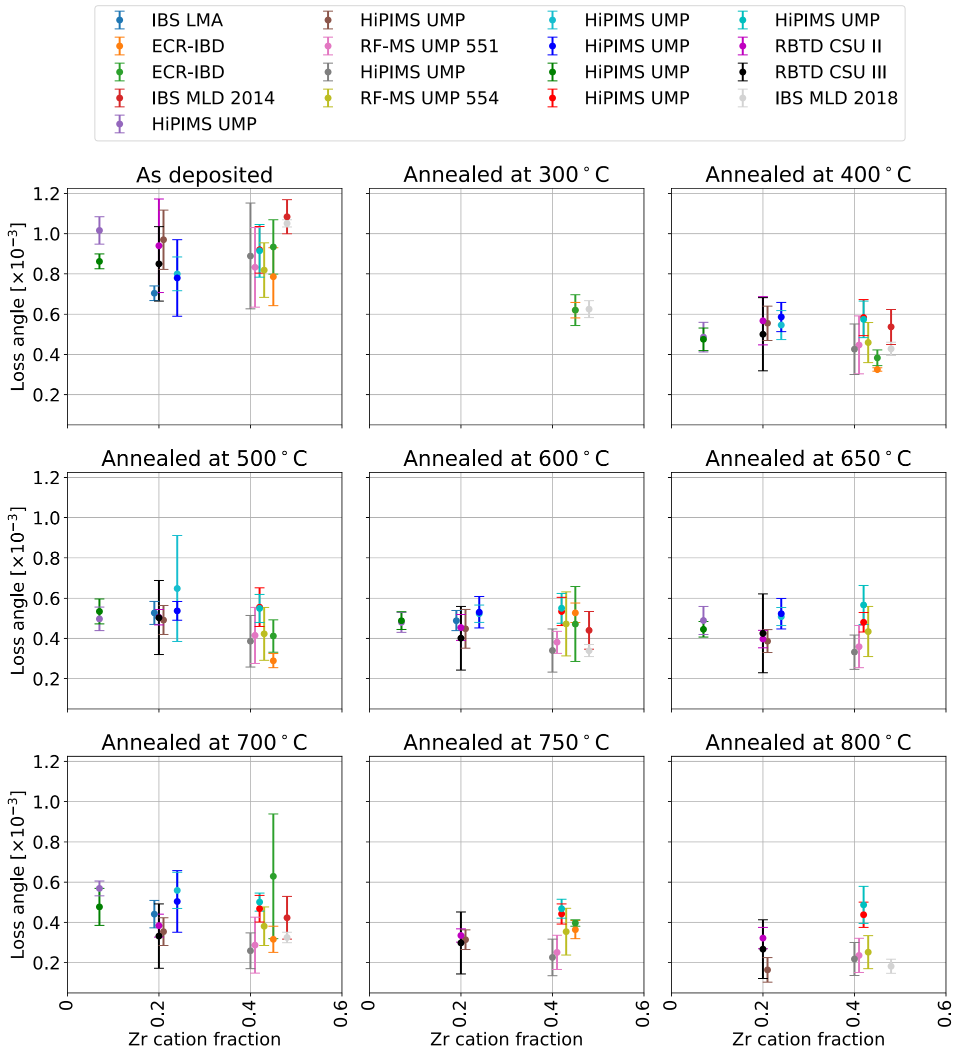

Figure 18. Frequency-averaged coating loss angle $\overline{\varphi}$ of all the Ta_2O_5–ZrO_2 coating samples considered in this work, as a function of cation ratio $\eta = \mathrm{Zr}/(\mathrm{Ta} + \mathrm{Zr})$. Each panel corresponds to a different annealing peak temperature T_a.

5. Effects of annealing

As expected, co-sputtering zirconia proved to be an efficient way to frustrate crystallization in tantala thin films, allowing for a substantial increase of the maximum annealing temperature T_a. Figure 20 shows that higher cation ratios $\eta = \mathrm{Zr}/(\mathrm{Zr} + \mathrm{Ta})$ allowed to increase T_a up to 800 °C, without crystallization occurring. More specifically, IBS samples have been tested up to 800 °C and no sign of crystallization was observed. RBTD sample CSU II ($\eta = 0.23$) was amorphous after treatment at 800 °C. HiPIMS/RF-MS samples showed signs of crystallization for temperatures ranging from 700 to 850 °C, depending on the cation ratio η.

Figures 18 and 19 show that annealing significantly reduced the coating mechanical loss, from about $\overline{\varphi} \sim 10^{-3}$ for the as-deposited samples down to $\overline{\varphi} \sim (2 - 4) \times 10^{-4}$ for the samples

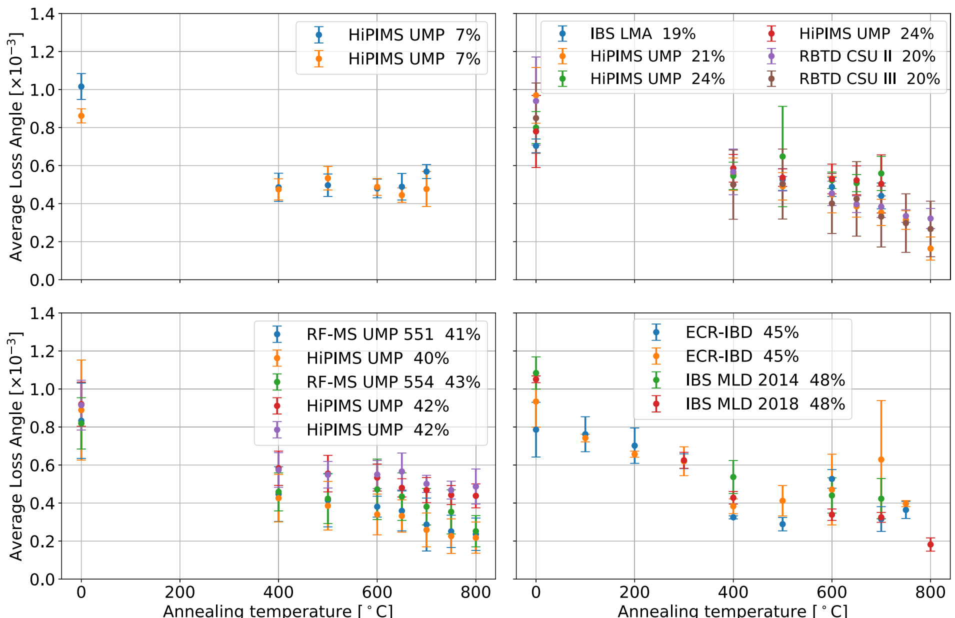

Figure 19. Frequency-averaged coating loss angle $\overline{\varphi}$ of all the Ta_2O_5–ZrO_2 coating samples considered in this work, as a function of the annealing peak temperature T_a (as-deposited samples are denoted by $T_a = 0$°C). The four panels group together different samples with similar cation ratio $\eta = Zr/(Ta + Zr)$.

treated at 800 °C, whereas, within the measurement uncertainties, the doping does not affect the loss angle for a given T_a.

However, cracks appeared on IBS (MLD), RBTD and HiPIMS/RF-MS samples after annealing at 500 °C, and on single-layer IBS samples (LMA) after annealing at 700 °C. By way of example, figure 21 shows the cracks observed on an IBS sample (LMA) with an optical microscope; such cracks covered the whole surface of the sample, and their width was of the order of 10^{-5} m. Likely, this happened because of a mismatch between the thermal expansion coefficients of the thin films and substrates, causing high thermal stress. Although in principle our mechanical loss measurements are sensitive to such defects, we found no evidence that our results were affected. At least for some IBS samples (LMA), we avoided the formation of cracks by decreasing the annealing heating and cooling rates down to 7 °C h^{-1}. Such samples could be annealed up to 800 °C without any cracks forming at their surface.

Nevertheless, starting from $T_a = 500$°C, bubble-like defects of different number and size, detected with an optical microscope, appeared at variable depth in the IBS HR coating samples, likely due to the presence of incorporated argon within the layers [29, 43, 70]. We observed no trace of such defects in the annealed IBS single-layer samples deposited under identical conditions, indicating that this phenomenon only occurs when layers are stacked. It is not clear how to avoid this issue yet, and we are currently working to solve this problem.

At the same time, annealing at $T_a = 500$°C decreased the optical absorption of the IBS HR samples down to 0.5 ppm.

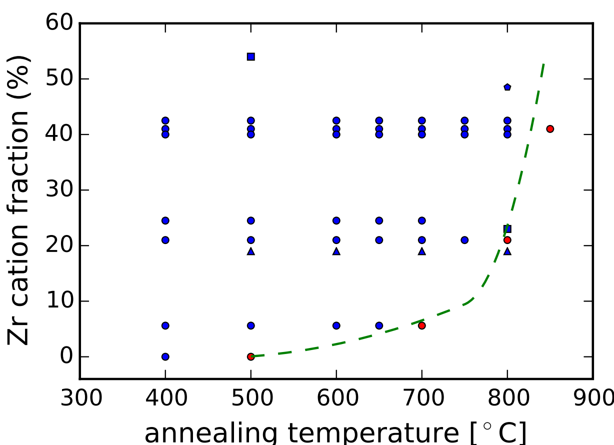

Figure 20. State of IBS, RBTD and HiPIMS/RF-MS Ta_2O_5–ZrO_2 thin films after annealing at temperature T_a, as a function of cation ratio $\eta = Zr/(Ta + Zr)$. Blue markers denote amorphous samples, while red ones indicate that the transition to a polycrystalline phase was observed. RBTD samples are denoted by squares, IBS samples by triangles (LMA) and pentagons (MLD), HiPIMS/RF-MS samples by circles. The dashed curve shows the approximate limit of the phase transition as a function of η.

Figure 21. Cracks observed on an IBS Ta_2O_5–ZrO_2 thin film (LMA) after annealing at $T_a = 700^\circ$C.

6. Raman spectroscopy

Raman spectroscopy probes the vibrational modes of a material constituents. In previous studies on amorphous silicon (a-Si), Roorda *et al* found a correlation between structural relaxation and the width of a peak in its Raman spectrum [51]. A sharpening of the peak was interpreted as the results of a decrease in the bond angle distribution upon annealing. Granata *et al* also

found a correlation between the mechanical loss and the normalized area of a Raman line in IBS and bulk silica [31]. Thus, it is of interest to see if there is a correlation between the Raman spectra of Ta_2O_5–ZrO_2 thin films and their loss angle, via structural relaxation.

Raman spectroscopy was performed on the coated silica disks with a Renishaw Invia Reflex microscope, with an Ar laser at a wavelength of 514 nm. The measurement was performed three times at different locations on each sample, then the spectra of each sample were averaged. It was carried out on all the MS as-deposited samples and on seven MS samples after annealing at 800 °C. Note that two of these annealed samples showed signs of crystallization, with significant change in the coating Young modulus and loss angle measurements (see table 6 and sections 4.4 and 4.5). Figure 22(a) presents an example of the Raman spectrum measured on a crystallized sample, where the arrows identify peaks associated with the crystal phase [45].

Tantala–zirconia has a complex structure, which translates into several peaks in the Raman spectrum, some of them overlapping, and makes the data analysis non-trivial. In addition, Ta_2O_5–ZrO_2 thin films are transparent at 514 nm, so that peaks from the underlying silica substrate also contribute to the measured spectra. Therefore, the initial step of the analysis was to decorrelate the contribution of the thin film from that of the substrate. Figure 22(a) shows a Raman spectrum of an amorphous sample (red curve), with, superimposed, a model (black) resulting from different contributions summed together: (i) the spectrum of a bare silica substrate (blue), (ii) the spectrum of a pure tantala thin film (green) obtained from a previous study [55], (iii) a background contribution represented by an exponential (dashed gray), (iv) additional contributions required so that the model correctly fit the data (purple), which are then assumed to be due to the addition of zirconia and which were modeled using four Lorentzian functions. Thanks to this model, we can identify where the thin film is the main contributor to the measured spectrum: referring to the purple curve of figure 22(a), this can be seen to happen in the interval from 600 to 750 cm^{-1}. An additional contribution from the thin film is observed near 900 cm^{-1}, but is less clearly separated from the substrate signal and was disregarded in the following analysis.

Next, we wanted to estimate the width of the Raman peak attributed to the thin film. However, trying to subtract substrate contributions or using a fit model would likely influence the shape of the peak, hence its width. To avoid this, we rather relied directly on the experimental data: we calculated the maximum slope of the raw signal on one side of the peak, at a location where the coating contribution to the spectrum is dominant. Indeed, the slope of a peak edge is a proxy for the peak width: for both Lorentzian and Gaussian functions, the maximum slope is proportional to the inverse squared width. Thus narrower peaks, which might be attributed to a more relaxed material, should feature a steeper slope on each side. To this end, the raw spectra were smoothed with a bi-cubic spline and normalized so that their maximum, in the 550 cm^{-1} to 750 cm^{-1} spectral region, where the contribution of the thin film is at the highest, is at unity. We then computed the derivative, an example of the result is found in figure 22(b).

In all panels of figure 22, the position of interest, i.e. the point where the slope of the signal related to the Zr contribution is the steepest, is represented by a vertical red line. In figure 22(c), we can see two raw spectra of the same sample, acquired before and after annealing. The slope computed using the spline fit at the Raman shift of interest is also plotted as a straight line, for each spectrum. We can observe from the raw data that the slope around 705 cm^{-1} changes upon annealing and is well represented by the first derivative deduced from the method illustrated in figure 22(b). If Raman peaks sharpen with relaxation, and relaxation decreases the loss angle, we expect a higher value of the derivative with decreasing loss angle.

Figure 23 shows the absolute value of the first derivative around 705 cm^{-1} as a function of the loss angle, where the color scale represent the cation ratio $\eta = \mathrm{Zr}/(\mathrm{Zr} + \mathrm{Ta})$. The red markers correspond to the two crystallized samples which show characteristic peaks in their

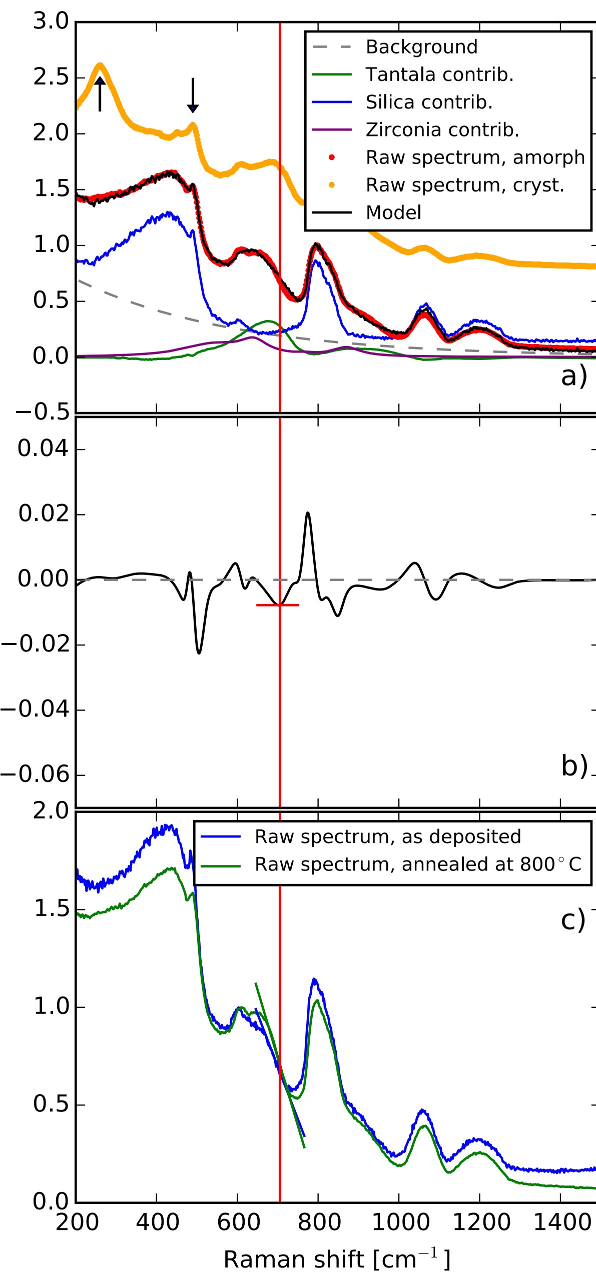

Figure 22. Measured Raman spectra of HiPIMS/RF-MS Ta_2O_5–ZrO_2 thin films and their analysis: (a) example of a spectrum obtained for an amorphous sample with, superimposed, a model resulting from different contributions summed together (see text for details); (b) derivative of the raw Raman spectrum, smoothed using bi-cubic splines; (c) raw, normalized spectrum of the same sample, as-deposited and annealed. The slopes extracted using the derivative method shown in (b) are represented by straight lines. The vertical red line across all panels is the position of the minimum of the first derivative of the Zr contribution shown in (a).

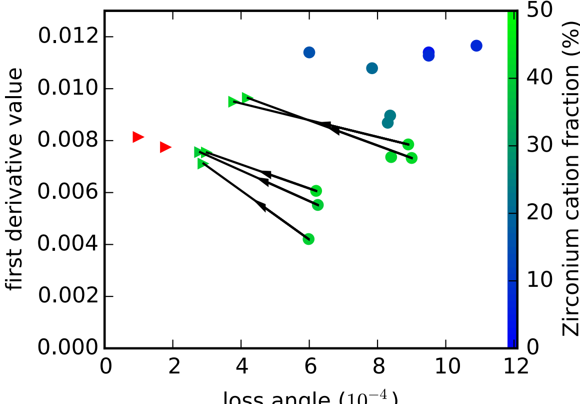

Figure 23. Absolute value of the minimum of the derivative of the Raman spectrum near 705 cm^{-1} as a function of the loss angle, for HiPIMS/RF-MS Ta_2O_5–ZrO_2 thin films. The color scale corresponds to the cation ratio $\eta = \mathrm{Zr}/(\mathrm{Zr} + \mathrm{Ta})$, circles denote spectra acquired on the as-deposited samples and triangles denote those acquired on the annealed samples, the same sample being linked by a black arrow. Red markers represent samples showing signs of crystallization.

Raman spectrum, and most probably some delamination, making their loss angle measurements unreliable. The circles are for measurements carried out on as-deposited samples while the triangles are for the annealed ones, and the same samples are linked by an arrow pointing toward the annealed one.

Figure 23 clearly shows that, upon annealing, each individual sample sees its peak slope increase and its loss angle decrease at the same time. Hence, the Raman peak sharpens upon relaxation, similar to what is observed in a-Si [51]. However, if one considers only the subset of the as-deposited samples (circles), it appears that the lower the loss angle, the lower the slope, which means the Raman peaks are wider. Also, samples that have the lowest loss angle are the ones with the highest cation ratio η (greener data points). Hence, the shape of the Raman peak near 705 cm^{-1} cannot be attributed solely to relaxation, as it is also clearly influenced by the micro-structural modifications that large amounts of Zr induce into the thin films, which in turn have an impact on the vibrational states distribution and hence on the shape of the Raman spectrum.

Therefore, these results show that Raman spectroscopy could be used as a probe to monitor the relaxation state of tantala-based alloys, and that relaxation is linked to the loss angle. Similar conclusions were reached using x-ray diffraction on tantala [55], where the x-ray peak of tantala sharpened with decreasing loss angle. However, the Raman peak shape is also influenced by the amount of doping, so while it can be used to monitor the evolution of a specific sample, it would be difficult to use it more generally as a probe of the state of relaxation in a material or a predictor of the loss angle.

7. Summary and conclusions

In order to decrease coating Brownian noise in current GW detectors, we developed a set of co-sputtered tantala–zirconia thin films. We extensively characterized these coatings for optical

and mechanical properties, to test their performances against the very stringent requirements of GW detectors.

As expected, co-sputtering zirconia proved to be an efficient way to frustrate crystallization in tantala thin films, allowing for a substantial increase of the maximum annealing temperature T_a, hence for a decrease of coating mechanical loss. The lowest average loss, $\overline{\varphi}_c = 1.8 \times 10^{-4}$ rad, was measured on IBS sample MLD2018 with cation ratio Zr/(Ta + Zr) = $48.5 \pm 0.4\%$ annealed at 800 °C. Higher annealing temperatures were prevented by the onset of crystallization.

The lowest loss value measured on co-sputtered tantala–zirconia thin films has to be compared to $\varphi_c = (2.3\text{–}3.4) \times 10^{-4}$ rad of tantala–titania layers in current GW detectors [32, 82], and to other high-index oxide coatings, either simple or co-sputtered [29, 33, 59–62]. Further coating loss reduction, down to 1×10^{-4} rad or lower, might be obtained with non-oxide coatings [33].

As measured on IBS HR samples with the same design of those of Advanced LIGO and Advanced Virgo, we observed as little optical absorption (0.5 ppm) as in current GW detectors [27, 46]. The same samples, however, featured an unusually high value of scattering, 45 ppm, compared to that of present detectors (5 ppm) [27, 46]. Indeed, part of the observed excess scatter might be ascribed to the presence of Ar bubbles formed upon annealing [29, 43, 70].

For some samples, we measured a refractive index at 1064 and 1550 nm higher than that of pure tantala thin films. This implies that HR stacks containing zirconia-doped tantala layers could be even thinner than HR coatings of present detectors, further decreasing coating Brownian noise [33].

For use in future GW detectors, further development will be needed to decrease scattering and to avoid the formation of bubble-like defects upon annealing. We are currently working to find appropriate solutions to these issues.

Acknowledgments

The research performed at the Laboratoire des Matériaux Avancés was partially supported by the Virgo Coating Research and Development (VCR & D) Collaboration. The work performed at Université de Montréal and École Polytechnique de Montréal was supported by the Natural Sciences and Engineering Research Council of Canada (NSERC), the Canadian foundation for innovation (CFI) and the Fonds de recherche Québec, Nature et technologies (FQRNT) through the Regroupement Québécois sur les matériaux de pointe (RQMP). These authors thank S Roorda, M Chicoine, L Godbout and F Turcot for fruitful discussions and technical support. The work performed at the University of Glasgow was supported by the Science and Technology Facilities Council (STFC, ST/N005422/1 and ST/I001085/1) and the Royal Society (UF100602 and UF150694). The research performed at Hobart and William Smith Colleges was supported by National Science Foundation Grant awards PHY-1307423, PHY-1611821, and PHY-1707863.

Data availability statement

The data that support the findings of this study are available upon reasonable request from the authors.

ORCID iDs

M Abernathy https://orcid.org/0000-0001-9805-4311
A Amato https://orcid.org/0000-0001-9557-651X
R Bassiri https://orcid.org/0000-0001-8171-6833
M Canepa https://orcid.org/0000-0002-5148-1233
A Di Michele https://orcid.org/0000-0002-0357-2608
M A Fazio https://orcid.org/0000-0002-9057-9663
M Granata https://orcid.org/0000-0003-3275-1186
A M Gretarsson https://orcid.org/0000-0003-3438-9926
E J Hough https://orcid.org/0000-0003-3242-3123
I W Martin https://orcid.org/0000-0001-7300-9151
B Maynard https://orcid.org/0000-0003-4799-1545
P G Murray https://orcid.org/0000-0002-8218-2404
S Penn https://orcid.org/0000-0003-4956-0853
S Rowan https://orcid.org/0000-0002-0666-9907
F Schiettekatte https://orcid.org/0000-0002-2112-9378
G Vajente https://orcid.org/0000-0002-7656-6882

References

[1] Callen H B and Welton T A 1951 Irreversibility and generalized noise *Phys. Rev.* **83** 34–40
[2] Oliver W C and Pharr G M 1992 An improved technique for determining hardness and elastic modulus using load and displacement sensing indentation experiments *J. Mater. Res.* **7** 1564
[3] Çetinörgü E, Baloukas B, Zabeida O, Klemberg-Sapieha J E and Martinu L 2009 Mechanical and thermoelastic characteristics of optical thin films deposited by dual ion beam sputtering *Appl. Opt.* **48** 4536
[4] Ceresoli D and Vanderbilt D 2006 Structural and dielectric properties of amorphous ZrO_2 and HfO_2 *Phys. Rev.* B **74** 125108
[5] Penn S D 2006 Frequency and surface dependence of the mechanical loss in fused silica *Phys. Lett.* A **352** 3–6
[6] Jellison G E and Modine F A 1996 Parameterization of the optical functions of amorphous materials in the interband region *Appl. Phys. Lett.* **69** 371
[7] Aasi J *et al* 2015 Advanced LIGO *Class. Quantum Grav.* **32** 074001
[8] Abbott B P *et al* 2016 Binary black hole mergers in the first advanced LIGO observing run *Phys. Rev.* X **6** 041015
[9] Abbott B P *et al* 2016 Observation of gravitational waves from a binary black hole merger *Phys. Rev. Lett.* **116** 061102
[10] Abbott B P *et al* 2017 GW170817: observation of gravitational waves from a binary neutron star inspiral *Phys. Rev. Lett.* **119** 161101
[11] Abbott B P *et al* 2017 Multi-messenger observations of a binary neutron star merger *Astrophys. J.* **848** L12
[12] Abbott B P *et al* 2018 GW170817: measurements of neutron star radii and equation of state *Phys. Rev. Lett.* **121** 161101
[13] Abbott B P *et al* 2019 GWTC-1: a gravitational-wave transient catalog of compact binary mergers observed by LIGO and Virgo during the first and second observing runs *Phys. Rev.* X **9** 031040
[14] Abbott B P *et al* 2021 GWTC-2: compact binary coalescences observed by LIGO and Virgo during the first half of the third observing run *Phys. Rev.* X **11** 021053
[15] Acernese F *et al* 2014 Advanced Virgo: a second-generation interferometric gravitational wave detector *Class. Quantum Grav.* **32** 024001
[16] Alexandrovski A *et al* 2009 Photothermal common-path interferometry (pci): new developments *Solid State Lasers XVIII: Technology and Devices* vol 7193 (Bellingham, WA: SPIE Optical Engineering Press) p 71930D

[17] Amato A *et al* 2018 High-reflection coatings for gravitational-wave detectors: state of the art and future developments *J. Phys.: Conf. Ser.* **957** 012006

[18] Amato A *et al* 2019 Optical properties of high-quality oxide coating materials used in gravitational-wave advanced detectors *J. Phys. Mater.* **2** 035004

[19] Amato A *et al* 2020 Observation of a correlation between internal friction and urbach energy in amorphous oxides thin films *Sci. Rep.* **10** 1670

[20] Birney R *et al* 2018 Amorphous silicon with extremely low absorption: beating thermal noise in gravitational astronomy *Phys. Rev. Lett.* **121** 191101

[21] Boccara A C, Jackson W, Amer N M and Fournier D 1980 Sensitive photothermal deflection technique for measuring absorption in optically thin media *Opt. Lett.* **5** 377

[22] Bräuer G, Szyszka B, Vergöhl M and Bandorf R 2010 Magnetron sputtering—milestones of 30 years *Vacuum* **84** 1354

[23] Buikema A *et al* 2020 Sensitivity and performance of the Advanced LIGO detectors in the third observing run *Phys. Rev.* D **102** 062003

[24] Cagnoli G *et al* 2018 Mode-dependent mechanical losses in disc resonators *Phys. Lett.* A **382** 2165

[25] Cesarini E, Lorenzini M, Campagna E, Martelli F, Piergiovanni F, Vetrano F, Losurdo G and Cagnoli G 2009 A ‘gentle’ nodal suspension for measurements of the acoustic attenuation in materials *Rev. Sci. Instrum.* **80** 053904

[26] Danilishin S L and Khalili F Y 2012 Quantum measurement theory in gravitational-wave detectors *Living Rev. Relativ.* **15** 5

[27] Degallaix J *et al* 2019 Large and extremely low loss: the unique challenges of gravitational wave mirrors *J. Opt. Soc. Am.* A **36** C85

[28] Evans M, Ballmer S, Fejer M, Fritschel P, Harry G and Ogin G 2008 Thermo-optic noise in coated mirrors for high-precision optical measurements *Phys. Rev.* D **78** 102003

[29] Fazio M A, Vajente G, Ananyeva A, Markosyan A, Bassiri R, Fejer M M and Menoni C S 2020 Structure and morphology of low mechanical loss TiO_2-doped Ta_2O_5 *Opt. Mater. Express* **10** 1687

[30] Granata M *et al* 2016 Mechanical loss in state-of-the-art amorphous optical coatings *Phys. Rev.* D **93** 012007

[31] Granata M *et al* 2018 Correlated evolution of structure and mechanical loss of a sputtered silica film *Phys. Rev. Mater.* **2** 053607

[32] Granata M *et al* 2020 Amorphous optical coatings of present gravitational-wave interferometers *Class. Quantum Grav.* **37** 095004

[33] Granata M *et al* 2020 Progress in the measurement and reduction of thermal noise in optical coatings for gravitational-wave detectors *Appl. Opt.* **59** A229

[34] Hála M, Vernhes R, Zabeida O, Bousser E, Klemberg-Sapieha J E, Sargent R and Martinu L 2014 Growth and properties of high index Ta_2O_5 optical coatings prepared by HiPIMS and other methods *Surf. Coat. Technol.* **241** 33

[35] Hála M, Vernhes R, Zabeida O, Klemberg-Sapieha J-E and Martinu L 2014 Reactive HiPIMS deposition of SiO_2/Ta_2O_5 optical interference filters *J. Appl. Phys.* **116** 213302

[36] Harry G M *et al* 2002 Thermal noise in interferometric gravitational wave detectors due to dielectric optical coatings *Class. Quantum Grav.* **19** 897

[37] Harry G M *et al* 2006 Titania-doped tantala/silica coatings for gravitational-wave detection *Class. Quantum Grav.* **24** 405

[38] Klemberg-Sapieha J E *et al* 2004 Mechanical characteristics of optical coatings prepared by various techniques: a comparative study *Appl. Opt.* **43** 2670

[39] Martin I W *et al* 2010 Effect of heat treatment on mechanical dissipation in Ta_2O_5 coatings *Class. Quantum Grav.* **27** 225020

[40] Miller J *et al* 2015 Prospects for doubling the range of Advanced LIGO *Phys. Rev.* D **91** 062005

[41] Murray P *et al* 2021 Mechanical loss reduction from crystallization in a Ta_2O_5–TiO_2 film (in preparation)

[42] Nakagawa N, Gretarsson A M, Gustafson E K and Fejer M M 2002 Thermal noise in half-infinite mirrors with nonuniform loss: a slab of excess loss in a half-infinite mirror *Phys. Rev.* D **65** 102001

[43] Paolone A *et al* 2021 Effects of the annealing of amorphous Ta_2O_5 coatings produced by ion beam sputtering concerning the effusion of argon and the chemical composition *J. Non-Cryst. Solids* **557** 120651

[44] Penn S D *et al* 2003 Mechanical loss in tantala/silica dielectric mirror coatings *Class. Quantum Grav.* **20** 2917
[45] Perez I, Carrejo J L E, Sosa V, Perera F G, Mancillas J R F, Galindo J T E and Rodríguez C I R 2017 Evidence for structural transition in crystalline tantalum pentoxide films grown by RF magnetron sputtering *J. Alloys Compd.* **712** 303
[46] Pinard L *et al* 2017 Mirrors used in the LIGO interferometers for first detection of gravitational waves *Appl. Opt.* **56** C11
[47] Prato M, Chincarini A, Gemme G and Canepa M 2011 Gravitational waves detector mirrors: spectroscopic ellipsometry study of Ta_2O_5 films on SiO_2 substrates *Thin Solid Films* **519** 2877
[48] Punturo M *et al* 2010 The Einstein telescope: a third-generation gravitational wave observatory *Class. Quantum Grav.* **27** 194002
[49] Reid S *et al* 2006 Mechanical dissipation in silicon flexures *Phys. Lett.* A **351** 205–11
[50] Reitze D *et al* 2019 Cosmic explorer: the U.S. contribution to gravitational-wave astronomy beyond LIGO (arXiv:1907.04833)
[51] Roorda S, Sinke W C, Poate J M, Jacobson D C, Dierker S, Dennis B S, Eaglesham D J, Spaepen F and Fuoss P 1991 Structural relaxation and defect annihilation in pure amorphous silicon *Phys. Rev.* B **44** 3702
[52] Tianjun L *et al* 2014 Measurements of mechanical thermal noise and energy dissipation in optical dielectric coatings *Phys. Rev.* D **89** 092004
[53] Travasso F, Amico P, Bosi L, Cottone F, Dari A, Gammaitoni L, Vocca H and Marchesoni F 2007 Low-frequency internal friction in silica glass *Europhys. Lett.* **80** 50008
[54] Vajente G, Ananyeva A, Billingsley G, Gustafson E, Heptonstall A, Sanchez E and Torrie C 2017 A high throughput instrument to measure mechanical losses in thin film coatings *Rev. Sci. Instrum.* **88** 073901
[55] Vajente G *et al* 2018 Effect of elevated substrate temperature deposition on the mechanical losses in tantala thin film coatings *Class. Quantum Grav.* **35** 075001
[56] Vajente G *et al* 2019 Chapter three—precision interferometry for gravitational wave detection: current status and future trends *Advances in Atomic, Molecular, and Optical Physics* vol 68 ed L F Dimauro, H Perrin and S F Yelin (New York: Academic) p 75
[57] Vajente G *et al* 2020 Method for the experimental measurement of bulk and shear loss angles in amorphous thin films *Phys. Rev.* D **101** 042004
[58] Villar A E *et al* 2010 Measurement of thermal noise in multilayer coatings with optimized layer thickness *Phys. Rev.* D **81** 122001
[59] Yang L, Randel E, Vajente G, Ananyeva A, Gustafson E, Markosyan A, Bassiri R, Fejer M M and Menoni C S 2019 Investigation of effects of assisted ion bombardment on mechanical loss of sputtered tantala thin films for gravitational wave interferometers *Phys. Rev.* D **100** 122004
[60] Yang L, Randel E, Vajente G, Ananyeva A, Gustafson E, Markosyan A, Bassiri R, Fejer M and Menoni C 2020 Modifications of ion beam sputtered tantala thin films by secondary argon and oxygen bombardment *Appl. Opt.* **59** A150–4
[61] Yang L *et al* 2020 Structural evolution that affects the room-temperature internal friction of binary oxide nanolaminates: implications for ultrastable optical cavities *ACS Applied Nano Mater.* **3** 12308–13
[62] Yang L *et al* 2021 Enhanced medium range order in vapor deposited germania glasses at elevated temperatures (arXiv:2102.08526)
[63] Zhurin V V, Kaufman H R, Kahn J R and Hylton T L 2000 Biased target deposition *J. Vac. Sci. Technol.* A **18** 37
[64] Fujiwara H 2007 *Spectroscopic Ellipsometry: Principles and Applications* (New York: Wiley)
[65] Arago D F J and Biot J-B 1806 *Memoire sur les affinites des corps pour la lumiere: et particulierement sur les forces refringentes des differens gaz* (Paris: Bachelier)
[66] Trinastic J personal communication
[67] Tewg J-Y, Kuo Y and Lu J 2005 Suppression of crystallization of tantalum oxide thin film by doping with zirconium *Electrochem. Solid State Lett.* **8** G27
[68] Chu W K 1978 *Backscattering Spectrometry* (New York: Academic) (https://doi.org/10.1016/B978-0-121-73850-1.X5001-7)
[69] Wood D L and Nassau K 1982 Refractive index of cubic zirconia stabilized with yttria *Appl. Opt.* **21** 2978
[70] Cevro M and Carter G 1995 Ion-beam and dual-ion-beam sputter deposition of tantalum oxide films *Opt. Eng.* **34** 596

[71] Fairley M 2005 http://www.casaxps.com
[72] Fejer M M 2016 Thermal noise in mirror coatings for gravitational wave detection *Optical Interference Coatings 2016* (Optical Society of America) p MB.1
[73] Gretarsson E M and Gretarsson A M 2018 Three methods for characterizing thermo-optic noise in optical cavities *Phys. Rev.* D **98** 122004
[74] Mayer M 1999 SIMNRA, a simulation program for the analysis of NRA, RBS and ERDA *AIP Conf. Proc.* **475** 541
[75] Kaiser N and Pulker H K 2003 *Optical Interference Coatings* (Berlin: Springer)
[76] NIST Standard Reference Database Number 20 2000 https://srdata.nist.gov/xps/
[77] Robie R 2018 Characterisation of the mechanical properties of thin-film mirror coating materials for use in future interferometric gravitational wave detectors *PhD Thesis* University of Glasgow
[78] Saulson P R 1994 *Fundamentals of Interferometric Gravitational Wave Detectors* (Singapore: World Scientific)
[79] Berry B S and Pritchet W C 1975 Vibrating reed internal friction apparatus for films and foils *IBM J. Res. Dev.* **19** 334
[80] Ferlauto A S, Ferreira G M, Pearce J M, Wronski C R, Collins R W, Deng X and Ganguly G 2002 Analytical model for the optical functions of amorphous semiconductors from the near-infrared to ultraviolet: applications in thin film photovoltaics *J. Appl. Phys.* **92** 2424
[81] Gilroy K S and Phillips W A 1981 An asymmetric double-well potential model for structural relaxation processes in amorphous materials *Phil. Mag.* B **43** 735
[82] Gras S and Evans M 2018 Direct measurement of coating thermal noise in optical resonators *Phys. Rev.* D **98** 122001
[83] Nowick A S and Berry B S 1972 *Anelastic Relaxation in Crystalline Solids* (New York: Academic)
[84] Reid S and Martin I 2016 Development of mirror coatings for gravitational wave detectors *Coatings* **6** 61
[85] Bright T J, Watjen J I, Zhang Z M, Muratore C, Voevodin A A, Koukis D I, Tanner D B and Arenas D J 2013 Infrared optical properties of amorphous and nanocrystalline Ta_2O_5 thin films *J. Appl. Phys.* **114** 083515
[86] Hong T 2013 Brownian thermal noise in multilayer coated mirrors *Phys. Rev.* D **87** 082001

A PUBLICATION FOR THE VACUUM COATING INDUSTRY FALL/WINTER 2022

BULLETIN

As seen in the Fall/Winter 2022 SVC Bulletin

Developing Optical Coatings for Gravitational Wave Detectors and Laser Optics using Next Generation Ion Beam Deposition Technique

By Chalisa Gier[1], Stuart Reid[1], Marwa Ben-Yaala[1], Svetoslava Angelova[1], Ross Birney[1,2], Paul Hill[1], Jim Hough[3], Iain Martin[3], Peter Murray[3], Sheila Rowan[3], Simon Tait[3], Gavin Wallace[1], Callum Wiseman[1]

[1]University of Strathclyde, Glasgow, United Kingdom

[2]University of the West of Scotland, Paisley, United Kingdom

[3]University of Glasgow, Glasgow, United Kingdom

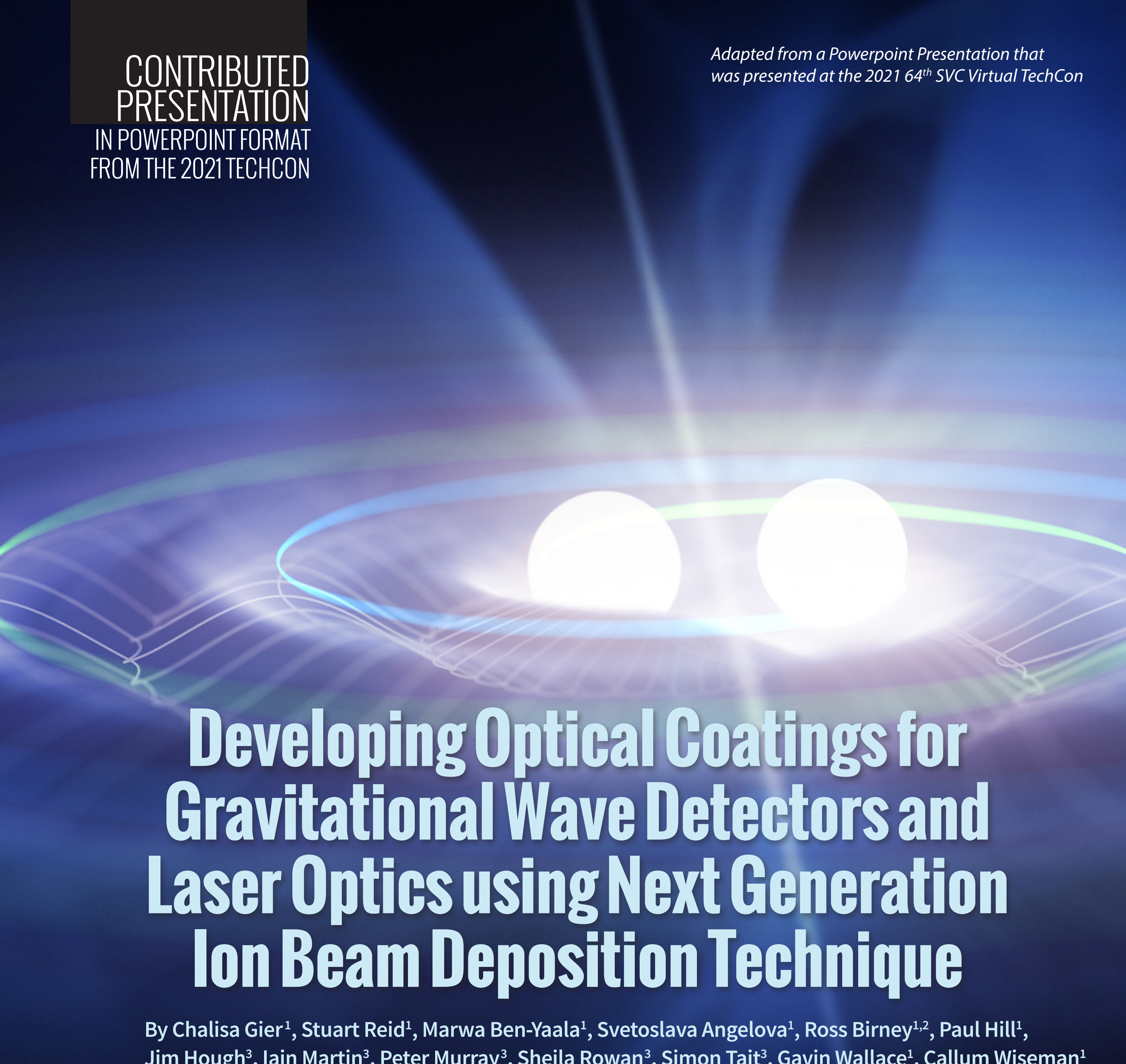

CONTRIBUTED PRESENTATION
IN POWERPOINT FORMAT
FROM THE 2021 TECHCON

Adapted from a Powerpoint Presentation that was presented at the 2021 64th SVC Virtual TechCon

Developing Optical Coatings for Gravitational Wave Detectors and Laser Optics using Next Generation Ion Beam Deposition Technique

By Chalisa Gier[1], Stuart Reid[1], Marwa Ben-Yaala[1], Svetoslava Angelova[1], Ross Birney[1,2], Paul Hill[1], Jim Hough[3], Iain Martin[3], Peter Murray[3], Sheila Rowan[3], Simon Tait[3], Gavin Wallace[1], Callum Wiseman[1]

[1]University of Strathclyde, Glasgow, United Kingdom;
[2]University of the West of Scotland, Paisley, United Kingdom;
[3]University of Glasgow, Glasgow, United Kingdom

Ion beam deposition (IBD) is a method generally used for the fabrication of Bragg reflectors with extremely low levels of optical loss. Gravitational wave detector mirrors are one example which requires high-reflectivity, through use of multilayer dielectric coatings, that require sub-ppm absorption over large area. Although, the Brownian thermal noise of typical coating materials, due to the mechanical dissipation, remains too high to allow future gravitational wave detectors to reach their quantum-limited sensitivities.

Therefore, the University of Strathclyde have developed a new IBD process to extend the available parameter range during manufacture, along with providing additional potential benefits. This technique utilized electron cyclotron resonance (ECR) plasma generation, alongside an extraction geometry which yields a cleaner and more precisely controlled extraction for generating an energetic ion beam for sputtering. This technique has been used to fabricate the lowest optical absorption amorphous silicon in the world; k = 1.2 x 10-5 at 1550 nm – a factor of 100 lower than standard RF-IBD. This talk will describe a new scaled-up deposition system being commissioned, with 6 independent ECR sources, enabling unique opportunities for developing novel alloys such as ultra-stable glasses. Relevance for other applications requiring ultra-low optical loss and high laser-induced damage threshold are discussed, along with the results obtained by manipulating the deposition parameters and the effect it has on the coatings' optical properties.

Note from Managing Editor: We are delighted to share with the readers of the Bulletin some of the interesting Powerpoint Presentations from past TechCons. We hope you find them as interesting as we do.

Sue Taube/Managing Editor

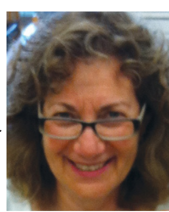

TechCon 2021 *Virtual*

64th Annual Technical Conference Proceedings Virtual Event: May 3 – 7, 2021
© 2021 Society of Vacuum Coaters all rights reserved ISSN 0737-5921, ISBN 978-1-878068-41-5

Developing Optical Coatings for Gravitational Wave Detectors and Laser Optics using Next Generation Ion Beam Deposition Technique

Chalisa Gier[1], Stuart Reid[1], Marwa Ben-Yaala[1], Svetoslava Angelova[1], Ross Birney[1,2], Paul Hill[1], Jim Hough[3], Iain Martin[3], Peter Murray[3], Sheila Rowan[3], Simon Tait[3], Gavin Wallace[1], Callum Wiseman[1]
[1]University of Strathclyde, Glasgow, United Kingdom; [2]University of the West of Scotland, Paisley, United Kingdom; [3]University of Glasgow, Glasgow, United Kingdom

Ion beam deposition (IBD) is a method generally used for the fabrication of Bragg reflectors with extremely low levels of optical loss. Gravitational wave detector mirrors are one example which requires high-reflectivity, through use of multilayer dielectric coatings, that require sub-ppm absorption over large area. Although, the Brownian thermal noise of typical coating materials, due to the mechanical dissipation, remains too high to allow future gravitational wave detectors to reach their quantum-limited sensitivities. Therefore, the University of Strathclyde have developed a new IBD process to extend the available parameter range during manufacture, along with providing additional potential benefits. This technique utilized electron cyclotron resonance (ECR) plasma generation, alongside an extraction geometry which yields a cleaner and more precisely controlled extraction for generating an energetic ion beam for sputtering. This technique has been used to fabricate the lowest optical absorption amorphous silicon in the world; k = 1.2 x 10^{-5} at 1550 nm – a factor of 100 lower than standard RF-IBD. This talk will describe a new scaled-up deposition system being commissioned, with 6 independent ECR sources, enabling unique opportunities for developing novel alloys such as ultra-stable glasses. Relevance for other applications requiring ultra-low optical loss and high laser-induced damage threshold are discussed, along with the results obtained by manipulating the deposition parameters and the effect it has on the coatings' optical properties.

www.svc.org https://doi.org/10.14332/svc21.proc.0047

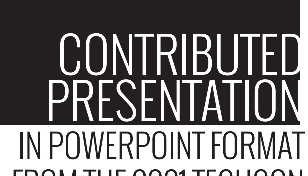

IN POWERPOINT FORMAT
FROM THE 2021 TECHCON

DEVELOPING OPTICAL COATINGS FOR GRAVITATIONAL WAVE DETECTORS AND LASER OPTICS USING NEXT GENERATION ION BEAM DEPOSITION TECHNIQUE

Outline

- Introduction
  - Our group
  - Laser Optics
  - Gravitational Waves & it's Detectors
- Technique
  - Ion Beam Deposition
  - Electron Cyclotron Resonance (ECR) Ion Source
- Set-up
  - RF Ion Beam Deposition
  - ECR Ion Beam Deposition
  - Characterisation
- Objectives
- Results
- Conclusion & Outlook

1. Introduction

Our Group
Laser Optics
Gravitational Waves & its Detectors

Our Group

Professor Stuart Reid
Group Leader &
Head of the Department

Chalisa Gier &
Dr. Marwa Ben Yaala
ECR-IBD for High Laser Damage Threshold Optical Coatings
ECR-IBD Coatings for GW Mirrors

Dr. Paul Hill &
Gavin Wallace
RF-IBD Mirror Coatings & Mechanical Loss Measurements for GWD

Callum Wiseman
Piezoelectric Coatings for Sensors
DLC Coatings for Biomedical Applications

Curtis Talbot
Thermal Annealing Impact on Optical Performance of Oxide Coatings

Optical Coatings for High Power Laser Optics

- High-power thin film optical coatings
  - Required for optics that must handle sustained high-power output from lasers
- The optical coating is generally the limiting factor in the output of a high-power laser system
- Hence, there is an increased requirement for coatings with high damage threshold

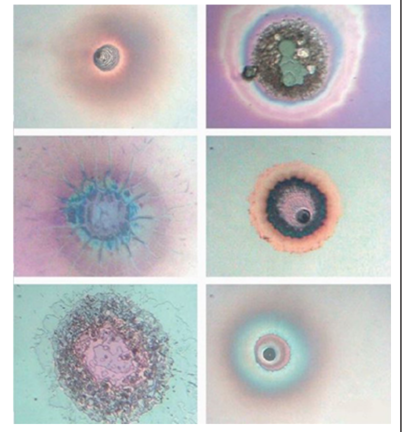

Gravitational Wave Detectors

High demanding key requirements for optical coatings:

- Very low absorption and scattering losses
- High reflectivity
- Low-loss dielectric mirrors

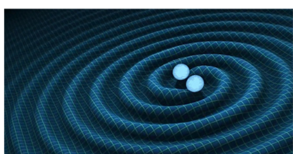

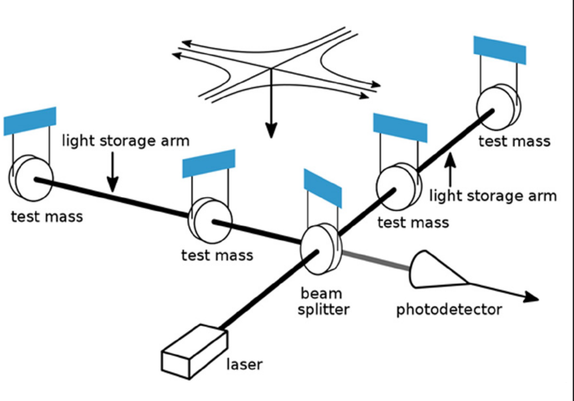

2. Technique

Ion Beam Deposition
Electron Cyclotron Resonance (ECR) Ion Source

DEVELOPING OPTICAL COATINGS FOR GRAVITATIONAL WAVE DETECTORS AND LASER OPTICS USING NEXT GENERATION ION BEAM DEPOSITION TECHNIQUE

Ion Beam Deposition

- Gas Injected
- Ionised Atoms
- Accelerated the created atoms
- Sputter the target
- Deposit on substrate

Ion beam
Ion Source
Target
Substrate

IBD: Highest quality optical coatings, with low absorption and scatter. Optical values close to those of bulk materials.

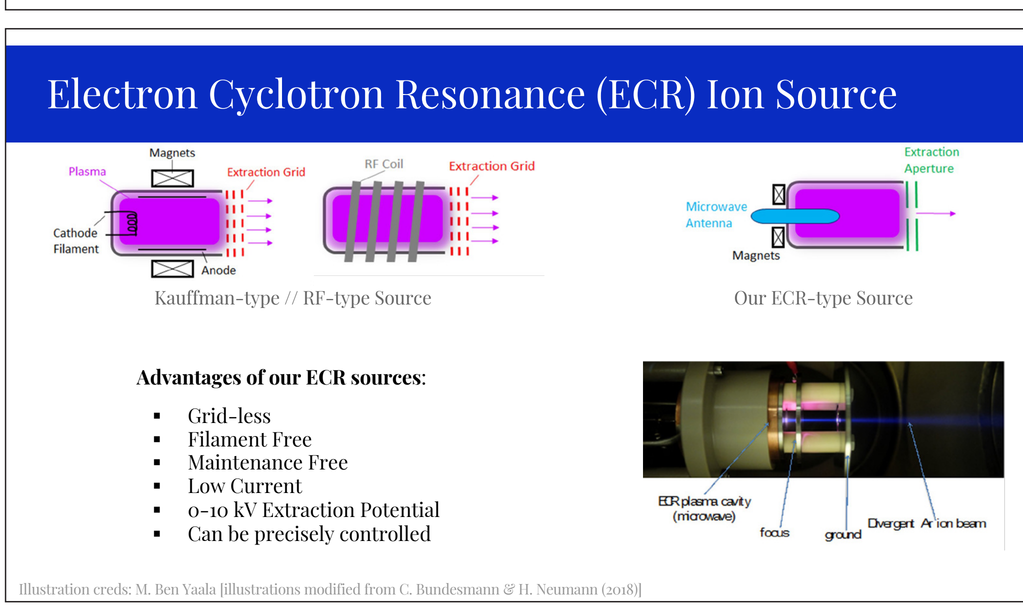

3. Set-up at Strathclyde University

RF-IBD
ECR-IBD
Characterisation

RF-IBD

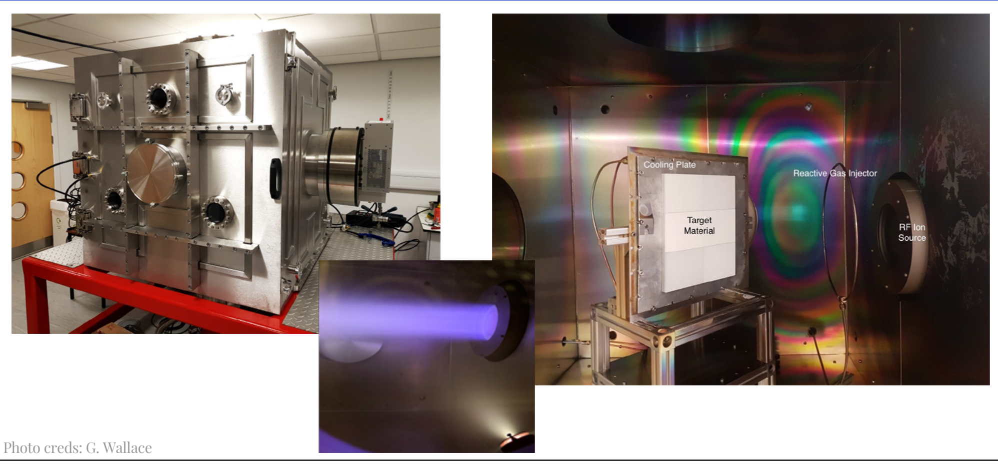

Photo creds: G. Wallace

Extreme Performance Optical coatings Centre (EPOC)

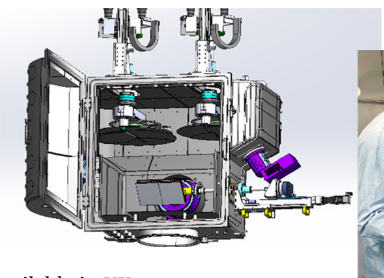

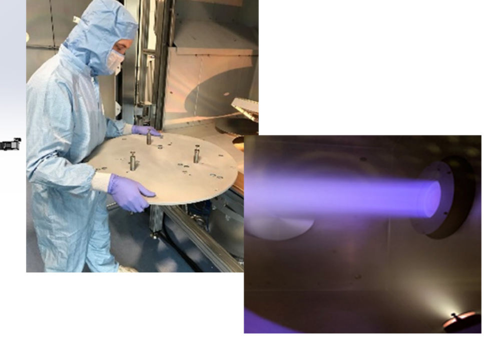

Industry best – unavailable in UK
EPOC aim: make available to UK photonics sector
(+ largest IBD in world)

Large-scale RF ion beam deposition
CEC/Strathclyde/Glasgow/UWS
amorphous coatings for up to 620 mm dia / 200 kg

ECR-IBD

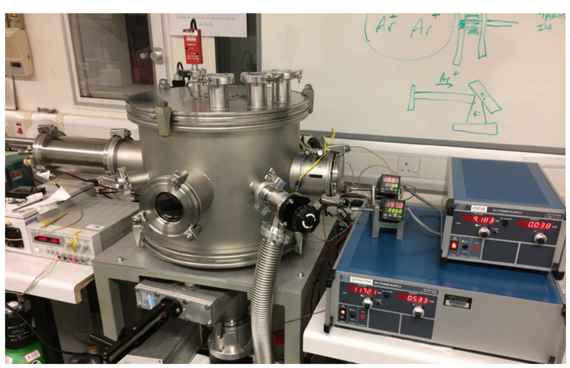

PHYSICAL REVIEW LETTERS **121,** 191101 (2018)

Amorphous Silicon with Extremely Low Absorption: Beating Thermal Noise in Gravitational Astronomy

R. Birney,[1,2,*] J. Steinlechner,[3,4,†] Z. Tornasi,[3] S. MacFoy,[1,2] D. Vine,[2] A. S. Bell,[3] D. Gibson,[2] J. Hough,[3] S. Rowan,[3] P. Sortais,[5] S. Sproules,[6] S. Tait,[3] I. W. Martin,[3] and S. Reid[1,2]

[1]*SUPA, Department of Biomedical Engineering, University of Strathclyde, Glasgow G1 1QE, United Kingdom*
[2]*SUPA, Institute for Thin Films, Sensors and Imaging, University of the West of Scotland, Paisley PA1 2BE, United Kingdom*
[3]*SUPA, Institute for Gravitational Research, University of Glasgow, Glasgow G12 8QQ, United Kingdom*
[4]*Institut für Laserphysik und Zentrum für Optische Quantentechnologien, Universität Hamburg, Luruper Chaussee 149, 22761 Hamburg, Germany*
[5]*Polygon Physics, 30 Chemin de Rochasson, 38240 Meylan, France*
[6]*WestCHEM, School of Chemistry, University of Glasgow, Glasgow G12 8QQ, United Kingdom*

(Received 9 July 2018; revised manuscript received 23 August 2018; published 6 November 2018)

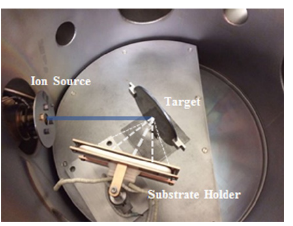

World record for the fabrication of the lowest absorption of amorphous silicon thin films (<20 ppm absorption at 1550 nm) – *Birney et al., PRL 2018*

IN POWERPOINT FORMAT
FROM THE 2021 TECHCON

DEVELOPING OPTICAL COATINGS FOR GRAVITATIONAL WAVE DETECTORS AND LASER OPTICS USING NEXT GENERATION ION BEAM DEPOSITION TECHNIQUE

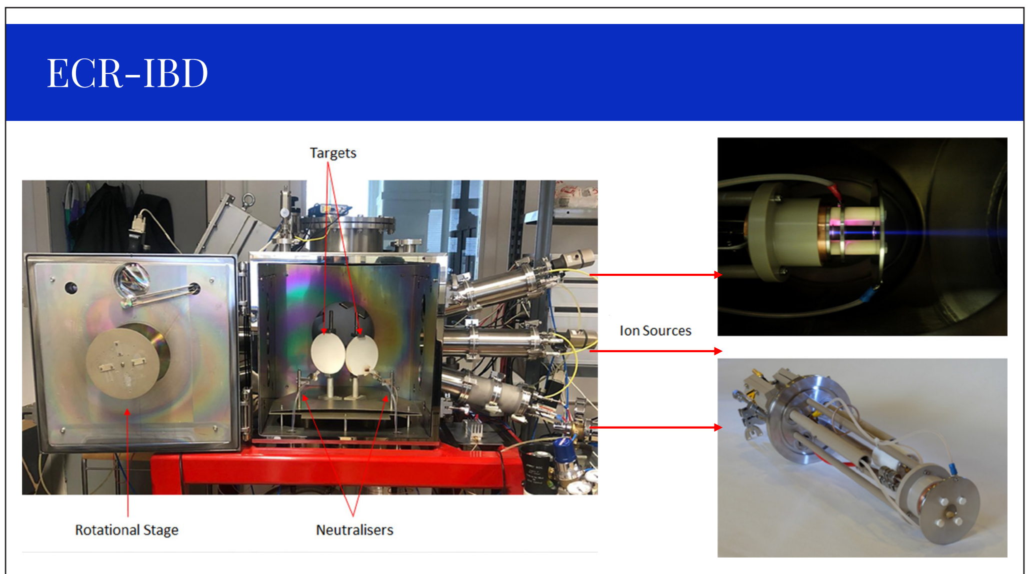

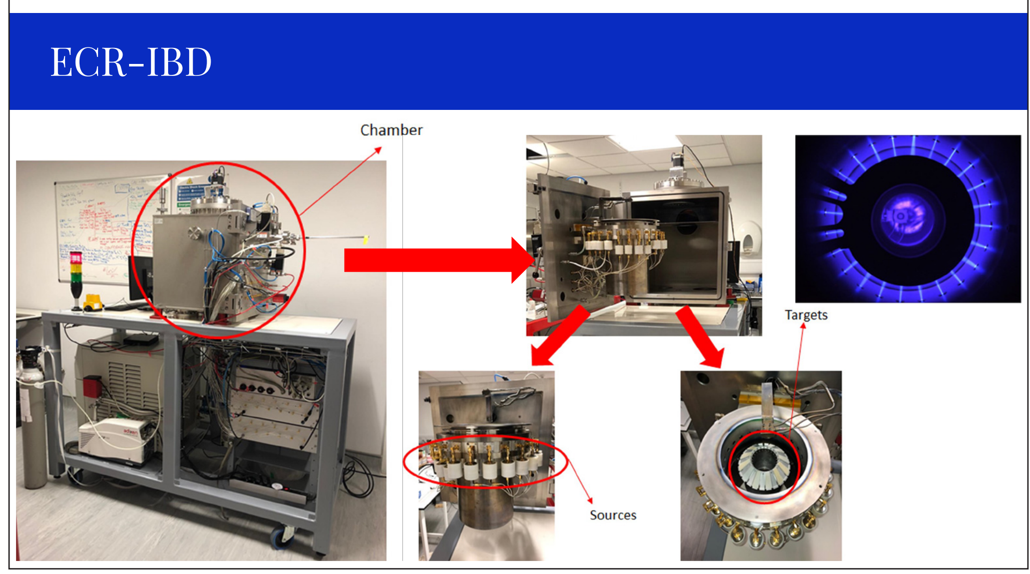

Characterisation

GeNS System commissioned at Strathclyde.

This system is use to measure the mechanical loss of coated discs (*experiment carried out by Gavin Wallace*)

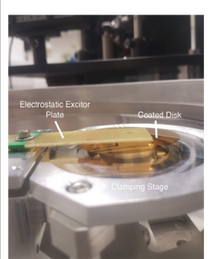

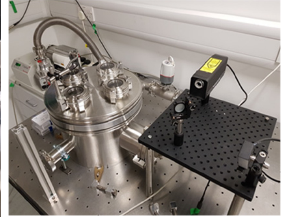

Photo creds: G. Wallace

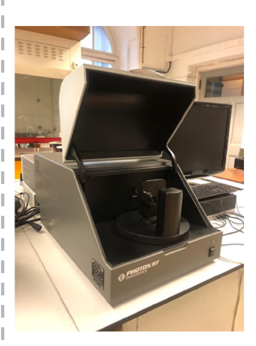

Photon RT (spectrophotometer) at Strathclyde.

The system is specially designed for optical coaters, with wide range of wavelength: 185-5000 nm

The Transmittance and Reflectance data obtained is then used in SCOUT to obtain optical parameters (n, k, and E_g)

4.
Objectives

Parameters for Tuning Coating's Properties

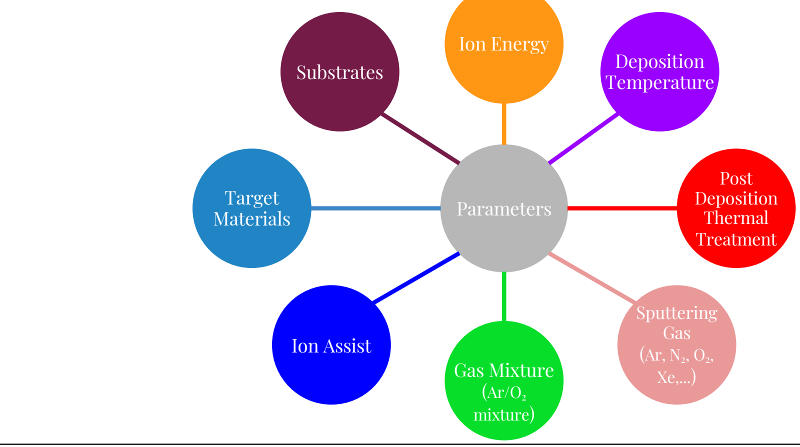

Materials that have been investigated

Gravitational Wave:
- GeO_2
- TeO_2
- TiO_2
- SiO_2
- a-Si
- SiN_x
- Ta_2O_3
- ZrO_2
- and mixed materials

LIDT:
- HfO_2
- Sc_2O_3
- SiO_2
- and mixed materials

Piezoelectric:
- ZnO
- AlN

Cardiovascular Implants:
- DLC

DEVELOPING OPTICAL COATINGS FOR GRAVITATIONAL WAVE DETECTORS AND LASER OPTICS USING NEXT GENERATION ION BEAM DEPOSITION TECHNIQUE

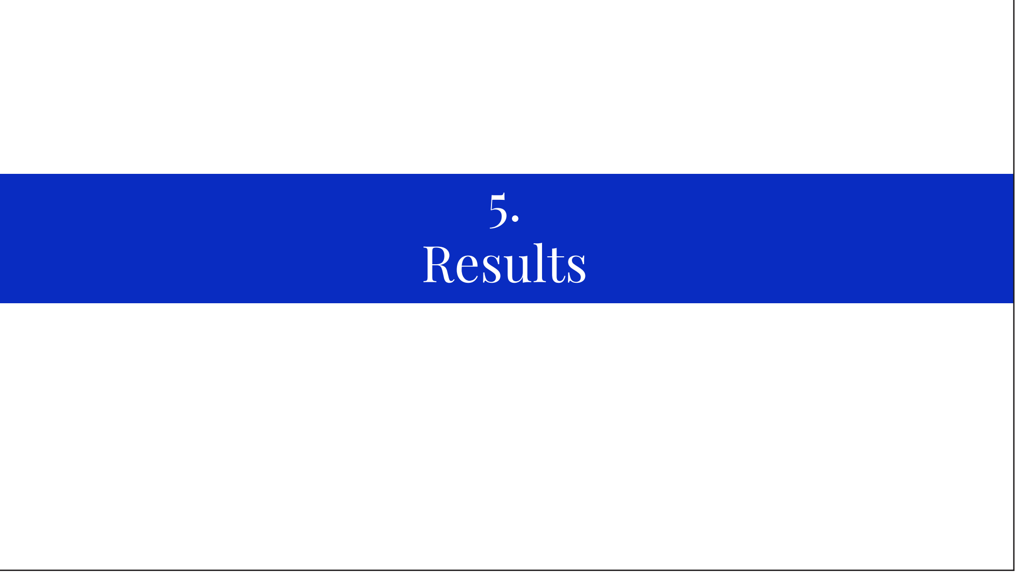

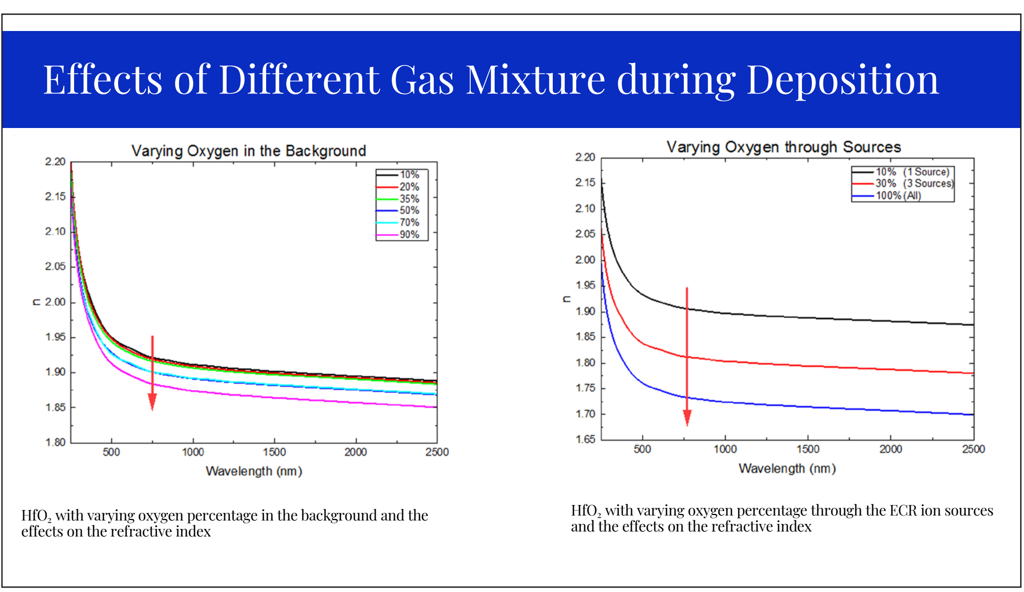

HfO_2 with varying oxygen percentage in the background and the effects on the refractive index

HfO_2 with varying oxygen percentage through the ECR ion sources and the effects on the refractive index

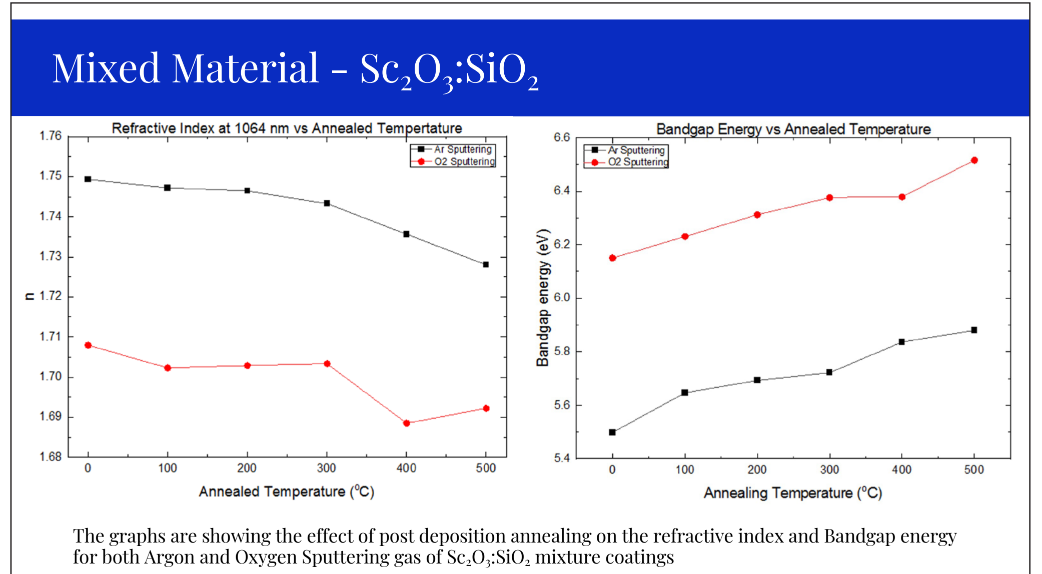

The graphs are showing the effect of post deposition annealing on the refractive index and Bandgap energy for both Argon and Oxygen Sputtering gas of Sc_2O_3:SiO_2 mixture coatings

a-Si

PHYSICAL REVIEW LETTERS **121,** 191101 (2018)

Amorphous Silicon with Extremely Low Absorption: Beating Thermal Noise in Gravitational Astronomy

R. Birney,[1,2,*] J. Steinlechner,[3,4,†] Z. Tornasi,[3] S. MacFoy,[1,2] D. Vine,[2] A. S. Bell,[3] D. Gibson,[2] J. Hough,[3] S. Rowan,[3] P. Sortais,[5] S. Sproules,[6] S. Tait,[3] I. W. Martin,[3] and S. Reid[1,2]

[1]*SUPA, Department of Biomedical Engineering, University of Strathclyde, Glasgow G1 1QE, United Kingdom*
[2]*SUPA, Institute for Thin Films, Sensors and Imaging, University of the West of Scotland, Paisley PA1 2BE, United Kingdom*
[3]*SUPA, Institute for Gravitational Research, University of Glasgow, Glasgow G12 8QQ, United Kingdom*
[4]*Institut für Laserphysik und Zentrum für Optische Quantentechnologien, Universität Hamburg, Luruper Chaussee 149, 22761 Hamburg, Germany*
[5]*Polygon Physics, 30 Chemin de Rochasson, 38240 Meylan, France*
[6]*WestCHEM, School of Chemistry, University of Glasgow, Glasgow G12 8QQ, United Kingdom*

(Received 9 July 2018; revised manuscript received 23 August 2018; published 6 November 2018)

Amorphous silicon has ideal properties for many applications in fundamental research and industry. However, the optical absorption is often unacceptably high, particularly for gravitational-wave detection. We report a novel ion-beam deposition method for fabricating amorphous silicon with unprecedentedly low unpaired electron-spin density and optical absorption, the spin limit on absorption being surpassed for the first time. At low unpaired electron density, the absorption is no longer correlated with electron spins, but with the electronic mobility gap. Compared to standard ion-beam deposition, the absorption at 1550 nm is lower by a factor of ≈100. This breakthrough shows that amorphous silicon could be exploited as an extreme performance optical coating in near-infrared applications, and it represents an important proof of concept for future gravitational-wave detectors.

DOI: 10.1103/PhysRevLett.121.191101

aSi
SiO₂

extinction coefficient k
commercial coating
our coating
heat treatment temperature [°C]

FIG. 2. Extinction coefficient k at 1550 nm as a function of heat treatment temperature for our coating and, for comparison, of a commercial coating (data from Ref. [15]).

Mixed Oxides - ZrO_2:Ta_2O_5

- By using mixed materials, this will gain the benefit of high n and low mechanical loss materials, without losing the required optical properties
  - This will reduce the coating thickness
    - Leading to the reduction of Brownian thermal noise

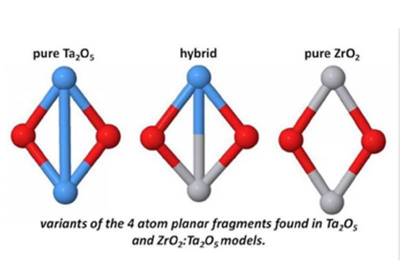

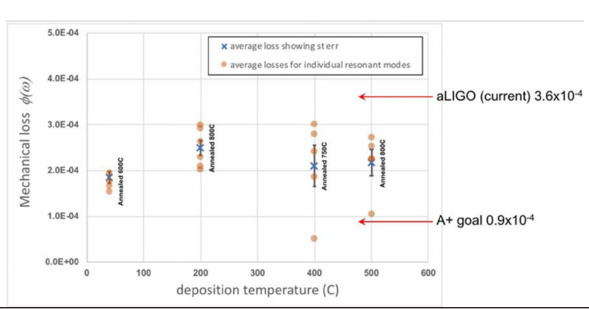

6. Conclusion & Outlook

DEVELOPING OPTICAL COATINGS FOR GRAVITATIONAL WAVE DETECTORS AND LASER OPTICS USING NEXT GENERATION ION BEAM DEPOSITION TECHNIQUE

Summary

- Successfully commission and develop two ECR-IBD systems
- RF & GeNS system has also been successfully commissioned by G. Wallace
- Different materials have been investigated
  - Laser Optics: HfO_2 ; Sc_2O_3 and mixing with SiO_2
  - Gravitational Waves: ZrO_2:Ta_2O_5 ; TeO_2 ; a-Si
- Investigated different parameters during and after deposition & investigate the effects it has on the coatings' optical parameters

Ongoing Research Activity

- For GW: Investigate materials with corner sharing properties & effects of post-deposition thermal treatment on optical properties & mechanical loss
  - GeO_2
  - GeO_2:TiO_2 alloys
  - TeO_2
- For Laser Optics: Investigate other mixed materials (including different mixing percentage) & the effects of post-deposition thermal treatment on the optical properties and LIDT

Contact Information:
Email: chalisa.gier@strath.ac.uk
LinkedIn: Chalisa Gier

About the Authors:
Chalisa Gier, Dr. Marwa Ben Yaala, Callum Wiseman, Gavin Wallace, Professor Stuart Reid

Chalisa Gier is a Ph.D. candidate, currently in her final year of studies, in the Biomedical Engineering department, at the University of Strathclyde. She first received her bachelor's degree in Physics from the University of the West of Scotland (2017) and her master's degree in Applied Physics at the University of Strathclyde the following year (2018). Her research is focused utilising the novel electron cyclotron resonance (ECR) ion beam deposition technology to fabricate thin film coatings, where this technique has previously been used to fabricate the lowest optical absorption amorphous silicon (2018). She has helped to developed and optimised two different ECR-systems during her Ph.D.: 6-ion beams and 24-ion beams ECR-systems. Currently, she is working on her thesis focusing on the fabrication and characterisation of thin films for both high laser damage threshold for optical coatings and low mechanical loss for gravitational wave mirrors, looking at both pure and mixed-oxide materials.

Dr. Marwa Ben Yaala is a research associate in the Biomedical Engineering Department, at the University of Strathclyde. She was awarded the doctoral degree "Summa Cum Laude" in experimental physics in 2019 from the University of Basel, working in the EuroFusion EC-funded project, following a research assistant position at Fraunhofer FEP, Dresden. Dr Ben Yaala pioneered various plasma-based etching/deposition technologies, and now leads the Electron cyclotron resonance (ECR) ion beam facility at the University of Strathclyde. She leads the development and commercialisation of ECR-IBD in relation to extreme performance optical coating fabrication, funded by STFC-IPS, in partnership with Gooch & Housego. Dr Marwa Ben Yaala developed the world's first 6-beam and 24-beam high-energy ECR systems, relevant for flexible, high-throughput use of ECR ion beam deposition technology.

Callum Wiseman is a Researcher in thin film design and development in the Biomedical Engineering department at the University of Strathclyde. He has experiences in wide range of material characterisation techniques. His main research focus: ZnO for piezoelectric applications and DLC coatings for biomedical applications, both deposited by ECR ion beam sputter deposition.

Gavin is a current Ph.D. candidate at the University of Strathclyde. He attained a physics honours degree in 2016 from University of the West of Scotland before working on non-dispersive infrared gas sensor technology at Gas Sensing Solutions Ltd. His current Ph.D. topic is the study of optical coatings with applications in gravitational wave research using RF ion beam deposition technology.

Professor Stuart Reid is the Head of the Department of Biomedical Engineering at the University of Strathclyde. He leads a multidisciplinary team working on both medical and astrophysics research:- Bone: He is co-inventor of "nanokicking", where nanoscale vibrations are used to persuade stem cells to turn into bone in the lab (ACS Nano 2013, Nature BME 2017). He is in the process of co-founding a company (www.nanokick.com) to help supply bone graft (the most transplanted tissue after blood) for regenerative medicine. UK Charity, Find A Better Way (https://www.findabetterway.org.uk) is funding the first-in-man study of nanokicked stem cells, planned for 2020, with the aim to provide bone graft for patients injured by land mines. IBD amorphous coatings: Reid's lab is also developing and manufacturing some of the most advanced laser mirrors in the world, to enable future gravitational wave detectors to be limited entirely by quantum effects. The team has pioneered the first ECR (electron cyclotron resonance) ion beam deposition facility, and the first elevated temperature ion beam deposition (up to 500C) for the fabrication of ultra-stable "ideal glasses". This technology has enabled the fabrication of the world's lowest optical absorption amorphous silicon (aSi), reaching <20ppm absorption at 1550nm for a quarter-wave layer. The group is also pioneering ultra-low mechanical dissipation mixed oxides, reaching levels of 1.3e-4 for Zr-doped Ta_2O_5 thin films. The group has now developed the world's first 6-beam and 24-beam high energy ECR systems. MBE crystalline mirror coatings: Working alongside local SME, Gas Sensing Solutions (GSS) Ltd, and Stanford, Glasgow, and West of Scotland Universities, we are developing AlGaP interference optics that can be integrated into silicon optoelectronic devices. Breath analysis (capnograph): Working with GSS Ltd and the University of the West of Scotland (UWS), we are developing optical coatings to tune (narrow) the spectral response of NDIR (non-dispersive infrared) CO_2 gas sensors for use in medical capnography.

Thin Solid Films 771 (2023) 139781

Contents lists available at ScienceDirect

Thin Solid Films

journal homepage: www.elsevier.com/locate/tsf

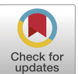

Controlling the optical properties of hafnium dioxide thin films deposited with electron cyclotron resonance ion beam deposition

Chalisa Gier [a], Marwa Ben Yaala [a,*], Callum Wiseman [a], Sean MacFoy [a], Martin Chicoine [c], François Schiettekatte [c], James Hough [b], Sheila Rowan [b], Iain Martin [b], Peter MacKay [d], Stuart Reid [a]

[a] *SUPA, Department of Biomedical Engineering, University of Strathclyde, Glasgow G1 1QE, United Kingdom*
[b] *SUPA, Institute for Gravitational Research, University of Glasgow, Glasgow G12 8QQ, United Kingdom*
[c] *Département de Physique, Université de Montréal, Montréal, QC H3T 1J4, Canada*
[d] *GOOCH & HOUSEGO PLC, Dowlish Ford, Ilminster TA19 0PF, United Kingdom*

A R T I C L E I N F O

Keywords:
Ion beam deposition
Electron cyclotron resonance
Hafnium oxide thin films
Refractive Index
Bandgap energy
Amorphous thin films

A B S T R A C T

The effects of reactive and sputtering oxygen partial pressure on the structure, stoichiometry and optical properties of hafnium oxide (HfO_2) thin films have been systematically investigated. The electron cyclotron resonance ion beam deposition (ECR-IBD) technique was used to fabricate the films on to JGS-3 fused silica substrates. The amorphous structure of HfO_2 films were determined by X-ray Diffraction. Energy-dispersive X-ray Spectroscopy and Rutherford Backscattering Spectrometry were carried out for the composition and stoichiometry analysis, where this suggests the formation of over-stoichiometric films. The data suggests that the O:Hf ratio ranges from 2.4 – 4.45 to 1 for the ECR-IBD fabricated HfO_2 films in this study. The transmission and reflectance spectra of the HfO_2 films were measured over a wide range of wavelengths ($\lambda = 185 – 3000$ nm) by utilizing a spectrophotometer. The measured spectra were analyzed by an optical fitting software, which utilizes the model modified by O'Leary, Johnson and Lim, to extract the optical properties, refractive index (n) and the bandgap energy (E_0). By varying the reactive and sputtering oxygen partial pressure, the optical properties were found to be $n = 1.70 – 1.91$, and $E_0 = 5.6 – 6.0$ eV. This study provides a flexible method for tuning the optical properties of HfO_2 coatings by controlling the mixture of reactive and sputtering gas.

1. Introduction

Hafnium oxide, also known as Hafnia (HfO_2), is one of the most attractive high refractive index materials, high-k dielectric, with excellent thermal and chemical stability [1] that are widely used in optical coating applications. They are also commonly used in multilayer optical coatings as the high index material, alongside low index material like silica, where it can be utilized in interference filters, anti-reflective coatings, metal-oxide-semiconductor transistors, and cameras that can be utilized for space applications [2–4]. Other applications that HfO_2 films has been utilized aside for optical coatings are memory applications [1,5,6], ferroelectrics transistors which can be used for in-memory computing devices, as well as neuromorphic devices [7–9] and as HfO_2 based nanoagent in clinical trials for radiosensitized tumor therapy [10]. HfO_2 has optical transparency over a wide spectral range, from ultraviolet (UV) to mid-infrared (mid-IR) region, due to its wide bandgap of 5.3 – 5.7 eV [11,12], alongside high laser induced damage threshold (LIDT), allowing it to often be utilized as the coating for optics in high power laser systems. These HfO_2 coated optics are utilize in filters or mirrors for laser spectroscopy, laser diodes, and multilayer high reflection mirrors for Gravitational-wave interferometers, for example [13–15]. Although, from previous studies by many authors over the years, it shows that HfO_2 has its favorable and advantages characteristics for different applications, but the optical and structural properties of the thin films can vary depending on the deposition methods, as well as the deposition parameters [1,2]. This leads to common deposition techniques, including electron beam evaporation [11,16,17], dual ion beam sputtering [18,19], reactive low voltage ion plating, radio frequency (RF) magnetron sputtering [20], high pressure reactive sputtering [21], pulsed laser deposition [1], and ion beam deposition (IBD)

* Corresponding author.
E-mail address: marwa.ben-yaala@strath.ac.uk (M. Ben Yaala).

https://doi.org/10.1016/j.tsf.2023.139781
Received 13 July 2022; Received in revised form 23 February 2023; Accepted 27 February 2023
Available online 5 March 2023
0040-6090/© 2023 The Author(s). Published by Elsevier B.V. This is an open access article under the CC BY license (http://creativecommons.org/licenses/by/4.0/).

[22,23], yielding inconsistent optical, electronic and structural properties. These inconsistencies reported in literature includes differences in films' stoichiometry due to the deposition method, crystalline phases, polycrystallinity, amorphous nature, density, and defect states [1,24,25]. With these inconsistencies reported in film properties, it has previously been demonstrated that IBD is a technique that is capable of the fabrication of high quality thin films, with properties close to those of bulk materials. The high quality includes low scattering, high density, high refractive index, low absorption, good mechanical structural properties, and good environmental stability. The investigation of the purity, stoichiometric defects, and optical properties are of great significance for the preparation of high-quality coatings.

Reported here is a strategy for the optimization of HfO_2 film properties by controlling the oxygen to argon ratio during the IBD process. The films were produced by utilizing electron cyclotron resonance (ECR)-IBD, which is a process that has previously yielded the lowest IR absorption in amorphous silicon thin films [26], but otherwise underexplored for optical coating development. The stoichiometry and elemental analysis of the films discussed were carried out by Energy-dispersive X-ray Spectroscopy (EDS) along with Rutherford backscattering spectrometry (RBS). The structural properties of the films were determined by X-ray Diffraction (XRD), and the optical properties, such as refractive index (n) and bandgap energy (E_0), were obtained by fitting the transmittance and reflectance spectra by using a commercial optical fitting software application. The aim of this work is to report the correlation between the reactive oxygen partial pressure and HfO_2 films' optical and structural properties and film composition by utilizing the ECR-IBD technique.

2. Materials and method

2.1. Thin film fabrication

The HfO_2 coatings presented in this study were fabricated in a custom-built IBD system [26], utilizing three compact ECR ion sources (all ECR sources from *Polygon Physics, France*), as shown in Fig. 1. These ion sources generate highly confined (mm-scale) parallel beams extracted through a single aperture and extracted with 10 kV potential. The three ion beams are directed onto a HfO_2 target, which is situated in the middle of the chamber. During the deposition process, everything inside the system was kept constant (i.e. target-to-substrate position, target angle, etc.). The ion sources parameters are controlled via a LabVIEW software (Version 16.0, NI): gas flow through the ion sources, the individual microwave power for plasma generation, beam voltage, and focus voltage. The microwave power input is between 3 – 5 W, the

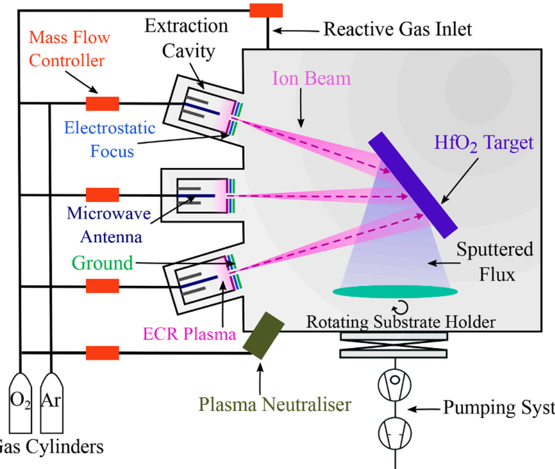

Fig. 1. Schematic diagram of the experimental setup for the HfO_2 study. The figure shows all the different components of the custom-built ECR-IBD system.

focus voltage is between 3 – 6 kV and the beam voltage is kept constant at 10 kV for all sources. The chosen parameters are used to provide the highest extraction current, minimal beam divergence, highest ion energies and to provide the most stable beam for each deposition.

The substrates used in this study are JGS-3 fused silica circular discs, 20-mm in diameter and 1-mm thick (*Changchun Qianhao Photoelectric Co., Ltd, China*). For improved thickness uniformity of the coatings, four samples are placed on a rotating substrate holder, on a ferrofluidic drive, driven by a stepper motor at 0.6 rpm for each deposition. Due to the nature of the ECR sources and their low deposition rate (~0.01 Å/s), the deposition time for each run is 72 h, where the thickness varies between 140 – 270 nm, dependent on the coating configurations. The growth rate was measured *in situ* by utilizing a quartz microbalance, and the thickness of the coatings were later determined by fitting the transmittance and reflectance measurements using SCOUT (Version 4.93, WTheiss Hardware and Software).

A hafnium oxide target with 99.99% purity was used for this investigation. A neutralizer was added to the setup to mitigate instabilities associated with plasma charging build-up, in addition to electrical discharging/arcing due to the accumulation of charge on the non-conductive target surface.

For the deposition process, the base pressure of the chamber was lower than 3×10^{-4} Pa and the deposition were carried out at room temperature. The total pressure was fixed to 2.5×10^{-2} Pa during deposition. The gasses were introduced in the chamber following three configurations:

(i) Varying the reactive oxygen background partial pressure from 10% to 90% of the fixed total pressure value, where argon is introduced through the sources and neutralizer, where this will be referred to as '*X*% Reactive Oxygen'
(ii) Varying the sputtering oxygen partial pressure through 1 or 3 sources with no background gas, where this will be referred to as: '10% Sputtering Oxygen' when 1 source is utilizing oxygen while the remaining 2 sources and the neutralizer are utilizing argon; and '30% Sputtering Oxygen' when all 3 sources are utilizing oxygen and the neutralizer is utilizing argon. For this configuration, the argon from the neutralizer is taken into account for the overall gas percentages and fixed total pressure value
(iii) Using pure oxygen gas for the full process through the sources and the neutralizer, where this will be referred to as 'Pure Oxygen Process'

2.2. Optical characterization

For the optical characterization of the deposited films, Photon RT spectrophotometer (*EssentOptics Ltd., Belarus*) was used to obtain the transmittance (T) and reflectance (R) of the coatings at the wavelength range of 185 – 5000 nm. Once both spectra were obtained for each substrate, the data is imported to the optical fitting software SCOUT to analyze the spectra [26,27].

There are many different methods which can be used to model the optical properties of amorphous semiconductors, based on the density of states (DOS) function, where Tauc-Lorentz model [28] and O'Leary, Johnson, and Lim (OJL) model [29] are typically used. Within this study, the OJL model has been utilized within SCOUT.

OJL model is used to describe the interband transition in the amorphous semiconductors [30,31]. This model assumes the parabolic shape valance and conduction band of the DOS, with tail states exponentially decaying into the bandgap [29–31]. The said tail states are the results of the disorder present in amorphous semiconductor, where this is also known as the Urbach tail [32]. The parameters of OJL DOS model are:

$$E_{m,c} = E_c + \frac{1}{2}\gamma_c \tag{2.2.1}$$

$$E_{m,v} = E_v - \frac{1}{2}\gamma_v \tag{2.2.2}$$

Where E_c and E_v are the conduction and valence band energy, γ_c and γ_v is the damping constant of the conduction and valence bands, and m_c and m_v are the conduction and valence band mass. Eqs. (2.2.1) and 2.2.2 represents the mobility edges of the conduction and valence bands, respectively. As for the bandgap energy (E_0), this is denoted by:

$$E_c + \frac{1}{2}\gamma_c - \left[E_v - \frac{1}{2}\gamma_v\right] = E_0 \tag{2.2.3}$$

Where E_0 can be acquired via SCOUT. The other OJL interband transitions within SCOUT are as follows [30,31,33,34]:

- OJL mass: this acts as the scaling factor in determining the shape of the DOS
- OJL gamma valence: this is the band tail width, or Urbach tail
- OJL decay: this is the number which ensures the imaginary part decays to zero for high frequency

As for the refractive index (n), this is calculated by utilizing the Kramers-Kronig Relation (KKR) implemented in SCOUT. The KKR connects the real and imaginary parts of the susceptibilities, and can be used to calculate the real and imaginary parts of the dielectric function. By utilizing both the KKR and OJL model implemented in SCOUT and fitting of T and R spectra, this allows for the extraction of n, E_0, and thickness, among other optical constants not discussed in this study.

The following steps were taken within SCOUT to carry out the optical fittings: (1) Introduce the OJL model, initial values of the complex refractive index (based on literature) and film thickness. (2) Insert the T and R spectra. (3) Run the "automatic fit", where the downhill simplex method is applied to vary the fit parameters in order to minimize the deviation between the experimental and simulated values, until an optimal fit is obtained. (4) The E_0, n and thickness values can now be obtained [30,31].

2.3. Elemental and structural characterization

The compositional elemental analysis and mapping of the samples were measured by Hitachi S3700-N Scanning Electron Microscope (SEM), equipped with an EDS system at room temperature, operated at an accelerating voltage of 10 kV. Further confirmation of the elemental analysis were carried out by RBS measurements, which were carried out using a 2 MeV ^{4}He beam. The beam was incident at an angle of 7° from the surface of normal to minimize channeling effects, and the detector was placed at a scattering angle of 170° Atomic concentrations were determined by fitting the experimental spectra with the SIMNRA program [35]. The structure of the films was determined by utilizing XRD method using Bruker D8 Advance with a Cu Kα X-ray source at λ = 1.541 Å. The XRD scans are measured in the standard Bragg-Brentano geometry, measured between the angles of $2\theta = 20 - 55°$

3. Results

Fig. 2 shows the XRD pattern of pure HfO_2 films with varying oxygen content: (i) in the background with argon as the sputtering gas, (ii) through the ion sources (1 and 3 sources), where argon is still present in the process through the neutralizer, and (iii) pure oxygen process, where there is no argon inside the chamber. As can be seen from the XRD data, all HfO_2 films show a broad weak band, which indicates that all of the films in this study are amorphous. XRD data for a blank substrate is also included to show the peak centered at ~21° in all samples is from the substrate. The XRD data shows minimal difference between the blank substrate and coated substrates, which further demonstrates that the HfO_2 thin films in this experiment are amorphous. Also included in the figure is a sample annealed to 500 °C from the pure oxygen process,

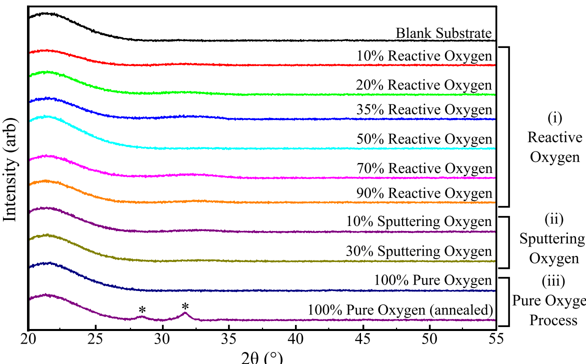

Fig. 2. XRD spectra of blank substrate and HfO_2 thin films deposited by ECR-IBD for the three different configurations of the introduction of oxygen in the system: (i) reactive gas, (ii) sputtering gas, and (iii) pure oxygen process with and without thermal annealing.

which shows the emergence of narrow peaks compared to the as-deposited films. These narrow peaks are an indicator to the increasing crystalline structure when the films are annealed, and are denoted by * in Fig. 2. This is further confirmation that the as-deposited samples investigated are in fact amorphous.

The atomic composition of the deposited hafnia films measured by EDS is shown in Fig. 3. The only elements detected by utilizing EDS in all coatings are O, Hf, and Ar. In Fig. 3a and b, the atomic percentage of oxygen and hafnium present in the films are provided. Fig. 3d shows the ratio between oxygen and hafnium present. By increasing the background oxygen partial pressure over 35%, an increase of the oxygen concentration in the films is observed. The highest value of oxygen concentration in the films was acquired by 30% sputtering oxygen, where the O:Hf ratio is 4.45:1 (*red circle*). Note that the composition for the pure oxygen process was not measured by EDS. From Fig. 3d, it can be seen that all coatings have an excess of oxygen, and are over-stoichiometric due to the measured O:Hf ratios being above 2:1, where the lowest is 2.4:1 at 20% background oxygen (*black square*). Fig. 3c shows the Ar atomic percentage measured by EDS. For all films within this study, the Ar concentration is lower than 2.5%. The decrease in Ar concentration is correlated with the oxygen increase, as shown in Fig. 3a. However, at 30% sputtering oxygen (*red circle*), there are no Ar incorporated within the films.

Due to the high O:Hf content shown in Fig. 3d, RBS measurements were also carried out to confirm the O:Hf content, and the stoichiometry of the films discussed within this paper. Fig. 4 shows the O:Hf content acquired by utilizing RBS method. As shown, the results are slightly different to that of EDS results (Fig. 3d). However, the RBS results are in agreement with EDS results, where the films discussed within this study are all over-oxygenated, and therefore, over-stoichiometric. As previously mentioned, for stoichiometric HfO_2 thin films, the O:Hf ratio must be 2:1, where in this case (based on RBS results, Fig. 4), the lowest O:Hf ratio in this study has the value of 2.65:1 at 10% background oxygen (*black square)*. Alongside, the highest O:Hf ratio in this study, based on RBS results, is 3.89:1 at pure oxygen process (*green triangle*).

The transmittance and reflectance measurements are shown in Fig. 5. The absorption peaks measured at 2700 nm (very predominant in the transmittance data) are the water absorption peaks, which are associated with the substrate material. As described in the materials and methods section, for varying oxygen content configuration (i) are shown as solid lines, where 10% and 90% reactive oxygen is shown in Fig. 5; configuration (ii) is shown as dashed lines; and configuration (iii) is shown as dotted lines. As shown in Fig. 5, the higher the oxygen content (for all three configurations), the transmittance also increases, and therefore, the reflectance decreases – where this can be seen most prominently in the range of 1500 – 3000 nm. In example, for configuration (i) 10% reactive oxygen (*red, solid line*) has a lower transmittance

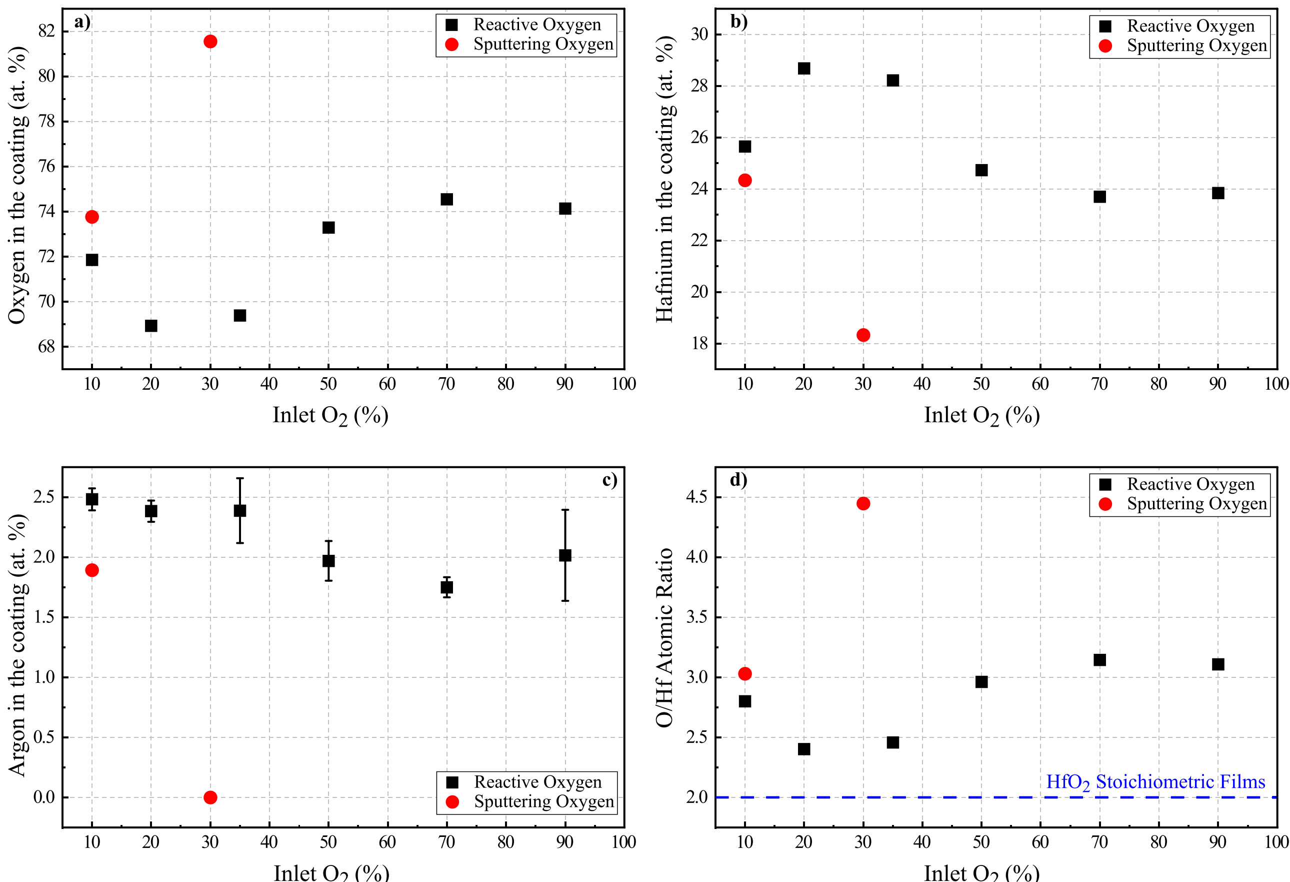

Fig. 3. EDS measurement of the atomic percentages of (a) oxygen, (b) hafnium, (c) argon in the coatings, and (d) atomic percentage ratio of oxygen over hafnium in the coatings.

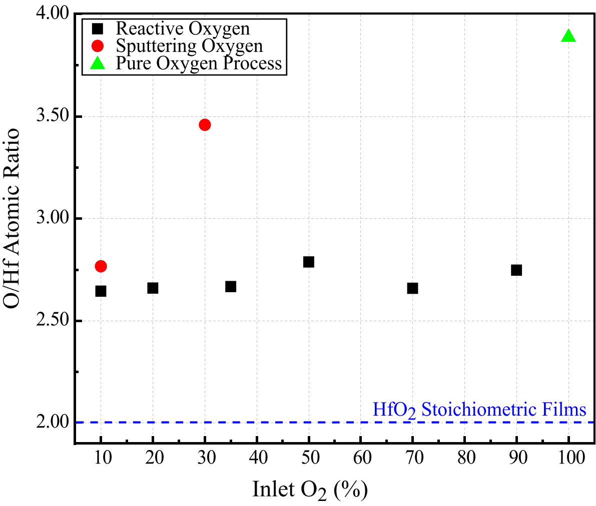

Fig. 4. Atomic percentage ratio of oxygen over hafnium in the coatings extracted by RBS measurements.

(and higher reflectance) than that of 90% reactive oxygen (*magenta, solid line*) in this wavelength range. This is also true for configuration (ii), where 10% sputtering oxygen (*blue, dashed line*) has a lower transmittance (and higher reflectance) than that of 30% sputtering oxygen (*green, dashed line*) within this wavelength range. Alongside, configuration (iii), where this is the pure oxygen process (*orange, dotted line*) has the highest transmittance, and lowest reflectance out of all three configurations.

It can also be observed that the transmittance data of samples shown exhibit interference effects. These interference fringes can be used as an indicator for the thickness of the films [31], where it can be observed that the films have different thickness due to the different configurations and oxygen percentages. As previously mentioned, all coatings have the same deposition time of 72 h, where the thicknesses varies between 140 – 270 nm, dependent on the coating configurations. From Fig. 5, the data shows that by varying the oxygen content, for all three configurations, this has an effect on the transmittance and reflectance data, along with other optical properties, which will be discussed further.

Fig. 6a shows the refractive index acquired from fitting via SCOUT for the wavelength range of 200–2500 nm, whereas Fig. 6b shows the refractive index extracted for a fixed wavelength of 1064 nm. This wavelength is chosen as Nd:YAG lasers operating at 1064 nm are widely used in many high power laser systems, including for military, medicine, and spectroscopy purposes. Fig. 6a shows that, as the oxygen concentration increases, the refractive index decreases for all three configurations (reactive oxygen, sputtering oxygen, and pure oxygen process), where the pure oxygen process possessing the lowest refractive index, and 10% reactive oxygen process possessing the highest refractive index. Fig. 6b also shows that at 10% reactive oxygen, the refractive index at 1064 nm is the highest ($n = 1.91$) and decreasing as the reactive oxygen percentage increases. The lowest refractive index at 1064 nm is for the pure oxygen process with the value of $n = 1.72$. The data shown in Fig. 6 are quoted from the average values from SCOUT fittings, where four coated substrates from each run are fitted five times each.

Fig. 7 shows the bandgap energy of HfO_2 films, extracted from the OJL gap energy model. For configuration (i) [*black square*], Fig. 7 shows that at 35% reactive oxygen partial pressure has the lowest bandgap energy of 5.6 eV, however, within the error range, from 10 – 50%

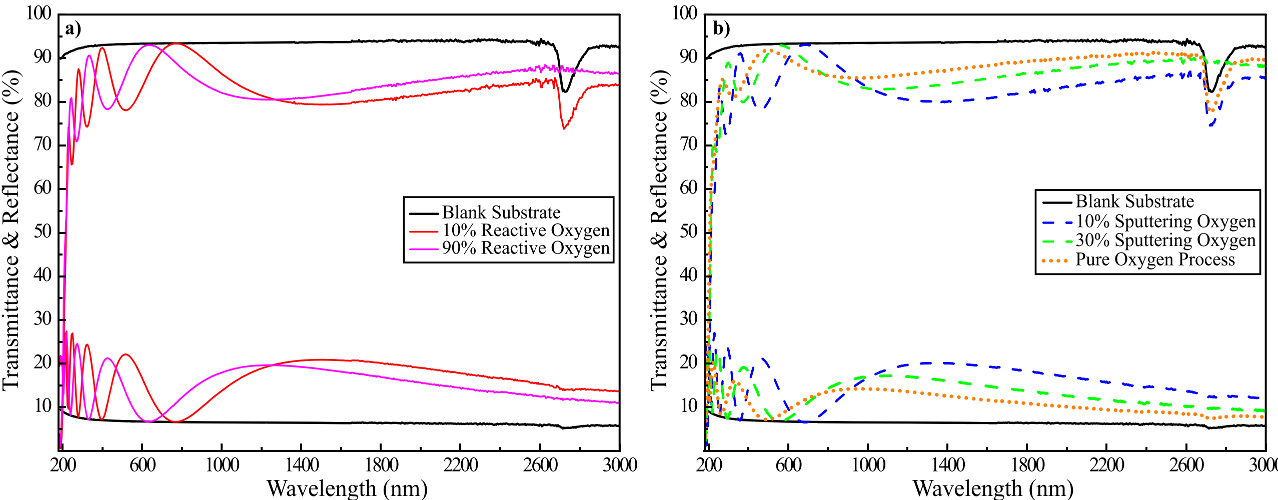

Fig. 5. Transmittance and reflectance data acquired from Photon RT spectrophotometer with wavelength range of λ = 185 – 3000 nm. Only a few selected samples used in this study are shown in the figure.

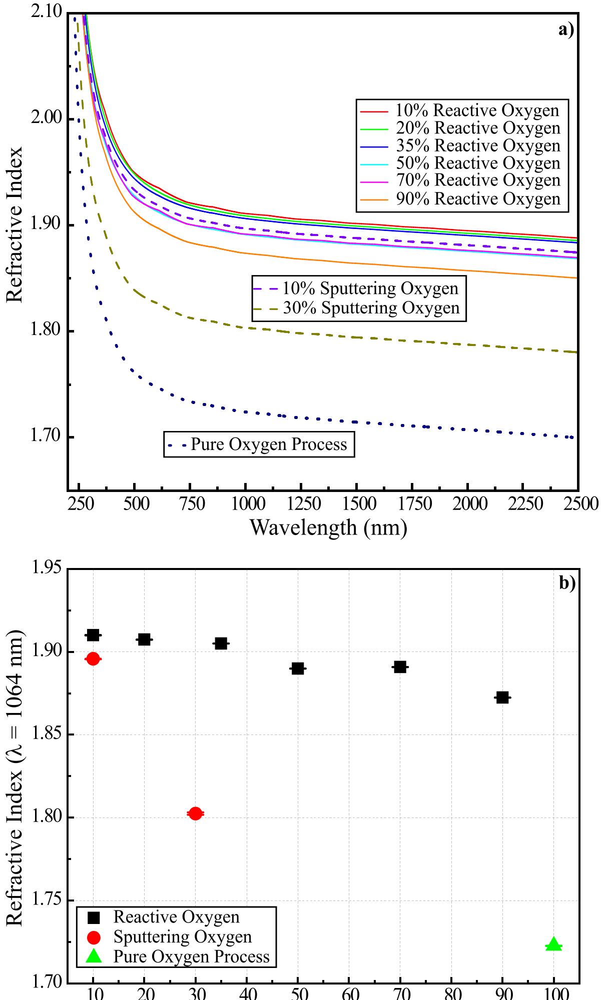

Fig. 6. Refractive index of the films acquired from SCOUT fittings: (a) dispersion of refractive index versus wavelength of HfO_2 films with different oxygen configurations, and (b) refractive index of each film at 1064 nm versus the oxygen percentage.

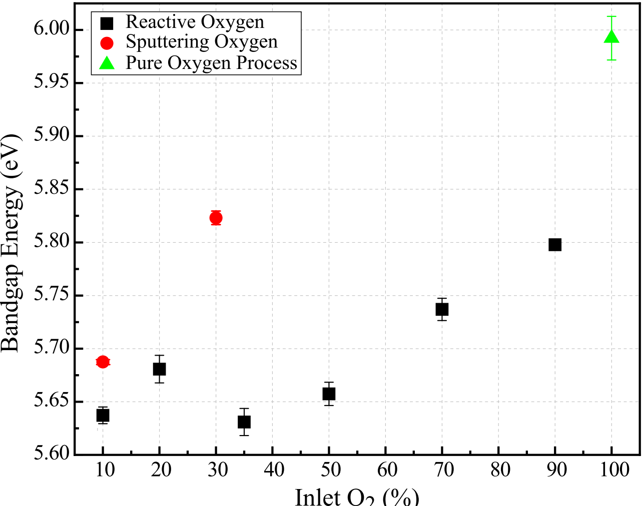

Fig. 7. OJL bandgap energy (E_0) versus oxygen percentage, where E_0 is acquired from the computed data from SCOUT.

reactive oxygen partial pressure, the bandgap energies are within the same values of 5.65 ± 0.05 eV. For configuration (ii) [*red circle*], the bandgap energy increases with the increasing percentage of oxygen used as sputtering gas, from 5.69 eV at 10% sputtering oxygen to 5.82 eV at 30% sputtering oxygen. As for configuration (iii) [*green triangle*], the pure oxygen process provides the highest bandgap energy at 6 eV. The overall trend that can be concluded from Fig. 7 is that as the oxygen concentration increases for each configuration, the bandgap energy also increases.

4. Discussion

The transmission spectra measured for all films presented in Fig. 5 show a high transmission from the UV to mid-IR (~300–3000 nm) which makes HfO_2 an interesting material for optical applications. At the wavelength of ~2700 nm, it can be seen that in the transmittance data, there are absorption peaks. This absorption is common in fused silica substrates, where this band corresponds to the OH absorption band (or "water band") [36]. It can also be seen that they are substrate-dependent, as not all of the transmittance data shown in Fig. 5 possess this absorption peak. As this absorption peak is only due to the

substrates, it is negligible when it comes to the discussion of the films optical constants in this study.

The XRD data in Fig. 2 shows that all coatings within this experiment exhibit a very broad wide band and minimal difference compared to blank substrates, which demonstrates that the HfO_2 films in this experiment are amorphous, similar to the amorphous glass substrate. The XRD data for annealed HfO_2 fabricated within the same pure oxygen process is shown to exhibit narrow peaks, where this shows that the film is becoming more crystalline in nature. This is in contrast to the broad peak of the films within this investigation, further verifying that the films are amorphous, even with the increase of oxygen content at room temperature.

The EDS compositional analysis presented in Fig. 3 shows that, within the measurement certainty of circa 0.1%, only Ar, O, and Hf species are observed. High purity films are expected from the ECR-IBD process, due to a highly confined, filament-free plasma generation in addition to the extraction of ions through a single aperture. The single aperture extraction allows high extraction potentials and eliminates the requirement for extraction grids that are a source of contamination in standard IBD processes. As shown in Fig. 3c, the films contain interstitial argon in the range 1.7 – 2.5%, which is typical in IBD processes, where inert gasses are used as the sputtering species, and trapped atoms can create "nanobubbles" [23]. However, the 30% sputtering oxygen process (configuration (ii), where argon is only utilized via the neutralizer) and pure oxygen process (configuration (iii), based on RBS results), does not have any Ar within the films, due to no use of argon during the deposition process. The amount of Ar that exists within the films in this study is slightly higher than the Ar solubility in solid materials (~1%) [23,37], however, this is still less than that of conventional RF-IBD systems (6 – 10%) [23]. This surplus of Ar quantity is associated with the implantation of the reflected neutral atoms with high kinetic energies, where the backscattered argon are incorporated into the coatings, along with the film-forming particles, as the angular distribution of each of these have some overlap as they leave the target surface [23,38,39]. These Ar atoms will accumulate to form bubbles within the HfO_2 matrix due to the inert nature of the gas. Whilst the fraction of argon in these samples are low, the quantity of implanted argon bubbles [23] decreases with increasing oxygen adsorption in the films. It is likely that the different oxygen regimes across the range of the samples reported in this paper play different roles in the deposition process and resultant thin film properties. The presence of nanobubbles, both due to the entrapment of Ar and O_2 molecules, may have an effect on the absorption of thin films, alongside the LIDT if used in laser systems, as the trapped nanobubbles can lead to optical breakdown due to laser exposure. Further investigation into the nanobubbles and the effect on absorption and LIDT results produced by films utilizing ECR-IBD will be of interest to study.

In addition, from both the EDS measurements and RBS measurements, the films presented in this paper are all over-stoichiometric in relation to the composition of the HfO_2 target (2:1 is the expected O:Hf ratio). Different mechanisms are thought to be the cause for the over-stoichiometry:

(I) Interstitial oxygen in the films, where the oxygen molecules are supplanted in the interstitial sites within the HfO_2 lattice, where the oxygen aggregates in the films [40];

(II) Higher coordination number compounds are bonded during the deposition due to the high energy process (e.g. HfO_x, where $x > 2$) [41].

Since Hf does not have a stable oxidation state to allow for bonding of three O atoms, the possibility of higher coordination compound like HfO_3 can be ruled out. In turn, this leads to the conclusion that the over-stoichiometry observed are due to the interstitial oxygen within the films.

The decreasing refractive index of the films at higher reactive oxygen partial pressure (Fig. 6), where the literature value reported is $n = 1.88$ at 1064 nm for HfO_2 thin films, and $n = 2.1$ (at 550 nm) for bulk HfO_2 [11,42–44] can be attributed to the interstitial oxygen that exists within the lattice. Alongside the decrease in refractive index observed due to interstitial oxygen, this also leads to the increasing bandgap behavior (Fig. 7), particularly increasing to greater than the reported bandgap values (5.3 – 5.7 eV) [11,12].

With the increase of oxygen content and O:Hf ratios, changes can be observed most prominently in the increased transmittance data (Fig. 5), especially in the mid-IR region of the samples deposited ($\lambda \approx 1300$ – 3000 nm). At 90% reactive oxygen (configuration (i)), where the O:Hf ratio is ~3:1, the transmittance has increased the most compared to other spectra in the same configuration (i), (Fig. 5a). At 30% sputtering oxygen (configuration (ii)), where the O:Hf ratio is ~4.45:1 (from EDS, and ~3.5:1 from RBS), provides an even higher transmittance than that of reactive oxygen configuration; and the pure oxygen process (configuration (iii)), where this has the highest transmittance out of all three configurations (Fig. 5b) with O:Hf ratio of ~4:1 (Fig. 4, *green triangle*).

Fig. 6 shows that as the oxygen content increases, for all configurations, the refractive index decreases. This reduction in refractive index related to the increase of reactive oxygen partial pressure in configuration (i) could also be associated to the reduced packing density, which also leads to the increase in the bandgap energy when comparing between the samples within the same configuration. As previously stated, in literature, the refractive index of HfO_2 thin films is $n = 1.88$ at 1064 nm for HfO_2 thin films, where the films were fabricated by electron beam evaporation [11,42]. For films in configuration (i), the overall refractive index at differing reactive oxygen percentages is higher than reported values, where this could be due to the higher overall packing density through the use of ECR-IBD when compared to films fabricated by other processes, such as electron beam evaporation or magnetron sputtering, when the films are still amorphous. Fig. 6 also shows that the refractive index is lower when utilizing oxygen as sputtering gas compared to argon, where this is most apparent in the pure oxygen process (configuration (iii)).

As for the optical bandgap energy, this is affected by many factors: defect density, purities, packing density, stoichiometry, etc. As previously stated, the bandgap energy of HfO_2 reported in the literature is 5.3 – 5.7 eV [11,12]. It can be seen that in this work, by increasing the oxygen content during the deposition, the bandgap energy can be manipulated to be higher than that of the reported values (Fig. 7). Other researchers [13] have reported the values of 5.59 – 5.68 eV with increasing reactive oxygen partial pressure, and another group [45] have reported the values of 5.58 – 5.83 eV, where in this work, the values are reported in the range of 5.6 – 5.8 eV by increasing the reactive oxygen partial pressure (configuration (i)). As for configuration (ii) and (iii), the bandgap energies are in the range of 5.69 – 6.0 eV. This shows that as the oxygen content increases, the bandgap energy increases, which is in agreement with other groups' findings [45]. In addition, there is also a slight blue-shift of the transmittance data (Fig. 5), at the UV range for the absorption edge, that can be seen with the increase of oxygen content. This absorption edge is associated with the bandgap energy, and the shift seen is known as Burstein-Moss shift, where this shift to lower wavelengths of the absorption edge is associated with the increase of bandgap energy.

As stated earlier, the decrease in refractive index and increase of bandgap energy as the oxygen content increases within this study can also be due to the decrease in the packing density of the films. Yoldas formula [45] can be utilized to calculate the packing density (p), where this is defined as:

$$p = \frac{n_p^2 - 1}{n_b^2 - 1} \tag{4.1}$$

Where n_p is the refractive index of the thin films at 600 nm, and n_b is the refractive index of bulk-HfO_2 in this case, where $n_b = 2.1$. By

utilizing this equation, it was found that the highest packing density within this study can be found for 10% reactive oxygen (configuration (i)) where $p = 0.81$, and the lowest packing density within this study is found when utilizing pure oxygen process (configuration (iii)) where $p = 0.6$. This is in agreement with the results extracted from SCOUT, where at highest packing density calculated (10% reactive oxygen, configuration (i)), the refractive index is highest (Fig. 6), with the lowest bandgap energy (Fig. 7). Alongside, at lowest packing density calculated in this study (pure oxygen process, configuration (iii)), the refractive index is lowest (Fig. 6), with the highest bandgap energy (Fig. 7).

The film growth rate for all films sputtered with argon is ~0.01 Å/s, which is around two orders of magnitude lower than that of conventional IBD. The slow deposition rate may be one of the reasons for the over-stoichiometry where the oxygen adatoms have a longer time for reacting and diffusing in the forming thin film. The high energy of the ECR process could also produce highly reactive oxygen that sputters the targets and are bonded to the hafnium atoms. The rate decreases further with the introduction of oxygen in the sources as sputtering gas (configuration (ii) and (iii)). This rate is directly related to the momentum transfer between the bombarding ions and the target atoms, which is directly correlated to the difference in atomic mass between the working gas and the target atoms. In particular, for Hf, the sputtering yield is ~3 times higher with Ar than with O_2 [46].

5. Conclusion

The effect of reactive oxygen partial pressure and sputtering oxygen through the ion sources plays an important role in the optical properties of HfO_2 thin films, fabricated by ECR-IBD technique. ECR gridless high-energy ion sources produced high-density pure hafnia films (with a lower backscattered Ar content at ~2.5% compared to the conventional IBD technique). The structural analysis carried out by XRD confirmed that all films within this study are amorphous. The compositional analysis demonstrated that the films in this study were all over-stoichiometric as the O:Hf ratio is higher than 2:1, even for reactive O_2 partial pressure as low as 10% from the total process pressure which was found to be 2.8:1. Further investigation into the over-stoichiometry were carried out by utilizing RBS, where the results are in agreement with EDS results, demonstrating over-stoichiometric films found in this study. By utilizing the OJL model implemented within SCOUT software, the refractive index were found to be in the range of $n = 1.70 – 1.91$, and the OJL bandgap energy were found to be in the range of $E_0 = 5.6 – 6.0$ eV for the different oxygen concentrations that were investigated. The results indicated that the refractive indices decreases with the increase of oxygen content within the chamber, whereas the bandgap energies increases. This shift of bandgap to higher energies can also be seen from the slight shift towards lower wavelengths (blue shift) in the transmittance measurement in the UV range as the oxygen content increases. From the optical characterizations, it was found that by controlling both the reactive and the sputtering oxygen concentration during deposition, the bandgap energy, and the refractive index, could be tuned to the desired value, depending on the application.

Future work will include chemical analysis to understand how the excess oxygen is incorporated in the films and how it affects the nature of the hafnia coatings deposited by the ECR-IBD method. Furthermore, as HfO_2 coatings are of interest for high-quality optical coatings for laser systems, LIDT studies will be carried out to compare the three different configurations discussed in this investigation. Along with this, the study of temperature treatment on these films will also be of interest to determine the optical, structural and the oxygen incorporation changes that may be observe, and in turn, the LIDT changes that may occur.

CRediT authorship contribution statement

Chalisa Gier: Conceptualization, Methodology, Software, Validation, Formal analysis, Investigation, Resources, Data curation, Writing – original draft, Writing – review & editing, Visualization. **Marwa Ben Yaala:** Conceptualization, Methodology, Validation, Investigation, Resources, Visualization, Writing – review & editing. **Callum Wiseman:** Validation, Formal analysis, Resources. **Sean MacFoy:** Software. **Martin Chicoine:** Validation, Formal analysis, Resources. **François Schiettekatte:** Validation, Formal analysis, Resources. **James Hough:** Funding acquisition. **Sheila Rowan:** Funding acquisition. **Iain Martin:** Funding acquisition. **Peter MacKay:** Funding acquisition. **Stuart Reid:** Supervision, Writing – review & editing.

Declaration of Competing Interest

The authors declare that they have no known competing financial interests or personal relationships that could have appeared to influence the work reported in this paper.

Data availability

Data will be made available on request.

Acknowledgments

The authors would like to acknowledge that the EDS and XRD work were carried out at the Advanced Materials Research Laboratory (AMRL), at the University of Strathclyde. This work was supported by the Science and Technology Facilities Council [grant numbers ST/S001832/1, ST/T003367/1], the University of Strathclyde, the University of Glasgow, and Gooch and House Ltd.

References

[1] L. Sun, J.G. Jones, J.T. Grant, N.R. Murphy, C.V. R.amana, K.G. Eyink, J.P. Vernon, P.R. Stevenson, Nanoscale-thick thin films of high-density HfO2 for bulk-like optical responses, ACS Appl. Nano Mater 4 (2021) 10836–10844, https://doi.org/10.1021/acsanm.1c02267.

[2] S. Fang, C. Ma, W. Liu, J. He, C. Wang, G. Chen, D. Liu, R. Zhang, Effect of oxygen flow on the optical properties of hafnium oxide thin films by dual-ion beam sputtering deposition, Appl. Phys. A Mater. Sci. Process. 128 (2022), https://doi.org/10.1007/s00339-022-06224-2.

[3] D. Wernham, A. Piegari, Optical Coatings in the Space Environment, Elsevier LTD., 2018, https://doi.org/10.1016/B978-0-08-102073-9.00022-9.

[4] A. Wiatrowski, A. Obstarczyk, M. Mazur, D. Kaczmarek, D. Wojcieszak, Characterization of HfO2 optical coatings deposited by MF magnetron sputtering, Coatings 9 (2019) 1–20, https://doi.org/10.3390/COATINGS9020106.

[5] C. Künneth, R. Materlik, M. Falkowski, A. Kersch, Impact of four-valent doping on the crystallographic phase formation for ferroelectric HfO2 from first-principles: implications for ferroelectric memory and energy-related applications, ACS Appl. Nano Mater. 1 (2018) 254–264, https://doi.org/10.1021/acsanm.7b00124.

[6] M.H. Park, Y.H. Lee, T. Mikolajick, U. Schroeder, C.S. Hwang, Review and perspective on ferroelectric HfO2-based thin films for memory applications, MRS Commun. 8 (2018) 795–808, https://doi.org/10.1557/mrc.2018.175.

[7] H. Joh, M. Jung, J. Hwang, Y. Goh, T. Jung, S. Jeon, Flexible ferroelectric hafnia-based synaptic transistor by focused-microwave annealing, Cite This ACS Appl. Mater. Interfaces. 14 (2022) 1326–1333, https://doi.org/10.1021/acsami.1c16873.

[8] I.-.J. Kim, J.-.S. Lee, Ferroelectric transistors for memory and neuromorphic device applications, Suparyanto Dan Rosad 5 (2020) (2015) 248–253, https://doi.org/10.1002/adma.202206864.

[9] Z. Li, T. Wang, Y. Liu, J. Yu, J. Meng, P. Liu, K. Xu, H. Zhu, Q. Sun, D.W. Zhang, L. Chen, Understanding the effect of oxygen content on ferroelectric properties of Al-doped HfO 2 thin films, (2022) 9–12. 10.1109/LED.2022.3226195.

[10] Y. Li, Y. Qi, H. Zhang, Z. Xia, T. Xie, W. Li, D. Zhong, H. Zhu, M. Zhou, Gram-scale synthesis of highly biocompatible and intravenous injectable hafnium oxide nanocrystal with enhanced radiotherapy efficacy for cancer theranostic, Biomaterials 226 (2020), 119538, https://doi.org/10.1016/J.BIOMATERIALS.2019.119538.

[11] M.F. Al-Kuhaili, S.M.A. Durrani, E.E. Khawaja, Characterization of hafnium oxide thin films prepared by electron beam evaporation, J. Phys. D. Appl. Phys. 37 (2004) 1254–1261, https://doi.org/10.1088/0022-3727/37/8/015.

[12] E. Bersch, S. Rangan, R.A. Bartynski, E. Garfunkel, E. Vescovo, Band offsets of ultrathin high-κ oxide films with Si, Phys. Rev. B. 78 (2008), 085114, https://doi.org/10.1103/PhysRevB.78.085114.

[13] S. Jena, R.B. Tokas, S. Tripathi, K.D. Rao, D.V. U.dupa, S. Thakur, N.K. Sahoo, Influence of oxygen partial pressure on microstructure, optical properties, residual

stress and laser induced damage threshold of amorphous HfO2 thin films, J. Alloy. Compd. 771 (2019) 373–381, https://doi.org/10.1016/j.jallcom.2018.08.327.
[14] D. Schiltz, D. Patel, C. Baumgarten, B.A. Reagan, J.J. Rocca, C.S. Menoni, Strategies to increase laser damage performance of Ta_2O_5/SiO_2 mirrors by modifications of the top layer design, Appl. Opt. 56 (2017) C136, https://doi.org/10.1364/ao.56.00c136.
[15] Z. Balogh-Michels, I. Stevanovic, A. Borzi, A. Bächli, D. Schachtler, T. Gischkat, A. Neels, A. Stuck, R. Botha, Crystallization behavior of ion beam sputtered HfO2 thin films and its effect on the laser-induced damage threshold, J. Eur. Opt. Soc. Publ. 17 (2021), https://doi.org/10.1186/s41476-021-00147-w.
[16] L. Gallais, M. Commandré, Laser-induced damage thresholds of bulk and coating optical materials at 1030nm, 500 fs, Appl. Opt. 53 (2014) A186, https://doi.org/10.1364/ao.53.00a186.
[17] A. Hervy, L. Gallais, D. Mouricaud, G. Chériaux, Electron-beam deposited materials for high-reflective coatings: femtosecond LIDT, Opt. InfoBase Conf. Pap. (2013) 4–6, https://doi.org/10.1364/oic.2013.fa.4.
[18] L. Gallais, B. Mangote, M. Zerrad, M. Commandré, A. Melninkaitis, J. Mirauskas, M. Jeskevic, V. Sirutkaitis, Laser induced damage of hafnia coatings as a function of pulse duration in the femto to picosecond regime, Opt. InfoBase Conf. Pap. (2010), https://doi.org/10.1364/oic.2010.fa7.
[19] A. Ciapponi, F.R. Wagner, S. Palmier, J.Y. Natoli, L. Gallais, Study of luminescent defects in hafnia thin films made with different deposition techniques, J. Lumin. 129 (2009) 1786–1789, https://doi.org/10.1016/j.jlumin.2009.02.026.
[20] L. Pereira, P. Barquinha, E. Fortunato, R. Martins, Influence of the oxygen/argon ratio on the properties of sputtered hafnium oxide, Mater. Sci. Eng. B Solid-State Mater. Adv. Technol. 118 (2005) 210–213, https://doi.org/10.1016/j.mseb.2004.12.030.
[21] F.L. Martínez, M. Toledano-Luque, J.J. Gandía, J. Cárabe, W. Bohne, J. Röhrich, E. Strub, I. Mártil, Optical properties and structure of HfO2 thin films grown by high pressure reactive sputtering, J. Phys. D. Appl. Phys. 40 (2007) 5256–5265, https://doi.org/10.1088/0022-3727/40/17/037.
[22] G. Abromavičius, S. Kičas, R. Buzelis, High temperature annealing effects on spectral, microstructural and laser damage resistance properties of sputtered HfO2 and HfO2-SiO2 mixture-based UV mirrors, Opt. Mater. 95 (2019), https://doi.org/10.1016/j.optmat.2019.109245 (Amst).
[23] C. Harthcock, S.R. Qiu, R.A. Negres, J.A. Hammons, T. Voisin, G. Guss, A. A. Martin, C.J. Stolz, M.G. Menor, G. Bhowmik, M. Huang, The impact of nano-bubbles on the laser performance of hafnia films deposited by oxygen assisted ion beam sputtering method, Appl. Phys. Lett. 115 (2019), https://doi.org/10.1063/1.5129454.
[24] T.J. Bright, J.I. Watjen, Z.M. Zhang, C. Muratore, A.A. Voevodin, Optical properties of HfO2 thin films deposited by magnetron sputtering: from the visible to the far-infrared, Thin Solid Films 520 (2012) 6793–6802, https://doi.org/10.1016/j.tsf.2012.07.037.
[25] J. Aarik, H. Mändar, M. Kirm, L. Pung, Optical characterization of HfO2 thin films grown by atomic layer deposition, Thin Solid Films 466 (2004) 41–47, https://doi.org/10.1016/j.tsf.2004.01.110.
[26] R. Birney, J. Steinlechner, Z. Tornasi, S. Macfoy, D. Vine, A.S. Bell, D. Gibson, J. Hough, S. Rowan, P. Sortais, S. Sproules, S. Tait, I.W. Martin, S. Reid, Amorphous silicon with extremely low absorption: beating thermal noise in gravitational astronomy, Phys. Rev. Lett. 121 (2018), 191101, https://doi.org/10.1103/PhysRevLett.121.191101.
[27] W. Theiss, (2022) SCOUT software. http://www.wtheiss.com/.
[28] G.E.U. Jellison, Spectroscopic ellipsometry data analysis: measured versus calculated quantities, Thin Solid Films 313314 (1998) 3339.
[29] S.K. O'Leary, S.R. Johnson, P.K. Lim, On the relationship between the distribution of electronic states and the optical absorption spectrum in amorphous semiconductors, Solid State Commun. 109 (1999) 589–594, https://doi.org/10.1016/S0038-1098(98)00605-X.
[30] A. Solieman, A.A. Abu-Sehly, Modelling of optical properties of amorphous selenium thin films, Phys. B Condens. Matter. 405 (2010) 1101–1107, https://doi.org/10.1016/j.physb.2009.11.014.
[31] A. Solieman, Extracting the optical parameters of thermally evaporated Se film by modelling of transmittance spectra: effect of heat treatment, J. Taibah Univ. Sci. 14 (2020) 470–478, https://doi.org/10.1080/16583655.2020.1746600.
[32] F. Urbach, The long-wavelength edge of photographic sensitivity and of the electronic absorption of solids [8], Phys. Rev. 92 (1953) 1324, https://doi.org/10.1103/PhysRev.92.1324.
[33] N. Musila, M. Munji, J. Simiyu, E. Masika, R. Nyenge, Optical properties and analysis of OJL model's electronic inter-band transition parameters of TiO2 films, Path Sci. 4 (2018) 3001–3012, https://doi.org/10.22178/pos.36-5.
[34] A. Solieman, A.A. Abu-Sehly, Determination of the optical constants of amorphous AsxS 100-x films using effective-medium approximation and OJL model, Mater. Chem. Phys. 129 (2011) 1000–1005, https://doi.org/10.1016/j.matchemphys.2011.05.047.
[35] M. Mayer, SIMNRA user's guide, Report IPP 9/113, Max-Planck-Institut für Plasmaphysik, Garching, Germany, (1997). http://home.mpcdf.mpg.de/~mam/Report-IPP-9-113.pdf.
[36] A.M. Efimov, V.G. Pogareva, A.V. S.hashkin, Water-related bands in the IR absorption spectra of silicate glasses, J. Non. Cryst. Solids 332 (2003) 93–114, https://doi.org/10.1016/j.jnoncrysol.2003.09.020.
[37] M.R. Carroll, E.M. Stolper, Argon solubility and diffusion in silica glass: implications for the solution behavior of molecular gases, Geochim. Cosmochim. Acta 55 (1991) 211–225, https://doi.org/10.1016/0016-7037(91)90412-X.
[38] R. Feder, C. Bundesmann, H. Neumann, B. Rauschenbach, Ion beam sputtering of Ag - Angular and energetic distributions of sputtered and scattered particles, Nucl. Instrum. Methods Phys. Res. Sect. B Beam Interact. with Mater. Atoms. 316 (2013) 198–204, https://doi.org/10.1016/j.nimb.2013.09.007.
[39] C. Bundesmann, H. Neumann, Tutorial: the systematics of ion beam sputtering for deposition of thin films with tailored properties, J. Appl. Phys. 124 (2018), https://doi.org/10.1063/1.5054046.
[40] A.S. Foster, F. Lopez Gejo, A.L. Shluger, R.M. Nieminen, Vacancy and interstitial defects in hafnia, Phys. Rev. B - Condens. Matter Mater. Phys. 65 (2002) 1741171–17411713, https://doi.org/10.1103/PhysRevB.65.174117.
[41] J. Zhang, A.R. Oganov, X. Li, K.H. Xue, Z. Wang, H. Dong, Pressure-induced novel compounds in the Hf-O system from first-principles calculations, Phys. Rev. B - Condens. Matter Mater. Phys. 92 (2015) 1–10, https://doi.org/10.1103/PhysRevB.92.184104.
[42] M.F. Al-Kuhaili, Optical properties of hafnium oxide thin films and their application in energy-efficient windows, Opt. Mater. 27 (2004) 383–387, https://doi.org/10.1016/j.optmat.2004.04.014 (Amst).
[43] M. Jerman, Z. Qiao, D. Mergel, HfO2 as a function of the films ' mass density, Appl. Opy. 44 (2005) 3006–3012.
[44] D.L. Wood, K. Nassau, T.Y. Kometani, D.L. Nash, Optical properties of cubic hafnia stabilized with yttria, Appl. Opt. 29 (1990) 604, https://doi.org/10.1364/ao.29.000604.
[45] J. Gao, G. He, B. Deng, D.Q. Xiao, M. Liu, P. Jin, C.Y. Zheng, Z.Q. Sun, Microstructure, wettability, optical and electrical properties of HfO2 thin films: effect of oxygen partial pressure, J. Alloy. Compd. 662 (2016) 339–347, https://doi.org/10.1016/j.jallcom.2015.12.080.
[46] N. Matsunami, Y. Yamamura, Y. Itikawa, N. Itoh, Y. Kazumata, S. Miyagawa, K. Morita, R. Shimizu, H. Tawara, Energy dependence of the ion-induced sputtering yields of monatomic solids, At. Data Nucl, Data Tables 31 (1984) 1–80, https://doi.org/10.1016/0092-640X(84)90016-0.